Petroleum and Coal

Article **Open Access**

ENHANCEMENT OF SEPARATION EMULSIFIABLE OIL FROM OIL/WATER EMULSION FROM WASTE WATER BY THE SURFACTANT AND BARITE

Noura El Mehbad

Najran University, Chemistry Department, Najran, Saudi Arabia

Received April 16, 2018; Accepted June 27, 2018

Abstract

The oil separation behavior of emulsifiable oil was studied using barium salt of heavy alkyl benzene sulphonate as the frother and calcium salt of heavy alkyl benzene sulphonate as de- emulsifier. In this research, the application of separation column technique was studied. A synthetic oil emulsion was prepared with different percentage of oil. The stability rate constant was determined under different conditions. The study showed that the critical concentration of the surfactant affects oil recovery depend on its critical micelle concentration CMC. The adsorption of the surfactant from the solution was investigated by measuring surface properties of the frother. The results were discussed in term of the adsorption isotherm and surface properties of the surfactant at the solution/oil/solid interfaces. The experimental data were analyzed as a first-order kinetic rate. The maximum oil removal obtained from the stable emulsion was 90% by weight. It can be enhanced by the addition 0.1% of barite.

Also, this paper deals with the influence of various thermodynamic parameters on the adsorption surfactant on the solid barite particles and will be discussed this synergism between the surfactant and the barite particles according to its adsorption isotherms at solid / oil interface and surface properties of the collector. It can be concluded that the column technique seems to be important separation methods and need to be modified using electro separation in the next research.

Keywords*: Oil emulsion; frother; wastewater; barite.*

1. Introduction

Microemulsion is formed when water is dispersed in a hydrocarbon-based continuous phase and is normally located towards the oil apex of an oil/surfactant. In this region, thermodynamically driven surfactant self-assembly generates aggregates known as reverse or inverted micelles, which minimize surface energy, are the most common form. Added amphoteric surfactants will become compartmentalized into the central cores of these reversed micelles. The oil-water emulsions are found in the petroleum industry, such as producing, and refining. The microemulsion is harmful to the environment. It is very important to develop different methods for destruction of oil emulsion for oil removal. Flotation technique which is used for recovering oil from clay and wastewater by Omar *et al.* [1]. The separation methods are developed, such as electroflotation and dissolved gas flotation [2-6]. The study of separation required preparation of the stable synthetic emulsion. Micelles in these systems can be described as "nanoreactors," providing a suitable environment for controlled nucleation and growth. Also, at the latter stages of growth, steric stabilization provided by the surfactant layer prevents the nanoparticles from aggregating. Some amphoteric surfactants such as N-octyl-N-benzyl-N-methyl glycine is used as oil separation. The physicochemical chemical characteristics were investigated. The adsorption behavior of these surfactants at oil/air interface was investigated by measuring the surface tension and interfacial tension as a function of concentration. Surface properties, in particular, the critical micelle concentration (CMC), the maximum surface excess (Γ_{CMC}) and the minimum surface area (A_{min}) were measured. It is found the surface, and thermodynamic properties of the prepared surfactants depend on its chemical structure.

Also, it is found that there is a good relationship between the surface properties of the surfactant and their efficiency in depressing oil recovery. The separation of waste oil from clay was studied using benzyl triethanol ammonium chloride as a phase transfer catalyst. The study showed that the surface tension affects oil recovery. The effects of various parameters including the concentration of catalyst, collector, and contact angle, and zeta potential for oil extraction were studied. The results depicted that, oil recovery increased with time of separation to a maximum and then levels off. The mechanism of oil separation was discussed according to micelle composition and the calculated oil recovery obtained was 87% [6].

This research aims to prepare stable oil emulsion at the optimum condition and studying the barium salt of heavy alkyl benzene sulphonate as anionic oil frother and its mixture with non ionic nonyl phenol ethoxylate at different mole fractions. Furthermore, at optimum conditions, addition different percentage of clay to best collector dose. Also, this paper suggests the relationship between the efficiency of adsorption at oil phase and solid phase. The used oil was pretreated with local clay by the Elmehbad [7].

2. Experimental

Triton x -100 is the nonylphenol ethoxylate with a mean of 10 ethoxy units per nonyl phenol was used and supplied from Aldrich. The barium and calcium salts of heavy alkyl benzene sulphonate as anionic oil collector and de-emulsifier were prepared and confirmed their structures.

The surface tensions for various concentrations of the frother was measured using a Kruss type 8451 Duy Noy tensiometer at different temperatures with an accuracy of 0.2 mN/L [8].

Table 1 lists the physical properties of the oil uses in forming an emulsion. The oil content of each sample was determined gravimetrically to an accuracy of ± 10mg /L [9]. Separation experiments were conducted using a column. The samples were conditioned with de-emulsifier for 10 minutes before separation. At optimum conditions, the recovered oil was collected, and its weight determined [9].

Emulsions were prepared from base oil and water, the emulsifier (Triton x 100) was used with a concentration of 50 μmol/L according to its CMC. The physicochemical properties of the base oil are listed in table 1. The oil content of the sample was determined gravimetrically to an accuracy of ± 10 mg/L [9].

Table1. Physical properties of emulsified oil

Properties	Base oil	Test ASTM
Density (g/mL) at 15.5°C	0.8951	D 1298
Refractive index nD_{20}	1.4954	D 1218
Kinematic viscosity cSt		
at 40°C	16.56	D 445
at 100°C	27.15	
Pour point, °C	14	D 97
Carbon residue content, wt%	1.5	D524
Ash content, wt%	0.0511	D482

In the separation process using the separation column. The emulsion poured in the column, different concentration of demulsifier was added and stirred at 1200 rpm with the pulp pH was adjusted only by adding, HCl. Then frother and barite added for 5- 20 min nitrogen was introduced.

3. Results and discussions

In the formation of emulsions, oil is broken up into particles that are dispersed into water. This emulsion is highly unstable according to the thermodynamic parameters. So addition Triton x-100 ethoxylate is to stabilize the emulsion for a definite time.

Figure 1, shows the change in oil concentration with time by adding this emulsifying agent. This compound adsorbs at the interface between oil/w interfaces. As the results, the interfacial tension between the two phases decreases. Furthermore, agent forming a barrier film around oil droplets As the results, the dispersed particles do not coalesce forming microemulsions. Flocculation or coagulation depends on interfacial tension and temperature. At low temperature, ethoxylate forming its micelle (CMC), then oil particles can be solubilized inside the micells and forming o/w emulsions. As the temperature is increased, the solubilization of oil increases until 50 C°. Furthermore, as the temperature increases, the structure of the micelle change to a sandwich like by increasing temperature and the phase inverse and the micelle change from hydrophilic to oleophilic micelles (Figure 2).

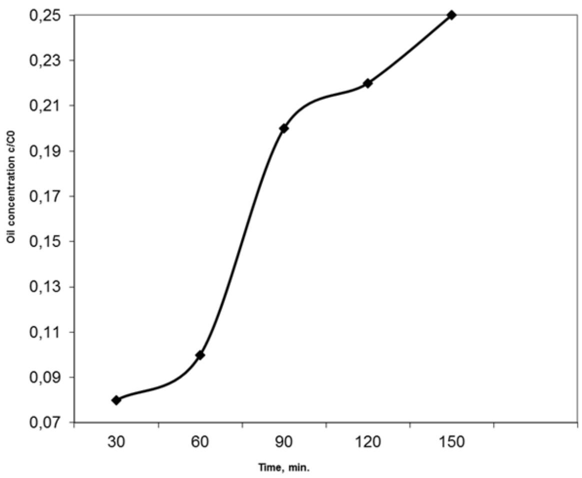

Figure 1. Effect different times on the oil concentration in oil/water emulsion, c/Co

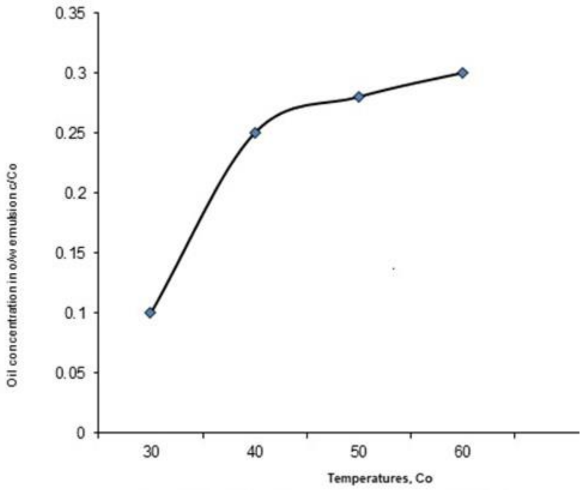

Figure 2. Effect different temperatures on oil content c/Co in o/w emulsion

At optimum conditions of formation emulsion o/w, the stable emulsion are conditioned with different concentration of demulsifier (calcium heavy alkylate sulphonate) for 10 min. and stirring rate 1200rpm. The results obtained are cleared in Figure 3.

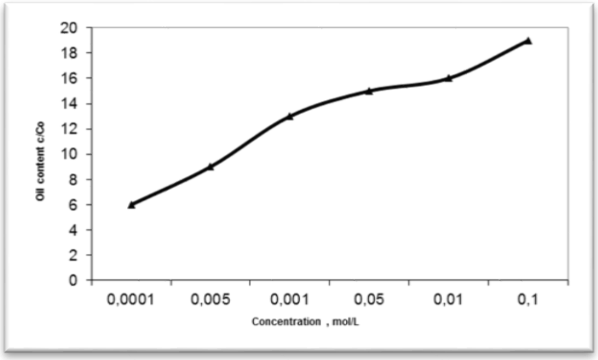

Figure 3. Effect of diferent concentration of the demulsifier calcium heavy alkylate sulphonate on oil separation

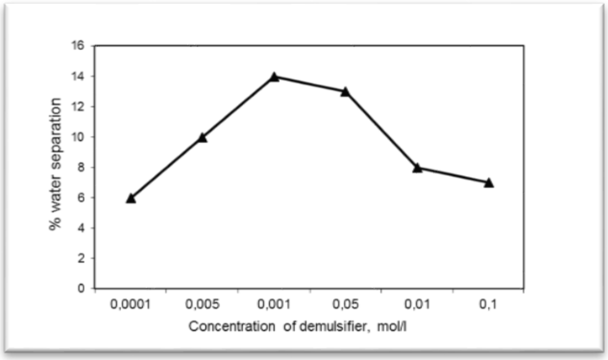

Figure 4. Effect different concentrations of the demulsifier in the presence of barite on oil content c/Co

The percentage of oil separation versus the concentration of demulsifier is depicted in the above figure. The oil separation was improved as the concentration of the demulsifer increased to 0.005 mol/L. These results can be discussed according to the role of the additive. The demulsifier is hydrophobic in nature, lead to the emulsion invert direction of its adsorption. As results, oil particles coagulate. The trapped water is surrounding by an interfacial film of demulsifier. As the results an increase in the interfacial tension between two phases, due to the rupture of a thin film formed between adjacent droplets. At the same time, the demulsifier counter acts as the emulsifier and promotes the formation of the aggregates oil and facilitate the rupture of the droplet interface film, lead to separation of oil from water.A sample of barite with size 150 mesh and its surface area 59.38 m^2g^{-1}.The addition of 10 g of barite enhances the role of demulsifier in oil separation as shown in Figure 4.

The synergies between the demulsifier and the fine particles of barite are depicted in Figure 5. The author suggests the barite particles capable of forming oleophilic colloidal suspensions, as the results, the oil particles aggregate, and water separate from emulsifier micelle in the core. The interaction of barite at the emulsion interface and wettability of the barite. At the same time, the demulsifier adsorbs at the barite with oil phase indicated by formation the fragment number of particulates at the oil-water interface. As the results, demulsifier is effective in changing the wet ability of barite.

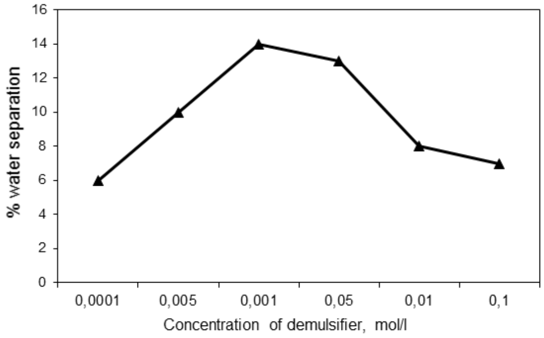

Figure 5. Relation between concentration of the de emulsifier and % water separation

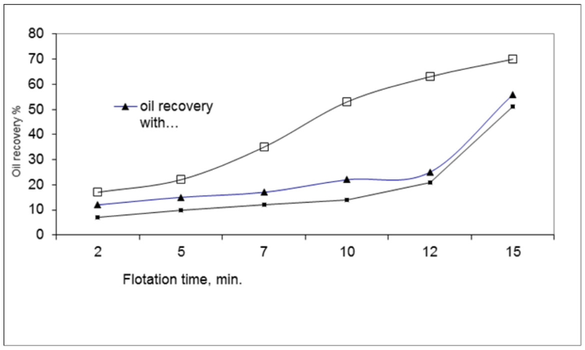

Figure 6. Effect of the separation time on the percentage of oil recovery at 0.01mole/l of collector, with and without the demulsifier and 1% of barite

At optimum conditions of demulsifying 1% of barite conditioned for 10 min. and stirring at 1200rpm. The effect of dose of barium heavy alkylate sulphonate as oil frother with a velocity of nitrogen 5l/s is shown in Figure 6. The percentage of oil recovery increase with increasing time of separation. We notice sharply increase in oil recovery after 2 minutes. The rate of oil recovery can be correlated to fit the first order kinetic rates the following:

$$dc/dt=-k$$

where the c is the oil concentration; t is separation time; k is removal rate constant.

$$Ln(c/c^o) = -kt$$

From the above equation, k value = 2.5 min^{-1}but by changing the dose of frother, the values of k increase as shown in Table 2 and Figure 7. The author calculates the degree of surface coverage of the additive on barite surface. It found that there is a good relationship between % of oil recovery and degree of surface coverage (Table 3).

Table 2. Effect of the separation time on rate constant

Dose of collector	k
0.0001	2 m^{-1}
0.001	2.2 m^{-1}
0.01	2.5 m^{-1}
0.1	3.1 m^{-1}

From the above equation, k value = 2.5 min^{-1}but by changing the dose of the frother, the values of k increase as shown in Table 2 and Figure 7.

The changes to the frother performance with an addition 1% of barite powder enhance separation and oil recovery as shown in figure 7. It found that, a significant increase in oil recovery and removal rate constants. The percentage of oil recovery changed from 45 to 73% for barite concentration 1%by weight and k changed from 3.1min $^{-1}$ to 5.1 min^{-1} (Table 3). These results can be discussed according to the adsorption isotherm of barium sulphonate on barite surface. The author suggests a method for measuring of the degree of surface coverage of the collector on barite surface according to Frumkin adsorption isotherm, the results are listed in Table 3. Which the oil recovery increases with increasing contact angle and degree of surface coverage. The author thinks the degree of surface coverage computable with a contact angle of oil barite surface.

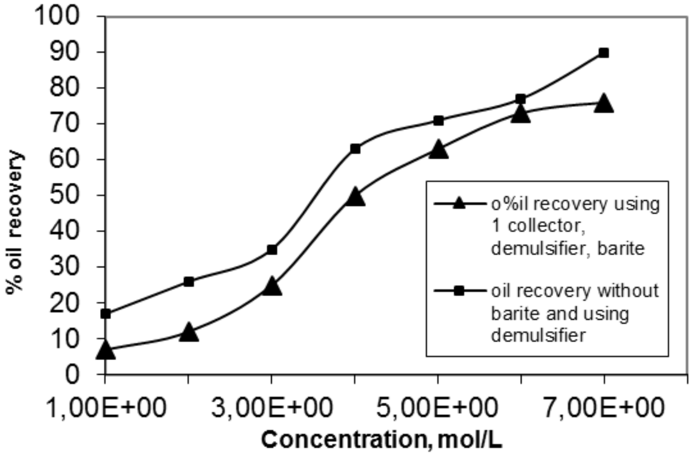

Figure 7. Effect of the frother concentration on % oil recovery in the presence demulsifier and with or without barite

Table 3. Effect degree of surface coverage of the additive at barite surface on % oil recovery

Dose of the frother	Degree of surface barite converge by the additiveø
0.0001	0.0042
0.001	0.00707
0.01	0.01
0.05	0.012

4. Conclusion

Further work will study removal oil without using additive by design electro separation column of the frother barium heavy alkylate sulphonate necessary to enhance of oil recovery by separation techniques. There is a good enhancement between addition fine powders of barite in the presence of the frother, where the yield of oil recovery increase. These results depend on the degree of surface coverage of collector on barite surface, which affect on the contact angle of oil.

References

[1] Omar AMA and Azzam EMS. Adsorption of some anionic surfactant on barite and at solution/air interfaces. J. of Surfactants and Detergents, 2004; 7(2): 141-145.

[2] Omar AMA and Nagui AAK. Surface and Thermodynamic Parameters of Some Cationic Surfactants. J. Chem. Eng. Data, 1998; 43: 117.

[3] Omar AMA, Mohamed MS and Ibrahim H. Recovery of Residual Emulsifiable Oil from Waste Water by Flotation. Lubric. Sci, 2001; 14(2):275-284.

[4] Omar AMA, El Adly RA, Keera RA and Mohamed MS. Recovery of Residual Lubricating Oil from Waste Clay by Flotation. Monatshefte für Chemie/Chemical Monthly, 1998; 129: 387-392.

[5] Omar AMA. Anionic/Nonionic Collector Efficiency as Related to the CMC of the Mixture. Afinidad, 1996; 53(464):262-266.

[6] El Morsi AK, Omar AMA. Development of a Method for the Extraction of Oil from Clay by Friendly Phase Transfer Catalyst. Petroleum Science and Technology, 2010; 28(16):1674-1680.

[7] El Mehbad N. Treatment and Refining of Used Lubricating Oil by Clay with Polymeric Surfactants.Research Journal of Applied Sciences, Engineering and Technology,14(1): 7-9.

[8] Gad EAM, Omar EAM and Zaki M. Surface and Thermodynamic Parameters Of Mixed N-Alkyl N- Trimethyl Ammonium-Chloride with Isooctyl Nonyl Phenol Ethoxylate. J. Surfactants and detergents, 1999; 2(1):39-43.
[9] Oldham GF. Seminar on aspects of prevention of oik pollution in the Mediterranean action plan. UNEP, Athens 11-13 February, pp 2-15., 1985.

To whom correspondence should be addressed: Dr. Noura El Mehbad, Najran University, Chemistry Department, Najran, Saudi Arabia

Petroleum and Coal

Article **Open Access**

DEVELOPMENT OF A SMART DIGESTER FOR THE PRODUCTION OF BIOGAS

Ilesanmi A. Daniyan[1], Akporode K. Ahwin[1], Adeyemi A. Aderoba[1] and Lanre Daniyan[2]*

[1] *Department of Mechanical & Mechatronics Engineering, Afe Babalola University, Ado-Ekiti, Nigeria*
[2] *Department of Instrumentation, Centre for Basic Space Science, University of Nigeria, Nsukka, Nigeria*

Received April 30, 2018; Accepted June 27, 2018

Abstract

Due to the rising need for alternative sources of energy, as a result of the challenges of fossil fuel, studies must forge on to explore other viable sources of clean and renewable energy like biogas. Biogas is a combustible mixture of bio-methane, carbon (IV) oxide, and other trace gases. It is produced as a result of anaerobic digestion of organic matter. This work develops a small-scale biogas plant with a smart system that was used to enhance the study of biogas production at the Department of Mechanical and Mechatronics Engineering, Afe Babalola University Ado-Ekiti (ABUAD). The plant was designed using Autodesk Inventor and fabricated with Stainless steel due to its high resistance to biological corrosion. An Arduino Uno Microcontroller was also connected to a pressure, pH and temperature sensors to monitor the process parameters of the developed biogas plant. Results obtained to validate the direct relationship between organic loading rate and biogas production. It also showed the interaction between temperature and pressure, temperature and pH, pH and pressure. Optimization of the process parameters was carried out using the central composite design model and response surface methodology. Taking the biogas yield as the response of the designed experiment, the data obtained were statistically analysed to obtain a suitable model for optimization of biogas yield as a function of the process parameters. For a sample 24-hour period the optimum values of the process parameters for the optimum yield of biogas (23 litres) were found to be: Loading rate (0.75 kgVDM/m^3), temperature (25.34^{o}C), pH (7.04) and pressure (4.84 kPa). The work has been able to lay a foundation for studies on biogas production using sensors and continuous parameter monitoring. It has also laid a foundation for research work by developing a small scale biogas plant for experimental purposes.

Keywords*: anaerobic digestion; biogas; organic matter; smart system; renewable energy.*

1. Introduction

Biogas is a combustible mix of gases produced by the natural fermentation of wet biomass in an anaerobic process [1]. Biogas production technologies are highly beneficial to society as they transform waste into useful energy while reducing environmental pollution. Furthermore, the digestate (decomposed substrate) provides a source of potent fertilizer for improving plant yield. Biogas is a sustainable source of energy and can be explored to end the dependence on energy from fossil fuels.

The average human being produces about 1.2 kg of waste each day [2]. In all parts of the world, increasing production and improper management of organic waste is a major environmental problem [3]. Even more troubling, according to the World Energy Council [4], more than 80% of the world's energy need is currently being met from non-renewable energy sources. It is thus imperative for the engineering profession to develop waste-to-energy systems to help meet the energy demands of society. In domestic application, heat energy is required each day for warmth and cooking. This energy can be provided in a sustainable manner with the implementation of a waste-to-energy conversion system using anaerobic digestion of organic waste to yield biogas for cooking, space heating and even powering of combined heat and power (CHP) engines, and organic fertilizer for improving plant yield.

This work develops a small-scale biogas plant that converts food waste and animal excreta to biogas via anaerobic digestion. According to Ramatsa *et al.* [5], anaerobic digestion is a four-stage process brought about by the combined action of several species of bacteria. The first stage called hydrolysis where long chain substances like carbohydrates, proteins, and fats are broken down into smaller fragments such as simple sugars, glycerol, fatty acids and amino acids [6]. In the second stage called acidogenesis and acidification, fermentative microorganisms convert these smaller fragments into short chain fatty acids such as acetic acid, propionic acid, and butyric acid [7]. In the third stage of acetic acid formation (acetogenesis), the products of the previous stage are the starting substrates. With these products, lactic acid, alcohols, and glycerol, these substances are converted by acetogenic microorganism into acetic acid, hydrogen and CO_2. In the fourth and final stage, methane bacteria act on the acetic acid, hydrogen, and CO_2 to produce methane [7-8]. This biogas typically contains 50 -70% of methane [9]. With the above process, it becomes evident that biogas production is a fairly complex process. According to Weise and Konig [9], without instrumentation and proper monitoring, biogas plants are often under-loaded i.e., the biomass feed rate (organic loading rate) are below required levels to make the process cost-effective. Thus, the biogas plant will also be incorporated with a monitoring system consisting of sensors and a microcontroller to continuously monitor the process parameters- pH, temperature and pressure and indicate plant malfunction.

The aim of this work is to develop and optimize a small-scale biogas plant with a smart system for use in small scale applications.

Since conventional biogas plants are not monitored, they are plagued with various challenges including the aforementioned under-loading of organic material (low organic loading rate) and overloading (excessive organic loading rate). Overloading slows down or stops the anaerobic digestion process and may cause a total system breakdown. Another considerable challenge that arises from lack of monitoring is diges-ter instability which arises as a result of unsuitable pH for biogas production. According to Weise and Konig [8], for the first and second stage of biogas production, the best pH is between 4.5 – 6.3. For the third and fourth stages where methane formation is evident, the optimal pH range is specified as 7.0 -7.7.

The anaerobic digestion process, however, self-regulates to achieve such a pH level, but it is common to have biogas plants fed with substrates that will make achieving this range difficult. This greatly increases the time needed for biogas production to commence. Furthermore, another challenge that arises from inadequate or non-existent biogas plant monitoring is poor production due to excessive temperature fluctuations or improper temperature range for various types of methanogenic bacteria. Methanogenic bacteria can either be psychrophilic (operating effectively between 12 to 24°C), mesophilic (operating optimally between 22-40°C) or thermophilic (thriving optimally between 50 – 60°C). All these points to a gap in cost-effective and easily accessible monitoring systems for biogas plants especially in the conventional pilot and small-scale biogas plants. With the recent national economic turbulence and a worldwide slump in oil prices, it has become evident that countries must look inward to renewable sources of wealth and energy that will be economical, socially and environmentally sustainable. According to Davidson [10], 'sustainable energy' is energy for 'sustainable development'. Hence, the development of this system that will minimize improper waste disposal in communities, while creating wealth from waste, reducing landfills and providing a potent organic fertilizer becomes not only attractive but needful. Since waste is generated on a daily basis in academic and industrial areas, the system becomes desirably sustainable to study the anaerobic digestion process continuously. The fertilizer output can then be used on farms to grow crops that will help meet the local nutritional needs of society. Incorporation of the monitoring system also becomes desirable in ensuring that the process is both safe and stable. The sensors can detect anomalies in operation, and warning alarms can be raised to prevent plant instability, accidents, and emergencies before they occur.

This research is limited to development of a small-scale biogas plant for studying biogas production using a variety of organic waste. The small-scale biogas plant is incorporated with a smart monitoring system that is limited to data acquisition and display.

Anaerobic digestion requires a vessel with an enclosed (i.e., air-tight) environment in which diverse microbial consortium which degrade organic material to generate biogas. When organic material including animal manure, agricultural residues, sewage sludge and food waste among others, undergo anaerobic digestion by the action of anaerobic bacteria, biogas is produced. According to Al Seadi *et al.* [3] and Friehe *et al.* [9], this gas mixture called biogas consists primarily of methane (50-75 % vol.) and carbon dioxide (25- 50 % vol.). Biogas also contains small quantities of hydrogen, hydrogen sulphide, ammonia and other trace gases. The composition of the gas is essentially determined by the substrate supplied, the fermentation (digestion) process and the technical design of the plant. According to Friehe *et al.* [9], monitoring biological processes is challenging. Despite this fact, however, a variety of options exist for monitoring of plants ranging from operating logs to fully automated data acquisition and control systems. In the small-scale application, however, complex systems are to be avoided due to cost implication.

According to Weise and Konig [8], to achieve optimal control of the biogas plant, detailed knowledge of key chemical and physical properties including temperature, pH, organic acid and fatty acid concentration, ammonium concentration and acid capacity. The sensors required for monitoring key process parameters including pH, pressure, and temperature will be studied subsequently. The process by which biogas is formed can be divided into four major steps as shown in Figure 1. These individual stages of decomposition (degradation) must be coordinated and harmonized with each other in the best way possible to ensure that the process completes smoothly without impediment or instability [9].

During the first stage, complex compounds of the starting material including carbohydrates, proteins, fats, and oils are broken down into simple organic compounds such as amino acids, sugars and fatty acids/glycerol. The hydrolytic bacteria involved in this stage releases enzymes that decompose the material by biochemical means.

During this acidification phase, the immediate products from hydrolysis are then further broken down by acid-forming (fermentative) bacteria to form lower fatty acids (acetic, propionic and butyric acid) alongside carbon dioxide and hydrogen. Also, small quantities of lactic acid and alcohols are also formed. The nature of products formed during this stage is influenced by the concentration of the intermediate hydrogen content.

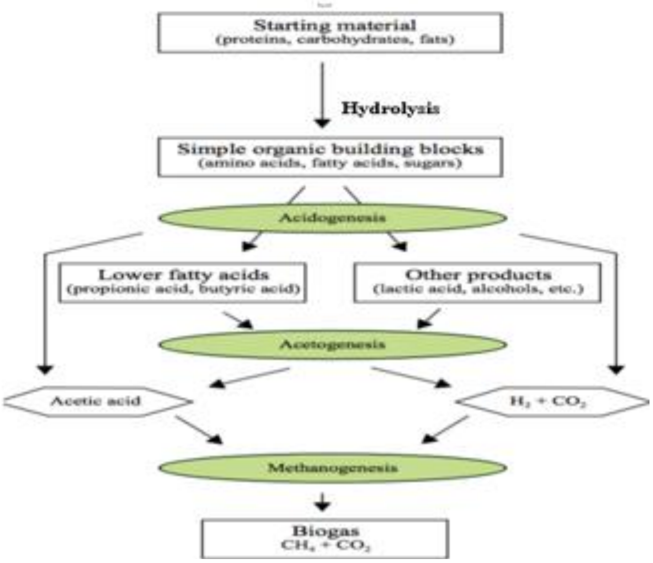

Figure 1. Schematic representation of anaerobic digestion *(Source: Friehe et al.* [9]*)*

In this stage, acetic acid forms. The products of the acidification phase (acidogenesis) are then converted by acetogenic bacteria into precursors of biogas (acetic acid, hydrogen, and carbon dioxide). The partial pressure of hydrogen is particularly important in this connection. Excessive partial pressure of hydrogen can prevent the conversion of the intermediate products of acidogenesis due to energy related reasons.

As a consequence of this excessive partial pressure, organic acids such as propionic acid, isobutyric acid, isovaleric acid and hexanoic acid accumulate and inhibit the formation of methane. For this reason, the hydrogen-forming (acetogenic) bacteria must co-exist in a close biotic community with the hydrogen-consuming methanogenic archaea, which consume hydrogen together with carbon dioxide during the formation of methane, thus ensuring an acceptable environment for the acetogenic bacteria.

This is the final stage of biogas generation. Acetic acid, hydrogen and carbon dioxide are converted into methane by strictly anaerobic methanogenic archaea. The hydrogenotrophic methanogens produce methane from hydrogen and carbon dioxide, whereas the acetoclastic methane-forming bacteria produce methane by acetic acid cleavage. At higher organic loading rates (usually obtainable in agricultural biogas plants), methane is formed primarily via the reaction pathway utilizing hydrogen, while it is only at relatively low organic loading rates that methane is formed via the reaction pathway involving the cleavage of acetic acid [11].

In an anaerobic digester or reactor, these four phases of anaerobic degradation take place simultaneously as a single-stage process. According to Vanek *et al.* [12], anaerobic digesters are open systems which means that diverse types of microbes can come in with the waste streams to circumvent the need to sterilize the inflow streams, and this eventually results in thousands of microbial species being present in a relatively stable consortium. This suggests that within the anaerobic digester, microbes comprise a food web, which means that a product from one microbe is the substrate (food) for another one.

According to Dobre *et al.* [13] and Friehe *et al.* [14], the following key factors affect the production of biogas via anaerobic digestion of organic waste. The hydraulic retention time (HRT) it is the mean range in which the substrate for anaerobic digestion process is retained in the digester, in contact with active bacterial mass. Substrates containing simple compounds are easily decomposed and require short HRT, while substrates containing complex compounds are harder decomposed and require a longer HRT. The retention time of the solids (SRT) is the measure of the biologic system capability to reach certain standards concerning the effluents and/or to maintain a satisfactory rate of pollutants biodegradation. SRT controls the microbial mass in the reactor in order to obtain a degree of waste stabilization.

Maintaining a high SRT translates to more stable running, better tolerance to toxic and shock loads and quick recovery after toxicity or instability. HRT is a key factor in the design process anaerobic digestion for digestible and hard complex organic pollutants, while SRT is the control parameter in the design process for readily digestible organic elements.

HRT is determined by the volume of the digester and the amount of substrate loaded per unit of time, according to the equation .1.

$$\mathrm{HRT} = \frac{V_d}{V_s}\ [\mathrm{days}], \qquad (1)$$

where: HRT is the hydraulic retention time [days]; V_d is the digester volume [m^3]; V_s is the amount of substrate loaded per time unit [m^3/s].

A short retention time determines a better flow rate of the raw material, but the low productivity of biogas.

In the production process of biogas, the pressure is of great significance. The experiments have shown that when hydrostatic pressure prevailing on the methanogenic bacteria increases over the range, 400 - 500 mm H_2O [13], biogas production ceases and is resumed when the hydrostatic pressure falls below that range. This is a critical component of the design work as it determines the height of fluid that the digester tank should operate with. For vertical digesters where the height can reach tens of meters, biogas is produced only up to maximum depth 4 – 5 m and the rest of the area occupied by the substrate does not produce biogas, which is why it is necessary to periodically bring to surface the material under the limit of reaction, by the stirring continued. The negative impact of this factor can also be avoided by using a horizontal tank whose height is typically below 3.5 m.

In anaerobic digestion all biological processes are carried out at well-defined values of pH. The pH of the optimal hydrolytic stage is between 5 - 6, and for methane production (methanogenesis) stage, the optimal pH value varies between 6.5 – 8. If the pH value decreases below 6, methane production is strongly inhibited. In the hydrolytic stage, the acidogenic bacteria require a pH in the range 5.5 – 7.0, and in the final stages, methanogenic bacteria require a pH value ranging between 6.5 - 8.0.

A major limitation to the processing of organic substrates through the process of anaerobic digestion in a single phase is a lower value of pH in the reactor due to rapid acidification by the production of volatile fatty acids. This effect hinders and inhibits the activity of methanogenic bacteria. At digesters operating in a single phase with the full mixing of the substrate, the pH must meet the requirements of the populations of micro-organisms that coexist in the digester. The temperature of the reaction medium influences the pH value. While the temperature is increasing, the carbon dioxide solubility decrease; this is why in the case of thermophilic digesters the pH value is higher than in the mesophilic ones where the carbon dioxide will dissolve easier and will produce carbonic acid in reaction with the water, increasing the acidity. During the digestion process, the pH value may increase because of the ammonia presence resulted either by the protein degradation or by its presence in the charging flux. The size of organic particles to be digested affects the rate of anaerobic digestion and thus the overall rate of biogas production. The smaller the particle size, the faster the rate of anaerobic digestion due to increasing in surface area. This smaller particle size increases biogas generation rate and reduces the amount of residue thus reducing digestion time overall. Smaller particles also mean shorter settling time since particles can be suspended in the fluid for greater digestion [15].

To achieve steady and increased biogas production rate, the substrate to be digested and the anaerobic bacteria must have extensive contact. This contact can be achieved by proper mixing of the substrate in the digester tank. If there is insufficient mixing, layers of sediments begin to form in the digester tank, trapping bacteria beyond the reach of the undigested substrate [14]. Due to differences in density, these various substrates form layers with the majority of the bacterial mass settling at the bottom of the tank out of reach of the majority of the substrates to be decomposed.

Solids that can float then form a layer of scum at the top of the slurry making it difficult for gas to escape from lower levels. The result of these factors is a significantly lower biogas production rate. Thus, mixing is essential for proper biogas production. Excessive mixing must, however, be discouraged in biogas plants as the bacteria that help form acetic acid (during acidogenesis) and the archaea responsible for methanogenesis form a close biotic community that can be destroyed by excessive stirring. A compromise thus must be reached between stirring time and stirring intensity.

Other factors that affect biogas production include mixing ratio, inoculums, loading rate, nitrogen inhibition, C/N ratio, agitation, toxicity, solid concentration, seeding, metal cations, additives, etc.

A wide array of research work has been carried out on biogas production in Nigeria and in other parts of the world. Biogas production and science have steadily progressed in the last four decades. However there is much room for innovation and creative thinking. Otaraku and Ogedengbe [16] studied the effect of Sawdust concentration in the co-digestion of sawdust, cow dung, and water hyacinth. This was done over a period of 64 days, and it was observed that about 40% of Sawdust in the total solids yielded optimum biogas production. Increased Sawdust content lowered biogas productivity due to the high lignin content of the sawdust which is difficult to digest.

Yavini *et al.* [17]studied the mesophilic biogas production potential of Groundnut shell, Maize cobs, Rice straw, and Bagasse. It was observed that the inoculation of these agricultural wastes with methanogenic bacteria sources such as cattle dung and poultry droppings had an important role and positive impact on biogas generation quantity. Rajendran *et al.* [18] gave an insightful overview into the various designs and operation of household biogas digesters, noting that moderate mixing is essential in biogas reactors as too much mixing stresses the microorganisms and too little mixing encourages foaming and even formation of scales.

Dahunsi and Oranusi [19]worked on co-digestion of food waste and human excreta for biogas production. They provided relevant data on the pH regime in the mesophillic temperature range for co-digestion of food waste and human excreta. The limitation of their research lies in the fact that temperature and pH were not continuously monitored but taken daily and weekly respectively. Ezeokoye and Okeke [20] worked on the design, construction, and performance evaluation of a Plastic Bio-digester and the Storage of Biogas. They Monitored parameters for biogas production from grains during batch digestion, but in their digesters, Practical digesters are mostly continuously fed, temperature monitored daily, pH monitored weekly. Dobre *et al.* [13] studied the overview of Main factors affecting biogas production. They highlighted lack of effective parameter monitoring to be a major cause of poor production and instability. Labatut and Gooch [21] monitored of anaerobic digestion process to optimize performance and prevent system failure. The work highlighted lack of process monitoring and operational management as a major cause of failure in most Biogas plants. They used analytical laboratories for onsite monitoring of large-scale plants which are too expensive for the domestic or small-scale application.

Despite the many benefits of biogas digesters, there are also a number of drawbacks that can make the implementation of this technology difficult. These difficulties include: Methanogens have many specific parameters, such as temperature and pH, this hinders widespread commercialization of anaerobic digesters [22]. The hydraulic retention time (HRT) poses a challenge, HRT which is the average time that the input slurry spends in the digester before it is removed, in tropical countries is 30 to 50 days, whereas in colder climates, it can be as long as 100 days, which requires a larger digester volume and raises costs [23]. While digesters can provide energy savings or even income to small-scale owners at farms—by way of selling electricity produced back to the power company—finding the right economies of scale possess yet another challenge. While biogas digesters do indeed offer a valuable way to reduce food waste and to capture energy that would otherwise be squandered, the actual potential of anaerobic digestion to produce a great deal of electricity is fairly limited. Even if the energy-producing capacity of biogas is small, given the waste-reducing benefits of anaerobic digestion, combined with its ability to slow climate change, pursuing policies to make digesters more common makes a great deal of sense. The main challenge is finding the right scale in order to make biogas digesters more economically feasible.

2. Materials and method

The biogas plant was designed as a continuously stirred reactor type (CSTR) due to its smaller footprint, ease of maintenance and improved gas production over the plug-flow mix type. A fixed-dome configuration was also selected over the floating-dome type due to its stability and relative ease of operation. A grinder was added to the digester vessel to reduce the particle size for improved biogas production. A stirrer system with an electric motor was also added to introduce substrate mixing that would boost biogas yield. The monitoring system was identified as a major improvement based on the limitations of other work and was implemented in the biogas plant.

The methodology employed for the design and construction is elucidated subsequently.

2.1. Materials

The following materials were used for the construction of a biogas plant:

i. Sparkless electric motor (1HP)
ii. Stainless steel type 316
iii. Stirrer

iv. Waste grinder
v. Hopper
vi. Valves and fittings
vii. Flashband sealing tape
viii. Arduino Uno Microcontroller
ix. pH Meter Kit
x. Pressure transducer sensor
xi. Temperature sensor

The part list of the developed small-scale biogas plant is presented in Table 1.

Table 1. Part list

S/N	Description	Quantity	Material	Remarks
1	Digestion tank	1	1 mm sheet metal	Stainless steel
2	Sparkless electric motor	1	Bought-out	0.35 kW
3	Stirrer	1	20 mm ø shaft	Stainless steel
4	Waste grinder	1	1 mm sheet metal for mesh. 125 mm diameter grater.	
5	Valves and fitting	2	Bought-out	½″ ball valve ½″ adapter ¾″ socket ¾″ X ½″ bushing ¼″ gas outlet valve ½″ T-fitting ½″ PVC pipe
6	Flashband sealing tape	2	Bought-out	Aluminum faced, bitumen backed sealing tape
7	Arduino Uno	1	Bought-out	
8	pH Meter Kit		Bought-out	
9	Pressure transducer sensor	1	Bought-out	
10	Temperature sensor	1	Bought-out	

2.1. Digestion tank

The digestion tank is the main reactor chamber where anaerobic digestion takes place. The material for fabrication is selected as stainless steel due to its ability to combine high strength, good formability and good resistance to biological corrosion [24] that can result from the metabolic activity of anaerobic microorganisms. Painting with a chromium oxide based paint will also improve the surface thermal absorptivity from solar insolation. The following design calculations were evaluated for the overall reactor tank design.

i. The volume of the reaction tank

According to Bachmann [25], to ensure that micro-organisms have a balance between the time needed to breakdown waste substrates and the concentration or quantity of substrates available (to avoid overloading the micro-organisms and hence inhibiting biogas production), two factors must be considered in sizing of biogas plants. These include the organic loading rate (OLR) and the hydraulic retention time (HRT).

The formula for calculating the volume of digester tank is given by equation 2.

$$V_d = \frac{I_w \times DM \times VDM}{OLR} \qquad (2)$$

where: V_d is the reactor volume [m^3]; I_w is the substrate input [kg/day]; DM is the dry matter content of the waste or total solids content expressed in %; VDM is the volatile dry matter content of the waste [% DM]; OLR is the theoretical organic loading rate [kgVDM/ m^3day] OLR for a continuously stirred tank can be as high as 4 kgVDM/ m^3day [25]. Assuming maximum substrate input (I_w) is 1.4 kg/day of food waste from home kitchens (small-scale application). DM for food waste can be estimated at 20% and VDM as 85% [3,26]. Thus,

$$V_d = \frac{1.4 \times 0.2 \times 0.85}{4} \qquad V_d \approx 0.06\, m^3$$

ii. Tank dimensions

For minimal footprint and aesthetic consideration we take heuristics:

$h = 1.75d = 3.5r$ (3) but, $V_d = \pi r^2 h = .5\pi r^3$ (4)

Equating equations (3.2) and (3.3) $0.6 = 3.5\pi r^3$

Hence $r \approx 0.175\, m$ and $h \approx 0.61\, m$

According to Moss [27], the thickness of the tank is estimated from equation 5.

$$t = \frac{P.r}{SE - 0.6P} \tag{5}$$

where: t is the minimum thickness of the cylindrical reactor wall (mm); P is the maximum internal pressure (N/mm^2); r is the internal radius of the reactor tank (mm); S is the maximum allowable working stress of the component (N/mm^2); and E is the joint efficiency.

Anaerobic digestion is favored by near-atmospheric pressure condition, and anaerobic bacteria thrive best below 1.2 bar (120 kPa). Consequently, beyond the accepted range above, the anaerobic digestion process stalls and eventually biogas production ceases. Thus, the maximum pressure the tank should withstand should be within a safety limit of 1.2 bar. Using a Factor of Safety of 3, a maximum design pressure P calculated as 3.6 bar (360 kPa) is utilized. The internal radius of the tank, r is 0.175 m assuming a joint efficiency of the weld, E is 0.8. The maximum tensile strength of stainless steel is obtained as 520 MPa [28].

The permissible working stress is calculated as:

$$S = \frac{Maximum\ Tensile\ Strength}{FOS} = \frac{520MPa}{5} = 104\ MPa$$

$$t = \frac{360 \times 10^3 \times 0.175}{(104 \times 10^6 \times 0.8) - 0.6(600 \times 10^3)} = 0.000765\ m\ or\ 0.765\ mm$$

Thus, the thickness of plate was thus selected as 1 mm to the nearest mm.

iii. Baffle design

The digestion reaction tank (reactor tank) is equipped with baffles to prevent swirling and to induce turbulence required for mixing in the tank. According to James [29], the following heuristics apply: 3 to 4 baffles are sufficient for a cylindrical tank, and the geometry is shown in Figure 2.

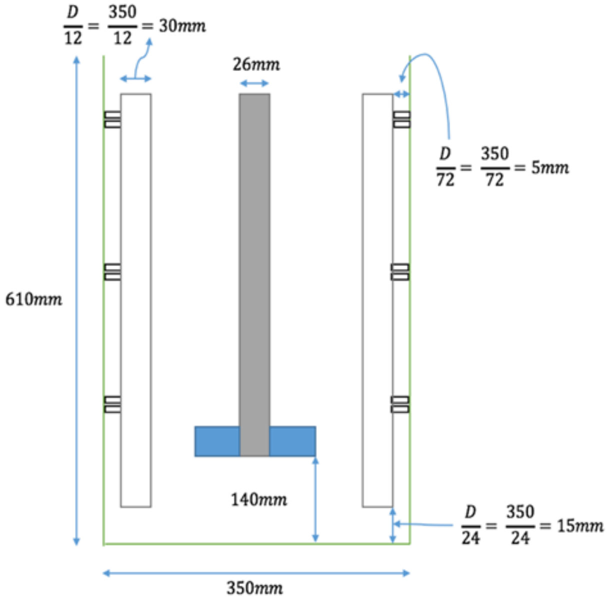

Figure 2. Baffle design for digester tank

The power requirement of the mixer was obtained using equation 6 according to Peters *et al.* [24].

$$P = \emptyset N_r^3 D_a^5 \rho \qquad (6)$$

where: P is the power required for mixing (kW); $\emptyset$ is the power function; N_r is the impeller rotation per unit time (rps); D_a is the impeller diameter (m); ρ_s is the density of slurry to be mixed (kg/m^3)

The power function can be estimated from charts using the Reynolds number and impeller characteristics. The Reynolds number for the flow is given by equation 7.

$$Re = \frac{D_a^2 N_r \rho_s}{\mu} \qquad (7)$$

The input waste is food waste of average density; $\rho_{fw} = 360$ kg/ m^3 [2] and water of density ρ_w= 1000kg/ m^3. With a mixture ratio 1:1, $c_{fw} = c_w$, the slurry density is given from equation 8.

$$\rho_s = \frac{\rho_w . \rho_{fw(c_{fw} + c_w)}}{\rho_{fw} c_{fw} + \rho_w c_w} \qquad (8)$$

$$\rho_s = \frac{1000 \times 360\ (2)}{360 + 1000} = 530\ \text{kg}/\ m^3$$

Slurry viscosity (μ) is approximately 650 cP or 0.65Ns/m^2 [29]. Assuming the impeller speed $N_r\ is\ 600\ rpm\ (10\ rps)$ and the diameter of impeller (D_{athe}) obtained from impeller sizing heuristics according to Peters *et al.* [24] is given as equation 9.

$$D_a = \frac{Tank\ Diameter\ (D_T)}{2.5} \qquad (9)$$

$D_a = \frac{Tank\ Diameter\ (D_T)}{2.5} = \frac{350}{2.5} = 140\ mm$. Therefore, the Reynolds number is calculated from equation 7 as: $Re = \frac{0.14^2 \times 10 \times 530}{0.65} = 160$

Since Froude's number is not a factor (Re < 300), the relation between power function and the Reynolds number for a paddle mixer is shown in Figure A1 from Appendix A. Thus, the power function $\emptyset\ is\ 6$ as obtained from the chart for Reynolds number Re of 54.

Assuming $N_r = 600\ rpm = \frac{600}{60}\ rps = 10\ rps$, $D_a = 0.14\ m$, and $\rho_s = 530\ kg/m^3$.

Using equation 6, the power required for mixing is calculated as:

$P = 6 \times 10^3 \times 0.14^5 \times 530 = 171\ W$

With loading of 80%, the motor power required will thus be:

$P_m = \frac{171}{0.8} = 250$ W (to the nearest standard). Using a safety factor of 2.5, $P_m = 250 \times 2.5 = 625$ W

Due to availability, a **1 HP** (750 W) motor is selected.

2.2. Stirrer

The stirrer consists of paddle-type impeller blades with a vertical shaft subjected to twisting moment only.

i. The diameter of impeller (D_a)

According to Peters *et al.* [24] (2003), the diameter of imthe peller is obtained from impeller sizing heuristics as 140 mm by recalling equation 9.

$$D_a = \frac{Tank\ Diameter\ (D_T)}{2.5} \qquad (Recall\ equation\ 9)$$

ii. Diameter of shaft

As the weight of the shaft is negligible and as the shaft is vertically oriented for mixing, it is subjected majorly to twisting moment. From Khurmi and Gupta [30], shafts may be designed on the basis of rigidity and strength. When subjected to twisting moment only, the following relation holds true:

$$\frac{T}{J} = \frac{\tau}{r} \qquad (10)$$

with little mathematical consideration it can be shown that:

$$d^3 = \frac{16T}{\pi\tau} \qquad (11)$$

where: T is the torque or twisting moment (Nm); τ is the allowable or permissible torsional shear stress (N/mm^2); J is the Polar moment of the shaft about its axis of rotation (mm^4); r is the radius of the shaft (mm); and d is the diameter of the shaft (mm).
The twisting moment T is calculated from equation 11 as

$$T = \frac{P}{2\pi N_r} \qquad (12)$$

$$T = \frac{750}{2\pi \times 10} = 11.94\ Nm$$

The allowable shear stress for stainless steel can be obtained as $\tau = 0.18\sigma_u$ (13)
where: σ_u is the ultimate tensile strength given as 520 MPa [28].
$\tau = 0.18 \times 520 = 93.6\ MPa$
Thus, the diameter of shaft the the for the mixer is calculated as:

$$d^3 = \frac{16 \times 11.94}{\pi \times 93.6 \times 10^6} \qquad d = \mathbf{10\ mm}\ (nearest\ standard\ size)$$

Using a safety factor of 2, $d = \mathbf{20\ mm}\ (nearest\ standard\ size)$

2.3. Water crusher

Since food waste is to be used as a substrate, provision is made for the easy crushing of food remains including cooked food and spoiled fruits. The waste crusher will also aid in the particle size reduction of various grains and nuts that will be fed to the biogas reactor. The crusher consists of a roller with a shaft for power transmission. The power required to actuate the crusher depends on the torque needed to rotate the roller cylinder when loaded to maximum. As the digester will be loaded daily in batches of 1.4 kg; the force F on the crusher is given by equation 14.

$$F = m.g \qquad (14)$$

$$F = 1.4 \times 9.81 = 13.74\ N$$

The torque T required is calculated from equation 15.

$$T = F.r \qquad (15)$$

$$T = 13.74 \times 0.1 = 1.374\ Nm$$

Assuming a moderate speed of 40 rpm, hence the minimum power requirement for the crusher can be obtained as:

$$P = \frac{2\pi NT}{60} \qquad (Recall\ equation\ 12)$$

$$P = \frac{2\pi \times 40 \times 1.374}{60} = 5.8\ W$$

Hence, hand grinding was evaluated as an ecoeconomicaltion and thus selected.

2.4. Valves

Two ball valves are utilized for fluid control in the system. One ¾″ valve serves as the drain or flush valve for emptying the contents of the tank after the design HRT is exceeded. A ¼″ gas outlet valve serves for the feeding of gas to the plant outlet.

2.5. Flashband sealing tape

This is a self-adhesive, aluminum faced bitumen backed sealing tape. It is a quick, efficient and cost effective method of flashing, sealing and repair that produces lasting protection in all climates. It provides a watertight seal that improves over time [31].

2.6. Arduino Uno microcontroller

The Arduino Uno is a microcontroller board that provides a simple and modular way of interfacing the real world with the computer to handle basic processing tasks on a chip while working with hardware sensors. The Arduino Uno uses the ATmega328 chip that supports 14 digital pins that can be configured as either input or output and 6 analog inputs [32]. Table 2 shows the technical features of the Arduino Uno.

Table 2. Technical Specifications of the Arduino Uno

S/N	Item	Value	Remarks
1	Micro-controller	8-bit Atmel ATmega328p	1 mm sheet metal
2	Operational voltage	5V	Input range: 7-12V
3	Digital GPIO	14	6 capable of PWM
4	Analog IO	6	10-bit
5	Program memory	Flash 32kb, EEPROM 1kb	SRAM 2kb
6	Clock speed	16MHz	
7	USB	Type B socket	
8	Programmer	In-system firmware	USB-based
9	Serial communications	SPI, I2C	Software UART
10	Other	RTC, watchdog, interrupts	

The Arduino is programmed using the Arduino IDE with source code written in C.

2.7. Pressure transducer sensor

This measures the pressure of the gas with a carbon steel alloy sensor material. It has a working pressure range of 0-1.2 MPa. The normal working temperature range is 0-85°C and the response time is approximately 2 ms.

It consists of an elastic material that deforms under the application of pressure and an electrical element which detects the deformation and transmits it as changes in voltage.

2.8. pH Meter Kit

This is a kit that measures pH of a substance. It is specially designed for the Arduino and has an accuracy of $\pm 0.1 pH$ (at 25°C). The kit has a range of 0 – 14pH. The kit consists of a pH sensor probe, a BNC connector and a pH 2.0 interface.

2.9. Temperature sensor

This takes temperature readings for the plant to aid process insights. It has a temperature range of -40°C - 80°C.

2.10. Construction of the biogas plant

The volume of digester constructed is 0.06 m^3. A 1 mm thick stainless steel sheet was used in the fabrication of the biogas reactor for the following reasons:

i. It has high resistance to biological corrosion which can arise due to anaerobic digestion process;
ii. It can withstand a wide range of temperatures and pressures.
iii. It also combines good strength with high formability.

In constructing the small-scale biogas plant, the following stages were undergone:

i. Construction of the cylindrical digester vessel of diameter 350 mm and height 610 mm;
ii. Construction of the grinding unit;
iii. The connection of the plant monitoring system circuit;
iv. Installation of the grinding unit on the digester vessel;
v. Installation of the electric motor;
vi. Installation of piping and fittings;
vii. Installation of plant monitoring circuit on digester vessel.

2.10.1. Construction of cylindrical vessel

The following steps are taken to construct the cylindrical biogas digester vessel:

i. The 1 mm stainless steel metal sheet was cut to size (1100 X 610 mm) using the Guillotine machine.
ii. The 1100 X 610 mm stainless steel sheet was rolled to shape using the metal rolling machine.

iii. The metal sheet was welded to form the cylindrical shape of the body plate.
iv. A separate stainless steel sheet was cut and welded into a conical shape for the bottom of the tank.
v. The circular metal plate of diameter 350 mm was marked out and cut as the top plate of the cylindrical vessel.
vi. Three stainless steel plates of dimension 94.5 X 580 mm were cut. These were rolled and welded into cylindrical baffles for the tank.
vii. The three cylindrical baffles were welded to the internal surface of the tank. Baffles at 90°, 180° and 270° relative to the circular top plate.
viii. The conical bottom plate was then welded to the cylindrical body plate.
ix. The stainless steel shaft was turned to 20 mm external diameter.
x. Two 140mm paddle impellers were welded to the stainless steel shaft.
xi. The mild steel square pipe was cut into three sections of length 300 mm These sections were then welded onto the cylinder as the vessel legs.
xii. A 20 mm bore was machined in the circular top plate for the stainless steel shaft.
xiii. The circular top plate was welded onto the cylindrical vessel and installation of a bearing assembly for the machined shaft.

2.10.2. Construction of the grinding unit

The following steps are taken to construct the grinding unit:

i. The side plates of the hopper were marked out with dimensions 70 X 65 mm for the square component and 130 X 70 X 110 mm for the trapezium component.
ii. The marked out shape was cut to specifications.
iii. The face plates of the hopper were marked out and cut with dimensions 90 X 65 mm for the square component and 175 X 90 X 110 mm for the trapezium component.
iv. The side plates were drilled to create a 25 mm bore for the shaft and cylindrical grinder mesh.
v. The cylindrical grinder mesh was developed with recommended 1.5 mm mesh basic size and 3mm clearance.
vi. The cylindrical mesh, shaft, and handle were assembled.
vii. The four plates (two side plates and two face plates) were welded together to obtain the hopper unit.

2.10.3. The connection of the biogas plant monitoring system circuit

The biogas plant monitoring system was connected on a breadboard for prototyping using the circuit diagram shown in Figure 3. Figure 3 show the connection of the ATmega328 chip on the Arduino Uno with the pH, pressure and temperature sensor.

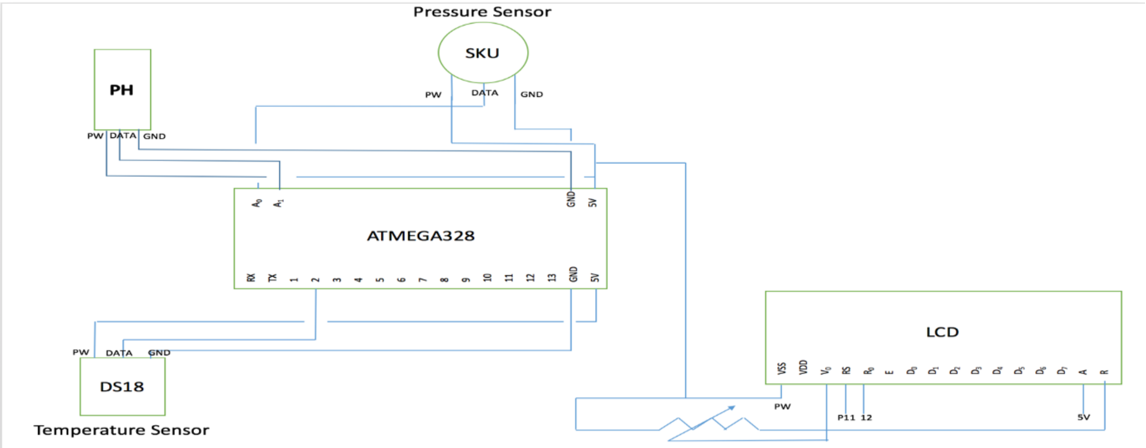

Figure 3. Monitoring system circuit with Arduino Uno microcontroller

2.11. Performance evaluation of the developed biogas reactor

This was done to evaluate the performance of the biogas plant in terms of effectiveness of the continuous monitoring system. Data were obtained from the pressure, pH and temperature sensors to determine their accuracy. The biogas yield is recorded to give daily and total biogas yield. The biogas yield is then evaluated with the pressure, pH and temperature variation per day.

2.12. Leak and integrity testing

After the electric motor, grinding unit and monitoring system are installed, the biogas plant is subjected to a leak and integrity test using the following steps:

i. Close all valves were closed and tighten all fitting joints.
ii. Introduce compressed air at a regulated pressure and inspect all fittings, valves, and joints for leakage.
iii. Mark out leaks if any.
iv. Tighten all joints and carry out final inspection on the entire plant.

2.13. Input Waste

The developed biogas plant was fed with 3.55 kg of food waste (comprising egg shells, cooked rice, pounded yam, etc.) and 11.45 kg of cassava waste water. The total input waste thus is about 15 kg.

2.14. Method

The waste material was gathered from the ABUAD Cafeteria 1 and the cassava waste water from a neighboring village close to the ABUAD community. The waste was prepared by removing foreign/non-organic materials and fed into the biogas plant and fed

The food waste material was fed by mixing with water in a ratio 1:1. The waste material is allowed to decompose for 7-14 days before biogas yield is evaluated. Immediately the waste was fed into the system, the biogas plant monitoring system was initiated to allow for data acquisition.

2.15. Determination of biogas yield

Biogas yield is determined using the water-displacement method. A known volume of water is used as a barrier and biogas is collected over it, and its volume is recorded daily. The correlation, prediction, modelling, and optimization of optimum process parameters and yield of biogas produced from food waste was done using the central composite design and response surface methodology.

The software employed was Design-Expert® (version 7) which is used for experiment design. A four-level-four factor central composite design model and response surface methodology were used to study the effect of independent variables such as organic loading rate (kgVDM/m^3), temperature (℃), pH and pressure (kPa) and on the biogas yield. The input process parameters varied and their range includes; organic loading rate (0.6-0.9 kgVDM/m^3); reaction temperature (24.27 – 26.42℃); pH (6.81-7.28) and pressure (4.20-5.48 kPa).

It is also used to investigate the quadratic cross effect of the four input process parameters earlier mentioned on biogas yield. Table 3 shows the input values for process parameters denoted as numeric factors over 4 levels. This generated a run of 30 experiments and the data obtained were statistically analyzed with the Design-Expert® software to get a suitable model for biogas yield (litres) as a function of the four independent variables.

The performance evaluation of the developed biogas plant was carried by introducing a total input waste of 15 kg. 3.55 kg of food waste material composing of 54% egg shells and 46% leftovers were sourced from the ABUAD Cafeteria. The food waste comprises egg shells, cooked rice, pounded yam, etc. 11.45 kg of cassava waste water was also fed into the plant.

3. Results and discussion

The developed biogas system with its associated expert system is shown in Figure 4.

Figure 4. Developed small-scale biogas plant

The system pressure, pH of the substrate and corresponding temperature variation were determined. The biogas yield per day for the given substrate was then obtained via collection over water as shown in Table 3.

Table 3. Methane yield per day

S/N	Time (days)	Weigh of input waste (kg)	Weight of consumed waste (kg)	Volume of methane generated (m^3)	Weight of methane generated (kg)	Amount of electricity generated (kWh)	Methane yield (%)
1	14	15	2.5	1.95	1.28	4.17	51.2
2	28	15	2.6	2.01	1.32	4.30	50.7
3	42	16	2.8	2.18	1.43	4.67	51.0
4	56	18	3.2	2.60	1.70	5.57	53.3
5	80	16	2.7	2.14	1.40	4.58	52.0
6	94	18	3.0	2.45	1.60	5.24	54.0

The volume of methane generated and the amount of electricity produced from 14-84 days is shown in Figure 5. High pressure favours the conversion of the substrate to methane gas. An optimum amount of 5.24 kWh of electricity was generated within 84 days which is sufficient for domestic applications.

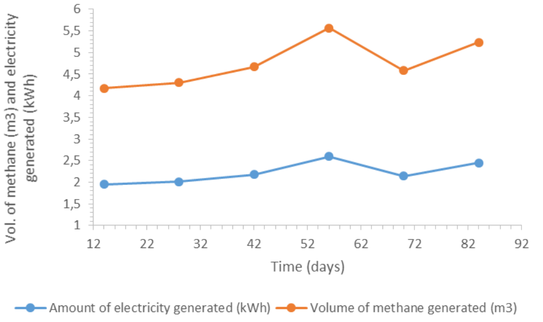

Figure 5. Volume of methane generated and amount of electricity produced

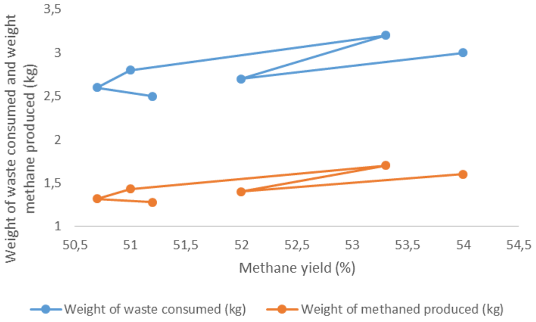

Figure 6. Methane yield for waste consumed and methane produced

Also, Figure 6 show the methane yield for the input waste consumed as well as the corresponding methane produced. The conversion efficiency of the consumed substrate to methane gas lies between 50-54%. This agrees with the findings of Banks [32] while evaluating the potential of anaerobic digestion to provide energy and soil amendment.

The summary of the designed experiment to predict biogas production in terms of study type using central composite as initial design and a quadratic design model was also given in Table 4.

Table 4. Numeric factors and levels

			S/N	Factor	Name	-alpha	+alpha
1.	A	Organic loading rate	kg/VDM/m^3	0.6	0.9	0.45	1.05
2.	B	Temperature	℃	24.27	26.42	23.195	27.495
3.	C	pH		6.81	7.28	6.575	7.515
4.	D	Pressure	kPa	4.20	5.48	3.56	6.12

The yield of the biogas from food waste was determined using equation 16.

$$Yield = \frac{Weight\ of\ biogas}{Weight\ of\ input\ waste} \times 100\% \qquad (16)$$

A predictive model for estimating the biogas yield in terms of the process parameters was obtained from Table 4 as given in equation 17.

$$Yield = 18.27 + 0.000 * A + 0.28 * B + 0.50 * C + 0.000 * D - 0.81 * A * B + 1.19 * A * C + 0.69 * A * D + 0.44 * B * C - 3.06 * B * D - 0.063 * C * D \qquad (17)$$

where: A denotes the organic loading rate (kgVDM/m^3); B is the temperature (℃); C is the pH and D is the pressure (kPa).

Figure 7 was a 3D response surface plot of the interaction effect loading rate and temperature when pH and pressure were held constant at 7.04 and 4.84 kPa respectively. The optimum yield of biogas was 23 litres. Increase in loading rate increases the temperature and increases the yield of the biogas.

7

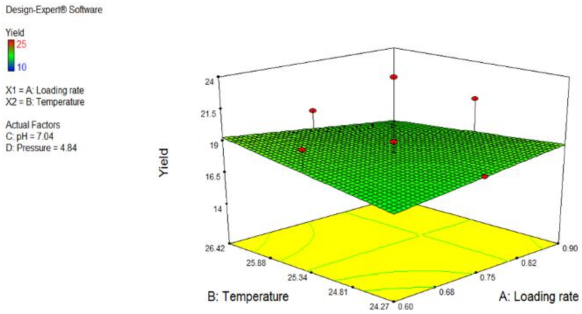

Figure 7. Effect of interaction of loading rate and temperature on biogas yield

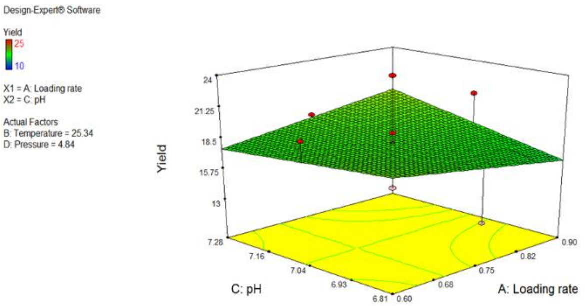

Figure 8. Effect of interaction of loading rate and pH on biogas yield

Figure 8 studies the interaction effect of loading rate and pH when temperature and pressure are held constant at 25.34°C and 4.84 kPa respectively. The optimum yield of biogas was 23 litres. Increase in loading rate increases the pH and increases the yield of the biogas up to the optimum yield point after which there is a sharp decrease in the yield with an increase in the loading rate and pH. This may be due to the fact that when the biogas is loaded beyond the optimum, the rate of decomposition decreases resulting in a decreased yield of the biogas.

Figure 9 is a 3D response surface plot of the interaction effect of the loading rate and pressure keeping temperature and pH constant at 25.34°C and 7.04 respectively. Increase in loading rate increases the pressure resulting in an optimum yield of biogas. Beyond the optimum yield of 23 litres, the yield of the biogas decreases with increase in loading rate and pressure.

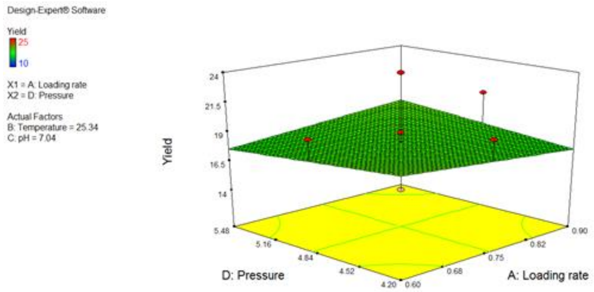

Figure 9. Effect of interaction of loading rate and pressure on biogas yield

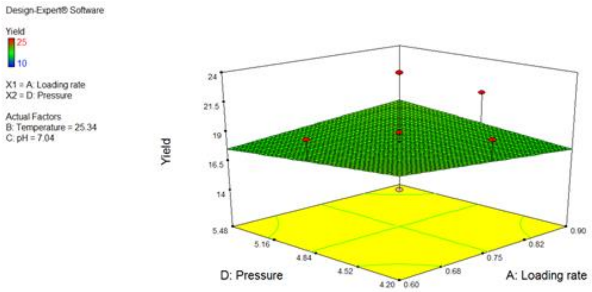

Figure 10. Effect of interaction of temperature and pH on biogas yield

Figure 10 was a 3D response surface plot of the interaction effect of temperature and pH when loading rate and pressure were held constant at 0.75 and 4.84 respectively. The value of pH is likely to be unaffected with an increase in temperature. Further increase in temperature beyond the optimum may kill the decomposition of anaerobic bacteria which will, in turn, slow down the rate of decomposition resulting in a decrease in the yield of the biogas.

Figure 11 is a 3D response surface plot of the interaction effect temperature and pressure on the yield of biogas when the loading rate and pH were held constant at 0.75 and 7.04 respectively. The interaction between the temperature and pressure was observed to be inversely proportional as an increase in temperature reduces the pressure and vice versa. The optimum yield of biogas was found to be 23 litres.

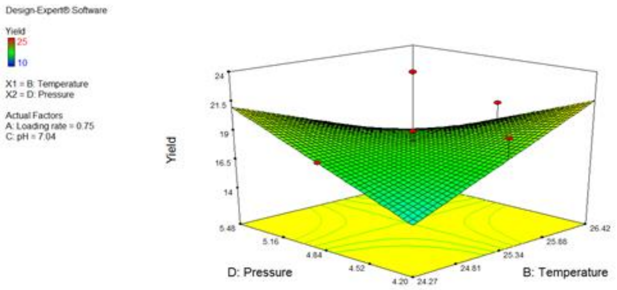

Figure 11. Effect of interaction of temperature and pressure on biogas yield

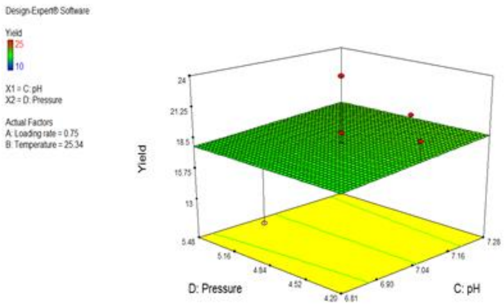

Figure 12. Effect of interaction of pH and pressure on biogas yield

Figure 12 is a 3D response surface plot of the interaction effect of pH and pressure on the yield of biogas. The variation in pH is unlikely to affect the pressure variation. Hence the optimum yield of biogas was found to be 23 litres.

From Figures 7-12, the optimum values of the process parameters for the optimum yield of biodiesel (23 litres) were found to be: loading rate (0.75 kgVDM/m^3), temperature (25.34°C), pH (7.04) and pressure (4.84 kPa).

4. Conclusion, recommendations, and contribution to knowledge

4.1. Conclusion

The successful completion of this work featured the design a biogas plant for use in ABUAD for studying biogas production, fabrication of the designed biogas plant, incorporation of a relatively low-cost continuous parameter monitoring system for the small-scale biogas plant and evaluation and optimization of the developed biogas plant. The optimum conversion of substrate to methane gas was 54% which generated 5.24 kWh of electricity within 84 days.

4.2. Recommendations

The following recommendations will be pivotal to further work on the development of biogas plants with monitoring system:

i. A metering system should be added to measure the amount of biogas produced on the gas outlet line per day as water displacement method requires close human monitoring.
ii. A wireless module should be added to the system to make the system fully smart and communicate to as an 'Internet of Things' device.
iii. A non-conventional heating system e.g., passive solar heating using water and solar insolation should be considered to raise the temperature to the thermophilic range for faster biogas production.
iv. Implementation of a packaging system that will enhance the value of the produced fertilizer.

4.3. Contribution to knowledge

The work contributes to knowledge as follows:

i. Improvement in process control and monitoring with the use of sensors and a micro-controller.
ii. Incorporation of a low-cost monitoring system for the small-scale biogas plant.
iii. Provision of a design framework for small-scale biogas plant for laboratory and experimental purposes.

References

[1] Gerlach F, Grieb B and Zerger U. Sustainable Biogas Production: A handbook for Organic Farmers. Frankfurt: FiBL Projekte GmbH 2014. Available from: http://www.ecofys.com/files/files/ecofys-2014-sustaingas_handbook.pdf [Accessed 4 December 2016].

[2] Hoornweg D and Bhada-Tata P. What a Waste: A Global Review of Solid Waste Management. World Bank: Urban Development Series, Knowledge Papers 2012. [Online]. Available from: http://siteresources.worldbank.org/INTURBANDEVELOPMENT/Resources/336387-1334852610766/What_a_Waste2012_Final.pdf [Accessed: 25 November 2016].

[3] Al Seadi T, Rutz D, Prass, H, Kottner M, Finsterwalder T, Volk S and Janssen R. Biogas Handbook. Esbjerg: University of Southern Denmark 2008. [Online]. Available from: Lemvig Biogas. http://www.lemvigbiogas.com/download.htm [Accessed 25 November 2016].

[4] World Energy Council. World Energy Resources: 2013 Survey. London: World Energy Council. [Online]. Available from: https://www.worldenergy.org/wp-content/uploads/2013/09/Complete_WER_2013_Survey.pdf [Accessed: 25 November 2016].

[5] Ramatasa IM, Akinlabi ET, Madyna DM, and Huberts R. Design of the Bio-digester for Biogas Production: A Review. Proceedings of the World Congress on Engineering and Computer Science. Vol. II WCECS 2014 22-2, San Francisco USA. pp. 1-4.

[6] Sharma D, and Samar K. Frequently Asked Questions on Biogas Technology. Department of Renewable Energy Engineering. Maharana Pratap University of Agriculture and Technology 2016, Udaipur. pp. 1-62.

[7] Lahlou Y. Design of a Biogas Pilot Unit for Al Akhawayn University 2017. pp. 1-65.

[8] Wiese J, and Konig R. (2007). Monitoring of digesters in biogas plants. [Online]. Available from: https://uk.hach.com/asset-get.download.jsa?id=25593611187 [Accessed 2 March 2017].

[9] Friehe J, Weiland P and Schaffer A. Guide to Biogas: From Production to use. Fachagentur Nachwachsende Rohstoffe e.V. (FNR) 2010, Gülzow.

[10] Davidson O. Sustainable energy and climate change: African perspectives. In: Davidson O., Sparks D. (eds.) Developing energy solutions for climate change: South African research at EDRC. Cape Town: Energy and Development Research Centre 2002. pp. 145–152.

[11] Bauer, C., Korthals, M., Gronauer, A. & Lebuhn M (2008) Methanogens in biogas production from renewable resources - a novel molecular population analysis approach. Water Sci Technol 58: 1433–1439.

[13] Dobre P, Nicolae F and Matei F. Main factors affecting biogas production – an overview. Romainian Biotechnological Letters. 2014; 19(3), pp 9283 – 9296.

[14] Friehe J, Weiland P. and Schreiber A. Guide to Biogas. Fachagentur Nachwachsende Rohstoffe e.V. (FNR) 2012, Gulzow

[15] Perera KUC. Investigation of Operating Conditions for Optimum Biogas Production in Plug Flow Type Reactor. KTH Industrial Engineering and Management 2011, Stockholm, pp. 1-46

[16] Otaraku IJ, and Ogedengbe EV. (2013) Biogas Production from Sawdust Waste, Cow Dung and Water Hyacinth – Effect of Sawdust concentration, International Journal of Application or Innovation in Engineering & Management. 2013; 2(6): 91-93.

[17] Yavini TD, Taura WH, Mohammed N. and Namo JM. (2014). Comparative Study of Mesophillic Biogas Production Potential of Selected Agro-Wastes. The International Journal of Engineering and Science, 214; 3(2): 1-6.

[18] Dahunsi SO, and Oranusi US. (2013). Co-digestion of Food Waste and Human Excreta for Biogas Production, British Biotechnology Journal,2013; 3(4). 485-499.

[18] Rajendran K, Aslanzadeh S, and Taherzadeh MJ. (2012). Household Biogas Digesters – A Review. Energies, 2012; 5(1): 2911-2942.

[19] Ezekoye VA, and Okeke CE. (2006) Design, Construction, and Performance Evaluation of Plastic Biodigester and the Storage of Biogas. [Online]. Available from: http://www.akamaiuniversity.us/PJST7_2_176.pdf [Accessed 10 March 2017].

[20] Labatut RA, and Gooch CA. (2014) Monitoring of Anaerobic Digestion Process to Optimize Performance and Prevent System Failure. [Online]. Available from: https://ecommons.cornell.edu/bitstream/handle/1813/36531/21.Rodrigo.Labatut.pdf?sequence=1 [Accessed 9 March 2017].

[22] Chen Y, Cheng JJ, and Creamer KS. Inhibition of Anaerobic Process: A review. Bioresource Technology,2018; 99(10): 4044-4064.

[23] Yadvika S, Sreekrishnan TR, Kohli S, and Rana V. (2004) Enhancement of biogas production from solid substrates using different techniques – a review. Bioresource Technology, 2004; 95: 1-10.

[24] Peters MS, Timmerhaus KD, and West RF. Plant Design and Economics for Chemical Engineers. 5th ed. New York 2003: Elsevier.

[25] Bachmann N. Design and Engineering of Biogas Plants, in: Wellinger, A., Murphy, J., Baxter, D. (eds.) The biogas handbook: Science, production and applications. Cambridge 2013: Woodhead Publishing.

[26] SEAI: Sustainable Energy Authority Ireland. Energy in the Residential Sector: 2013 Report. September 2013. pp. 1-2.

[27] Moss DR. Pressure Vessel Design Manual: Illustrated procedures for solving major pressure vessel design problems. 3rd ed. Oxford 2004: Elsevier.

[28] James B. (2012). Mixing 101: Baffled by Baffles? How Baffle Configuration can Optimize Industrial Mixing. [Online]. Available from: http://www.dynamixinc.com/baffled-by-baffles[Accessed 11 March 2017].

[28] Wendt U. Materials Science and Engineering: Materials in Mechanical Engineering, in Grote, K., Antonsson, E. K. (eds.) Springer Handbook of Mechanical Engineering. New York 2009: Springer.

[29] ATS Rheosystems (2017). Viscosity Profile of Food Waste Slurry: Application Proof. [Online]. Available from: http://www.atsrheosystems.com/app_proofs/food/viscosity_profile_of_a_food_waste_slurry.pdf [Accessed 28 February 2017].

[30] Khurmi RS, and Gupta JK. A Textbook of Machine Design. New Delhi 2005: Eurasia Publishing House.

[31] Andek Corporation. (2015). Flashband. [Online]. Available from: http://www.andek.com/AProducts/flash.html [Accessed 14 April 2017].

[31] Goodwin S. Smart Home Automation with Linux and Raspberry Pi. 2nd Ed. New York 2013: Apress.

[32] Banks C. Optimising Anaerobic Digestion. University of Reading 2009, UK. pp. 1-39.

To whom correspondence should be addressed: Dr. I. A. Daniyan, Department of Mechanical and Mechatronics Engineering, Afe Babalola University Ado Ekiti

Petroleum and Coal

Article **Open Access**

A STUDY ON THE DIFFERENT REFORMING TECHNIQUES IN GAS TO LIQUID TECHNOLOGY

*Mohamed A. Ayad**, *Nour A. El-Emam, Tarek M. Aboul-Fotouh*

Mining and Petroleum Engineering Department, Faculty of Engineering, Al-Azhar University, Cairo, Egypt

Received May 14, 2018; Accepted June 25, 2018

Abstract

Gas-to-liquid (GTL) is the chemical conversion of natural gas into high-quality liquid products. The most important reforming technologies used are autothermal reforming (ATR), Partial oxidation (POX), and Steam methane reforming (SMR). A process flowsheet based on each reforming technique is designed with parameters and operating conditions obtained from the industry field data and simulated with ASPEN plus V8.6. A comparative analysis is mainly developed for assessing the different reforming technologies based on syngas ratio (H_2/CO) that is a favorable value of 2, and the results are documented and provide that ATR and POX techniques have a value equal or close to 2, then an additional comparison between ATR and POX based on Amount of Syngas, amount of heat saving and greenhouse gas emissions. POX is the most influential technique that has a large amount of syngas and heat saving and low CO_2 content and should be expanded use in industry.

Keywords: *Gas-to-liquid; Steam Methane Reforming; Partial Oxidation; Autothermal Reforming.*

1. Introduction

The gas-to-liquid (GTL) technology, it chemically converts natural gas into clean-burning liquid products [1]. This chemical liquefaction technique produces sulfur-free transportation fuels with a high cetane number suitable for blending or as a direct fuel for combustion engines [2-4]. By converting natural gas into liquid fuels, the technology greatly reduces high transport costs which in the past prevented its access to distant markets. It also facilitates fuel tran-sport; thus benefits the environment in two ways. First, the resulting liquid hydrocarbons are pure and burn cleanly. Second, converting gas to liquid allows producers to transport and market associated gas that would otherwise be flared into the atmosphere [5]. Due to the removal of impurities before the gas is converted to liquid, GTL products have superior properties regarding combustion efficiency and emission of some pollutants [6].

A GTL process mainly comprises of three parts as shown in Figure 1. which are reforming of natural gas to syngas (CO and H_2 mixture) by different technologies, subsequent Fischer-Tropsch reaction of syngas to hydrocarbons (also called syncrude), conversion of syngas into chains of hydrocarbon products takes place on a catalyst surface, and upgrading of syncrude by fractionation, hydrotreating, hydro-cracking, and hydroisomerization to yield products that meet the market specifications Before these three steps of a GTL process, the acid gas removal unit is existed to turn the natural gas feedstock from sour gas to sweet gas. A sulfur compound in sour gas will poison the active sites of catalyst used in the subsequent process [7-8].

2. Syngas production for GTL

The most important reforming technologies currently used for syngas production are Steam Methane Reforming (SMR), Partial Oxidation (POX) and Auto Thermal Reforming (ATR). These different technologies are employed by several industries such as Shell which uses POX [3], Rentech which uses SMR [9], and Sasol [10] and Exxon Mobil [4] which use ATR.

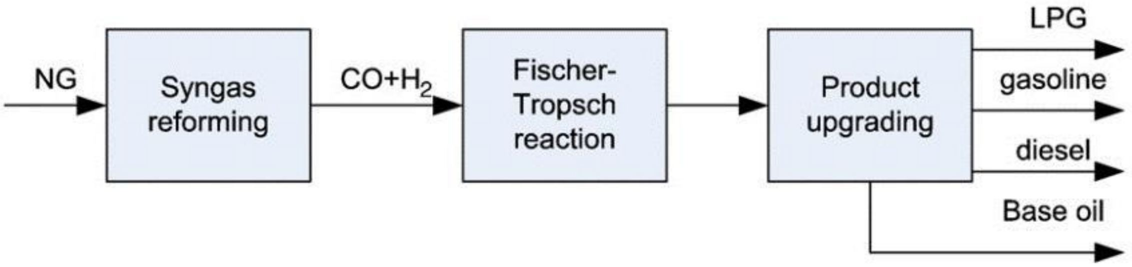

Figure 1. Gas-To-Liquids process diagram

2.1. Autothermal reforming (ATR)

During ATR, a mixture of steam, methane, and oxygen is reacted adiabatically over a fixed bed of nickel-based catalyst. ATR has a combination of reactions [2].

To avoid the potential problem that the ATR works as a steam cracker, which produces olefins from higher hydrocarbons in the feed, a pre-reformer is introduced.

In the pre-reformer, all higher hydrocarbons (C_{2+}) are converted into a mixture of methane, hydrogen, carbon monoxide and carbon dioxide according to the following reactions [11].

$C_nH_m + n\ H_2O \rightarrow n\ CO + (n + m/2)\ H_2$ for $n \geq 2$ Eq. (1)

Equilibrium reaction (exothermic):

$CO + 3\ H_2 \leftrightarrow CH_4 + H_2O$ $\Delta H = -210$ kJ/mol Eq. (2)

$CO + H_2O \leftrightarrow CO_2 + H_2$ $\Delta H = -41.2$ kJ/mol Eq. (3)

The key part of the syngas unit is the autothermal reformer [12-14]. The chemical reactions carried out in this option are below:

$CH_4 + ½\ O_2 \rightarrow CO + 2H_2O$ $\Delta H = -519$ kJ/mol Eq. (4)

$CH_4 + H_2O \rightarrow 2CO + 3H_2$ $\Delta H = 206$ kJ/mol Eq. (5)

$CO + H_2O \rightarrow CO_2 + H_2$ $\Delta H = -41$ kJ/mol (WGS) Eq. (6)

2.2. Partial oxidation (POX)

This reforming technique employs an air separation unit because nitrogen-free oxygen is required in the feed. The partial Oxidation can be catalytic or noncatalytic [15-16]. Efforts have been made to achieve the partial oxidation at low temperatures (for range between 300 and 1000°C with a rhodium catalyst [16] or using platinum as catalyst with a temperature lower than 1200°C [17]) because the high reaction temperatures that are currently used (between 1200 and 1500 °C) the operating cost is high and soot formation is observed [18].

Syngas can be directly produced by the following exothermic reaction:

$CH_4 + 0.5\ O_2 \rightarrow CO + 2\ H_2$ $\Delta H = -36$ kJ/mol Eq. (7)

2.3. Steam Methane Reforming (SMR)

SMR is a widely practiced technology for hydrogen-rich syngas production. This reaction is strongly endothermic. Thus the major challenge, and often the limiting factor in the selection of the SMR process, is providing sufficient heat into the reactor system to maintain the required reaction temperature [19]. This Reforming Technique is a catalytic process which carried out in a multitubular reactor commonly packed with a catalyst. Most commercial steam reforming catalysts are nickel-based and use carriers such as alumina, zirconia, etc. [18, 20]. The chemical reaction carried out in this option is below

$CH_4 + H_2O \rightarrow CO + 3H_2$ $\Delta H = 206$ kJ/mol Eq. (8)

$CH_4 + CO_2 \rightarrow 2CO + 2H_2$ $\Delta H = -41$ kJ/mol Eq. (9)

$CO + H_2O \rightarrow CO_2 + H_2$ $\Delta H = 247$ kJ/mol (WGS) Eq. (10)

A water-gas shift (WGS) reaction is part of this process [20].

3. Simulation and analysis

3.1. Feed conditions and specifications

The case study deals with a feedstock of natural gas. Table 1 lists the characteristics of the natural gas fed to the process.

Table 1. Typical feed gas conditions for the case study [21]

Flowrate (kmol/hr)	3 000
Temperature (°C)	22
Pressure (bar)	63
Component	Composition (mol %)
Methane	92.4
Ethane	3.6
Propane	1.6
N_2	1.0
CO_2	1.3
H_2S	0.1

3.2. Modeling environment

The Aspen plus V 8.6. Simulation tool has been used to develop a process model to determine the best Reforming technique according to technicality analysis.

Natural gas is sweetened for acid gas removal then preheated and sent into a reformer to react with steam and/or oxygen.

3.3. Simulation of Acid Gas Removal Process

The model consists of an absorber and a stripper. Moreover, a simulation of this unit is modeled by aspen technology and check for the model is achieved as shown in results which the sweet gas contains a traces of H_2S and CO_2 less than the standard requirements.

Table 2. Key simulation results of acid gas removal

Process stream	CO_2 mole fraction	H_2S mole fraction
Gas in	0.013	0.001
Gas out	164 ppm	1.25 ppm
CO_2 out	0.9	0.07

3.4. Simulation of syngas production by different reforming routes

As mentioned earlier, there are currently three reforming technologies used on a commercial scale, namely SMR, POX, and ATR.

3.4.1. Design basis and specifications

Peng Robinson equation of state was used as the property method for the physical property calculations. The reformer is simulated with the ASPEN Plus REquil model which is an equilibrium-based calculation.

3.4.2. Simulation of syngas production by ATR technology

The process flow diagram for ATR (including the acid gas removal process) is shown in Figure 2.

3.4.2.1.Process description

The sweet gas leaves from the top of the absorber column with a temperature of 45ºC and pressure of 63 bar at the flowrate of 2 965 kmol/hr. After reducing the pressure to 30 bar through a valve and preheating the temperature to 455ºC, the sweet gas entered the pre-reformer with steam and recycled CO_2 stream (both at 455ºC and 30 bar). All hydrocarbons heavier than methane are converted to CO and H_2.

The exit temperature of pre-reformer is usually lower than the desired ATR inlet temperature. Thus a heater is needed to increase the outlet stream temperature to a desired level (655ºC in this work). The oxygen stream from the cryogenic air separation unit (ASU) section is blown to the burner of ATR reactor at a temperature of 200ºC.

The ATR converts the methane into syngas by reacting with steam and oxygen; all the reactions reach equilibrium. Because of the large heat released by the partial oxidation reaction, the overall reaction of ATR is exothermic, and the hot syngas leaves the reactor at 1300 K that is cooled to ambient temperature of 28°C for the removal of water and CO_2 then the syngas is ready to enter the FT Reactor.

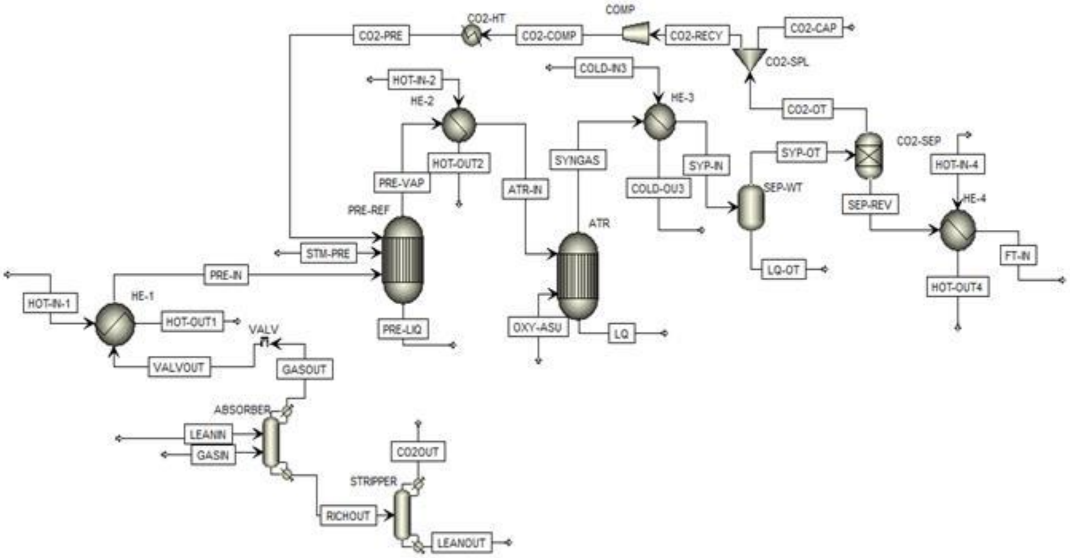

Figure 2. Process flow diagram for ATR

3.4.2. Simulation of syngas production by partial oxidation reformer (POX) Technology

The process flow diagram for POX (including the acid gas removal process) is shown in Figure 3.

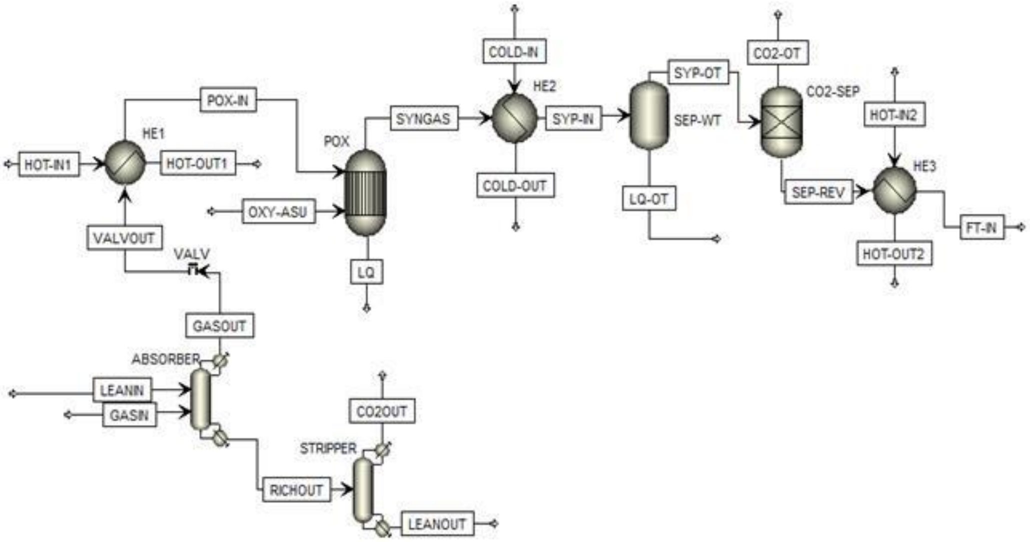

Figure 3. Process flow diagram for POX

3.4.2.1. Process description

The partial oxidation reformer is modeled similarly as in the ATR case with the REquil model, which is driven by an equilibrium-based calculation.

Sweet gas is preheated to 455°C, while oxygen from the air separation unit (ASU) is compressed to the pressure of Reformer. Both components are sent to the partial oxidation reformer where an exothermic reaction takes place. The reformer pressure was set to 30 bar, which also corresponds to industrial practice. The POX converts the methane into syngas by reacting with oxygen.

3.4.3. Simulation of syngas production by steam-methane reformer (SMR) technology

The process flow diagram for SMR (including the acid gas removal process) is shown in Figure 4.

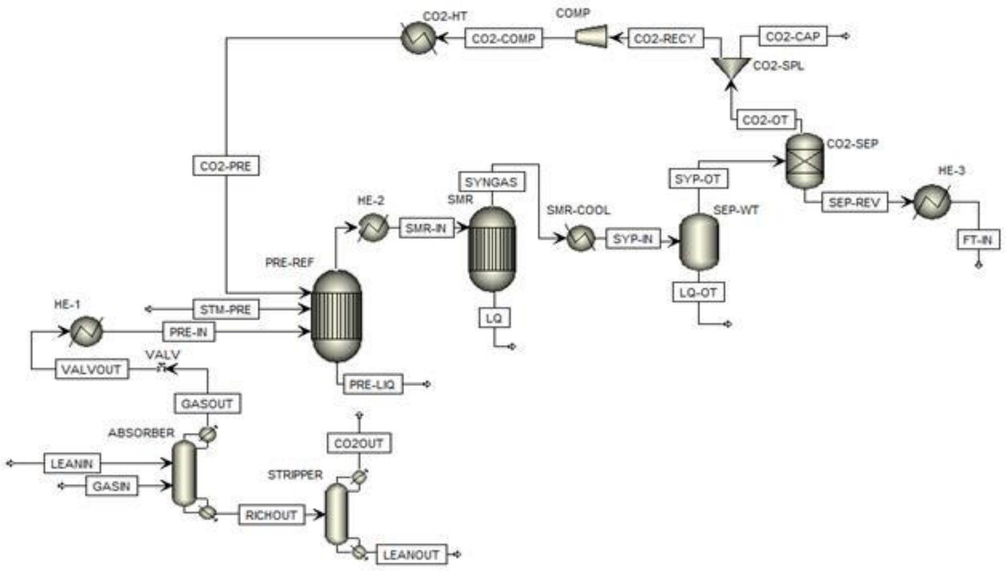

Figure 4. Process flow diagram for SMR

3.4.3.1 Process description

The pre-reformer and steam reformer are modeled similarly as in the ATR case except that the reformer operates at a lower pressure 18 bar concerning the other two cases.

4. Results and discussion

4.1. Key simulation results

The key simulation results are presented in Table 3.

Table 3. The key simulation results of different reforming techniques

Composition	ATR Technique		POX Technique		SMR Technique	
	Mole flow (Kmol/hr)	Mole per-cent %	Mole flow (Kmol/hr)	Mole per-cent %	Mole flow (Kmol/hr)	Mole per-cent %
H_2	5 032	57.2	6 058	65.66	4 932	59.7
CO	2 516	28.6	3 131	33.93	1 670	20.2
CH_4	457	5.3	-	-	1 429	17.3
CO_2	166	1.9	-	-	33	0.4
O_2	-	-	1	0.01	-	-
H_2O	579	6.6	7	0.08	164	2
N_2	30	0.4	30	0.32	30	0.4
Total Flow	8 780	100	9 227	100	8 258	100

The syngas ratio is adjusted to 2 which a low (H_2O/CH_4) ratio and (O_2/CH_4) ratio of 0.53 is adapted for the base case of ATR. The molar ratio of (O_2/CH_4) ratio is adapted to 0.66, and the syngas ratio is 1.93 for the base case of POX. The molar ratio of (H_2O/CH_4) is 0.68, and the syngas ratio is 2.93 for the base case of SMR so the treated gas must be taken for H_2 removal to adjust the H_2: CO ratio to 2; 31% of the H_2 contained in the syngas is remo-ved, along with traces of water, CO_2, and CH_4. The adjusted syngas is heated to 227°C and fed to the FT reactor.

4.2. Effect of parameters on syngas ratio

4.2.1. Effect of temperature on syngas ratio

It can be seen that a reduction of the H_2/CO ratios with increasing temperatures reaching a favorable value of 2 for ATR, as expected, the conversion of the reactants also increased with temperature, with syngas ratio reaching a value of 2.91 for *SMR* as the temperature reaches 1300 K. Hence, the temperature is an important parameter in determining the H_2/CO ratio of the product gas.

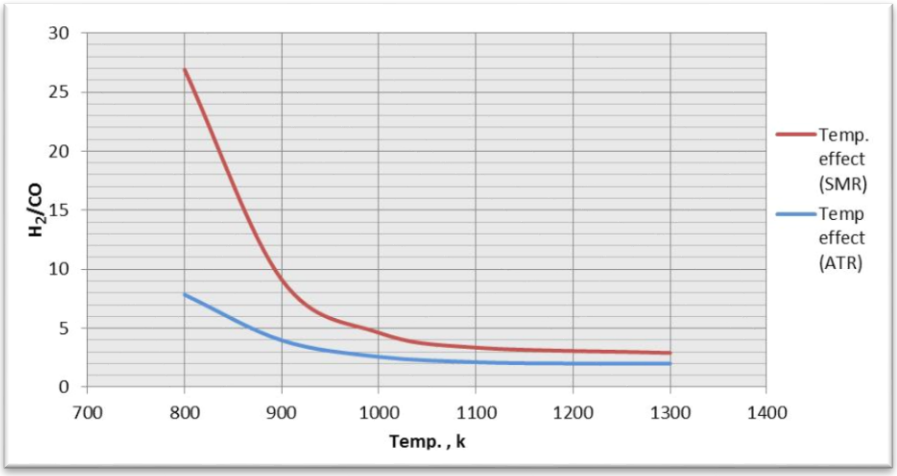

Figure 5. Effect of temperature on syngas ratio

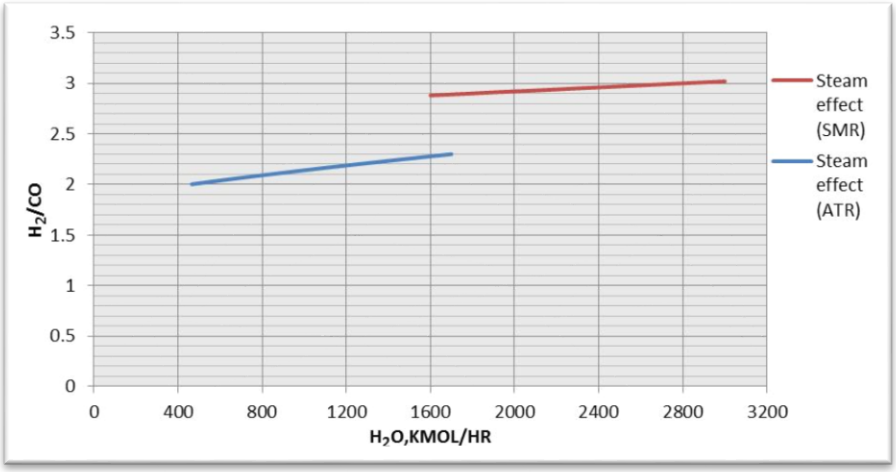

Figure 6. Effect of steam on syngas ratio

4.2.2. Effect of steam on syngas ratio

It can be seen that increasing of the H_2/CO ratios with increasing steam. The suitable syngas ratio is 2.91 at a steam value of 1890 kmol/hr which represent H_2O/CH_4 of 0.68 for SMR technique. Hence, the steam is an important parameter in determining the H_2/CO ratio of the product gas.

4.2.3. Effect of oxygen on syngas ratio

It can be seen that increasing of the H_2/CO ratios with increasing oxygen values up to a certain value of oxygen which over this value a syngas ratio still constant for POX Technique. Hence, the oxygen value is an important parameter in determining the H_2/CO ratio of the product gas.

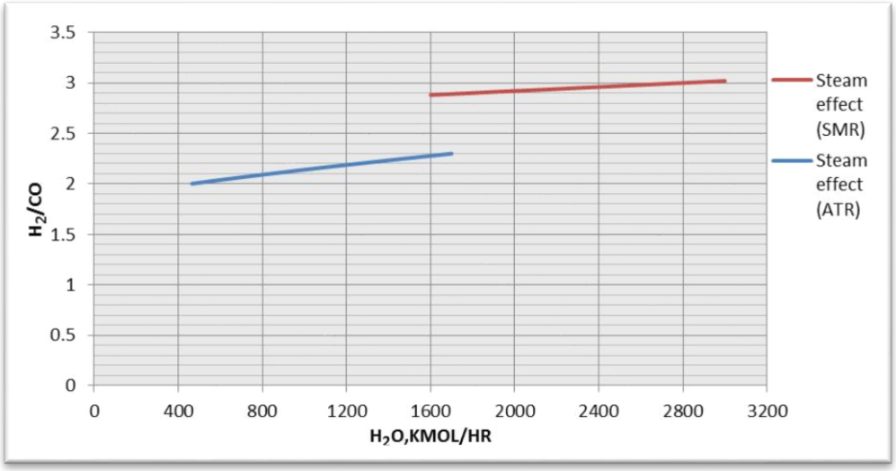

Figure 7. Effect of oxygen on syngas ratio

4.3. Comparison and analysis of three syngas production techniques

The choice of reforming technology is determined by balancing between the characteristics of each one. The product syngas composition from each reforming technologies can be manipulated by altering various process conditions and/or by means of additional process steps as shown in Table 4.

Table 4. Simulation parameters for each syngas configuration

Simulation parameter	ATR	POX	SMR
Operation conditions			
Operating pressure [bar]	30	30	18
Operating Temperature [K]	1300	1300	1300
Steam to carbon ratio	0.17	-	0.68
Oxygen to carbon ratio	0.53	0.57	-
Results			
Syngas ratio	2	1.93	2.91

From Table 4, SMR Technique is not ideally suited to GTL plants. This is due to the fact that FT. Synthesis requires an H_2/CO ratio of about 2, which is lower than that obtainable with SMR which has a value of 2.91. For a complete reaction of conversion of methane to syngas, it is needed to a large amount of steam, and the reaction is endothermic. POX Technique has a syngas ratio slightly lower than that is required for FT synthesis which has a value of 1.93. ATR Technique has a syngas ratio value of 2 which is typically suited to FT synthesis

4.4. The additional study focused on ATR and POX Techniques

The most favorable syngas ratio for the cobalt-based catalyst is a value of 2. The additional study focused on ATR Technique is executed and also focused on POX which has a value of syngas ratio closed to the desired value.

4.4.1. Greenhouse gas emissions

Table 5. The CO_2 emissions of feed and product streams

Stream Type	ATR Technique		POX Technique	
	flow(kg/sec)	CO_2e (kg/sec)	flow(kg/sec)	CO_2e (kg/sec)
Total feed	18 0193.1	309	126 145.8	309
Total product	18 0193.1	53.4	126 145.8	0.56

4.4.2. Process heat duty

There is a majority of heat was produced which may be used for power cogeneration. Also, when a simulation model completed the F-T reactor produces a higher amount of heat. The process net heat that is excess in ATR Technique = 1.26E+08 Btu/hr and in POX = 1.56 E+08 Btu/hr.

Table 6. Heat duty for each unit

ATR Technique		POX Technique	
Units	Enthalpy (kJ/hr)	Units	Enthalpy (kJ/hr)
Heat 1	6.36E+07	Heat 1	6.36E+07
Heat 2	4.39E+07	Heat 2	5.371 E+07
Heat 3	5.07E+07	Cool 1	-2.822E+08
Heat 4	3.61E+04	-	-
Cool 1	-2.91E+08	-	-

4.4.3. Heating and cooling utilities

As thermal pinch analysis is conducted to determine the potential heat that could be exchanged among the hot and cold streams. The grand composite curves for ATR and POX are shown in Figure 8, 9.

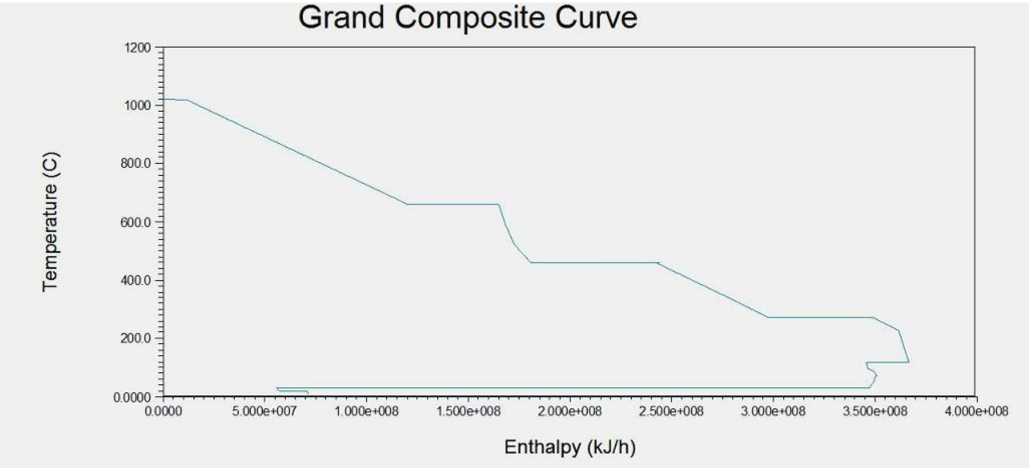

Figure 8. The grand composite curve of ATR

From ATR diagram it indicates that after heat integration, the minimum cooling utility is 68.1million Btu/hr and the minimum heating utility is zero. From POX diagram the minimum cooling utility is zero, and the minimum heating utility is 1.49 million Btu/hr. The savings for heating and cooling utilities resulting from heat integration are listed in Table 7.

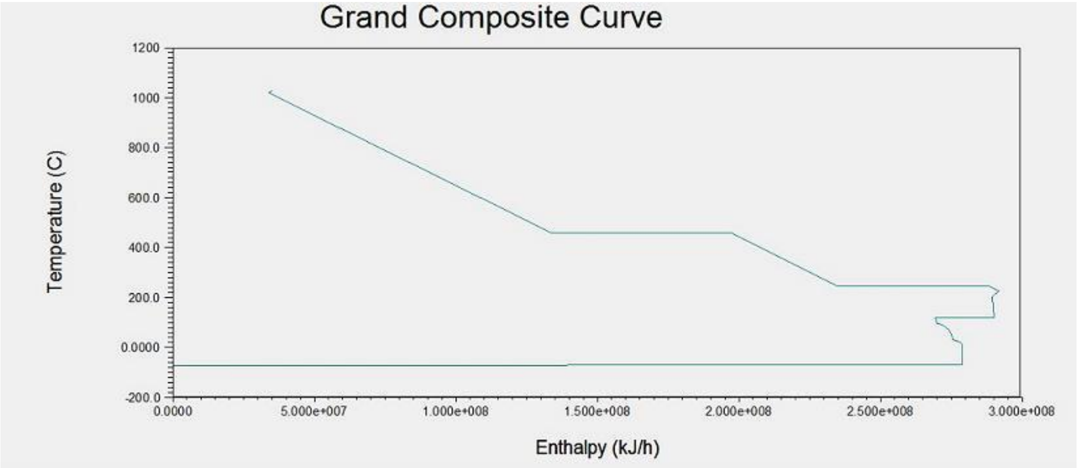

Figure 9. The grand composite curve of POX

Table 7. Heating and cooling utility savings

	ATR technique		POX technique	
	Hot utilities (kJ/hr)	Cold utilities (kJ/hr)	Hot utilities (kJ/hr)	Cold utilities (kJ/hr)
Before integration	8.68E+07	3.13E+07	5.12E+07	10.31E+06
After integration	0	7.18E+07	1.57E+06	0
Savings ($/yr)	2,957,764	1,043,276	6,761,871	127,238

5. Conclusion

A gas to liquid process (GTL) based on different reforming techniques has been simulated and optimized by Aspen Plus. The parameter study conducted through the use of case studies was found to give the best one. The Results of The different reforming techniques are conducted and compared, and the following is concluded:

- The results for the SMR base case GTL process indicate that technologies for monetizing stranded natural gas via the SMR route would be intrinsically disadvantaged by the net requirement for Syngas ratio and the reaction is strongly endothermic.
- POX Technique has the largest amount of syngas, a small content of CO_2 emissions and a large amount of saving heat as compared with ATR Technique but syngas ratio is slightly smaller than the desired value.
- ATR Technique needs to amounts of both steam and oxygen while POX needs to only oxygen and total amounts ATR need are more than required for POX Technique.
- The choice between ATR and POX Techniques is based on availability and flexibility and POX is the best reforming one and it has to be expanded.

References

[1] Hall KR. A new gas to liquids (GTL) or gas to ethylene (GTE) technology. Catal. Today, 2005; 106 (1-4), 243-246.
[2] Keshav TR, Basu S. Gas-to-liquid technologies: India's perspective. Fuel Process. Technol. 2007; 88 (5), 493-500.
[3] Senden MMG, Martens FJA, Steenge WDE, Nagelvoort RK. Shell's GTL: Its Technology and Design, Its Operation and Products. International Petroleum Technology Conference, Doha, Qatar, 2005.
[4] Fiato RA, Sibal PW. ExxonMobil's Advanced Gas-to-Liquids Technology - AGC21. SPE Middle East Oil and Gas Show and Conference, Kingdom of Bahrain, Society of Petroleum Engineers, 2005.
[5] Bassey ME. Economic viability of a floating gas-to-liquids (GTL) plant. PhD diss., North-West University, 2007.

[6] Muonagor CM. An Appraisal of the Economic Viability Of Producing Synthetic Diesel From Natural Gas, Nigeria. Pet Coal, 2013; 55(4): 338-350.
[7] Panahi M, Rafiee A, Stogestad S, Magne H. A natural gas to liquid process model for optimal operation. Industrial & Engineering Chemistry Research, 2012; 51: 425–433.
[8] David AW, Chikezie N, Brian FT., Gas-to-liquids (GTL): A review of an industry offering several routes for monetizing naturl gas. Journal of Natural Gas Science and Engineering, 2012; 9: 196 – 208
[9] Dennis L. Real Fischer-Tropsch Technology for Real Projects. Howard Weil Conference, Rentech. Inc, Houston, TX, U.S.A., 1999.
[10] Heydenrich P. Sasol's Slurry Phase Process - The Challenge of Putting It Together. AIChE Spring Meeting, Houston, TX, U.S.A., 1999.
[11] Bakkerud PK. Upadate on synthesis gas production for GTL. Catalysis Today, 2005; 106: 30-33.
[12] Christensen TS, Primdah I. Improve syngas production using autothermal reforming. Hydrocarbon Processing, 1994; 73(3): 39-46.
[13] Christensen TS, Østberg M, Bak Hansen J.-H. Process Demonstration of Autothermal Reforming at Low Steam-to-Carbon Ratios for Production of Synthesis Gas. In AIChE Annual Meeting, Reno, USA, 2001.
[14] Ernst WS, Venables SC, Christensen PS, Berthelsen AC. Push synthesis gas production limits. Hydrocarbon Processing, 2000; 79(3): 100.
[15] Rhamim II. Gas-to-liquid technologies: Recent advances, economics, prospects, 26th IAEE Annual International Conference, Prague, Houston, TX, U.S.A., 2003.
[16] Silberova B, Venvik HJ, Holmen A. Production of hydrogen by short contact time partial oxidation and oxidative steam reforming of propane. Catal. Today, 2005; 99(1-2): 69-76.
[17] Korup O, Goldsmith CF, Weinberg G, Geske M, Kandemir T.;, Schlögl R, Horn R. Catalytic partial oxidation of methane on platinum investigated by spatial reactor profiles, spatially resolved spectroscopy, and microkinetic modeling. J. Catal., 2013; 297: 1-16.
[18] Wood DA, Nwaoha C, Towler BF. Gas-to-liquids (GTL): A review of an industry offering several routes for monetizing natural gas. J. Nat. Gas Sci. Eng., 2012; 9: 196-208.
[19] Steynberg A, Dry M. Fischer-Tropsch Technology; Elsevier Science: Amsterdam, 2004.
[20] Wilhelm DJ, Simbeck DR, Karp AD, Dickenson RL. Syngas production for gas-to-liquids applications: technologies, issues and outlook. Fuel Processing Technology 2001; 71(1-3): 139-148.
[21] Butwell FB, Perry CR. Performance of Gas Purification Systems Utilizing DEA Solutions. In Laurence Reid Gas Conditioning Conference, 1975.

To whom correspondence should be addressed: Dr. Mohamed A. Ayad, Mining and Petroleum Engineering Department, Faculty of Engineering, Al-Azhar University, Cairo, Egypt, eng_m.ali2012@yahoo.com

Petroleum and Coal

Article **Open Access**

ASPHALTENE MODELING BY SARA TEST RESULTS, AN INTRODUCTION OF SIMPLE AND ACCURATE EMPIRICAL MODEL

Mahdi Hasanvand[1]*, Mohammad Shadadeh*[1]*, Mohammad Ali Ahmadi*[2]

[1] *Research Institute of Petroleum Industry, Tehran, Iran*
[2] *Petroleum University of Technology, Ahvaz,Iran*

Received April 11, 2018; Accepted June 27, 2018

Abstract

Asphaltene precipitation problems cause millions $ of cost annually. Reservoir skin effect, Well inflow capacity decreasing, Oil flow decreasing, and well column blockage and production facilities break-out are examples of asphaltene related problems. The basic step to control and solve these problems is accurate prediction of asphaltene molecule precipitation. Asphaltene content oil is experience different thermodynamic conditions in the flow path from underground original reservoir zone to oil and gas separation facilities. It is obvious that thermodynamic instability of asphaltene is related to oil composition and its fraction entities. Although the direct effect of different fraction of crude oil (Saturate, Aromatics, Resins and Asphaltene (SARA)) may be unclear but by increasing the experimental data of precipitation an empirical model can be developed. The developed empirical model is the first model to predict the weight percent of asphaltene in a wide range of temperature and pressure (130-250 ^{0}F and 600-8600 Psi). The correlation is proposed based on 84 precipitation data point of 10 different crude oils. The least square of errors (R^2) of correlation is more than 93% which is so accurate rather than common thermodynamic models of asphaltene precipitation.

Keywords: .

1. Introduction

Asphaltene related problems are going to increase every day, as the oil fields production life becomes more, and reservoirs become more depleted. The cost of wellbore tubing washing, oil production delay and environment damages are dramatic tragedies associated with asphaltene precipitations. So the best solution here is to avoid asphaltene precipitation and deposition rather than thinking of removal methods.

There are different ways to avoid asphaltene precipitation such as inhibitor and solvent injection, thermal ways like heating and ultrasonic methods and finally making conditions out of Asphltane Deposition Envelope (ADE). In all of this ways, the knowledge of asphaltene thermodynamic behavior is essential. To optimize these processes, it is necessary to have accurate predictions of the amount of asphaltene precipitation as a function of the amount of solvent, temperature, and pressure [1].

The thermodynamic behavior of asphaltene molecule is unique and vague from an oil field to another. The common trend is precipitating in a pressure above bubble point as onset pressure, increasing asphaltene precipitation to bubble point and deceasing after that. The temperature trend is vague and it is believed that in heavy crude oils by increasing the temperature the asphaltene precipitation increased and in light crude oils the trend is contradict. Some different cases are reported in literature [2-3].

To modeling and simulating asphaltene behavior some experiments are defined. Onset pressure of this molecule is detected by Near Infra-Red ray in solid detective suspended equipment [4]. Additionally, asphaltene weight precipitation change by pressure is detected by High Pressure High Temperature (HPHT) Filtration device and associated IP143 tests [5] or by Visual

HPHT microscope [6]. All of these experiments are special, time consuming and done in high pressure and temperature conditions. The results of these Laboratory studies are used to modeling of molecule behavior. But the common models have failed to produce a consensus about the physical state of asphaltenes in crude oil. Most of these models need special properties such as molecular weight, enthalpy of fusion, volume shift and so on of asphaltene molecule which is not identical during precipitation, so it makes procedure more problematic [7-9]. The number of variables is another problem of common models of asphaltene behavior[10]. A list of common models of asphaltene behavior is taken in table 1. All together it can be said that estimates of models to asphaltene properties are more speculative than conclusive [9,11]. This is mainly due to the extreme chemical complexity of both the asphaltenes and crude oil [12-13].

So there are two problem in asphaltene modeling, the hardship of laboratory experiment and the ease of procedure and precise of thermodynamic model.

Table 1. Asphaltene Mmain models, type, properties, advantages and disadvantages

Model name	Proposer	Type	Summary
Hirschberg model	[14]	Based on Flory (1953) lattice theory.	The parameters are mole fraction, molar volume, and solubility parameter for each individual component. The entropy of mixing of mono-disperse polymer-like molecules can be accounted by using Flory (1953) lattice theory. He investigated the effect of temperature and pressure on the asphaltene color and precipitation.
Micellization Models	[10]	Based on minimum Gibbs Energy theory.	The liquid phase Consists of a mixture of monomer asphaltenes, monomer resins, asphalteneresin micelles, and Other oil species. Total Gibbs Energy of system is calculated by fugacity calculation. a large number of parameters such as interaction parameters, the size of the micellar core, the average characteristic length of molecules, the interfacial tension, the thickness of micelle, and the adsorption energy, are needed in the model
Statistical Thermodynamic model	[36]	Based on Statistical Associating Fluid Theory (SAFT)	Asphaltenes are assumed to be large spherical molecules with multiple association sites that can bind to other asphaltenes and resins. An advantage of the SAFT approach is that the complexity of the problem can be significantly reduced by formulating molecular theory. Furthermore, the model can account for the effects of resins addition and asphaltene solvent addition on the solubility of asphaltenes.
Oligimerization Model	[37]	Based on Colloidal theory.	Asphaltene association was modeled analogous to linear polymerization. This model is very complex and need lots of parameters for modeling. It can fit the molar mass data and solubility so.
Developed Oligimerization Model	[1]	Based on Colloidal theory.	This model requires two fit parameters (the association constant and molar ratio of terminator to propagator) and two estimated parameters (the monomer molar masses of terminators and propagators). The model can predict the effect of carbon number precipitant, temperature, solvent and resin concentrations.
Micellar Models	[38]	Based on surfactant behavior.	Asphaltene is a very large structure that made of several monomers it can act as a surfactant, this model explain micellar structure for asphaltene. Akbaezadeh 2005 showed neither molar mass nor IFT variation show the existence of CMC. Therefore, asphaltene cannot have the micellar structure.
Regular Solution Model	[8]	Based on vapor-liquid-liquid equilibrium.	The model uses the concept of material balance by coupling with thermodynamic model. The separate VLE and LLE can be used to find the composition of different fractions (vapor, asphaltene, crude oil). By some assumption the predict precipitation of asphaltene in different pressure and temperature.

Our alternative way is modeling of asphaltene behavior by the results of concentration of Saturates, Aromatics, Resins and Asphaltene fraction of crude oil (SARA Test). This test is an easy handling experiment and is a standard of heaviness of crude oil. This experiment includes titration or addition of solvents and is a basic experiment that most of models about asphaltene precipitation are using. These tests are mostly conducted in atmospheric pressure or low pressures.

In this work we present a correlation model based on results of SARA test of more than 10 different crude oils. This model is a predictive empirical correlation on asphaltene precipitation behavior due to reduction or increase of pressure. The model has appropriate results for reservoir natural depletion cases or in reverse during secondary recovery when trying to increase reservoir pressure for improves recovery without considerable change in temperature.

Unfortunately in this study we could not do any predictions about onset of asphaltene precipitation due to lack of experimental data, however we believe that we can have a rough estimate which is not too bad to have an estimate of onset pressure.

2. Thermodynamic modeling of asphaltene precipitation

Today still there is not a unique predictive model that could describe asphaltene behavior at different conditions for different oil samples. This is due to complexity and nature of asphaltene and crude oils [12]. Different thermodynamic models have been proposed to predict asphaltene phase behavior. Precipitation is the formation of an asphaltene solid phase (or possibly dense liquid) due to change in the thermodynamic equilibrium between the oil components. Three general categories of thermodynamic models are 1-EOS approach, 2-Polymer solution models and 3-Colloidal models. As models become more complicated sometimes accuracy improves, but generally new parameters introduced are not available in the literature and should be determined experimentally for each sample, and this will limit their application.

An earlier model [14], which has been used for predicting asphaltene solution data by several investigators [15] employs the Flory - Huggins model of polymer solubility [16]:

$$\ln \phi_{a,\max} = \left(V_a / V_I - 1\right) + \left(\phi_a - \chi \phi_I^2\right) \ldots \qquad (1)$$

where $\phi_{a,\max}$ the maximum volume fraction of asphaltene solute; V_a and V_I are the molar volume of asphaltene and liquid solvent, respectively; χ is the Flory interaction parameter and ϕ_I is the solvent volume fraction. The Flory interaction parameter, χ, can also be estimated from:

$$\chi = V_a / RT\left(\delta_a - \delta_I\right)^2 \ldots\ldots \qquad (2)$$

The two parameters which are essential in the performance of this model are the molar volume and solubility parameter of the asphaltene components. The molar volume is dependent on the molecular weight and the density. Density is a measurable parameter whereas the molecular weight is much more difficult to measure with any degree of accuracy. Most methods for the determination of molecular weight produce data that show a dependence on the ability of the asphaltenes to aggregate [17]. The solubility parameter is depended to aggregation and this dependency makes the results of modeling inexact.

The simplest model for precipitated asphaltene is the single-component solid model that was tried by [18] and [19]. The precipitated asphaltene is represented as a pure solid while the oil and gas phases are modeled with a cubic EOS [20]. The fugacity of the pure solid is given by:

$$\ln f_s = \ln f_s^o + \frac{v_s\left(P - P^o\right)}{RT} \ldots\ldots\ldots \qquad (3)$$

where f_s^o is reference solid fugacity and v_s is solid molar volume.

The model basically uses the same calculation as vapor liquid equilibrium calculation, but here it uses another flash calculation between solid and liquid. It could be assumed that solid liquid has an effect on liquid vapor equilibrium or not. The method uses EOS parameters of heavy or plus fraction as tuning parameters to predict the experimental data. Large number of tuning parameters limits the ability of the model to predict different condition. This model is not able to predict the effect of temperature on asphaltene precipitation.

Colloidal model for prediction of asphaltene precipitation has been used as a model which has a focus on effect of resin on asphaltene precipitation and deposition. This model is presented by [21]. The model is based on the assumption that asphaltenes exist in the oil as solid particles in colloidal suspension, stabilized by resins adsorbed on their surface. It is also assumed that the short range intermolecular repulsive forces between resin molecules adsorbed on different asphaltene particles keep them from flocculating. This repulsive force can be overcome or neutralized by mechanical (large pressure drop, agitation) or electrical (opposing streaming potential) means.

The modeling of precipitation needs to calculate the concentration of the resins in the liquid phase. In the absence of the equilibrium constant data for resin adsorption on the surface of asphaltene particles for calculating the critical chemical potential of the oil mixture, implementation of the proposed model will require some experimental data of the onset of asphaltene deposition for fitting purposes. The model can then be used to predict the onset at different liquid compositions, provided that the resin and asphaltene fractions remain as they were when the fitting point was determined.

All above models are consuming time, have try and error steps, needs expensive and time consuming experiments background and have many variables.

3. Data gathering

The SARA separation was originally designed for characterization of residuals [22]. The heavy end of a crude oil can be separated into four distinct fractions namely saturates, aromatics, resins, and asphaltenes using the experimental SARA procedure. SARA analysis separates the sample in saturated, aromatics, resins, and asphaltenes compounds through the action of n-alkane solvents, toluene and dichloromethane, and the interaction between the oil with a stationary phase. The SARA analysis starts with the precipitation of asphaltenes in n-alkane solvents such as pentane or heptane. Subsequently, the de-asphalted oil is separated by chromatography methods with the help of different stationary phases and solvents of varied polarity [23-25].

A crude oil usually contains a considerable amount of volatile material that must be removed prior to performing SARA separation of the crude oil. Although there are different and accurate method to investigate the SARA weight fractions of crude oil [26-27], Vazquez and Mansoori [28], proposed a simple, inexpensive, forward standard method to separate SARA fractions based on liquid absorber chromatography. This is accomplished by performing a vacuum batch distillation at 10 mm Hg and room temperature until the weight of the residue reaches a constant value.

The first fraction to be separated from the vacuum residue is the nC_5-asphaltenes. The 0.2 micro meter filtrate collected from the separation of the nC-$_5$ asphaltenes is commonly known as maltenes. It contains the remaining three fractions, saturates, aromatics and resins. These three fractions are separated using open-column liquid chromatography.

Saturate hydrocarbons in present of n-pentane as solvent phase, are not absorbed on activated silica under the conditions specified. The saturate fraction of the oil is eluted from the column with 1/L of n-pentane volume at 5 mL/min. The solvent is removed using a rotary vacuum evaporator to recover saturates fraction.

Aromatic hydrocarbons are adsorbed on activated silica in the presence of n-pentane, and desorbed by toluene after removal of the Saturates under the conditions specified. The aromatic fraction of the oil is eluted from the chromatographic column using toluene at 5 mL/min. The resin fraction of the oil is eluted from the chromatographic column using a 90/10 toluene/MeOH solution at 5 mL/min. This fraction is reported as wt.%. prepared Silica gel column and separation of maltene fractions during SARA test.

This procedure is done for 10 crude oil sample before HPHT filtration to develop Asphaltene Deposition Envelope (ADE). The results of SARA test and specific properties of crude oils are presented in Table 2.

Table 1. SARA test results of 10 crude sample and their specifications such as GOR, Ps and density

Crude No	Saturated wt.%	Aromatic wt.%	Resin wt.%	Asphaltene wt.%	GOR Scf/Stb	Saturation pressure, psia	Density, g/cc
1	63.79	31.67	2.61	0.89	1300	4260	0.829
2	60.49	33.84	3.23	2.11	1100	3290	0.865
3	55.14	30.73	10.88	3.25	1120	2980	0.861
4	54.67	28.89	12.66	3.8	1080	2513	0.857
5	52.49	41.04	5.48	0.99	1037	6267	0.898
6	52.07	35.87	8.93	3.17	900	3045	0.865
7	50	25	21	3.9	654	1963	0.873
8	44.84	34.83	12.21	8.10	240.43	1067	0.987
9	30.1	42.1	13.36	13.75	450	1722	1.076
10	26.82	67.69	4.47	0.66	540	1524	1.103

After SARA test, the high pressure high temperature set up was prepared for measuring Asphaltene Precipitation in different thermodynamic conditions. The Whatman paper filter of 0.2 micrometer diameter was pert by helium gas between two thick steal cylinders. After crude oil stabilization in specific thermodynamic condition, the crude oil is transported through paper filter and the asphaltene content of filtrated oil is measured by IP143 procedure. The difference of asphaltene contents before and after filtration is equal to asphaltene precipitation in specific temperature and pressure. This test is done and repeat for each crude oil in reservoir temperature and 8 different pressures. At the final, 84 data point is resulted and reported in 8 series: temperature, pressure, saturates, aromatic, resins, asphaltenes content, and asphaltene precipitation wt% .

4. Methodology

Genetic programming (GP) [29] is an exciting method to model various petroleum engineering issues. The major benefit of the GP-based models against other intelligent based solutions like as artificial neural network, fuzzy logic and least square support vector machine (SVM) is their capability to create estimation correlations without presuming first form of the existing correlation like as previous work of the authors [30-31]. Gene expression programming (GEP) is a new division or branch of Genetic Programming which evolved by Ferreira [32]. This approach has capability to generate computer programs with various sizes and shapes while conventional Genetic Programming and other intelligent tools like as fuzzy logic are restricted to fewer engineering areas [30-31].

Genetic Programming is a branch of genetic algorithms (GAs) which is a modern regression approach with a giant capability to automatically develop computer programs. It worth mentioning that, the evolutionary algorithm followed by the GP procedure is inspired from the Darwinian theory of natural collection [30].

Based on symbolic regression experiments by Koza in 1992, Genetic Programming (GP) was introduced and developed [29]. The major difference between the original Genetic Algorithm (GA) and Genetic Programming (GP) methods is that the developing programs in Genetic Programming (GP) are parse trees rather than fixed-length binary strings in conventional Genetic Algorithm (GA) [30]. A typical pc programme based on the Genetic Programming (GP) formula is demonstrated in Figure 1, [29,31] .

Gene expression programming (GEP) is a new subarea of Genetic Programming (GP) was firstly introduced and evolved by Ferreira, [30,32]. Gene expression programming (GEP) consist Function set, terminal set, fitness function, control parameters, and termination condition which are the main parameters of the addressed method. The generated outcomes of Genetic Programming (GP) are depicted as tree topologies and presented in a functional programming language [29-30]. It should be noted that the genetic operators perform on the chromosome level in GEP approach which leads to an extreme simplification in the generation of genetic diversity [30]. As known Gene Expression Programming (GEP) has a multi-genic nature. Therefore; more complicated models with various sub-models can be created through the evolutionary process. A gene in Gene Expression Programming (GEP) is comprised a list of symbols while the addressed symbols are parameters of function or terminal sets. A typical GEP gene is illustrated as following as [30]:

+./.×.√.^.5.X.Y ……… (4)

where X, Y and 5 are elements of the function set; +, /,√, × and ^ are the terminal nodes, and "." is the element separator for user friendly reading [30]. The above addressed expression is called Karva notation or K-expression [32]. A K-expression can be demonstrated by a diagram as an Expression Tree (ET) while the first position in the K-expression stands for the root of the addressed Expression Tree (ET) [30]. i.e. example, the pure mathematical equation $\sqrt{\frac{(X\times Y)}{(X^Y)}}$ can be easily demonstrated as an expression tree (ET) which depicted in Figure 2, with the Karva language illustration of */Q ^ X Y (Q represents the square root function).

It worth mentioning that, the size of the relevant Expression Trees changes through the GEP evolutionary process while the valid length of each expression is same to or less than the length of the gene [30].

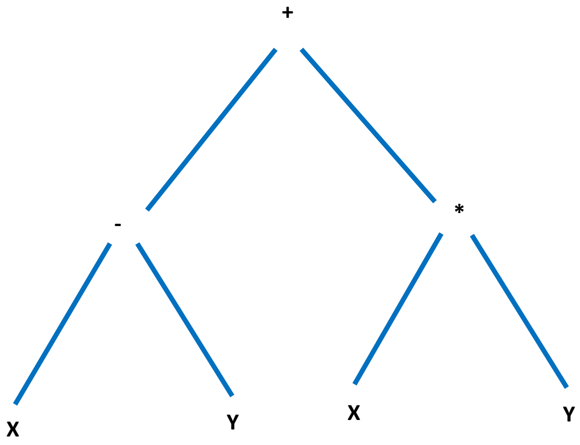

Figure 1. A typical computer LISP program in the GP algorithm represented as a parse tree (expression tree), which stands for the algebraic expression [(X-Y)+(X*Y)] by a two-gene chromosome

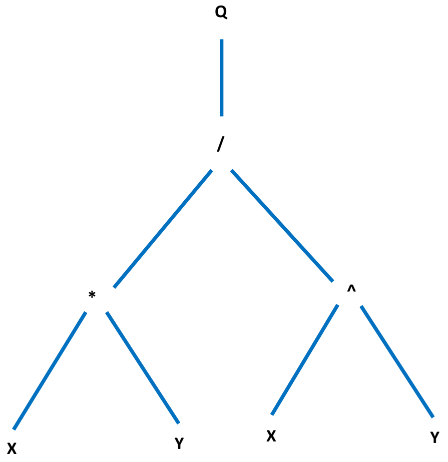

Figure 2. A typical Karva Language program in the GEP strategy, which represents the algebraic expression [$\sqrt{\frac{(X\times Y)}{(X^Y)}}$] by a two-gene chromosome

5. Results and discussion

One of the exciting advantages of the GEP method [33] is that there is no need to take on special functional topologies to gain the best prediction/estimation of the real measured data. As a result, the most integrate and robust and effective correlation topologies consisting of the most efficient independent parameters are figured out through the evolutionary algorithm itself [34]. As illustrated earlier in this text, no accurate and integrate model or correlation exist for prediction of amount of asphaltene precipitation of crude oil samples. The majority of the amount of asphaltene precipitation of the crude oils can be correlated by the GEP principle parameters such as saturates, aromatics and resins. In this paper, it is firstly assumed that the RI can be formulated as the functions of the addressed parameters as follows:

Amount of asphaltene precipitation =*f(*saturates, aromatics, resins, . . . *)* (5)

Based on the above assumption and GEP procedure which demonstrated in Figure 3, the required correlation was developed. Results of the evolved correlation discussed in detail in next section.

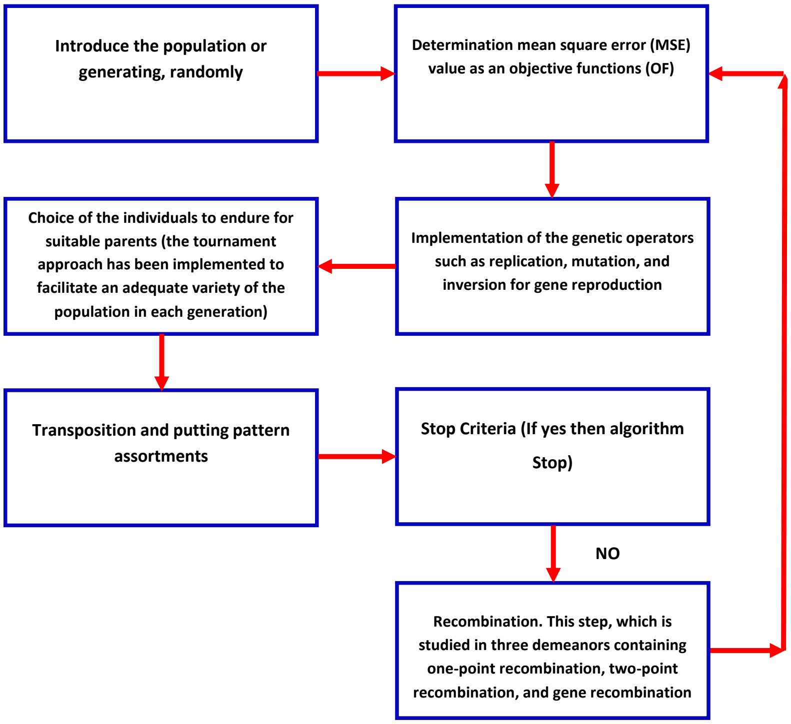

Figure 3. Chart box of the gene expression programming (GEP)

The asphaltene weight percent for 9 crude oils in reservoir temperature and different pressures have been resulted by HPHT filtration experiment. For crude oil number 10 the lower and upper onset pressures for 4 different temperatures have been got, and finally 84 different data point is developed for all 10 crudes. Each data point has 7 data includes Saturates wt%, Aromatic wt%, Resin wt%, Asphaltene wt%, Pressure, Temperature and finally precipitated Asphaltene wt%. The results of crudes oil are quantitatively follows known trend of pressure effect in literatures [35]. In high pressures by decreasing the pressure the asphaltene precipitation increased to reach a summit on bubble point. After that the amount of precipitated asphaltene decreased to reach the lower onset pressure. As it is shown in figure 6 all crude oils except crude number 8 follow this trend so this exception may be because of laboratory errors and we can ignore this test.

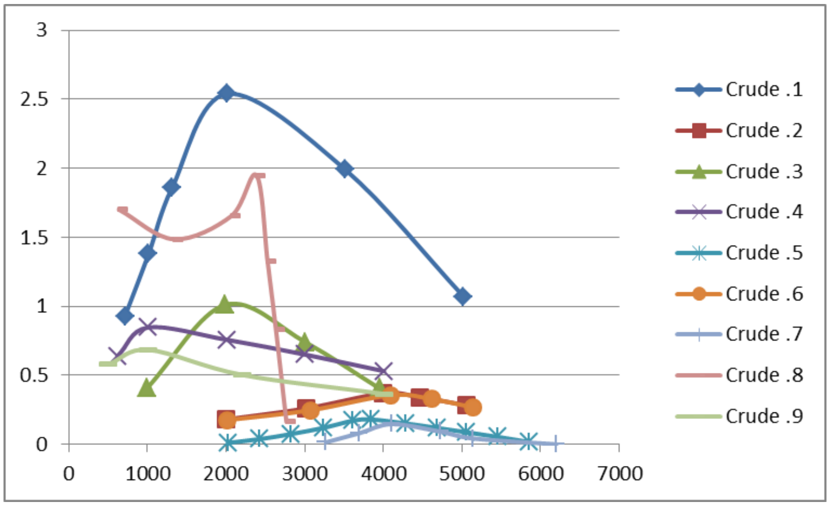

Figure 4. Asphaltene precipitation weight percent vs. pressure for different crude oils

The results of filtration and SARA tests are used for developing an algorithm to predict the asphaltene precipitation. The following correlation is the best match for the data points. In this correlation the input data are SARA fractions, temperature and pressure and in other hand Asphltene weight precipitation is the output.

$$\text{Asp Precipitation wt\%} = 0.048694 - 3.61035\times B\times A + 0.923329\times A^2 + 19.3559\times B\times C$$

$$-7.96925\times C^2 + 0.590678\times B - 8.37478\times B^2$$

$$A = 0.164042 - 0.0160959\times R\times As - 6.62471\times 10^{-6}\times R\times P + 0.00555145\times R^2 + 0.0193652\times As^2$$

$$B = -0.0242789 + 5.29966\times D^2 + 0.574105\times E - 5.34385\times E^2 + 0.530724\times F$$

$$C = -0.257337 + 0.13385\times R + 0.0149444\times R\times D + 0.182241\times R\times G - 0.0107369\times R^2$$

$$+1.22226\times D\times G - 0.558429\times G - 1.77068\times G^2$$

$$D = -38.621 + 1.16607\times S + 0.00405818\times A\times S - 0.156774\times S\times As - 0.00814875\times S^2 - 0.699435\times A$$

$$-0.0578714\times A\times As + 0.0110473\times A^2 + 12.342\times As - 0.285922\times As^2$$

$$E = -4.33206 + 0.134702\times S - 0.00867193\times S\times R - 0.0266438\times S\times As - 0.000960369\times S^2$$

$$+0.404947\times R + 0.00290696\times R^2 + 1.78279\times As - 0.0695639\times As^2$$

$$F = -3.1253 + 0.134334\times S - 0.00629117\times S\times R - 0.001273119\times S^2 + 0.268575\times R$$

$$-1.69761\times 10^{-6} R\times P + 0.00465625\times R^2 + 2.1573\times 10^{-5} P$$

$$G = -0.913686 + 0.119983\times S - 0.000701052\times S\times T + 2.26418\times 10^{-6} T\times P + 6.6136\times 10^{-5} T^2$$

$$-0.000644618\times P + 1.58863\times 10^{-8} P^2$$

which A, B, C, D, E, F and G are variable coefficients of S, Ar, R, As, P and T. S, Ar, R, As, P and T are Saturates, Aromatic, Resins, Asphaltenes, Pressure and Temperature respectively.

The results of comparison between estimated and actual data are depicted in figure 5. The least square average of correlation is $R^2=0.9384$.

The deviation of correlation data and actual data is presented in figure 6. The figure shows there is an accurate prediction in correlation results.

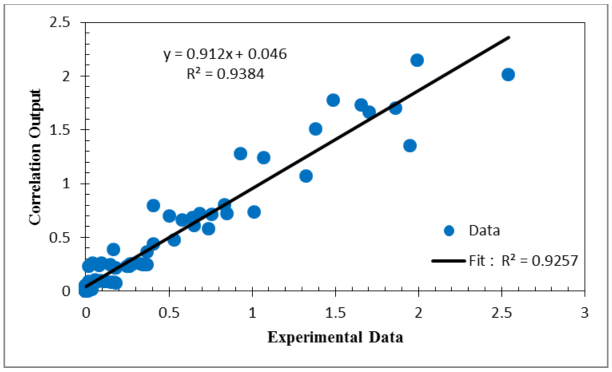

Figure 5. Comparison of correlation output vs. experimental data

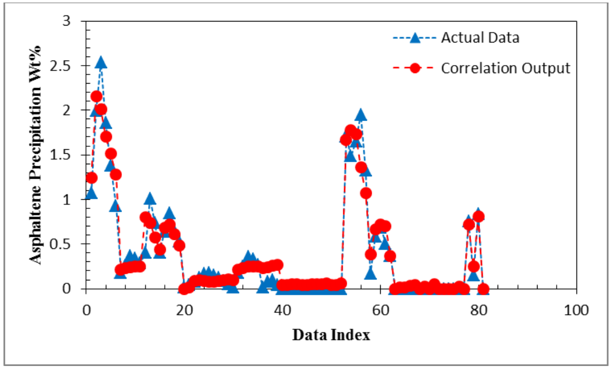

Figure 6. Predicted data and actual data of asphaltene precipitation

Before this study the SARA fraction is routinely used for qualitative analysis of stability of asphaltene in crude oils at reservoir conditions. De-Boer, proposed 4 plots based on SARA results to predict stability of asphaltene molecules [36]. But in this study it is proved that SARA results could predict asphaltene precipitation quantity rather than qualitatively analysis.

6. Conclusion

In this study a novel empirical correlation to model asphaltene precipitation based on SARA fraction test is developed. The developed empirical model is the first model to predict the weight percent of asphaltene in a wide range of temperature and pressure (130-250^{0}F and 600-8600 Psi). The correlation is proposed based on 84 precipitation data point of 10 different crude oils. The least square of errors (R^2) of correlation is more than 93% which is so accurate rather than common thermodynamic models of asphaltene precipitation.

References

[1] Agrawala M, Yarranton HW. An Asphaltene Association Model Analogous to Linear Polymerization. Ind. Eng. Chem. Res., 2001; 40: 4664-4672.

[2] Nakhli H, Alizadeh A, Moqadam SM, Afshari S, Kharrat R, Ghazanfari MH. Monitoring of asphaltene precipitation: Experimental and modeling study. Journal of Petroleum Science and Engineering, 2011; 78(2): 384-395. .

[3] Hasanvand M, Shahsavani B, Anooste A. Study of temperature effect on asphaltene precipitation by visual and quantitative methods. Journal of Petroleum Technology and Alternative Fuels, 2012; 3(2): 8-18.

[4] Hasanvand MZ, Kharrat R, Behbahani SS. Thermodynamic Modeling of Asphaltene Precipitation, the Role of Pressure and Temperature. 2012: LAP LAMBERT Academic Publishing, ISBN-10: 384849244X.

[5] ASTM, Standard Test Method for Determination of Asphaltene (Heptane Insolubles) in Crude Petroleum and Petroleum Products. 2000.

[6] Zanganeh P, Ayatollahi S, Alamdari A, Zolghadr A, Dashti H, and Kord S. Asphaltene Deposition during CO_2 Injection and Pressure Depletion: A Visual Study. Energy & Fuels, 2012; 26(2): 1412-1419.

[7] Shirani B, Nikazar M, Naseri N, Ali, Mousavi-Dehghani SA. Modeling of asphaltene precipitation utilizing Association Equation of State. Fuel, 2012; 93: 59–66.

[8] Pazuki GR, Nikookar M. A modified Flory-Huggins model for prediction of asphaltenes precipitation in crude oil. Fuel, 2006; 85(7-8): 1083-1086.

[9] Speight JG, and Plancher H. Molecular Models for Petroleum Asphaltenes and Implications for Asphalt Science and Technology. in Proc., Internat. Symp. on the Chemistry of Bitumens. 1991.

[10] Pan H, Firoozabadi A. Thermodynamic Micellization Model for Asphaltene Aggregation and Precipitation in Petroleum Fluids. SPE Prod. & Fac, 1998: 118.

[11] Cimino R, Correra S,Del Bianco A, and Lockhart TP. Solubility and Phase Behavior of Asphaltenes in Hydrocarbon Media. in Asphaltenes: Fundamentals and Applications, E.Y.S.a.O.C. Mullins, Editor. 1995, Plenum Press: NY: 97-130.

[12] Mullins OC, Seifert DJ. Zuo JY, and Zeybek M. Clusters of Asphaltene Nanoaggregates Observed in Oilfield Reservoirs. Energy Fuels, 2013; 27(4): 1752–1761.

[13] Groenzin H, and Mullins OC. Asphaltene Molecular Size and Structure. J. Phys. Chem. A, 1999; 130(50): 11237–11245.

[14] Hirschberg A, de Jong LN, Schipper BA, Meijer JG. Influence of Temperature and Pressure on Asphaltene Flocculation. 1984, KoninWijke/Shell E&P Laboratorium.

[15] Burke NE, Hobbs RE, and Kashou SF. Measurement and modeling of asphaltene precipitation. Journal of Petroleum Technology, 1990; 42(11): 1440-1446.

[16] Prausnitz JM, Lichtenthaler RN, and Azevedo EGD. Molecular Thermodynamics of Fluid Phase Equilibria. 3rd ed. 1999, Upper Saddle River,NJ: Prentice Hall PTR.

[17] Speight JG, Long RG, and Trawbridge TD. Factor Influencing the Separation of Asphaltenes from Heavy Petroleum Feed stocks. Fuel, 1984; 5: 616.

[18] Gupta AK. A model for Asphaltene Flocculation Using an Equation of State. in Department of Chemical and Petroleum Engineering. 1986, University of Calgary: Calgary, Alberta.

[19] Thomas FB, Bennion DW, and Hunter BE. Experimental and Theoretical Studies of Solids Precipitation from Reservoir Fluid. Journal of Canadian Petroleum Technology, 1992; 31: 22-31.

[20] Nghiem L. Phase Behavior Modeling and Compositional Simulation of Asphaltene Deposition in Reservoirs. 1999, University Of Alberta: Edmonton, Alberta.

[21] Leontaritis KJ, and Mansoor, GA. Asphaltene Flocculation during Oil Recovery and Processing: A Thermodynamic-Colloidal Model. in SPE International Symposium on Oil Field Chemistry. 1987, SPE: San Antonio, TX,.

[22] Jewell DM, Albaugh EW, Davis BE, Ruberto RG. Integration of chromatographic and spectroscopic techniques for the characterization of residual oils. Ind. Eng. Chem. Fundam, 1974; 13(3): 278–282.

[23] ASTM, Standard Test Method for Separation of Representative Aromatics and Non-aromatics Fractions of High-Boiling Oils by Elution Chromatography. 1995.

[24] ASTM, Standard Test Methods for Separation of Asphalt into Four Fractions. 1997.

[25] ASTM, Standard Test Method for Characteristic Groups in Rubber Extender and Processing Oils and Other Petroleum Derived Oils by the Clay–Gel Absorption Chromatographic Method. 2008.

[26] Meléndez LV, Lache A, Orrego-Ruiz JA, Pachon Z, Mejia-Ospino E. Prediction of the SARA analysis of Colombian crude oils using ATR–FTIR spectroscopy and chemometric methods. Journal of Petroleum Science and Engineering, 2012; 90-91: 56–60.

[27] Sanchez-Minero F, Anachyeta J, Silva-Oliver G, Flores-Valle S. Predicting SARA composition of crude oil by means of NMR. Fuel, 2013; 110: 318–321.

[28] Vazquez D, Mansoori GA. Identification and measurement of petroleum precipitates. Journal of Petroleum Science and Engineering, 2000; 26(1-4), 49-55.

[29] Koza JR. Genetic programming, on the programming of computers by means of natural selection. Cambridge (MA. 1992, MIT Press.

[30] Mollahasani A, Alavi AH, Gandomi AH. Empirical modeling of plate load test moduli of soil via gene expression programming. Computers and Geotechnics, 2011; 38(281-286).

[31] Ahmadi, M. A., Zendehboudi, S., Bahadori, A., James, L., Lohi, A., Elkamel, A., & Chatzis, I. Recovery Rate of Vapor Extraction in Heavy Oil Reservoirs – Experimental, Statistical, and Modeling Studies. Industrial & Engineering Chemistry Research, 2014; 53(41), 16091-16106.

[32] Ferreira C. Gene expression programming: a new adaptive algorithm for solving problems. Complex Syst., 2001; 13(2): 87–129.

[33] Ferreira C. Gene Expression Programming: Mathematical Modeling by an Artificial Intelligence. 2nd ed. ed. 2006, Berlin/New York: Springer-Verlag.

[34] Gharagheizi F, Ilani-Kashkouli P, Farahani N, Mohammadi AH. Gene expression programming strategy for estimation of flash point temperature of non-electrolyte organic compounds,. Fluid Phase Equilibria, 2012; 329: 71– 77.

[35] Zhang X, Pedrosa N, and Moorwood T. Modeling Asphaltene Phase Behavior: Comparison of Methods for Flow Assurance Studies. Energy & Fuels, 2012; 26: 2611−2620.

[36] de Boer RB, Leerlooyer K, Eigner MRP, van Bergen ARD. Screening of Crude Oils for Asphalt Precipitation: Theory, Practice, and the Selection of Inhibitors. SPE Production & Facilities, 1995. SPE 24987,: 55-61.

[37] Sako T, Wu AH, and Prausnitz JM. Modelling of high-pressure phase equilibrium using the Sako–Wu–Prausnitz equation of state I. Pure-components and heavy n-alkanes solutions. Fluid Phase Equilibrium, 1999;163(1):61–77.

[38] Yarranton HW, Alboudwarej H, Jakher R. Investigation of Asphaltene Association with Vapor Pressure Osmometry and Interfacial Tension Measurements. Ind. Eng. Chem. Res., 2000; 39: 2916-2924.

[39] Akbarzadeh K, Alboudwarej H, Svrcek WY, Yarranton HW. A generalized regular solution model for asphaltene precipitation from n-alkane diluted heavy oils and bitumens. Fluid Phase Equilibria, 2005; 232: 159–170.

To whom correspondence should be addressed: Dr. Mohammad Shadadeh, Research Institute of Petroleum Industry, Tehran, Iran, mohamad.shadadeh@gmail.com; shadadehm@ripi.ir

Petroleum and Coal

Article **Open Access**

SYNTHESIS, CHARACTERISTICS AND KINETIC STUDY AND APPLICATION OF HETEROGENEOUS NANO-CATALYST

Masoumeh M. Mirzaeian, Ali Morad Rashidi, Mahshad Alaei

Department of Chemical Engineering, Islamic Azad University, Shahrood Branch, Shahrood, Iran

Received May 21, 2018; Accepted June 27, 2018

Abstract

Mercaptan removal from a gas stream using multi-walled carbon nanotubes (MWCNTs) supported cobalt nanocatalyst in fix bed reactor is discussed in this paper. MWCNTs as support were first functionalized with carboxylic acid then cobalt particles that are supported by MWCNTs are prepared using impregnation technique.

The nanocatalysts were characterized by Fourier transform infrared spectroscopy (FTIR), Raman spectroscopy, and X-ray diffraction (XRD) and transmission electron microscopy (TEM) analysis. The TEM analysis showed that functionalized MWCNTs were well covered with homogeneously distributed of cobalt particles. The influence of temperature and gas hour space velocity (GHSV) parameters on mercaptan removal under nanocatalysts was investigated. Moreover, the kinetic parameters related to catalytic reaction for mercaptan removal in present of Co-MWCNT nanocatalyst was reported.

The results displayed the concentration of mercaptan from a gas stream is reduced from 16 800 ppm to less than 15 ppm by Co/MWCNTs in temperature of 100°C and GHSV of 1000 h^{-1}.

Keywords*: nanocatalyst; removal of mercaptan; multi-walled carbon nanotubes; cobalt particles; kinetic study; heterogeneous catalyst.*

1. Introduction

Mercaptans are sulfur-containing organic compounds with the general R-SH formula. They are relatively common in natural gas and petroleum systems as naturally occurring species in low concentrations. Mercaptans are also added to gas products as an odorants for leak examination [1]. Mercaptans a higher concentration become very toxic and may cause harmful health effects. There are difficult methods for removing of mercaptans like as: oxidation, chemical, and absorption. These methods have particular defect and disadvantages, therefore, in order to reduce mercaptans content of stream to desired value must use of the perfect process. Adsorption is one of the most widely applied control technologies for removal of volatile sulfur compounds.

In adsorption procedures for mercaptans removal from gas stream many different catalysts have been applied. Carbon nanotubes as a new type of carbon material have interesting properties such as mesoporosity, high purities, high thermal stability, high surface areas and high pore volume [2-3]. Their morphology and structural characteristics are shown to be quite suitable for use as catalytic support materials and improve catalytic activity and also are insoluble in most organic and aqueous solvents Thus, the surface of CNTs can be modified through different treatment to improve the compatibility and solubility and make a good distribution of metals on their therein [4-5].

In this paper, with an attempt to show the effects of different experimental condition in the removal of mercaptans from gas stream under performance of MWCNT-supported Co nanocatalyst, we functionalized MWCNT- COOH then prepared MWCNT- Co using the impregnation method for produce nanoparticle catalyst, finally used it as catalyst for the adsorption of mercaptans in fix bed reactor.

2. Experimental

In section experimental first, MWCNT-supported were prepared by impregnation synthesis method and used as catalysts for mercaptan removal in a fix bed reactor and concentration of mercaptans was measured with a potentiometer. All reagents including sulfuric acid (H2SO$_4$) 96%, nitric acid (HNO_3) 64%, cobalt nitrate $Co(NO_3)_2 \cdot 6H_2O$, potassium hydroxide (KOH) were purchased from Merck Company. Aqueous solutions were prepared using Millipore water from Milli-Q water systems. MWNTs Multi-walled carbon nanotubes (MWNTs) with purity > 90%, (size 10 µm; diameter 10 –30 nm; specific surface area 270 m^2/gr and thermal conductivity 1500 w/mv) were prepared in Research Institute of Petroleum Industry of Iran (RIPI) were prepared and MWCNT-Co synthesized using the impregnation method.

In a first step, the carbon nanotubes (CNTs) were synthesized using chemical vapor deposition (CVD) method using (Co-Mo/Mg) catalyst and methane as carrier gas at temperature 900°C for 30 min.

In the next step, carbon nanostructures were functionalized by using acid oxidation method. Carbon nanostructures were added to an aqueous acid solution of H_2SO_4/HNO_3 mixture with the ratio of 1:3 by volume. The mixture is ultrasoniced at a temperature of 60°C for 1 hour then it is filtered and neutralized by being washed with distilled water. The product was dried in an oven at 90ºC for 12 h.

For the synthesis of the metallic nanoparticle of cobalt supported on Multi-Wall Carbon Nanotubes (MWNTs) was used impregnation method. For this purpose, cobalt nitrate was dissolved in a certain volume of distilled water and stirred until a homogenous solution was created, then the resulting solution by the method of impregnation slowly was added to carbon nanotubes. Nanocatalysts was dried at a temperature of 120°C. The chemical structure of MWCNT/Co is shown in Scheme 1.

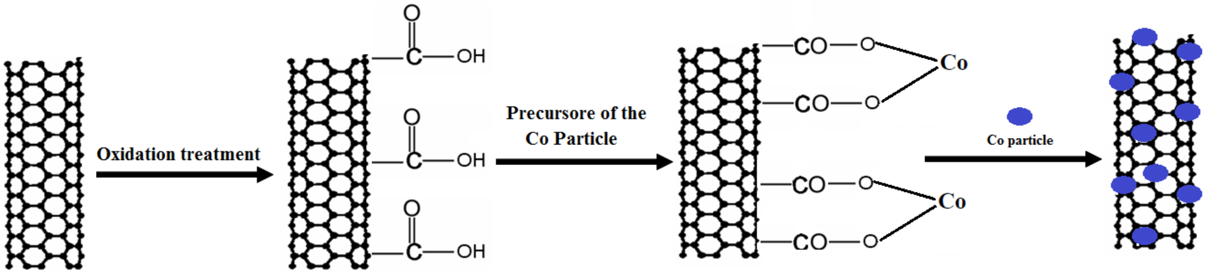

Scheme 1. Schematic illustration of the synthesis of MWCNT/Co composites

The morphology and structure characterizations of MWCNT, MWCNT-COOH, and MWCNT-Co were performed using transmission electron microscopy (TEM), X-ray diffraction, Fourier transform infrared spectroscopy (FTIR). The tests for mercaptans removal from the gas stream has been accomplished in an operating condition like as reaction temperature and gas hour space velocity (GHSV h^{-1}). The catalyst was loaded in a fixed-bed reactor that constructed from the stainless steel-314 tube. The reactor vertically takes placed in an electrical furnace. The temperature of the furnace was controlled by a thermal indicator controller (TIC).

The gas stream was containing hydrocarbon mixture (98.29wt %) and mercaptan (0.0168 wt %) with mercaptans content of 16 800 ppm. Gas flow to the reactor was regulated by the mass flow controller (MFC). The catalyst was heated from room temperature to the reaction temperature, and amount of GHSV was characterized regarding the volume (mL) of the catalyst and inlet gas velocity (mL/min).

Then the gas stream passes downwards through the catalytic bed. The product stream has been passed through KOH solution (20%) in different times each time for 20 min. The time of the process and operating pressures were 120 min and 1 bar, respectively. Mercaptan concentration is determined by KEM potentiometric (AT-500) titration method according to UOP 163 method. The experimental setup for mercaptan adsorption shows in Fig1.

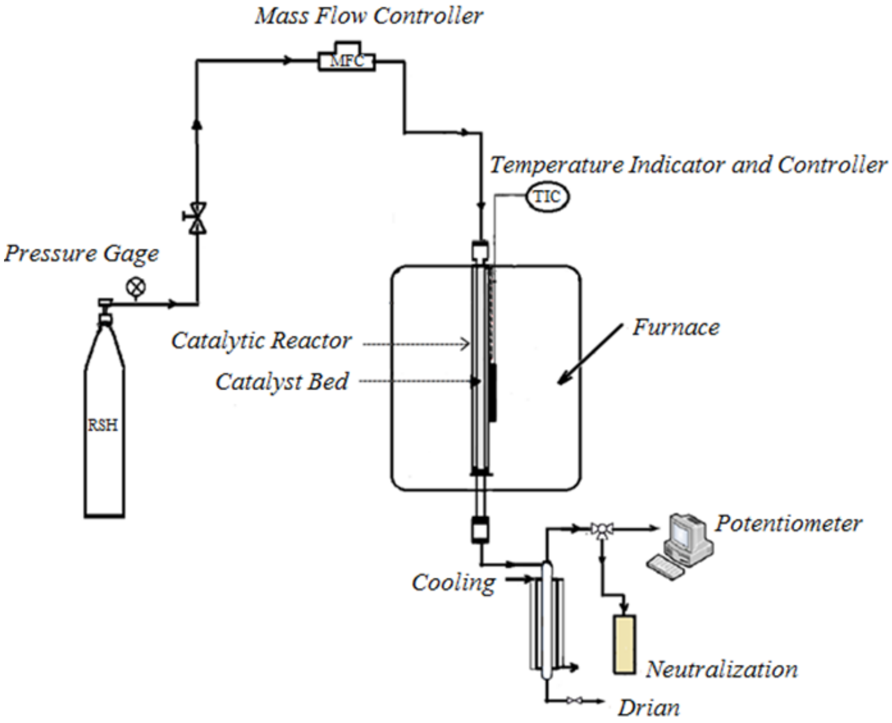

Figure 1. Experimental set-up

3. Results and discussion

The preparation of MWCNT-Co involves the introduction of the MWCNTs of acid groups through sulfuric acid treatment, the development of Co nanoparticles. CNTs are functionalized with functional groups to improve its dispersion into solvents. Acid treatment removes the impurities as amorphous carbon particles and also introduces the –COOH groups on the surface of MWCNTs. The crystallinity formation of Co nanoparticles on the MWCNTs surface is confirmed by X-ray powder diffraction (XRD) results.

The XRD patterns of as-synthesized MWCNTs (a), MWCNT-COOH (b), MWCNT-Co (c) are displayed in Figure 2. The diffraction peaks at 2θ of 26.24° and 42.58° are due to the (002) and (110) planes of MWNTs. As shown in Figure 2(a), 2 (b) XRD patterns of functionalized MWNTs are similar to that of as-synthesized MWCNTs. The intensity of the diffraction peak at (002) in acid functionalized MWCNTs was increased as compared to the as-synthesized MWCNTs. [6-7]

As shown in Figure (2c), two peaks 2θ=26°, 44° is related to the structure of the carbon nanotube, and the rest of the peak is related to the different pages of crystalline Co_3O4. Its dominant peak is in 2θ = 37°, and the other peaks at 45° and 51.5 ° is related to cubic cobalt structures [8-9].

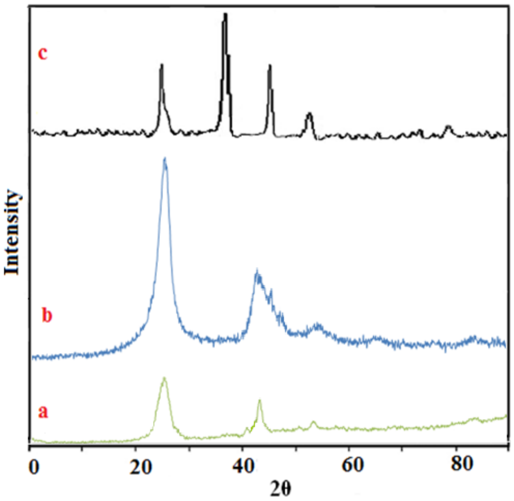

Figure 2. XRD spectra of a) as- synthesized MW-CNTs, b) MWCNT-COOH, c) MWCNT-Co

The surface morphologies and composite properties of MWCNTs, MWCNT-COOH, and MWCNT-Co were investigated by transmission electron microscopy (TEM) measurement. The multiwalled tubes range in length from a few tens of nanometers to several micrometers, and in outer diameter from about 2.5 to 30 nm. The flawless surface in purified condition was clearly observed in TEM image of Fig.3 (a), no destruction occurred on the side wall fig a. Based on the all morphological surface analysis Fig. 3(b), it is mentioned that nanotube functionalization process functionalization leading to shortening and defect to create functional groups on the side wall and at the end of the tube. Fig. 3(c) shows the TEM image of the MWCNTs modified with Co particles. It can also be seen that the f-MWCNTs are well covered with homogeneously distributed of particles because the functional groups on the MWCNT surface cause a uniform distribution of cobalt particles. The average size of Co nanoparticles is within the range of (5-11 nm). Similar to previously reported work, the small particles interact with inside wall and larger particles with an outside wall [10-11].

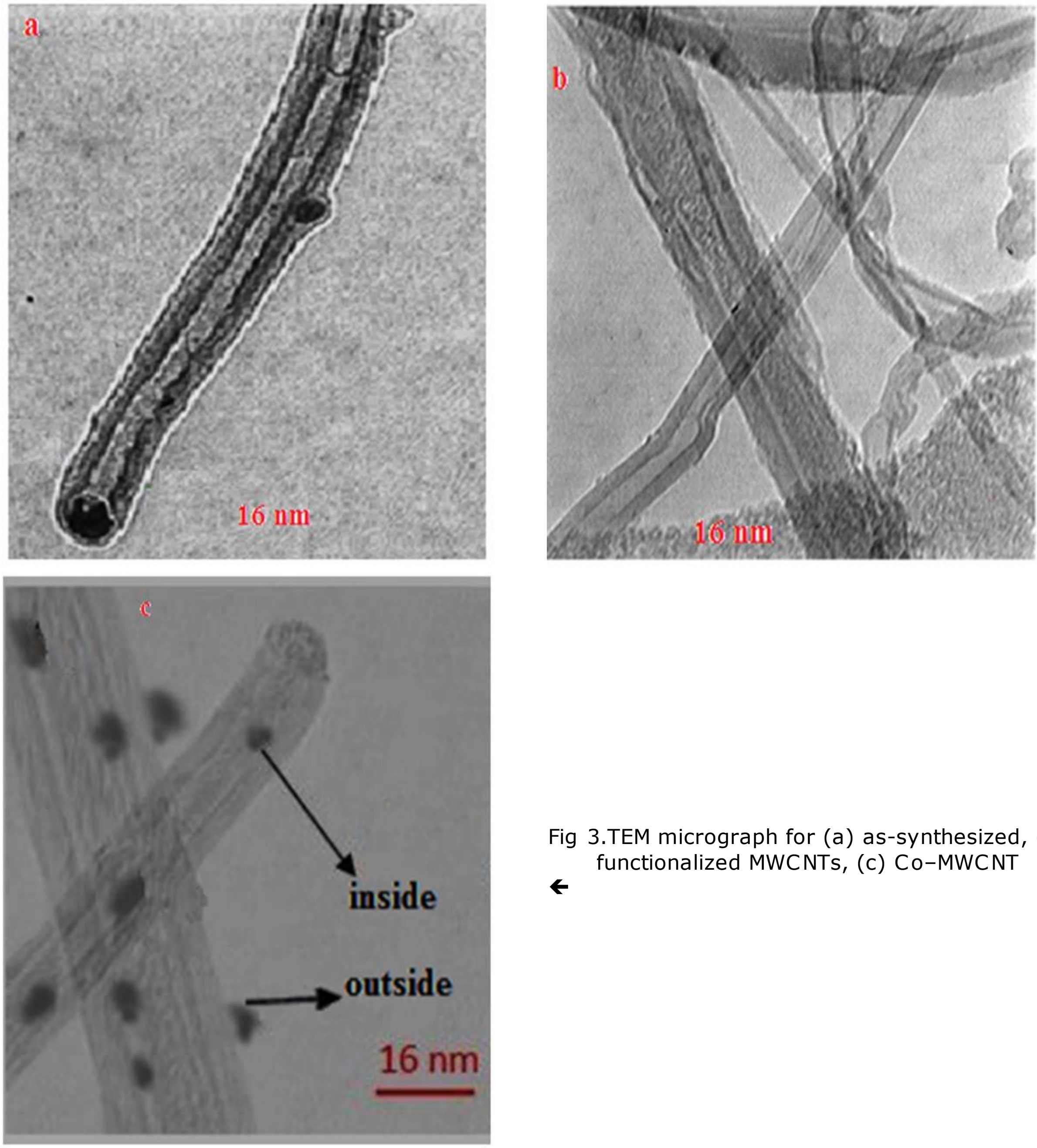

Fig 3.TEM micrograph for (a) as-synthesized, (b) functionalized MWCNTs, (c) Co–MWCNT

←

Figure 4 illustrates the IR spectra of raw, oxidized and Co- MWCNTs. The IR spectra of raw, oxidized MWCNTs showed similar characteristic peaks, indicating the similarity in the structure of the MWCNTs. These results indicate that after the oxidation step, the oxygen functional groups such as carboxylic and hydroxy acids are formed on the surface of purified MWCNTs.

The FTIR spectra of the pristine MWNTs and after functionalization with carboxylic and MWCNT-Co are shown in Fig (4a-c). Concerning pristine and oxidized MWNTs as shown in Fig (4a, b), the peak at 1570 cm^{-1} is associated with the graphitic structure of CNTs (C=C stretch). The peak at 3400 cm^{-1} is attributed to OH group on the surfaces of pristine MWNTs.The presence of carboxylic C=O (1726 cm^{-1}), C-O (1188 cm^{-1}) and OH (2400-3400 cm^{-1}) vibrations in the spectrum of oxidized MWNTs indicated carboxyl groups are formed to the tip and sidewalls of the MWNTs [12-13]. The spectrum of MWCNTs-Co nanocatalyst Fig. 4(C) exhibit the presence of bands at 506, 572 and 660 cm^{-1}. These bands are the feature of a metal–oxygen bond in a spinel-type crystal structure [14].

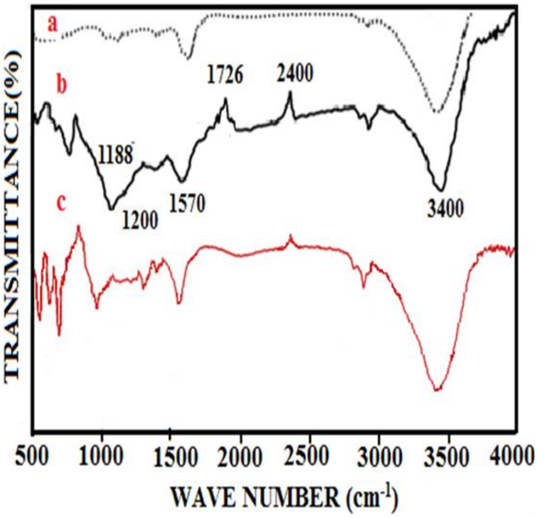

Fig.4. FT-IR spectra of a) MWCNT, b) MWCNT-COOH, c) Co-MWCNT

In compared with MWCNT, there is a slight shift of the skeletal vibration of the graphite sheets for the Co/MWCNT nanocatalyst, which may be due to the introduction of cobalt. Also, the conformational changes observed by shifting of bands in MWCNTs-Co nanocatalyst indicate the formation of stable nanocatalysts by the deposition of Co nanoparticles on the surface of MWCNTs.

The Raman spectra of pristine MWCNTs, MWCNT-COOH, and MWCNT-Co is shown in Figure 5. As can be seen from the Figure 5a, the Raman spectra of the pristine MWCNTs show bands at about 1347, 1573 and 2661 cm^{-1} are the D band, G band and 2D band of MWCNTs, respectively. This strongly supports the fact that MWCNTs were produced. Furthermore, The MWCNT-COOH (Fig. 5b) showed bands at 1352, 1583 and 2750 cm^{-1}. After the junction of cobalt nitrate with MWCNT, the Raman spectrum (Fig. 5c) shows characteristic peaks around 465,671,512 cm^{-1}corresponding to different vibrational modes of Co particles. All the aforementioned characterizations confirm the interaction between Co and MWCNT and matches up well with the reported cobalt oxide spectrum. The relative intensity ratio of the D- and G-bands (I_D/I_G) is used to probe the effectiveness of functionalization. The I_D/I_G band ratios as an indication of the quality of carbon nanotubes for catalyst supports increased with acid treatment. Acid treatment increased the I_D/I_G from 0.11 to 0.19. This shows that the amount of defects on the MWCNT surface increases with acid treatment, which in turn leads to better metal dispersion on the acid-treated MWCNT surface and as well as higher catalyst activity. The formation of particles on the MWCNTs was achieved with some disruption of the graphitic CNTs, and the I_D/I_G varied

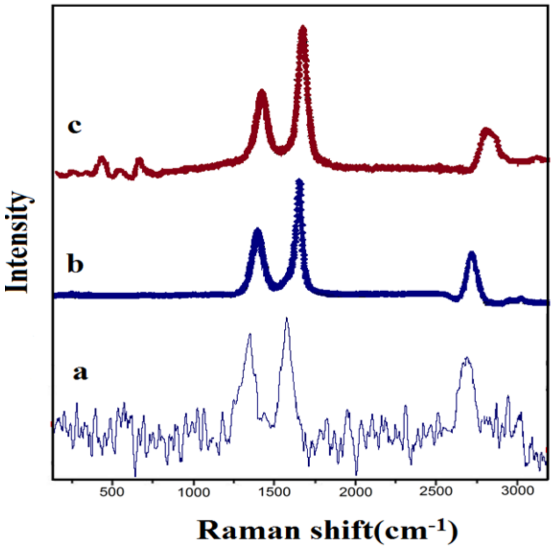

Fig. 5. Raman spectra of a) MWCNT, b) MWCNT-COOH, c) Co-MWCNT

to 0.25 for the Co-MWCNT nanocatalyst. It is indicating that some additional disorder was introduced by a synthesis procedure [15-16].

Mercaptan removal from hydrocarbon mixture was carried out under the different operating conditions in the presence of heterogeneous catalyst of Co-MWCNT. The results of some experiments have been shown in Fig.6.

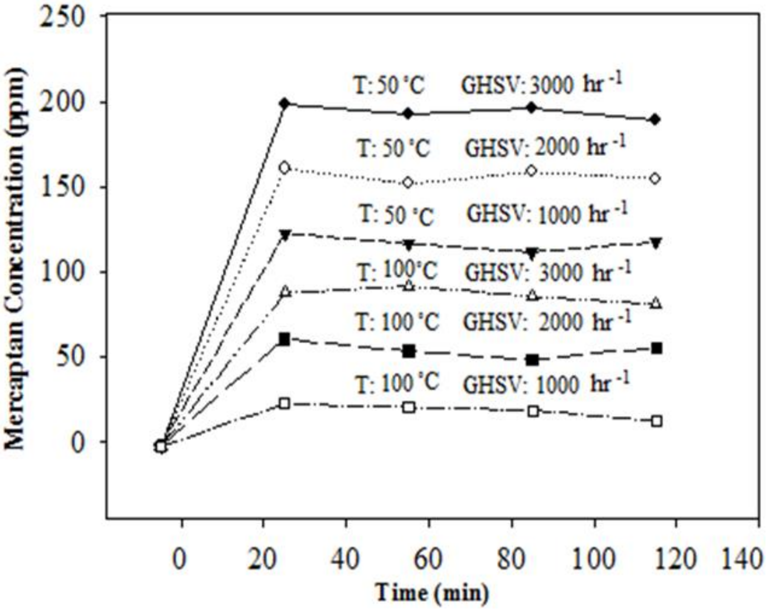

Fig 6. Variation of mercaptan concentration content in exit stream with time

The process was carried out in the temperature of 50 to 100°C and GHSV of 1 000 to 3 000 hr $^{-1}$. In time 0 min mercaptan concentration in outlet stream was 16,800 ppm. At the beginning of the process, maximum adsorption of mercaptan occurs, while after passing time the adsorption process becomes less effective due to saturation of the catalyst surface with mercaptan and as a result mercaptan increases in the exit stream. According to the obtained results, increasing temperature and decreasing GHSV cause better contacting of the gas stream with catalyst and in the result of that better conversion of mercaptan to disulfide. Also, increasing temperature causes an increase in the reaction rate and by increasing the GHSV the residence time of the gas reduces. The maximum concentration of mercaptan in products can be reduced from 16 800ppm to less than 15 ppm under Co - MWCNT nanocatalyst in the best condition of temperature (100°C), and GHSV (1000 hr $^{-1}$).

Mechanism of the oxidation of mercaptan into disulfides in present of Co-MWCNT nanocatalyst are listed below:

The general reaction:

$$RSH \xrightarrow{Ca\,,O2} RSSR + H_2O \qquad (1)$$

Mechanism:

$$RSH + OH^- \leftrightarrow RS^- + HO2 \qquad (2)$$

$$RS^- + Co\ (II)\text{-}MWCNT + O_2 \rightarrow RS^-\_\ Co\ (III) - MWCNT\_\ O_2^- \qquad (3)$$

$$RS^-\ \_Co\ (III) - MWCNT\ \_O_2^- \rightarrow RS^0 + Co\ (II) - MWCNT\ \_\ O_2^- \qquad (4)$$

$$2RS^0 \rightarrow R\text{-}S\text{-}S\text{-}R \qquad (5)$$

In this mechanism, the formation of disulfide result from generation of free radicals (RS^0) which formed from mercaptide ions (RS^-) under Co -MWCNT nanocatalyst. Co (III) -MWCNT are generated by the oxidation of Co (II) -MWCNT by molecular oxygen then the reduction of mercaptide ions by Co (III) –MWCNT gives RS^0 radicals. Finally, the production of disulfides former results in recombination of the RS^0 radicals.

3.1. Estimation of kinetic parameters

Kinetic study of the mercaptans removal lead to optimizing operating conditions, catalyst performance, and determine parameters for better removal of sulfur compounds.

The integral method is a general and better manner for the determination of experimental rates and kinetic parameters of a reaction than the conventional methods. Four models were suggested for the estimation of the order of reaction in term of mercaptan concentration (Table.1).

Table 1. Integrated form of the rate law for rate equation

Order	Rate Law	Integrated Rate Equation
0	Rate= k	$[C_0]-[C_{merc}]=kt$
1	Rate= $k[C_{merc}]$	$Ln([C_0]/[C_{merc}])= -kt$
2	Rate= $k[C_{merc}]^2$	$(1/[C_{merc}]) - (1/[C_0]) = kt$
n	Rate= $k[C_{merc}]^n$	$C_{merc}^{1-n} - C_0^{1-n} = (n-1)\, kt$

n-order, 0, 1 and 2 rate reaction is done using curve fitting then by plotting the power model and experimental data and compare two graphs. It is indicated that the reaction rate is a first-order equation Fig.7.

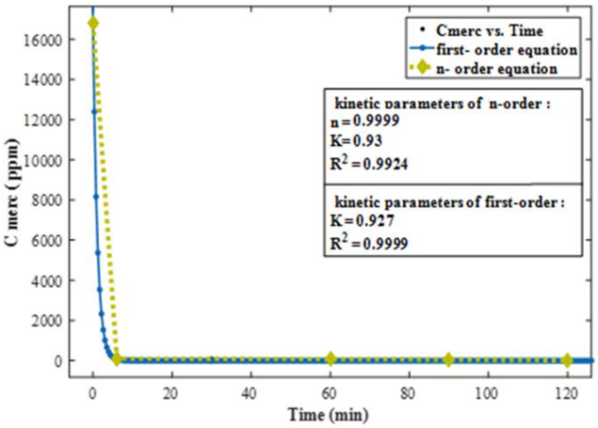

Fig. 7. Comparison n – order equation with experimental data for Co-MWCNT nanocatalyst

Using equations in (Table.1) the data was plotted for each model. The kinetic parameter in the term of R^2 for zero, first and second order guesses are reported in Fig. 8. According to the results, the value of k, n with best-fitted results of R^2 (0.99) for least square is reported for the first-order equation in the present of Co-MWCNT nanocatalyst. Also, it can be concluded that the rate of n, k, R^2 obtained for n – order reaction extremely is similar to the value of n, k, R^2 for first order reaction.

According to Fig. 8, in the first-order reactions the slope is $(-m.K_1)$:

Slope= $-m \times K1 = -0.93\ min^{-1}$ (6) $m = 10^{-3}\ kg / 4 \times 10^{-3}\ m^3 = 0.25$ (7)

$K_1 = 0.062\ m^3/Kg\ cat.sec$ (8)

Amount of the activation energy be calculated by Arrhenius' law:

$K_1 = K_0 \exp(-ER/T)$ (9)

So it's logarithm can be written as:

$Ln(K_1) = (-ER/T) + Ln(K_0)$ (10)

By having all the other parameters fixed and testing experiments in various temperatures, the amount of the activation energy and the effect of temperature on the rate of reaction is obtained.

Fig.9 indicates the experimental data and the best line that passes through Ln (K_1) versus 1/T for removal of mercaptan under Co – MWCNT nanocatalyst. In accordance with the obtained results, the rate of mercaptan removal reaction intensifies with increasing the temperature.

Thus, the suggested kinetic model of K_1 and the reaction rate equation is presented as follows:

$K_1 = 15.51 \exp(-2049/T)$ (11) and, $-r = 15.51 \exp(-2049/T)[C_{merc}]^{0.99}$ (12)

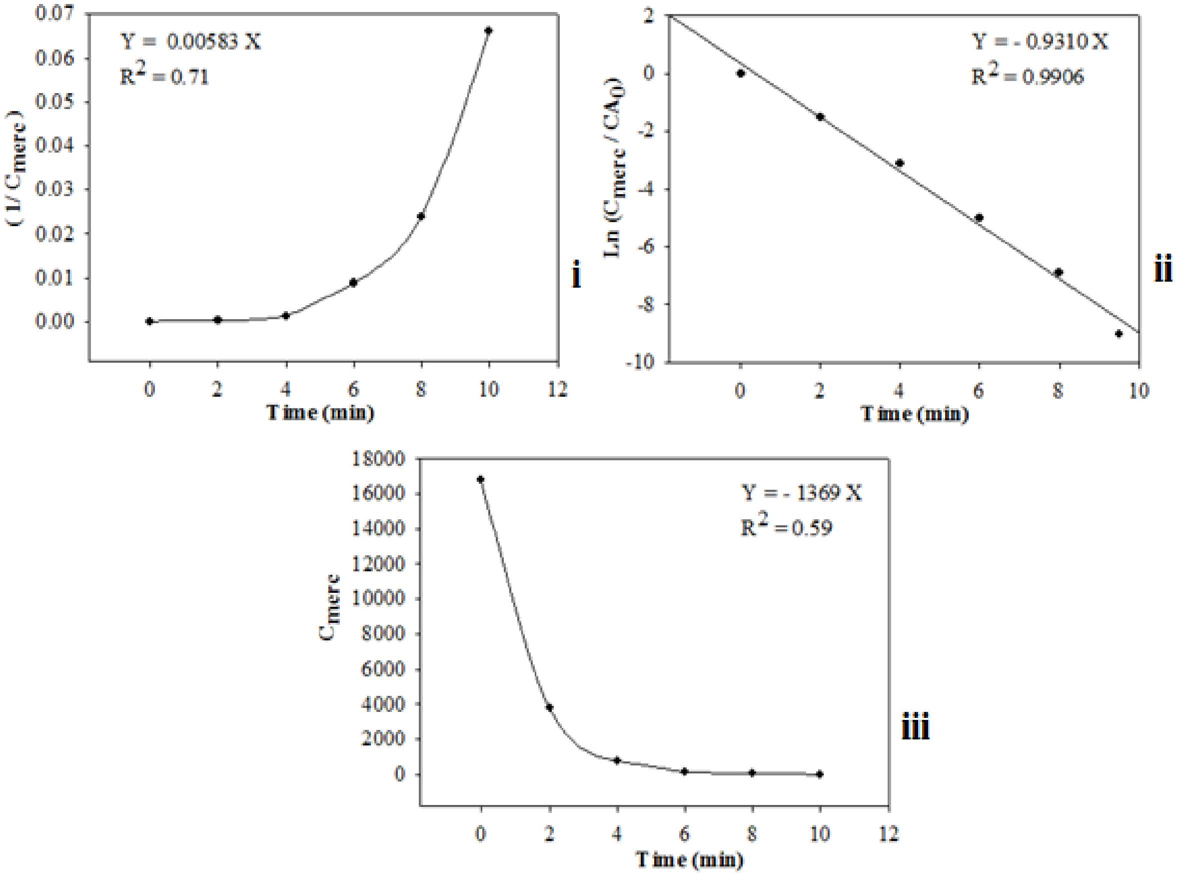

Fig. 8. Estimation of the rate constant of the catalytic reaction using an integral method under Co - MWCNT nanocatalyst for (i) zero-order reaction, (ii) first-order reaction, and (iii) second – order reaction

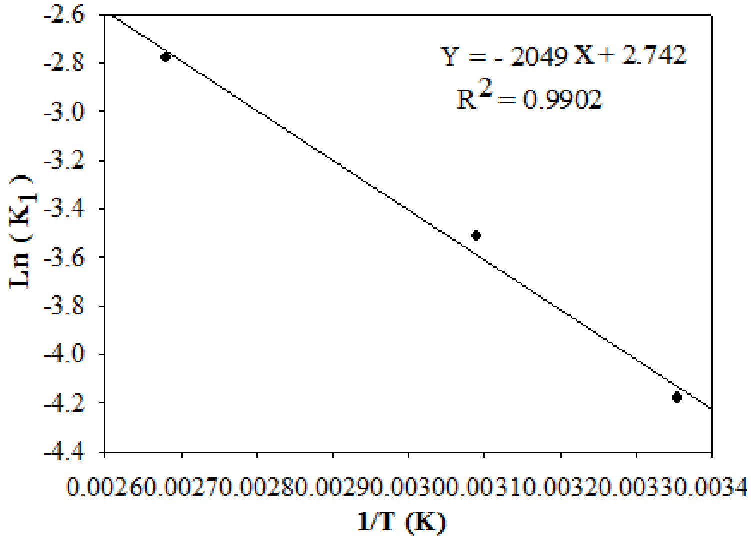

Fig. 9.Arrhenius curve for mercaptan removal in present of Co-MWCNT nanocatalyst

4. Conclusions

Cobalt nanocatalysts that are supported by carbon nanotubes (CNTs) are prepared using an impregnation technique, and their performance in mercaptan removal have been appraised.

The results show that average size of Co nanoparticles is within the range of (5-11 nm) and the small particles interact with inside wall and larger particles with an outside wall. Catalytic test result show mercaptan was removed from a gas stream using Co- MWCNT nano-catalyst. Unreacted mercaptan is reduced with increasing temperature and decreasing GHSV. Decreasing GHSV cause is increasing residence time of gas and better catalytic activity. Temperature has the most effects in mercaptan conversion, and Increasing of it causes an increase in adsorption and reaction rate. In addition, the minimum unreacted mercaptan in outlet gas stream is obtained at a temperature of 100°C and GHSV of 1000 h^{-1} and the concentration of mercaptan under Co-MWCNT nanocatalyst reduced from 16 800ppm of the gas to less than 15 ppm. On the other hand, the kinetic study of mercaptan removal in the present of Co-MWCNT nanocatalyst was investigated, and kinetic parameters related to catalytic reaction for Co-MWCNT nanocatalyst was obtained. By comparing the obtained results for models of 0, 1, 2 and n order of reaction, It was indicated first-order reactions, as the best result, for removal mercaptan in present of Co-MWCNT nanocatalyst in a fix bed reactor.

Nomenclature

E	*Activation energy*	*J. mol^{-1}*
K	*Rate constant*	*mol. m^{3}.Sec^{-1}.Kg $^{-1}{}_{cat}$*
k	*Arrhenius' constant*	*mol. m^{3}. Sec^{-1}.Kg $^{-1}{}_{cat}$*
r	*Rate of reaction*	*mol. Kg cat. Sec^{-1}. L^{-1}*
R	*Universal gas constant*	*J. mol^{-1} K^{-1}*
T	*Temperature*	*°C*
Time		*Sec*
M	*catalyst weight*	*Kg*
V	*volume of*	*L*
M	*M.V^{-1}*	*kg.m^{-3}*
C	*Concentration of mercaptan*	*mol.L^{-1}*
C_0	*Initial concentration of mercaptan*	*mol.L^{-1}*
Cat	*Catalyst*	
GHSV	*Gas Hour Space Velocity*	*mL.min^{-1}*

References

[1] Man F, Carroll J. Limitations and Challenges Associated with the Disposal of Mercaptan-Rich Acid Gas Streams by Injection, Gas Liquids Engineering Ltd., Calgary, AB, Canada: A Case Study, 2009.
[2] Baughman RH, Zakhidov AA, Heer WA. Carbon nanotubes the route toward.applications, Science, 2002; 297:787–792
[3] Sun P, Fu KF, Lin Y, Huang WJ. functionalized carbon nanotubes: Properties and application. Acc. Chem. Res, 2002; 35: 1096–1104.
[4] Tavasoli A, Rashidi AM, Zadeh KS, Karimi A, Kodadadi AA, Mortazavi Y. Carbon nanotubes supported cobalt catalyst for converting synthesis gas into hydrocarbons, EP patent 1782885 A1, 2007.
[5] Pan X, Fan Z, Chen W, Ding Y, Luo H, and Bao X. Enhanced ethanol production inside carbon-nanotube reactors containing catalytic particles. Nature material, 2007; 6: 507-511.
[6] Lee GW, Kim J, Yoon J, Bae JS, Shin BC, Kim IS, Oh W, Ree M. Structural characterization of carboxylated multi-walled carbon nanotubes. Thin Solid Films, 2008; 516: 5781-5784.
[7] Wu FY, Cheng HM. Structure and thermal expansion of multi-walled carbon nanotubes before and after high-temperature treatment. J. Phys. D: Appl. Phys, 2008; 38: 4302-4307.
[8] Jacobs G, Das TK, Zhang Y, Li J, Racoillet G, and Davis BH. Fischer-Tropsch synthesis: support, loading, and promoter effects on the reducibility of cobalt catalysts. Applied Catalysis A: General, 2002; 233: 263-281

[9] Tavasoli A, Irani M, Abbaslou MMR, Trépanier M, Dalai AK. Morphology and deactivation behavior of Co-Ru/Al2O3 Fischer-Tropsch synthesis. The Canadian Journal of Chemical Engineering, 2008; 86:1070-1080.

[10] Trépanier M, Tavasoli A, Dalai A.K, Abatzoglou N. Fischer-Tropsch synthesis over carbon nanotubes supported cobalt catalysts in a fixed bed reactor: Influence of acid treatment. Fuel Processing Technology, 2009; 90: 367-374.

[11] Trépanier M, Tavasoli A, Dalai A.K, Abatzoglou N. Co, Ru and K loadings effects on the activity and selectivity of carbons nanotubes supported cobalt catalyst in FTS. Applied Catalysis A.General, 2009; 353: 193-202.

[12] Shaffer MSP, Fan X, Windle AH. Dispersion and packing of carbon nanotubes. Carbon, 1988; 36: 1603-1612.

[13] Liu L, Qin Y, Guo Z. Reduction of solubilized multiwalled carbon nanotubes. Carbon, 2003; 41: 331-335

[14] Sun L, Li H, Ren L, Hu C. Synthesis of Co_3O_4 nanostructures using a solvothermal approach. Solid State Sci, 2009; 11:108– 112.

[15] Yu T, Zhu Y, Xu X, Shen Z, Chen P. Controlled Growth and field emission properties of cobalt oxide nanowalls. Adv. Mater, 2005; 17: 1595–1599.

[16] Xu Zh, Li Z, Tan X. Supercapacitive carbon nanotube-cobalt molybdate nanocomposites prepared via solvent-free microwave synthesis. Royal Society of Chemistry, 2012; 2: 2753-2755.

To whom correspondence should be addressed: Dr. Masoumeh M. Mirzaeian, Department of Chemical Engineering, Islamic Azad University, Shahrood Branch, Shahrood, Iran

Petroleum and Coal

Review **Open Access**

AN OVERVIEW OF COAL ENERGY SOURCES AND SUPPLY IN THAILAND

Kittiphop Promdee[1]***, *Apisake Monthienvichienchai*[2], *Thitirat Panbamrungkij*[3]

[1] *Department of Environmental Science, Chulachomklao Royal Military Academy, Nakhon Nayok, 26001, Thailand*
[2] *Department of History, Chulachomklao Royal Military Academy, Nakhon Nayok, 26001, Thailand*
[3] *Department of Geography, Chulalongkorn University, Bangkok 10330, Thailand*

Received May 11, 2018; Accepted June 27, 2018

Abstract

This study introduces the key facts on the current proven reserves, production, sources, and supply of coal. The research provides an overview of the energy situation in Thailand; how the demand for coal and the clean coal activities being undertaken in Thailand. Coal production is currently a large industrial of energy source. In recent years Thailand's economy has grown rapidly, resulting in increased energy demand. This demand is met almost entirely by fossil fuels which provide 90% of the country's supply; gas makes up 70%, coal 20%, and there are some oil-fired plants. The remaining 10% comes mainly from hydroelectricity and other renewables. Several international institutions operating in Southeast Asia play an important role in contributing to the long-term energy strategy in Thailand. However, their work on promoting the use of clean coal technologies is limited in Thailand. The use of coal in Thailand will increase if all the planned new coal-fired power stations are built. Therefore, it is important that information on, and research into, the use of clean coal technologies within Thailand are supported and increased to better inform the wider community

Keywords: *Coal; Energy Sources; Power Generation; Energy Policy.*

1. Introduction and overview

1.1. Coal energy sources in Thailand

Coal, which is primarily used for the generation of electricity. Thailand will look to develop new coal-fired power plants as gas reserves decrease in the country. According to a recent report from the Electricity Generating Authority of Thailand (EGAT), the country will consider clean coal technologies to help reduce carbon dioxide and other greenhouse gas emissions. using imported coal to fuel power plants is the best option for Thailand to provide reliable energy to the grid. Current drilling in the Gulf of Thailand was expected to be productive in a decade, as the gas reserves run dry. This will affect the security of our power supply [12-15]. Using imported liquefied natural gas, which costs double that of natural gas, will push power tariffs to rise. The most appropriate solution is to find other fuels such as coal as a substitute for gas. These fuels should make the power system more sustainable with low tariff rates. In addition to increasing its coal-fired power generation, Thailand hopes to use more renewable energy sources within the next decade [16]. The EGAT report stated the country has a goal to have 25 percent of its energy mix coming from renewable sources within the next 10 years.

Coal was used for power generation for a century [17-22]. Currently, 70% of the electricity used in the world was from coal, and it tended to increase 5-7% annually as the world still had the abundant coal reserve, contrary to oil and natural gas which clearly decreased [23-27]. Thailand lost the chance in using the coal for power generation but let other countries consumed it. Actually, coal was the cheap fuel, leading to the low price of electricity, but people were still concerned about the pollution [28-29]. However, presently there was the clean coal technology that could get rid of pollutant and heavy metal very well, which was different from

Mae Moh Power Plant case 40 years ago when the technology was not modern. EGAT did not use the good technology, scientist, would also protest. Anyway, for the Krabi Power Plant development, EGAT applied the clean technology, so it was the chance for Thailand to have the clean coal power plant enhancing the security of the southern Thailand power system. The example from Japan, in which the Government saw the importance of power. Japan needed to have sufficient power, while social and environmental care was also necessary.

1.2. Energy policy of Thailand

The government anticipated that energy prices would be one of the key concerns due to limited energy resources, environmental issues, global warming and climate change challenges which affect people's quality of life and the country's competitiveness [30-35]. Therefore, the 20-year Energy Efficiency Development Plan 2015-2036 (EEDP) was developed by the Energy Policy and Planning Office, Ministry of Energy (Thailand) to address the issues. The objectives of the EEDP are as follows:

- To establish the energy conservation targets (heat and electricity) in the short term 5 years and long term 20 years where the aim is to reduce energy intensity (EI) by 30 percent in the year 2036 compared with that in the year 2010 for overall country and energy intensive sectors such as industrial, business, and residential.
- To define strategies and guidelines in the energy conservation promotion to achieve the aforementioned targets and to formulate operation plans of the relevant organizations.

In order to formulate the 20-year Energy Efficiency Development Plan 2015-2036, the Ministry of Energy revised the 20-year Energy Efficiency Development Plan 2011-2030 by adjusting the baseline data and assumptions. Therefore, the target of the EEDP 2015-2036 becomes to reduce energy intensity by 30 percent in the year 2036 compared with that in the year 2010 or accounting for 56,142 kilo tons of oil equivalent (ktoe). However, energy savings estimated by an energy intensity reduction during the year 2010-2013 was 4,442 ktoe. Thus, the energy conservation target would be achieved by measures and projects during the year 2015-2036 accounting for 51,700 ktoe where around 15 percent or 7,641 ktoe (89,672 GWh) would be in electricity sectors and around 85 percent or 44,059 ktoe would be in thermal sectors (Table 1).

Moreover, the energy conservation plans of 4 economic sectors; residential, industrial, business, and transportation were revised. Therefore, 6 guidelines were stated to encourage energy conservation as follows:

1) Removing / Revising energy price subsidies to create the market price
2) Introducing tax incentives / to encourage the use of efficient appliances
3) Introducing monetary incentives / grants or soft loan along with energy management consulting to encourage the use of high-efficiency appliances
4) Defining Industrial Factory and Building Energy Code to be under obligations
5) Building public awareness of energy conservation
6) Defining Energy Efficiency Resources Standard (EERS) for power producers and distributors

1.3. Assumptions and frameworks of Thailand power development

The National Energy Policy Council (NEPC) approved assumptions and frameworks to formulate the Thailand Power Development Plan 2015-2036 (PDP2015) (Table 2). In addition, the Alternative Energy Development Plan (AEDP) and the Energy Efficiency Development Plan (EEDP) were also formulated along the timeframe between the year 2015 and 2036. The new Thailand's load forecast was formulated in line with the potential and target of the AEDP and the EEDP, economic growth, changes in economic structure, infrastructure development projects, the performance of the EEDP measures and Very Small Power Producer (VSPP) power purchase plan. The power demand forecast was formulated as the business as usual case (BAU) according to the average forecasted GDP growth during the year 2014-2036.

Table 1. Energy conservation targets classified by economic sector (GWh) [37]

Economic sector	Energy conservation targets				
	2016	2021	2026	2031	2036
Industrial	2,174	9,420	17,497	22,845	31,843
Business	853	5,156	12,687	22,406	36,052
Residential and agricultural	395	1,914	4,877	8,760	13,633
Government	302	1,713	2,960	4,683	7,144
Total	3,724	18,203	38,021	58,694	89,672

Table 2. Estimated energies requirement for the PDP2015 [37]

Energies	Percentage in 2014	Percentage in 2026	Percentage in 2036
Imported hydropower	7	10-15	15-20
Clean coal including lignite	20	20-25	20-25
Renewable energy including hydro	8	10-20	15-20
Natural gas	64	45-50	30-40
Nuclear	-	-	0-5
Diesel/Fuel oil	1	-	-

In addition, population growth, urbanization, and growth rate of electricity customers by economic sectors were also considered [38-42]. Consequently, End-use model and Econometrics model were used for the formulation of the power demand forecast development with the assumptions as follows:

- The power demand forecast models for long-term energy efficiency were used to estimate the power demand of the Provincial Electricity Authority (PEA) distribution system and the Metropolitan Electricity Authority (MEA) distribution system. Assumptions required for the models are growth rates of Residential, Business, Industrial, and Other Customer in the distribution system which changes according to economic and population growth.
- The estimated GDP growth during the year 2014-2036 in which the outcomes from the infrastructure development projects excluding high-speed train projects were included in the estimation. The estimated GDP growth during the year 2014-2036 expected to grow on the average of 3.94 % annually was used in the power demand forecast models.
- The power demand from BTS sky train, MRT train, and 10 mass rapid transit projects in Bangkok were counted in the model except those of the unclear high-speed train projects.
- The target of the EEDP is to reduce the energy intensity of the year 2036 by 30 % from that of the year 2010. Thus, the measures of the EEDP on electricity focus mainly on industrial, building, residential, and government sector

2. Scenario and analyses

Throughout history, coal has been used as an energy resource, primarily burned for the production of electricity and heat, and is also used for industrial purposes, such as refining metals [43-48]. Coal is the largest source of energy for the generation of electricity worldwide, as well as one of the largest worldwide anthropogenic sources of carbon dioxide releases [49-54].

In this study, fuel options for power generation are simulated using a scenario-based approach. The impact of major fuel options, e.g. natural gas, coal and nuclear, on the perspectives of the overall generation cost, demand, and supply was considered [55-61]. For the application of power generation, peak load requirement can be evaluated directly using the product of electricity demand and the assigned load duration curve. The additional capacity for power generation technology can be calculated based on the merit order with the constraint of planning reserve margins [62-63]. The primary resource is a withdrawal by the required feedstock during the transformation process. Moreover, targets of electricity import and export are also allowed for the target planning of power purchasing in the future [64-66]. As a result, total generation cost, demand, and supply can be calculated from the electricity generation process using each individual technology. The deviation can be presumed by the averaged properties of power production by generation type.

The scenario relies on the target-based future prospect. Ambitious macroeconomic growth causes a rise in electricity demand in the long-run. The needs of diversification on the supply side lead to a lower share of natural gas. The coal options are the considered to be the major alternative fuels in the plan. In this case, the peak power requirement relies on the recent official load forecast. The key assumptions of economic growth and overall energy elasticity for the moderate case and beyond the planning period of 2010 to 2020, it is assumed that the driver of electricity demand remains unchanged from the year 2010.

Capacity expansion of the scenario is referred to in the existing power development plan of which the increase of base-load capacity is mainly from the natural gas combined cycle, coal-fired power plant, expected to be commissioned in 2020.

In this scenario, it is assumed that the coal option becomes favorable to reduce the portion of natural gas utilization in power generation in long-term. Only coal-fired power plants will be installed for the incremental capacity of baseload requirement after the year of 2010. All of the installed capacity and imported capacity during the period remain identical to the scenario.

3. Goal target and the future

3.1. Coal-fired power plant in Thailand

Compared to Indonesia, a nation with approximately 70 coal-fired power plants, Thailand currently has five coal-fired power plants over 300 megawatts and nine smaller plants of around 100 megawatts or less (Table 3, 4). But like Indonesia, the Thai government has approved the new power development plan (PDP2015) to expand the use of coal power with large coal-fired power plants of 7,390 MW combined within the next 21 years. As has already been noted, these coal plants don’t just lead to the premature deaths of thousands of Thai people, they also foul the air, water and immediate surroundings, they displace entire communities, destroy some of Thailand’s most renowned tourist destinations and contribute to global warming [67-68].

Table 3. Operating coal-fired power plants in Thailand [69]

Power plant name	Capacity, (MW)	Power plant name	Capacity, (MW)
Mae Moh	2,400	Bangkok HSFC plant	50
BLCP	1434	Kaeng Khoi factory	17
Gheco one	700	Ban Pong spi	15
Glow SPP phase 3-5	431	Amphar Sampran	15
Tha Toom	300	Ban Pong ski	15
Muang IRPC	108	Elite kraft factory	10
Wang Sala mill	60	Prachin Buri IPC	10
Ayuthaya mill	57	Prachin Buri UTP	8

Table 4. New coal-fired power plant projects in Thailand [69]

Project name	Status	Sum of capacity, MW
Thap Sakae power station	announced	2,800
Thepa power station	announced	2,000
Krabi new	Planning	800
Mae Moh power station	Pre-permit development	600
Prachin Buri TCP	Pre-permit development	600
Prachin Buri electricity TCP	Planning	20
Grand total		5,020

The mine mouth coal-fired power generation plant in Mae Moh region is the biggest thermal power generation plant in Thailand (Fig. 2), which has used coal-lignite as fuel. It has held the second share of utility power generation about 22.7% of all utility-produced electricity referred from EGAT.

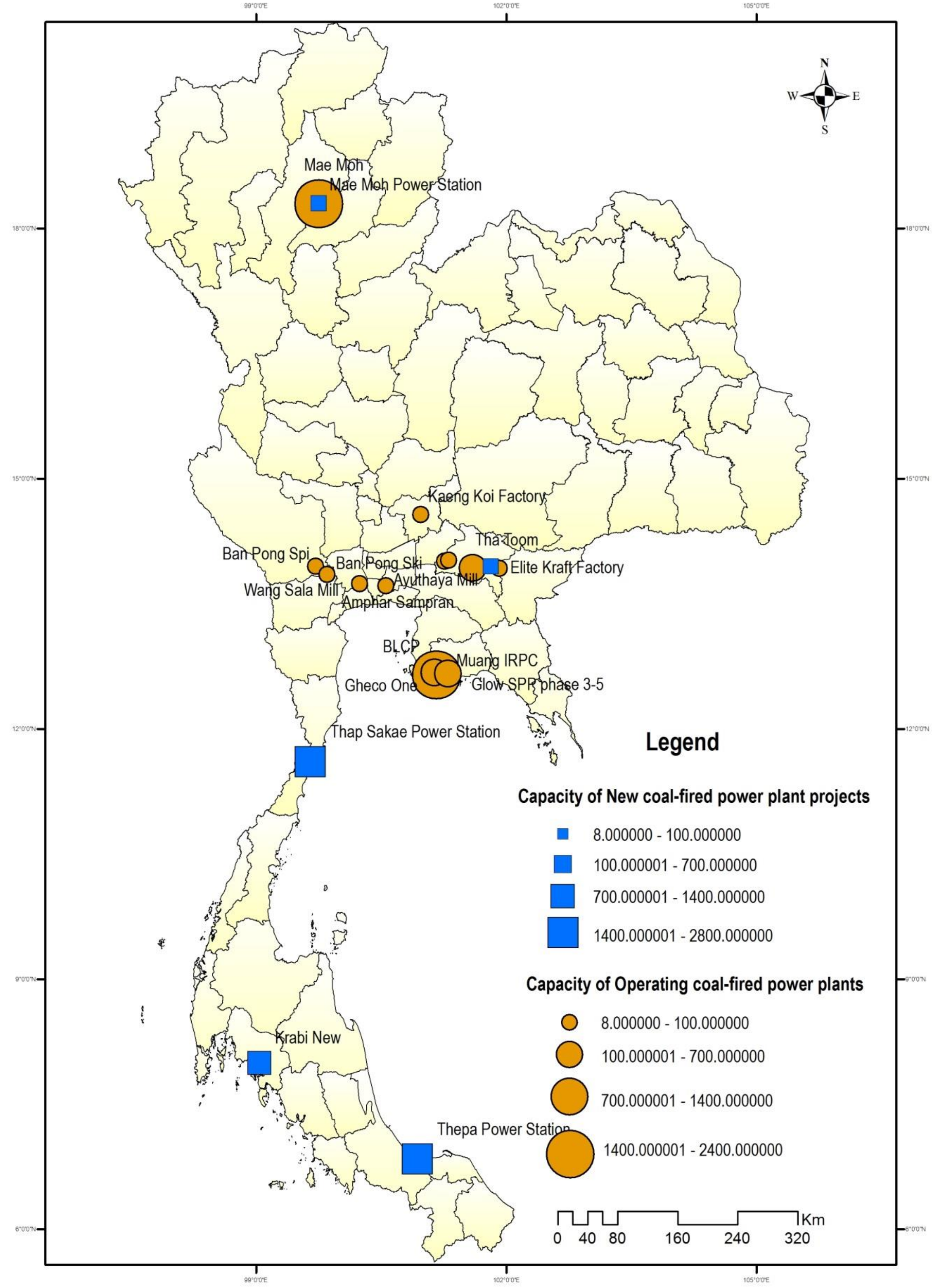

Figure 1. The coal-fired power plant in Thailand with a capacity of operating coal-fired power plants

In the year 2000, the gross electricity production by type of fuels used is approximately from natural gas, lignite, fuel oil, hydro, diesel oil and others about 52.5%, 22.7%, 16.8%, 7.8%, 0.2% and 0.0026%, respectively. Due to the lignite fuel in Mae Moh region contains a high amount of sulphur about 3% therefore, in some year, the number of health complaints have increased during the cool season when high concentrations of SO_2 has been emitted [70-74]. EGAT responded to this problem by gradually installing the flue gas desulphurization systems (FGD) (Fig. 3) in the power generation unit. Sulphur dioxide has been controlled by FGD and produced satisfactory results. On the other hand, Life cycle thinking point of view, it is important to study and understand about the environmental impacts of the power generation plant after installation of FGD in the whole life cycle (from cradle to grave) [75-78]. Moreover, when EGAT installed and operate the FGD, it has also required high investment budget, operation cost, maintenance cost and other cost. Therefore, the externality analysis of SO_2 ought to be investigated for the whole life span of the FGD. This paper discussed about Life Cycle Assessment (LCA) and externality study, in which focus on Mae Moh lignite-fired power generation plant with the generated capacity of 2,625 MW and generated electricity 15,547.56 GWh.

Figure 2. Top 3 largest coal-fired power plant in Thailand

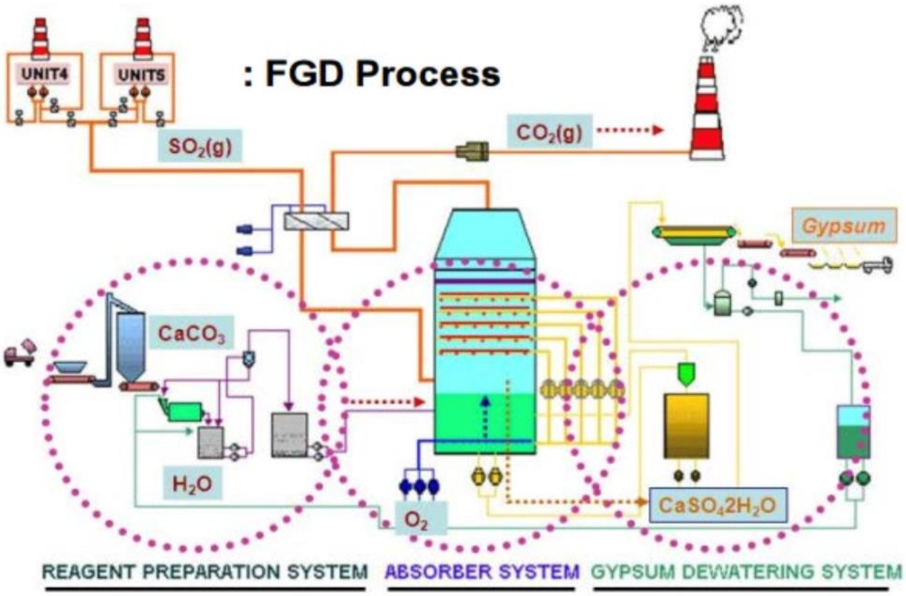

Reaction; $CaCO_3 + SO_2(g) + (1/2)O_2 + 2H_2O \longrightarrow CaSO_4.2H_2O(s) + CO_2(g)$
(Limestone) (Oxidation air) (Gypsum)

Figure 3. The flue gas desulphurization systems (FGD) in the power generation unit of Mae Moh

The 2 x 700 MW power plant of BLCP (Fig. 2), that can produce approximately 10,000 gigawatt hours (GWh), is designed to achieve the maximum efficiency consistent with reliability and cost factors [79-80], thereby, gaining the greatest possible economic utilization of the imported coal [81-88].

The raw material for BLCP power plant will be bituminous coal imported from Australia and Indonesia. The coal will be transported by ships to the berth located at the southwest of the project by coal unloaders. It will be transported and separated into 3 piles at the coal yard. The total storage capacity will be 662,000 tons in which are sufficient for 60-days continuous electricity generation. From the coal yard, the coal will be transported via conveyors to bunkers and coal pulverizers where it will be ground to a suitable size for putting into boiler furnace in suspension in transport air. Combustion of coal provides heat which is transferred to demineralized water in the tubes surrounding the furnace [89-92]. Boiling water and steam will be separated in the boiler drum located at the top of the boiler.

BLCP Power Station controls the percentage of sulfur content on per shipment basis within the range of 0.27-0.70%, and the average limit of 0.45% on per year basis. Based upon the plant design and the technical calculation, it is estimated that the Station can outperform all key parameters or limits as stipulated by the EIAs as follows.

- Dust at 43 mg/m^3 against the regulatory limit of 120 mg/m^3. Simply put, it is 64% better than the standard.
- Oxide of sulfur (SO_2) at 262 ppm. against the regulatory limit of 320 ppm. It is 18% better than the standard. (However, the annual average is at 124 ppm., or 61% better than the standard).
- Oxide of nitrogen (NO_x) at 241 ppm against the regulatory limit of 350 ppm. It is 31% better than the standard.

GHECO-One plant is designed and will be operated in line with international standards (Fig. 2), using high-quality coal and state of the art and environmentally friendly technology including NOx, SO_2 and Dust emission reduction facilities and Supercritical Pulverized Coal Boiler Technology with high efficiency reducing consumption of fuel and all emissions (Fig. 4). The project has been granted the Environment Impact Assessment (EIA) approval and Environmental

Health Impact Assessment (EHIA) approval by the Office of Natural Resources and Environmental Policy and Planning (ONEP). GHECO-One Co. Ltd (GHECO-One) is proceeding with construction activity of its coal-fired power station even though it is waiting for the opinion of the Council of State regarding which state agencies can grant permission for construction. To solve the issue GHECO-One sought authorization from the Industrial Estate Authority of Thailand (IEAT) or the National Energy Regulator agencies. The plant is located in Map Ta Put industrial zone in Thailand.

GHECO-One is the owner of the project, which will have a 660 megawatts (MW) generation capacity. GHECO-One is a joint venture company formed by Hemaraj Land and Development Public Company Limited and the Glow Group that own 35% and 65% of it respectively. GHECO-One has already signed the power-purchase deal with EGAT for the supply of electricity.

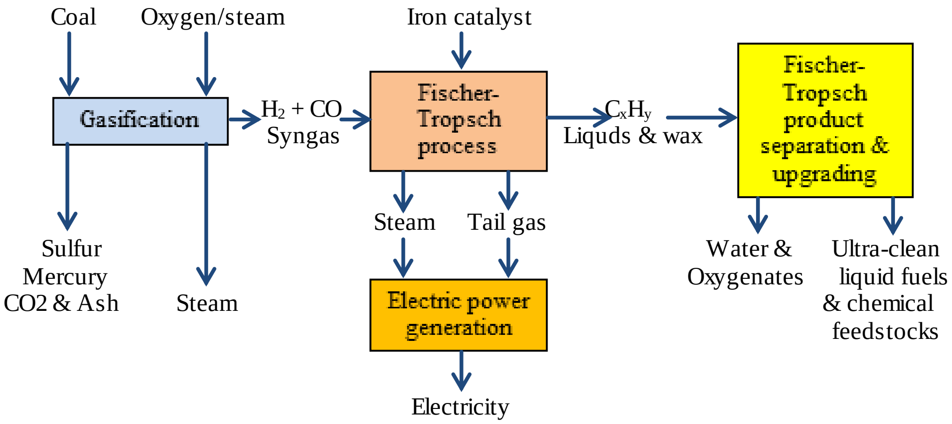

Figure. 4. Producing liquid fuels from coal – two approaches

Coal unloading facility as a precautious measure, the station will engage an independent party to perform and check the quality of every shipment of imported bituminous coal. The objective is to ensure full compliance, particularly to the sulfur content limit, at the early stage of the electricity generation process [93-95]. During the unloading, water spray equipment is also installed at the unloaded hopper in order to prevent dust dispersal.

All coal will be carefully unloaded and transported to the direction of the plant or the coal stockyard, by belt conveyor with wind protection sheet in order to prevent diffusion, spreading of dust, and falling of objects [96-97]. Water from spraying will be pumped back for treatment first before being recycled for future usage in order to save operating cost. As a result, water will be wisely used and conserved without the need for drainage into the sea. The station is also required to monitor and to check the quality of seawater around the unloading port on a regular basis.

All power station is also required to keep and maintain coal stockyards at the appropriate volume to ensure continuity of electricity generation without interruption caused by shortage during the normal and abnormal time [98]. The coal stockyard is designed to consist of three piles; the first two piles will be actively used for generating electricity and the last pile to be pressed and covered by grasses, for the purpose of back up during the fuel shortage or emergency. Water spray system is also installed with technical flexibility for constant adjustment to match with the wind speed. The 6-meter high wind protection wall is also constructed along the length of the stockyard in order to avoid dust dispersal or heat combustion [99-100].

3.2. Coal market policy

Thailand has no explicit policy on coal production or imports, and no government department is tasked with overseeing coal imports specifically [101-103]. Coal mining and transport regulations, however, are in place. As Thailand has very limited domestic coal resources, the planned increase in coal-fired generation will necessitate an increase in coal imports. Given the fairly liquid global market for coal, this is unlikely to raise any supply concerns. There are, however, environmental concerns associated with coal, in particular the climate change impacts of emissions. As the agreement signed at COP21 in Paris in December 2015 requires future climate change targets to be more stringent than current targets, any coal generation developed in Thailand will have to coexist with increasingly ambitious climate goals. Any new coal generation should be high efficiency, low-emissions (HELE), which, in addition to emitting significantly less CO_2 emissions than subcritical units, could also potentially be retrofitted to include Carbon Capture and Storage (CCS) at some later stage.

3.3. Coal-fired generation

Coal-fired generation accounts for 19.9% of total power production in Thailand. In 2014, demand for coal amounted to 25.6 million tons of coal equivalent (Mtce), and was evenly split between industrial and power generation uses. Thailand expects demand for coal to increase at an average annual rate of 1.8% per year, reaching 36.1 Mtce by 2036. While increasing industrial demand accounts for some of this growth, the majority is due to increases in coal used for power generation.

Thailand is in the process of replacing old and inefficient coal-fired generation units, such as the Khrabi power plant. This is being heavily opposed by the Thai public and non-governmental organizations, which fear detrimental health and environmental impacts from coal-fired generation [104-105]. PDP2015 calls for additional replacements and new coal-fired generation in Thailand up to 2036. In the face of domestic opposition, the government of Thailand and EGAT are building coal-fired generation units outside Thailand and importing the electricity generated via IPPs and PPAs. The first such plant is the mine-mouth Hongsa power station in Xaignabouri, Lao PDR, with another planned in Myanmar. Hongsa is being developed by Ratchaburi Electricity Generating Holding, Banpu Power and Lao Holding State Enterprise (LHSE), and will export 1,473 MW of power to Thailand with EGAT as the purchaser. A similar project is underway in Myanmar, where PTT Energy and Ratchaburi Electricity Generating Holding plan to invest in a 600 MW coal-fired power plant in Kyaing Tong, of which about 500 MW would be exported to Thailand.

The most common approach for studying the health impacts of coal-fired power plants is the "impact pathway" approach, which follows air pollution from emissions from the studied sources, to the dispersion and chemical transformation of emissions, to resulting pollution levels in different locations, to population exposure, resulting increase in health impacts, and finally to the total health impacts on the population-level [106-07]. The impact pathway approach with information sources used in the study.

The national emission standards applied to each power plant were identified and were used to calculate air pollutant emissions as a first approximation. Indonesia's state power company, PLN, has designed their power plants for 4,300 kcal coal with 0.35% sulfur, so emission rates for plants for which Plant reports compliance fuel as the SO_2 control method were calculated on this basis. Non-PLN plants without SO_2 controls were assumed to burn average Indonesian coal with 0.6% sulfur.

4. Electricity transmission and distribution

Electric power distribution is the final stage in the delivery of electric power; it carries electricity from the transmission system to individual consumers. Distribution substations connect to the transmission system and lower the transmission voltage to medium voltage with the use of transformers [108]. Distribution transformers lower the voltage to the utilization voltage of household appliances and typically feed several customers through secondary distribution lines at this voltage. Commercial and residential customers are connected to the secondary distribution lines through service drops. Customers demanding a much larger amount of power may be connected directly to the primary distribution level.

Once the power is generated, it is delivered over national and regional transmission systems to cooperative-owned substations. A number of partners are involved in this process and a portion of what is collected in your monthly bill is returned to these partners for their role in service delivery. Transmission systems, like distribution systems, are comprised of poles, wires and other equipment that are vulnerable to environmental elements and failure due to age, technical or mechanical issues [109]. When transmission-related outages occur, the operative is dependent on the transmission provider for both information and restoration. Transmission-related outages tend to be larger and more widespread than distribution system outages (Fig. 4).

This is our piece of the delivery pie. Transmission providers deliver power to our substations. The power for ultimate delivery over our distribution system to individual homes or business [110]. A portion of your monthly payment, specifically the service charge and distribution kWh charge, are used to cover the many expenses of daily operation of your cooperative, including the cost of providing and maintaining our distribution system (Fig. 4).

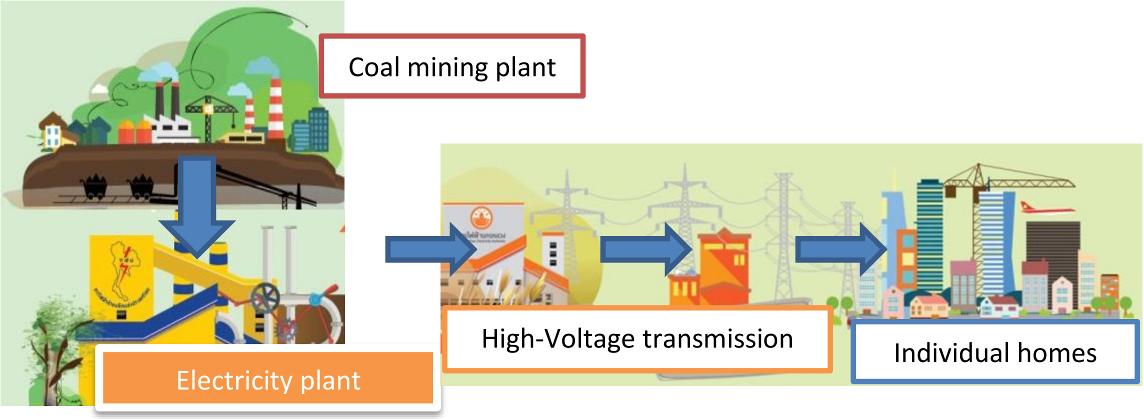

Figure 5. Coal and electricity transmission and distribution of Thailand

EGAT is the country's system operator, managing and controlling, via the National Control Center and five regional control centers, the dispatch of power generation both from both EGAT's own power plants and from private power plants to meet the country's demand in the most efficient, reliable, and environmentally-responsible way. It also owns and operates the national transmission network which includes transmission lines and substations of various high voltage levels which covers all parts of the country (Fig. 5).

5. Energy efficiency demand and power demand forecast

As an economy situated within ASEAN, the relative performance of Thailand compared to its neighbors is an important consideration with respect to the nature of domestic demand. Competition from countries such as Myanmar – which is relatively less developed but which is undergoing reforms that may increase economic development in the near term – may force Thailand to move up the economic value chain. If so, this could change the nature of electricity demand within the country, potentially reducing or even breaking the link between economic growth and growth in electricity consumption. Indeed, it is possible that the economy of Bangkok may have already experienced such a decoupling. Certain parts of Thailand, however, remain relatively underdeveloped. It is therefore possible that a decline in demand growth in some parts of Thailand could be offset by an increase in demand growth elsewhere (Fig. 6).

The Thai government should therefore be commended for taking a strong and approach to energy efficiency. Energy efficiency combines all the guiding principles of PDP2015, and is a key component of improving Thailand's electricity security. The EEP is ambitious and comprehensive and, implemented as planned, will decrease Thailand's energy intensity and increase demand for energy-efficient products and services. Achieving the reduction targets outlined by the EEP would avoid the equivalent of 16 new coal plants, and decrease greenhouse gas and other environmentally destructive emissions. A number of factors continue to constrain the implementation of energy efficiency markets in Thailand. A lack of coordination between government agencies could have an impact on the effectiveness of policies and programmes, as could a lack of energy efficiency finance, particularly for small and medium-sized enterprises [102-104].

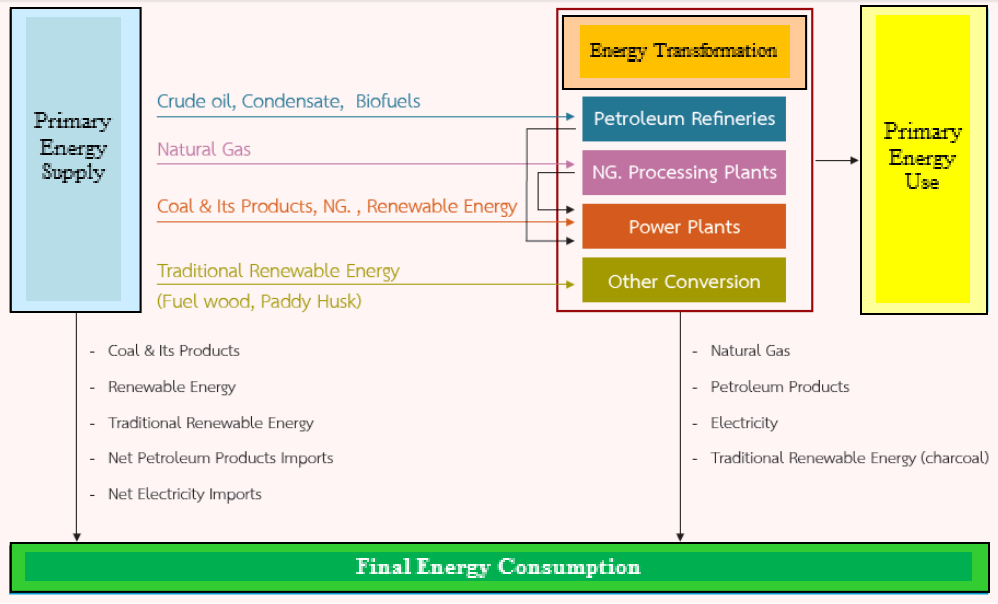

Figure 6. Flow diagram of energy supply and consumption in Thailand

Energy providers have taken an active role in demand-side energy efficiency, sustaining and expanding this role requires a system that would make reducing energy demand, and capturing the other benefits of energy efficiency, a viable business opportunity. Barriers to energy efficiency include a lack of manpower, lack of awareness on the part of the public, the relative expense of more efficient technologies, the length of payback periods and the opportunity cost of installing energy-efficient equipment versus avoiding associated downtime. Experts within Thailand have expressed concern that the easiest energy efficiency measures have already been exploited, and that it is becoming more difficult to find projects with a high enough internal rate of return to justify the investment. This is partly because the economics of energy efficiency program is undermined by Thailand's relatively low electricity tariffs. The country's tariff structure already differentiates between peak and off-peak periods. As a further step, Thailand could move to provide more granular real-time pricing in particular to large consumers, who may be in a better position to react to real-time price changes than smaller consumers. Thailand should also work to ensure that tariffs are truly cost-reflective.

Finally, with regard to demand forecasts, certain parties outside government are concerned that current projections overestimate long-term growth rates. If actual demand growth is lower than projections suggest, this could have a profound impact on the relevance of the PDP.

World production and consumption of coal declined in 2015, by 4% and 1.8%, respectively. Production fell for the first time since 1998, with large declines in the Asia Pacific (-2.9%) and North America (-10.3%). China remained by far the world's largest producer even though output fell by 2%. Coal consumption declined in all regions except South & Central America and the Asia Pacific [105-108]. The US and China accounted for all of the net declines in global consumption.

World primary energy consumption grew by a below-average 1.0% in 2015, the slowest rate of growth since 1998. Growth was below average in all regions except Europe & Eurasia. All fuels except oil and nuclear power grew at below-average rates. Oil remained the world's dominant fuel and gained global market share for the first time since 1999, while coal's market share fell to the lowest level since 2005. Renewables in power generation accounted for a record 2.8% of global primary energy consumption [109-110].

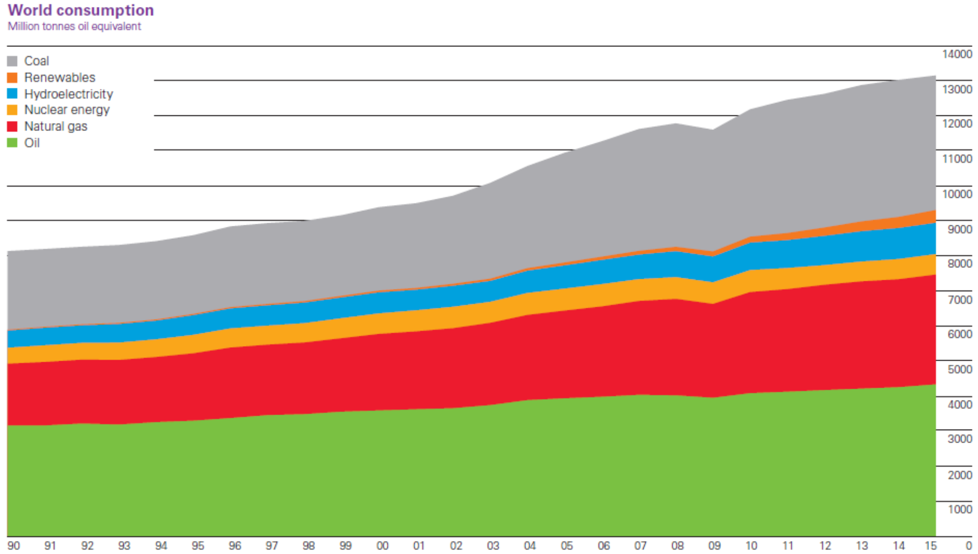

Figure 7. World consumptions of energy [3]

Coal reserves are available in almost every country. The biggest reserves are in the Asia & Oceania region [3, 111-114].

In projecting the energy demand during 2010-2020, consideration is also given to key energy policy issues of the government, for example, the energy efficiency improvement, the promotion of new & renewable energy development, the assumption that after 2011 there would be more imports of electricity from neighboring countries and that the major fuels used by new Independent Power Producers (IPPs) would be natural gas at a share of 70% and coal at a share of 30% [4-5, 115].

The overall growth in primary energy demand in Thailand is projected to be at an average rate of 4.3% during the forecast period, with oil still accounting for the largest share up to the year 2010. Then, natural gas demand would surpass oil demand from the year 2010 onwards. The demand of lignite/coal would grow, but its share in the energy mix would be rather stable and would slightly increase to 15% by the year 2020, with an average growth rate of 6% during the forecast period [Fig. 8].

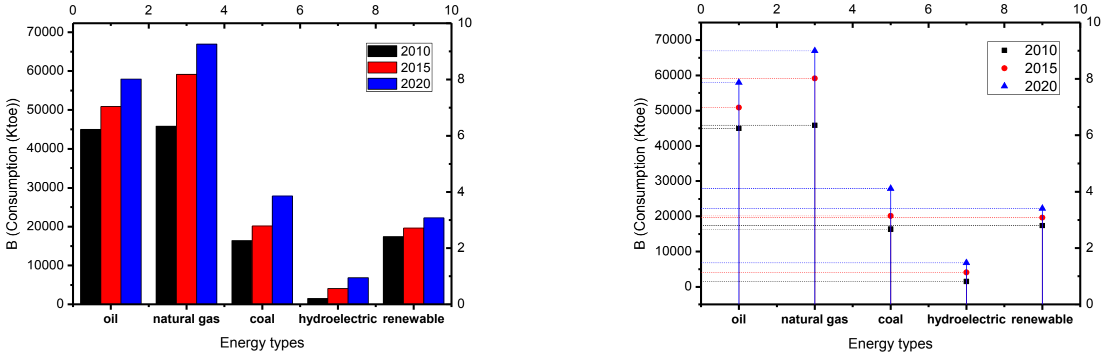

Figure 8. Projection of the share of primary energy demand during 2010-2020

The cumulative average growth rate of the overall final energy demand during the forecast period is projected to be 4.5%. The growth rate of natural gas demand during the forecast period would be the largest, i.e. 13.7%, followed by that of electricity at 5.8% and lignite/coal at 5.6%. Oil consumption would grow but its cumulative average growth rate would be only 2.8% [Fig. 9].

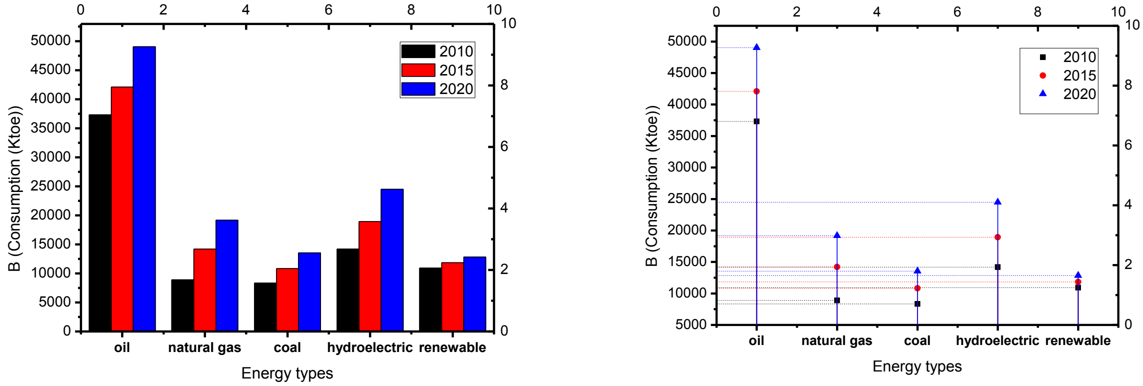

Figure 9. Projection of the share of final energy demand during 2010-2020

Using lignite & coal as fuel for power generation is a means to diversify fuel types to increase the power system security with the minimum generating cost and to stabilize the power tariffs. However, the share of coal used in power generation is now still below 20%. In the future, coal will play a greater role in the power generation in Thailand. With the full steam operation of 1,400-MW BLCP coal-fired power plant this year, a demand of 3.5 million tons of imported coal is expected for the plant. The government will encourage EGAT and new IPPs to use imported coal for power generation to be supplied to the grid after 2011. Also, the use of clean coal technology will be required to enhance the operating efficiency while reducing the environmental impact.

Given the forecast on energy demand and supply of Thailand, as mentioned earlier, together with the policy on the fuel mix of the government, it is expected that the use of coal & lignite for power generation will gradually increase in the near future. Especially for imported coal for use by IPPs, its share is projected to increase apparently from 7% in 2010 to 12% in 2020.

Table. 5 as shown the forecasting on primary energy demand and coal demand outlook according to Consumption and Compound Annual Growth Rate in Thailand. The forecasting on final energy demand and coal demand outlook according to Consumption and Compound Annual Growth Rate in Thailand, the data shown in table 6.

Table. 5. Forecast on primary energy demand

Energy types	Consumption (Ktoe)			Compound Annual Growth Rate [CAGR (%)]		
	2010	2015	2020	2010	2015	2020
Oil	44,954	50,846	57,967	2.6	2.5	2.7
Natural gas	45,852	59,145	66,955	10.1	5.2	2.5
Coal	16,355	20,141	27,881	7.1	4.3	6.7
Hydroelectric	1,510	4,061	6,835	-1.5	21.9	11.0
Renewable	17,371	19,620	22,223	1.8	2.5	2.5
Total	126,405	153,813	181,860	5.4	4.1	3.4

Table. 6. Forecast on final energy demand

Energy types	Consumption (Ktoe)			Compound Annual Growth Rate [CAGR (%)]		
	2010	2015	2020	2010	2015	2020
Oil	37,311	42,099	49,038	2.8	2.4	3.1
Natural gas	8,905	14,204	19,169	26.9	9.8	6.2
Coal	8,333	10,817	13,532	6.9	5.4	4.6
Hydroelectric	14,186	18,930	24,474	6.3	5.9	5.3
Renewable	10,917	11,832	12,838	1.6	1.6	1.6
Total	79,652	97,882	119,051	5.2	4.2	4.0

In the industrial sector, the government targets to replace 5% of oil consumption by natural gas which can be produced domestically. The gas district cooling and cogeneration will be promoted in large industries and buildings and in the industrial estates. The use of renewable energy, especially biomass, is being promoted for heat generation [116-118]. Several measures are introduced, such as, the establishment of the minimum efficiency of the combined heat and power system, measures on biomass management in industrial factories, a tax incentive for industries using biomass fuel, and legal measures on wastewater treatment and waste disposal [119-120]. Coal will be another fuel option in this sector. Imported coal of which the quality is better than domestically produced lignite has been widely used in various industries in Thailand. At present, the government has promoted greater use of clean coal technology to reduce the environmental impact resulting from the use of coal.

6. Conclusions

Thailand’s renewable energy framework is supply-side oriented. Policy measures have been designed to focus on incentivizing the increase in supply. The demand for increased renewable energy generation in Thailand has been limited to a small circle of investors. In this case, the role of consumers of electricity is merely as the bearers of costs of renewable energy investment. Hence continuous support for renewable in Thailand should include initiatives to call for more strategic planning, better regulatory support, better governance, and better public communication.

Thailand electricity generating development focuses on sustainability, the efficiency of supply and demand-side management, and public participation, with the aim to save the energy resources and reduce the effects on the environment that are accepted by the whole world as the most suitable way for the good life quality of global populations.

Thailand’s renewable energy framework still needs improvement for the following:

- Planning and strategy; the lack of strategic integration in Thailand’s energy policies and measures serve as an impediment to renewable energy growth in Thailand overall. In particular, major policies that affect the renewable power industry are not unified, including Thailand’s long-term power procurement plan.
- Policy and regulatory framework; though Thailand has made advances in putting in place an attractive feed-in tariff measure. Unforeseen problems that arose during the implementation process included the problem of speculation. Ad hoc and non-transparent responses to these caused delays in the application process for adder support and led to public criticism of poor governance.
- Financing options; financial support does exist from both the private and public sector, both domestically and from international financiers. In order for the market to expand in a continuous and sustainable manner, there is a need for an increase in capacity building in private and public financial institutions to evaluate risks and opportunities in renewable energy.

References

[1] Polachan S. The Sustainable, Security of Thailand Energy Sector. Geological Society of Thailand. International Geoscience Conference: GEOSEA 2012, Bangkok, Thailand. 22 p.
[2] Wangjiraniran W, and Euaarporn B. Study on fuel options for power generation in Thailand. Engineering Journal, 2010; 14 (3): 36-44.
[3] Dudley B. BP Statistical Review of World Energy 2016. BP p.l.c. St James’s Square, London SW1Y 4PD, UK. 48 p.
[4] Suksumek S. Coal Demand Outlook in Thailand. Energy Policy and Planning Office (EPPO), Ministry of Energy (MOE) 2007. Thailand, 40 p.
[5] Achawangkul Y. Alternative energy development plan (AEDP) 2015. Thailand Integrated Energy Blueprint, Ministry of Energy 2015, Thailand. 27 p.
[6] Wangjiraniran W, Nidhiritdhikrai R, Eua-Arporn B. Scenarios on Power Generation in Thailand. 2012 International Conference on Future Environment and Energy, IPCBEE 28 : 1-5, IACSIT Press, Singapoore.
[7] Birol F. Thailand Electricity Security Assessment 2016. International Energy Agency (IEA). 86 p.

[8] Kessels J. Prospects for coal and clean coal technologies in Thailand. IEA Clean Coal Centre (CCC). 14 Northfields, London 2010, SW18 1DD. UK. 2 p.

[9] Energy Policy and Planning Office. 2015. Thailand Power Development Plan 2015-2036. Ministry of Energy, Thailand. 78 p.

[10] Haema S. Renewable energy in Thailand. Department of Alternative Energy Development and Efficiency (DEDE), Ministry of Energy 2012, Thailand. 22 p.

[11] Alternative Energy and Efficiency Information Center. 2014. Energy of Thailand. Department of Alternative Energy Development and Efficiency, Ministry of Energy. 12 p.

[12] Song X, Yang S, Shao L, Fan J, Liu Y. PM_{10} mass concentration, chemical composition, and sources in the typical coal-dominated industrial city of Pingdingshan, China. Science of The Total Environment. 2016; 571: 1155–1163.

[13] Shakeel SR, Takala J, Shakeel W. 2016. Renewable energy sources in power generation in Pakistan. Renewable and Sustainable Energy Reviews, 2016; 64: 421–434.

[14] Hu Y, Cheng H. Control of mercury emissions from stationary coal combustion sources in China: Current status and recommendations. Environmental Pollution,2016; 218: 1209–1221.

[15] Corrêa da Silva R, de Marchi Neto I, Seifert SS. Electricity supply security and the future role of renewable energy sources in Brazil. Renewable and Sustainable Energy Reviews, 2016; 59: 328–341.

[16] Limanskiy AV, Vasilyeva MA. Using of low-grade heat mine water as a renewable source of energy in coal-mining regions. Ecological Engineering, 2016; 91: 41–43.

[17] Qin S, Sun Y, Li Y, Wang J, Zhao C, Gao K. 2015. Coal deposits as promising alternative sources for gallium. Earth-Science Reviews, 2015; 150: 95–101.

[18] Hu L, Shi X, Qiao S, Lin T, Li Y, Bai Y, Wu B, Liu S, Kornkanitnan N, Khokiattiwong S. Sources and mass inventory of sedimentary polycyclic aromatic hydrocarbons in the Gulf of Thailand: Implications for pathways and energy structure in SE Asia. Science of The Total Environment, 2017; 575: 982-995.

[19] Chan HR, Fell H, Lange I, Li S. Efficiency and environmental impacts of electricity restructuring on coal-fired power plants. Journal of Environmental Economics and Management 2017; 81: 1-18.

[20] Weldu YW, Assefa G. Olivier Jolliet. Life cycle human health and ecotoxicological impacts assessment of electricity production from wood biomass compared to coal fuel. Applied Energy, 2017; 187: 564-574.

[21] Śliwińska A, Burchart-Korol D, Smoliński A. Environmental life cycle assessment of methanol and electricity co-production system based on coal gasification technology. Science of The Total Environment, 2017; 574: 1571-1579.

[22] Sarhosis V, Jaya AA, Thomas HR. 2106. Economic modelling for coal bed methane production and electricity generation from deep virgin coal seams. Energy, 2016; 107: 580-594.

[23] Burchart-Korol D, Krawczyk P, Czaplicka-Kolarz K, Smoliński A. Eco-efficiency of underground coal gasification (UCG) for electricity production. Fuel, 2016; 173: 239-246.

[24] Li HZ, Tian XL, Zou T. Impact analysis of coal-electricity pricing linkage scheme in China based on stochastic frontier cost function. Applied Energy, 2015; 151: 296-305.

[25] Hancevic PI. Environmental regulation and productivity: The case of electricity generation under the CAAA-1990. Energy Economics, 2016; 60: 131-143.

[26] Craig CA, Feng S. Exploring utility organization electricity generation, residential electricity consumption, and energy efficiency: A climatic approach. Applied Energy, 2017; 185: 779-790.

[27] Guo Z, Cheng R, Xu Z, Liu P, Wang Z, Li Z, Jones I, Sun Y. A multi-region load dispatch model for the long-term optimum planning of China's electricity sector. Applied Energy, 2017; 185: 556-572.

[28] Zhang C, Zhong L, Liang S, Sanders KT, Wang J, Xu M. 2017. Virtual scarce water embodied in inter-provincial electricity transmission in China. Applied Energy, 2017; 187: 438-448.

[29] Gökgöz F, Atmaca ME. Portfolio optimization under lower partial moments in emerging electricity markets: Evidence from Turkey. Renewable and Sustainable Energy Reviews, 2017; 67: 437-449.

[30] Bigerna S, Bollino CA, Ciferri D, Polinori P. Renewables diffusion and contagion effect in Italian regional electricity markets: Assessment and policy implications. Renewable and Sustainable Energy Reviews, 2017; 68: 199-211.

[31] Gal N, Milstein I, Tishler A, Woo CK. Fuel cost uncertainty, capacity investment and price in a competitive electricity market. Energy Economics, 2017; 61: 233-240.

[32] Iychettira KK, Hakvoort RA, Linares P, de Jeu R. Towards a comprehensive policy for electricity from renewable energy: Designing for social welfare. Applied Energy, 2017; 187: 228-242.

[33] Eren S, Küçük D, Ünlüer C, Demircioğlu M, Yanık Y, Arslan Y, Özsoy B, Güverçinci AH, Elma İ, Tanıdır Ö, Ölmez YC, Sönmez S. A ubiquitous Web-based dispatcher information system for effective monitoring and analysis of the electricity transmission grid. International Journal of Electrical Power & Energy Systems, 2017; 86: 93-103.

[34] Tayal D, Rauland V. Future business models for Western Australian electricity utilities. Sustainable Energy Technologies and Assessments, 2017; 19: 59-69.

[35] Bhattacharyya R, Ganguly A. 2017. Cross subsidy removal in electricity pricing in India. Energy Policy 2017; 100: 181-190.

[36] Craig CA, Feng S. An examination of electricity generation by utility organizations in the Southeast United States. Energy, 2016; 116: 601-608.

[37] Chen H, Wang C, Ye M. An uncertainty analysis of subsidy for carbon capture and storage (CCS) retrofitting investment in China's coal power plants using a real-options approach. Journal of Cleaner Production, 2016; 137: 200-212.

[38] Ming Z, Lilin P, Qiannan F, Yingjie Z. Trans-regional electricity transmission in China: Status, issues and strategies. Renewable and Sustainable Energy Reviews, 2016; 66: 572-583.

[39] Pean E, Pirouti M, Qadrdan M. Role of the GB-France electricity interconnectors in integration of variable renewable generation. Renewable Energy, 2016; 99: 307-314.

[40] Matar W, Echeverri R, Pierru A. The prospects for coal-fired power generation in Saudi Arabia. Energy Strategy Reviews, 2016; 13–14: 181-190.

[41] Shim C, Hong J. Impact of a national plan for future electricity supply on ambient air quality in South Korea. Energy Policy, 2016; 88: 278-288.

[42] Long N, Duncan A. Oregon’s new clean energy law: Broad coalition wins with groundbreaking bill to cut coal-fired electricity, double renewable energy. The Electricity Journal2016; 29 (3): 19–20.

[43] Song M, Cui L. Economic evaluation of Chinese electricity price marketization based on dynamic computational general equilibrium model. Computers & Industrial Engineering, 2016; 101: 614-628.

[44] Şengül H, Bayrak F, Köksal MA, Ünver B. A cradle to gate life cycle assessment of Turkish lignite used for electricity generation with site-specific data. Journal of Cleaner Production, 2016; 129: 478-490.

[45] Tahmasebi A, Zheng H, Yu J. The influences of moisture on particle ignition behavior of Chinese and Indonesian lignite coals in hot air flow. Fuel Processing Technology,2016; 153: 149-155.

[46] Lechner AM, Kassulke O, Unger C. Spatial assessment of open cut coal mining progressive rehabilitation to support the monitoring of rehabilitation liabilities. Resources Policy, 2016; 50: 234-243.

[47] Rybak A, Rybak A. Possible strategies for hard coal mining in Poland as a result of production function analysis. Resources Policy2016; 50: 27-33.

[48] Salmi EF, Nazem M, Karakus M. The effect of rock mass gradual deterioration on the mechanism of post-mining subsidence over shallow abandoned coal mines. International Journal of Rock Mechanics and Mining Sciences, 2017; 91: 59-71.

[49] Zhang D, Wang J, Zhang P, Shi B. Internal strain monitoring for coal mining similarity model based on distributed fiber optical sensing. Measurement, 2017; 97: 234-241.

[50] He F, Gu L, Wang T, Zhang Z. The synthetic geo-ecological environmental evaluation of a coastal coal-mining city using spatiotemporal big data: A case study in Longkou, China. Journal of Cleaner Production, 2017; 142: 854-866.

[51] Howladar MF, Deb P, Muzemder ATMSH. Monitoring the underground roadway water quantity and quality for irrigation use around the Barapukuria Coal Mining Industry, Dinajpur, Bangladesh. Groundwater for Sustainable Development, 2017; 4: 23-34.

[52] Liu X, Bai Z, Zhou W, Cao Y, Zhang G. Changes in soil properties in the soil profile after mining and reclamation in an opencast coal mine on the Loess Plateau, China. Ecological Engineering, 2017; 98: 228-239.

[53] Chong T, Yi S, Heng C. Application of set pair analysis method on occupational hazard of coal mining. Safety Science,2017; 92: 10-16.

[54] Calvo JAP, Pérez AMJ. Optimal extraction policy when the environmental and social costs of the opencast coal mining activity are internalized: Mining District of the Department of El Cesar (Colombia) case study. Energy Economics,2016; 59: 159-166.

[55] Norman H. Coal Mining and Coal Seam Gas on Gomeroi country: Sacred lands, economic futures and shifting alliances. Energy Policy, 2016; 99: 242-251.

[56] Karan SK, Samadder SR. Reduction of spatial distribution of risk factors for transportation of contaminants released by coal mining activities. Journal of Environmental Management,2016; 180: 280-290.

[57] Espitia-Pérez L, Sosa MQ, Salcedo-Arteaga S, León-Mejía G, Hoyos-Giraldo LS, Brango H, Kvitko K, da Silva J, Henriques JAP. Polymorphisms in metabolism and repair genes affects DNA damage caused by open-cast coal mining exposure. Mutation Research/Genetic Toxicology and Environmental Mutagenesis,2016; 808: 38-51.

[58] Burchart-Korol D, Fugiel A, Czaplicka-Kolarz K, Turek M. Model of environmental life cycle assessment for coal mining operations. Science of The Total Environment,2016; 562: 61-72.

[59] Hendrychová M, Kabrna M. An analysis of 200-year-long changes in a landscape affected by large-scale surface coal mining: History, present and future. Applied Geography, 2016; 74: 151-159.

[60] Yaylacı ED, Düzgün HŞ. Indicator-based sustainability assessment for the mining sector plans: Case of Afşin-Elbistan Coal Basin. International Journal of Coal Geology, 2016; 165: 190-200.

[61] Gao W, Ge M. Stability of a coal pillar for strip mining based on an elastic-plastic analysis. International Journal of Rock Mechanics and Mining Sciences, 2016; 87: 23-28.

[62] Jiang B, Wang L, Lu Y, Sun X, Jin G. Ground pressure and overlying strata structure for a repeated mining face of residual coal after room and pillar mining. International Journal of Mining Science and Technology, 2016; 26(4): 645-652.

[63] Yao B, Ma Q, Wei J, Ma J, Cai D. Effect of protective coal seam mining and gas extraction on gas transport in a coal seam. International Journal of Mining Science and Technology,2016; 26 (4): 637-643.

[64] Deng X, Zhang J, Kang T, Han X. Strata behavior in extra-thick coal seam mining with upward slicing backfilling technology. International Journal of Mining Science and Technology, 2016; 26(4): 587-592.

[65] Korski J, Tobór–Osadnik K, Wyganowska M. Reasons of problems of the polish hard coal mining in connection with restructuring changes in the period 1988–2014. Resources Policy, 2016; 48: 25-31.

[66] Meng Z, Shi X, Li G. Deformation, failure and permeability of coal-bearing strata during longwall mining. Engineering Geology, 208: 69-80.

[67] Gautam S, Prasad N, Patra AK, Prusty BK, Singh P, Pipal AS, Saini R. Characterization of $PM_{2.5}$ generated from opencast coal mining operations: A case study of Sonepur Bazari Opencast Project of India. Environmental Technology & Innovation, 2016; 6: 1-10.

[68] Wang S, Li X, Wang D. Mining-induced void distribution and application in the hydro-thermal investigation and control of an underground coal fire: A case study. Process Safety and Environmental Protection, 2016; 102: 734-756.

[69] Suchowerska Iwanec AM, Carter JP, Hambleton JP. Geomechanics of subsidence above single and multi-seam coal mining. Journal of Rock Mechanics and Geotechnical Engineering, 2016; 8: 304-313.

[70] Ribeiro J, Suárez-Ruiz I, Flores D. Geochemistry of self-burning coal mining residues from El Bierzo Coalfield (NW Spain): Environmental implications. International Journal of Coal Geology, 2016; 159: 155-168.

[71] Zhao Z, Zhu J, Xia B. Multi-fractal fluctuation features of thermal power coal price in China. Energy, 2016; 117: 10-18.

[72] Yang S, Qian Y, Liu Y, Wang Y, Yang S. Modelling, simulation, and techno-economic analysis of Lurgi gasification and BGL gasification for coal-to-SNG. Chemical Engineering Research and Design, 2017; 117: 355-368.

[73] Holuszko ME, Leeder WR, Mackay M, Giroux L, McPhee T, Ng KW, Dexter H. Effects of organic liquids on coking properties of a higher-inert Western Canadian coal. Fuel Processing Technology, 2017; 155: 225-231.

[74] Zhao Y, Sun Y, Liu S, Wang K, Jiang Y. Pore structure characterization of coal by NMR cryoporometry. Fuel, 2017; 190: 359-369.

[75] Jiang W, Jia K, Chen Z, Deng Y, Rao P. Using spatiotemporal remote sensing data to assess the status and effectiveness of the underground coal fire suppression efforts during 2000–2015 in Wuda, China. Journal of Cleaner Production, 2017; 142: 565-577.

[76] Wu XD, Xia XH, Chen GQ, Wu XF, Chen B. Embodied energy analysis for coal-based power generation system-highlighting the role of indirect energy cost. Applied Energy, 2016; 184: 936-950.

[77] Tang L, Shi J, Yu L, Bao Q. Economic and environmental influences of coal resource tax in China: A dynamic computable general equilibrium approach. Resources, Conservation and Recycling, 2017; 117: 34-44.

[78] Li Y, McCalley JD. An innovative disjunctive model for value-based bulk transmission expansion planning. Electric Power Systems Research, 2017; 143: 7-13.

[79] Zhu J, Wu G, Shi Ch, Gan D, Cao Y, Wu C. Research on the electric unbalance degree of multiple transmission lines non-parallelly erected entirely in one common corridor. International Journal of Electrical Power & Energy Systems, 2017; 85: 67-76.

[80] Saikia J, Narzary B, Roy S, Bordoloi M, Saikia P, Saikia BK. Nanominerals, fullerene aggregates, and hazardous elements in coal and coal combustion-generated aerosols: An environmental and toxicological assessment. Chemosphere, 2016; 164: 84-91.

[81] Pearse R. The coal question that emissions trading has not answered. Energy Policy, 2016; 99: 319-328.

[82] Siriwardane R, Benincosa W, Riley J, Tian H, Richards G. Investigation of reactions in a fluidized bed reactor during chemical looping combustion of coal/steam with copper oxide-iron oxide-alumina oxygen carrier. Applied Energy, 2016; 183: 1550-1564.

[83] Guo Z, Ma L, Liu P, Jones I, Li Z. A multi-regional modelling and optimization approach to China's power generation and transmission planning. Energy, 2016; 116: 1348-1359.

[84] Li Y, Lukszo Z, Weijnen M. The impact of inter-regional transmission grid expansion on China’s power sector decarbonization. Applied Energy, 2016; 183: 853-873.

[85] Zhang L, Li Z, Yang Y, Zhou Y, Kong B, Li J, Si L. Effect of acid treatment on the characteristics and structures of high-sulfur bituminous coal. Fuel, 2016; 184: 418-429.

[86] Rioux B, Galkin P, Murphy F, Pierru A. Economic impacts of debottlenecking congestion in the Chinese coal supply chain. Energy Economics, 2016; 60: 387-399.

[87] Tian L, Gai X, Qu B, Li H, Zhang P. Influence of spatial variation of ground motions on dynamic responses of supporting towers of overhead electricity transmission systems: An experimental study. Engineering Structures, 2016; 128: 67-81.

[88] Arora V, Cai Y, Jones A. The national and international impacts of coal-to-gas switching in the Chinese power sector. Energy Economics, 2016; 60: 416-426.

[89] Misch D, Gross D, Huang Q, Zaccarini F, Sachsenhofer RF. Light and trace element composition of Carboniferous coals from the Donets Basin (Ukraine): An electron microprobe study. International Journal of Coal Geology, 2016; 16: 108-118.

[90] Yuan J, Li P, Wang Y, Liu Q, Shen X, Zhang K, Dong L. Coal power overcapacity and investment bubble in China during 2015–2020. Energy Policy, 2016; 97: 136-144.

[91] Saikia BK, Dalmora AC, Choudhury R, Das T, Taffarel SR, Silva LFO. Effective removal of sulfur components from Brazilian power-coals by ultrasonication (40 kHz) in presence of H_2O_2. Ultrasonics Sonochemistry, 2016; 32: 147-157.

[92] Tang S, Wang L, Feng X, Feng Z, Li R, Fan H, Li K. Actual mercury speciation and mercury discharges from coal-fired power plants in Inner Mongolia, Northern China. Fuel, 2016; 180: 194-204.

[93] Hu S, Wei Z, Chang Q, Trinchi A, Yang J. A facile and green method towards coal-based fluorescent carbon dots with photocatalytic activity. Applied Surface Science, 2016; 378: 402-407.

[94] Chen Z, Zhang X, Gao L, Li S. Thermal analysis of supercritical water gasification of coal for power generation with partial heat recovery. Applied Thermal Engineering, 2017;111: 1287-1295.

[95] Ahmed U, Kim C, Zahid U, Lee C, Han Ch. Integration of IGCC and methane reforming process for power generation with CO_2 capture. Chemical Engineering and Processing: Process Intensification, 2017; 111: 14-24.

[96] Liu Y, Cai YP, Yang ZF, Tan Q, Lin X. Identification of optimal recourse strategies for power generation under a government-guided coal-pricing mechanism in north China. International Journal of Electrical Power & Energy Systems, 2016; 79: 210-227.

[97] Wu J, Hou H, Yang Y. Annual economic performance of a solar-aided 600 MW coal-fired power generation system under different tracking modes, aperture areas, and storage capacities. Applied Thermal Engineering, 2016; 104: 319-332.

[98] Zhai R, Liu H, Li C, Zhao M, Yang Y. Analysis of a solar-aided coal-fired power generation system based on thermo-economic structural theory. Energy, 2016; 102: 375-387.
[99] Wang K, Wang S, Liu L, Yue H, Zhang R, Tang X. Environmental co-benefits of energy efficiency improvement in coal-fired power sector: A case study of Henan Province, China. Applied Energy, 2016; 184: 810-819.
[100] Xu C, Xu G, Zhao S, Dong W, Zhou L, Yang Y. A theoretical investigation of energy efficiency improvement by coal pre-drying in coal fired power plants. Energy Conversion and Management, 2016; 122: 580-588.
[101] Godby R, Coupal R. The potential impact of rate-based or mass-based rules on coal-producing states under the Clean Power Plan. The Electricity Journal, 2016; 29: 42-51.
[102] Yuan J, Lei Q, Xiong M, Guo J, Hu Z. The prospective of coal power in China: Will it reach a plateau in the coming decade? Energy Policy, 2016; 98: 495-504.
[103] Mylläri F, Karjalainen P, Taipale R, Aalto P, Häyrinen A, Rautiainen J, Pirjola L, Hillamo R, Keskinen J, Rönkkö T. Physical and chemical characteristics of flue-gas particles in a large pulverized fuel-fired power plant boiler during co-combustion of coal and wood pellets. Combustion and Flame, 2017; 176: 554-566.
[104] Yan Y, Yang C, Peng L, Li R, Bai H. Emission characteristics of volatile organic compounds from coal-, coal gangue-, and biomass-fired power plants in China. Atmospheric Environment, 2016; 143: 261-269.
[105] Zhao Y, Hong H, Jin H. Appropriate feed-in tariff of solar–coal hybrid power plant for China’s Inner Mongolia Region. Applied Thermal Engineering, 108: 378-387.
[106] Meng M, Mander S, Zhao X, Niu D. Have market-oriented reforms improved the electricity generation efficiency of China's thermal power industry? An empirical analysis. Energy, 2016; 114: 734-741.
[107] Hinojosa VH, Velásquez J. Improving the mathematical formulation of security-constrained generation capacity expansion planning using power transmission distribution factors and line outage distribution factors. Electric Power Systems Research, 2016;140: 391-400.
[108] Cho B, Choi G, Uruno Y, Kim H, Chung J, Kim H, Lee K. One-dimensional simulation for attemperator based on commissioning data of coal-fired steam power plant. Applied Thermal Engineering, 2016; 113: 508-518.
[109] Ma S, Zhao Y, Yang J, Zhang S, Zhang J, Zheng C. Research progress of pollutants removal from coal-fired flue gas using non-thermal plasma. Renewable and Sustainable Energy Reviews, 2017; 67: 791-810.
[110] Wei M, Zhao X, Fu L, Zhang S. Performance study and application of new coal-fired boiler flue gas heat recovery system. Applied Energy, 2017; 188: 121-129.
[111] Hao R, Zhang Y, Wang Z, Li Y, Yuan B, Mao X, Zhao Y. An advanced wet method for simultaneous removal of SO_2 and NO from coal-fired flue gas by utilizing a complex absorbent. Chemical Engineering Journal, 2017; 307: 562-571.
[112] Xue Y, Tian H, Yan J, Zhou Z, Wang J, Nie L, Pan T, Zhou J, Hua S, Wang Y, Wu X. Temporal trends and spatial variation characteristics of primary air pollutants emissions from coal-fired industrial boilers in Beijing, China. Environmental Pollution, 2016; 213: 717-726.
[113] Li Y, Yan M, Zhang L, Chen G, Cui L, Song Z, Chang J, Ma Ch. Method of flash evaporation and condensation – heat pump for deep cooling of coal-fired power plant flue gas: Latent heat and water recovery. Applied Energy, 2016; 172: 107-117.
[114] Mun T, Tumsa TZ, Lee U, Yang W. Performance evaluation of co-firing various kinds of biomass with low rank coals in a 500 MWe coal-fired power plant. Energy, 2016; 115: 954-962.
[115] Starkloff R, Postler R, Al-Maliki WAK, Alobaid F, Epple B. Investigation into gas dynamics in an oxyfuel coal fired boiler during master fuel trip and blackout. Journal of Process Control, 2016; 41: 67-75.
[116] Valentić V, Žiković S, Višković A. Can CCS save coal fired power plants – The European perspective. International Journal of Greenhouse Gas Control, 2016; 47: 266-278.
[117] Li S, Chen Z, He E, Jiang B, Li Z, Wang Q. Combustion characteristics and NO_x formation of a retrofitted low-volatile coal-fired 330 MW utility boiler under various loads with deep-air-staging. Applied Thermal Engineering, 2017; 110: 223-233.
[118] Zhai R, Li C, Chen Y, Yang Y, Patchigolla K, Oakey JE. Life cycle assessment of solar aided coal-fired power system with and without heat storage. Energy Conversion and Management, 2016; 111: 453-465.
[119] Zhang Y, Shi M, Wang J, Yao J, Cao Y, Romero CE, Pan W. Occurrence of uranium in Chinese coals and its emissions from coal-fired power plants. Fuel, 2016; 166: 404-409.

[120] Gu Y, Xu J, Chen D, Wang Z, Li Q. Overall review of peak shaving for coal-fired power units in China. Renewable and Sustainable Energy Reviews, 2016; 54: 723-731.

To whom correspondence should be addressed: Dr. Kittiphop Promdee, Department of Environmental Science, Chulachomklao Royal Military Academy, Nakhon Nayok, 26001, Thailand

Petroleum and Coal

Article **Open Access**

TRANSFORMER OIL DEGRADATION STUDY BY CHROMATOGRAPHY, SPECTROSCOPY AND DISSOLVED GAS ANALYSIS

*Reena R. Meena *, Sunil Chaki, Ankurkumar J. Khimani, M. P. Deshpande*

P.G. Department of Physics, Sardar Patel University, Vallabh Vidyanagar - 388 120, Gujarat, India

Received May 22, 2018; Accepted August 27, 2018

Abstract

Transformer oil is a very important component of the transformer. The oil acts as an insulator and heat exchanger. This paper compares and evaluates the analytical observations of two transformer oils. The two transformer oils taken as samples for the study are; one a non-used transformer oil of the make year 1997 and another a fresh transformer oil of 2017 make. The transformer oil used in India is paraffin based having long chains of hydrocarbon, with general chemical formula, C_nH_{2n+2}. In the present study, gas chromatography – mass spectrometry (GC-MS) technique was employed to determine the compositional constituents of both the oils. The Fourier transformed infrared (FTIR) and ultra violet – visible (UV-Vis) spectroscopy techniques were employed to characterize both the oils. Dissolved gas analysis (DGA) technique was employed to analyze the oils conditions. The obtained results for the old and new oils have been deliberated and compared in this paper.

Keywords: *Transformer oils; GC-MS; FTIR; UV-VIS spectroscopy; DGA.*

1. Introduction

Transformer oils are highly refined mineral oil possessing excellent insulating properties. It also works as a coolant and as a heat exchanger when in operation in a transformer. The transformer oil is of two types, the naphthenic based and the paraffinic based oil. In India the transformer oil generally used is paraffin based and is labeled as IS-335:1993. The transformer oil contains long chains of hydrocarbons possessing general chemical formula as C_nH_{2n+2}, where n varies from 11 to 44.

The working of transformer leads to degradation of the transformer oil. Due to degradation, it loses its insulating property. This degradation is due to hydrogenation and oxidization [1-2]. It has been observed that high voltage and temperature of operation hastens the deterioration of the transformer oil. This deterioration results into the change in the chemical composition of the oil which ultimately results into the generation of new degradation by-products such as carbon monoxide (CO), aldehydes, ketones, etc. [3]. As a result of the change in the chemical composition of the oil, the different gases are evolved and are responsible for the worsening of the insulating property of the oil [4-7]. There are also changes in the physical properties like the color of the oil, density, viscosity and flash point due to its aging process. Because of the changes in the chemical and physical composition of the insulating oil, there is furthermore a change in the electrical property of the insulating oil. These changes affect one of the important parameters, its break down voltage (BDV). Hence one can say owing to working of transformer there is an overall change in the physical, chemical and electrical properties of the insulating transformer oil. As the transformer oil properties change with the operation, there is always a possibility of the oil to alter its properties with the passage of time [8-9]. Sensing to the possibility of transformer oil properties modification with the passage of time the authors studied the properties of two transformer oils of different ages.

The authors were fortunate to have an unused transformer oil of the year 1997 make, which was used as one sample. The 20 years old transformer oil was compared with new transformer oil of 2017 make. Thus, the new transformer oil was the second sample.

There are various techniques to analyse insulating oil, but the methods are costly, laborious and time-consuming. Therefore, the authors employed simple spectral analytical techniques like gas chromatography – mass spectrometry (GC-MS), Fourier transformed infra-red (FTIR) spectroscopy and UV-Vis spectroscopy to characterize the two transformer oil samples.

This paper highlights the chromatographic, spectral and dissolved gas analysis data of the two transformer oils. The effort has been made to compare and analyse both the data.

2. Experimental

An old transformer oil of the year 1997 make was labeled as T1 and was used without any purification or treatment for analysis and study. Similarly, the fresh, pure transformer oil of 2017 make was labeled as T2 and was procured from the local market; APAR Industries, Vadodara, Gujarat, India. Both are branded in India market as IS-335:1993. The photographs of both the samples are shown in Figure 1.

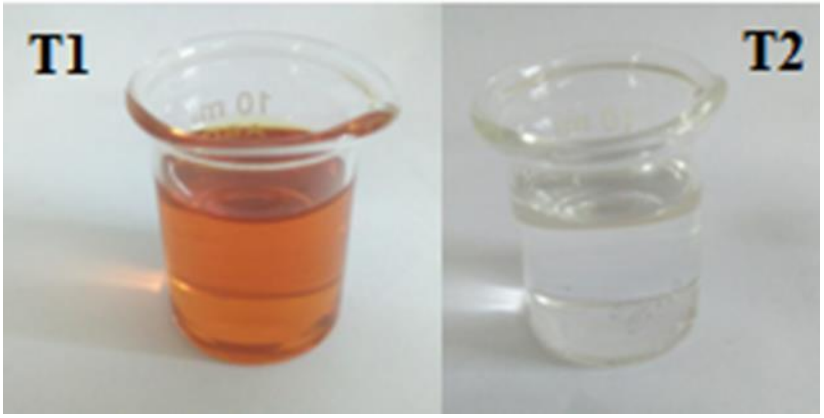

Figure 1. Photography of transformer oils T1 and T2

The photography of the oils, Figure 1, shows that the old oil T1 appears to be darker than the new oil T2. The visual observation seems to indicate that the old oil T1 has colloidal suspension due to degradation. The new transformer oil T2 appeared colorless and transparent.

The chemical composition determination of T1 and T2 oil samples were done by Gas-Chromatography attached with Mass Spectrometry (GC-MS) technique. In this GC-MS analysis, Perkin Elmer Auto system XL GC with Turbo mass was employed. Reason for selection of this technique was the ease and simplicity of analysis. The GC-MS analysis gives instantaneousness, efficient identification, and quantification of oil components and compositions [10-11].

The different chemical bonds present in the T1 and T2 samples were studied by Fourier transformed infra-red (FTIR) technique. The Shimadzu FTIR – 8400S was employed for the analysis of both the transformer oil T1 and T2 samples.

The ultraviolet – visible (UV-Vis) spectroscopy was carried out on T1 and T2 oils using Systronics Double beam UV-Vis Spectrometer 2202. The UV-Vis Spectroscopy measurement was done in the wavelength range of 200nm to 600nm. In general practice, the UV-Vis spectroscopy is employed as an on-line diagnostic tool to detect early abnormalities in transformers [12-18].

The dissolved gas analysis (DGA) is one of the basic and best techniques to determine the degradation of the oil. The transformer oil composition undergoes lots of chemical changes under the influence of operating temperature and high voltage. Gases evolve due to excessive thermal or electrical stress. The generated dissolved gases are in low concentrations (ppm), and its proper analysis can allow the early intervention before the degradation of the oil sets in and lead to failure of the electrical apparatus. The level of these generated gases will decide the incipient fault [19]. The DGA for both the samples T1 and T2 was performed employing

Perkin Elmer, ARNEL CLARUS 580. The break down voltage (BDV) and moisture content of the oil samples were also determined.

3. Results and discussion

The obtained GC-MS spectra of both the transformer oil samples, T1 and T2, are shown in Figure 2(a, b). The analysis of the GC-MS spectra shows that the sample consists of hydrocarbon with different units of carbon. The thorough analysis of the spectra showed that both the transformer oil samples are liquid paraffin based having chemical formula as C_nH_{2n+2}. The analysis showed that the value of n ranges from 11 to 45 for the analyzed sample T1 (old), whereas in the case of sample T2 (new) it ranges from 14 to 44. The mass spectroscopy of gas chromatography of the sample T1 showed a prominent peak having a retention time of 10.23 minutes. This peak is due to the presence of sulfurous acid, 2-ethylhexyl nonyl ester having molecular formula $C_{17}H_{36}O_3S$. The analysis by GC-MS corroborates the presence of sulphurous acid in T1. This proves that the sulphur content of T1 oil sample has converted to acid. While in the case of T2 no sulfurous compound was observed in the GC-MS analysis.

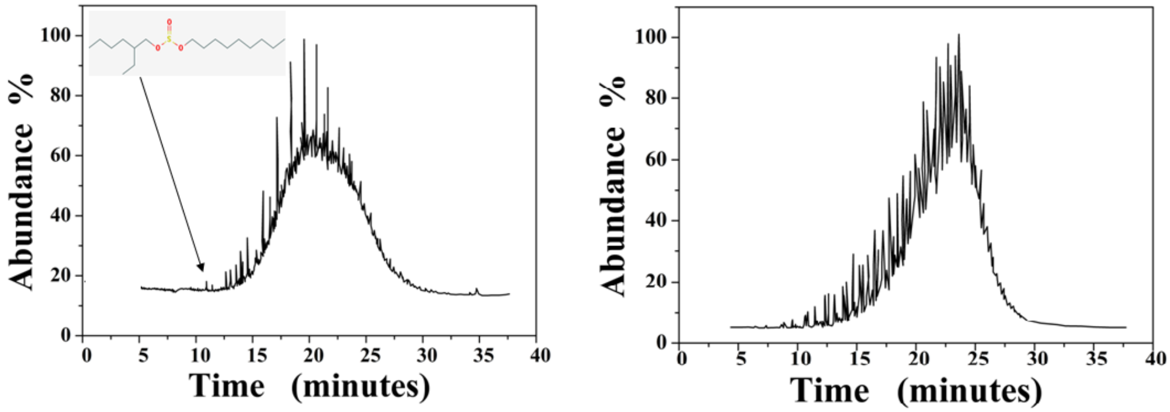

Figure 2. The GC-MS spectra of (a) transformer oil T1 and (b) transformer oil T2

The FTIR spectra recorded for transformer oil samples T1 and T2 are shown in Figure 3(a, b). The FTIR spectra give the qualitative measurement, and the peak sizes directly indicate the specific chemical bonds present in the sample.

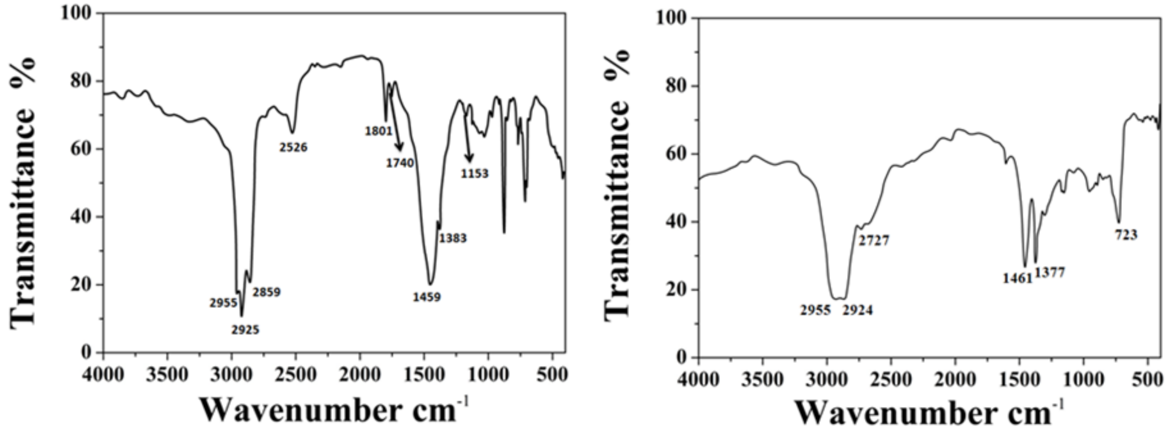

Figure 3. FTIR spectra for (a) transformer oil T1 and (b) transformer oil T2

The observed peaks in recorded FTIR of T1 and T2 samples were assigned bonds [20]. The vibrational and stretching bonds assigned to the observed FTIR peaks of the samples T1 and T2 are tabulated in Table – 1(a, b) [21].

Table 1(a). The FTIR peaks and assigned bonds of transformer oil sample T1

FTIR peak position (cm^{-1})	Assigned Bonds
2955	=C-H stretching of the carbon-carbon double bonds
2925 and 2859	CH stretching, CH_3 methylene group
1801	-C=O stretch
1740	Oxidation of oil (carbonyl group, ketones)
1469	C-H symmetric bend
1373	CH_3 bend
1153	Sulphonation of the oil
900 -680	Aromatic compounds. Shows the position of the benzene ring.

Table 1(b) The FTIR peaks and assigned bonds of transformer oil sample T2

FTIR peak position (cm^{-1})	Assigned Bonds
2955	=C-H stretching of the carbon-carbon double bond
2924 and 2727	C-H stretching of the saturated carbon – carbon bonds
1461	C-H symmetric bending (alkanes) methyl and methylene
1377	C-H bending of the alkanes (iso-propyl split)
733	C-H out of the plane stretching of the standard carbon – carbon bond.

The analysis of Table 1(a, b) shows that many observed peaks remain common in both the samples T1 and T2. The common FTIR peaks of the samples T1 and T2 lies near to wave-number positions 2955, 2924, 2727, 1461, 1373 cm^{-1}. These peaks are present in the old sample T1 and new sample T2, stating them to be standard peaks arising due to a paraffinic compound of which the oils are composed. All these peaks have been assigned with various bonds.

The table shows three extra peaks in the old transformer oil sample T1. They lie at the wave-number positions 1801, 1740 and 1153 cm^{-1}. The peak at wave-number 1801 cm^{-1} is due to -C=O stretch, thus stating oxygen reacting with the oil and forming a bond. The peak observed at wave-number 1740 cm^{-1} is due to the oxidation caused by the carbonyl and carboxyl compound [22-24]. The transformer oil modification also leads to an increase in acidic and aromatic (pungent) content. This increase in acidic and aromatic content increases the C=O and C=C double bond. The thermal aging of a paraffinic compound of the transformer oil dehydrogenates and forms naphthenic compounds. These naphthenic compounds get further dehydrogenated and form conjugated C=C double bond [24-25].

The peak observed at wave-number 1153 cm^{-1} arises due to the sulphonation of the oil. The introduction of sulphur increases the sludge formation and leads to degradation of the oil. They reacted with water to produce powerful inorganic acids such as sulfuric acid (H_2SO_4) [21]. This states that water content in the oil has increased leading to the formation of sulphuric acid. The presence of the sulphuric acid compounds was also confirmed by the GC-MS analysis. The FTIR analysis substantiates that with the passage of time, the transformer oils undergo oxidation as well as sulphonation. The oxidation leads to an acid formation that can corrode the transformer. The sulphonation increases sludge formation which leads to sedimentation and degradation of transformer operation.

Along with the FTIR spectroscopy, the UV-Vis spectroscopy is employed for the study of T1 and T2 transformer oils. The obtained spectra for T1 and T2 oils are shown in Figure 4.

The UV-Vis spectra show that T2 oil has lower absorbance compared to T1 oil. Lower absorbance in T2 oil means more transparency in T2 oil compared to T1 oil. The higher absorbance in T1 clearly shows the oil is less transparent compared to T2. This UV-Vis spectra analysis of less transparency of T1 oil compared to T2 oil substantiates the visual observation of the oil, Figure 1. The decrease in transparency in T1 is due to sludge formation as observed in FTIR spectroscopy analysis. The UV-Vis spectra clearly corroborate the FTIR observations. The higher absorbance indicates the variation in the oil which is due to the increased dissolved decay products as well as the impurities in it due to its ageing [26-27].

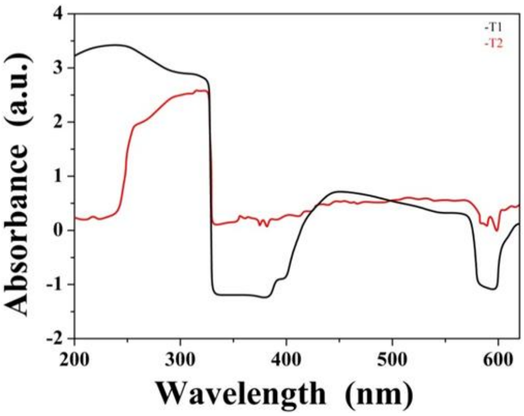

Figure 4 The UV-Vis NIR for the sample T1 and T2

The obtained results of the DGA analysis of both the transformer oil samples T1 and T2 are tabulated in Table 2.

Table 2. The DGA analysis data for T1 and T2 oil samples

Sr. No.	Name of the gas	T1 (old) oil(ppm)	T2 (new) oil(ppm)
1	Hydrogen	5	Traces (<1)
2	Methane (CH_4)	8	Traces (<1)
3	Ethylene (C_2H_4)	Traces(<1)	Nil
4	Ethane (C_2H_6)	Nil	Nil
5	Acetylene (C_2H_2)	Nil	Nil
6	Carbon dioxide (CO_2)	633	53
7	Carbon monoxide (CO)	45	4
8	Oxygen (O_2)	7 774	6 893
9	Nitrogen (N_2)	24 091	18 350

The analysis of DGA data, Table 2, firstly confirms the non use of both the oils. This is confirmed by the absence of ethylene, ethane, and acetylene in case of both the transformer oil samples. This ethylene, ethane and acetylene hydrocarbon compounds get formed due to the high temperature of the transformer oil. Since the oils are non used samples, the temperature has never increased, and thus ethylene, ethane, and acetylene hydrocarbon compounds have not been formed.

More amount of carbon dioxide (CO_2) and carbon monoxide (CO) in old oil sample T1 compared to new oil sample T2 is due to over exposure of T1 to the atmosphere. Due to the exposure to the atmosphere, the C-C single bond breaking in the hydrocarbon chains of the sample T1 takes place, which further leads to the formation of CO_2 and CO. On the other side the sample T2 is fresh oil and is not exposed more to the atmosphere leading to less formation of CO_2 and CO. The DGA analysis furthermore revealed that oxygen (O_2) and nitrogen (N_2) content is more in T1 oil compared to T2 oil. This further confirms over exposure of T1 oil sample to the atmosphere. The exposure leads to percolation of atmospheric oxygen and nitrogen into the oil.

Other than the chemical constituents present in the oil samples, the standard basic data like break down voltage and moisture content of both the samples were evaluated and are tabulated in Table 3.

Table 3. Basic data of T1 and T2 transformer oils

Sr. No.	Parameter	Test method	T1 (old) oil	T2 (new) oil
1	Break down voltage (BDV)	IS: 6792: 1992	28 kV	60 kV
2	Water content	IS: 13567: 1992	90ppm	< 30ppm

The analysis of the data of Table 3 shows that the BDV value has decreased more than half in case of old transformer oil T1 compared to new oil T2. This corroborates the degradation of transformer oil over time. Similarly, the water content data shows nearly three times more water content in old transformer oil T1 compared to new transformer oil T2. This further confirms the degradation of transformer oil with the passage of time. The water content increase is due to long exposure of old transformer oil to the atmosphere leading to hydration of the oil.

4. Conclusion

Two paraffinic based transformer oils, one of make year 1997 that is 20 years old and another of make year 2017 that is a fresh oil were comprehensively characterized. The visual observation of the oil showed the old transformer oil to be yellowish brown colloidal compared to the new oil which was near colorless transparent. The GC-MS analysis showed the presence of the sulphurous complex in old oil, whereas in new oil no such amalgam was observed. The FTIR analysis further confirmed the presence of the sulphurous complex in the old oil. The old oil was found to be less transparent compared to the new oil analyzed by the transmission spectra analysis employing UV-Vis spectroscopy. The DGA analysis of the transformer oils showed the presence of atmospheric gases in the old oil. The DGA observations clearly stated over exposure of old oil to the atmosphere. The determined standard parameters of the studied transformer oil samples showed that water content has increased in the old oil compared to the new oil. Even the BDV has decreased to more than half in case of old transformer oil, whereas BDV of new transformer oil remained satisfactory. All these observations clearly state that the old transformer oil has degraded due to over exposure to the atmosphere. The degradation is by the formation of different unwanted complexes, leading to colloidal oil and impoverished standard parameters.

Acknowledgments

The authors are grateful to the APAR Industries Ltd. Vadodara, Gujarat, India for providing the fresh transformer oil as sample; Sardar Vallabhbhai National Institute of Technology (SVNIT), Surat, Gujarat, India, Sophisticated Instrumentation Centre for Applied Research & Testing (SICART), Vallabh Vidyanagar, Anand, Gujarat, India and Electrical Research and Development Association (ERDA), Vadodara, Gujarat, India for the analytical measurements.

References

[1] Cackova V, Dedinska L, Kvakovsky M. Degradation mechanism in transformer oil. 9th Scientific Conference of Young Researchers, FEI Tu of Kosice (2010).

[2] Wang M, V Andermaar AJ, Srivastava KD. Review of condition assessment of power transformer in service. Electrical Insulation Magazine, IEEE (2002) 12-25.

[3] Chernozhukov NI, Krein SE, Losikov BV. Oxidizability of Mineral Oils. Gostoptekhizdat, Moscow (1955) 121–126.

[4] Duval M. Dissolved gas analysis: It can save your transformer. Electrical Insulation Magazine IEEE 5 (1989): 22-27.

[5] Pandey R, Deshpand MT. Dissolved gas analysis (DGA) of mineral oil used in transformer. Int. J. of Appl. or Innovation in Engg. & Management ;1: 208-212.

[6] Kelly J. Transformer fault diagnosis by dissolved gas analysis. Transactions on Industry Applications IEEE,1980; 16: 777-782.

[7] Hussain K, Karmakar S. Dissolve gas analysis of aged transformer oil: a case study. J. of Elect. Engg., 2015: 1-10.

[8] Missas S, Danikas MG, Liapis I. Factors affecting the ageing of transformer oil in 150/20kV transformers. Int. Conf. on Dielectric Liq. IEEE (2011).

[9] Liapis I, Danikas MG. A study of parameters affecting the ageing of the transformer oil in distribution transformer. Int. Conf. on Dielectric Liq. IEEE (2011).

[10] Blomberga J, Schoenmakersb PJ, UA Th. Brinkmanc. Gas chromatographic methods for oil Analysis, J. of Chromatography A, 2002;972: 137-173.

[11] Kaplan IR, Rasco J, Lu. Shan Tan. Chemical characterization of transformer mineral insulating oils. J. Environmental Forensics, 2010; 11: 117-145.

[12] Palmer JA, Wang X, Shoueshi RA, Mander A, Torgerson DRC. Effect of aging on the spectral response of transformer oil. Electrical Insulation, Conference Record of the 2000 IEEE International Symposium on Electrical Insulation. Anaheim, CA, USA (2002)

[13] Siada AA, Lai Sin SP, Islam S. Remnant life estimation of power transformer oil using UV-Vis spectral response. Power Systems Conference and Exposition, IEEE/PE Conference , Seattle, WA, USA (2009).

[14] Lai SP, Siada AA, Islam SM., Lenc G. Correlation between UV-Vis spectral response and furan measurement of transformer oil. International Conference on Condition Monitoring and Diagnosis, Beijing, 2008.

[15] Karthik R, Raja T, Shunmugam S. Performance evaluation of transformer oil using UV-Vis spectrophotometer. Acta Scientiarum Technology, 2014; 36: 245-250.

[16] Gafiyatullina LG. UV Spectroscopy of GK Transformer Oil. Opt. and Spect., 2010; 109: 97–100.

[17] Hussain K, Karmakar S. Condition assessment of transformer oil using UV-Visible spectroscopy. Power Systems Conference, IEEE, (2014) 1–5.

[18] Malika H. UV/VIS response based fuzzy logic for health assessment of transformer oil. Procedia Engineering, 2002; 30: 905-912.

[19] Duval M. A review of faults detectable by gas in oil analysis in transformers. electrical insulation magazine. IEEE, 2002; 18: 8-17.

[20] Drago RS. Physical method in inorganic chemistry (Chapter 7). East-West Press Pvt. Ltd., New Delhi (1968).

[21] http://machinerylubricationindia.com/magazine/108-2015/sep-oct/302-benefits-of-ftir-oil-analysis”

[22] Georgiev A, Karamancheva I, Topalova L. Determination of oxidation products in transformer oils using FT-IR spectroscopy. J. of Mol. Structure, 2008; 872: 18–23.

[23] Mihalcova J. Study of degradation of mineral oils product by FTIR Method. Chem. pap.,2003; 57: 211-215.

[24] Zakharich MP, Zaitsev II, Komar VP, Nikonovich FN, Ryzhkov MP, Skornyakov IV. Analysis of transformer oil using IR analyzers. J. of Applied Spectroscopy, 2001; 68: 61-65.

[25] Benounis M, Aka-Ngnui T, Jaffrezic N, Dutasta JP. NIR and optical fiber sensor for gases detection produced by transformation oil degradation. Sensors and Actuators,2008; 141: 76–83.

[26] Karmakar S, Roy NK, Kumbhakar P, Effect of ageing in transformer oil using UV-visible spectrophotometeric technique, J. Optics, 2011; 40: 33-38.

[27] Ghalkhani M, Fofana I, Bouaicha A, Hemmatjou H. Influence of aging by-products on the gassing tendency of transformer oils. Electrical Insulation and Dielectric Phenomena, 2012: 870–873, DOI: 10.1109/CEIDP.2012.6378919.

To whom correspondence should be addressed: Dr. Reena R. Meena, P.G. Department of Physics, Sardar Patel University, Vallabh Vidyanagar - 388 120, Gujarat, India, reenameena_001@yahoo.co.in

Petroleum and Coal

Article **Open Access**

THE PROSPECTS OF OBTAINING PLASTIC GREASES FROM SECONDARY HYDROCARBON RAW MATERIAL

Andrey B. Grigorov[1], Oleg I. Zelenskii[2], Alexey V. Sytnik[2]

[1] National Technical University «Kharkov Polytechnic Institute», 61002, 2 Kirpichova str., Kharkov, Ukraine
[2] Ukrainian State Coal-Chemistry Institute, 61023, 7 Vesnina Str., Kharkov, Ukraine

Received June 5, 2018; Accepted August 27, 2018

Abstract

The paper presents the results of producing lubricating grease from industrial and household waste in the laboratory. Partially prepared diesel engine oil SAE 10W-40 was used as a dispersion environment, and high and low pressure polyethylene (household polyethylene bags used) was used as thickener. It has been established that by using selected base oil, thickener and anti-wear additive DF-11, recycling oils can be obtained, which will be classified according to DIN 51502 to K2PF-30 and K3PF-30. It is proposed to expand the raw material base for the production of recycling oils through the using of waste industrial, hydraulic, transmission oils, as well as high-boiling petroleum fractions extracted from oil sludge or acidic tar and selective waste distillate oils. On the basis of the analysis of the researching results, it was established that on the basis of exhausting motor oil and polyethylene with the addition of additives of different functional purpose, it is possible to obtain a number of antifriction plastic lubricants used in swing bearings, railway and protective greases that can be used in the range of operating temperatures, on average up to 100ºC.

Keywords: *exhausting motor oil; thickener; plastic grease; polyethylene; additives; optical density; express analysis.*

1. Introduction

With the modern development of the techno sphere, there is a tendency to increase the volume of industrial and domestic household waste. Their accumulation has a negative impact on the environment and directly on humans. However, these wastes can be considered as an alternative source of hydrocarbon raw material for many technological processes for the production of various materials of the broad functional value. These materials can be realized in chemical industries. At the same time, waste processing improves the global environmental situation significantly and brings a significant revenue to the budget of the country developing this direction.

2. The purpose and objectives of the research

A very promising direction in the use of the secondary hydrocarbon raw material is the production of plastic greases, which in their properties are not inferior to products obtained during the oil processing. They also have a much lower cost of production.

In general, any plastic grease contains in its composition 70-90 % (mass) of the base oil (mineral or synthetic nature), 5-15 % (mass) of the thickener (metallic soaps) and 1-5 % (mass) of various additives. In addition to these constituents, 3-10 % (mass) of other components are present in oils. They are fillers that improve the performance properties of the final commercial product [1-2].

Drawing on long-term experience in the production and application of greases in various industries, it should be noted that the main components, of which today lubricants are produced, can be replaced by cheap analogs with storage of the required quality level. One of the many-tonnage industrial wastes, which on the one hand is a rather dangerous waste, and on the other hand is a valuable resource for many manufacturing processes, is used lubrication oils [3]. These oils can be successfully used as a base oil (dispersion medium) in the technology of greases production.

Thus, for example, it has been investigated the possibility of using used motor oils after regeneration and hydrocarbon distillation from the sludge of the purification unit for the production of highly alkaline sulfonate additives as a dispersion medium of hydrocarbon and soap greases. Solid oil paraffin, petrolatum, and calcium stearate were used as a thickener [4].

Dry and calcium-rich and hydrocarbon preservative greases with enhanced protective properties are known in comparison with oils on base distillates based on the use of used motor oils as a dispersion medium. Obtained lubricants in terms of their bulk and surface properties are similar to the lubricants "EXXON Estan 1.2" and "SHELL Ossagl V (00)" [5].

In work [6], it is proposed to obtain preservative lubricants for the protection of agricultural machinery with the use of purified waste motor oils and thickeners – stillage bottoms from the production of synthetic fatty acids and metallic soaps Ca, Li. The proposed lubricants inhibit the anodic dissolution of the steel due to both the oil itself and the action of antioxidant, anticorrosive additives, and are similar in properties to commercial greases "AGIP Grease CC 2.3", "Texas Hytex EP-2".

Based on purified waste motor oils, thickener, graphite and complex antiwear additive the authors of the work [7] obtained greases in appearance and basic properties similar to general-purpose commercial lubricants.

For thickening by greasing of threaded joints, in particular for conical threaded connections of pipes and equipment used in wells, a lubricant containing the oil base and a powder filler (graphite, zinc, lead, aluminum, etc.) is used [8].

Today used polyethylene products are the most common solid domestic waste that accumulates in the countries of the European Union and is a cheap source of hydrocarbon raw materials. Taken into consideration some properties of polyethylene itself (resistance to organic and inorganic solvents, the melting point is 103-140°C), these products can be used as a thickener in the grease production.

It is shown that the addition of recycled polymers (polyethylene, polypropylene and EVA copolymer) to lithium grease improves its rheological properties significantly [9]. Based on the mixture of paraffinic mineral oils of Group I and II (kinematic viscosity at 40 °C is equal to 160 mm^2/s), they are produced by Indian Oil Corporation Ltd. (Faridabad, India) and blends of polypropylene and high-density polyethylene, greases with high rheological properties were obtained [10].

Also, in work [11] plastic greases were synthesized, they correspond to the classification DIN 51502, K5S-60 according to their properties, and contain low molecular weight polyethylene and up to 30 % (mass) oils (dewaxed oil, residual extract of selective oil purification and used oils).

In the field of railway transport, namely, for lubricating rails on the curved sections of the track, a composition consisting of low molecular weight polyethylene is used – a waste product for the production of high-density polyethylene 15-25 % (mass) of hydrolytic lignin, 10-25 % (mass) of the spent diesel oil are added to this waste [12].

3. Results and discussion

Having analyzed the information given above, it is possible to propose a conditional technological classification of plastic greases according to the main components from which it was obtained, namely, base oil and thickener:

Group I plastic greases – classic greases obtained from distillate petroleum or synthetic oils, which as a thickener contain metallic soaps, solid hydrocarbons, and inorganic substances;

Group II plastic greases – combined greases in which the base oil and thickener can be partially replaced by industrial waste, by-products, and substances found in other industries;

Group III plastic greases – recycling greases, in which the base oil and thickener can be completely replaced with industrial and household waste.

The share of recycling greases in the total volume of production and consumption of lubricants is very small, but at the moment the certain conditions have already been created under which this direction is a priority in scientific research of the countries of the European Union.

Considering this, it is possible to propose a scheme for the grease production (Fig. 1), in which the base oil is the partially prepared semisynthetic motor oil SAE10W-40 API SL/CF, and the thickener is high pressure polyethylene or low pressure polyethylene, or their mixture.

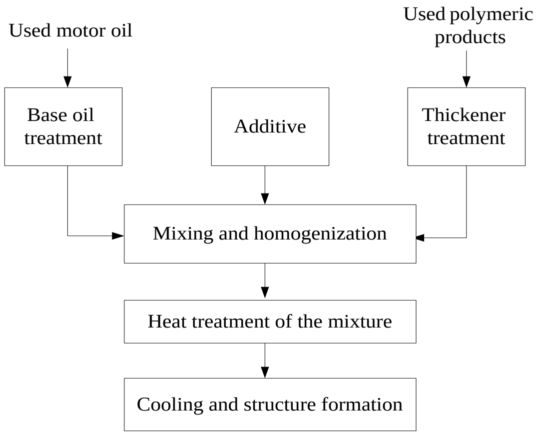

Fig. 1. The structural scheme for obtaining recycling grease

First, the dispersion medium – used motor oil SAE10W-40 API SL/CF, undergoes a preparatory stage, including the removal of water and mechanical impurities from its composition by settling and centrifuging the oil. At this stage, also used polyethylene products – packaging film, bags, etc., are crushed.

Further, the prepared components (base, thickener, and complex additive) are fed into mixing and homogenization, where the thermal dissolution of the thickener with a certain concentration of polyethylene occurs at a temperature of at least 110 °C. Then the reaction mixture undergoes heat treatment at a higher temperature. The final stage in the scheme is cooling and forming the final structure of the grease with the properties given in Table. 1.

Table 1 Quality indicators of obtained plastic greases

Indicator name	Numerical values of indicators for grease compositions	
Thickener mark	Polyethylene of high pressure	Polyethylene of low pressure
Concentration of thickener, % (mass)	7	5
External view	Homogeneous ointment, black	Homogeneous ointment, black
Penetration at 25 ºC, mm·10^{-10}	273	235
Droplet temperature, ºC	95	110
Corrosion effect on metals (carbon steel)	Withstands, no traces of corrosion	Withstands, no traces of corrosion
Evaporation at 120 ºC	0,72	0,43
Content, % (mass):		
free alkalis	0,04	0,04
water	not available	not available
mechanical impurities	0,10	0,10
water-soluble acids and alkalis	not available	not available
Colloidal stability, %	6,34	3,67

It should be noted that in the grease production with the use of polyethylene as a thickener, unlike lubricants where metal soaps are used [13], it is not necessary to conduct a deep preparation (cleaning) of the dispersion medium. It is enough to remove only water and mechanical impurities.

Polar tar-asphaltene substances, which are the products of oxidation of hydrocarbon crude, they also have a positive effect on the properties of the grease, since they cause high adhesion to metal surfaces. Another oxidation product is carboxylic acids. They are corrosion inhibitors [14], and these acids improve the volumetric properties of lubricants [15]. Also, the grease has good low-temperature properties due to the depressant additives that make up the base oil.

The results of the laboratory tests show that a lubricant thickened with 7 % by weight of high pressure polyethylene and 4.0 % of an antiwear additive according to DIN 51502 refers to K2PF-30, and a lubricant with 5 % by weight of low pressure polyethylene and 4.0 % of an antiwear additive can be attributed to K3PF-30.

Also, compared «EXXON Estan 1.2» this lubricant has a higher value of the dropping point (at 15°C), which extends the upper temperature limits of its application. Also, the greases obtained have a lower value of colloidal stability (by 3.66-9.33 % of the removed oil) than "EXXON Estan 1.2". According to other indicators, the obtained greases have values close to those of "EXXON Estan 1.2".

The adhesive properties of the obtained lubricants were tested by applying the grease to a degreased metal plate, followed by testing it in a laboratory centrifuge for discharge at 3000 rpm. within 3 minutes. The undertaken study has shown that the grease layer is completely preserved on the metal plates. Hence the lubricants withstand the tests.

It is possible to expand the raw material base for the production of recycled oils of thickened high pressure polyethylene and low pressure polyethylene by using other raw materials (used industrial, hydraulic, transmission oils, as well as high boiling petroleum fractions isolated from oil sludge or acid sludge, and wastes of selective purification of distillate oils), but, this requires additional research.

4. Conclusion

The development and introduction of recycling grease production technologies in the industry will allow reducing the harmful impact on the environment from the accumulation of industrial and domestic waste, using them as raw materials in manufacturing processes aimed at obtaining fuels and lubricants.

It is possible to get a number of antifriction plastic greases on the basis of large-tonnage waste, used motor oil and used polyethylene products, which are a valuable source of secondary hydrocarbon raw materials, including the additives of various functional purposes. These lubricants are used in rolling bearings, as rail and protective lubricants, which can be used in the range of operating temperatures to an average of 100°C. Due to the low cost and simplification of the raw material preparation technology, the obtained greases will be much cheaper compared to analogues made from oil according to the classical technology.

References

[1] Rizvi SQA. Lubricant Chemistry, Technology, Selection and Design; ASTM International: West Conshohocken, PA, USA, 2009; p. 443.

[2] Donahue CJ. Lubricating Grease: A Chemical Primer. J. Chem. Educ. 2006; 83(6): p. 862.

[3] Diphare M, Pilusa J, Muzenda E, Mollagee M. A Review of Waste Lubricating Grease Management. 2nd International Conference on Environment, Agriculture and Food Sciences (ICEAFS'2013), Kuala Lumpur (Malaysia), 2013, p. 131-134.

[4] Pokrovskaya SV, Bulavka YuA, Bogdanovich AI, Zubova AV. The use of regenerated spent engine oil and organic sludge removal in the production of soap and hydrocarbon grease. The Bulletin of the Polotsk State University. 2012; 11: 104-108.

[5] Skobeltsin AS, Nemets VL. Study of the possibility of using used motor oils as a dispersion medium of soap greases. Oil refining and petrochemistry. 2005; 9: 32-37.

[6] Ostrikov VV, Matyitsin GD, Guschina AI. Preservative lubricants based on products of cleaning of used motor oils. Practice of anti-corrosion protection. 1999; 12(2): 5-17.

[7] Kornev AYu, Shihalev IN, Ostrikov VV. Preparation of greases based on used oils. Science in Central Russia. 2013; 4: 227-228.

[8] Lyubinin IA, Misyura VV, Korotkova NP, Kravets EA. Graphite and its modifications - antifriction filler of greases. Questions of chemistry and chemical technology. 2013; 3: 121-129.

[9] Martin-Alfonso JE, Valencia C, Sanchez MC, Franco JM, Gallegos C. Rheological modification of lubricating grease with recycled polymers from different plastic waste. Ind. Eng. Chem. Res. 2009; 48: 4136-4144.

[10] Dixena R, Sayanna E, Badoni R. Recycled and Virgin HDPEs as Bleed Inhibitors and Their Rheological Influences on Lubricating Greases Thickened with PP and mPP. Lubricants. 2014; 2: 237-248.

[11] Pokrovskaya SV, Oschepkova NV, Bulavka YuA. Plastic lubricants based on low-molecular polyethylene at the Polymir plant. The Bulletin of the Polotsk State University. 2009; 8: 173-176.

[12] Tuvshintur B, Vinokurov DI, Yakimova GA, Gozbenk VE. Application of lubricant for the system "wheel-rail". Solving the problem of wear with the use of production waste. Systems. Methods. Technologies. 2015; 27(3): 23-31.

[13] Shihalev IN. A method for obtaining a dispersion medium of lubricants based on used motor oils and evaluating the performance of a grease in a friction unit. Science in Central Russia. 2015; 17(5): 98-104.

[14] Prokhorenkov VD, Ostrikov VV, Knyazeva LG. Use of used motor oils as a basis for conservation materials. Practice of anti-corrosion protection. 2000; 16(2): 40-45.

[15] Golovnikov AV, Filippova OP, Yamanina NS, Kopyilov AB. Investigation of the structure, properties and physico-chemical characteristics of used oils. Proceedings of the Tula State University. 2012; 1: 120-126.

To whom correspondence should be addressed: Dr. Andrey B. Grigorov, National Technical University «Kharkov Polytechnic Institute», 61002, 2 Kirpichova str., Kharkov, Ukraine, grigorovandrey@ukr.net

Petroleum and Coal

Article **Open Access**

GENERAL ALGORITHM FOR EFFICIENCY EVALUATION OF MULTI-COLUMN DISTILLATION FLOWSHEETS

Marina A. Samborskaya, Inga A. Gryaznova[1], Andrey V. Volf, Evgeniy V. Popok*

Division for Chemical Engineering, Tomsk Polytechnic University, Russia

Received May 25, 2018; Accepted August 27, 2018

Abstract

The paper shows the development and application of a general algorithm for efficiency evaluation (AEE) of distillation sequences. The algorithm provided consideration of energy efficiency, flowsheet structure, and product specifications. In Aspen HYSYS^{TM}, we developed two "first principle" models of crude oil distillation units with and without heat integration. We have applied the AEE to compare the effectiveness of their performance for different types of oil. The effectiveness was higher for heat integrated unit, so its model was adopted as basic. Six alternative retrofit flowsheet models were developed for the purposes of preliminary optimization. Preliminary optimization was a combination of predesign optimization of unit flowsheet structure and apparatus design to create the optimal crude oil distillation unit and to provide the process flexibility in respect of feed flowrate and oil quality. Parametrical optimization was performed for all configurations of flowsheet structure. Maximum feed flowrates and the product yields were defined for all flowsheet structures. Relative total investments for retrofits of the basic flowsheet were estimated. They consider the cost of distillation columns, the internal device, pumps, heat exchangers, piping. AEE application to all retrofit flowsheets allows designing effective and relatively inexpensive refinery unit.

***Keywords**: crude oil distillation unit; multi-column distillation sequences; general algorithm for efficiency evaluation; preliminary optimization; parametrical optimization; thermodynamic efficiency.*

1. Introduction

Distillation technologies and oil fractionation is not an exception. Energy consumption in the fractionation units determines the energy efficiency of a refinery in whole. The feed rate of the refineries, as a rule, exceeds one million ton per year. According to the data [1] average feed rate of a refinery in the Russian Federation is 8.72 million tons per year.

Numerous studies are conducted in order to increase the energy efficiency of oil fractionation since the even slight reduction in energy consumption delivers sufficient benefits. Increase in efficiency of the fractionation units executes both in the way of efficient utilization of external heat and in high recovery of light oil distillates.

Complex oil composition and complexity of a flowsheet structure along with heat integration and recovery require both preliminary optimization on the design stage and optimization during a unit performance [2].

Optimization based on the simulation is executed with the use of technologic, thermodynamic or economic criteria. The aim of thermodynamic analysis is to minimize energy consumption by means of optimal flowsheet development.

The authors [3] noted that the energy consumption for the distillation column is proportional to the minimum number of transfer units and the minimal reboiler duty. They proposed the original methods to calculate these values based on thermodynamic analysis for the initial design stage. The authors [4] performed an algorithm for the optimal design of thermally coupled distillation sequences. The criterion of optimality was the minimal reboiler duty corresponding to maximal thermodynamic efficiency.

A thermodynamic analysis is widely used to evaluate and minimize irreversibility in the distillation systems, for the decrease in the operation costs and ecological expenses. In paper [5], the author has reviewed conventional methods and case studies of thermodynamic analysis for binary and multicomponent systems and for refinery as well. Authors [6] performed the exergy analysis of single- and two-stage crude oil distillations, showed the sufficiently lower exergy lost for the two-stage flowsheet.

However, the energy efficiency of a unit performance depends considerably on a heat recovery for which rigorous simulation of the whole flowsheet is required. Economic criteria are formulated in terms of investments and operation cost.

In the paper [7], alternatives of representation were examined for economic optimization of a single distillation column. The objective function – the total annualized cost (TAC) was the sum of equipment and heat transfer fluid costs. The algorithm requires sufficient CPU time and faces a convergent problem. Authors [8] performed the hybrid algorithm, which used the results of simulation the distillation flowsheets in Aspen HYSYS^{TM} to minimize TAC. TAC is the sum of investments and operation costs. Investments are the sum of vessels cost, reboilers and condensers cost. Operation costs are the sum of the energy dependent of condensers' and reboilers' load. The algorithm allows optimizing the flowsheets of simple structure with a limited set of equipment neglecting heat recovery and column piping.

The main drawback of the approaches mentioned above is neglect of heat recovery and column piping that limits the ability to calculate the effectiveness of the whole unit. Technologic criteria, as a rule, are expressed by the product specifications and recovery efficiency.

In this paper, we developed the general algorithm for efficiency evaluation and showed its application to choose an optimal mode and flowsheet structure of oil fractionation unit.

2. Thermodynamic efficiency of oil fractionation units

Thermodynamic efficiency criteria reflect the relation between external and utilized heat flow. Thermodynamic efficiency can be calculated as:

$$\eta_T = \frac{q_0 - q_k}{q_0} * 100\% \qquad (1),$$

Thermodynamic efficiency criterion reflects both heats utilized for distillation and heat recovery rate in a unit. Consequently, the criterion implies the flowsheet structure.

Product specifications and recovery affect the criterion value as well, since the increase in recovery requires an increase in reflux flow, hence increase in condensers and reboilers loads. The part of recovered heat decreases that results in a decrease in the thermodynamic efficiency criterion.

In Aspen HYSYS^{TM}, we developed two "first principle" models of crude oil distillation units with and without heat integration in order to find optimal flowsheet structure.

Simplified flowsheet structure without heat integration is shown in Fig. 1. Optimization of operation mode was carried out for different types of crude oil.

Thermodynamic efficiency of the flowsheet without heat integration does not exceed 50% because of low heat recovery.

The fractionation unit shown in Fig. 2 is of the more complex structure with an atmospheric column equipped with two stripping and two intermediate pump rounds. The heat of all intermediate and product flows is utilized in heat recovery. The model was verified for all types of oil, for different product specifications and meteorological conditions [9]. Average thermodynamic efficiency was about 70%, for this reason, this structure was taken as basic. Developed "first principle" model of the unit includes all equipment, e.g. columns, separators, vessels, heat exchangers, pumps. The sizing and hydraulic calculation for internals (valve trays) of the columns were carried out as well. The possibility to set the value of ambient temperature on the air coolers' inlet was included into the model as far as the temperature affects substantially over vapor loads, separators' performance and heat exchange. A detailed description of the flowsheet and product set are performed in [2].

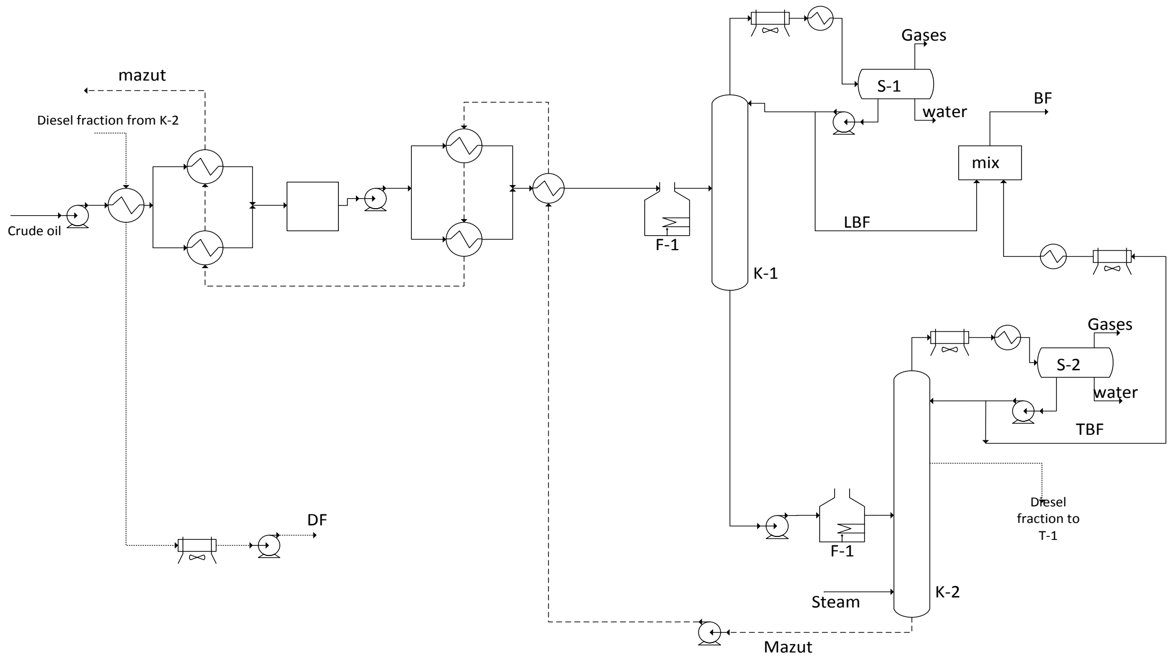

Fig. 1. Structure of crude oil distillation unit without heat integration

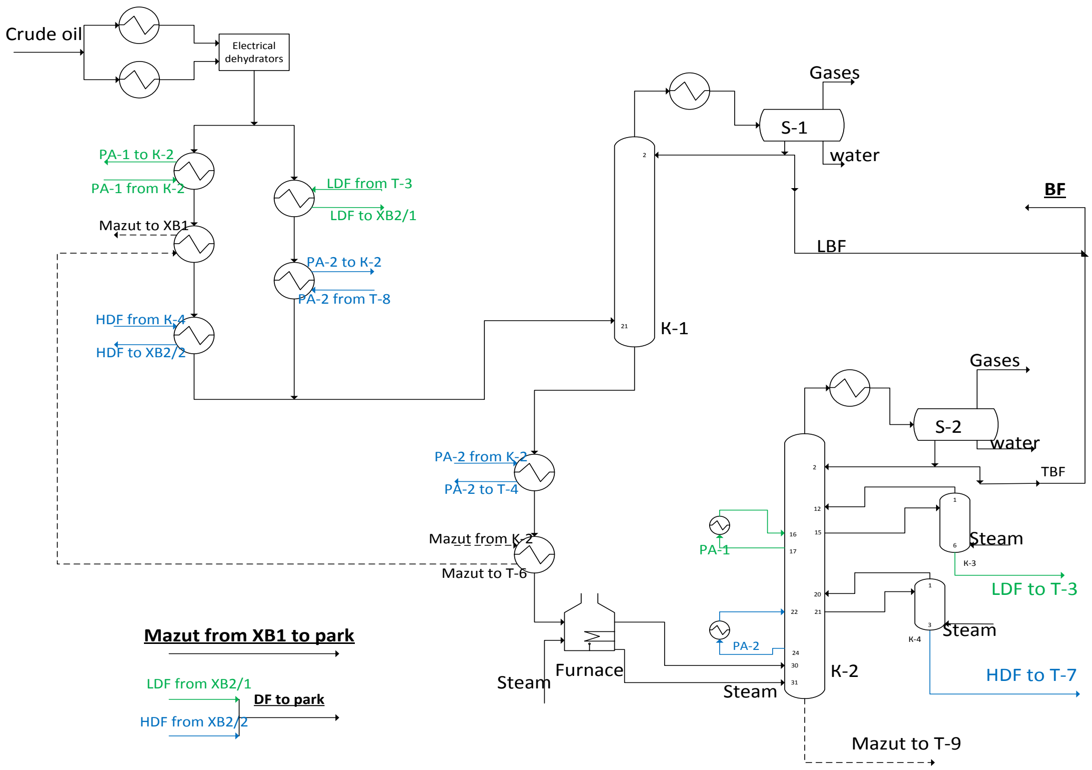

Fig. 2. Basic distillation unit with heat integration

3. Alternatives for retrofit

Performance of the basic unit was studied on the model in a wide range of feed load between 500 000 and 900 000 tons per year. Stage increase in load was used along with detection of “pinch points” and parametrical (technologic) optimization on each stage.

Based on the obtained results, we proposed six alternatives to retrofit:

1. The process flow diagram (PFD) equipped with an additional tray column, working in parallel with the main column K2 (Fig.3).
2. The PFD equipped with an additional packing column, working in parallel with the main column K2.
3. The PFD equipped with a main tray column K2 of a greater diameter.
4. The PFD equipped with a main packing column K2 of a greater diameter.
5. The PFD with an additional side-draw from the main tray column K2 equipped with a stripping (Fig.4).
6. The PFD with an additional side-draw from the main packing column K2 equipped with a stripping.

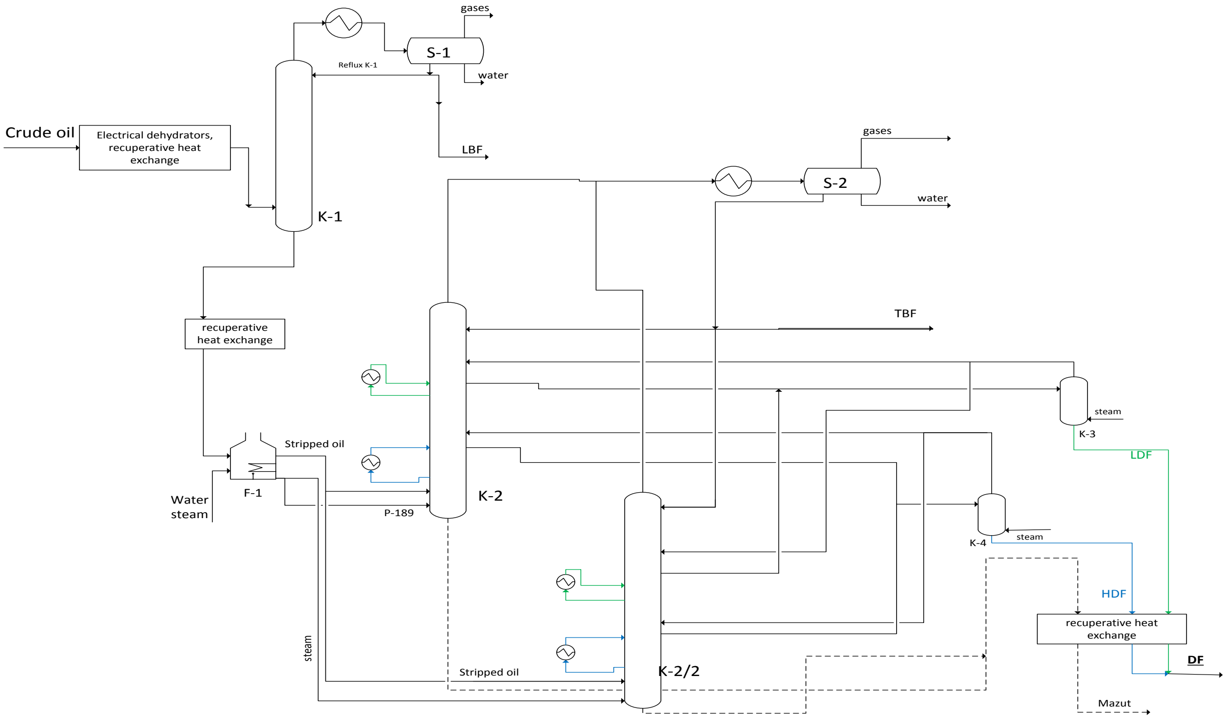

Fig. 3. The PFD equipped with an additional tray column, working in parallel with the main column K2 Alternatives of retrofit number 1, 2

4. Algorithm implementation

4.1. Parametrical optimization

The aim of parametrical optimization was a maximum yield of light distillates under sustainable operating and facing product specification. The conditions of overheated steam to columns and stripping were considered during optimization [10]. We used the algorithms previously tested and performed in [2, 9, 10].

4.2. Economic and thermodynamic optimization

For economic optimization, we estimated the sums of relative capital investments and operating costs above the basic flowsheet costs. Investments included the cost of additional equipment, cost of the unit construction and installation. Additionally, the annual operation cost and increase in the value of the product were calculated. Calculations were referred to the economic performance of the basic flowsheet.

The surface of the thermodynamic efficiency criterion in the space of economic parameters is shown in Fig. 5. Maximum of the criterion corresponds to the most effective alternative. Flowsheet numbering in Fig. 5 corresponds to the mentioned above numbering (Chapter 3).

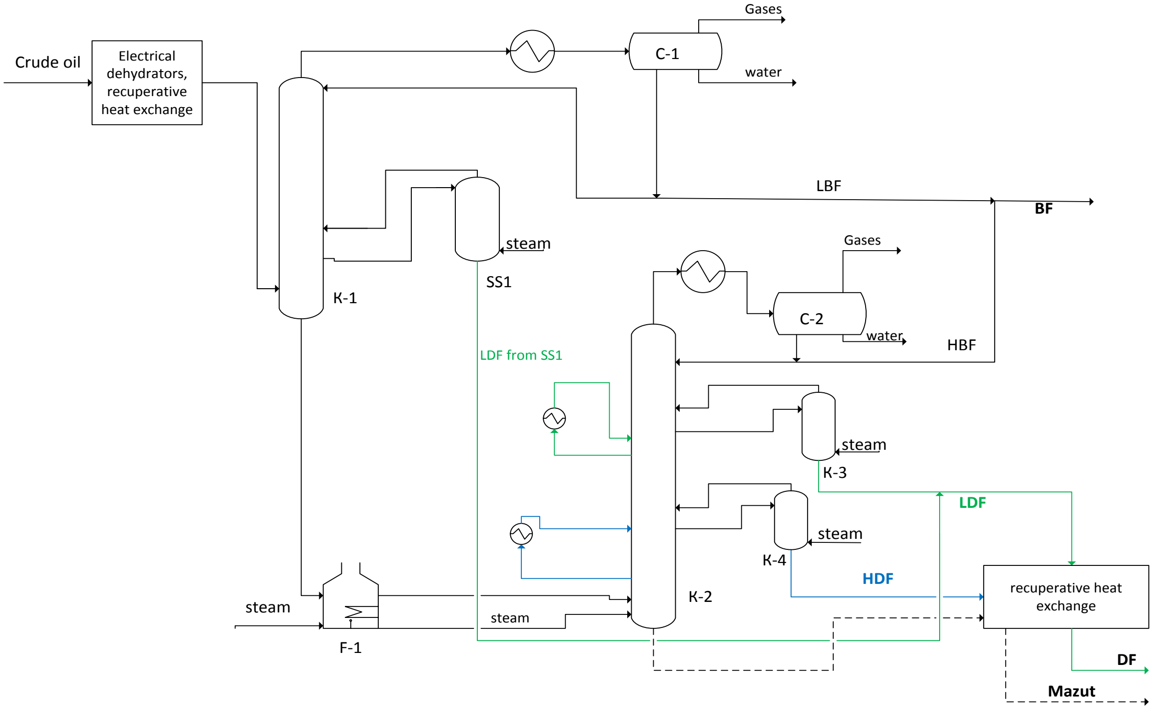

Fig. 4. The simplified scheme of the crude oil distillation unit with pre-fractionator and extra stripping (SS1). Alternatives of retrofit number 5, 6

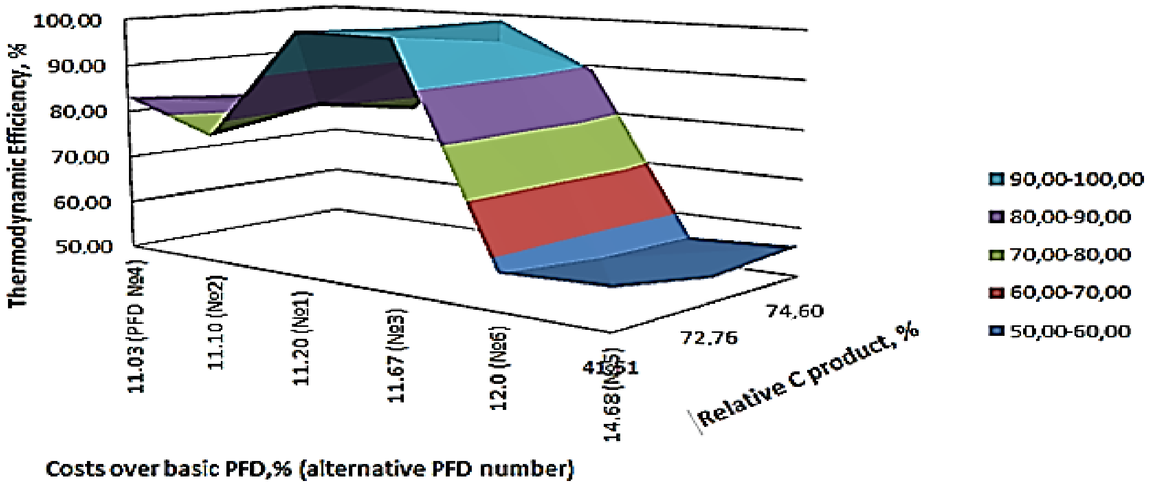

Fig. 5. Thermodynamic efficiency criterion in the space of economic parameters

5. Conclusion

The general algorithm for efficiency evaluation of multi-column distillation flowsheets was developed on the basis of designed thermodynamic, economic, technological optimization criteria using the results of the simulation. This hybrid algorithm for efficiency evaluation (AEE) was applied to select the optimal distillation sequence with heat integration and recuperative heat exchange from the proposed alternative flowsheets. The alternatives for retrofit were selected to provide the process flexibility in respect of flowrate of crude oil (load) and oil quality. The optimal operation modes were defined with consideration of the product quality.

The best distillation sequence for the design is characterized by relatively low total cost with maximum light product yields. Operating mode optimization of this flowsheet makes it possible to obtain energy efficiency higher than 90% without loss of product quality.

Symbols

η_T	*thermodynamic efficiency, %;*
q_0	*total external heat flow, kWt;*
q_k	*heat flow withdrawn by heat exchangers and air coolers and unutilized for heating feed or intermediate streams, kWt.*

References

[1] http://bcs-express.ru/show_res_ru.asp?id=5230. Rossijskie NPZ. Equity Research.
[2] Samborskaya MA, Gryaznova IA, Volf AV. Procedia Chemistry, 2015; 15: 134–142.
[3] Pleşu V, Bonet Ruiz AE, Bonet J, Llorens J, Iancu P. Minimum number of transfer units and reboiler duty for multicomponent distillation columns. University Politehnica of Bucharest, Centre for Technology Transfer in Process Industries (CTTPI).
[4] Calzon-McConville CJ, Rosales-Zamora MB, Segovia-Hernández JG, Hernández S, Rico-Ramírez V. Design and Optimization of Thermally Coupled Distillation Schemes for the Separation of Multicomponent Mixtures. Ind. Eng. Chem. Res.,2006; 45 (2): 724–732.
[5] Demirel DY. Thermodynamic Analysis of Separation Systems (2004). Papers in Thermal Mechanics. Paper 2. http://digitalcommons.unl.edu/chemengthermalmech/2.
[6] Al-Muslim H, Dincer I, Zubair SM. Exergy analysis of single-and two-stage crude oil distillation units. J. Energy Resour. Technol., 2003; 125(3):199-207.
[7] Barttfeld M, Aguirre PA, Grossmann IE. Alternative Representations and Formulations for the Economic Optimization of Multicomponent Distillation Columns, Computers & Chemical Engineering, 2003; 27(3): Pages 363-383.
[8] Caballero JA. Logic hybrid simulation-optimization algorithm for distillation design // Computers & Chemical Engineering, 2015; 72: 284-299.
[9] Samborskaya MA, Volf AV, Gryaznova IA, Vdovushkina NS. Parametricheskaya optimizatsiya integrirovannyih shem fraktsionirovaniya nefti. Fundamentalnyie issledovaniya, 2013; (8-3): 714-719.
[10] Samborskaya MA, Gusev VP, Gryaznova IA, Vdovushkina NS, Volf AV. Crude oil distillation with superheated water steam: parametrical sensitivity and optimization. Procedia Chemistry, 2014; (10): 337 – 342.

To whom correspondence should be addressed: Dr. Marina A. Samborskaya, Division for Chemical Engineering, School of Earth Science & Engineering, Tomsk Polytechnic University, 43a, Lenin Avenue, Tomsk, 634050, Russia; tel.: +7-903-954-683-6; e-mail: sma@tpu.ru

Petroleum and Coal

Article **Open Access**

ASSESSMENT OF LEACHATE CONTAMINATION OF GROUNDWATER AROUND THE IGBENRE EKOTEDO DUMPSITE, OTA, SOUTHWEST NIGERIA

Anthony Aduojo Ameloko[1], Elijah Adebowale Ayolabi[2], Efeoghene Enaworu[1], Eniola Bolujo[1]

[1] Department of Petroleum Engineering, Covenant University Ota, Nigeria
[2] Department of Geosciences, University of Lagos, Nigeria

Received May 31, 2018; Accepted August 27, 2018

Abstract

The study was initiated at the instance of the Local Authority, to evaluate the physico-chemical parameters (quality) of groundwater used by residence living around the Igbenre Ekotedo dumpsite. Nine (9) groundwater samples were collected randomly from boreholes around the dumpsite and were analysed for heavy metals including Fe, Pb, Mn, Cu, Cr, and Zn, using Atomic Absorption Spectroscopy. Other elements analysed for include Mg^{2+}, Na^+, K^+, Ca^{2+}, and anions such as PO_4^{3-}, SO_4^{2-}, NO_3^-, and Cl^-.The physical properties tested for are their total dissolved solid (TDS), pH values, temperatures, hardness and electrical conductivity (EC). The results showed that the TDS, NO_3^-, hardness and EC concentrations of the water samples fell below the permissible limits set by the WHO standards for drinking water quality for the area except at location BH 3, BH 4 and BH 5. The concentrations of Ca^{2+}, Na^+, Cl^-, SO_4^{2-}, Zn and Cr are found to be below the WHO standard for all locations, but with relatively higher concentration values of Ca^{2+}, and, Cl^- at locations BH 3, BH 4 and BH 5. Also, the concentrations of PO_4^{3-}, Mg^{2+}, K^+ and Fe are significantly higher than the prescribed WHO standard but with relatively higher values of Mg^{2+} and Fe associated with locations BH 3, BH 4 and BH 5. The spatial distribution maps of the examined parameters show a general increase in concentration towards the Southwest and Southern directions of the study area. This implies the likely direction of groundwater flow around the area since contaminants are usually mobilised and moved in the direction of groundwater flow. At the moment, the contamination is localised and limited to the South-western part of the study area and boreholes can safely be located at the North-Western and South-Eastern parts of the surveyed area.

Keywords: *Contamination; groundwater; metal; dumpsite; concentration.*

1. Introduction

The Igbenre Ekotedo dumpsite in Ota, Ogun State is an open dumpsite and currently receives industrial, institutional and domestic wastes from communities, industries and institutions located around the area. The landfill is improperly designed and therefore not protected by either impermeable soil or polyethylene geomembrane liner, thus allowing for environmental pollution around the vicinity where the site is located. Public concerns regarding the contamination of soil and ground water by leachates emanating from the dumpsite has recently increased in the area and this drew the attention of the Local Authorities. To address the issue, there is therefore the need for constant information on the status of groundwater quality around the dumpsite. In dumpsites that are not constructed according to international standard (without liners), leachates that are formed within the waste materials eventually find their way into the subsurface environment, where they contaminate groundwater bodies Municipal landfill leachates are highly concentrated complex effluents which contain dissolved organic matters; inorganic compounds, such as ammonium, calcium, magnesium, sodium, potassium, iron, sulphates, chlorides and heavy metals such as cadmium, chromium, copper, lead, nickel, zinc among others [1-3]. The greatest contamination threat to groundwater comes from the leachate generated from the materials which most often contain toxic substances especially when wastes of industrial origins are land filled [4]. However, it has been widely reported that leachates from landfills for non-hazardous waste could as well contain complex organic compound, chlorinated hydrocarbons and metals at concentrations which pose a threat to both surface and groundwater. The produced leachate is normally composed of organic and inorganic compositions. In addition, with increase in time, the produced leachate permeates into ground systems leading to change of physical and chemical properties of groundwater. Lee *et al.* [5], stated that heavy metals such as cadmium, arsenic, chromium have been reported at excessive level in groundwater due to landfills operation. With respect to Longe *et al.* [4], the volume of leachate depends principally on the area of the landfill, the meteorological and hydrogeological factors and effectiveness of capping. According to Kostova [6], concentration (mg/L) of leachate constituent are in phases namely transition (0-5years), acid-formation (5-10years), methane fermentation (10-20years) and final maturity (>20years). The age of a landfill also significantly affects the quantity of leachate formed. The ageing of a landfill is accompanied by increased quantity of leachate. Leachates generated in the initial period of waste deposition (up to 5 years) in landfills have pH-value range of 3.7 to 6.5 indicating the presence of carboxylic acids and bicarbonate ions. With time, pH of leachate becomes neutral or weakly alkaline ranging between 7.0 and 7.6. Landfills exploited for long period of time give rise to alkaline leachate with pH range of 8.0 to 8.55 [7-8]. Excessive content of these chemical compounds may be associated with contaminants around the Igbenre Eotedo dumpsite and so, this study was initiated at the instance of the Local Authorities to determine the physico-chemical parameters (quality) of groundwater used by residence living around the dumpsite. They intend to rely on the results from this study and other geophysical investigation around the area to determine appropriate locations to provide boreholes as a way of intervention. []

1.1. Study area

The Igbenre Oke-tedo Landfill is located in Ota along the Sango-Idiroko road (Figs. 1 and 2). It is about 800 m away from the major express road by the High Court, opposite Nestle Company. The landfill is bounded by residential buildings and a very deep gulley. Currently, waste is indiscriminately being dumped on the ground surface without any compaction effort in the site, and most often the waste materials are constantly being burnt by fire. Geologically, the study area falls within the sedimentary basin of southwestern Nigeria popularly called the Dahomey Basin. The Dahomey Basin constitutes part of the system of West African precratonic (marginal sag) basin developed during the commencement of rifting, associated with the opening of the Gulf of Guinea in the early Cretaceous to late Jurassic. The Basin is very extensive and consists of Cretaceous Tertiary sedimentary sequence that thin out on the east and are partially cut off from the sediment of the Niger Delta Basin by the Okitipupa ridge. In general, rocky outcrops are poor due to the thick vegetation and soil cover. The knowledge of the geology of this basin had been improved through the availability of boreholes and recent road cuts. Major lithological sequences associated with the Basin are Abeokuta Formations (Ise, Afowo and Araromi Formations), and Ewekoro, Akinbo, Oshoshun, Ilaro and Benin Formations. The lithology is composed of loose sediment ranging from silt, clay and fine to coarse grained sand, called coastal plain sand. The exposed surface consists of poorly sorted sands with lenses of clays. The sands are in part cross-bedded and show transitional to continental characteristics [9-13].

2. Materials and methods

Groundwater samples were collected at about 50 to 600 m radius (Figure 1) from the landfill under study during the month of August, 2014. Nine (9) groundwater samples were collected randomly around the study area. Some of the sampling points were located far away from the sites to possibly determine the lateral extent of the spread and also to serve as control. The water samples were analysed to determine their heavy metal contents such as iron, lead, manganese, copper, chromium, cadmium, and zinc, according to international standards for the examination of water and wastewater quality [14].

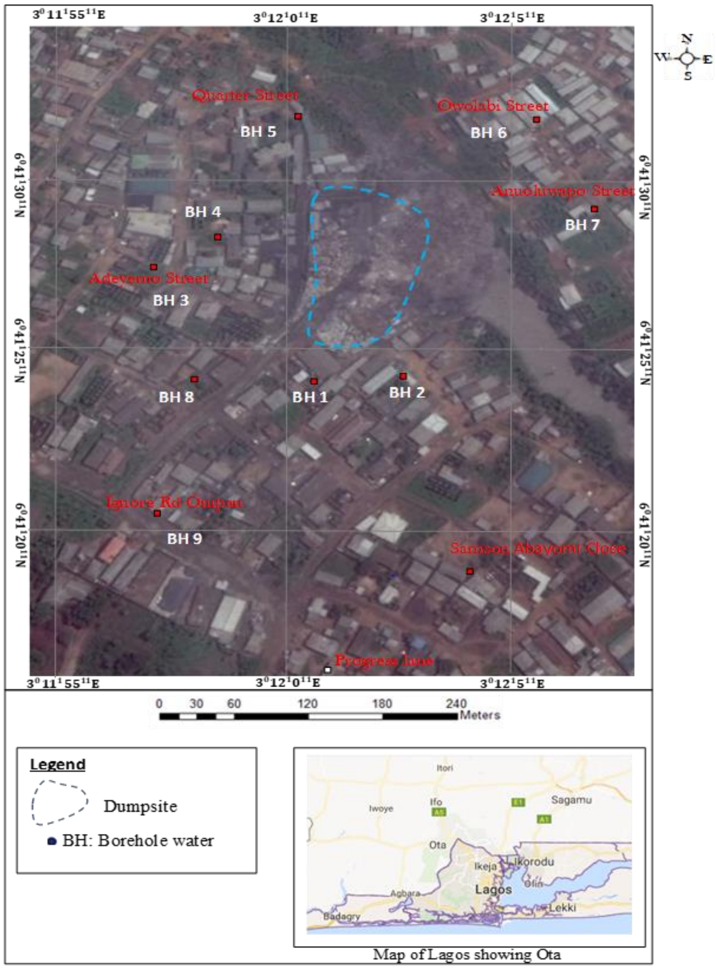

Figure 1. Data acquisition map showing location of dumpsite

Figure 2. Pictorial view of Igbere Eko-tedo dumpsite, Ota

Other elements analysed for include Mg^{2+}, Na^+, K^+, Ca^{2+}, hardness, and anions such as PO_4^{3-}, SO_4^{2-}, NO_3^-, Cl^-. The physical properties obtained in-situ were their TDS, pH values, temperatures, and EC. Samples were collected in a 7.5 litre polyethylene bottles after rinsing with the water being sampled and were properly sealed. Samples were labelled and stored until they were eventually transferred to the Chemistry Department, University of Lagos, Akoka for laboratory analysis. Global Positioning System (Garmin GPS Channel 76 model) was used to measure the coordinates of the sampling points. The field data were later interpolated using Kriging technique to produce the elemental distribution maps of the area using ArcGIS software.

3. Results and discussion

Tables 1, 2 and 3 present the results and descriptive statistics of the physico-chemical properties of water samples collected from the boreholes around the dumpsite.

Table 1. Hydrophysical analysis of water samples from boreholes around Igbenre Ekotedo landfill

Sample	Location	Coordinate	pH	Temp (°C)	EC (µS/cm)	TDS (ppm/mg/L)	Hardness (mg/L)
BH 1	Progress Lane	06^0 41′ 17.14″N 003^0 12′ 01.15″E	5.47	25.2	60	29	85.0
BH 2	Samsom Abayomi Close	06^0 41′ 20.91″N 003^0 12′ 04.56″E	5.18	25.2	23	11	75.0
BH 3	Adeyemo Street	06^0 41′ 26.48″N 003^0 11′ 56.22″E	4.52	26.1	1385	692	212.0
BH 4	Adeyemo Street (by sch.)	06^0 41′ 28.96″N 003^0 11′ 55.25″E	6.01	25.6	1053	575	175.0
BH 5	Quarter Street	06^0 41′ 31.48″N 003^0 11′ 58.90″E	5.79	25.0	1272	836	155.0
BH 6	Owolabi Street (Hill top)	06^0 41′ 34.31″N 003^0 12′ 04.36″E	5.53	26.1	30	15	90.0
BH 7	Anuoluwapo Street	06^0 41′ 32.24″N 003^0 12′ 07.58″E	5.27	24.4	15	8	10.0
BH 8	Igbenre Rd Oni-pan	06^0 41′ 23.38″N 003^0 11′ 55.87″E	5.65	24.8	50	25	40.0
BH 9	Igbenre Rd Oni-pan	06^0 41′ 24.00″N 003^0 11′ 54.60″E	5.95	24.0	83	42	40.0
Mean			5.48		474.55	248.11	99.67
Range			4.52-6.01		15-1572	8-836	10-212
SD			0.46		441.36	220.51	56.72
CV			8.39		174.91	175.16	73.24
WHO/SON standard			6.5-8.5	-	1000	500	150

SD- standard deviation; CV-coefficient of variation, %

Table 2. Macro elements and anions content of water samples obtained from boreholes around Igbenre Ekotedo dumpsite

Samples	Ca^{2+} (mg/L)	Mg (mg/L)	K (mg/L)	Na (mg/L)	Cl^- (mg/L)	SO_4 (mg/L)	PO_4 (mg/L)	NO_3 (mg/L)
BH 1	34.72	12.38	2.67	7.04	159.53	38.0	40.6	2.2
BH 2	30.06	10.19	2.81	5.91	106.35	26.0	39.2	5.9
BH 3	89.97	13.11	2.57	7.02	159.53	45.0	10.8	14.9
BH 4	30.06	10.92	2.71	7.08	186.58	27.0	11.10	11.8
BH 5	28.07	10.19	2.31	6.04	106.35	11.0	32.40	16.7
BH 6	36.07	13.11	2.07	7.11	70.90	278.0	10.3	3.4
BH 7	4.01	1.46	2.94	5.82	88.63	125.0	22.4	6.2
BH 8	16.03	5.83	2.82	5.89	88.63	33.0	42.3	1.3
BH 9	16.03	5.83	2.56	6.71	159.53	22.0	38.5	2.8
Mean	31.67	9.22	2.61	6.51	125.11	67.22	27.51	7.58
Range	4.01-89.97	1.46-13.11	2.1-2.94	5.82-7.1	70.9-186.58	11-278	10.3-42	1.3-16.7
St. Dev.	24.23	4.00	0.27	0.58	41.28	85.74	13.88	2.36
CV	7	43	10	9	33	128	21	57
WHO*	50	2.0	1.0-2.0	200	250	200/100	5.0	10

*SD- standard deviation; CV-coefficient of variation, %; *WHO/SON standard*

Table 3. Heavy metal contents of water sample obtained from boreholes around Igbenre Ekotedo dumpsite

Samples	Fe (mg/L)	Zn (mg/L)	Mn (mg/L)	Cu (mg/L)	Pb (mg/L)	Ni (mg/L)	Cr (mg/L)
BH 1	3.91	2.30	0.71	0.52	0.01	0.02	0.02
BH 2	3.34	2.02	0.92	0.67	ND	0.02	0.01
BH 3	4.50	2.07	0.84	0.44	ND	0.02	0.02
BH 4	3.02	2.11	0.98	0.36	ND	0.02	0.02
BH 5	2.91	2.01	0.72	0.29	0.01	0.01	0.03
BH 6	2.39	3.11	0.91	0.57	0.02	0.01	0.01
BH 7	2.56	2.91	0.77	0.32	0.01	0.02	0.01
BH 8	3.11	3.08	0.78	0.58	0.02	0.03	0.01
BH 9	3.49	2.07	0.87	0.53	0.03	0.03	0.02
Mean	3.25	2.41	0.83	0.48	0.01	0.02	0.02
Range	2.39-4.5	2.01-3.11	0.71-0.98	0.29-0.67	0-0.03	0.01-0.03	0.01-0.03
SD	0.66	0.48	0.09	0.13	0.01	0.007	0.005
CV	20	20	11	27	1.0	35	5
WHO*	0.3	5.0	0.5	0.5	0.01	0.02	0.05

*SD- standard deviation; CV-coefficient of variation, %; *WHO/SON standard; ND -Not Detected*

The results show that the water samples collected around the waste dumpsite have higher concentrations of most of the analysed parameters. From Table 1, the temperature of the groundwater samples ranged from 24^{0C} to 26.1°C. The pH values of the groundwater samples are all acidic and ranging from 4.52 to 6.01. The effects of acidic waters on human health and the environment have been widely reported. For example, acidic waters have been known to be aggressive and enhance the dissolution of iron and manganese causing unpleasant taste in water [15]. The EC is a function of the degree of dissolved matters in water. Chemically pure water has a very low EC. The EC of water around the dumpsite ranged between 15 and 1385 μS/cm, and except at BH 3, BH 4 and BH 5, all other values are found to be below the permissible standard of 1000 μS/cm, set by WHO (Fig. 3). The TDS concentration showed strong positive linear relationship with the EC (suggesting common source) and was found to be low at all the locations also and less than standard limit of 500 ppm/mg/L except at location BH 3, BH 4 and BH 5 (Fig. 3). The high concentration of TDS and EC at locations BH 3, BH 4 and BH 5 may be an indication of contamination due to high content of inorganic salts such as; calcium, magnesium, potassium, sodium, bicarbonates, chlorides, and sulphates in the groundwater. It also implies likely westward direction of groundwater flow around the area since contaminants are usually mobilised and move in the direction of groundwater flow. This was also inferred from the geophysical study around the site (Not shown). Hardness is normally expressed as the total concentration of Ca^{2+} and Mg^{2+} in mg/L, equivalent $CaCO_3$. Hardness ranged from 10 to 212 mg/L and all values are below the standard limit of 150 mg/L except also at BH 3, BH 4 and BH 5 (Fig. 3). Strong linear relationship exists between the observed hardness of water and the TDS and EC concentration from all the locations.

Table 2 provides the major elemental compositions and anion contents of water from the boreholes. Ca^{2+} and Mg^{2+} concentrations in groundwater samples from all the sampling points have mean values of 31.67 mg/L and 9.22 mg/L respectively. The Mg^{2+} content of all the water samples have elevated values above the standard limit of 2.0 mg/L in about 88.8% of the locations except at location BH 7 (fig. 3), while Ca^{2+} concentration exceeded the standard limit at location BH 3 (Fig. 3). Ca^{2+} and Mg^{2+} do not pose potential adverse health effects in drinking water. The presence of both ions in water increases its hardness, which results in the use of more soaps than what is necessary for bathing and washing [16]. Both Ca^{2+} and Mg^{2+} are beneficial to human health. Past epidemiological studies have supported the hypothesis that extra magnesium and or calcium in drinking water can contribute to reduced cardiovascular disease and other health benefits in populations [16]. K^+ values are higher than the standard limit for all the locations. Na^+ and Cl^-concentrations in all sampled locations are all below the WHO minimum requirement of 200 mg/L and 250 mg/L (Fig. 3) respectively.

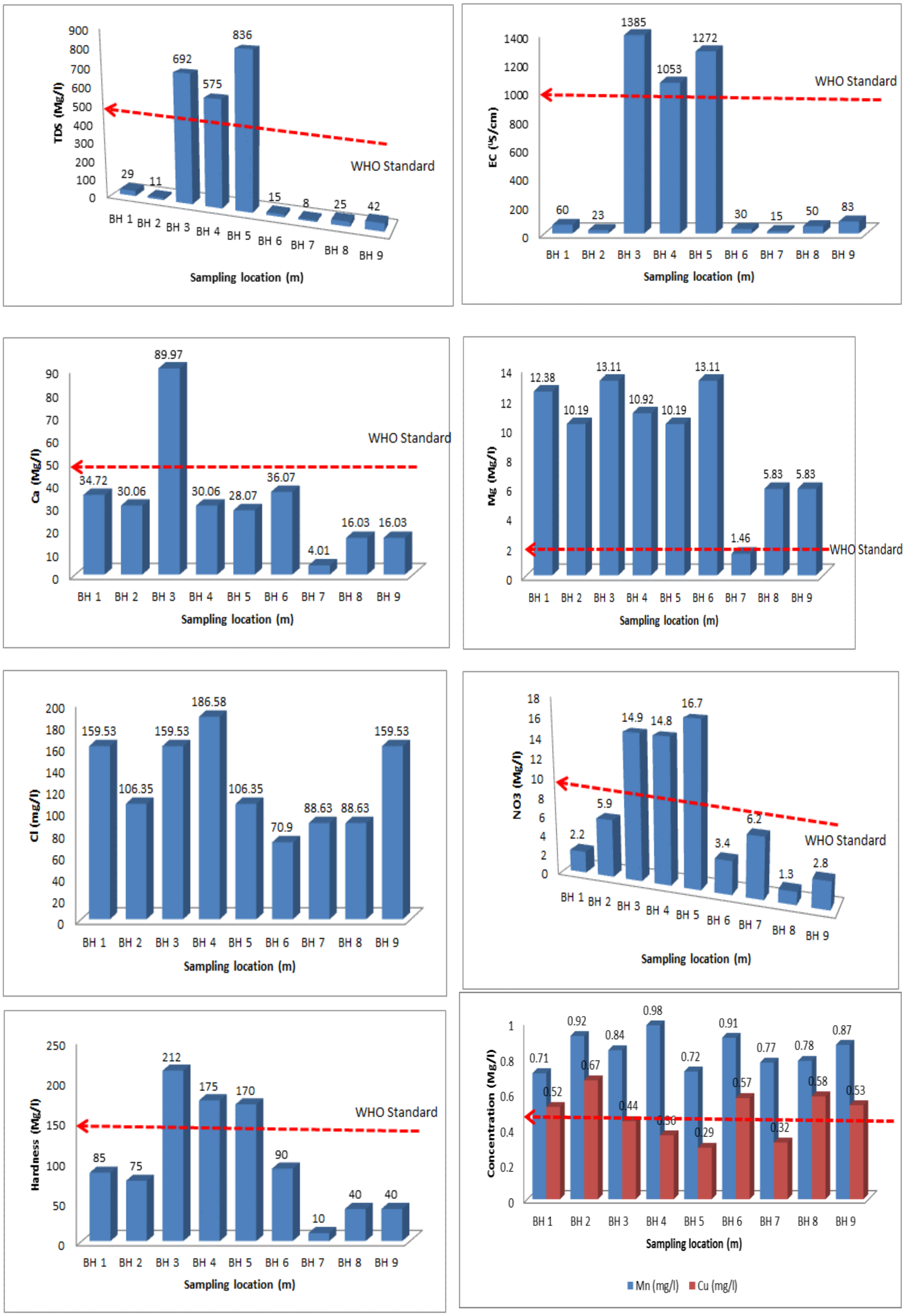

Figure 3. Concentration of other physicochemical properties of water samples versus WHO standard

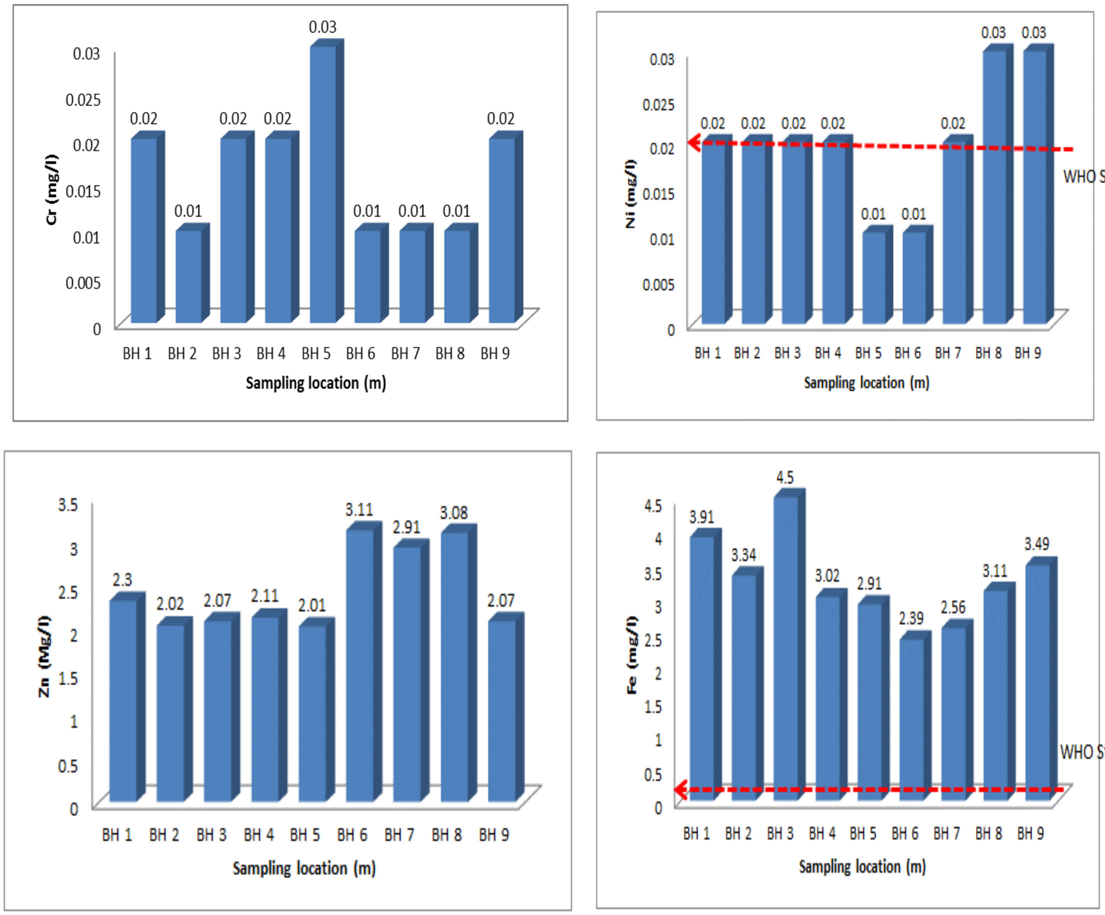

Figure 4. Concentration of EC and hardness in borehole water sample versus WHO standard

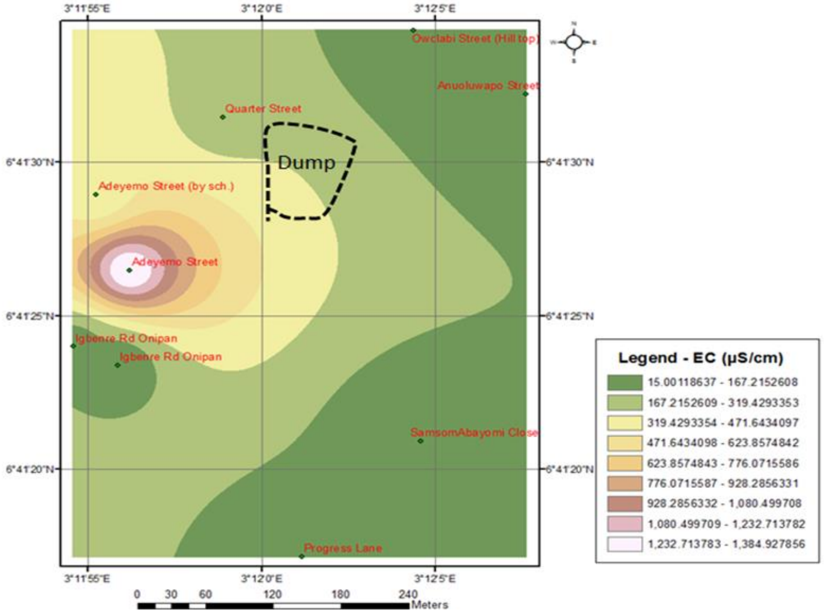

Figure 5. EC concentration distribution map around the Igbenre Ekotedo dumpsite

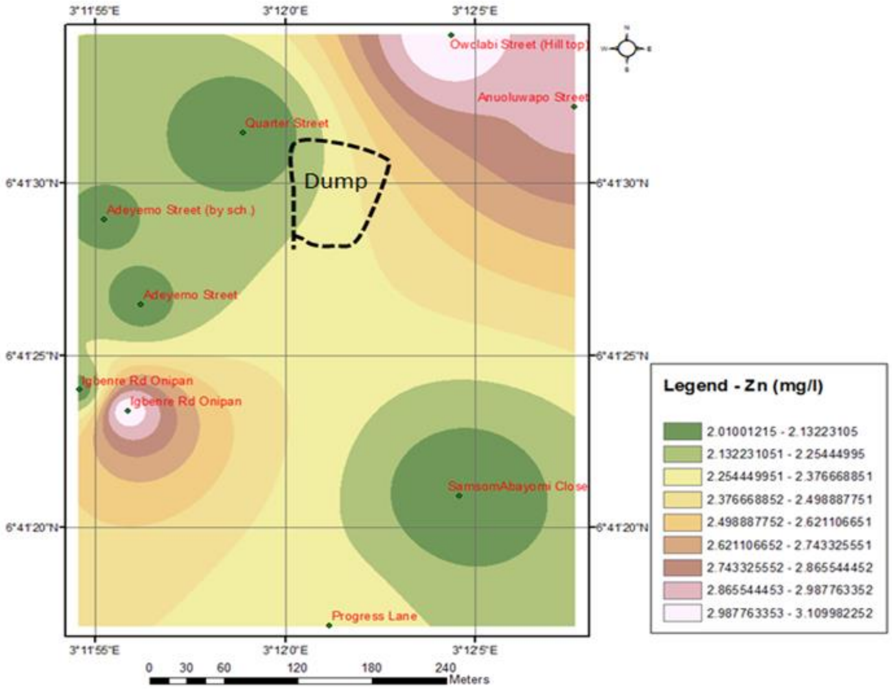

Figure 6. Zn concentration distribution map around the Igbenre Ekotedo dumpsite

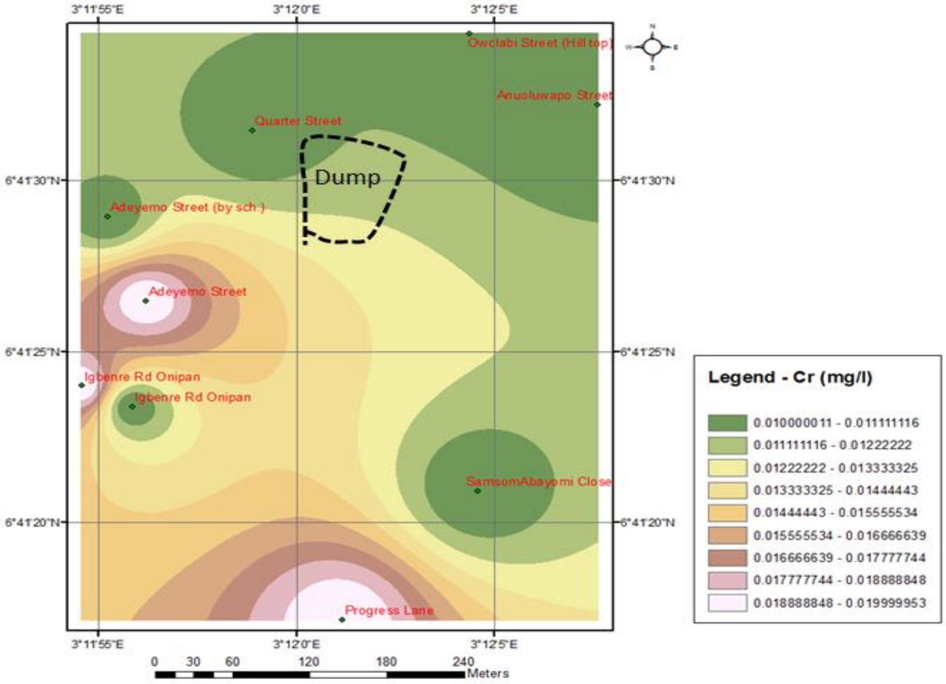

Figure 7. Cr concentration distribution map around the Igbenre Ekotedo dumpsite

Excess NO_3^- concentration in water samples are key indicators of contamination. Their values in all the locations are below the WHO limit but are elevated at locations BH 3, BH 4 and BH 5 (i.e. about 33.3% of the locations) beyond the standard limit (Fig. 3). The measured SO_4^{2-} ion exceeded the prescribed standard limits of (100-200 mg/L) set by WHO (2007) in about 11.11 % (BH 6) from the investigation.

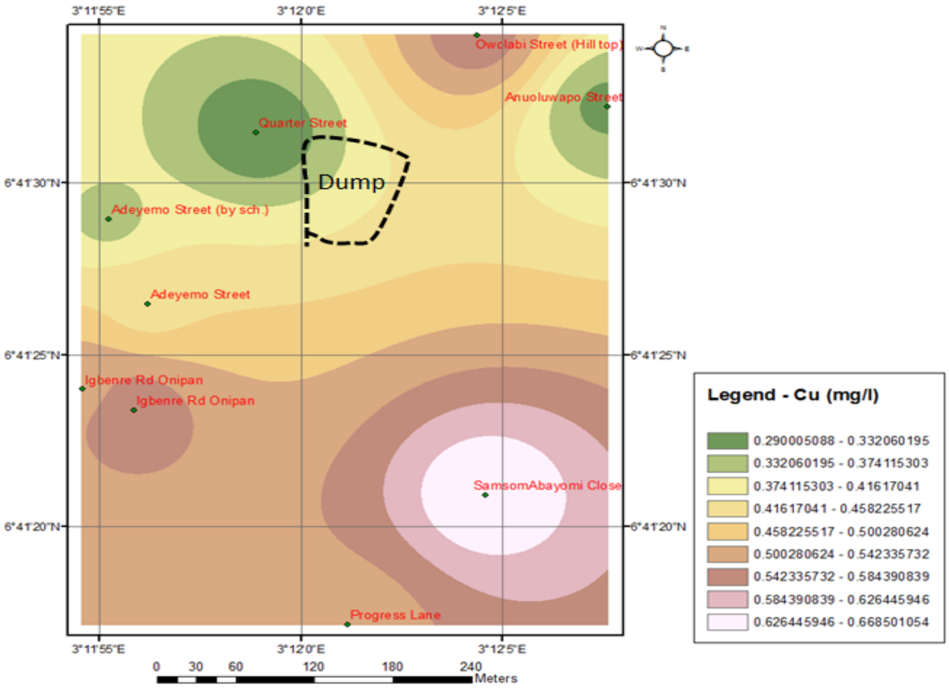

Figure 8. Cu concentration distribution map around the Igbenre Ekotedo dumpsite

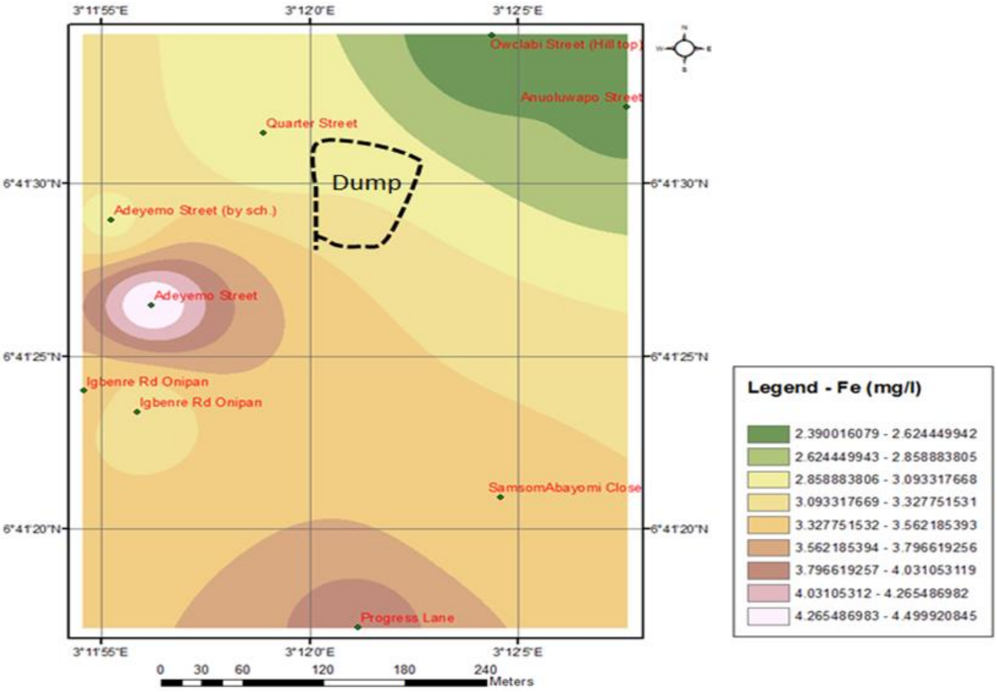

Figure 9. Fe concentration distribution map around the Igbenre Ekotedo dumpsite

Table 3 presents the descriptive statistics and standard values of heavy metals in groundwater around the site. Among the examined variables, Fe has the highest mean (3.25 mg L^{-1}), followed by Zn (2.41 mg L^{-1}) while Pb and Cr remained the least (0.01 mg L^{-1}). Also, Fe recorded the highest standard deviation (0.66 mg L^{-1}) followed by Zn (0.48 mg L^{-1}). Cr and Ni recorded the least values of standard deviation (0.005 mg L^{-1} and 0.007 mg L^{-1} respectively).

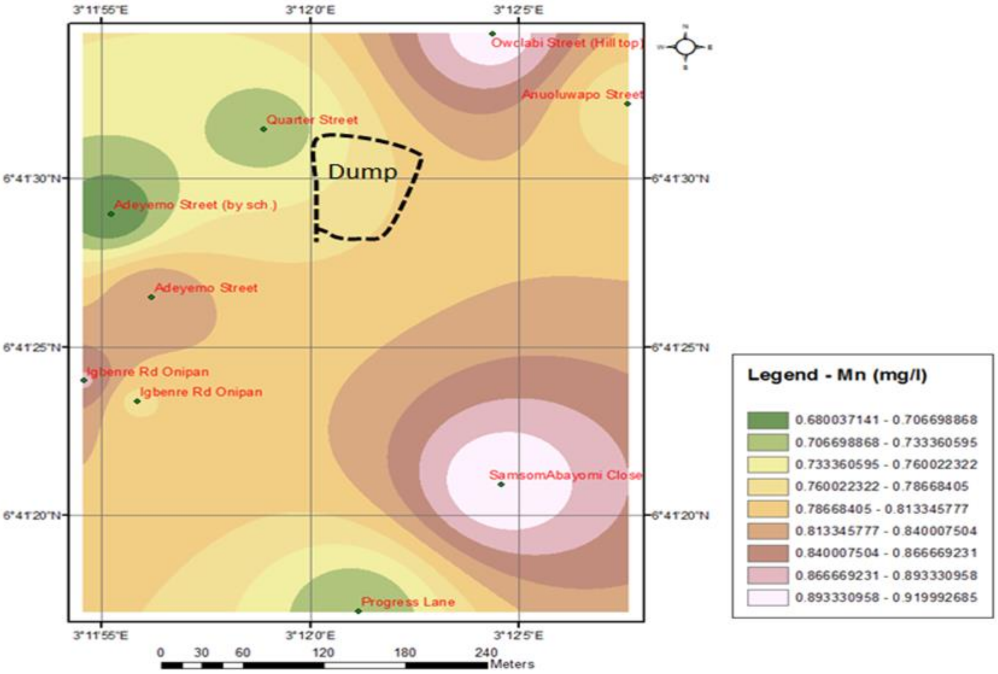

Figure 10. Mn concentration distribution map around the Igbenre Ekotedo dumpsite

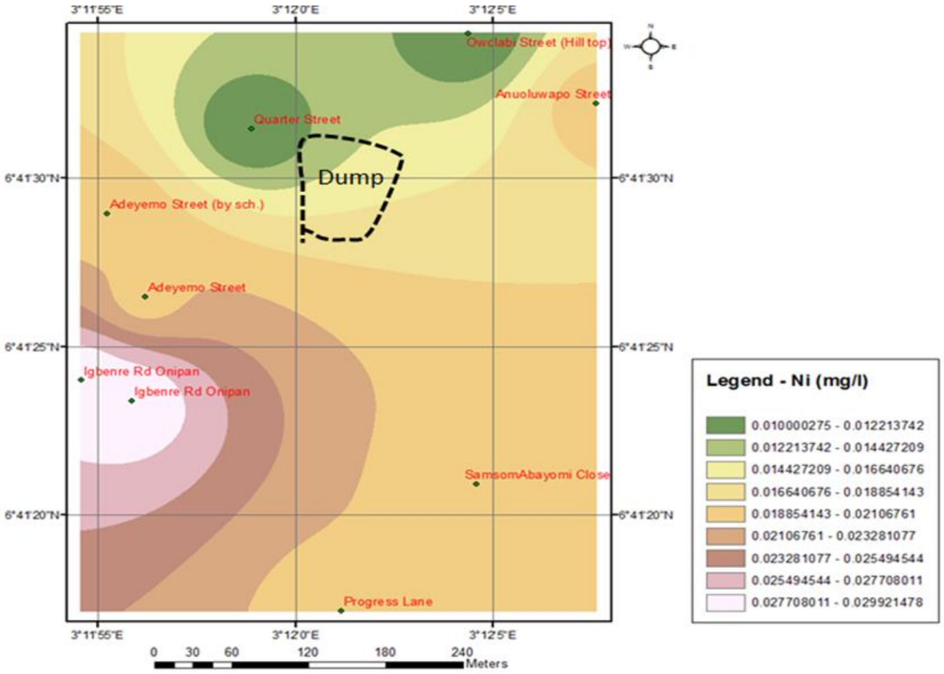

Figure 11. Ni concentration distribution map around the Igbenre Ekotedo dumpsite

Furthermore, on the pattern of relative variation, the result of the coefficient of variation shows that all the examined variables are heterogeneous. Ni and Cu for example top the list with values of 35 % and 27 % respectively. The WHO permissible level of Chromium (0.05 mg L^{-1}) is not exceeded in all the sampled boreholes in the study area, while that of Ni was below the standard limit for all locations except at BH 8 and BH 9 (Fig. 4). The spatial distribution map of Cr is presented in figure 7 with a general increase towards the Southern and Southwest parts of the study area while that of Ni indicates more concentration towards the

Southwest (Fig. 11). The concentration of Pb exceeded the WHO permissible limit (0.01 mg L^{-1}) at locations BH 6, BH 8 and BH 9, but within limit at about 33.33 % of the locations (BH 1, BH 5 and BH 7), and not detectable in the remaining locations (Table 3). Toxic concentration of Pb (≥ 0.01mg/L) in human beings has been implicated for causing anaemia, kidney damage and cerebral oedema [17-18]. The mean concentration of Cu exceeded the WHO permissible level of 0.5 mg L^{-1} for all samples at the site except at BH 3, BH 4, BH 5 and BH 7 (Fig. 3). The spatial distribution map of Cu indicates an increase towards the South-eastern part of the study area (Fig. 8). The WHO permissible level of Fe (0.3 mg L^{-1}) was exceeded in all the sampled borehole water around the study area with values ranging from 2.39-4.5 (Fig. 4).

Presence of Fe in water can lead to change of colour of groundwater [20]. These high values of Fe also support the results of previous research that concluded that water in Nigeria generally has high Fe content. The spatial distribution map of Fe in figure 9 shows more of the concentration towards the Southern and Southwest parts of the study area. The WHO permissible level of Zn (5.0 mg L^{-1}) is not exceeded in sampled groundwater in all the locations while that of Mn (0.5 mg L^{-1}) is exceeded in all sampled borehole in the study area (Figs. 3 and 4). Concentrations of Mn in excess of 0.2 mg L^{-1} make water distasteful to drinking with no specific toxic effects [4]. The spatial distribution map of Zn is shown in figure 6 with a general increase towards the Southwest and Northeast directions of the study area while that of Mn indicates a Southeast and Northeast distributions (Fig. 10). Very low correlations exist between Cu, Zn, $Cl^-$and EC, TDS and $SO_{4'}$ indicating multiple anthropogenic source, while moderate correlations exist between hardness and Mg^{2+}, Na and Cl (Fig. 12).

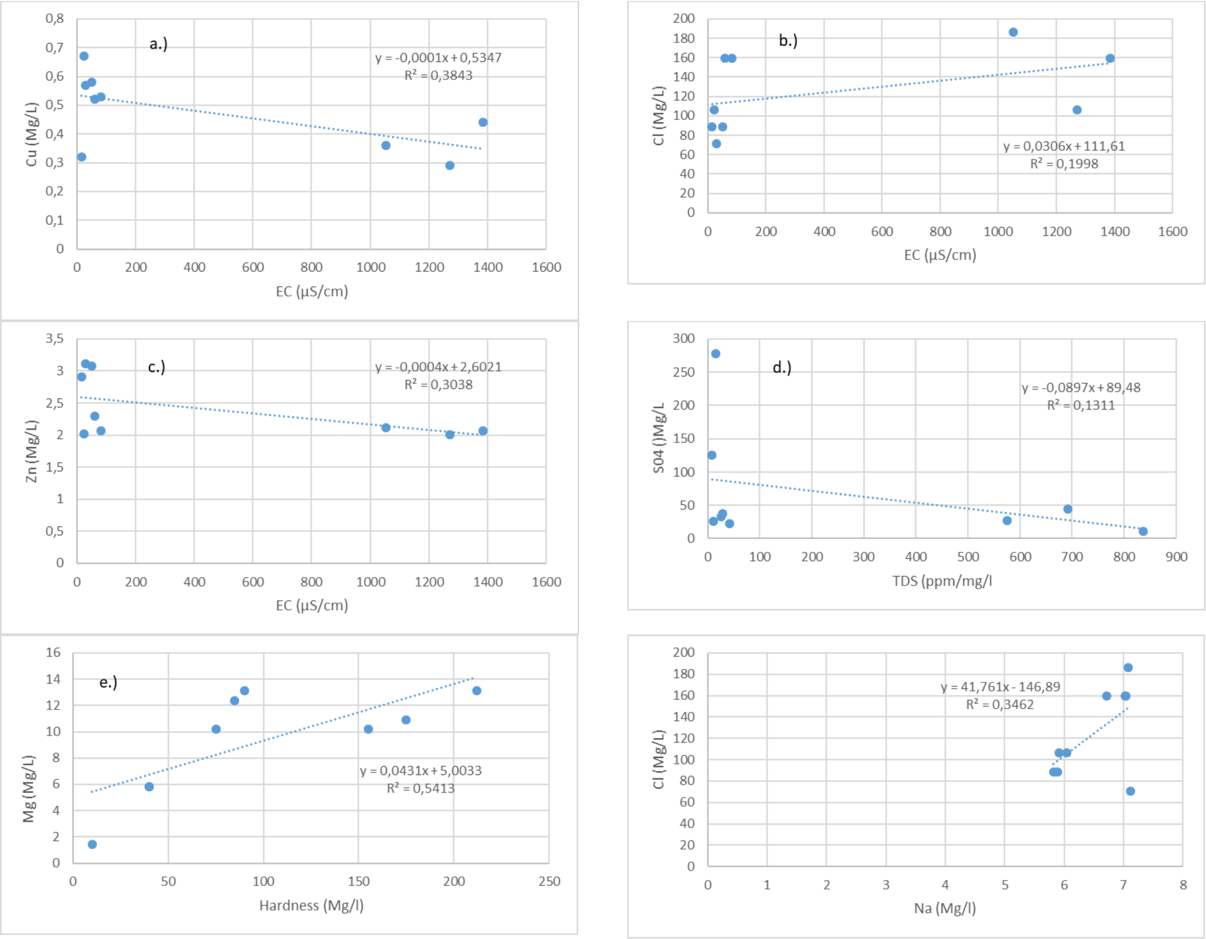

Figure 12. Scatter plot for the correlation between EC and Cu (a), Cl (b) Zn (c) and between TDS and SO4 (d), hardness and Mg (e), Cl and Na (f)

4. Conclusion

The borehole water from all the dumpsites have been analysed and the various elemental compositions determined. The physical properties of water obtained around the dumpsite showed TDS, hardness, NO_3^-, and EC values greater than the standard limit at BH 3, BH 4 and BH 5. There is a corresponding increase in value for Ca^{2+}, Mg^{2+}, Cl^- and SO_4^{2-} for these same locations. The high values of most of the physicochemical properties at BH 3, BH 4 and BH 5 locations is not unconnected with contamination arising from the release of leachate generated at the dumpsite. It also implies likely Southwest direction of groundwater flow around the area since contaminants are usually mobilised and move in the direction of groundwater flow. At the moment, the contamination is localised and limited to the Southwestern part of the study area and boreholes can be safely located at the North-eastern and South-eastern parts of the surveyed area. Public complaints regarding the colour and taste of water from their borehole confirms the results around this area. The pH values obtained from water samples indicates high acidic content. The heavy metals analysis and subsequent evaluation revealed that Fe and Mn concentration from all the water samples have exceeded their background levels. This further supports the report of high iron concentrations in groundwater in Nigeria according to WHO and UNICEF, 2006. The spatial distribution of all the examined parameters shows a Southwest/Southern increase around this waste site. The proximity of the dumpsite to residential areas is a potential danger and proactive measures must be put in place by the appropriate authorities to avoid epidemic outbreak that might result from the consumption of the contaminated groundwater around this area.

Acknowledgment

The authors acknowledge the funding support offered by Covenant University for the project and also to Ogun State Waste Management Authority for the permission to work on their site.

References

[1] Christensen JB, Jensen DL, Gron C, Filip Z and Christensen TH. (1998): Characterization of the dissolved organic carbon in landfill leachate-polluted groundwater, Water Res., 1998; 32: 125-135.
[2] Lee GF, Jones RA and Ray C. Sanitary landfill leachates recycle. Biocycle, 1986; 27: 36-38.
[3] Ogundiran OO, and Afolabi TA. Assessment of the physicochemical parameters and heavy metal toxicity of leachates from municipal solid waste open dumpsite. Int. J. Environ. Sci. Tech., 2008; 5(2): 243-250.
[4] Longe EO and Enekwechi LO. Investigation on potential groundwater impacts and influence of local hydrogeology on natural attenuation of leachate at a municipal landfill. Int. J. Environ. Sci. Tech., 2007; 4(1):133-140.
[5] Lee S and Kitanidis PK. Analysis of Groundwater Flow and Travel Time for a Landfill Site in an Arid Region with a Thick Vadose zone. Hydrological Processes, 1993; 7: 373-387.
[6] Kostova I. Leachate from sanitary landfills - origin, characteristics, treatment, Assoc. Prof. at University of Architecture, Civil Engineering and Geodesy, "Iskar's Summer School"– Borovetz, 26-29 July 2006.
[7] Longe EO and Balogun MR. Groundwater Quality Assessment near a Municipal Dumpsite, Lagos, Nigeria. Research Journal of Applied Sciences, Engineering and Technology, 2010; 2(1): 39 – 44.
[8] Slomczynska B and Slomczynski T. Physicochemical and Toxicological Characteristics of Leachate from MSW Landfills. Polish J. Environ.Stud., 2004; 13(6):637.
[9] Agagu OK. A Geological Guide to Bituminous Sediments in Southwestern Nigeria, (Unpubl Monograph 1985). Dept. of Geology, University of Ibadan.
[10] Enu EI. Nature and occurrence of tar sands in Nigeria. In: Ako BD, Enu EI (eds) Occurrence, utilization and economics of tar sands. Nigeria Mining and Geosciences Society publication on tar sands workshop 1990. Olabisi Onabanjo University, Ago-Iwoye, pp 11–16.
[11] Jones HA, Hockey RD. (1964). The geology of part of south-western Nigeria. Geol Survey Nigeria Bulletin, 1964; 31: 1–101
[12] Nton ME. Sedimentological and geochemical studies of rock units in the eastern Dahomey Basin, south western Nigeria. Unpublished Ph.D thesis. University of Ibadan 2001, pp 315.

[13] Omatsola ME, Adegoke OS. Tectonic evolution and cretaceous stratigraphy of Dahomey Basin. Journ Min Geol., 1981; 18: 130–137.

[14] American Public Health Association. American Water Works Association, Water Environment Federation (1998). Standard methods for examination of water and wastewater (20th Ed.). New York, USA: American Public Health Association.

[15] Edwards KA, Classen GA, Schroten EHJ. The water resource in tropical Africa, and its exploitation, ILCA – Int. Livestock Centre for Africa 1983, Res. Rep., Addis Ababa p. 28.

[16] World Health Organization. Calcium and magnesium in drinking water (Public Health Significance 2009).
Retrieved from:http://whqlibdoc.who.int/publications/2009/9789241563550_eng.pdf

[17] Egborge ABM. Industrialisation and heavy metal pollution in Warri River. University of Benin Press 1991, Inaugural lecture series 32.

[19] Townsend A. Encyclopaedia of Analytical Science, Academic Press 1991, London.

[20] Rowe RK, Quigley RQ, and Booker JR. Clay Barrier Systems for Waste Disposal Facilities. E & FN Spon, London 1995, UK.

[21] WHO, (2004). Guidelines for Drinking Water Quality. 3rd Edn. Vol. 1 Recommendation, Geneva, 515.

[22] World Health Organization (WHO) and UNICEF, (2006). Rapid Assessment of Drinking Water Quality. Country Report, Nigeria, 82.

[23] WHO (2007). Water for Pharmaceutical Use in Quality Assurance of Pharmaceuticals. A Compendium of Guidelines and Related Materials, 2nd Updated Edition, World Health Organization, Geneva, 170-187.

To whom correspondence should be addressed: Dr. Anthony Aduojo Ameloko, Department of Petroleum Engineering, Covenant University Ota, Nigeria, Email: tonyameloko@yahoo.com

Petroleum and Coal

Article **Open Access**

ASSESSMENT OF SANDING POTENTIAL OF UNCONSOLIDATED SANDSTONE RESERVOIRS USING MODIFIED HOEK-BROWN FAILURE CRITERION

Fred Temitope Ogunkunle[1], *S. O. Isehunwa*[2], *D. O. Orodu*[1], *Oluwasanmi Olabode*[1]

[1] *Department of Petroleum Engineering, Covenant University, Ota, Nigeria*
[2] *Department of Petroleum Engineering, University of Ibadan, Ibadan, Nigeria*

Received May 10, 2018; Accepted July 27, 2018

Abstract

Assessment of sanding tendency during field development planning and completion design of oil and gas wells is very paramount because sanding tendency significantly impact on well completion choices and overall field development economics. Production of sand occurs in zones of failure creating perforation cavity and wellbore instabilities. The starting point of most predictive tool is identifying the stres-ses at the perforation cavity, failure prediction around such cavity and applying appropriate failure criterion. Most of the existing sand predictive tools are anchored on Mohr-Coulomb failure criterion which assumes a linear failure envelope but does not represent the response of reservoir rocks to induced stress.

Therefore, this work presents the results of a study investigating the potential of sand production in a Niger Delta field using modified Hoek-Brown failure criterion in developing a new geomechanical sanding predictive model that describes the non-linear increase in peak strength of isotropic rocks with increase in confining stress. The condition for sanding was formulated to be minimum well pressure at/below which sanding is to be expected. Based on Hoek-Brown material constant (a) which describes the rock mass quality, three (3) sanding criteria were developed and verified by comparing the results with existing numerical the model result and field scenario.

From the comparison with numerical model result, the three (3) sanding criteria gave the same result when Biot's constant is taken to be one (unity) but generally close to the numerical result. The results from the field case study, for the two wells evaluated indicates field well pressures that fall below the minimum well pressure at sanding predicted by the sanding criteria developed. This shows why they were both sand producers and this was in agreement with the production data from both wells. However, the model with exponent ($a = 0.5$) gave the closest to the field well pressure. The good agreement between the results from numerical/field case study and current work augurs well for its application when Hoek-Brown material constants can be accurately predicted.

Keywords*: Sand Production; Modified Hoek-Brown; Minimum well pressure; Wellbore Stability.*

1. Introduction

Every year, the upstream petroleum industry spends in excess of $6 billion US dollars on wellbore stability issues [10]. Many rock stability issues, some of which are sand production, borehole collapse otherwise called breakout, casing shear, rock compaction, and so on., are to be expected starting from the beginning of oil exploration operations such as; drilling and completion operations down to workover operations. Sand production is a usual production challenge observed in weakly consolidated and unconsolidated formation which play host to around 70 percent of global oil production [2].

Sand production arises when reservoir fluid flowing under high velocity removes a quota of the reservoir rocks creating continuous influx of formation materials. Production of sand occurs in zones of failure creating perforation cavity and wellbore instabilities. Sand production tendency over the life of the well has significant impact on completion choices. As we work in more challenging environments such as deep water, heavy oil, and high-pressure high-temperature wells, reservoirs are more complex and costlier to drill and complete. Downhole sand control methods significantly increase the complexity and cost of the completion and challenge the economics of the field development. This poses questions like do we need downhole sand control on all wells that have potential to produce sand? When the produced sand volume is not significant can the sand be managed at surface? Completions and workovers would be much simpler and cheaper without downhole sand control. Well production would also increase without downhole sand control, however, sand production could increase the risk of sanding up in wells [13]. It also increases the risk of eroding chokes, surface flow-lines, and equipment. Operational costs would increase due to sand transportation and disposal.

Numerous work has been done on the subject for so long, but despite that, accurately addressing this problem has remained unsolved because of its complexity. Several predictive tools are already been utilized in the industry to gain meaningful information about sanding potentials in oil and gas wells, most of which are limited in use because (1) they require information about the well that are not available until the well is completed and produced for a reasonable time frame, or not routinely measured on field [1,7], (2) some of the models are complex and requires extensive laboratory studies to determine the input data from core samples, which tend to affect the predictive accuracy [3,11], (3) inappropriate use of failure mechanism, (4) assuming a linear failure envelope for failure criterion which does not represent the response of reservoir rocks to induced stress (5) and finally considering intact rocks.

Chin and Ramos [4] developed a model for predicting sand production by coupling both geomechanical properties of rock and fluid flow parameters to estimate volumetric sand production in the early draw-down stage, bean-up, down to depletion stage. The work shows the influence of rock strength, flow properties, fluid properties and time on sand production from weak reservoirs. The model can serve as a guide to the quantity of sand to be expected. Mcphee and Enzendorfer [8] reported application of fuzzy logic computing techniques to correlate wireline log responses with core measurements to establish a field calibrated continuous sand production throughout the reservoir intervals. They used this method coupled with geomechanical models to analyse if selective perforation could guard well deliverability and equally ensure production without sand issues. The integrated sand management technique helped deliver production rate of over 100MMScf/d without sand production problems and also saved cost and lowering completion failure risk by using the fuzzy logic model to determine and avoid zones of thin sand which could lead to sand production. Isehunwa *et al.* [7] develop an analytical model to predict sand production in oil wells from the Niger/Delta oil fields, Nigeria. The model share input parameters close to Bratli *et al*. [2], with rock and fluid properties the major factor affecting sanding in their model. Their results show that maintaining cavity height below 30ft is important for sand free production.

In this paper, an analytical sand production onset prediction model is developed based on the popular theory of poro-elasticity and assuming shear failure induced sanding, the applicability of modified Hoek-Brown failure criterion rather than the popular Mohr-coulomb in predicting sand production onset was investigated.

2. Theoretical framework

The onset of sand production is the failure of intact rock, thus, if this can be predicted and prevented, then the sand production becomes no issue. Therefore, the starting point for most predictive tool for predicting sanding potentials in unconsolidated sandstones is identifying the stresses at the perforation cavity and failure prediction around the perforation cavity or open hole. The stepwise process in the model development is listed as follows:

1. Identifying the in situ stress magnitude.
2. Assessing the stress state at the borehole wall or perforation tunnel, having in mind the orientation of the borehole.
3. Applying appropriate failure criterion.

Assumptions

The approach in this model will be based on the listed assumptions:

- The horizontal stress is isotropic at far field
- The rock is a homogenous, unconsolidated or poorly consolidated sandstone
- The formation is in a geologically relaxed environmental, there is no active tectonic regime.
- Shear failure corresponds to initiation of sand production, i.e. no drag forces.
- Stress-controlled failure process around the perforation cavity is dominated by cohesion loss (i.e. not by frictional strength loss).
- The wellbore/perforation tunnel-formation structure is axisymmetric.
- Formation rock failure can be described by modified Hoek-Brown failure criterion.

2.1. Borehole stress (Isotropic In-situ stress)

The in-situ stresses in this study will be considered at points ($\sigma_{\theta=0}$). The three principal stresses can then be written in borehole geometry coordinates for conveniences and then transpose into radial systems of tangential, radial and overburden coordinates. For this study, the maximum induced stresses is taken to occur in the tangential coordinate. The borehole wall is assumed to be permeable, therefore, the pore pressure at the borehole wall is equal to the well pressure. The derivation of poro-elastic solution to stresses around the borehole according to Fjaer [5] given in terms of radial and tangential stresses are as follows,

$$\sigma_r{}' = (1-\alpha)P_{wf(t)} \tag{1}$$

$$\sigma_\theta{}' = \frac{P_{wf(t)}{R_w}^2 - \left(2\sigma_{h(t)} - P_{wf(t)}\right){R_e}^2}{{R_w}^2 - {R_e}^2} - \alpha\frac{1-2\nu}{1-\nu}\bar{P}_{(t)} - \alpha\frac{\nu}{1-\nu}P_{wf(t)} \tag{2}$$

In this study, it is assumed that reservoir radius is in order magnitude greater the wellbore radius i.e., $R_e \gg R_w$, therefore, the above equation is simplified as follows;

$$\sigma_\theta{}' = 2\sigma_{h(t)} - \alpha\frac{1-2\nu}{1-\nu}\bar{P}_{(t)} - \left(1+\alpha\frac{\nu}{1-\nu}\right)P_{wf(t)} \tag{3}$$

2.2. Failure criteria

Several empirical criteria exist in the literature that describes the onset of rock failure, among these are the Mohr-Coulomb failure criterion; Mogi-Coulomb failure criterion; Ducker Prager failure criterion; Von Mises failure criterion and Hoek-Brown failure criterion which all give material behaviour of rocks at failure. The most common failure criterion used in theoretical modelling of sand production and any other geo-mechanical related problems is the Mohr-Coulomb failure criterion. It accounts for 80% of existing models while other criteria accounts for the remaining 20%, the major reasons for the use of Mohr-Coulomb failure criteria according to Oluyemi *et al.* [9] are (1) simplicity and ease of use (2) mathematical simplicity, which expressed shear stress as a linear function of normal stress. This thus implies a linear failure envelope and also only applicable when considering intact rocks. However, it has been proven that petroleum reservoir rocks do not exhibit linear failure envelope as such, modeling sand production while using Mohr-Coulomb or any modified version cannot be relied upon to fully capture failure behavior of rocks under imposed stress. Therefore, in this study, Hoek Brown failure criterion will be adopted, which is an empirically derived failure criterion that describes the non-linear increase in peak strength of isotropic rock with increasing confining stress.

The original non-linear Hoek Brown failure expression for intact was introduced in 1980 as;

$$\sigma_1 = \sigma_3 + \sqrt{mC_o\sigma_3 + s{C_o}^2} \tag{4}$$

where: σ_1 = major principal stress; σ_3 = minor principal stress;
C_o = uniaxial compressive strength of the intact rock; m and S are dimensionless empirical constants.

To account for reservoir rocks that are no longer intact, Hoek Brown criterion was updated in response to experience gained with its use and to address the practical limitation of friable rocks [6]. In achieving this, a generalized form of the criterion was reported in 1995 as follows;

$$\sigma_1{}' = \sigma_3{}' + C_o\left(m_b\frac{\sigma_3{}'}{C_o} + s\right)^a \qquad (5)$$

mb=is a reduced value of M in the original Hoek-Brown equation for failure,which accounts for the strength reducing effects of the rock mass conditions; a =empirical constant to account for system' s bias towards hard rock.

In terms of borehole stress,

$$\sigma_\theta{}' = \sigma_r{}' + C_o\left(m_b\frac{\sigma_r{}'}{C_o} + s\right)^a \qquad (6)$$

$$m_b = m_i exp\left(\frac{GSI - 100}{24 - 14D}\right) \qquad (7)$$

$$S = exp\left(\frac{GSI - 100}{9 - 3D}\right) \qquad (8)$$

2.3. Critical Wellbore pressure failure model

If we assume isotropic in-situ stresses, and that the effective tangential stress is the maximum principal stress and the effective radial stress is the minimum principal stress, and if we assume sanding occur at shear failure condition, using Modified Hoek-Brown criterion, stability occur when RHS of equation 8 is equal the LHS as follows;

$$\sigma_r{}' = (1 - \alpha)P_{wf} \qquad (9)$$

$$\sigma_\theta{}' = 2\sigma_{h(t)} - \alpha\frac{1 - 2\nu}{1 - \nu}\bar{P}_{(t)} - \left(1 + \alpha\frac{\nu}{1 - \nu}\right)P_{wf(t)} \qquad (10)$$

$$2\sigma_h - \alpha\frac{1 - 2\nu}{1 - \nu}\bar{P} - \left(1 + \alpha\frac{\upsilon}{1 - \upsilon}\right)P_{wf} = (1 - \alpha)P_{wf} + C_o\left[m\frac{(1 - \alpha)P_{wf}}{C_o} + S\right]^a \qquad (11)$$

To simplify equation 8 further, the Hoek-Brown material constants a, mb and s for the rock mass has to be evaluated. These constants are determined for the rock mass using Geological Strength Index (GSI) as defined in Hoek *et al.* [6] (Table 1). Exponent "a" according to Hoek *et al.* was added to the failure criterion to address the system's bias towards hard rock and to better predict the behavior of poorer quality rock masses by enabling the failure envelope's curvature to be adjusted, especially under very low normal stresses. Since it is extremely difficult to estimate or predict the general state of reservoir rock downhole (rock quality) and especially when core examinations are not available. It will be inaccurate to assume reservoir rocks quality is 100% (hard rock, i.e a = 1) or that the rock mass is of very poor quality (a = 0). Therefore, for this research, two extreme scenarios and one average value of exponent "a" was used to simplify equation 8 further and hence, the derivation of critical well pressure that will give a safe margin was evaluated. The estimated values of the material constants (Table 1) are representation of the level of disturbance within the rock mass. The critical well pressures at different rock conditions are presented in table 2, derivations presented in appendix A.

3. Model verification

The validation process for models presented in Table 2 strictly relies on well log information (specifically sonic and density log). These data set are obtained during drilling process and provides specific data for the well before completion. In this case, the model can be used as a quick check for evaluating the potential for sanding across different reservoirs penetrated by a well, in terms of minimum allowable well pressure at/below which shear failure of the reservoir rocks will be triggered. With this, the completion team has a sanding predictive tool that can help in taking completion strategy decisions for well development. The sanding onset model presented in this study was verified using a field case study (Niger Delta) and data for numerical analysis from Yi [12].

Table 1. Hoek-Brown material constants for rock mass

Rocks	Carbonates Rocks	Shale	Sandstone	Fine Grained Igneous Rocks	Coarse Grained Igneous Rocks
Intact Rocks	M = 6 S =1	M = 8 S =1	M = 11 S =1	M =16 S =1	M = 18 S =1
Undisturbed Rocks	M = 3 S = 0.189	M = 4.39 S = 0.189	M = 5.59 S = 0.189	M = 7 S = 0.189	M = 12.56 S = 0.189
Moderately Weathered Rocks	M = 7 -1.6. S = 0.00198 – 0.0205	M = 1 -0.923. S =0.00198 – 0.0205	M = 1.6 - 3.02 S = 0.00198 – 0.0205	M = 1.6 - 4.81 S = 0.00198 – 0.0205	M = 3.3 - 6.51 S = 0.00198 – 0.0205
Heavily Weathered Rocks	M = 0.03 S = 0.00002	M = 0.043 S = 0.00002	M = 0.65 S = 0.00002	M = 0.0746 S = 0.00002	M = 0.109 S = 0.00002

Table 2. Conditions for sanding in wells with isotropic in-situ stresses and permeable borehole wall

Case	Material Constant (a)	Minimum bottom-hole pressures at failure
Isotropic In-situ Stress	$a = 0$	$P_{wfc} = \frac{2\sigma_h - \alpha n\bar{P} - C_o}{2 - \alpha n}$
Isotropic In-situ Stress	$a = 0.5$	$P_{wfc} = \frac{mC_oU - 2RY \pm \sqrt{mC_oU - 2RY^2 - 4R^2\left(Y^2 - S{C_o}^2\right)}}{2R^2}$
Isotropic In-situ Stress	$a = 1$	$P_{wfc} = \frac{2\sigma_h - \alpha n\bar{P} - SC_o}{2 - \alpha n + m(1 - \alpha)}$
Yi [12]		$\frac{P_{wf}}{C_o} = (1 - \nu)\left[2\frac{\sigma_h}{C_0} - \frac{1 - 2\nu\bar{P}}{1 - \nu C_0} - 1\right]$

Case study 1 (Yi’s numerical result)

The result from current study was compared with Yi’s numerical prediction of minimum well pressure. The numerical results of Yi [12] were chosen because (Table 2), it shares similar boundary condition and physical geometry with the current work, except that the material failure criterion for the two models is different as discussed earlier in the introduction.

Using the data presented in Tables 3 and 4, critical wellbore pressure analysis was performed for the model and compared with Yi’s numerical results. Based on the two models assumption, sand production is caused by wellbore shear failure, using the sanding models derived in this study and Yi’s analytical model, together with his numerical results, the minimum well pressure for the three methods are presented in Table 4.

Table 3. Reservoir and production parameters from Yi [12]

Reservoir parameters	Value	Reservoir parameters	Value
Wellbore radius (ft)	0.25	X Direction permeability (mD)	5
Drainage area (acre)	40	Y Direction permeability (mD)	10
Aspection ratio	0.5	Z Direction permeability (mD)	0.1
Reservoir thickness (ft)	20	Porosity (fraction)	0.12
Gas specific gravity (fraction)	0.7	Reservoir temperature (°F)	108
Initial production rate (Mscf/Day)	1000	Formation compressibility (1/psi)	10e-6
Intial reservoir pressure (psi)	2800		

Table 3. Rock Mechanical properties used for comparison

Mechanical properties	Value	Mechanical properties	Value
Young Modulus (psi)	1.4E+6	Overburden Stress (psi)	3400
Poisson Ratio (fraction)	03	Min. Horizontal Stress (psi)	3060
Cohesive Strength UCS (psi)	1500	Poro-elastic constant	1
Friction Angle (Degree)	30		

Table 4. Comparison of current model with existing model and numerical result

This study			Numerical result
a = 0	a = 0.5	a = 1	$Pw_{f\,(}$(psi)
$Pw_{f\,(}$(psi)	$Pw_{f\,(}$(psi)	$Pw_{f\,(}$(psi)	
2114	2114	2114	2175

From Table 4, it can be seen that the onset of sand production for the three methods is not too different when Biot's constant $(\propto)$ is taken to be 1 for all the models. The results are quite different for this current study when Biot's constant is not unity. Assuming Biot's constant to be 1 reduced the non-linear increase in peak strength of isotropic rock with increasing confining stress to a more general form of Mohr-coulomb linear failure envelope, which is the condition at which a = 0 in this current study. This understanding prompted us to carry out sensitivity study on the Biot's constant and its effect on the predicted minimum well pressure. The result of this is presented in Figure 1.

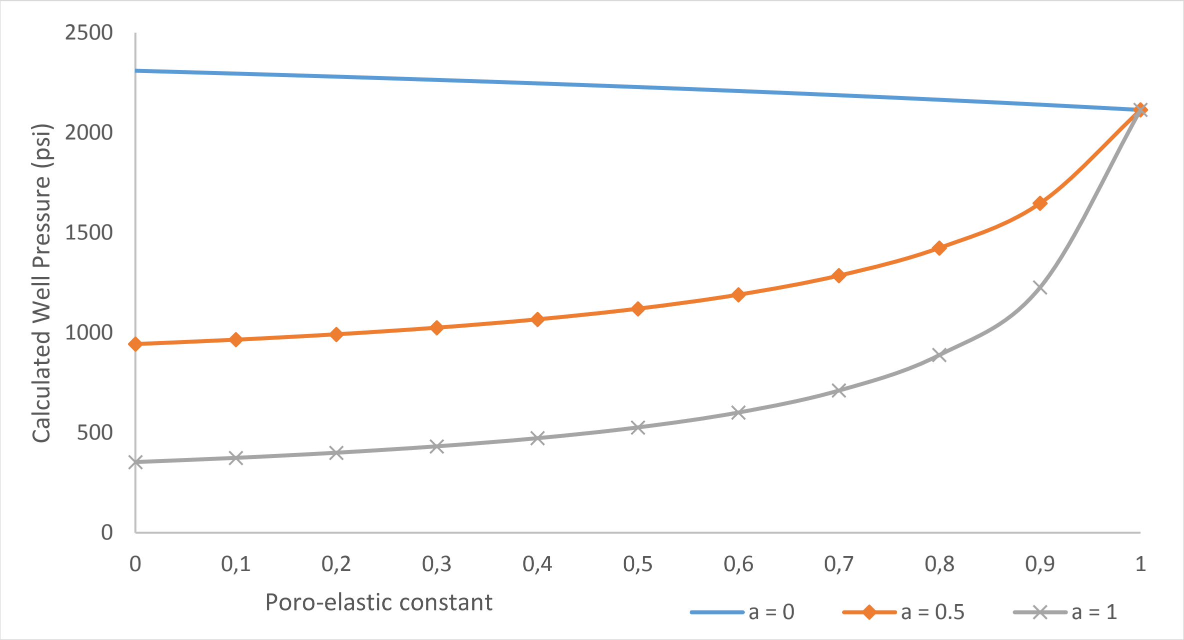

Figure 1. Effect of poro-elastic constants on calculated well pressure

In unconsolidated or weak formations, the Biot's constant α which is the ratio of bulk modulus at constant pore pressure to the bulk modulus at constant confining pressure is generally approximated to be 1. Figure 1 shows the effect of Biot's constant on the calculated well pressures. It can be observed from the Table 4 that, for the special case of $(\propto = 1)$, the three conditions of rock mass quality according to table 2 gave the same minimum well pressure. This is due to the fact that Biot's constant was assumed to be 1, which eliminates the effect of other rock condition parameters according to Heok-Brown failure criterion for the cases of exponent "a" = 0.5 and 1. Sentivity study on Biot's constant between 1 and 0 shows two different trends for different conditions of exponent a; at a = 0, which is a typical case of linear failure envelope, reduction in poro-elastic constant resulted into increase in the calculated minimum pressure (Figure 1). Whereas at a = 0.5 and 1 shows similar trend of reduction in the calculated well pressure because the effect of Hoek-Brown material constants M and S which represent the frictional strength of the rock and measures of how fractured a rock is' respectively, are been accounted for. This implies that accurate estimation of Biot's constant is essential in accurately predicting the minimum well pressure below which sand is to be expected.

Case study 2 (Niger Delta)

Data from two exploration boreholes (well A and B) were used in this aspect. The strength of the reservoir rocks are direct results of compaction of the sand grains and effects of overburden and was found to be strongly correlated to depth as a function of burial. Tables 5 and 6 records the extracted sand production data for wells A and B, with the gas to liquid ratio. Proposed model for the current study presented in Table 2 was used to perform analysis of critical well pressure at onset of sanding on wells A and B. Table 7 through 10 present the in-situ stress data used in calculating the borehole stresses and the dynamic elastic properties used in the model.

Table 5. Sand production data for well A

Sand (PPTB)	Oil (bbl/m)	Water (bbl/m)	Water-cut (%)	Gas (Msc/m)	GLR (Scf/bbl)
2	54279	31	0	11063	204
0	21540	8	0	9525	442
1	13506	5814	30	5550	287
1	3646	1497	29	1024	199
2	39280	16440	30	7541	135
2	38743	7399	16	6933	150
2	23049	4228	15	4778	175

Table 6. Sand production data for well B

Sand (PPTB)	Oil (bbl/m)	Water (bbl/m)	Water-cut (%)	Gas (Mscf/m)	GLR (scf/bbl)
40	13081	36322	74	5919	120
34	17137	14032	45	82393	2643
33	15323	11686	43	2899	107
33	14850	10520	41	19075	752
33	19788	14790	43	14550	421
33	18150	13607	43	15624	492
33	18615	13327	42	5813	182

Table 7. In-situ stress data for well A

Depth(ft)	Overburden (Psi)	Pore Pressure (psi)	Min Horizontal Stress (psi)	Max Horizontal Stress (psi)
5842.9	4797.605	2752.006	3585.203	3877.348
5979.9	4975.875	2524.714	3765.543	4064.538
6059.9	5090.922	2580.002	3897.122	4200.117
6159.9	5179.737	2603.551	3981.947	4289.942
6259.9	5268.708	2626.481	4067.438	4380.433
6359.9	5357.834	2648.794	4153.595	4471.59
6459.9	5447.117	2670.49	4240.418	4563.413
6559.9	5536.556	2691.567	4327.908	4655.903
6659.9	5626.151	2712.027	4416.063	4749.058
6759.9	5715.902	2731.868	4504.884	4842.879
6859.9	5805.809	2751.093	4594.372	4937.367
6959.9	5895.872	2769.699	4684.526	5032.521
7059.9	5986.09	2787.688	4775.345	5128.34
7159.9	6076.465	2805.058	4866.831	5224.826
7200.9	6113.564	2812.002	4904.533	5264.578
7270.9	6260.245	2925.083	5267.767	5631.312
7344.9	6478.202	2917.982	5457.995	5825.24
7483.9	6750.478	2933.614	5583.738	5957.933
7574.9	7287.054	2794.987	6154.606	6533.351
7637.9	7492.78	2927.454	6424.238	6806.133

Table 8. Calculated dynamic elastic properties for well A (extracted for the reservoir)

Poisson ratio	Young modulus (Mpsi)	Shale Content (%)	Shear Modulus G (Mpsi)	Bulk Modulus K (Mpsi)	Biot's Constant
0.28	671.9335	0.113	262.4631	509.0334	0.46
0.28	687.6885	0.113	268.6171	520.9689	0.46
0.28	696.8885	0.113	272.2107	527.9385	0.46
0.28	708.3885	0.113	276.7027	536.6505	0.46
0.28	719.8885	0.113	281.1947	545.3625	0.46
0.28	731.3885	0.113	285.6867	554.0745	0.46
0.28	742.8885	0.113	290.1787	562.7865	0.46
0.28	754.3885	0.113	294.6707	571.4985	0.46
0.28	765.8885	0.113	299.1627	580.2105	0.46
0.28	777.3885	0.113	303.6547	588.9225	0.46
0.28	788.8885	0.113	651.1417	597.6345	0.46
0.28	800.3885	0.113	660.6337	1281.248	0.46
0.28	811.8885	0.113	670.1257	1299.657	0.29
0.28	823.3885	0.113	679.6177	1318.066	0.29
0.28	1749.819	0.3765	683.5094	1325.614	0.29
0.28	1766.829	0.3765	690.1538	1338.5	0.29
0.28	1784.811	0.3765	697.1779	1352.123	0.29
0.28	2334.977	0.221	912.1377	1768.895	0.2
0.28	2363.369	0.221	923.2288	1790.403	0.2
0.28	817.2553	0.1024	319.2642	619.1282	0.47

Table 9. In-situ stress data for well B

Depth(ft)	Overburden (Psi)	Pore Pressure (psi)	Min Horizontal Stress (psi)	Max Horizontal Stress (psi)
5694	4675.3	2448.4	4071.2	4355.9
5794	4675.3	2491.4	4205.6	4494.5
5894	4675.3	2534.4	4406.6	4701.3
5994	4675.3	2577.4	4581.8	4881.5
6094	4675.3	2620.4	4659.5	4986.8
6194	4675.3	2663.4	4786.7	5090.8
6280	4675.3	2700.4	4848.8	5162.8
6687	4675.3	2875.4	5283.4	5617.7
6931	4675.3	2911.0	5631.4	5978.0
7123	4675.3	2991.7	5991.2	6347.3
7809	4675.3	3201.7	6577.5	6968.0

Table 10. Calculated dynamic elastic properties for well B (extracted for the reservoir)

Poisson ratio	Young modulus (Mpsi)	Shale Content (%)	Shear Modulus G (Mpsi)	Bulk Modulus K (Mpsi)	Biot's Constant
0.28	654.81	0.113	255.7	495.9	0.46
0.28	666.31	0.113	260.2	504.7	0.46
0.28	905.8941	0.214	264.6	513.4	0.46
0.28	1456.542	0.214	568.8	1103.5	0.29
0.28	1480.842	0.214	578.3	1121.9	0.29
0.28	1505.142	0.214	587.8	1140.3	0.29
0.28	1526.04	0.214	765.5	1484.6	0.29
0.28	2086.344	0.532	815.1	1580.8	0.2
0.28	2162.472	0.221	289.7	562.1	0.2
0.28	762.161	0.221	297.7	577.7	0.47
0.28	835.563	0.221	326.4	633.3	0.47

Using three conditions for sanding (Table 2), the critical pressures at which sanding is to be expected were calculated and compared with field well pressure at sanding as shown in

Figure 2 and 3 for well A and B respectively. For well A, the condition for sanding as estimated from the sanding models developed gave the range of pressures for sanding to be between 1600 – 2200 psi using the 3 equations in this study, field data indicate that sand production occurs at well pressure of 2000 psi for perforated interval between 6843 ft to 6923 ft. From 2, a good match between field observed well pressure at sanding assuming shear failure and model predictions was observed which in turns induced sand production.

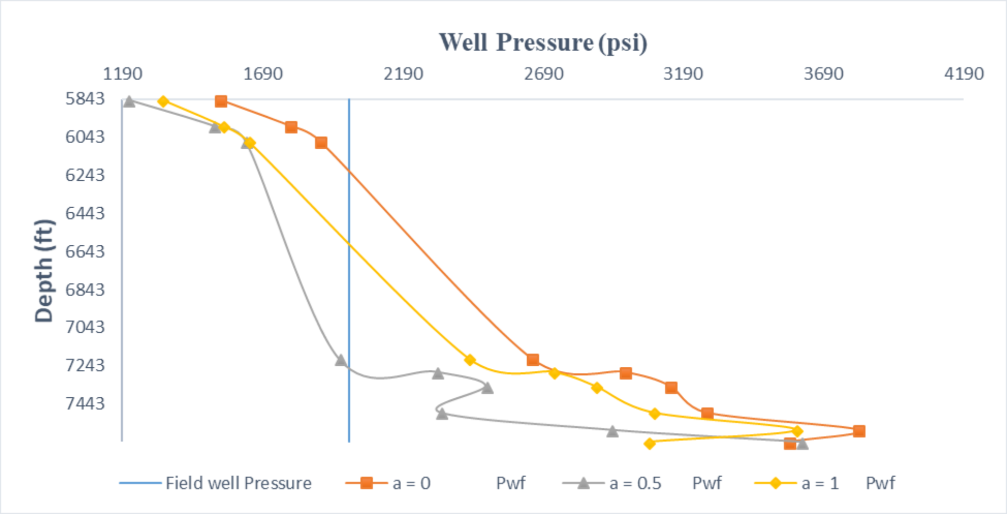

Figure 2. Plot of predicted and field measured well pressure at sanding onset assuming shear induced stress sanding for well A

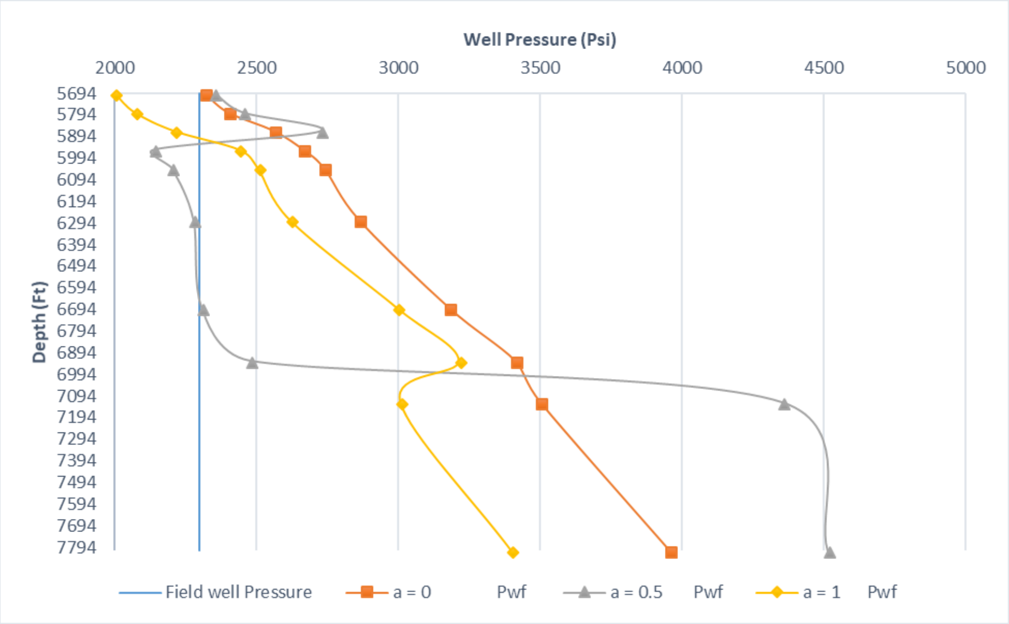

Figure 3. Plot of predicted and field measured well pressure at sanding onset assuming shear induced stress sanding for well B

For well B, sanding condition at a = 0.5 correspond to the field observed well pressure at sand production onset for perforation depth between 6294 ft to 6344 ft, while sanding onset at a = 0, 1 predicted slightly above the field observed minimum well pressure at sanding onset.

4. Conclusion

In this paper, the applicability of modified Hoek-Brown failure criterion in geomechanical modelling of sand production in unconsolidated sandstone reservoirs rock was explored and a new shear failure induced sanding onset prediction model is derived. The analytical model compared with the numerical result before been applied to field data to verify its field applicability. The results from the comparison were encouraging and very close. For field applications, the results were in agreement with field observed well pressure for the reservoirs penetrated. Therefore, this model is recommended for prediction of sanding potentials in unconsolidated sandstone reservoirs in real-time.

Nomenclature

$\sigma_r{}' = Effective\ Radial\ Stress$
$\sigma_\theta{}' = Effective\ Tangential\ Stress$
$\sigma_h = Minimum\ horizontal\ stress$
$\nu = Poisson's\ Ratio$
$\lambda = Lame\ Parameter$
$E = Young's\ Modulus\ (psi)$
$\alpha = Poro - elastic\ constant$
$\bar{P} = Far - field\ pore\ pressure\ or\ Average\ Reservoir\ Pressure\ (Psi)$
$P_{wf} = Bottom - hole\ Pressure\ (psi)$
$P_w = Well\ Presssure\ (Psi)$
$C_o = Uniaxial\ Compresive\ Strength$
$M = Hoek - Brown\ Material\ Constant\ (rock\ mass)$
$S = Hoek - Brown\ Material\ Constant$
$Re\ =\ reservoir\ boundary\ radius, L, ft$
$Rw\ =\ cavity\ (wellboe, perforation\ tunnel\ or\ perforation\ tip)\ radius, L, ft$

Appendix A

If we assume isotropic in-situ stresses, and that the effective tangential stress is the maximum principal stress and the effective radial stress is the minimum principal stress, and if we assume sanding occurs at shear failure condition, using Modified Heok-Brown criterion, stability occur when (eqn 8);

$$2\sigma_h - \alpha\frac{1-2\nu}{1-\nu}\bar{P} - \left(1+\alpha\frac{\upsilon}{1-\upsilon}\right)P_{wf} = (1-\alpha)P_{wf} + C_o\left[m\frac{(1-\alpha)P_{wf}}{C_o} + S\right]^a$$

ISOTROPIC IN-SITU STRESS

For $a = 0$ and solve for P_{wf}

$$2\sigma_h - \alpha\frac{1-2\nu}{1-\nu}\bar{P} - \left(1+\alpha\frac{\upsilon}{1-\upsilon}\right)P_{wf} = (1-\alpha)P_{wf} + C_o$$

$$2\sigma_h - \alpha\frac{1-2\nu}{1-\nu}\bar{P} - P_{wf}\left[1+\frac{\alpha\upsilon}{1-\upsilon}+1-\alpha\right] = C_o$$

$$P_{wf}\left[1+\frac{\alpha\upsilon}{1-\upsilon}+1-\alpha\right] = 2\sigma_h - \alpha\frac{1-2\nu}{1-\nu}\bar{P} - C_o$$

$$P_{wf} = \frac{2\sigma_h - \alpha\frac{1-2\nu}{1-\nu}\bar{P} - C_o}{\left[1+\frac{\alpha\upsilon}{1-\upsilon}+1-\alpha\right]}$$

Expanding the de-numerator yield;

$$\left[1+\frac{\alpha\upsilon}{1-\upsilon}+1-\alpha\right] = \frac{2(1-\upsilon)+\alpha(2\upsilon-1)}{1-\upsilon}$$

$$= 2+\alpha\left(\frac{2\upsilon-1}{1-\upsilon}\right)$$

$$= 2-\alpha\left(\frac{1-2\upsilon}{1-\upsilon}\right)$$

Let $n = \frac{1-2\upsilon}{1-\upsilon}$

Then the expansion above can be simplified as;

$2-\alpha n$

Therefore, $P_{wf}\ is;$

$$\boldsymbol{P_{wf}=\frac{2\sigma_h-\alpha n\bar{P}-C_o}{2-\alpha n}}$$

ISOTROPIC IN-SITU STRESS

For $a={}^1\!/_2$ and solve for P_{wf}

$$2\sigma_h-\alpha\frac{1-2v}{1-v}\bar{P}-\left(1+\alpha\frac{v}{1-v}\right)P_{wf}=(1-\alpha)P_{wf}+\sqrt{mC_o(1-\alpha)P_{wf}+SC_o{}^2}$$

$$2\sigma_h-\alpha\frac{1-2v}{1-v}\bar{P}-\left(1+\alpha\frac{v}{1-v}\right)P_{wf}-(1-\alpha)P_{wf}=\sqrt{mC_o(1-\alpha)P_{wf}+SC_o{}^2}$$

Squaring both sides and re-arranging

$$\boldsymbol{P_{wf}}^2\left[\left(1+\frac{\propto v}{v}\right)^2+2\left(1+\frac{\propto v}{1-v}\right)(1-\propto)+(1-\propto)^2\right]$$
$$-\boldsymbol{P_{wf}}\left[4\sigma_h\left(1+\frac{\propto v}{1-v}\right)+4\sigma_h(1-\alpha)-2\propto\left(\frac{1-2v}{1-v}\right)\left(1+\frac{\propto v}{1-v}\right)\bar{P}-2\right.$$
$$\left.\propto\left(\frac{1-2v}{1-v}\right)(1-\propto)\bar{P}+mC_o(1-\propto)\right]+4\sigma_h{}^2-4\sigma_h\alpha\frac{1-2v}{1-v}\bar{P}+\propto^2\left(\frac{1-2v}{1-v}\right)^2\bar{P}^2-SC_o{}^2=0$$

Expanding the coefficients of $\boldsymbol{P_{wf}}^2$ and $\boldsymbol{P_{wf}}$ yields the following

Coefficient of $\boldsymbol{P_{wf}}^2$

$$\left[\left(1+\frac{\propto v}{v}\right)^2+2\left(1+\frac{\propto v}{1-v}\right)(1-\propto)+(1-\propto)^2\right]$$

This can be written as;

$A^2+2AB+B^2$

Where

$A=\left(1+\frac{\propto v}{v}\right)$ $\quad$ $A^2=\left(1+\frac{\propto v}{v}\right)\left(1+\frac{\propto v}{v}\right)$

$B=(1-\propto)$ $\quad$ $2AB=2\left(1+\frac{\propto v}{1-v}\right)(1-\propto)$

$$A^2=1+2\frac{\propto v}{1-v}+\frac{\propto^2 v^2}{(1-v)^2}$$

$$AB=1-\propto+\frac{\propto v}{1-v}-\frac{\propto^2 v}{1-v}$$

$$2AB=2-2\propto+\frac{2\propto v}{1-v}-\frac{2\propto^2 v}{1-v}$$

$$B^2=(1-\propto)^2=1-2\propto+\propto^2$$

Putting all these together gives;

$$1+2\frac{\propto v}{1-v}+\frac{\propto^2 v^2}{(1-v)^2}+2-2\propto+\frac{2\propto v}{1-v}-\frac{2\propto^2 v}{1-v}+1-2\propto+\propto^2$$
$$=\frac{4(1-v)^2+\propto^2(2v-1)^2+4\propto(2v-1)(1-v)}{(1-v)^2}$$
$$=\frac{[2(1-v)+\propto(2v-1)]^2}{(1-v)^2}P_{wf}{}^2$$

Coefficient of $\boldsymbol{P_{wf}}$

$$P_{wf}\left[4\sigma_h\left(1+\frac{\propto v}{1-v}\right)+4\sigma_h(1-\alpha)-2\propto\left(\frac{1-2v}{1-v}\right)\left(1+\frac{\propto v}{1-v}\right)\bar{P}-2\propto\left(\frac{1-2v}{1-v}\right)(1-\propto)\bar{P}+mC_o(1-\propto)\right]$$

Re-arranging this gives;

$$4\sigma_h\left[1+\frac{\propto v}{1-v}+1-\propto\right]-2\bar{P}\propto\left[\left(\frac{1-2v}{1-v}\right)\left(1+\frac{\propto v}{1-v}\right)+\left(\frac{1-2v}{1-v}\right)(1-\propto)\right]+mC_o(1-\propto)$$

Similar to P_{wf}^{2} the coefficients of $\boldsymbol{P_{wf}}$ can be simplify thus;

$$A=\left[1+\frac{\propto v}{1-v}+1-\propto\right]=\frac{2(1-v)+\propto(2v-1)}{1-v}$$

$$B=\left(\frac{1-2v}{1-v}\right)\left(1+\frac{\propto v}{1-v}\right)+\left(\frac{1-2v}{1-v}\right)(1-\propto)=\left(\frac{1-2v}{1-v}\right)\left[1+\frac{\propto v}{1-v}+1-\propto\right]$$

$$=\frac{(1-2v)\left[\left(2(1-v)\right)+\propto(2v-1)\right]}{(1-v)^2}$$

$$=4\sigma_h A-2\bar{P}\propto B+mC_o(1-\propto)$$

$$=4\sigma_h\left[\frac{2(1-v)+\propto(2v-1)}{1-v}\right]-2\bar{P}\propto\left[\frac{(1-2v)\left[\left(2(1-v)\right)+\propto(2v-1)\right]}{(1-v)^2}\right]+mC_o(1-\propto)$$

$$=\frac{2(1-v)+\propto(2v-1)}{1-v}\left[\frac{4\sigma_h-2\bar{P}\propto(1-2v)}{1-v}\right]+mC_o(1-\propto)$$

$$=P_{wf}\left[\frac{2(1-v)+\propto(2v-1)}{1-v}\left[\frac{4\sigma_h-2\bar{P}\propto(1-2v)}{1-v}\right]+mC_o(1-\propto)\right]$$

Constants

$$4\sigma_h^{2}-4\sigma_h\alpha\frac{1-2v}{1-v}\bar{P}+\propto^2\left(\frac{1-2v}{1-v}\right)^2\bar{P}^2-SC_o^{2}$$

$$\boldsymbol{let\ n}=\frac{1-2v}{1-v}$$

The equation above can be written thus;

$4\sigma_h^{2}-4\sigma_h\alpha n\bar{P}+\propto^2 n^2\bar{P}^2-SC_o^{2}$

To factor **n** into the expressions for P_{wf} and P_{wf}^{2} the expressions can be written as;

Coefficient of P_{wf}

$$=\left[2+\propto\frac{(2v-1)}{1-v}\right]\left[4\sigma_h-2\bar{P}\alpha\left(\frac{1-2v}{1-v}\right)\right]+mC_o(1-\propto)$$

$[2-\propto n][4\sigma_h-2n\bar{P}\alpha]+mC_o(1-\propto)P_{wf}$

Coefficient of P_{wf}^{2}

$$=\left[\frac{2(1-v)+\propto(2v-1)}{1-v}\right]\left[\frac{2(1-v)+\propto(2v-1)}{1-v}\right]P_{wf}^{2}$$

$$=2-\propto\left(\frac{1-2v}{1-v}\right)^2P_{wf}^{2}$$

$(2-\propto n)^2P_{wf}^{2}$

The final expression is as follows

$(2-\propto n)^2P_{wf}^{2}-\big[[2-\propto n][4\sigma_h-2n\bar{P}\alpha]+mC_o(1-\propto)\big]P_{wf}+4\sigma_h^{2}-4\sigma_h\alpha n\bar{P}+\propto^2 n^2\bar{P}^2-SC_o^{2}=0$

To simplify the above expression further;

$let\ k=(2-\propto n)^2$

$l=[2-\propto n][4\sigma_h-2n\bar{P}\alpha]+mC_o(1-\propto)$

$w=4\sigma_h^{2}-4\sigma_h\alpha n\bar{P}+\propto^2 n^2\bar{P}^2-SC_o^{2}$

Simplifying constant w, yields;

$w=\propto^2 n^2\bar{P}^2-4\sigma_h\alpha n\bar{P}+4\sigma_h^{2}-SC_o^{2}$

$w=(\propto n\bar{P}-2\sigma_h)^2-\ SC_o^{2}$

$l=[2-\propto n][4\sigma_h-2n\bar{P}\alpha]+mC_o(1-\propto)$

$=(2-\propto n)-2[\propto n\bar{P}-2\sigma_h]+mC_o(1-\propto)$

Substituting the above simplifications back into the final equation gives;

$(2-\propto n)^2P_{wf}^{2}-(2-\propto n)-2[\propto n\bar{P}-2\sigma_h]+mC_o(1-\propto)P_{wf}+(\propto n\bar{P}-2\sigma_h)^2-\ SC_o^{2}=0$

Re-arranging this equation gives a quadratic equation that can be solve using general formula.

$$(2-\propto n)^2P_{wf}^{2}-P_{wf}[mC_o(1-\propto)-2(2-\propto n)(\propto n\bar{P}-2\sigma_h)]+(\propto n\bar{P}-2\sigma_h)^2-\ SC_o^{2}=0$$

$$x=\frac{b\pm\sqrt{b^2-4ac}}{2a}$$

$a=(2-\propto n)^2$

$b = [mC_o(1{-}\propto) - 2(2{-}\propto n)(\propto n\bar{P} - 2\sigma_h)]$
$c = (\propto n\bar{P} - 2\sigma_h)^2 - SC_o{}^2$
Let $R = 2{-}\propto n$ $\quad Y = \propto n\bar{P} - 2\sigma_h$ $\quad U = 1{-}\propto$
Then;
$a = R$ $\quad b = mC_oU - 2RY$ $\quad C = Y^2 - SC_o{}^2$
Therefore, P_{wf} is given as;

$$\boldsymbol{P_{wf} = \frac{mC_oU - 2RY \pm \sqrt{mC_oU - 2RY^2 - 4R^2\left(Y^2 - SC_o{}^2\right)}}{2R^2}}$$

ISOTROPIC IN-SITU STRESS

For $a = 1$ and solve for P_{wf}

$$2\sigma_h - \alpha\frac{1-2\nu}{1-\nu}\bar{P} - \left(1 + \alpha\frac{\upsilon}{1-\upsilon}\right)P_{wf} = (1-\alpha)P_{wf} + C_o\left[m\frac{(1-\alpha)P_{wf}}{C_o} + S\right]^a$$

$$2\sigma_h - \alpha\frac{1-2\nu}{1-\nu}\bar{P} - \left(1 + \alpha\frac{\upsilon}{1-\upsilon}\right)P_{wf} = (1-\alpha)P_{wf} + C_o\left[m\frac{(1-\alpha)P_{wf}}{C_o} + S\right]^1$$

$$2\sigma_h - \alpha\frac{1-2\nu}{1-\nu}\bar{P} - SC_o = P_{wf}\left[1 + \frac{\alpha\upsilon}{1-\upsilon} + 1 - \alpha + m(1-\alpha)\right]$$

$$P_{wf} = \frac{2\sigma_h - \alpha\frac{1-2\nu}{1-\nu}\bar{P} - SC_o}{\left[1 + \frac{\alpha\upsilon}{1-\upsilon} + 1 - \alpha + m(1-\alpha)\right]}$$

Let $n = \frac{1-2\upsilon}{1-\upsilon}$

Then the expansion above can be simplified as;

$$\boldsymbol{P_{wf} = \frac{2\sigma_h - \alpha n\bar{P} - SC_o}{2 - \alpha n + m(1-\alpha)}}$$

References

[1] Al-Awad MN and Desouky SEM. Prediction of Sand Production from a Saudi Sandstone Reservoir. Saudi Arabia: Revue de Institute français du petrole, 1997; 52(4): 407-414.

[2] Bianco LCB and Halleck PM Mechanisms of arch instability and sand production in two-phase saturated poorly consolidated sandstones. The SPE European Formation Damage Conference 2001. Hague, Netherlands: SPE-68932-MS, https://doi.org/10.2118/68932-MS.

[3] Bratli RK and Risne R. Stability and Failure of Sand Arches. Society of Petroleum Engineers Journals 1981, Pp. 236-248.

[4] Chin LY and Ramos GG. Predicting Volumetric sand Production in Weaak Reservoirs. SPE/ISRM Rock Mechanics Conference 2002. Trving, Texas: SPE/ISRM.

[5] Fjaer ERM. Holt,Horsud P, Raaen AR and Risnes R. Petroleum Related Rock Mechanics. Amsterdam, The Netherlands: Elsevier Science Publishers 1992.

[6] Hoek E, Carranza-Toress, CT & Corkum, B. Hoek-Brown failure criterion. 5th North American Rock Mechanics Symposium (NARMS-TAC) 2002. Pp. 00. 267 - 273). University of Toronto, Canada: Toronto Press.

[7] Isehunwa, SO, and Olanrewaju, O. A Simple Analytical Model for Predicting Sand Production in a Niger/Delta Oil Field. International Journal of Engineering, Science & Technology, 2010; 2(9): 4379 - 4387.

[8] Mcphee, CA and Enzendorfer CK. Sand Management Solutions for High Rate Gas Wells, Sawan Field Pakistan. *SPE International S*ymposium and Exhibition on Formation Damage Control 2004. Louisiana, USA: SPE.

[9] Oluyemi, GF & Oyeneyin, MB. Analytical critical drawdown (CDD) failure model for real time sanding potential prediction based on Hoek-Brown failure criterion. Journal of Petroleum and Gas Engineering, 2010; 1(2): 16 - 27.

[10] Powers, J. Halliburton and Geomechanics International Announce strategic partnership. Dallas, TX, USA: Press Release of Halliburton June 15, 2000.

[11] Weingarten, JS and Perkins TK. Prediction of Sand Production from Gas Wells: Methods and Gulf of Mexico Case Studies. Journal of Petroleum Technology, 1995; 596 -600.

[12] Yi X. Numerical and analytical modeling of sanding onset prediction. Texas: PhD Dissertation Submitted to the office of graduate Studies of Texas A & M University, 2003.
[13] Fadairo A, Oyedele-Adeyi O, Oladepo A, & Ogunkunle TF. Modeling the effect of entrained sand particles on pressure transverse in a flowing gas well. World Journal of Engineering, 2017; 14(5): 406-413.

To whom correspondence should be addressed: Frederick Temitope Ogunkunle, Department of Petroleum Engineering, Covenant University. Ota, Ogun State, Nigeria

Petroleum and Coal

Article **Open Access**

WAVE CHANGES IN PETROGRAPHIC COMPOSITION OF DONBAS MIDDLE CARBONIFEROUS COAL SEAMS

V. S. Savchuk, V. F. Prykhodchenko, D. Prykhodchenko, L. Tokar

National Mining University, Department of General and Structural Geology, Dnipro

Received June 13, 2018; September 5, 2018

Abstract

Availability of wave changes in petrographic composition in a stratigraphic section of Donbas has been determined for the first time in terms of the Middle Carboniferous coal seams of Lozova coal area. Data concerning the type petrographic composition of coal seams at the level of cycles confirm periodical character of the changes. Stratigraphic zones have been singled out according to the intensity and direction of changes in the petrographic composition of coals.

Keywords*: coal; petrographic composition; Donets Basin; vitrinite; inertinite; liptinite.*

1. Introduction

The paper continues the studies dealing with the analysis and systematization of the data on the petrographic composition of the Middle Carboniferous coals of northern borders of the Donets Basin [1-2].

Having generalized the available material on the petrographic composition of coal basins, Yu.A. Zhemchuzhnikov determined that the coals of various ages are characterized by a peculiar petrographic composition being unique for each coal type. Secondary unit of the planetary stratigraphic scale was taken as a basic stratigraphic unit [3]. Owing to the fact that petrographic composition of the Lower Carboniferous coals differed considerably from one of the Middle Carboniferous coals, they were studied separately. Hence, it was pointed out that petrographic composition of coals could change within a much narrower stratigraphic interval. That was proved further while generalizing the data on the petrographic composition of coals in basins of different geological eras.

An integrated approach to the study of the petrographic composition lets us to identify the genetic coal (similar studies were conducted for coals of the Lviv-Volyn basin [4]), determine their typical macerals' composition and establish regional and stratigraphic patterns of change.

Thus, detailed studies of the petrographic composition of the Permian coals of the Pechora Basin have defined the difference between the coals of different series of the system. It was determined that the Upper Permian coals are characterized by far less content of inertinite group [5]. Similar results were obtained in cases of Karaganda and Kuznetsk Basins [5].

It is considered that the Middle Carboniferous coals of Donbas are characterized by uniform appearance and petrographic composition [6]. They have minor changes being relatively constant both in terms of area and stratigraphic section [7].

Analysis of petrographic features of coals of the Bashkirian and Moscovian Stages has shown that they have practically no differences either in microstructure or in substance and petrographic composition [8]. The average content of gelified substance of the Middle Carboniferous coals is 80-90%. As a rule, the amount of inertinite group (3-15%) exceeds the one of liptinite group (2-10%). Coals are mainly clarain and duroclarain ones of mixed or spore composition [8].

According to the majority of researchers, the main differences in the petrographic composition of the Middle Carboniferous coals are insignificant [6-7, 9]. That is why for a long time various researchers have tried to determine specific conditions for the formation of genetic coal types as well as to define areal and stratigraphic regularities for their distribution [8].

Moreover, much attention was paid to the study of stratigraphy and correlation of seams as for their lithological and coal-petrographic features. Generalization of the data concerning changes in the petrographic composition of specific plies within the thickness of the Middle Carboniferous coal seams of Donbas has made it possible to determine certain peculiarities of their structure [8].

The generalizing paper considering coal-bearing formations of the Upper Paleozoic Era concludes that it is very important for scientific and practical purposes to carry out coal-petrographic analysis within a stratigraphic section of one of Donbas areas containing the most appropriate section. In this context, one should try to notice the difference in petrographic composition of the coals formed before and after great saltation in the development of coal-bearing plantation. Leading experts believe that the era of the accumulation of C_2^4 suite coal seams is that very boundary in terms of Donbas. According to their opinion, it is expedient to compare coals of suites C_2^1 – lower strata C_2^3 on the one hand, and suite C_2^5 and upper strata on the other hand [5]. Such a comparative analysis of the features of petrographic compositions of various-suite coal seams will make it possible to see the uniqueness and progressive development as well as to trace the geological history of coal accumulation [5].

Detailed studies of coal composition of Lozovaia coal-bearing area have allowed determining that the seams of the Bashkirian and Moscovian Stages differ in terms of micro- and macrostructure [1]. For the first time, it has been defined that changes in petrographic composition within the stratigraphic section of the Middle Carboniferous Series of Lozovaia coal-bearing area are of complex and periodic nature [1].

2. Objectives and objects

The objective of the paper is to trace the changes in type petrographic composition at different levels of the Middle Carboniferous Series of the Donets Basin.

One of the reasons of the lack of such studies may be explained by the fact that in terms of their area and stratigraphic section coal seams are distributed nonuniformly within the territory of Donbas [5]. Suites C_2^3, C_2^5, C_2^6, and C_2^7 are the ones containing most coal seams. Formations of suites C_2^1, C_2^2 demonstrate coal least often. Thus, there are practically no areas with the occurrence of commercial coal-bearing capacity within the whole coal-bearing thickness.

Lozova coal area located to the north from Western Donbas was selected as the object of the research. Within the territory of Lozova coal area, the Middle Carboniferous deposits are represented by suites of the Bashkirian (C_2^1, C_2^2, C_2^3, C_2^4) and Moscovian (C_2^5, C_2^6, C_2^7) stages (Fig. 1).

Maximum commercial coal-bearing capacity is associated with the deposits of the Moscovian stage [1]. However, almost all the suites except suite C_2^0 contain commercial coal seams. That makes it possible to determine petrographic features of various-age coals and trace stratigraphic changes of type petrographic composition of coals as well as to define their petrogenetic features in general.

We have collected and generalized the data on the petrographic composition of the Middle Carboniferous coals of Lozova coal area; the data were obtained in the process of geological-surveying and scientific and research activities [1].

3. Results and discussion

Figure 2 demonstrates averaged data on the total petrographic composition of coal seams of different stratigraphic units of the Middle Carboniferous series of Lozova coal area.

It has been pointed out that according to their total petrographic composition, the Middle Carboniferous seams of Lozova coal area differ slightly from the Middle Carboniferous seams of Donbas (Fig. 2). They contain more macerals of inertinite group (9.9%) and liptinite group (6.2%) and fewer macerals of vitrinite group (83.9%). According to the classification by Yu.A. Zhemchuzhnikov [3], Lozova coal area seams, as well as the coals of the Middle Carboniferous seams of Ancient Donbas, are represented by clarain; however, according to the classification by A.P. Karpinsky Russian Geological Research Institute [6], all of them belong to the subclass of gelites being represented by fusinite-lipoid-gelite type.

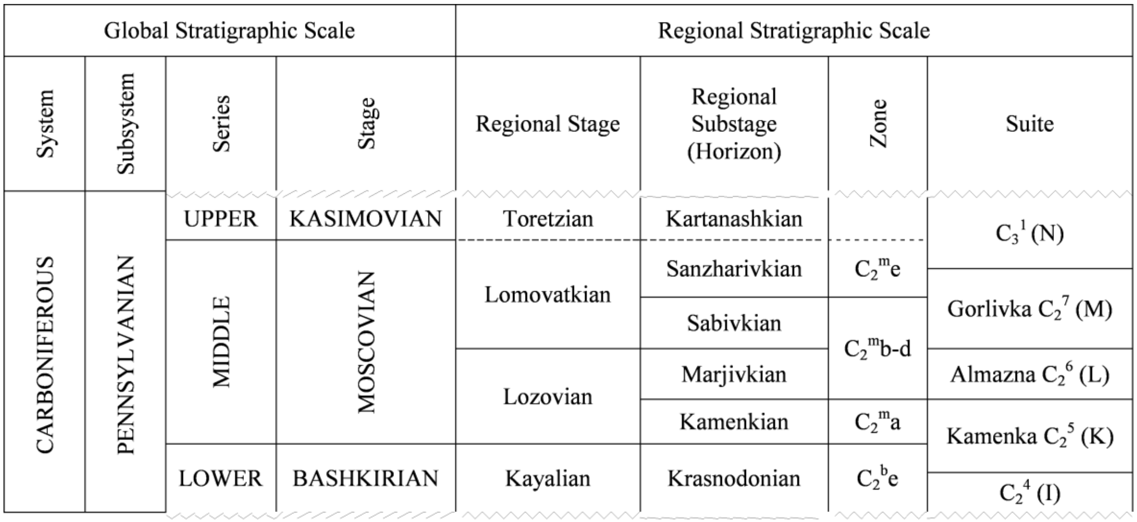

Global Stratigraphic Scale				Regional Stratigraphic Scale			
System	Subsystem	Series	Stage	Regional Stage	Regional Substage (Horizon)	Zone	Suite
CARBONIFEROUS	PENNSYLVANIAN	UPPER	KASIMOVIAN	Toretzian	Kartanashkian		C_3^1 (N)
		MIDDLE	MOSCOVIAN	Lomovatkian	Sanzharivkian	C_2^me	Gorlivka C_2^7 (M)
					Sabivkian	C_2^mb-d	
				Lozovian	Marjivkian		Almazna C_2^6 (L)
					Kamenkian	C_2^ma	Kamenka C_2^5 (K)
		LOWER	BASHKIRIAN	Kayalian	Krasnodonian	C_2^be	C_2^4 (I)

Figure 1. General stratigraphic chart of the Middle Carboniferous of the Donets Basin [10]

It has been proved that according to their total petrographic compositions, coals of the Bashkirian and Moscovian stages of Lozova coal area have practically no differences (Fig. 2).

It should be noted that numerous studies carried out in different basins, including the Donets one, have determined that changes in petrographic composition of coals are closely connected with the differences in paleographic and tectonic conditions of the development of coal-bearing formations; in addition, the changes are controlled by complex-cyclic development of the sedimentation [8]. That is why, to have further thorough studies of changes in petrographic composition in a stratigraphic section of the Middle Carboniferous series, we have decided to use cycles.

According to the conditions of the development of the Bashkirian Stage formations, Lower Bashkirian cycle (F_1 – H_4) and Upper Bashkirian cycle (F_1 – K_4) are singled out [6].

Type petrographic composition of the Lower Bashkirian cycle coals (suites C_2^1 and C_2^2) is as follows (%): vitrinite – 88.0, inertinite – 7.0, and liptinite – 5.0 (Fig. 2). The cycle differs from the Bashkirian Stage coals in a higher content of the vitrinite group and lower value of the inertinite and liptinite groups. The amount of inertinite group excesses insignificantly the amount of the liptinite group (Fig. 2).

According to the classification by A.P. Karpinsky Russian Geological Research Institute [11], the coals in its petrographic composition belongs to the subclass of gelites being represented mostly by such coal types as fusinite-lipoid-gelites and fusinite-gelites [1]. According to the classification by Yu.A. Zhemchuzhnikov, the coals belong to a mixed subgroup of clarain group.

The petrographic composition of the Upper Bashkirian cycle coals (suites C_2^3 and C_2^4) demonstrates a decrease in the content of microcomponents of vitrinite group (80.0%) with a parallel increase in the number of microcomponents of inertinite group (12.4%) and liptinite group (7.6%). According to the classification by A.P. Karpinsky Russian Geological Research Institute, the coal in its petrographic composition belongs to the subclass of gelitites being represented mostly by such coal types as fusinite-gelitites and lipoid-fusinite-gelitites [1]. According to the classification by Yu.A. Zhemchuzhnikov and others, the coals belong to a mixed subgroup of the duroclarain group.

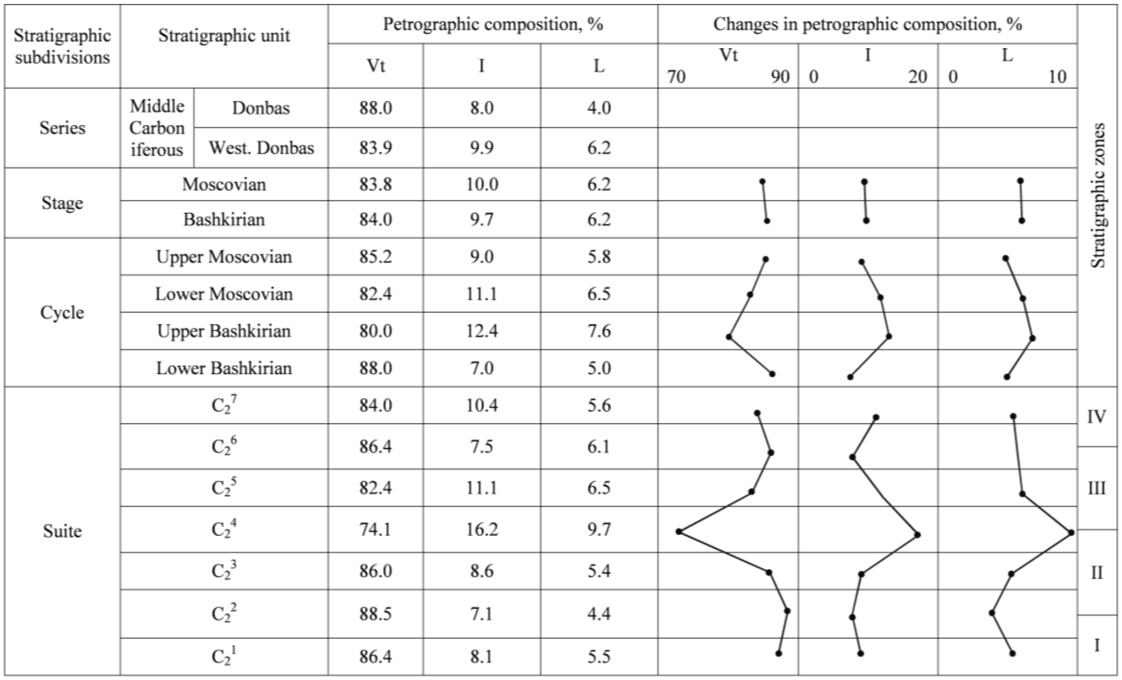

Stratigraphic subdivisions	Stratigraphic unit		Vt	I	L	Stratigraphic zones
Series	Middle Carboniferous	Donbas	88.0	8.0	4.0	
		West. Donbas	83.9	9.9	6.2	
Stage	Moscovian		83.8	10.0	6.2	
	Bashkirian		84.0	9.7	6.2	
Cycle	Upper Moscovian		85.2	9.0	5.8	
	Lower Moscovian		82.4	11.1	6.5	
	Upper Bashkirian		80.0	12.4	7.6	
	Lower Bashkirian		88.0	7.0	5.0	
Suite	C_2^7		84.0	10.4	5.6	IV
	C_2^6		86.4	7.5	6.1	
	C_2^5		82.4	11.1	6.5	III
	C_2^4		74.1	16.2	9.7	
	C_2^3		86.0	8.6	5.4	II
	C_2^2		88.5	7.1	4.4	
	C_2^1		86.4	8.1	5.5	I

Figure 1. The petrographic composition of the Middle Carboniferous coals and its changes in a stratigraphic section of Lozova coal-bearing area

Consequently, type petrographic composition of the Upper Bashkirian cycle coals (suites C_2^3 and C_2^4) demonstrate a considerable decrease in macerals of vitrinite group and increase in the number of macerals of inertinite and liptinite groups comparing to the coals of the Lower Bashkirian cycle. Changes in the petrographic composition of the coals of those cycles result in certain changes in the petrographic types and coal groups as well.

According to the conditions of the development of the Moscovian Stage formations, Lower Moscovian cycle (K) and Upper Moscovian cycle (L – M) are singled out.

The Lower Moscovian cycle (suite C_2^5) within the territory of Lozova coal area is represented by 13 coal seams and coal interlayers. Only coal seam k_8 is the one to be mined commercially. The petrographic composition of seam k_8 is as follows (%): vitrinite (Vt) – 82.4, inertinite (I) –11.1, and liptinite (L) – 6.5 (Fig. 2). In terms of petrographic composition, the seam belongs to clarain group. According to the classification by A.P. Karpinsky Russian Geological Research Institute, the coal is represented mostly by gelitite class in terms of great availability of gelite class. Such coal types as fusinite-lipoid-gelitites and fusinite-gelitite are the most abundant ones. There are also minor amounts of fusinite-lipoid-gelites and fusinite-gelites [1].

Comparing to the petrographic composition of the Moscovian Stage coals, the coals of the considered cycle are characterized by a lower content of microcomponents of vitrinite group and the available large amounts of microcomponents of inertinite group and liptinite group (Fig. 2).

On average, the petrographic composition of the Moscovian Upper cycle coals (suites C_2^6-C_2^7) demonstrates following content of macerals: macerals of vitrinite group – 85.2%, macerals of inertinite groups – 9.0, and macerals of liptinite group – 5.8% (Fig. 2). The seams are represented mostly by gelite coal type, especially coal of suite C_2^6. Comparing to the petrographic composition of the Moscovian Stage, the Upper Moscovian Cycle coals are characterized by the increased content of microcomponents of vitrinite group and slightly decreased the content of microcomponents of inertinite and liptinite groups (Fig. 2). Consequently, the petrographic composition of coal seams demonstrates an increase in the amount of vitrinite group along with the decrease in the amount of inertinite and liptinite groups from the Lower Moscovian cycle to the Upper Moscovian cycle.

The obtained data show that there is a clear wave change in the petrographic composition of coal seams at the level of cycles in a stratigraphic section of the Middle Carboniferous series of Lozova coal area.

To trace the periodicity of different orders in terms of changes in petrographic composition in stratigraphic section, petrographic compositions of different suites and their separate intervals were compared.

Petrographic composition in suites changes within a wider range of values. In that way, the content of vitrinite group varies within the limits of 14.4%, the content of inetrinite group varies within the limits of 9.2%, and content of liptinite group varies within the limits of 5.3%. It has been determined that there are different directions and intensity of the change within certain intervals of suites.

We have singled out four stratigraphic zones according to the changes in intensity and direction of the petrographic composition of coals in the stratigraphic section.

Stratigraphic zone one (I), (suites C_2^1 and C_2^2), is singled out within the boundaries of the Lower Bashkirian cycle. It is defined that there is a slight increase in the content of vitrinite group along with the decrease in the number of macerals of inertinite and liptinite groups from seams of suite C_2^1 to seams of suite C_2^2.

Stratigraphic zone two (II) of changes in petrographic composition is associated with the section of the Upper Bashkirian cycle (suites C_2^3 and C_2^4). Petrographic composition within that time limits changes unidirectionally and within large ranges. The content of vitrinite group over suites varies from 86.0% (suite C_2^3) to 74.1% (suite C_2^4). Considerable changes are also defined in the content of vitrinite group. Its maximum average values (16.2%) are observed for coals of suite C_2^4. Coals of suite C_2^3 contain a little less amount of it (8.6%). The amount of liptinite group varies within the range from 5.4% (suite C_2^3) to 9.7% (suite C_2^4). In general, there is a clear increase in the content of inertinite and liptinite groups along with the decrease in the amount of vitrinite from the lower suites to the upper ones within the limits of the singled out stratigraphic zone (Fig. 2).

There is a gradual increase in the amount of vitrinite group from 82.4 to 86.4% within the interval of C_2^5-C_2^6 suites. The content of the inertinite group in this stratigraphic section drops from 11.1% to 7.5%. The decrease in the amount of liptinite group takes place within a much narrower range of values from 9.7% to 6.1%. That was the basis to single out stratigraphic zone three (III) in petrographic composition changes.

Stratigraphic zone four (IV) from seams of suite C_2^6 to seams of suite C_2^7 demonstrates a minor decrease in the amount of vitrinite and liptinite groups at the expense of the increase in the amount of inertinite group from 7.5% up to 10.4% (Fig. 2).

4. Conclusions

The obtained data make it possible to draw the following conclusions:

1. In terms of averaged petrographic composition, coal seams of the Middle Carboniferous series of Lozova coal area of Western Donbas differ insignificantly from the petrographic composition of the Middle Carboniferous coals of Donbas; thus, the coal seams belong to one petrographic type.
2. In the stratigraphic section, changes in the petrographic composition of the Middle Carboniferous coals of Western Donbas are of wave nature.
3. Data on averages petrographic composition of coal seams at the level of cycles demonstrate the periodical character of the changes.
4. Different directions of changes in cycle compositions result in the leveling of differences in the total petrographic composition of coal seams determined for the stages.
5. Changes in the petrographic composition of coal seams in suites make it possible to single out stratigraphic zones characterized by a different direction and nonuniform degree of petrographic composition variation.

Further studies should be aimed at the determination of petrogenetic features of coals of different stratigraphic units and singling out of the reasons for complex and periodic changes in petrographic composition.

Symbols

Vt vitrinite, %;
I inertinite, %;
L liptinite, %.

References

[1] Savchuk V, Prykhodchenko V. Prykhodchenko D. Features and basic laws of changes in coal petrogenetic composition of the Moscow stage Lozovsky carboniferous area of Donbass, Journal of Geology, Geography, and Geoecology. 2014; 22(3/2): 15-21.

[2] Savchuk V, Prykhodchenko V, Buzylo V, Prykhodchenko D and Tykhonenko V. Complex use of coal of Northern part of Donbass. Annual Scientific-Technical Collection Mining of Mineral Deposits. Leiden, The Netherlands: CRC Press / Balkema, 2013; 185–191.

[3] Zhemchuzhnikov YuA. Razvitiye uglenakopleniya v geologicheskoy istorii, Izvestiya AN SSSR (Development of coal accumulation in geological history). News of the USSR AS. Series of Geology, 1955; 3: 57 – 82.

[4] Savchuk V, Prykhodchenko V, Prykhodchenko D. Petrographic composition of coal seams of mine lubelskaya no. 1-2 of the Lvov-Volyn basin and the basic laws of its change, Naukovyi Visnyk Natsionalnoho Hirnychoho Universytetu, 2013; 4: 22-27.

[5] Kler VR. i dr. Uglenosnyye formatsii verkhnego paleozoya SSSR (Coal-bearing formations of the Upper Paleozoic Era of the USSR). M.: Nedra, 1975.

[6] Sachsenhofer RF, Privalov V1, Izart A, Elie M, Kortensky J, Panova EA, Sotirov A, Zhykalyak MV. Petrography and geochemistry of Carboniferous coal seams in the ' Donets Basin (Ukraine): implications for paleoecology. Int. J. Coal. Geol., 2003; 55: 225-259.

[7] Izart A, Sachsenhofer RF, Privalov VA, Elie M, Panova EA, Antsiferov VA, Alsaab D, Rainer T, Sotirov A, Zdravkov A, Zhykalyak MV. Stratigraphic distribution of macerals and biomarkers in the Donets Basin: Implications for paleoecology, paleoclimatology, and eustacy. Int. J. of Coal Geol., 2006; 66(1-2): 69-107.

[8] Makedonov AV. Korrelyatsiya uglenosnykh otlozheniy i ugolnykh plastov v Donetskom basseyne (Correlation of the coal-bearing strata and coal seams in the Donets Basin), L.: Nauka, 1972.

[9] Sachsenhofer RF, Privalov VA, Zhykalyak MV, Bueker C, Panova E, Rainer T, Shymanovskyy VA, Stephenson R. The Donets Basin (Ukraine/Russia): Coalification and thermal history, Int. J. Coal. Geol., 2002; 49:33-55.

[10] Menning M, Alekseev AS, Chuvashov BI, Davydov VI, Devuyst F.-X, Forke HC, Grunt TA, Hance L, Heckel PN, Izokh NG, Jin Y-G, Jones PJ, Kotlyar GV, Kozur HW, Nemyrovska TI, Schneider JW, Wang X-D, Weddige K, Weyer D, Wor, DM. Global time scale and regional stratigraphic reference scales of Central and West Europe, Tethys, South China, and North America as used in the Devonian-Carboniferous-Permian Correlation Chart (DCP 2003). Palaeogeography, Palaeoclimatology, Palaeoecology, 2006; 240: 318-372.

[11] Ginzburg AI, Korzhenevskaya ES, Volkova IB. Petrograficheskiye tipy ugley SSSR (Petrographic types of the USSR coals), M.: Nedra. 1975.

To whom correspondence should be addressed: Professor V. S. Savchuk, National Mining University, Department of General and Structural Geology, Dnipro, Ukraine.nmugeology@gmail.com

Petroleum and Coal

Article **Open Access**

THE CONTROL METHOD OF THE PRESSURE OF COAL BURSTING TO COMPOSE THE COAL CHARGE, AS A WAY OF EXTENDING THE WORKING SERVICE OF COKE OVENS

Alexey Sytnik[1], Igor Shulga[1], Oleg Zelenskii[1], Elena Spirina[1], Andrey Grigorov[2]

[1] Ukrainian State Coal-Chemistry Institute, 61023, Kharkov, 7 Vesnina Str., Ukraine
[2] National Technical University «Kharkov Polytechnic Institute», 61002, 2 Kirpichova str., Kharkov, Ukraine

Received May 15, 2018; September 5, 2018

Abstract

In the process of operating coke ovens, various loads influence a blast-furnace masonry. They lead to the gradual destruction of the masonry. It is generally accepted that the most destructive effect on the cladding of furnace chambers is the excessive pressure of bursting of coked coal charges. Dynamic loads from the falling stream of the charge during loading of furnaces are also quite dangerous. Due to such unbalanced, transverse pressure on the walls of the chambers coking, which starts when the batch is loaded and continues during the development of the burst pressure when coking, the deflection of the heating wall occurs, and it leads to its destruction. In the article, the method has been given for determining the bursting pressure of a coked coal load, which makes it possible to control this value, in order to ensure the safety of the masonry of oven walls of coke ovens.

Keywords*: coal, coal charge; the process of coking; plastic mass; bursting pressure.*

1. Introduction

The modern technological process of blast-furnace production puts forward high requirements to the quality of coke, as it is the main costly component of the blast furnace charge. It is known that the quality of domain coke is influenced by two groups of factors. The first of them is related to the properties of the processed raw materials (coals and charge), and the second one is related to the coking mode and the post-furnace coke treatment (quenching, sorting, etc.). This fully applies to the mechanical "cold" strength of coke. Taking into account the fact that all over the world there are requirements for the "hot" strength of coke, determined by the indicators of CRI and CSR (18894 Coke - Determination of coke reactivity index (CRI) and coke strength after reaction (CSR)) by the method of Nippon Steel Corporation (Japan), and the quality of coke is determined mainly by the quality of the coal charge used in the coking feedstock. Coals are increasingly used to produce high-quality coke with CRI ≤ 30 % and CSR ≥ 70 % [1]. Studies have shown that these coals are characterized by high bursting pressure, which has a destructive effect on the masonry of the oven walls of coke oven batteries. In this regard, it is necessary to monitor the exponential pressure of the coal blends used for the coking process continuously. The extension the working service of coke ovens is the main task, and in this respect, the selection of coal concentrates with normal, i.e., a safe bursting pressure for the preparation of charge is urgently needed to ensure the integrity of the masonry walls of the furnaces. Since reliable methods for determining the magnitude of bursting pressure, at least in Ukraine, do not exist, we have set the goal of solving this problem ourselves.

Taking into account the availability of several technologies for the coke production in the production process – charge loading in the furnace in bulk and using the technology of ramming the charge, the method for determining the pressure of the batch is to be unified, i.e. allow determining in one apparatus the pressure of the expansion of both bulk and tamped charge (coals). In work [2], the authors give an overview of the known methods for determining the bursting pressure in experimental semi-industrial and laboratory furnaces. They make it possible to determine the bursting pressure of both bulk and tamped charges. However, charge loading in semi-industrial furnaces is 200–300 kg, and it results in a long duration of the determination, the unwieldiness of the instrumentation, the high cost of maintaining such an installation, and, consequently, the cost of one determination of the bursting pressure.

2. Experimental

To study the coal pressure and charge extrusion in the Ukrainian State Coal-Chemistry Institute, we have developed a universal laboratory setup, depicted in Fig. 1. It makes it possible to determine the value of the bursting pressure for the bulk and tamped method of loading coal (charge) [3-4]. Its design is protected by the patent of Ukraine [5], the results obtained allowed to develop, agree, approve in accordance with the established procedure and put into operation from 01.01.2018 DSTU 8724:2017 Coal and charge based on it. It is the method for determination of bursting pressure that occurs while coking.

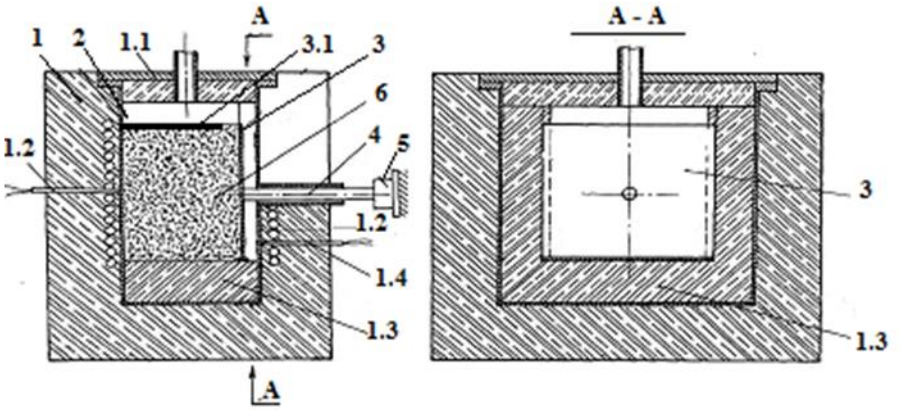

Fig.1. Unified furnace for determining the bursting pressure of tamped and bulk coal loading: 1 - electric furnace; 1.1 – an adiabatic cover with a gas bleeding branch pipe; 1.2 - electric heaters; 1.3 - thermal insulation; 1.4 - thermocouple; 2 - metal retort; 3 – steel plate l; 3.1 - steel perforated plate; 4 - quartz rod; 5 - pressure sensor; 6 - coal loading

The method consists in two-sided heating of the retort with coal loading at a given temperature, the sample parameters are given in Table 1, and the measurement of the bursting pressure by means of a piezoelectric pressure sensor in the range from 1 kPa to 70 kPa. The total time for determining the bursting pressure together with the preheating of the electric furnace to the set temperature is 4 hours.

Table 1. The parameters of the coal sample loaded into the retort

Loading	Loading weight, g	Mass fraction of particles by size <3 mm, %	Humidity of a coal sample (charge), %	Load density, g/cm^3
In bulk	600 ± 2	80 ± 3	10 ± 0,2	0,80 ± 0,01
Stamped	740 ± 2	90 ± 2	11 ± 0,2	1,13 ± 0,01

With two-sided heating of the coal loading, the peak of the bursting pressure (maximum) occurs at the moment of the merging of the plastic layers moving towards the heating walls from the axial plane. Such peaks are especially characteristic of coals or batch materials with high values of bursting pressure. With one-sided heating of the charge, there is no such peak; the pressure increases monotonically to the maximum value, and then begins to decrease.

3. Results and discussion

The conducted researches made it possible to simulate the process of coke formation, in such a manner that in the furnace chamber the coal charge is in different phases of thermal transformations, when the layer of initial coal coexists simultaneously (along the axial plane of the furnace), then in the direction of the heating wall, the plastic layer (the temperature range 330–510 °C) and a layer of semi-coke that passes into coke (Fig. 2).

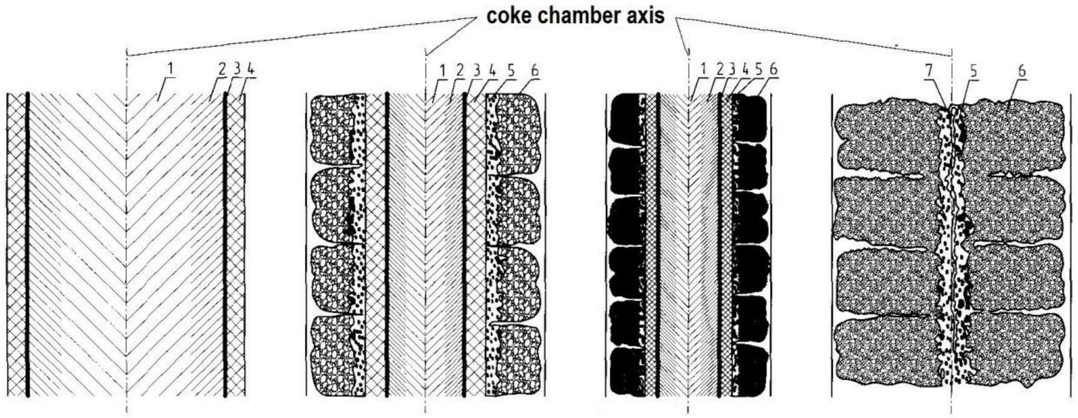

Fig. 2 shows a scheme of matter layers distribution in the load along the width of the coking chamber: 1 - moist coal (20°C); 2 - dry coal (200°C); 3 - coal in the softening state - swelling (330°C); 4 - hardening of the softened mass (510°C); 5 - semi-coke (600°C); 6 - coke (900°C); 7 - shrinkage seam along the axis of the chamber

The pressure of the pyrolysis gases formed in the plastic layer is transferred from one side to the initial coal charge, and on the other to the formed layer of coke, which adjoins the heating wall. The pressure exerted on the charge loaded with the bulk results in insignificant densification of the layer adjacent directly to the "cold" side of the plastic layer. In the case of a tamped charge compacted to high densities, this phenomenon does not occur, and all pressure of the vapor-gas products of the plastic layer is transferred through the coke layer to the heating wall.

The mechanism of development of the bursting pressure is the following: coal loading 2 at the boundary with the plastic layer 3 is initially a layer of slightly expanded grains, and it smoothly passes (toward the heating wall) into a layer of maximally expanded grains. Swelling of coal grains occurs as a result of the destruction of macromolecules of coal matter with the release of gaseous products. Acquisition of fluidity by the coal matter as a result of the destruction of rigid bonds between macromolecules and their fragments and accumulation of gaseous products in the coal grain leads to its swelling. As the temperature rises, the swelling of the grains increases, the porosity between them decreases, the grains crumble into each other. Sealing a layer of softened expanded grains from the "cold" side of the plastic layer creates a barrier that hinders the vapor-gaseous products from leaving the plastic layer. The plastic layer includes a layer of maximally expanded merged grains; this layer is formed as a result of rupture of the surface of the carbon grains and the release of the substance of coal that has passed into the liquid-mobile state. Later this layer passes into the foamed layer as a result of accumulation in it of a large quantity of vapor-gaseous products. As a result of the mass transfer of the coal substance from this layer towards the heating wall, a compacted layer of plastic mass is formed which, with a further increase in temperature, is converted into semi-coke 5, and then to coke 6, which is a solid porous substance. The barrier to the release of continuously generated gases from the plastic layer on the "hot" side is a compacted semi-hardened layer of plastic mass, characterized by low porosity. Semi-coke and coke as a result of further temperature transformations acquire a sufficiently high porosity (40–45 %), notably about 80 % of these pores being communicating, and therefore sufficiently gas permeable.

The strength of semi-coke and coke is high enough for them to transfer pressure from the plastic layer to the heating wall. Thus, on the one hand, a layer of softened swollen fused carbon grain prevents the free release of vapor-gaseous products from the plastic layer, and on the other hand, it is a layer of the primary semi-coke. The stronger and less gas-permeable these layers, the higher the gas pressure developed in the plastic layer, which is transferred through the semi-coke and coke to the heating wall. It should be noted that the rate of gases formation in the plastic layer is not a determining factor in the development of a large bursting pressure. This is confirmed, for example, by the fact that coals with the release of volatile substances 40 % develop a bursting pressure of the order of 2.5–4.0 kPa, while coals with V^{daf} =25 % – up to 20 kPa. The main condition is the gas tightness of the barriers on the "cold" and "hot" side of the plastic layer. Thus, the development of a particular magnitude of the bursting pressure is associated with the structure of the plastic layer, the properties of the plastic mass and the character of the coke formation.

After the test has been completed, the heating of the furnace is turned off, and the retort is left for another three hours for the thermal aging of the coke. After that, the retort already cooled to ~ 300°C, is removed from the furnace and left in the air for final cooling. Thus, "dry" quenching of coke is provided. If necessary, the resulting coke is tested for mechanical strength in a special drum and examined by other methods.

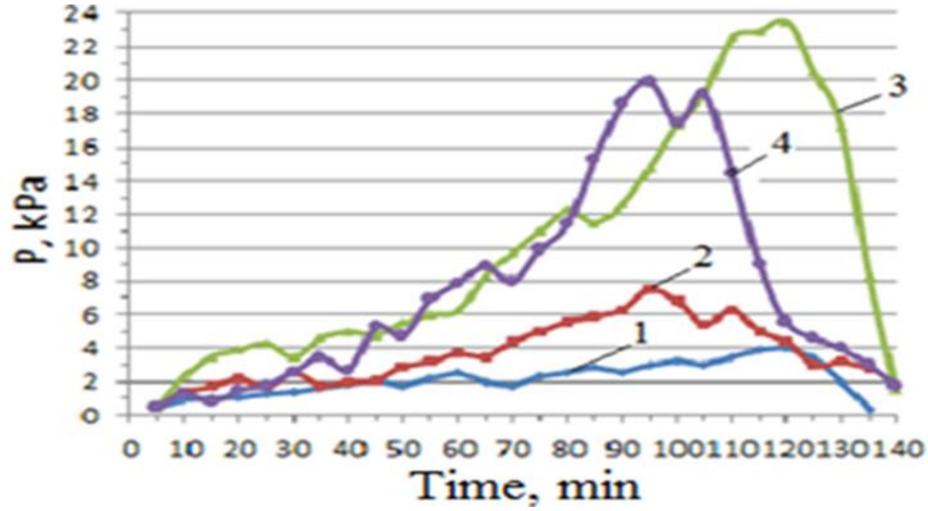

Fig. 3. The development dynamics of the pressure of coal extrusion in the coking process: 1 – Mine "Raspadskaya" (Russia); 2 – "Carter Rogue" (USA); 3 – LOV VOLATILE CC (USA); 4 – "Pocahontas" (USA)

Table 2. Characteristics of bituminous coals (B)

Sample (grade)	Supplier	Technical analysis, %			Petrographic composition, %						Plastic layer characteristics, mm	
		A^d	S^d_t	V^{daf}	R_0	V_t	S_v	I	L	Σ FK	x	y
B-1	Mine «Raspadskaya» (Russia)	8,6	0,47	37,3	0,83	88	1	8	3	9	40	16
B-2	«Karter Roag» (USA)	8.5	0.69	31.8	1.02	92	0	7	1	7	29	17
B-3	«LOV VOLATILE CC» (USA)	9,3	0,82	19,0	1,40	74	0	26	0	26	27	14
B-4	«Pocahontas» (USA)	8,9	0,94	18,0	1,54	69	2	29	0	31	10	10

In industrial coking chambers, the maximum burst pressure as a result of the combined effect of processes occurring in different loading layers is reached at the end of the second hour after charging the batch at the oven sole. In calculating the strength of heating sections, the maximum allowable bursting pressure is assumed to be 7 kPa [6]. The obtained results on a unified laboratory installation indicate that the coals develop a much higher pressure – up to 15–20 kPa, and therefore coking of the charge with their participation leads to a bursting pressure exceeding the permissible level. For example, Fig. 3 shows the dynamics of the bursting pressure in the process of coking coal during bulk loading, i.e., at an apparent density of 800 kg/m^3. The characteristics of coal concentrates are given in Table. 2.

4. Conclusion

The obtained practical results of the pressure of the coal extrusion allowed to conclude that the weakly baking coal of grade B1 is characterized by small values of the expansion pressure (0.9÷4.0 kPa), coal of grade B2 develop the average burst pressure (4.0÷8.0 kPa), and grades B3, B4 is the most open (6.0÷24.0 kPa). Moreover, due to the fact that many differently directed factors affect the expansion pressure, this quantity is not additive. Therefore, the only reliable way to estimate the bursting pressure is to determine it experimentally, to select, on the basis of the results obtained, the charge compositions that provide safe pressure values, and to use the results of the studies in the strength calculations of the heating sections.

Symbols

A^d	*ash content of coal in the dry state, %;*
V^{daf}	*volatile matter in the dry ash-free state, %;*
S_t^d	*sulphur of coal in the dry state, %;*
R_0	*mean vitrinite reflection coefficient, %;*
V_t	*vitrinite, %;*
S_v	*semivitrinite, %;*
I	*inertinite, %;*
L	*liptinite, %;*
ΣFC	*sum of fusinized components, %;*
x	*plastometric shrinkage, mm;*
y	*thickness of the plastic layer, mm;*
DSTU	*Ukrainian State Standard*

References

[1] Nomura S, Matsuzaki S, Naito M. Enhancement of Blast Furnace Reaction Efficiency throughte Use of Highly Reactive Coke. AISTech Proceedings. 2006; 1: 31-37.
[2] Sytnik AV, Kuznichenko VM. Determining the Expansion Pressure of Coking Batch: An Analytical Review. Coke Chem. 2011; 54(9): 323-330.
[3] Kuznichenko VM, Shulga IV, Sytnik AV. Laboratory method for determining the bursting pressure of coke coal loading with various bulk density. Journal of Coal Chemistry. 2007; 3-4: 29-33.
[4] Zelenskii OI, Sytnik AV. Development of methods modify the properties of the coal charge and create optimal conditions for coke ovens produce high quality coke. Journal of Coal Chemistry. 2016; 1: 26-30.
[5] Sytnik AV, Kuznichenko VM, Shulga IV. Ukraine Patent 57708, 2011.
[6] Rudyka VI. Coke chemical handbook, Publishing House INGEK: Kharkov, 2014; Vol. 2, Chapter 1; p. 728.

To whom correspondence should be addressed: Dr. Alexey Sytnik, Ukrainian State Coal-Chemistry Institute, 61023, Kharkov, 7 Vesnina Str., Ukraine tel.: +3-8050-933-68-76; e-mail: aleksejsytnik48@gmail.com

Petroleum and Coal

Article **Open Access**

CALCULATION OF RESERVOIR PARAMETERS IN GURPI AND PABDEH FRACTURED FORMATIONS, MARUN OIL FIELD, SW IRAN

*Shakiba Soltani Galoogerdi, Hossein Tabatabaei**

Department of Petroleum Engineering, Gachsaran Branch, Islamic Azad University, Gachsaran, Iran

Received June 4, 2018; Accepted September 5, 2018

Abstract

Marun oil field is one of the biggest Iranian oil fields (65 kilometers length and 7 kilometers wide), is located about 40 kilometers southwest of Ahwaz. Pabdeh and Gurpi Formations are mainly shale and marl and played the role of a fractured reservoir in this field. Estimation of fluid saturations for evaluation of hydrocarbon reservoirs is very important. The presence of clay in fractured and shaly reservoir formations makes the estimation of fluid saturation more complicated. According to the surveys carried out in Maroon oilfield, wells 38 and 48 at depths 3795-3854 and 3834-3799 m in Pabdeh formation are reservoir zones, and hydrocarbon saturations are 45 and 41%, respectively. This study showed that the Gurpi Formation had no significant hydrocarbon fluid, and the fractures contained brine only.

***Keywords**: fractured reservoirs; petrophysics; Pabdeh and Gurpi Formations; fluid saturation.*

1. Introduction

Studies and researches in the Zagros area are due to the existence of significant oil reservoirs in this area. In the meantime, the study of formations that have been considered as oil reservoirs is very significant, but other formations have been less considered. Formations of Gurpi and Pabdeh in the southwest of Iran are source rock and are among the formations that have not been studied more. In some oilfields, these two formations, have some reservoir properties and is some parts of the Dezful embayment are classified as fractured oil reservoirs. Generally, the porosity found in these reservoirs is mainly due to fractures.

According to the Gurpi Formations lithology (the major lithology of marl and calcareous shale) and Pabdeh (shaly lithology) and the manner and amount of stress in these regions, it is likely that these formations are considered as fractured reservoirs and considering the presence of Servak and Asmari reservoirs in this area, these two formations may contain hydrocarbons. By studying a well in the southwestern margin of Marun oil field, which drilled in asmari formations (as the main reservoir of Zagros) and Pabdeh and Gurpei, it was found that the fracture pattern in the Asmari and Pabdeh formations is almost the same, but the fractures condition in the Gurpi Formations which has more depth is different.

The highest fractures density is located in the lower part of Asmari formation and the whole of Pabdeh formation [6]. The highest number of fractures detected in image logs is the open type. The fractures of Asmari and Pabdeh formations have the same pattern, while the pattern of fractures in Gurpi Formation is completely different. Fractures of the Gurpi Formation have been created before or at the same time as the folds. The large dispersion of the directional fracture of the Gurpi Formation may be due to their non-systematic nature. The mechanism of fractures formation is flexural and bending-slip [6].

In this study, using log data and Geolag software (version 6.7.1), lithology, shale volume, porosity, water saturation related to Pabdeh and Gurpi Formations in Marun field have been calculated. The calculation of water saturation in shale-free formations is easily accomplished, but the presence of clay in fractured reservoir formations makes the estimation of fluid saturation more complicated.

2. Marun oil field

Marun oil field is located South of the Dezful Embayment and in the middle part of this structural zone along the Aghajari and Ramin anticlines (Figure 1). This large oil field was discovered by a two-dimensional seismic method in 1963. After drilling the first well, the presence of hydrocarbon in the Asmari reservoir was confirme [4]. The geographic location of this field is limited to Ramin field from the North, Kopal field from the East, Shadegan and Ahwaz fields from the west and northwest and Ramshir field from the south [5].The structure of Maroun Field is an anticline with low width and longitudinal with northwest- southeast direction in western and central parts and northeast-southwest direction in eastern end, with very distinct torsion in the middle of structure that has given to quadrilateral mode to the north direction. The vertical distance between the reservoir crest and the deepest surface of water oil contact in Asmari Formation is about 2000 meters. The construction gradient of the Marun Field varies in cross sections. It has a symmetrical state at the eastern nose, asymmetric state at the western nose to the center (the bending point with a maximum slope of 70°) and semi-symmetric state at north-east [5].

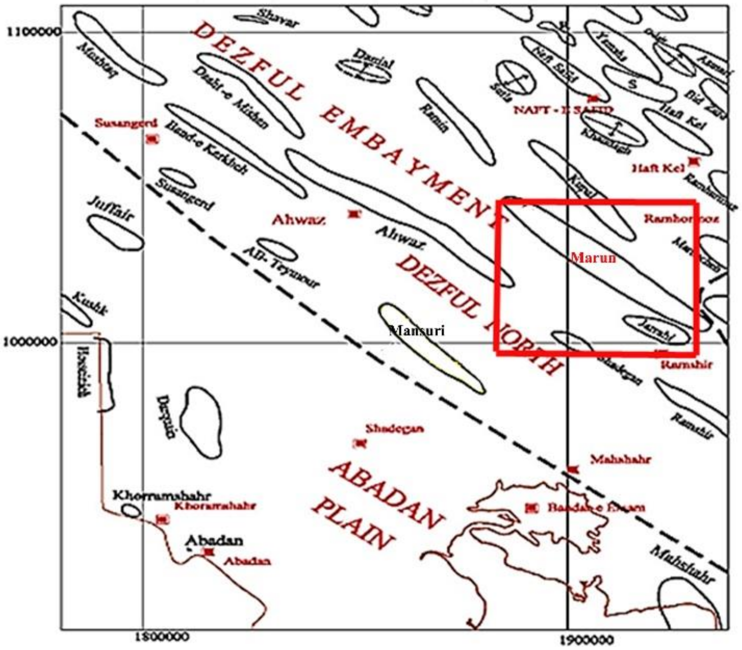

Figure 1. Location of oil fields in the southwest of Iran and Maroon oil field

3. Results and discussion

In this research, 2 wells in Maroon oilfield have been considered for petrophysical studies. These wells have almost complete information and logging data. The most important results of this project are as follows:

3.1. Shale volume

Shale volume is one of the most important parameters in all petrophysical studies and reservoir quality. The volume of shale means the number of clay minerals in the reservoir. In fact, accurate determination of reservoir quality and other petrophysical parameters such as porosity, type, and distribution of reservoir fluid, lithology and permeability are mainly based on the evaluation and determination of this parameter. In addition, the effect of the presence of shale as one of the important components of the rock on porosity and permeability in the analysis of well logging charts, their electrical properties also have a great influence on the calculated strength.

Due to small porosities of clay minerals, the petrophysical properties of the reservoir and so computation of parameters such as saturation and porosity is also affected [8]. Therefore, the calculation of shale volume for accurate estimation of the porosity, based on Well log data are needed. If the effect of shale volume in the formation is not considered, it will have a significant impact on the results of calculated porosity, permeability and water saturation of reservoir [1].

The most common method for calculating shale volume is the linear method using the corrected gamma ray chart (CIR) [8]. The volume of shale from the CGR chart was measured by the following equation.

$$V_{sh} = \frac{CGR - CGR_{min}}{CGR_{max} - CGR_{min}} \quad (1)$$

In this correlation, CGR_{max} is for the shale section, CGR_{min}: for the clean section and CGR: reading the gamma log at the desired depth.

Regarding the fact that the amount of shale volume decreases the reservoir properties, its amount in Pabdeh and Gurpi Formations can be considered as a negative factor in the change of reservoir properties. The average values of shale content in the Gurpi and Pabde Formations of Maroon Oilfield are presented in the tables below (Tables 1 and 2). The high amount of shale volume indicates the non-reservoir properties of these two formations.

Table 1. Average Shale Volume Percentage in Pabdeh Formation of Maroon Oilfield

Name of Formation	Sub-section (Zone)	Average Shale volume
Pabdeh	Zone 1	20.75
	Zone 2	16.5
	Zone 3	29

Table 2. Average Shale Volume Percentage in Gurpi Formation of Maroon Oilfield

Name of Formation	Average Shale volume
Gurpi	25.7

3.2. Calculation of porosity

Porosity is one of the essential parameters for reservoir rock because it represents the amount of hydrocarbon storage. This index is controlled by two factors of sedimentation and diagenetic processes [7]. The porosity of the rock and some hydrocarbon occupied portions are determined by logs. The porosity and percentage of hydrocarbons can be measured directly or indirectly through electrical, nuclear and acoustic logs. Depends on shaly or free from shale formation, the presence of hydrocarbons, as well as the use of different graphs and tools, methods for calculating porosity are different. To calculate porosity, neutron, density, sound, and resistivity logs are mainly used. It is possible to use a combination of some logs to perform this calculation [7].

In this study, cross-plots of neutron-density and neutron-sound have been used for calculation of porosity, which is discussed below.

3.2.1. Calculation of porosity using cross-plots of neutrons-density

The neutron and density logs can measure the total porosity, which can be the total initial porosity (intergranular or inter-crystalline) and secondary porosity (cavity, fracture, fracture) [1].

In this method, the porosity is determined by drawing the neutron values versus the density log. The presence of gas reduces the density of the rock.

The presence of shale in the formation causes the transfer of points to the south-east of the cross-plot. Therefore, before using cross-plots, both neutron and density diagrams must be corrected for shale [3]. Using the RHOB diagram versus NPHI, the total porosity for the Gurpi and Pabdeh Formations was 12% and 17%, respectively (Figures 2 and 3). Using the software and the density and neutron data, the porosity graph was drawn, and its lithology was determined. The major recognized lithologies for the Gurpi Formation are Shale, Marl, and Clay limestones and for Pabdeh Formation are Shale and Calcareous shale. These are shown in figures 2-4 for wells No. 38, 54, and 48.

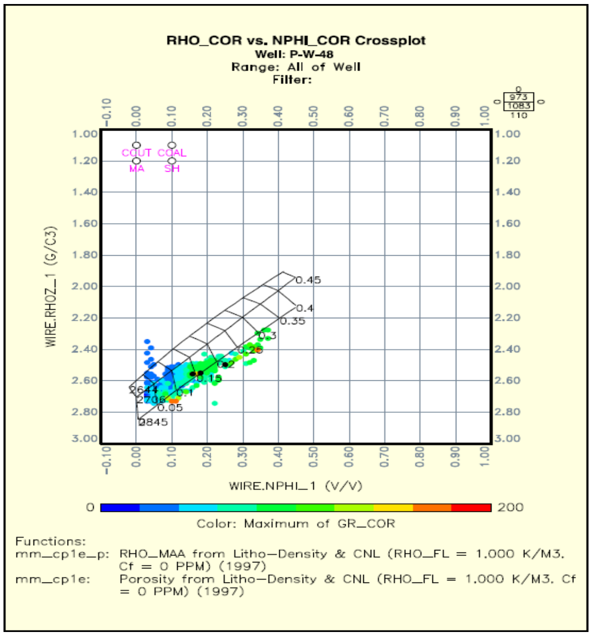

Figure 2. Porosity and lithology determination using software and NPHI, RHOB data for well 48 of Pabdeh formation in Marun oil field

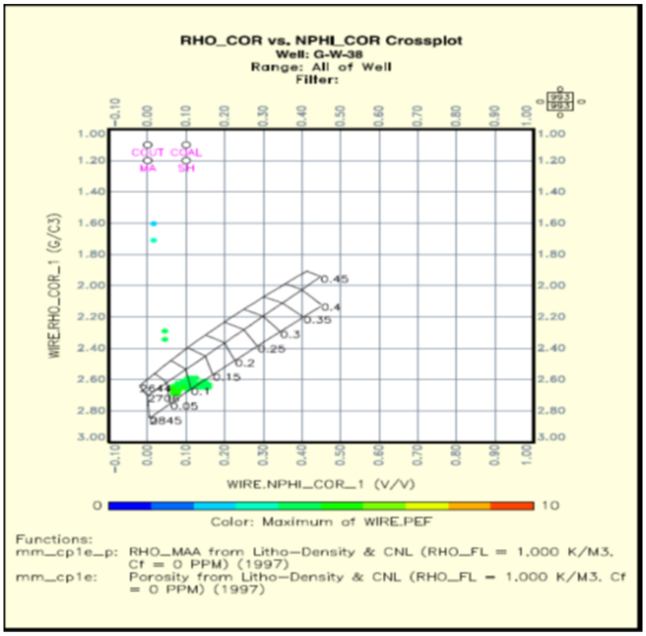

Figure 3. Porosity and lithology determination using software and NPHI, RHOB data for well 38 of Gurpi Formation in Marun oil field

3.2.2. Calculation of porosity using the neutron-sound cross-plot

The sound velocity in sedimentary formations is a function of several parameters, which are essentially dependent on the rock matrix components (sandstone, limestone, dolomite, etc.) and porosity distribution.

In this method, porosity is determined based on drawing of the values of neutron log versus sound log. If the neutron porosity of the shale and matrix Δt are different, the calculated porosity will not be correct. Therefore, shale correction is necessary first [2].

Neutron, density and neutron-sound cross-plots are used for determination of porosity and lithology [3]. Neutron-sound diagrams for wells No. 38 and 48 are shown in Figures 4 and 5.

Secondary porosity can be calculated using this cross-plot and the values for wells No. 38 and 48 of Gurpi and Pabdeh Formations are given in Table 3. This porosity is a result of tectonic activities and has the properties of a fractured formation. The electric illustrator diagram (Figure 6) shows the presence of these gaps in the Pabdeh Formation.

Table 3. Secondary porosity calculated by software and NPHI and DT data for wells 38 and 48 of Gurpi and Pabdeh formations in Maroon Oilfield

Name of Formation	Well no.	Secondary porosity
Gurpi	38	9.7
	48	11
Pabdeh	38	12.13
	48	12.66

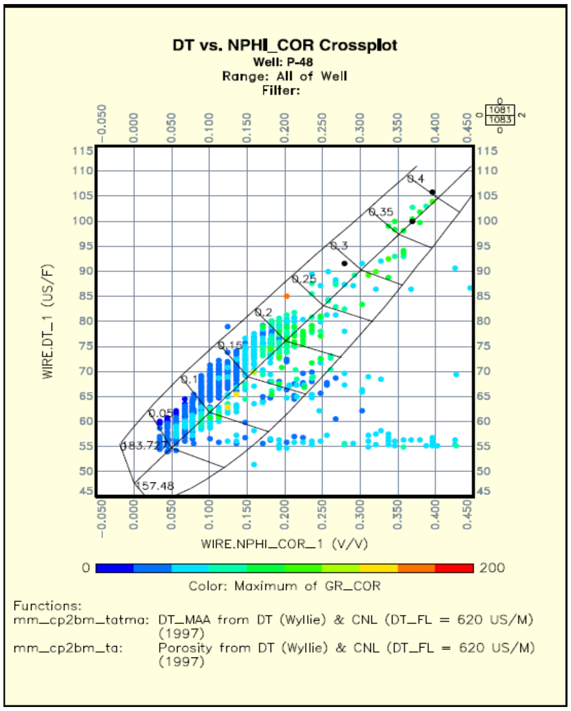

Figure 4. Porosity determination using software and NPHI and DT data for well 48 of Pabdeh formation in Marun oil field

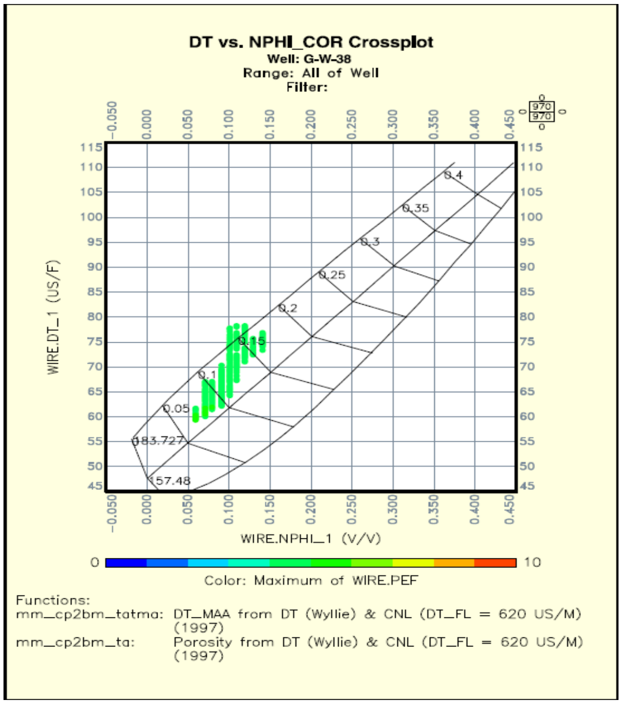

Figure 5. Porosity determination using software and NPHI and DT data for well 38 of Gurpi Formation in Marun oil field

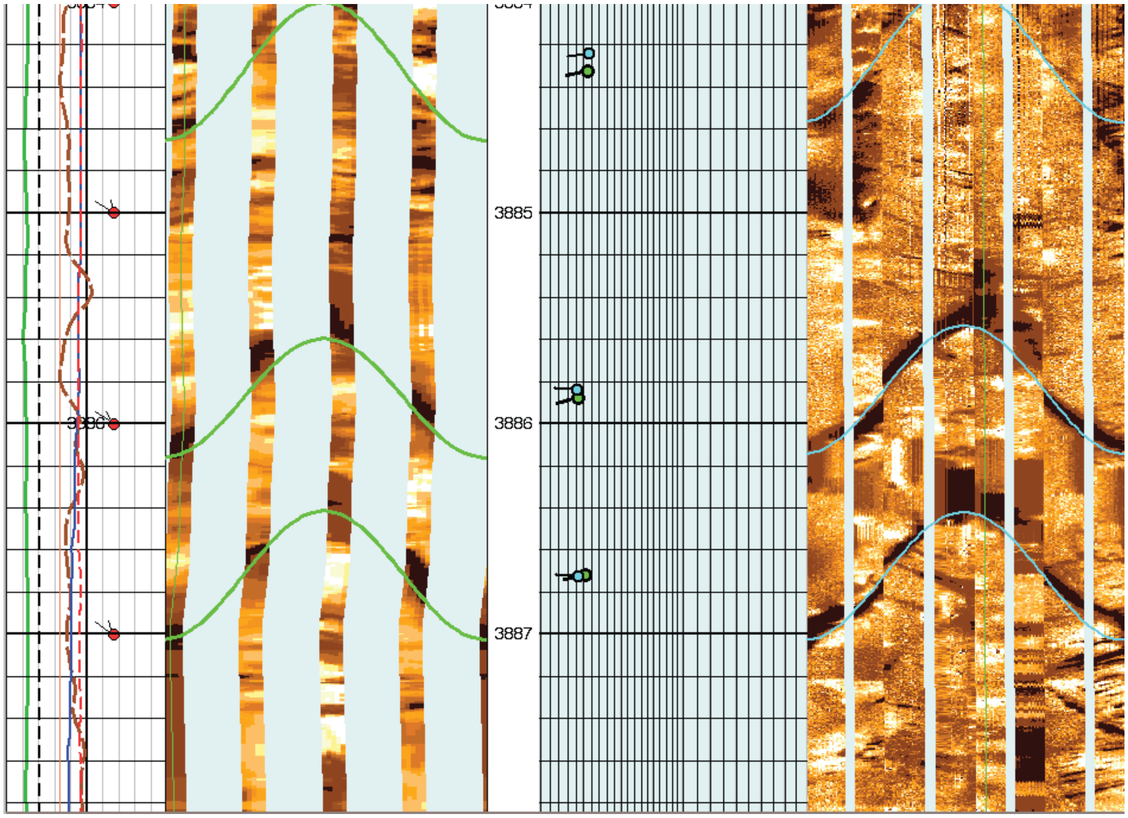

Figure 6. Fractures view in Pabdeh formation of Marun oil field for well No. 38

3.3. Calculation of water saturation

Saturation is one of the parameters that must be calculated using resistive log data. All methods of calculating water saturation are based on the Archie method, which was presented during the years 1941-1942. The Archie Formula does not apply to the depths that shale minerals or shale layers exist along with the matrix. If the Archi formula is used in these layers, the calculated saturation percentage will be unrealistic, because some parts of the water saturation are the water associated with shale minerals, along with the Matrix. Therefore, other methods are used to calculate the saturation of water. The best option is to use the Indonesia formula, which will provide more accurate calculations regarding the presence of shaly minerals in the matrix [1].

In this method, if we determine the electric conductivity of the hydrocarbon from equation (2) and real electrical conductivity from equation (3), the amount of water saturation is calculated from equation (4), which is done by the Geolag software.

$$\sqrt{C_o} = \sqrt{C_w/F} + V_{sh}^{1-V_{sh/2}} \times \sqrt{C_{sh}} \tag{2}$$

$$\sqrt{C_t} = \sqrt{C_w/F \times S_w^{n/2}} + V_{sh}^{1-V_{sh/2}} \times \sqrt{C_{sh} \times S_w^{n/2}} \tag{3}$$

In this equation, C_o: hydrocarbon electrical conductivity, C_w: electrical conductivity of water, F: coefficient of formation, V_{sh}: shale volume, C_{sh}: electrical conduction of shale, C_t: real electric conductivity of the formation and S_w is water saturation.

$$S_w = \left[\frac{R_w}{R_t} \times \frac{R_{sh}}{\left({V_{sh}}^{1-V_{sh/2}}\sqrt{R_W} + Q_e^{m/2}\sqrt{R_{sh}}\right)^2}\right]^{1/n} \tag{4}$$

According to the researches carried out in the studied wells in Pabdeh Formation of Marun oil field, in well no. 48 from depths of 3791 m to 3834 m, which is a reservoir zone, the saturation of water and hydrocarbon were 59% and 41% and in the well No. 38 from depths of 3795 m to 3854 m, which is the reservoir zone, the saturations of water and hydrocarbon are 55% and 45%, respectively (Figure 7 and 8). The Gurpi Formation has no hydrocarbon volumes but contains saline water.

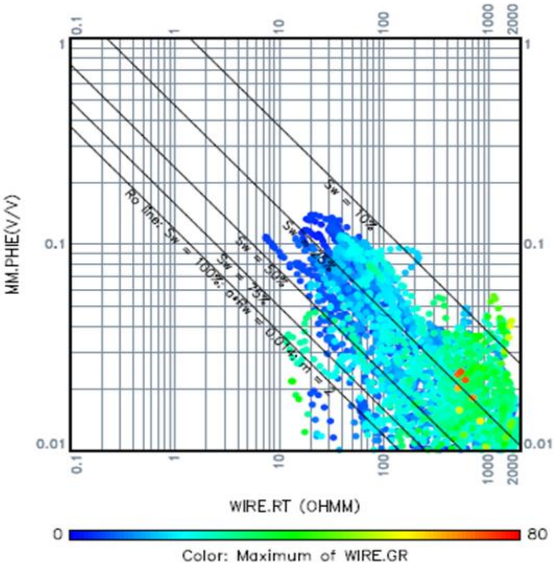

Figure 7. Determination of water saturation using software and data of PHIE, RT, and GR for well 38 of Pabdeh formation at Marun oil field

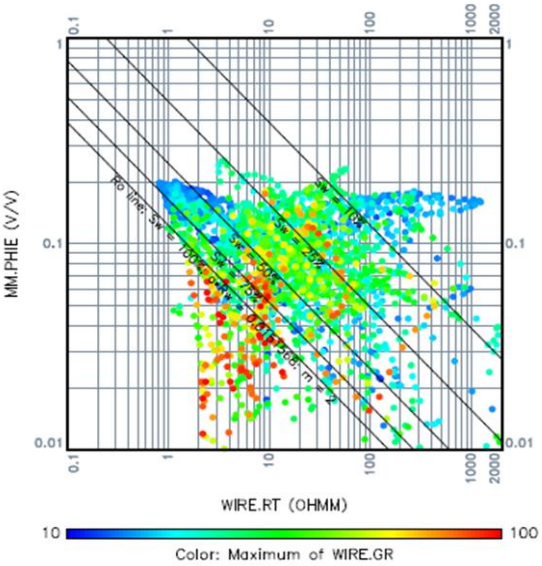

Figure 8. Determination of water saturation using software and data of PHIE, RT, and GR for well 48 of Pabdeh formation at Marun oil field

3.4. Identification of permeable zones

In this research, for the detection of non-reservoir permeable zones, caliper, bit size charts, and CGR diagram have been used. After calibrating these three diagrams, the best location for permeable zones is determined. Typically, when the size of the caliper diagram is less than the size of bit size diagram, the zone is said permeable and porous. In these surveys, the thickness of permeable zones in the studied wells was calculated so that well no. 48 has the maximum permeability. Using these three graphs, reservoir and non-reservoir sections were separated from each other. The whole Pabdeh formation in the studied wells was divided into three zones: Zone No. 1, from a depth of 3752 to 3795 m, is a non-reservoir zone and from depth of 3795 Up to 3828 m is a hydrocarbon reservoir zone (zone 2) and zone number 3 from depth 3828 to 3896 m is a porous zone without hydrocarbon but contains brine, and also the Gurpi Formation in the studied wells has a zone with relatively low porosity and free of hydrocarbons. Due to the lack of information, permeability has not been provided for these zones. Based on the existence of shale amount of 26.3%, well No. 38 in Gurpi Formation, according to the classification, is considered as a clay formation. The sound log in this formation has not many changes and is relatively flat and low, which indicates an increase in speed, that is, porosity is low. On the other hand, the resistance logs (shallow and deep) matched to each other and show a low resistance, indicating a hard and dense zone with saline water.

The calculated water saturation in this well was 99%, and the dominant lithology detected by the PEF graph was marl and clay lime. Well, No. 48 of the Gurpi Formation has a shale volume of 25.1% and water saturation of 99% and has the same lithology and fluid type as well No. 38. Due to lack of information, well No. 54, cannot be accurately evaluated. In well No. 48, Pabdeh formation from the depth of 3733 m to 3753 m contains high shale and low reservoir quality. The sound log in this region is sometimes irregular and distorted in some distances, which can be an indication of fractures. Also, the resistance curves are not consistent and relatively spaced apart, which is also an indication of the fractured zone. Regarding 100% water saturation, this region has no hydrocarbons and only contains saline water. The PEF chart also shows no. 10, which can be due to the penetration of barite into the fractures in this area. From the depths of 3753 m to 3791 m, the CGR decreases from top to bottom, and the average shale volume is 18, which represents a clay zone. The sound log is relatively smooth, and the resistance logs match, which unlike the upper part, is a uniform zone without fracture. This area also has a high water saturation and contains only salt water. By use of PEF chart, the dominant lithology was identified lime and shale lime. At a depth of 3791 m to 3834 m, the shale volume is 20%, which indicates poor reservoir quality. The sound log increases at the beginning of the zone and then decreases rapidly, indicating fluid in the porous space. In this zone, the resistance logs are matched and reduce from up to down, and with a précised look in the neutron and density logs that are almost parallel and the water saturation diagram in this zone, it can be said, this fluid is a most likely hydrocarbon. The PEF chart also shows the lithology of rock in this area is lime and shaly lime. From depths of 3834 m to 3900 m, regarding a high water saturation of 97%, as well as a reducing resistivity log, formation contains saline water, and the dominant lithology by the PEF chart was determined the shaly lime. In well No. 38, like well No. 48 in Pabdeh Formation the same zoning was observed, with the difference that at the top of this well, the fractured zone similar to well No. 48 was not observed and also differs from the depth mentioned for well No. 48. due to the lack of information in well No. 54, it is impossible to accurately evaluate the wells.

4. Conclusions

In this research, we used Geolag software version 6.7.1 for investigation of the reservoir properties, especially fluid saturation, lithology and calculation the amount of shale and porosity in Pabdeh and Gurpi Formations in Marun oilfield and so, the following results have been obtained. The amount of shale volume is 20.75%, 16.5%, 29%, and 25.7%. in the first, second and third zones of Pabdeh and the Gurpi Formation, repectively. In this method, the maximum and minimum CGR values are obtained in Pabdeh and Gurpi Formations in areas where there is no wellbore Collapse. Considering the fact that the existence of shale decreases the reservoir properties, its amount in Pabdeh and Gurpi Formations can be considered as a negative factor in the change of reservoir properties. The average porosity for the Gurpi and Pabdeh formations were 12% and 17%, respectively. The calculated values of the secondary porosity for wells No. 38 and 48 are equal to 9.7 and 11 % in the Gurpi Formation and 12.13 and 12.66 % in Pabdeh formation, respectively. This secondary porosity gives the reservoir properties to these formations, and so they can be classified as fractured reservoirs. According to the studies carried out in Marun oil field, in wells 48 and 38 of Pabdeh formation, the hydrocarbon saturation is 41% and 45%, respectively. Gurpi Formation contains only salt water.

References

[1] Deli LWX. Present exploiting situation and application prospects of software "geolog system". Computing Techniques for Geophysical and Geochemical Exploration, 1993; 1, 015.

[2] Bassiouni Z. Theory, measurement, and interpretation of well logs (Vol. 4). Henry L. Doherty Memorial Fund of AIME, Society of Petroleum Engineers 1994.

[3] Schramm LL. Fundamentals and applications in the petroleum Industry. Advances in Chemistry, 1992; 231, 3-24.

[4] Chegny SJ, Tahmasbi K, Arsanjani N. The possibility of replacing OBMs with emulsified glycol mud systems in drilling low-pressure zones of Iranian oilfields. in: IADC/SPE Asia Pacific Drilling Technology Conference and Exhibition, Society of Petroleum Engineers, 2008.

[5] Johnson SY, Schenk CJ, Anders DL, Tuttle ML. Sedimentology and Petroleum Occurrence, Schoolhouse Member, Maroon Formation (Lower Permian), Northwestern Colorado (1). AAPG Bulletin, 1990; 74: 135-150.

[6] Darvishzadeh A. Geology of Iran, Neda Publication. Tehran, (1991) 1-901.

[7] Hearst RB, Morris WA, Schieck DG. Reflection seismic profiling for massive sulphides in the high Arctic. in: SEG Technical Program Expanded Abstracts 1994, Society of Exploration Geophysicists, 1994, pp. 531-533.

[8] Tiab D, Donaldson EC. Petrophysics: theory and practice of measuring reservoir rock and fluid transport properties, Gulf professional publishing, 2015.

To whom correspondence should be addressed: Dr. Hossein Tabatabaei, Department of Petroleum Engineering, Gachsaran Branch, Islamic Azad University, Gachsaran, Iran

Petroleum and Coal

Article **Open Access**

RESERVOIR SIMULATION AND DECLINE CURVE ANALYSIS: A CASE STUDY OF "DER" FIELD, NIGER DELTA BASIN

Eseoghene R. Diaso, Efeoghene Enaworu, Ifeanyi Seteyeobot, Charles Y. Onuh*

Petroleum Engineering Department, Covenant University, Ota. Nigeria

Received May 5, 2018; Accepted September 5, 2018

Abstract

This research project gives an insightful glimpse into reservoir simulation using the Material Balance (MBAL) software. The software was used to confirm Stock Tank Oil Initially In-Place (STOIIP) for volumetric analysis. MBAL was used to apply the material balance method, decline curve analysis method, check the aquifer size of the field, and carry out production forecasts. Data from the field was inputted into MBAL and results acquired. These results were used in simulating the reservoir in order to carry out production forecasts. The research showed the impact of MBAL in predicting reservoir performance and carrying out reservoir simulation. The predictions were made based on field data. STOIIP was estimated using non-linear regression with a plot of average reservoir pressure against cumulative oil produced. The history matching tool and the production prediction tool were used to estimate the expected STOIIP, judging from the previous performance of the reservoir and the well. With the use of the analytical tool, the predominant reservoir driving mechanism was determined. This project will focus on the use of reservoir simulation in reservoir engineering and how MBAL can be used as a tool in reservoir simulation.

Keywords*: Simulation; Decline curve analysis; Volumetric analysis; History matching; Reservoir performance; Material balance.*

1. Introduction

During the development of oil and gas reservoirs, drainage challenges occur. Reservoir engineers then come up with scientific principles to these challenges. Reservoir engineering is the subsurface science of the oil and gas industry. It tries to explain what goes on underground in the reservoir. The main job of the reservoir engineer is to estimate the amount of hydrocarbon in place. Factors that assist in this estimation are subsurface geology, applied mathematics, basic chemistry, and physics. These factors affect the behaviour of the liquid and gas phases of the hydrocarbon [1].

Reservoir simulation is important because it gives us better control of the reservoir. A model is a copy of something original with respect to known parameters. In the oil and gas industry, profit is made by extracting hydrocarbon from a reservoir which is underground. Describing the reservoir is usually difficult because of the in accuracy in measuring parameters. This occurs because the reservoir is underground and the parameters are measured indirectly.

In the estimation of reserves, there might be errors in data collation which may lead to inaccurate estimation, i.e. overestimation or underestimation. Therefore, there is a need to accurately estimate the reserves to determine the viability of the field. This work is focused on the application of the MBAL software in reservoir engineering. The software will be used to carry out reserve estimation using both the decline curve analysis and the material balance methods. Several objectives have been considered which included the confirmation of STOIIP for volumetric analysis, confirmation of aquifer size and driving mechanism of the reservoir, and production forecasting under different scenarios.

2. Review of literature

Reservoir simulation involves the use of a mathematical model in analyzing and predicting fluid behaviour. The model is expected to replicate the geological and petrophysical characteristics of the reservoir. Reservoir Simulation has two main objectives - to optimize development plans in new fields and to delegate on operational and investment decisions [2]. The objective of their experiment was to carry out simulation tasks usually performed with simulators. MBAL is primarily used for reservoir simulation. It is an analytical tool that is used in reserve estimation, determination of drive mechanism, aquifer size assessment and in carrying out production forecast. MBAL can also be used for existing reservoirs, as it provides varied matching facilities. It can run production profiles with or without history matching. MBAL is a good tool in reservoir characterization and simulation under different scenarios. Despite its simplicity, it is still able to predict pressure depletion like other simulators [3]. Another limitation that was discovered was that the single tank does not take account of the heterogeneities of the field that was under study, whereas the multi-tank model had values which were in the range of the results gotten from the single grid model.

In early years, it was discovered that the material balance equation could not be used to determine the size of the field during the early years of production, this was accurate at the time because of the limited data that was available and the change in pressure that was required in the Schilthuis material balance equation [4]. The solution was to find the pressure value that would give the uniformity required in the equation. A relationship between reservoir pressure and oil saturation was developed. The relationship proved that oil saturation doesn't depend on the change in pressure of the reservoir, but the reservoir pressure. It is understandable that due to the limited data available in the early stages of production, material balance can be inaccurate. The subsidiary equation can be used in cases where there is no significant pressure drop [4]. Methods have been developed to examine material balance in oil and gas reservoirs. A new method of carrying out a material balance method in reservoir simulation is the dynamic material balance method. By combining the solution of the material balance equation with pressure test analysis theory, the dynamic material balance method can be used in estimating the initial oil in place, *N,* initial gas in place, *G, the* ratio of the oil to gas *m,* permeability, *K* and skin factor, *s*. It makes use of cumulative production history with PVT data with little or no pressure data. The dynamic material balance method will be able to improve the problem-solving capabilities of the material balance method especially in marginal fields and fields with limited pressure data [5]. Material balance approach was compared with reservoir simulation. It is believed that since the development of reservoir simulation, that material balance is not seen as a modern approach anymore in reservoir analysis. Material balance calculations depend on the uniformity of total pore volume, pressure, temperature, fluid composition and accurate values of volumetric estimation [6].

3. Methodology

The transient rate and the pseudo-steady state decline curves were combined and used in a single graph. Also, the material balance equation was employed. The dataset used for this work are; PVT, reservoir pressure. Production history and geologic data.

The concept of decline curve analysis involves fitting a line through the production history and assuming that the field will continue to behave in that manner. If there is in an inconsistency with the historical trend, then the result will not be reliable. The main assumption of this method is that what controls the trend of a curve in the past will continue to control the trend in the future.

For the material balance method, its calculations are very useful; they provide a method of estimating the oil, water, and gas that can be compared to volumetric estimates. The form of the material balance equation can be adjusted to fit oil or a gas reservoir.

3.1. Material balance for oil reservoirs

The general material balance equation

$$N(B_t - B_{ti}) + N_m B_{ti}\left(\frac{B_{gc}-B_{gi}}{B_{gi}}\right) + N\frac{B_{ti}S_{wio}}{1-S_{wio}}\left(\frac{B_{tw}-B_{twi}}{B_{twi}}\right) + N\frac{mB_{ti}S_{wig}}{1-S_{wig}}\left(\frac{B_{tw}-B_{twi}}{B_{twi}}\right) + N\left(\frac{1}{1-S_{wio}} + \frac{m}{1-S_{wig}}\right)B_{ti}c_f\Delta P = N_pB_o + \left[G_{ps}B_g + G_{pc}B_{gc} - G_iB_g'\right] - N_pR_{so}B_g - \left(W_e + W_i - W_p\right)B_w \quad (1)$$

For simplification purposes, some terms are defined:

$$E_o = B_t - B_{ti}\ ,\ E_{go} = mB_{ti}\left(\frac{B_{gc}-B_{gi}}{B_{gi}}\right)\ ,\ E_w = \frac{B_{ti}S_{wio}}{1-S_{wio}}\left(\frac{B_{tw}-B_{twi}}{B_{twi}}\right)\ ,\ E_{gw} = \frac{mB_{ti}S_{wig}}{1-S_{wig}}\left(\frac{B_{tw}-B_{twi}}{B_{twi}}\right)\ ,\ E_r = \left(\frac{1}{1-S_{wio}} + \frac{m}{1-S_{wig}}\right)B_{ti}c_f\Delta P \quad (2)$$

Substitute equation (2) in (1) changes the general material balance equation to:

$$N\left[E_o + E_{go} + E_w + E_{gw} + E_r\right] = N_pB_o + \left[G_{ps}B_g + G_{pc}B_{gc} - G_iB_g'\right] - N_pR_{so}B_g - (W_e + W_i - W_p)B_w \quad (3)$$

The terms on the right side of (2) represent fluid injection and production, the terms on the left represent volume change.

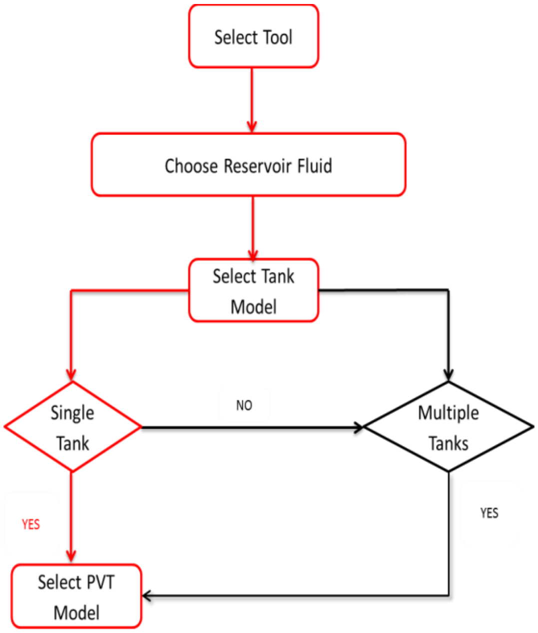

Figure 1a. Material balance workflow in estimating the initial oil in place.

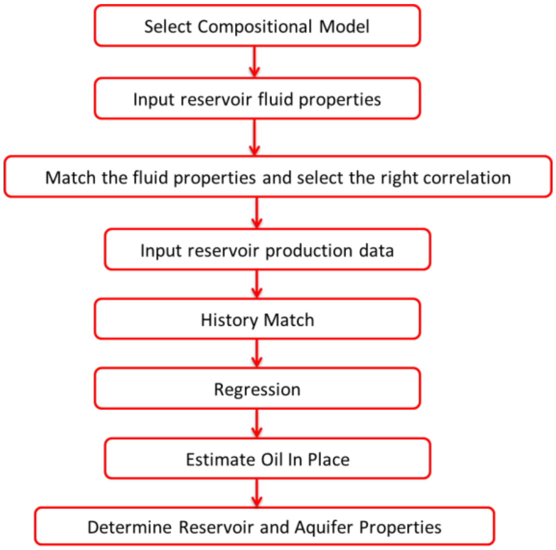

Figure 1c. Material balance workflow in estimating the initial oil in place

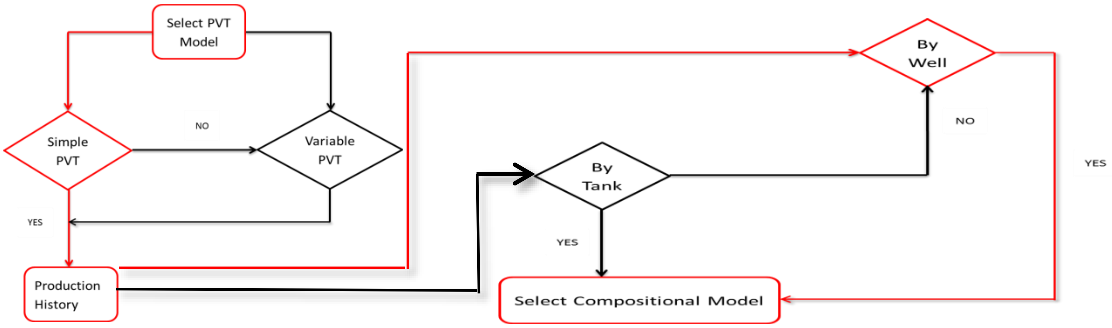

Figure 1b. Material balance workflow in estimating the initial oil in place

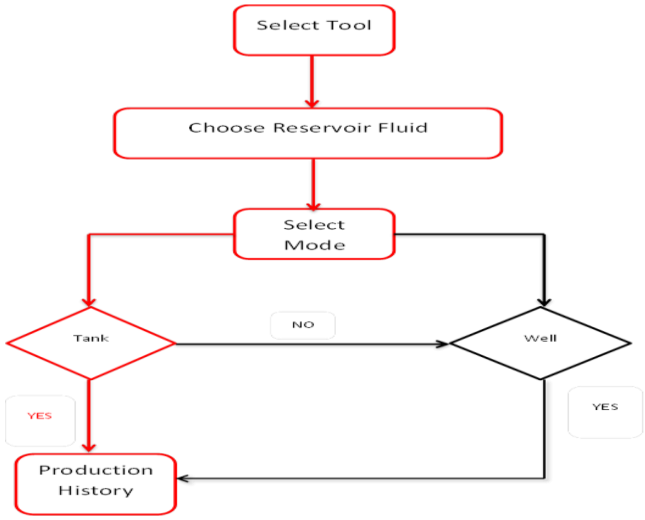

Figure 2a. Workflow for decline curve analysis.

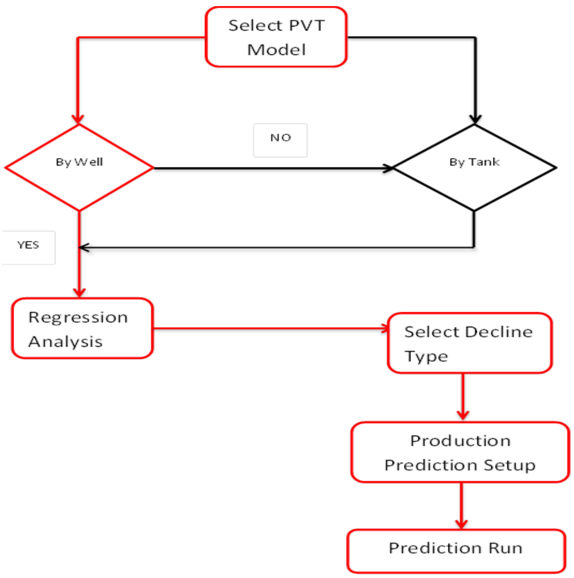

Figure 2b. Workflow of decline curve analysis

4. Results and discussion

The geology, PVT, and relative permeability data are presented in Table 1, Table 2 and Table 3 respectively.

Table 1. Geologic data

Thickness	100ft
Porosity	0.19
Saturation	0.15

Table 2. PVT data

Formation GOR	1589scf/stb
Oil gravity	39API
Gas gravity	0.875spg
Water Salinity	100000spm
Viscosity	0.28cp
Oil Formation Volume Factor	1.89rb/stb

Table 3. Relative permeability data

	Residual Saturation	End Point	Exponent
Krw	0.15	0.0284564	0.01002
Kro	0.15	0.8	2.25388
Krg	0.05	0.000328963	0.01002

From the energy plot (Figure 3), there is a pictorial representation of the different drive mechanisms and their contribution to the energy of the reservoir.

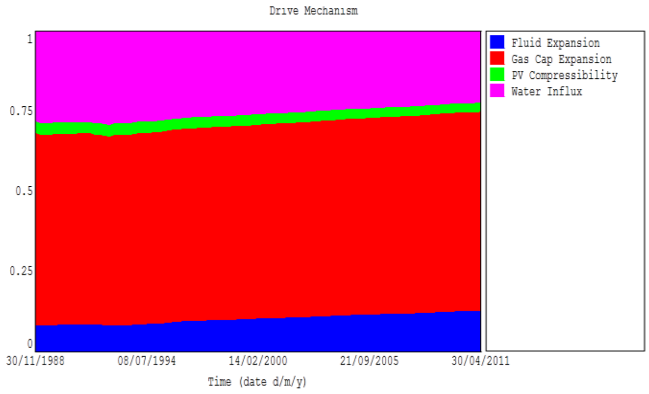

Figure 3. Energy plot

4.1. Graphical method

In this field, an additional energy mechanism went through a turn up seen in Campbell plot (Figure 4.). The aquifer then compensated the turn up in order to get a good history match.

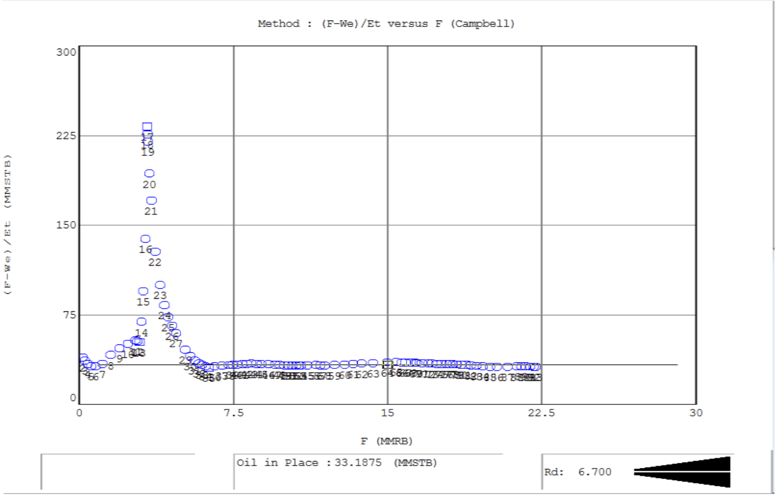

Oil in Place : 33.1875 (MMSTB)

Figure 4. Campbell plot

Analytical plot

This gives an analytical history matched model before and after regression analysis. To improve the quality of the history match regression analysis was carried out.

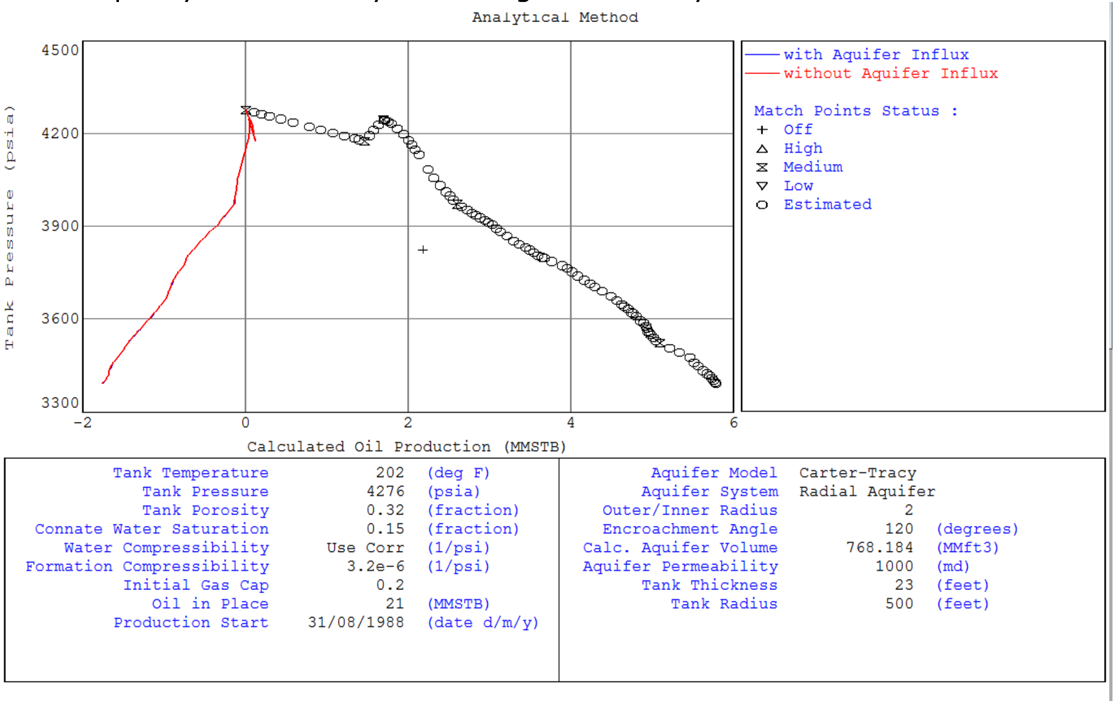

Tank Temperature	202	(deg F)
Tank Pressure	4276	(psia)
Tank Porosity	0.32	(fraction)
Connate Water Saturation	0.15	(fraction)
Water Compressibility	Use Corr	(1/psi)
Formation Compressibility	3.2e-6	(1/psi)
Initial Gas Cap	0.2	
Oil in Place	21	(MMSTB)
Production Start	31/08/1988	(date d/m/y)

Aquifer Model	Carter-Tracy	
Aquifer System	Radial Aquifer	
Outer/Inner Radius	2	
Encroachment Angle	120	(degrees)
Calc. Aquifer Volume	768.184	(MMft3)
Aquifer Permeability	1000	(md)
Tank Thickness	23	(feet)
Tank Radius	500	(feet)

Figure 5. Analytical plot before regression

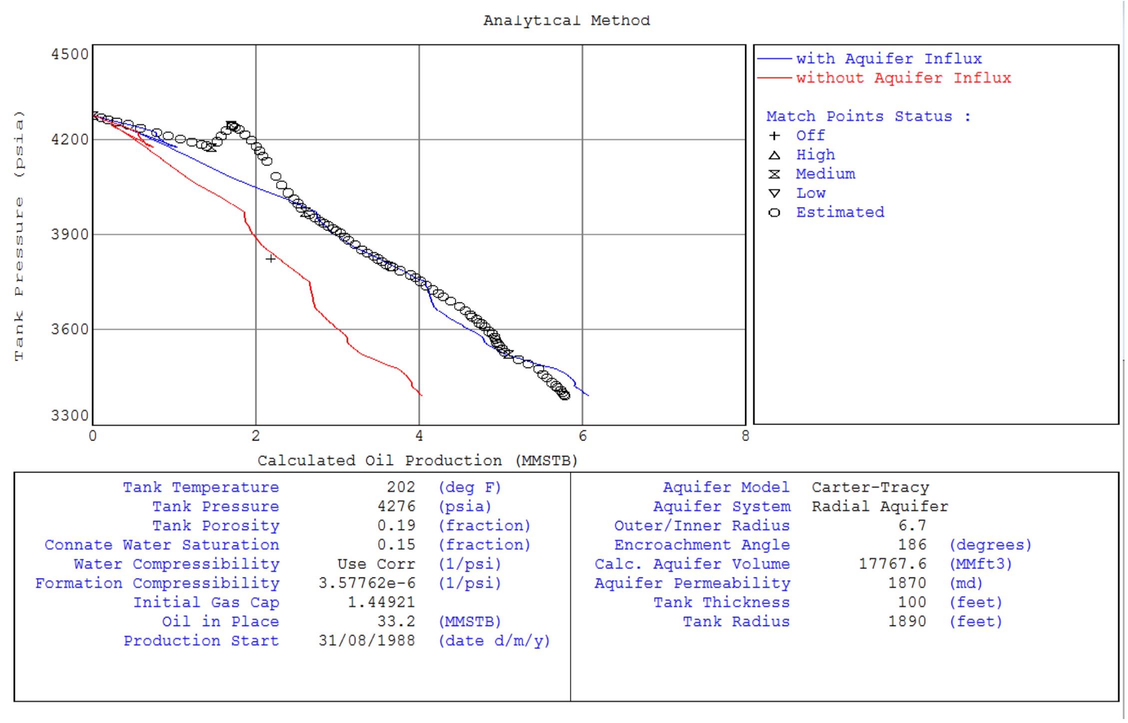

Tank Temperature	202	(deg F)	Aquifer Model	Carter-Tracy	
Tank Pressure	4276	(psia)	Aquifer System	Radial Aquifer	
Tank Porosity	0.19	(fraction)	Outer/Inner Radius	6.7	
Connate Water Saturation	0.15	(fraction)	Encroachment Angle	186	(degrees)
Water Compressibility	Use Corr	(1/psi)	Calc. Aquifer Volume	17767.6	(MMft3)
Formation Compressibility	3.57762e-6	(1/psi)	Aquifer Permeability	1870	(md)
Initial Gas Cap	1.44921		Tank Thickness	100	(feet)
Oil in Place	33.2	(MMSTB)	Tank Radius	1890	(feet)
Production Start	31/08/1988	(date d/m/y)			

Figure 6. Analytical plot after regression

History match

This gives a graphical representation of the historical production data; it tries to create a model that closely mirrors the reservoir behaviour in order to carry out predictive analysis on the reservoir.

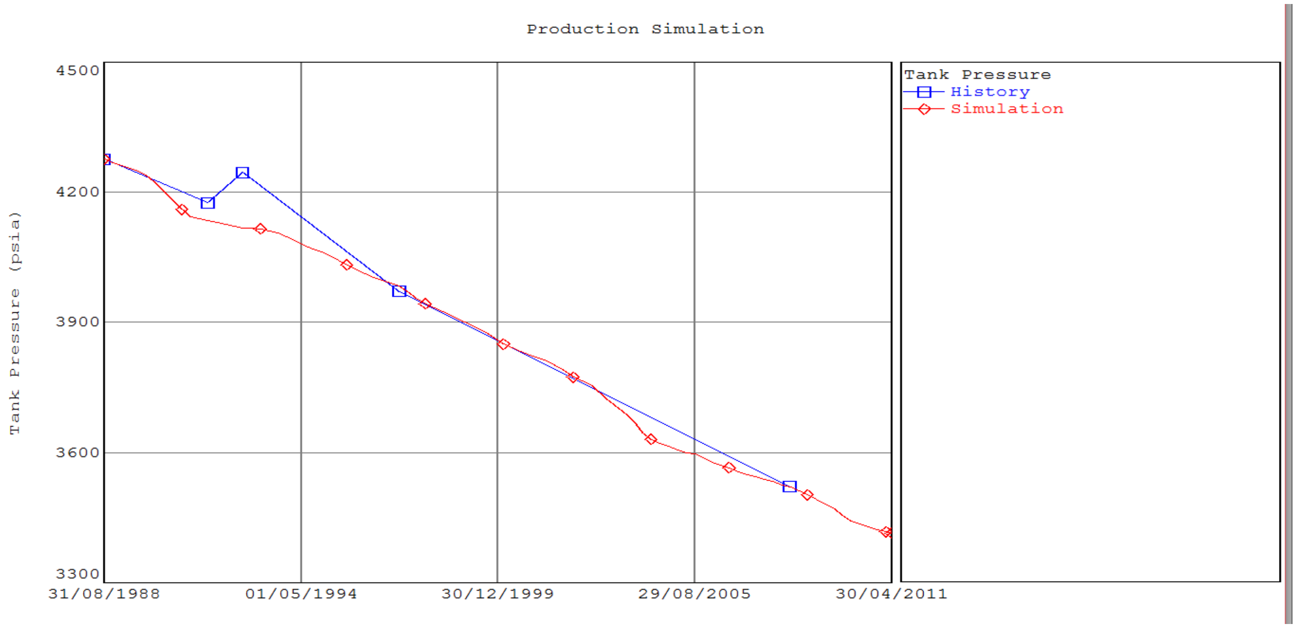

Figure 7. Graph of production simulation

Predictive Analysis

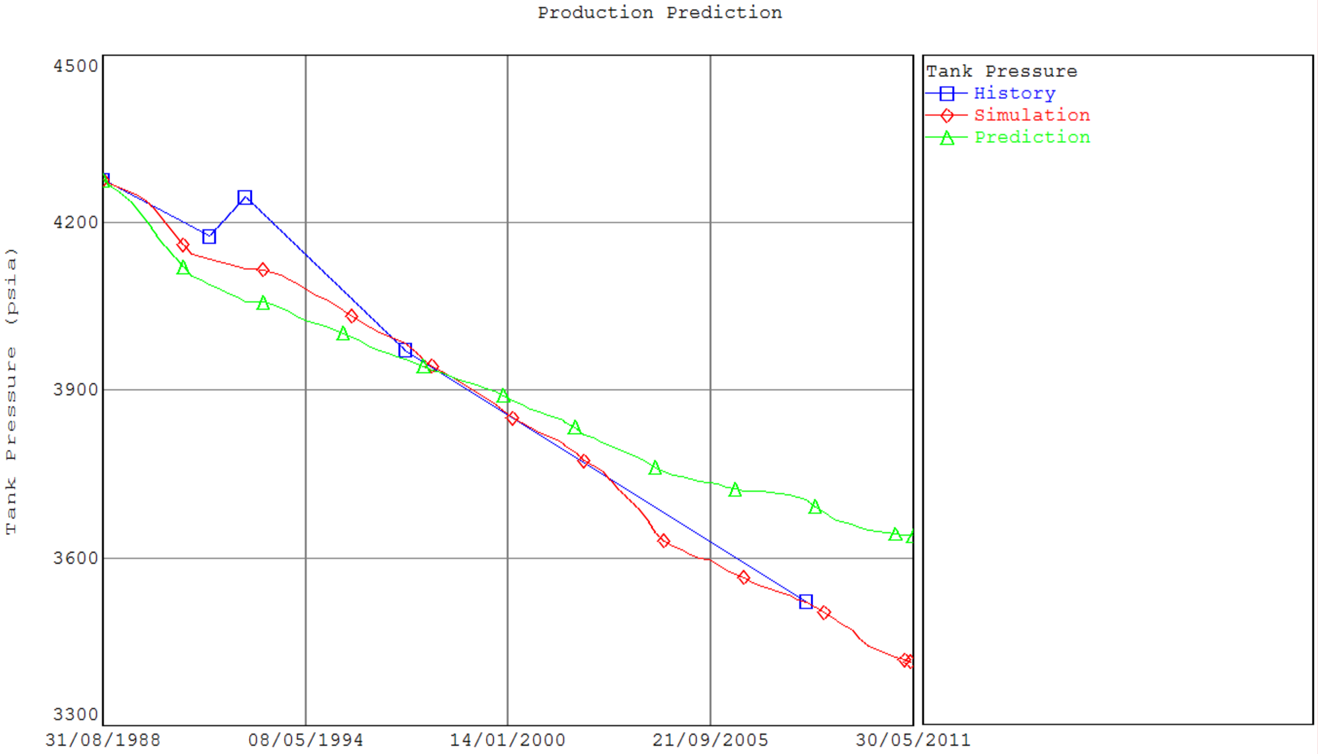

Figure 8. Production prediction of tank pressure from start to end of production

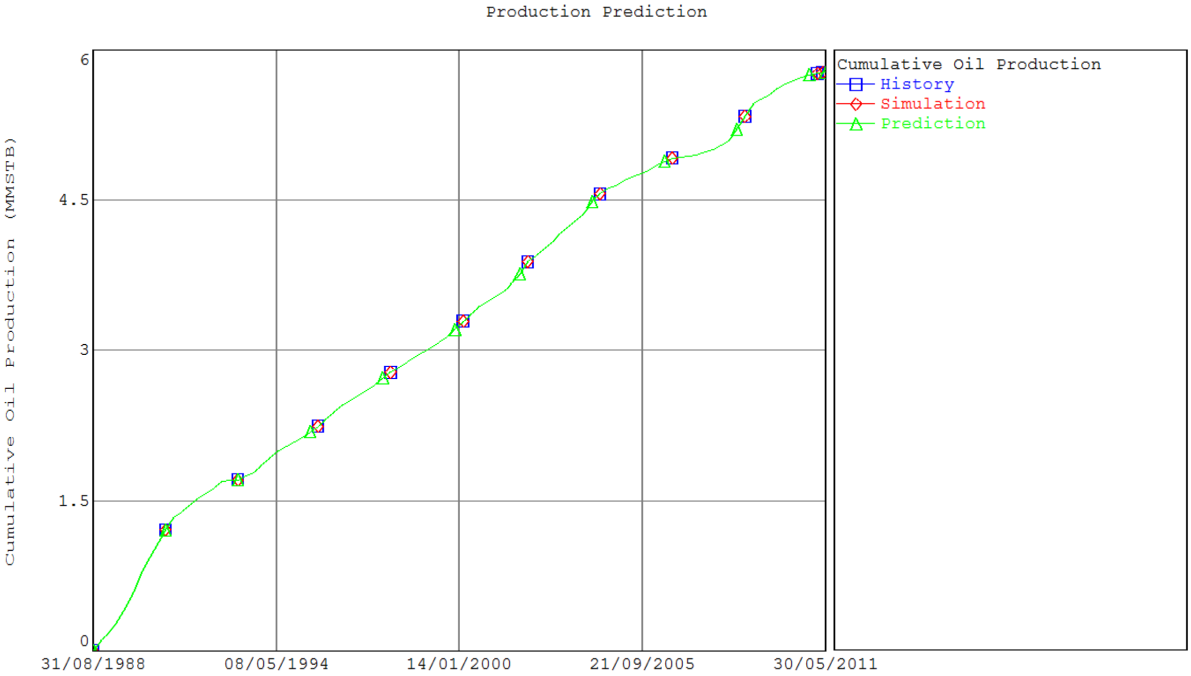

Figure 9. Production prediction of oil production from start to end of production

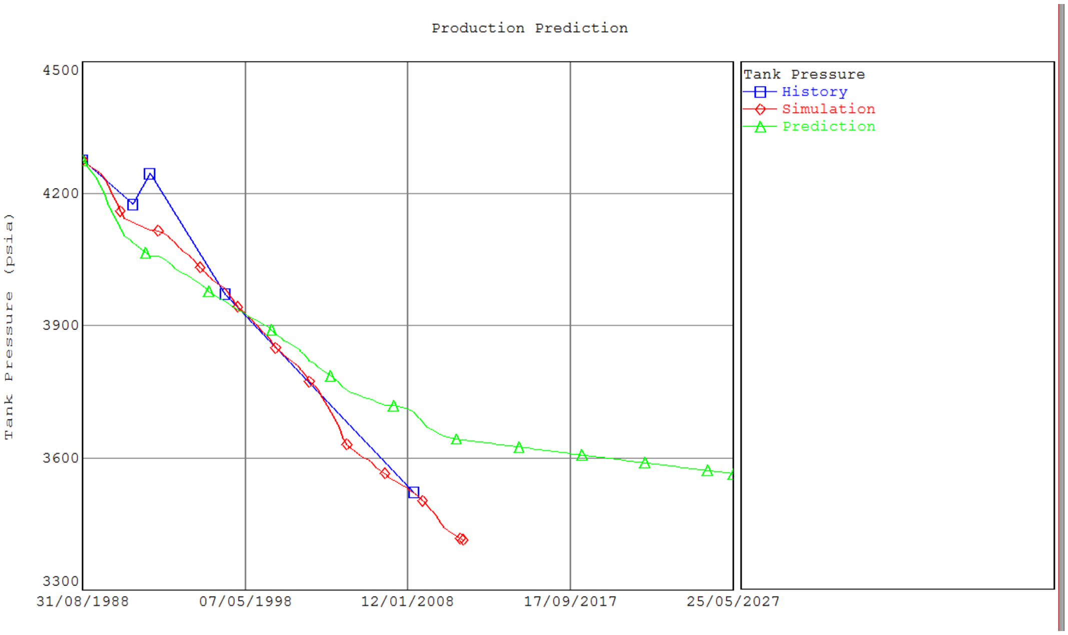

Figure 10. Production prediction of reservoir pressure from start to the year 2027

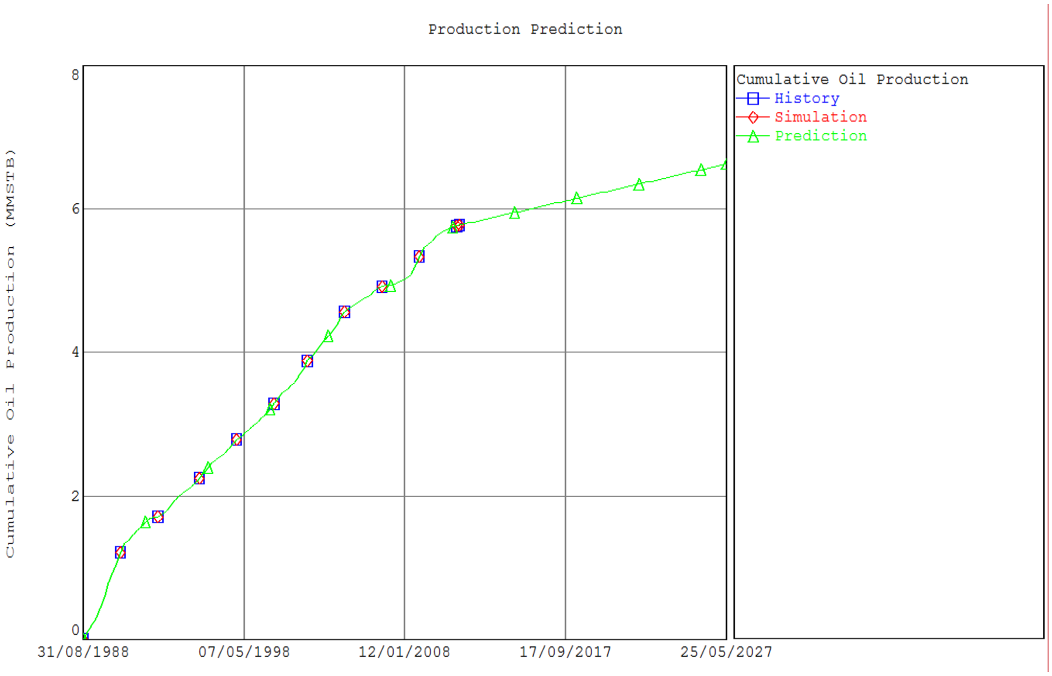

Figure 11. Production prediction of oil production from start to the year 2027

Table 4. Summary of results

Parameter	MBAL estimate	Parameter	MBAL estimate
STOIIP (MMSTB)	33.2	Encroachment Angle (degree)	186
Initial Gas cap (MMSCF)	1.44921	Porosity	0.19
Inner outer radius ratio	6.7	Aquifer Volume (mmft^3)	17767.6
Reservoir Radius (ft)	1890		

Production forecast

In carrying out the predictive analysis, both methods - the material balance method and the decline curve analysis were utilized. Using the material balance and applying MBAL, an estimated date of May 2027 was selected, and this resulted in an estimate of 6.5MMSTB. But by carrying out decline curve analysis and comparing the results, an estimate of 4.5MMSTB was obtained.

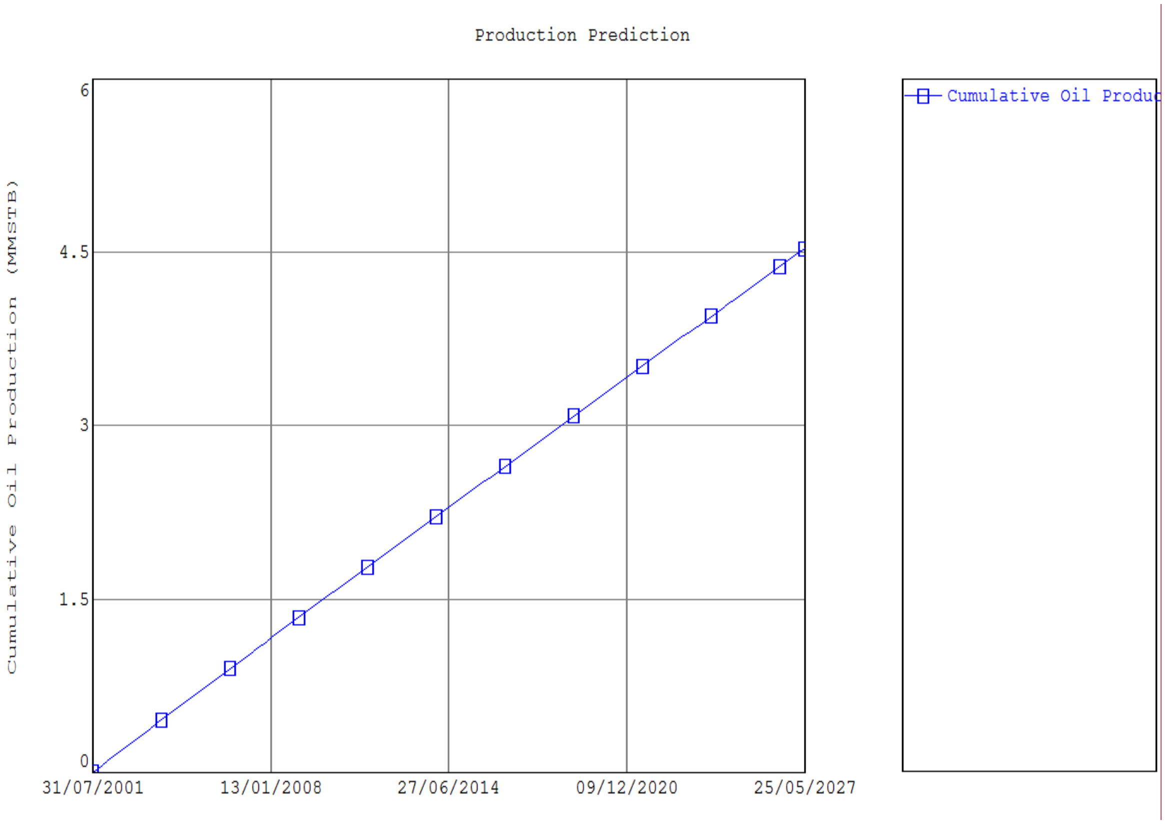

Figure 12. Production prediction based on decline curve analysis

The material balance method gave a STOIIP estimate of 33.5MMSTB. This estimate was made based on dynamic modelling and by utilizing petrophysical and geological properties obtained from a static model. When carrying out the production forecast, the decline curve analysis gave an estimate of 4.5MMSTB by the year 2027; while the material balance software gave an estimate of 6.25MMSTB. The aquifer was radial and with a size of 7767.6mmft^3. It had a permeability of 1870md with a large encroachment angle of 187.63^0. Due to the radial nature of the aquifer, it could be said that the aquifer is a large one and this is why the reservoir pressure was still high in the year 2027. From the energy plot, water influx was one of the major contributors to the drive mechanism, and this must have been due to the size of the aquifer.

5. Conclusion

Reserve estimation is a subsection of reservoir simulation. Material balance and decline curve analysis is based on most of the mathematical equations used for modern petroleum engineering. The material balance method and decline curve analysis method are two different methods of carrying out reserve estimation. The material balance value was higher than the decline curve analysis value. This could have been caused by inaccuracy in the production data. There was also a presence of a strong aquifer; this might have influenced the production history data. The main contributor to the energy of the reservoir was the gas cap expansion and the water influx, as seen from the energy plot in MBAL.

6. Recommendation

From this work, the following recommendations are made:

- Since there is such a large variance between the two methods, (material balance method and decline curve analysis used in the field), further analysis should be carried out on the reservoir. MBAL may not be exactly accurate so a larger simulator could be used.
- Discrepancies in the data can be minimized by the acquisition of more data.
- Monte Carlo analysis is advised to act as another validator; it will enhance the credibility or viability of the estimate.

NOMENCLATURE

MBAL = Material balance software developed by Petroleum Experts (PETEX)
STOIIP =Stock Tank Oil in Place
MMSTB = Million Stock tank Barrel
MMSCF= Million Standard cubic feet
$N(E_w+E_{gw})$ = *Change in volume of connate water*
NE_r = *Change in formation pore volume*
N_pB_o = *Cumulative oil production*
$N_pR_{so}B_g$ = *Cumulative gas produced with oil*
$G_{ps}B_g$ = *Cumulative solution gas produced as evolved gas*
$G_{pc}B_g$ = *Cumulative gas cap gas production*
G_iB_g' = *Cumulative gas injection*
W_eB_w = *Cumulative water influx*
W_iB_w = *Cumulative water injection*
W_pB_w = *Cumulative water production*
N = Original oil in place, STB

References

[1] Dake LP. The practice of reservoir engineering (revised edition). Amsterdam - London- New york- Oxford- Paris- Shannon-Tokyo: Elsevier 2001.
[2] Mallison TB, Knut-Andreas L. Mathematical Models For Oil Simulation. San Ramon: Chevron Energy Technological Company 2013.
[3] Gulnar Y. Late Life Field Material Balance Analysis – Statfjord Fm. Stavanger: University of Stavanger Press 2012.
[4] Hurst W. The Material Balance Equation. Houston: Society Of Petroleum Engineers 1973. ID:SPE-4920-MS.
[5] Ojo KP, Osinsaya SO. Material Balance Revisited. 30th Annual SPE Technical International Conference (p. 2). Abuja: Society of Petroleum Engineers 2006.
[6] Farouq AS, Nielsen RF. The Material Balance Approach vs. Reservoir Simulation As An Aid To Understanding Reservoir Drive Mechanics. Houston, Texas 1970: Society of Petroleum Engineers.

To whom correspondence should be addressed: Eseoghene R. Diaso, Department of Petroleum Engineering, Covenant University, Ota, Nigeria. eseoghenediaso97@gmail.com

Petroleum and Coal

Article **Open Access**

STRATIGRAPHIC CHARACTERIZATION OF A FLUVIAL RESERVOIR USING SEISMIC ATTRIBUTES AND SPECTRAL DECOMPOSITION: AN EXAMPLE FROM THE NORTHERN MALAY BASIN

Ismailalwali A. M. Babikir, Ahmed M. A. Salim, and Deva P. Ghosh*

Centre of Excellence in Subsurface Seismic Imaging & Hydrocarbon Prediction (CSI), Department of Geosciences, Institute of Hydrocarbon Recovery, Universiti Teknologi PETRONAS (UTP), 32610 Bandar Seri Iskandar, Malaysia

Received May 16, 2018; Accepted August 27, 2018

Abstract

The addition of new reserves from mature basins such as Malay basin requires a stratigraphic approach that encompasses locating subtle stratigraphic traps and improving the reservoir characterization of the producing fields to deliver more production. Seismic attributes controlled by well information and aided by many interpretation and visualization tools can provide a lot of geological and stratigraphic information from a 3D seismic volume. In this study, a number of seismic attributes that has a demonstrated ability to delineate stratigraphic elements and lithological variations have been applied to investigate the stratigraphic architecture and sand distribution of an Upper Miocene reservoir in an undeveloped field, Northern Malay Basin. The interpretation of the attributes (i.e. spectral decomposition, coherence, RMS amplitude, and sweetness) along with the fluvial geomorphology analysis indicated that the reservoir interval is a meandering fluvial system. Fluvial depositional elements that include channels, point bar, scroll bar, and crevasse play have been interpreted. The Sweetness attribute highlighted high amplitude anomalies related to the sand-prone depositional features. These anomalies interpreted as hydrocarbon sweet spots.

Keywords: *seismic attributes; spectral decomposition; reservoir characterization; fluvial reservoirs.*

1. Introduction

The Northern Malay Basin is a prolific gas region. Most of the fields are non-associate gas fields. The coal and coaly shale gas-prone is the main source rock in the area. The main producing strata are of Middle Miocene to Lower Pliocene age, namely E, D, and B stratigraphic groups. These sequences are characterized by thinly-bedded sand reservoirs along with a remarkable occurrence of coal in group E [1].

In the past, the interpretation of the subsurface was largely controlled by the existing geological models. This was due mainly to the limited resolution and quality of the data. The continuous development of the 3D seismic data quality in the Malay Basin made it possible to obtain robust interpretation for the subsurface. The seismically-driven geological interpretation considerably impacted the hydrocarbon exploration and production in the area. It is possible now, by using many interpretation methods and visualization techniques to understand the reservoir compartmentalization and external geometry, predict the sedimentary facies and pore-fill, and image the depositional evolution of a reservoir.

The area under investigation is an undeveloped gas field, located in the Northern Malay Basin. It is a faulted anticline, has gas discoveries in several reservoir intervals along with minor oil in group E. reservoir heterogeneity due to the stratigraphic complexity is the main challenge in this field, in addition, the presence of coal layers in group E, that interferes seismic signal and affects lithology and hydrocarbon prediction.

This study examined the depositional architecture and facies distribution of B100 reservoir of an undeveloped field, Northern Malay Basin. It is an Upper Miocene reservoir interpreted to be deposited in a fluvial environment.

A number of seismic attributes that has a demonstrated ability to delineate stratigraphic elements and lithological variations have been applied. The analysed attributes (i.e. spectral decomposition, coherence, RMS amplitude, and sweetness) showed that the reservoir is a complex meander fluvial system and the gas charge is mainly associated with the sand-prone fluvial facies such as point bar, channel-fill, and crevasse splay.

2. Geological setting

The Malay, offshore Malaysia, is a northwest-trending rift basin, developed by extensional tectonic along a shear zone during the early Tertiary (Figure1). This tectonics is believed to be related to the collision of the Indian plate with the Eurasian plate [2]. After the rift phase, the basin underwent a thermal sagging followed by a structural inversion. This structural inversion has created a series of anticlinal traps and half-grabens [1]. The Northern Malay Basin encompasses three structural trends, centre, west and east flanks. The centre is characterized by thick Tertiary section and steeply dipping basement faults, whereas the flanks are relatively gently dipping towards the centre, with a few major normal faults and half-grabens [3].

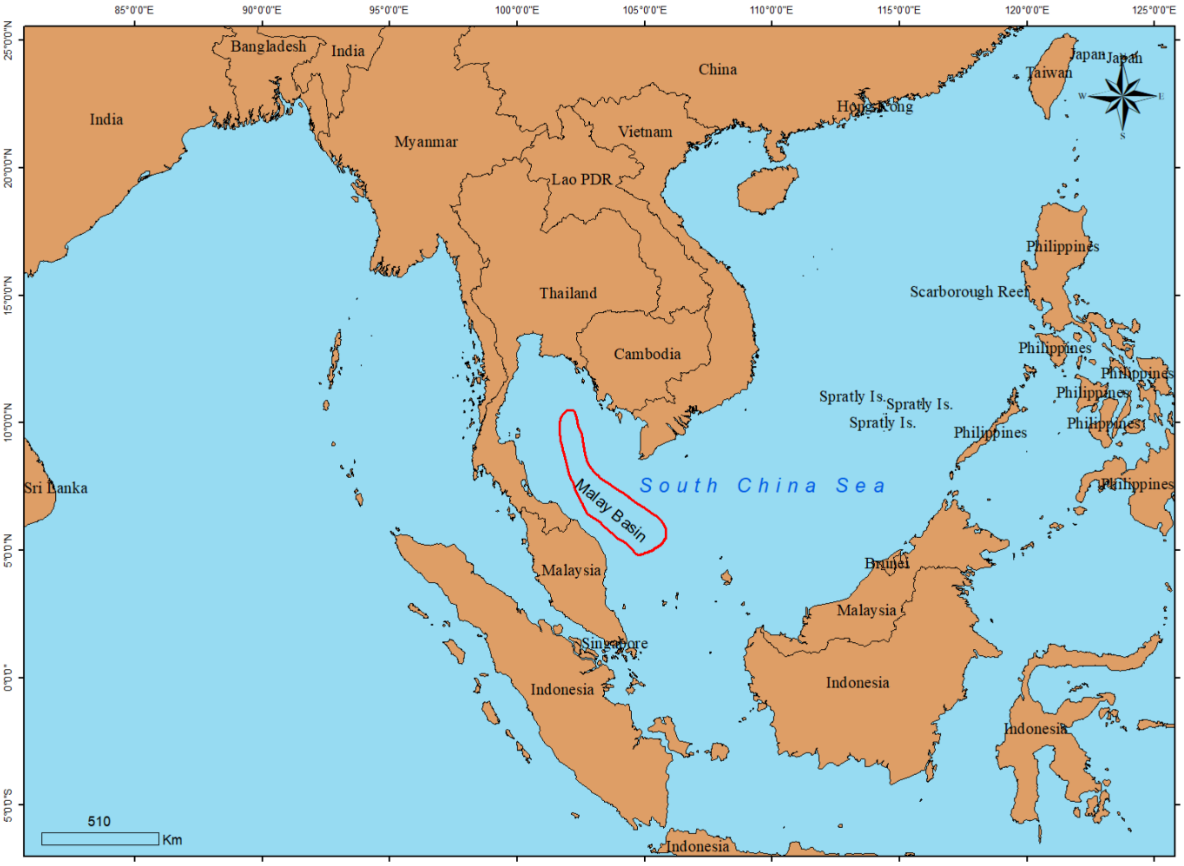

Figure 1. The location map of the Malay Basin. It is located offshore the peninsular Malaysia in the South China Sea

The field under investigation is located in the central structural domain, namely Cakerawala-Bujang trend (Figure2). The stratigraphy of the basin is from Oligocene to Recent. Based on seismic stratigraphy and biostratigraphy, the stratigraphic scheme of the basin is divided alphabetically, the older M to the younger A [4] (Figure3).

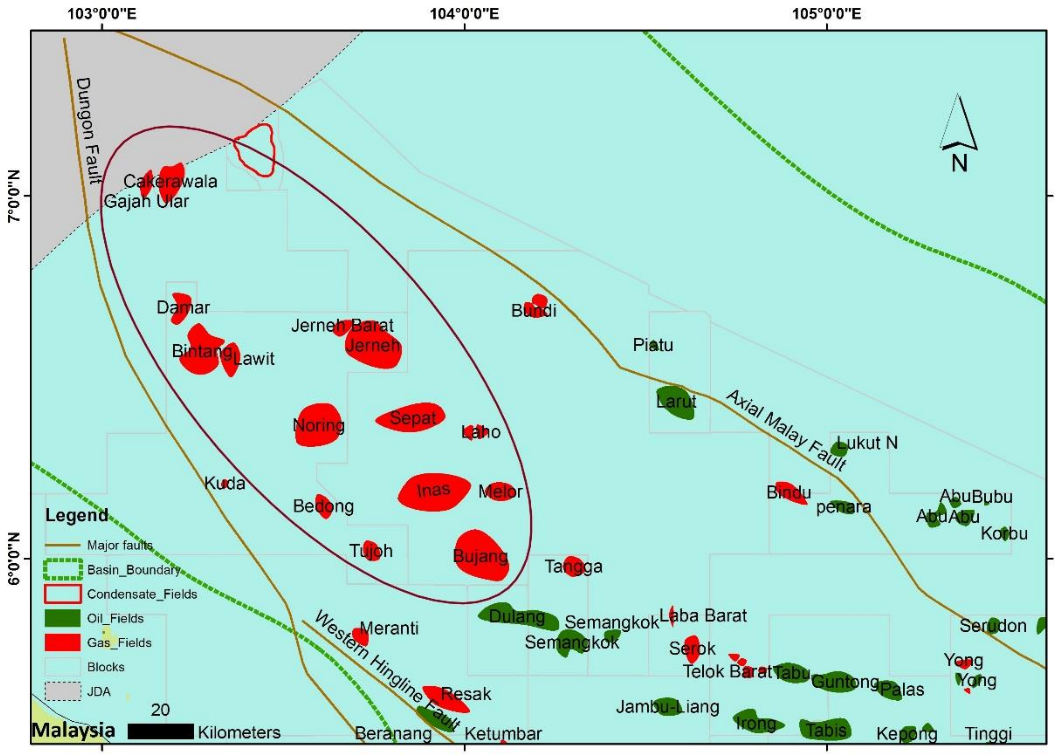

Figure 2. Location map of the Northern Malay basin. The field under study is located in the basin central part, namely Bujang-Cakerawala trend (dashed oval). After Madon et. al. [8]

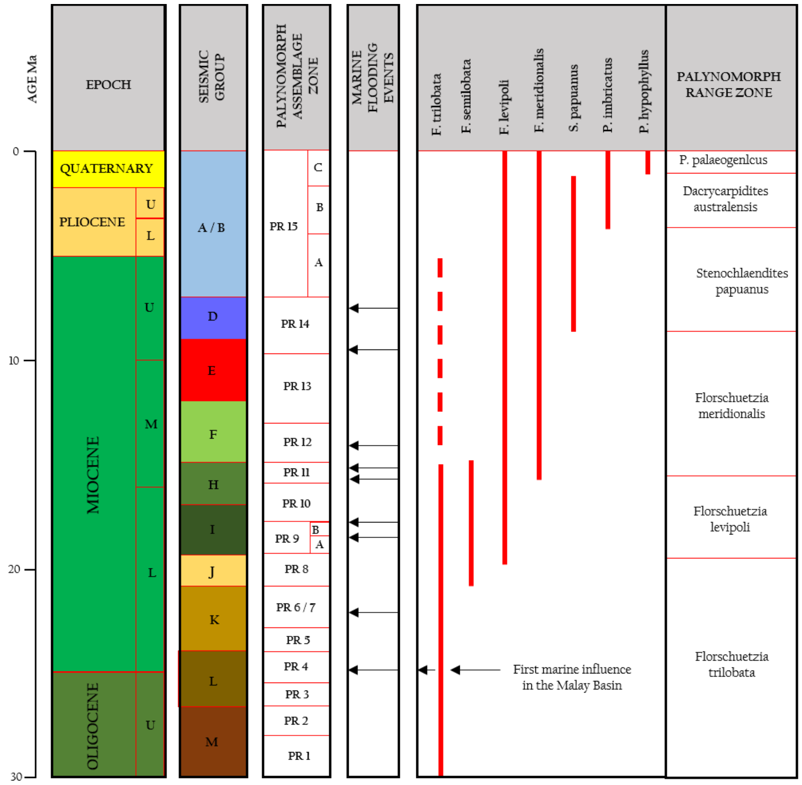

Figure 3. Stratigraphic scheme of the Malay Basin. The seismic groups correlated to the main palynomorphs assemblage zones (PR). The marine flooding events are also indicated. After Madon et. al. [8]

The petroleum system elements of the Northern Malay Basin include a mature and effective source rock (coal and carbonaceous shale) of group H and I that provide the hydrocarbon charge to reservoirs in E, D, and B groups. The hydrocarbon in the Northern Malay Basin is mainly gas, being trapped in the stratigraphically shallower units, E, D, and B. this is possibly due to the regional overpressure seal in the below group F. These reservoir sequences are interpreted to be deposited in continental, coastal, and shallow marine environments [1].

3. Methodology

A full-stack 3D seismic cube covering 400 km^2 and eight wells have been utilized in this study. The B100 reservoir ranges in two-way time between 1150 and 1600 ms. The top of the reservoir was picked on a strong trough that has been tied to the well-defined stacked gas sand characterized by a sharp base on gamma-ray (Figure 4). The horizon was auto-tracked and interpolated into continuous surface for attribute extraction (Figure 5).

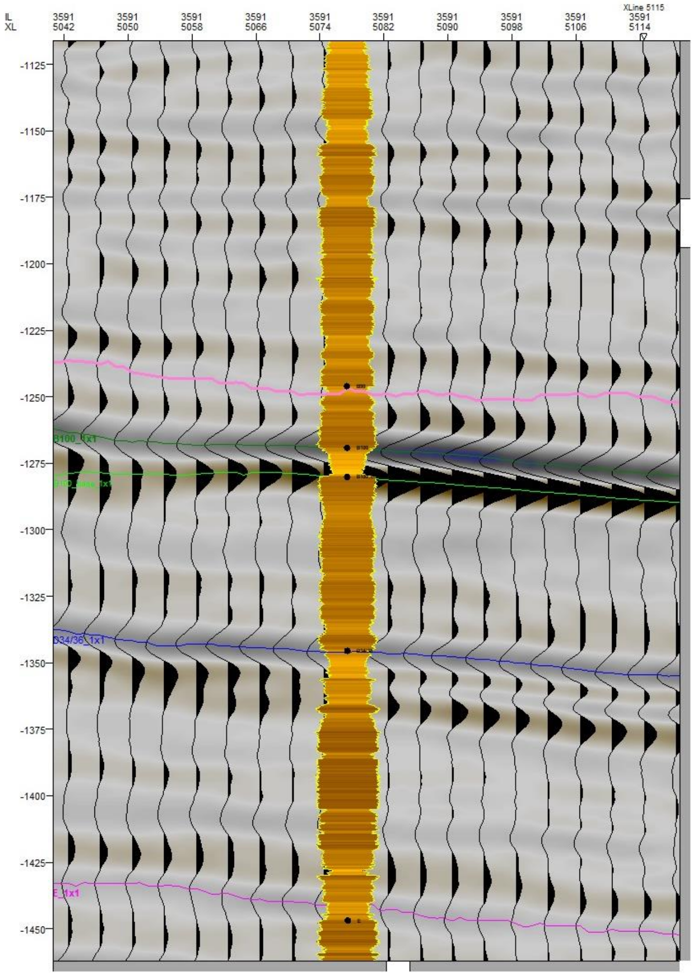

Figure 4. The top of the reservoir is tied to a well-defined gamma ray fining-upward parasequence at Well-8

🡐

3.1. Seismic attributes generation

This study integrates many seismic attributes that have a proven capability to delineate stratigraphic features and lithological variations. Coherence, RMS amplitude, and sweetness were generated and analysed in this study.

Coherence or variance attribute is a post-stack seismic attribute that measures the similarity between seismic waveform in a specified interval [5]. The coherency of a 3D seismic cube is done by computing local waveform similarity in different directions. The geological discontinuities such as faults, fractures, and stratigraphic boundaries are characterized by low coherence. The quality of the generated coherence map is largely affected by signal-to-noise ratio, static and stacking velocity errors [6]. Coherence attribute map was used to highlight channels edges and map the morphological variations.

RMS amplitude attribute calculates the root mean square (RMS) of single-trace samples T[i], over a user-specified vertical window with a length of n samples, for each sample in an input trace [5]. Sweetness attribute is the ratio between response amplitude and RMS response frequency. Strong amplitude anomalies of sweetness attribute are interpreted as good quality reservoir spots whereas clay rich areas are characterized by low amplitude [5]. RMS amplitude, reflection strength and sweetness attributes have a popular application as reservoir quality and fluid indicator and for channels detection in the Malay Basin. Gas-prone channel sand usually has strong anomalies, whereas the floodplain and the mud-filled channels have weaker response [7].

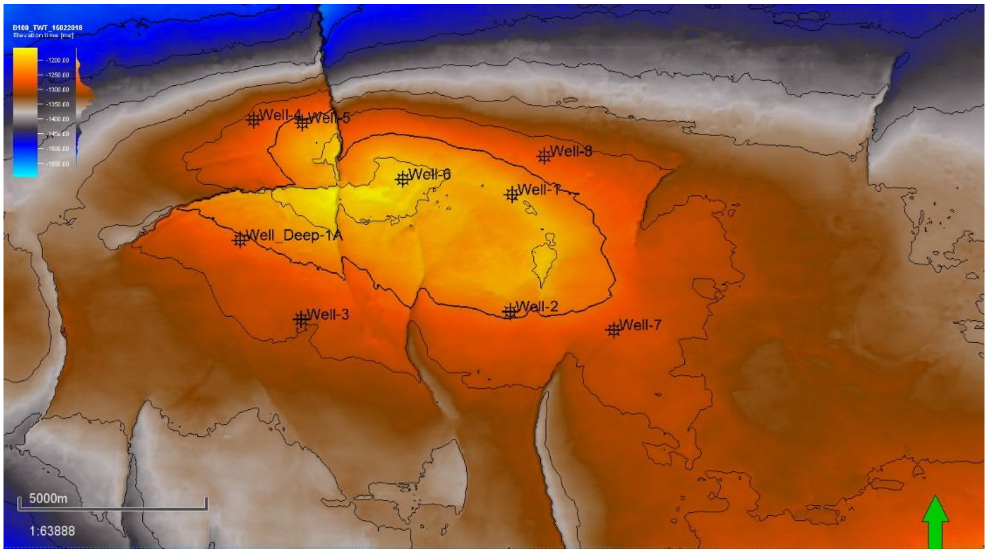

Figure 5. Time structure map of top B100 reservoir, showing an anticlinal structure crossed by numerous faults

3.2. Spectral decomposition and colour blending

Spectral decomposition is an efficient geophysical method for seismic geomorphology and reservoir characterization. It is a time-frequency analysis aims to break down the seismic trace into band-limited frequencies to highlight specific geological features [8]. The methodology followed for spectral decomposition includes extracting a sub-seismic volume (500 ms) for the zone of interest from the whole survey, Frequency selection is a crucial step in spectral decomposition. In order to get the best RGB color combination for imaging different geological variations, the frequencies of the red, green, and blue bands must be tuned and optimized. Frequency selection was performed interactively over the zone of interest and discrete frequencies of 25, 35, and 45 Hz were chosen for red, green, and blue channels respectively (Figure 6).

3.3. Iso-proportional slicing

Iso-proportional slicing also known as stratal slicing is an imaging tool that employed to generate attribute maps between two reference horizons [9]. Stratal slice is aimed to overcome the limitations of the time and horizon slices when the strata are not sheet-like or flat-lying. This method linearly samples the seismic attribute between two reference horizons in an equally-spaced interval to generate seismic attribute maps on phantom surfaces [10]. Four slices were extracted from all the generated attribute volumes to delineate channel bodies and their associated depositional features, predict lithology, and to carry out morphometric measurements of the channel width, depth, and sinuosity (Figure7).

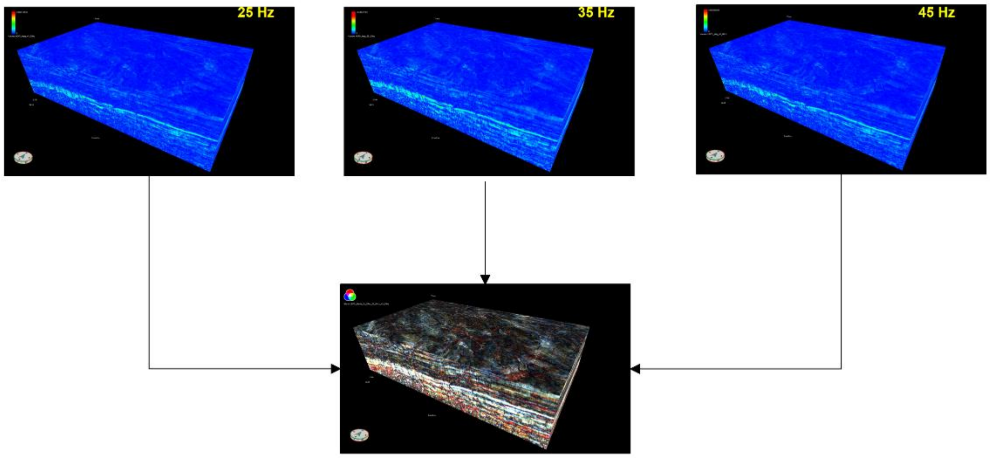

Figure 6. Spectral decomposition of a 500ms sub-volume at discrete frequencies of 25, 35, and 45 Hz. These volumes were combined together into an RGB color blended volume

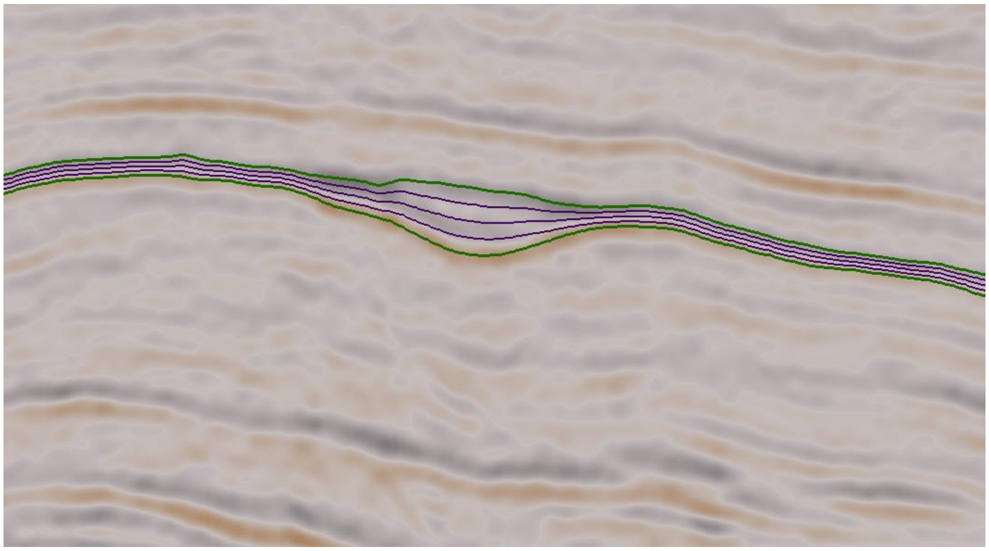

Figure 7. Stratal slicing process. It is a linear sampling of the seismic attributes between two reference horizons in an equally-spaced interval to generate seismic attribute maps on phantom surfaces

4. Results and discussion

Many details about B100 reservoir external geometry and the internal architecture have been obtained by the generated seismic attribute maps. On the basis of seismic geomorphology and well information, many features that related to the meander system were highlighted and different facies and geometries were interpreted. These maps showed that the reservoir interval is occupied by meander channel system. Stratal slicing is a very useful interpretation and visualization tool that aimed to provide a more precise representation of the stratigraphic elements and the depositional history interpretation. Four slices have been generated through B100 reservoir interval to study the stratigraphic evolution and channels development. The observed fluvial features include meandering channel, meander belt, meander scrolls, low sinuosity channel, point bar, abandoned channel, crevasse splay and so on Figure 8

A typical meander system is clearly visible in the RGB blended map. A large meander belt is present in the SE part of the area with meander radius about 500m. Meander scrolls are clearly visible within this belt indicating a lateral channel migration through time. The low amplitude response of the channel-fill is most probably due to the presence of mud, nevertheless, meander scrolls and point bar have a higher amplitude response indicating deposition of sand. Small incised tributary channels that feed the major meander belt are also observed. A meander loop exposure in the north-central part, containing 3 to 4 adjacent point bars was highlighted on the map. Isolated scattered point bars in the central part of the area can be seen as well. Floodplain crevasse splays are observed in the central part of the area. They are common in numerous fluvial environments and characterized by thin sand layers as confirmed by wells.

Figure 8. Stratal slice map of B100 reservoir on an RGB color composite volume. Frequencies of 25, 35, and 45 Hz were selected and blended into an RGB colour composite volume to image the zone of interest. The interpreted fluvial depositional elements include: ((M.Ch=meandering channel, L.S.Ch.=low sinuosity channel, P.B.=point bar, C.S.= crevasse splay, M.S.= meander scrolls, Ab.Ch.= abandoned channel)

The RMS amplitude and sweetness attributes were utilized to detect the sand distribution that related to channels and its depositional elements. Several high-amplitude anomalies over B100 reservoir interval were highlighted. The well data confirmed that these amplitude anomalies might be related to gas-charged sand bodies Figure 9. The attribute maps also showed that the sand distribution and hydrocarbon occurrence are very patchy due to the stratigraphic nature of the meander system. Most of the drilled wells were not in optimum locations to this hydrocarbon target. Mud-filled channels showed very weak amplitude response.

5. Conclusion

Seismic geomorphology has proven to be a very powerful interpretation tool. The produced highly detailed attribute maps with the aid of stratal slicing and visualization tools were capable to map and delineate B100 reservoir architecture. The generated attribute maps revealed that the B100 reservoir interval is predominantly occupied by a fluvial meandering-rivers system. RMS amplitude and sweetness attributes controlled by well information were used to highlight the reservoir sweet spots where good sand and probably hydrocarbon occur. This analysis showed that the drilled wells were not in the optimum location to test the hydrocarbon in this interval. The result of this study must significantly improve our knowledge and understanding and help to predict reservoir quality and lead to an accurate wellbore placement in the future.

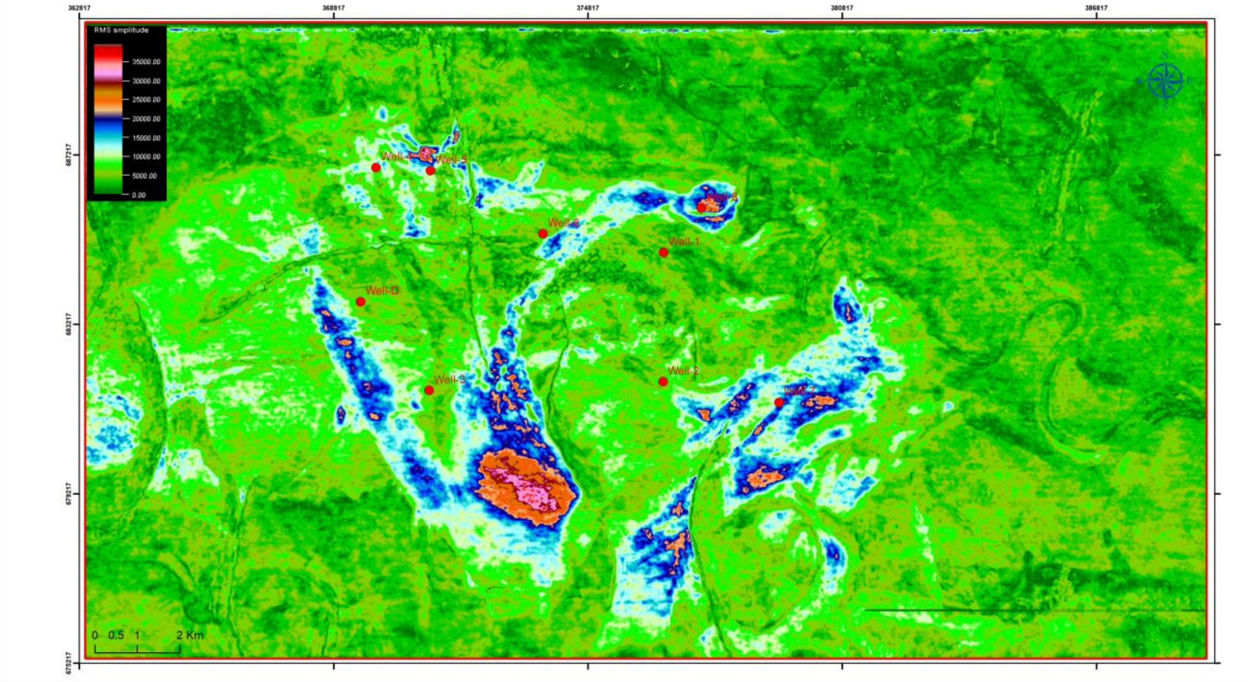

Figure 9. Sweetness attribute map of B100 reservoir, showing high amplitude anomalies and patchy distribution related to the sand-prone facies

Acknowledgments

The authors would like to thank PETRONAS and Universiti Teknologi PETRONAS for providing the data and fund for the study as well as the permission to publish this paper.

References

[1] Madon M, Abolins P, Hassan RA, Yakzan AM, Yang JS, Zainal SB. Petroleum systems of the Northern Malay Basin. Pet. Geol. Conf. Exhib. Bull., 2004; 49: 125–134.
[2] Mansor M, Rahman AHA, Menier D, and Pubellier M. Structural evolution of Malay Basin, its link to sunda block tectonics. Mar. Pet. Geol., 2014; 58(PB): 736–748.
[3] Ghosh D, Halim MFA, Brewer M, Viratno B, and Darman N. Geophysical issues and challenges in Malay and adjacent basins from an E & P perspective. Lead. Edge, 2010; 29(4): 436–449.
[4] Madon M. et al. The Petroleum geology and resources of Malaysia. Petronas, 1999.
[5] Barnes AE. Ed., Handbook of Poststack Seismic Attributes. Society of Exploration Geophysicists, 2016.
[6] Chopra S and Marfurt KJ. Seismic Attributes for Prospect Identification and Reservoir Characterization. Society of Exploration Geophysicists and European Association of Geoscientists and Engineers, 2007.
[7] Ghosh D, Sajid M, Ibrahim NA, and Viratno B. Seismic attributes add a new dimension to prospect evaluation and geomorphology offshore Malaysia. Lead. Edge, 2014; 33(5): 536–545.
[8] Castagna J and Sun S. Comparison of spectral decomposition methods. First Break, 2006; 24: 75–79.
[9] H Zeng, MM Backus, KT Barrow, and N. Tyler Stratal slicing, Part I: Realistic 3-D seismic model. Geophysics, 1998; 63(2):502–513.
[10] Zeng H. Stratal slice: The next generation. Lead. Edge, 2013; 32(2):140–144.

To whom correspondence should be addressed: Ismailalwali A. M. Babikir, Centre of Excellence in Subsurface Seismic Imaging & Hydrocarbon Prediction (CSI), Department of Geosciences, Institute of Hydrocarbon Recovery, Universiti Teknologi PETRONAS (UTP), 32610 Bandar Seri Iskandar, Malaysia

Petroleum and Coal

Article **Open Access**

INVESTIGATION OF COAL-METHANOARCHAEAL ASSEMBLAGE IN DEEP SUBSURFACE UNDERGROUND USING ENRICHMENT CULTURE TECHNIQUE

Diptangshu Mukherjee[1], *Vetrivel Anguselvi*[1*], *Reginald Ebhin Masto*[1], *Jhuma Ganguly*[2]

[1] *Industrial Biotechnology and Waste Utilization Research Group, CSIR-Central Institute of Mining and Fuel Research, Digwadih Campus, PO- FRI, Dhanbad-828108, Jharkhand, India*

[2] *Department of Chemistry, Indian Institute of Engineering Science and Technology, Shibpur, PO- Botanical Garden, Howrah- 711103, West Bengal, India*

Received June 22, 2018; Accepted September 3, 2018

Abstract

Enrichment culture of coal samples from underground mines (Jitpur and Moonidih underground mines) located in Dhanbad region, the Indian state of Jharkhand was tested positive for the presence of living microbial lineage capable of producing methane from coal during energy metabolism under laboratory condition. Accordingly, two gram negative, mesophilic, penicillin G and streptomycin resistant strain (BC/CIMFR-ana-CH4-12 and 14) derived from preferred sites were produce methane from acetate. They assimilated complex proteinaceous substances (yeast extract, beef extract, tryptone, and peptone) and amino acids (alanine, cysteine, and methionine) for energy metabolism. The pH ranges for growth were 6.0-7.5 for strain BC/CIMFR-ana-CH4-12 and 6.5-8.5 for strain BC/CIMFR-ana-CH4-14, with the fastest growth at pH 7.5 for BC/CIMFR-ana-CH4-12 and pH 7.0 for strain BC/CIMFR-ana-CH4-14. During growth, doubling time was observed 13.702-14.005 hours under the optimal condition, and specific growth rate was recorded 0.021/hour for both strains. Based on the study strains were belongs to *Methanococcus spp.* and *Methanobacterium spp.*, associated with numerous aerobic and anaerobic microbial community in deep subsurface coal deposits as suitable habitat. The ecological implication of their habitat also discussed. The study suggests that there is intense biogenic methane generation activity in a selected environment which may me enhance by stimulating the activity of existing methanoarchaeal consortia.

Keywords: *Coal bed; Archaea; Methane; Habitat; Substrate; Growth.*

1. Introduction

Archaea constitute the third fundamental domain of life, it comprises methanogens, red extreme halophiles, and the thermoacidophiles, playing a great impact on global nutrient cycling as well as a geochemical cycle in the biosphere. These diverge from other bacteria at the very early stage of evolution and habitat under extreme condition [1-2].

Generally, coal is made up of decomposed plant materials that initially form peat. After peatification, it metamorphosed into different ranks of coal as a complex heterogeneous ultra structure according to its burial depth and temperature [3]. About 85 to 95% (wt/wt dry coal) organic materials in coal are known as macerals which composed of plant material, and the inorganic materials are present as aluminosilicates and pyrites. Therefore, coal could be considered a very attractive carbon source for microbial biodegradation [4-5]. Studies revealed that a portion of coal bed methane is biological origin occurred by microbial consortia habitat in coal deposits [6-7]. Accordingly, high diversity of bacteria, firmicutes, spirochetes, bacteroides and all subgroups of proteobacteria are reported in the coal bed. Contrasts with archaeal linage, methanogens are common habitat, and only a few are characterized [8-10]. For example, sub-surface coal deposits were found to be the habitat of diverse acetoclastic, methylotrophic and hydrogenotrophic methanoarchaeal assemblages [11]. The members of

Methanosarcina spp. can take up H_2/CO, acetate, methanol, and methylamines as substrate habitat in coal beds of Alberta, Canada [5]. The Methanosarcinales [8], Methanobacteriales and Methanococcales [12] were reported from Powder River Basin, Wyoming. Kai *et al.* [13] stated that rod shaped methanogens are generally affiliated to the order of Methanobacteriales, which belongs to three mesophilic genera as *Methanobacterium*, *Methanobrevibacter* and *Methanosphaera*, and two thermophilic or hyperthermophilic genera as *Methanothermobacter* and *Methanothermus*. Indeed, archaebacteria residences under extra eme environment are undertaken for extensively exploration [14].

The goals of the current study were to confirm the presence of methane generating archaea in coal bed (Jitpur and Moonodih underground coal mine) of Dhanbad coal fields using culture dependent method to explore their physiology, growth kinetics and to emphasize their habitat for ecological point of view. The study further expands our knowledge and the value of archaea kingdom.

2. Experimental

2.1. Study sites

Dhanbad is a city in the Indian state of Jharkhand and recognized as coal capital of India. The region is endowed with huge resources of bituminous coal and having an area of 453Sq. Km bounded by latitudes 23° 37' and 23° 50' N and longitudes 86° 07' and 86° 28' E [15]. It is well known for coal mining and having some of the largest mines in India. Accordingly, two different coal mines namely Jitpur underground mine and Moonidih underground mine located in Dhanbad region have been selected for the study (Figure 1).

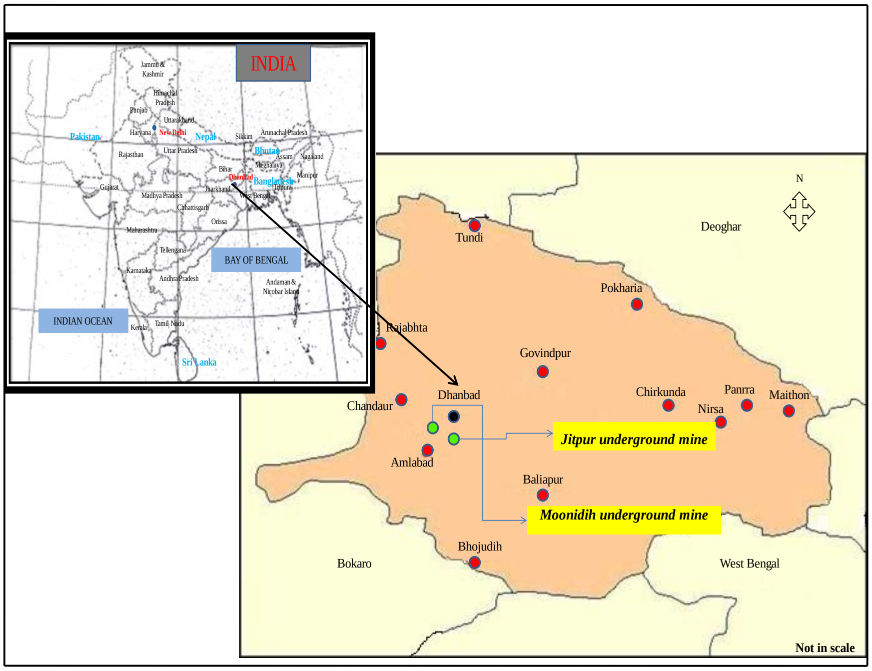

Figure 1. Map indicates the selected study sites

2.2. Microbial enrichment and isolation of a pure culture

Coal as inoculum source was collected (25-30cm deep) in polyethylene bag followed by flushing with 99.99% carbon dioxide (CO_2), sealed and kept at room temperature in dark condition until use. The basal medium [8-16] for enrichment was contained the following (g/L) ingredients was selected for enrichment and isolation: KCl (0.1), $MgCl_2$, $2H_2O$ (0.2), NH_4Cl (1), $CaCl_2$, $2H_2O$ (0.04), KH_2PO4 (0.1), NaCl (0.8), and yeast extract (2.0). The final concentration of trace metal in the medium (mg/L) were: Nitrilotriacetic acid, 10; $MnSO_4$, H_2O 5;

$Fe(NH_2)_4(SO4)_2.6H_2O$, 4; $CoCl_2.6H_2O$, 1; $ZnSO_4.7H_20$, 1; $CuCl_2.2H_2O$, 0.1; $NiCl_2.6H_2O$, 0.1; $Na_2MoO_4.2H_2O$, 0.1; Na_2SeO_4, 0.1 and Na_2WO_4, 0.1. Vitamin concentrations (mg/L) in the final medium were: Pyridoxine-HCl, 0.1; Thiamine-HCl, 0.05; Riboflavin, 0.05; Calcium pantothenate, 0.05; Thioctic acid, 0.05; p-aminobenzoic acid, 0.05; Nicotinic acid, 0.05; Vitamin B12, 0.05; Mercaptoethanesulfonic acid (coenzyme M), 0.05; Biotin, 0.02 and Folic acid, 0.02. The pH was adjusted 7.2 by 0.5N H_2SO_4 and NaOH. Finally, sodium bi-carbonate at a concentration of 2.0 g/L was added. A drop of resazurin (0.001g/L) was added as an oxygen indicator and autoclaved. After cooling 0.5mL reducing solution (1.25% cysteine-1.25% Na_2S) was added. Immediately 1g of powder sample was transferred into each flask and sealed by filling the headspace with pure CO_2. The flask was kept at 37°C in a dark place for one month. Pure culture was obtained by serial dilution technique on solid medium under anaerobic condition. Furthermore, screening was achieved through methane production potentiality by utilizing anaerobic basal liquid medium as described earlier supplemented with sodium acetate trihydrate at a concentration of 5g/L. The pure isolates were preserved at 4°C for characterization. Colony and cellular morphology were determined according to Balows *et al.* [17] using pure isolate. The cell aggregate formation of purely isolated methanogenic strains was determined in liquid basal medium supplemented with acetate at a concentration of 5gm/L. After commencing growth in liquid medium, the granule formation or cell aggregation was recorded [18].

2.3. Headspace gas analysis

Headspace gas was studied by using a gas analyzer (Madur, GA 21 Plus, Poland). For that, gas was sucked by 50mL injection syringe and directly injected to the sampling port of gas analyzer. Methane was detected through MadIR methane sensor and analyzed by Madcom software.

2.4. Phase-contrast and Scanning electron microscopy

Gram staining was performed according to Dubey, and Maheswari [19] and the cells were analyzed by phase-contrast microscope (Olympus BX53, Japan). The sample was prepared for scanning electron microscopy followed by user guideline of the instrument. For that, a thin bacterial smear was prepared on a glass slide, and it was dried completely. Then the smear was gold coated (15-20 nm) using a coater (Q1SOR). Finally, the slide was placed into vacuum created sample chamber of the instrument (Supra 55; Zeiss-Germany) and the image was taken at a suitable magnification.

2.5. Biochemical test, nutritional requirement, growth kinetics, and membrane study

Biochemical characterization as an enzymatic test, antibiotic sensitivity test, optimal growth condition, growth kinetics, and the nutritional requirement was performed as described by Dubey and Maheswari; Marteinsson *et al.;* Balows *et al.* [19-20-17]. Substrate utilization (as different compounds) was tested by using a basal medium with the addition of each tested compound and omitting one of the components in each test. All tests were performed in duplicate, and a control in which no substrate was added was used as a baseline. The pH of the medium was adjusted by 1N H_2SO_4 and NaOH. Penicillin G and streptomycin was added at a concentration of 0.5gm/L [9] into liquid basal medium. The turbidity of the medium was determined by UV/Vis spectrophotometer (CECIL C-7500 series, UK) at 610 nm. Doubling time (t_d), specific growth (μ) and generation time (g) were calculated according to Meher and Ranade, 1992; Tortara *et al.* [21-22]. The archaeal membrane lipid was extracted by a modification of Bligh and Dyer (chloroform-methanol) method [23-24] and analyzed by Fourier Transform Infrared Spectrophotometer (IRAffinity-1S, Shimadzu, Japan).

2.6. Habitat characterization

Characterization of archaeal habitat was performed by selecting different physicochemical and biological parameters. Accordingly, pH and electrical conductivity (EC) was measured by pH meter (Thermo-Scientific, Orion Star-A214) and EC meter (PCS Tester35, Multi parameter). Total organic carbon was determined by rapid dichromate oxidation technique and total nitrogen content was analyzed by alkaline potassium permanganate method [25] using Kjeldahl instrument (Pelican, Kelplus, Distyl-EM). Humic acid (HA) was estimated according to Mesa Verde Resources humic acid methodology [26]. The optical density was measured at 450nm using spectrophotometer and quantified through standard curve. Biological parameter as dehydrogenase activity was determined by utilizing 2,3,5-triphenyltetrazolium chloride (TTC) as a substrate followed by standard curve [27]. Total aerobic and anaerobic microbes were counted on nutrient agar and anaerobic basal agar plate (Hi-Media) using serial dilution method [19]. Serial dilution for anaerobic organisms was made by using sterile anoxic water solution. For that, pure nitrogen gas was bobbling in boiling stage of pre-sterilized distilled water containing resazurin at a concentration of 0.001g/L in serum vial (20mL capacity, Borosil) under aseptic condition. When the solution turned pink to colorless the vial was capped using rubber stopper and crimped. After cooling, trace amount of reducing solution was added into it and dilution was achieved by using glass injection syringe. Active microbial biomass carbon (AMBC) was measured by glucose nutrient induced respiration method [28]. Media was composed of peptone, (10g); yeast extract, (5g); glucose, (5g); sodium chloride (5g); Potassium di-hydrogen ortho-phosphate (0.21g) in 1000ml de-ionized water. Basal soil respiration (BSR) was measured as the CO_2 evolved from moist soil (60% water holding capacity), over an incubation period of 10 days at 25°C, in the dark condition [28]. For element analysis, ICP-OES (Thermo Scientific, iCAP 6000 series spectrometer) was used and the sample was prepared as described in ASTM D-4638 method [29].

3. Results and discussion

Generation of methane in empty space of enrichment culture flask was taken as evidence and screening tool for methanogenic archaea. Accordingly, two obligate anaerobic methane generating pure isolates were successfully received from selected habitat and referred as BC/CIMFR-ana-CH4-12 and 14 respectively.

3.1. Colony and cellular morphology

Isolated pure culture was considered for characterization in compare to colony and cellular morphology, summarized in Table 1.

Table 1. Characteristics of isolated methanoarchaeal strains from underground coal mines of Dhanbad

Strains	Habitat	Colony characteristics	Methane generation	Gram reaction	Shape	Cell-cell aggregation	Endospore
BC/CIMFR-ana-CH4-12	Coal surface of Jitpur underground mine	Colony was 0.5-1mm diameter, round and smooth. The color was off white with entire edge and texture was moist with flat elevation.	Positive	Gram Negative	Rod	Dispersed	Not found
BC/CIMFR-ana-CH4-14	Coal surface of Moonidih underground mine	Round-smooth colony and 0.5-1mm elongated on solid medium with entire edge. It was off white in color and the elevation was flat with moist texture.	Positive	Gram Negative	Spherical or cocci	Dispersed	Not found

Accordingly, the colony of both strains was found to be round shaped, off white color and exhibited 0.5-1.0mm in diameter with entire edge. The texture was noticed as moist with flat elevation on solid medium for the same. Methanogenic archaeal colony was observed grayish white color, opaque and round shaped with entire edges and the diameter was reached up to 0.5–1.0 mm [30]. The isolates grew as dispersed in liquid medium when supplemented with acetate and granule formation or cell aggregation was not observed during growth cycle. Cells of both strain stained gram negative. Further, clear and details image for gross cell morphology was studied by scanning electron micrograph and revealed that strain BC/CIMFR-ana-CH4-12 was rod shaped and BC/CIMFR-ana-CH4-14 exhibited cocci in shape (Figure 2).

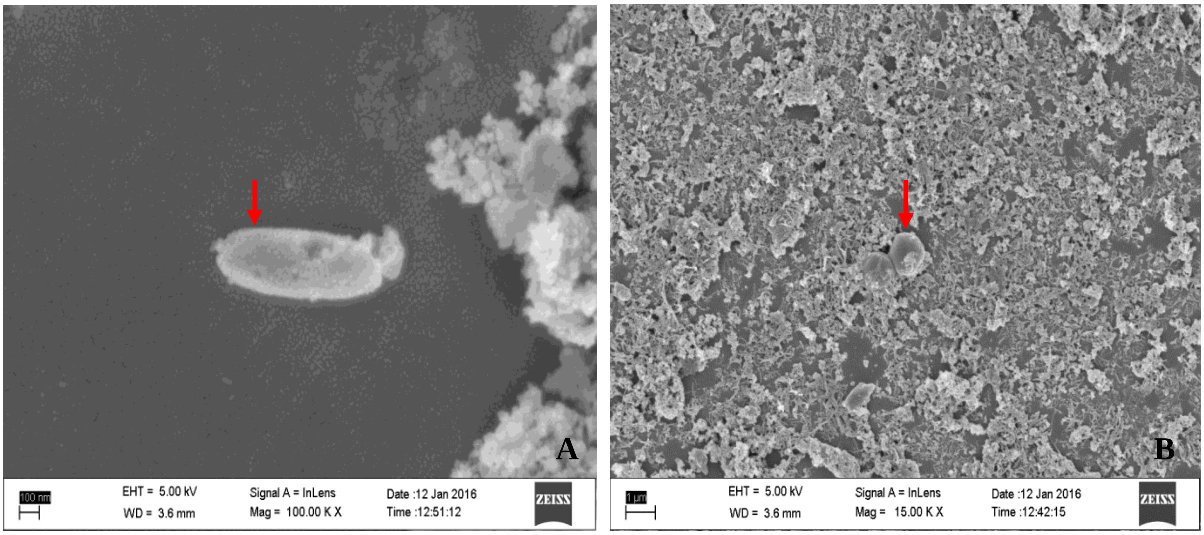

Figure 2. Scanning electron micrograph of isolated methanoarchaeal strains (A- BC/CIMFR-ana-CH4-12 and B- BC/CIMFR-ana-CH4-14)

3.2. Nutrient utilization

Methanogen can utilize various substrates for energy metabolism such as CO_2 reduction with hydrogen, formate as electron donors, methanol reduction, fermentation of acetate and dismutation of methylated compounds [31-32]. Substrate utilization by isolated strains as different carbon and nitrogen source was investigated during the course of growth and presented in Table 2. Accordingly, luxuriant growth was observed in presence of acetate to the growth medium for selected isolates. However, citrate was taken poorly by both strain and formate was moderately assimilated by strain BC/CIMFR-ana-CH4-12. Furthermore, the isolates were able to utilize selected complex proteinaceous substances (yeast extract, beef extract, tryptone and peptone) for energy metabolism. Yeast extract was luxuriantly assimilated by strain BC/CIMFR-ana-CH4-14, while tryptone was taken as good for both strains. The isolates further exploited selected amino acids (alanine, cysteine and methionine) as sole carbon and energy source. Although growth was generally weaker than the growth observed with complex substrates. Comparatively, strain BC/CIMFR-ana-CH4-12 respond luxuriantly in presence of L-methionine to the medium. Since, bacterial growth is depending upon the media composition as well as substrate composition. These differences may be attributed to differences in substrate composition [33].

Table 2. Utilization of different compounds as growth factor

Strains	Formate	Acetate	Citrate	YE	BE	Tryptone	Peptone	L-alanine	L-cysteine	L-methionine
BC/CIMFR-ana-CH4-12	+ +	+ + + +	+	+ + +	+ + + +	+ + +	+ + ++	+ + +	+ + +	+ + + +
BC/CIMFR-ana-CH4-14	+	+ + + +	+	+ + + +	+ + +	+ + +	+ + + +	+ + +	+ + +	+ + +

YE- Yeast extract, BE- Beef extract; growth was expressed as ++++ (luxuriant growth), +++ (good), ++ (moderate), + (poor) and – (no growth). Concentration of each proteinaceous substrate was tested at 0.5% (wt/vol) and amino acid was at a concentration of 0.1 mM [20]

3.3. Temperature and pH range

After temperature optimization in laboratory it was observed that isolated strains grew well under mesophilic condition in basal medium (Table 3). Culture of BC/CIMFR-ana-CH4-12 was found to sustain in a temperature range between 32-42°C while the optimum growth was recorded at 36°C. Strain BC/CIMFR-ana-CH4-14 was able to grow between 29-39°C and achieved fastest growth at 34°C. In addition, the pH is an important parameter for growth of microorganisms. Each bacterium is having a definite pH growth range and growth optimum [34]. Therefore, pH tolerance limit for isolates was found to be diverse. Strain BC/CIMFR-ana-CH4-12 thrived in a pH range 6.0-7.5 followed by optimal growth at pH 7.5. Further, the isolate BC/CIMFR-ana-CH4-14 tolerated pH range 6.5-8.5 and attained its fastest growth at pH 7.0.

Table 3. Optimal growth condition and biochemical characteristics of isolated strains

Parameters	BC/CIMFR-ana-CH4-14	BC/CIMFR-ana-CH4-12
Temperature range (°C)	29-39	32-42
Optimum temperature (°C)	34	36
pH range	6.5-8.5	6.0-7.5
Optimum pH	7.0	7.5
Catalase test	-	-
Indole test	-	-
Lipase activity	-	-
Protease activity	-	-
Starch hydrolysis	-	-
Urea hydrolysis	-	-
Penicillin G	Resistant	Resistant
Streptomycin	Resistant	Resistant
Doubling time (t_d)	14.005	13.702
Specific growth rate (µ)	0.021	0.021
Generation time (g)	32.255	31.556

3.4. Biochemical tests

Microorganisms play extremely versatile role to their lifecycle and their range of metabolic capacities are diverse [35]. The metabolic diversity of isolates was demonstrated by utilizing exceptional biochemical tests (Table 3). Accordingly, nitrogen metabolism was determined by means of iodole test and both strains were negative for the test, representing that they cannot act upon amino acid tryptophan due to the deficient in tryptophanase in their cell. Further, catalase and urease activity were also accounting negative for the isolates due to lack of that particular enzymes [19]. Additionally, the enzyme activity such as lipase, protease and starch hydrolysis were also considered for the study and none of the strain was found to be positive for those tests. Moreover, both strains were observed to be penicillin G and streptomycin resistant at a concentration of 0.5g/L, may be due to the diverse structure of their cell wall [36].

3.5. Growth kinetics

Microbial growth refers to increasing the cell number and it was performed in anaerobic basal medium supplemented with acetate under optimum growth condition. Consequence to this, growth kinetics was demonstrated as doubling time (t_d), specific growth rate (µ) and generation time (g), listed in Table 3. The isolates grew with a doubling time between 13.702-14.005 hours under optimal condition. The doubling time was 14 hours [37] and 11hours was reported for formate grown *Methanobacterium formicicum* [38]. Further, specific growth rate (µ) was recorded 0.021/hour for both strains. However, generation time (g) was noticed longer for isolated methanoarchaeal strains (31.556-32.255/hour). The specific growth rate of methanogenic archaea was reported as 0.049, 0.030, 0.023 and 0.021/hour which were variable according to the substrate composition [30]. Additionally, archaebacteria especially methanogens are very slow growing organism [39]. Therefore, doubling time and generation time was found to be longer during the course of growth.

3.6. Membrane study

The membrane of strain BC/CIMFR-ana-CH4-12 was analyzed by FT-IR and the data were collected over the frequency range of 3600-400 cm^{-1} in order to display the details of spectral changes (Figure 3). During study, the bands such as alkyl (1377, 1463, 2856, 2926 and 2952cm^{-1}), primary carbinol (1051cm^{-1}), ether (1115cm^{-1}) and hydroxyl functional groups (3450cm^{-1}) are very much identical in membrane spectrum [24]. Archaea especially methanogens characteristically possess isoprenoid branched ether linkethe d membrane lipids which were also identical [40].

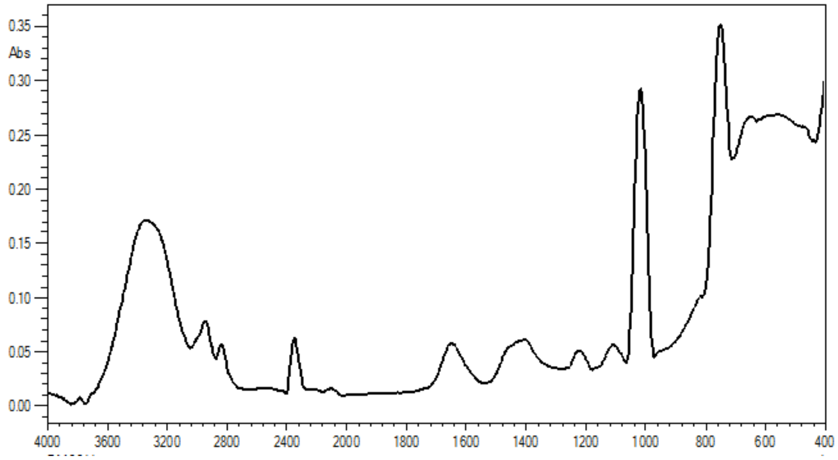

Figure 3. FT-IR spectra of isolated methanoarchaeal (BC/CIMFR-ana-CH4-12) membrane

3.7. Habitat characterization

Physico-chemical characterization of the environmental sample can influence the growth, behavior, interactions, and existence of the organisms where they residence that environment. During energy metabolism, they obtain nutrients from that particular habitat for the biosynthesis of cellular macromolecules [41-34]. Therefore, an attempt has been to understand the ecological significance of preferred archaeal habitat by exploration of different physico-chemical and microbiological parameters, presented in Table 4. Accordingly, the pH was found to be slightly basic in nature for both habitats. Further, EC was recorded 137 µS for Jitpur underground mines and 343.5 µS Moonidih underground mines. Carbon, nitrogen, hydrogen, phosphorus, and sulfur are the essential ingredients for biosynthesis of protein, nucleic acid, coenzymes and phospho-lipids [41]. Total organic carbon was measured at 3.13% and 9.55% for Jitpur and Moonidih underground mines. Comparatively, nitrogen content was found to be higher in Moonidih underground coal deposit. In addition, P and S were found to be rich in selected habitat for a cellular biosynthetic pathway in the archaeal cell. Further, Humic acid content was recorded nearly same for both chosen habitats which serve as a catalyst for microbial activity [42]. The element such as Fe, Ni, Co, Mo, Cu, Zn, W, Se, and B is vital for bacterial growth and metabolism [43-44]. Among them, Fe, Ni, Co, Zn, Cu, Mo, and W are very significant for enzymatic activity in the methanogenic pathway [44-46]. After analysis, it was experimental that Fe, Ni, Cu, Zn, B, and Se are sufficient to support methanoarchaeal growth in the selected environment. Microbiological data revealed that methanogenic isolates were found to associate with numerous aerobic and aerobic microbial linages in deep subsurface coal deposits. Further, actively microbial biomass carbon and basal soil respiration also reflect the availability of carbon for microbial maintenance in selected coal deposits [47].

Table 4. Physicochemical and microbiological characteristics of isolated methanoarchaeal habitat located in Dhanbad coal field

Parameters	Habitat	
	Jitpur underground mines	Moonidih underground mines
pH	8.22	8.15
Electrical conductivity (μS)	137	343.5
Total Organic Carbon (%)	3.13	9.55
Total nitrogen (%)	0.228	0.342
Humic acid (%)	0.0075	0.008
Sodium (Na)	30.612	22.286
Phosphorous (P)	75.608	91.052
Potassium (K)	7.756	6.350
Calcium (Ca)	31.053	36.651
Magnesium (Mg)	16.608	26.288
Iron (Fe)	72.009	61.026
Zinc (Zn)	0.124	0.153
Copper (Cu)	0.105	0.103
Manganese (Mn)	1.001	1.005
Nickel (Ni)	0.100	0.011
Boron (B)	0.030	0.031
Selenium (Se)	0.593	0.824
Sulfur (S)	48.356	41.299
Microbiological parameters		
Aerobic microbial count	1.2×10^8	9.5×10^7
Anaerobic microbial count	2.0×10^7	2.8×10^7
Dehydrogenase activity (μg TPF/g/h)	10.7	10.7
Soil respiration:		
AMBC (mg/kg)	31.13	62.26
Total BSR (mg/kg)	1.0	1.4
BSR (mg/kg)	484	396

Data are taken as mean value of triplicate. Elements were expressed as ppm. Microbial count was expressed as CFU (Colony Forming Unit); AMBC- Actively Microbial Biomass Carbon; BSR- Basal Soil Respiration; TPF- Tri-phenyl fomazon

4. Conclusion

The study confirms the presence of active methane generating archaeal lineage in underground coal deposits located in Dhanbad which have great ecological importance. Additionally, the archaeal assemblage was found to be associated with numerous aerobic and anaerobic microbial communities in coal bed as significant habitat. Based on the study isolated strains belonged to the genera of *Methanococcus spp.* and *Methanobacterium spp.* The research is also suggesting that there is intense methane generation activity through the microbial origin in a particular environment. Further, it is recommended for chemical measurements to stimulating the activity of existing methanoarchaeal consortia which can improve the understanding of these organisms in the environmental sample.

Acknowledgments

The authors would like to thank the CSIR, Government of India for its financial support and Dr. P. K. Singh, Director of CSIR-CIMFR for permitting this paper to be published.

References

[1] Pelczar JM, Chan ECS and Krieg NR. Microbiology, 5th ed., TATA McGRAW-Hill publication, New York, 1993.

[2] Offre P, Spang A and Schleper C. Archaea in biogeochemical cycles. Annl. Rev. Microbiol., 2013; 67: 437–457.

[3] Faison BD. The chemistry of low rank coal and its relationship to the biochemical mechanisms of coal biotransformation; Microbial transformations of low rank coals. In: Crawford DL ed., p. 1-26, CRC Press, Boca Raton, 1993.

[4] Strąpoć D, Picardal FW, Turich C, Schaperdoth I, Macalady JL, Lipp JS, Lin YS, Ertefai TF, Schubotz F, Hinrichs KU, Mastalerz M and Schimmelmann A. Methane producing microbial community in a coal bed of the Illinois Basin. Appl. Environ. Microbiol., 2008; 74 (8): 2424-2432.

[5] Penner TJ, Foght JM and Budwill K. Microbial diversity of western Canadian subsurface coal beds and methanogenic coal enrichment cultures. Int. J. Coal Geol., 2010; 82: 81–93.

[6] Smith JW and Pallasser RJ. Microbial origin of Australian coalbed methane. Am. Assoc. Pet. Geol. Bull., 1996; 80: 891–897.

[7] Ahmed M and Smith JW. Biogenic methane generation in the degradation of eastern Australian Permian coals. Organic Geochem., 2001; 32: 809–816.

[8] Green MS, Flanegan KC and Gilcrease PC. Characterization of a methanogenic consortium enriched from a coal bed methane well in the Powder River Basin, U.S.A. Int. J. Coal Geol., 2008; 76: 34–45.

[9] Kotelnikova A, Macario AJL and Pedersen K. *Methanobacterium subterraneum sp.* nov., a new alkaliphilic, eurythemic and halotolerant methanogen isolated from deep granitic groundwater. Int. J. Syst. Evol. Microbiol., 1998; 48: 357–367.

[10] Strapoc D, Mastalerz M, Dawson K, Macalady JL, Callaghan A, Wawrik B and Ashby M. Biogeochemistry of coal bed methane. Ann. Rev. Earth Planetary Sci., 2011; 39(1): 617-656.

[11] Shimizu S, Akiyama M, Naganuma T, Fujioka M, Nako M and Ishijima Y. Molecular characterization of microbial communities in deep coal seam ground-water of northern Japan. Geobiol., 2007; 5: 423–433.

[12] Klein D, Flores RM, Venot C, Gabbert K, Schmidt R. Stricker GD, Pruden A and Mandernack K. Molecular sequences derived from Paleocene Fort Union Formation coals vs. associated produced waters: implications for CBM regeneration. Int. J. Coal Geol., 2008; 76: 3–13.

[13] Kai M, Xiaoli L and Xiuzhu D. *Methanobacterium beijingense* sp. nov., a novel methanogen isolated from anaerobic digesters. Int. J. Syst. Evol. Microbiol., 2005; 55: 325–329.

[14] DeLong EF. Oceans of Archaea. Features ASM News, 2003; 69(10): 503-511.

[15] Central Mine Planning and Design Institute (CMPDI) Ltd, Ranchi, India, 2010.

[16] Tanner RS. Cultivation of bacteria and fungi. In: Hurst CJ, Crawford RL, Knudsen GR, Mclnerney MJ and Syetzenbach LD ed., Manual of Environmental Microbiology, 2nd ed., Australian Society of Microbiology (American Society of Microbiology) Press, p. 62-70, Washington DC, 2002.

[17] Balows A, Truper HG, Dworkin M, Harder W and Schleifer KH. The prokaryotes, 2nd ed., A hand book on biology of bacteria: Ecophysiology, isolation, applications. Springer-Verlag, New York, 1992.

[18] Wu WM, Jain MK and Zeikus JG. Formation of fatty acid degrading, anaerobic granules by defined species. Appl. Environ. Microbiol., 1996; 62(6): 2037–2044.

[19] Dubey RC and Maheswari DK. Practical Microbiology, 2nd ed., S. Chand publication, New Delhi, 2008.

[20] Marteinsson VT, Watrin L, Prieur D, Caprais JC, Raguenes G and Erauso G. Phenotypic characterization, DNA Similarities, and protein profiles of twenty sulfur-Metabolizing hyperthermophilic anaerobic archaea isolated from hydrothermal vents in the southwestern Pacific Ocean. Int. J. Syst. Bacteriol., 1995; 45(4): 623-632.

[21] Meher KK and Ranade DR. Isolation of propionate degrading bacterium in co-culture with a methanogen from a cattle dung biogas plant. J. Biosci., 1992; 18(2): 271 -277.

[22] Tortara GJ, Funke BR and Case CL. Microbiology: An introduction, 12th ed., Benjamin Cumming publication, San Francisco, 2007.

[23] Bligh EG and Dyer WJ. A rapid method of total lipid extraction and purification. Can. J. Biochem. Physiol., 1959; 37: 911–917.

[24] Mancuso CA, Nichols PD and White DC. A method for the separation and characterization of archaebacterial signature ether lipids. J. Lipid Res., 1986; 27: 49–56.

[25] Nelson DW and Sommers LE. Total carbon, organic carbon, and organic matter. In: Sparks DL, Page AL, Helmke PA and Loeppert RH eds., Methods of soil analysis. Part 3. Chemical methods. p. 961–1010, SSSA Book Ser. 5.3., ASA and SSSA, Madison, WI, 1996.

[26] Mesa Verde Resources Humic acid Methodology, Procedure for determination of humic acid content, Placitas, NM-87043. www.humates.com/methodology.htm/

[27] Casidajr LE, Klein DA and Santoro T. Soil dehydrogenase activity. Soil Sci., 1964; 98: 371–376.

[28] Islam KR and Weil RR. Land use effects on soil quality in a tropic forest ecosystem of Bangladesh. Agri. Ecosyst. Environ., 2000; 79: 9–16.

[29] ASTM D 4638 – 11. Standard guide for preparation of biological samples for inorganic chemical analysis, Volume: 11.01.

[30] Ma K, Liu X and Dong X. *Methanobacterium beijingense* sp. nov., a novel methanogen isolated from anaerobic digesters. Int. J. Syst. Evol. Microbiol., 2005; 55: 325–329.

[31] Ferry JG. How to make a living by exhaling methane. Annu. Rev. Microbiol., 2010; 64: 453–73.

[32] Liu Y and Whitman WB. Metabolic, phylogenetic and ecological diversity of the methanogenic archaea. Ann. N. Y. Acad. Sci., 2008; 1125: 171–89.

[33] Maestrojuan GM and Boone DR. Characterization of *Methanosarcina barkeri* MST and 227, *Methanosarcina mazei* S-6T, and *Methanosarcina vacuolata* Z-76IT. Int. J. Syst. Evol. Microbiol., 1991; 41(2): 267–274.

[34] Prescott LM, Harley JP and Klein JP. Microbiology, 5th ed., McGrawHill publication, New York, 2002.

[35] Norrell SA and Messley KE. Principles and applications: Microbiology laboratory manual, 2nd ed., Upper Saddle River, Prentice Hall, New Jersey, 2003.

[36] Dridi B, Fardeau ML, Ollivier B, Raoult D and Drancourt M. The antimicrobial resistance pattern of cultured human methanogens reflects the unique phylogenetic position of archaea. J. Antimicrob. Chemother., 2011; 66: 2038–2044.

[37] Neil L, Schauer D, Brown P and James GF. Kinetics of formate metabolism in *Methanobacterium formicicum* and *Methanospirillum hungatei*. Appl. Environ. Microbiol., 1982; 44(3): 549-554.

[38] Schauer NL and Ferry JG. Metabolism of the formate in *Methanobacterium formicicum*. J. Bacteriol., 1980; 142: 800-807.

[39] Kim CC. Identification of rumen methanogens, and characterization of substrate requirements and measurement of hydrogen threshold. Massey University, New Zealand, 2012.

[40] Koga Y, Nishihara M, Morii H and Akagawa-Matsushita M. Ether polar lipids of methanogenic bacteria: structures, comparative aspects and biosyntheses. Microbiol. Rev., 1993; 57 (1): 164–182.

[41] Atlas RM and Bartha R. Microbial ecology- fundamental and applications, 4th ed., Pearson education, 2009.

[42] Bhardwaj KK and Gaur AC. The effect of HA on the growth and efficiency of nitrogen fixation of *Azotobacter ohroococum*. Folia, 1970; 15(5): 364-367.

[43] Goodwin J, Wase D and Forster C. Effects of nutrient limitation on the anaerobic up flow sludge blanket reactor. Enzyme Microb. Technol., 1990; 12: 877–884.

[44] Takashima M, Speece RE and Parkin GF. Mineral requirements for methane fermentation. Crit. Rev. Environ. Control, 1990; 19: 465–479.

[45] Zhang Y and Gladyshev VD. Comparative genomics of trace elements: emerging dynamic view of trace element utilization and function. Chem. Rev., 2009; 48(28): 4828–4861.

[46] Glass JB and Orphan VJ. Trace metal requirements for microbial enzymes involved in the production and consumption of methane and nitrous oxide. Front. Microbiol., 2012; 61: 1–20.

[47] Menyailo OV, Lehmann J, Cravo M, Silva D and Zech W. Soil microbial activities in tree-based cropping systems and natural forests of the Central Amazon, Brazil. Biol. Fertility of Soils, 2003; 38: 1–9.

To whom correspondence should be addressed: Dr. (Mrs) V A Selvi, Senior Scientist, CSIR-CIMFR, Industrial Biotechnology & Waste Utilization Division, PO. FRI 828108, Dhanbad, Jharkhand, India

Petroleum and Coal

Article **Open Access**

AIR TO LIQUID PERMEABILITY CONVERSION FORMULA PROVES EFFECTIVE FOR NIGER DELTA SANDSTONE RESERVOIR OFFSHORE NIGERIA

Augustine Okechukwu Chukwuemeka[1], Goodluck Amede[2], Mustapha Abdulsalam[2], Kazeem Alani Odunlami[2], Eganoba Shada Oyintinloy[2]*

[1] *Akwa Ibom State University Ikot Akpaden*
[2] *Institute of Oil, Gas and Energy, Kuban State Technological University Krasnodar, Russia*

Received July 3, 2018; Accepted September 21, 2018

Abstract

As the petroleum industry strives to make more accurate estimation of in-place amount of reservoir fluid and predict their recoverability/ recovery ratio by use of computer simulation, liquid permeability data is of non-negligible importance for both sandstone and carbonate reservoir. The liquid permeability of a reservoir rock could be determined either by a direct core sample analysis in the laboratory or estimated by using a correlation, which connects air permeability to liquid permeability. Given that the industry already has a large amount of air permeability data, the correlation approach for determining liquid permeability is less capital intensive since it eliminates the need for expensive laboratory procedures that would otherwise have been involved in determining this value. In this work, we tested the validity of two previously proposed conversion formulae (equation 2 and 4) on a set data acquired from the Niger Delta sandstone reservoir in Nigeria and some carbonate reservoirs in the Middle East. While equation 2 proves very effective in converting the Niger Delta sandstone reservoir's air permeability data to liquid permeability at various intervals and varied pressure with a maximum absolute average error of 9.65%, equation 4 is ineffective in doing same, giving a minimum average error of 153.7%. Applied to data from carbonate reservoir, equation 2 also became ineffective. In this case, giving a minimum average error value of 69.2%. The results are further indication that carbonate and sandstone reservoirs differ significantly in their nature and thus properties; and therefore, behave differently when subjected to same conditions; in this case conversion formulae of air permeability to liquid permeability.

Keywords: *Air permeability; Liquid permeability; core samples; carbonate reservoir; sandstone reservoir; Niger Delta.*

1. Introduction

The most common types of reservoir rocks are the sedimentary rocks. Sedimentary rocks are made up of sediments that have been compacted closely by natural forces. Reservoir sedimentary rocks are classified into sandstones and carbonates (limestone and dolomite). There are different types of sandstone reservoir rocks such as river sandstones, dune sandstones, shoreline sandstones, and delta sandstones. But of primary importance is the delta sandstone which is the type of sandstone located in the Niger delta region of Nigeria, where rock samples were studied and data acquired for this article.

The Niger delta sandstone, which is one of the largest oils producing delta sandstones in the world with an approximate 34.5 billion barrels of recoverable oil, and 94 trillion feet^3 of natural gas [1], was formed by a periodic deposition of sediments from rivers (Niger and Benue) flowing into the Atlantic Ocean and wave erosion. The fact that wave erosion shapes the delta makes the Niger delta a destructive type. The river being rich in organic sediments flows into the Atlantic Ocean and deposits its organic content at the bottom of the ocean which gets covered in mud and over time forms black shale which is a source rock where oil and gas can be formed. The formed oil and gas over time find their ways to the overlying sedimentary rocks and get trapped by the rock cap.

In the determination of the productivity and economic viability of reservoir rock, one of the major characteristics taken into consideration is its ability to allow fluid transmission through it: a phenomenon termed permeability, which is represented by the letter "K." Without sufficient formation permeability, oil and gas production, secondary and tertiary recovery, and carbon sequestration are impossible [3]. To determine the value of this property, core samples are taken to the laboratory for analysis.

For an oil reservoir, of course, it is most desirable that the permeability of the reservoir to oil (K_{oil}) is deter-mined to a high degree of accuracy. However, in some cases, a correlation approach becomes an important, if not the only method for estimating K_{oil} especially during simulation or modeling of the reservoir rock.

If a reliable formula is established for converting air to liquid permeability, the need for expensive experimental procedures for determining liquid permeability during core sample testing will not be necessary. This also will be of great value during side tracking for enhanced recovery in mature fields where liquid permeability data may not be available, saving time on reservoir re-evaluation before side-tracking. This approach cuts down on drilling time and resources, which is of great economic importance to drilling contractors.

Up to this point several attempts have been made in converting between gas and liquid permeability. In this article, core sample data from a sandstone reservoir located in Delta State of the Niger delta region mentioned above shall be used to test the validity of conversion formulae put forward in previous articles.

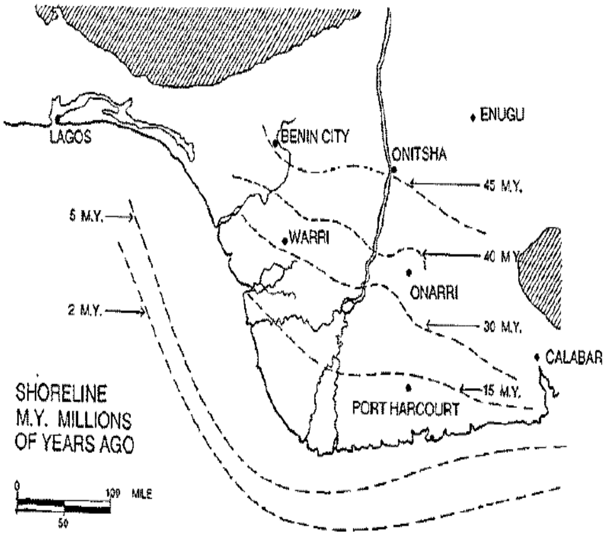

Fig.1. Present day and ancient shorelines of the Niger River Delta, Nigeria (*modified from Burke, 1972*) [2]

2. Overview of permeability and air to liquid permeabiity conversion formulae

With the discovery of crude oil and the increased use of its products as a primary source of energy for humanity came the need for detailed understanding of reservoir petrophysical properties such as porosity, permeability, relative permeability, capillarity, and saturation. Methods of measuring these properties in the laboratory have been developed with yet a constant attempt at improving on existing methods for enhanced accuracy.

The fundamental law of fluid motion in porous media is Darcy's law. The mathematical expression developed by Darcy in 1956 states that the velocity of a homogeneous fluid in a porous medium is proportional to the pressure gradient and inversely proportional to the fluid viscosity. For a horizontal linear system, this relationship is:

$$v = \frac{q}{A} = -\frac{k}{\mu}\frac{dp}{dx} \qquad (1)$$

where: v is the apparent velocity in centimeters per second and is equal to q/A, where q is the volumetric flow rate in cubic centimeters per second, and A is the total cross-sectional area of the rock in square centimeters.

In other words, A includes the area of the rock material as well as the area of the pore channels. The fluid viscosity, μ, is expressed in centipoise units, and the pressure gradient, dp/dx, is in atmospheres per centimeter, taken in the same direction as v and q. The proportionality constant, k, is the permeability of the rock expressed in Darcy units [4].

With increasing demand on the industry and a need to cut costs of data acquisition and improve reservoir fluid production efficiency, attempts have been made in the past to estimate permeability from porosity data. However, it has been proven that a direct proportionality does not always exist between porosity and permeability since a sample may have large pores which are either totally unconnected or have little interconnectivity thereby giving rise to low permeability.

By definition, any fluid can be used to measure absolute permeability. In practice, absolute permeability is measured by flowing air through a core sample that has been completely dried [5]. However, in laboratory conditions, replacing air with brine or oil in the experiment we get permeability to brine and permeability to oil respectively.

These forms of permeability vary both in the degree of difficulty and cost of measurement as well as their values; permeability to air, being the least capital intensive. In as much as permeability to air does give an idea of the reservoir rocks' permeability to liquid, depending totally on its value fails to provide a perfect prediction of reservoir fluid productivity especially if the liquid is to be produced from the reservoir. This is partly due to the fact that adhesion forces between air and reservoir vary significantly to that between reservoir fluid and the reservoir rock. At low rates, air permeability will be higher than brine permeability. This is because gas does not adhere to the pore walls as the liquid does, and the slippage of gases along the pore walls gives rise to an apparent dependence of permeability on pressure. This is called the Klinkenberg effect, and it is especially important in low-permeability rocks [6].

This, therefore, increases the need for a more accurate and cheaper method of either measuring or estimating the permeability of the reservoir to the liquid expected to be produced from it. In an attempt to solve this problem, a number of researchers have studied the possibility of deriving a formula which, when given the reservoir permeability to air, can estimate the reservoir's permeability to liquid with great accuracy.

In his study Macary [7], working on sandstone reservoirs from different parts of the world, applied equation (2) for estimating permeability to brine and equation (3) for permeability to oil of a sandstone reservoir from permeability to air with an average error value of 19.21%.

$$\text{Log } K_{brine}=1.0488 \text{ Log } K_{air} - 0.7222;\ R^2 = 0.85; \qquad (2)$$

$$\text{Log } K_{oil} = 1.0913 \text{ Log } K_{air} - 0.4946;\ R^2 = 0.95; \qquad (3)$$

Another researcher Al-Sudani *et al.* [8], in his study on reservoir samples, from different oil fields around the Middle East, applied equation (4).

$$K_l = A \cdot k_a \cdot \varphi^{0.09} \qquad (4)$$

where Ka and K_l are the air and liquid permeabilities respectively in millidarcy (md). (A = 0.73) for air permeability values less than unity, and (A = 1.002) for air permeability values greater than unity [8]. With this formula, the average absolute error was 4.16%. Further investigation into the nature of the reservoirs reveals that they are mostly carbonate reservoirs. This, however, was not clearly stated in work; giving an impression of general applicability.

As expected, the above formulae vary greatly given that carbonate and sandstone reservoirs differ in their composition and structure: from their chemical components to their physical characteristics. Table 1 below summarizes the differences between these reservoir rock types.

The two major differences between carbonate and sandstone reservoirs can be summarized as follows:

1. the site of sediment production,
2. the greater chemical activity of carbonate minerals [9-10].

Carbonate reservoirs which hold more than 60% of the world's oil are of immeasurable importance to the oil and gas industry and studying their productivity and permeability should take their porosity into account. This is because unlike sandstone reservoirs, carbonate reservoirs have varied forms of porosity. These include:

1. connected porosity existing between carbonate grains
2. vugs which are unconnected pores resulting from dissolution of calcite by water during diagenesis
3. fracture porosity which is caused by stress after deposition [11].

Table 1. Comparison of carbonate and sandstone reservoirs

Reservoir type	Main mineral composition	Site of sediment deposition	Wettability	Effect of diagenesis	Chemical activity of mineral
Carbonate	Calcite ($CaCO_3$)	authochthonous	Oil wet/mixed wet	Reduces porosity	Highly active
Sandstone	Sand (SiO_2)	allochthonous	Water wet	Hardly noticeable	Comparatively inactive

3. Data acquisition and methodology

The set of data used for calculations in this article includes air permeability, porosity, depth, and pressure. In acquiring data for this article, we examined core samples (Figures 3.-5.) from three different wells in the Niger Delta region of Nigeria, namely: Freeman1, Freeman 2ST1, and Freeman 3ST1. The samples were taken at different depths, and air permeability and porosity measurements were carried out at different pressures.

As to Freeman1 well the core samples were taken from the interval 8100ft to 8111ft and measurements were carried out at 1000psi. The resulting air permeability data fluctuate from 8160md to 4590md. At 3000psi from interval 8100ft to 8111ft measured air permeability data fluctuate between 7200md to 3280md. At 4500psi from interval 8100ft to 8111ft measured air permeability data fluctuate between 6640md to 2480md.

As to Freeman-2ST1 well the core samples were taken from the interval 9351ft to 9363ft and measurements were carried out at 1000psi. The resulting air permeability data fluctuate from 6280md to 1540md. At 3000psi from interval 9351ft to 9363ft measured air permeability data fluctuate between 4010md to 955md. At 4500psi from interval 9351ft to 9363ft measured air permeability data fluctuate between 3640md to 741md.

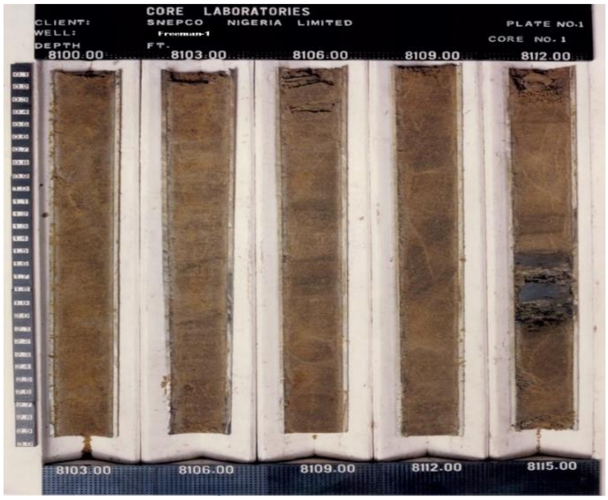

Fig.3. Core sample from FREEMAN 1 (8100-8111 ft).

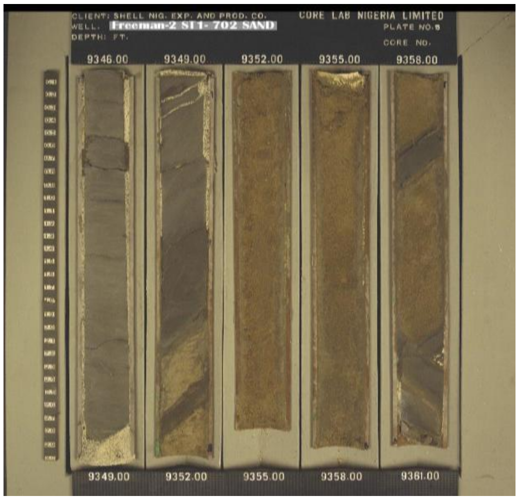

Fig.4. Core sample from FREEMAN 2 ST1 (9346-9361 ft)

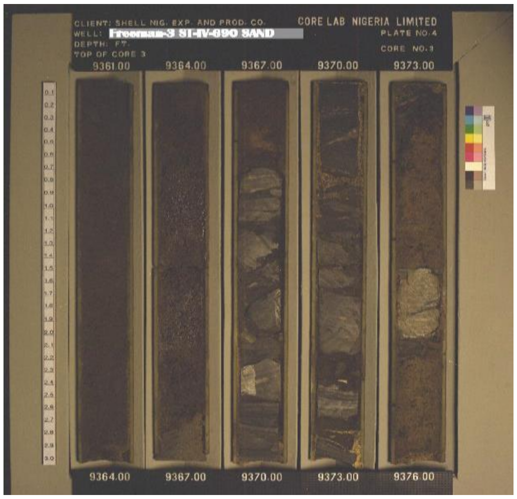

Fig.5. Core sample from FREEMAN 3ST1 (9361-9376 ft).

In addition to this, core sample data were taken from areas within the Middle East as stated by Al-Sudani *et al.* [7].

As to Freeman-3ST1 well the core samples were taken from the interval 9363ft to 9557ft and measurements were carried out at 1000psi. The resulting air permeability data fluctuate from 9610md to 321md. At 3000psi from interval 9363ft to 9557ft measured air permeability data fluctuate between 5610md to 226md. At 4500psi from interval 9363ft to 9557ft measured air permeability data fluctuate between 4760md to 139md.

We applied the conversion formulae by Macary [7] (equation 2) and (equation 4) by Al-Sudani *et al.* [8] to our data.

4. Results and discussion

Refer to appendix for tables and graphs.

The tables 2 to 10 show the result of applying equation 2 to core sample data from wells in the sandstone reservoir of the Niger delta region of Nigeria. Tables 11 to 13 show the results of applying equation 4 to the same reservoir, while table 14 and 15 show the results of applying equation 2 to data from carbonate reservoirs from locations within the Middle East.

The maximum average absolute percentage error for a chosen interval on the sandstone reservoirs from table 2 to 10 is 9.65%. This is obtained from Freeman 2ST1 at a pressure of 3000 psi. On the other hand, tables 11 to 13 show a minimum average absolute error of 153.7%; a very significant deviation reflecting the inapplicability of equation 4 to sandstone reservoirs. Tables 14 and 15 show a minimum average error of 69.2%.

The average absolute error observed when applying equation 2 to data from Freeman1 and freeman3st well decreases with an increase in the pressure of liquid permeability measurement from 1000psi to 4500psi. However, on applying equation 2 to data from Freeman2st1, the average absolute error increases with increasing pressure.

On each of the intervals examined under fixed pressure of measurement, the change in absolute error values does not follow a particular trend with increasing depth.

The above suggests that the accuracy of equation 2 for converting air to liquid permeability is affected by the depth from which the core sample was taken and the pressure at which laboratory liquid permeability data is conducted. The inconsistency in the pattern of their effects suggests the possibility of another factor (s) that affect the accuracy of the equation 2. The large error values encountered when equation 2 is applied to carbonate reservoirs suggest that the accuracy of the equation is affected by the chemical composition of the core sample.

In addition to the above, the large errors seen when equation 2 and equation 4 are applied to carbonate and sandstone reservoirs respectively underscores the difference between carbonates and sandstone reservoirs. None of the two equations can be universally applied to both sandstones and carbonate reservoirs. However, when applied independently to the sandstone reservoirs of Nigeria, equation 2 shows a high accuracy and extends its applicability beyond the areas on which it was first applied by Macary [7].

5. Limitations

While the data pool is not large enough to represent the entire reservoir structure of the Niger Delta region of Nigeria, by applying the formula at varying intervals and different pressure conditions, we have tried to accommodate varying reservoir conditions.

Bearing in mind that the main reservoir rock of the Niger Delta is the Agbada formation, it is reasonable to assume that the calculations fairly represent the applicability of this formula for converting air to liquid permeability in the Niger Delta. This work has calculated liquid permeability to brine and has made no attempt at calculating liquid permeability to oil. Though the formula for the later calculation is stated in work, laboratory data is not available to us, and we, therefore, cannot estimate errors.

6. Recommendations

To further solidify the veracity of this formula, more data from other sandstone reservoirs from around the world should be tested. In addition to this, further research should be carried out to understand the relationship between porosity and the accuracy of the formula and find the possible air permeability range for which the formula is most accurate. These recommendations are made on the following observations:

In Freeman1 well, the highest percentage error was 8.20% at a porosity of 32.5 and air permeability of 4160 milli Darcy at a pressure of 3000 psi while the lowest was -5.117% at a pressure of 3000 psi, permeability of 4760 mD and porosity of 31.1 such trends are visible throughout the entire tables.

With shale content likely not playing a significant role in the accuracy of the formula because of brine, the chances are that the formula has limitations to either porosity, pressure or air permeability values. These factors may act independently or in combination to affect the accuracy of the formula.

7. Conclusions

1. Equation 2 which was initially proven to be effective in Nubia “C” reservoir extends its validity and consistency to sandstone reservoir of the Niger Delta region of Nigeria under varying pressure conditions and reservoir depths.
2. Application of equation 4 to sandstone reservoir of the Niger delta region of Nigeria, showed a considerably large error margin in comparison to its application in some Iraqi and Egyptian oil fields with predominantly carbonate reservoir rocks.
3. Application of equation 2 to data from the Iraqi and Egyptian oil fields proves to be ineffective for conversion of air permeability to liquid permeability.
4. The above observations suggest that due to the varying nature of sandstone and carbonate reservoirs, a formula developed for converting air permeability to liquid permeability in carbonate reservoirs cannot be applied effectively for the same conversion in sandstone reservoirs and vice-versa.
5. This method of estimating liquid permeability from core sample air permeability data which has been proven effective in a good number of oil fields goes a long way to save cost and time. This is valuable for the development of new oil fields and revitalization of mature fields.

APPENDIX

APPLICATION OF EQUATION 2 TO SANDSTONE RESERVOIRS

(** where* Log Kbrine *is the calculated brine-permeability using equation 2)*

Table 2. Application of equation 2 to FREEMAN-1 at a depth range of (8100.15ft - 8111.05 ft) and pressure of 1000psi

well	depth	por_1000	ka_1000	kb_1000	Logkb_1000	Log Kbrine	error %	absolute error
Freeman-1	8100.15	33.8	4590	1166	3.06669855	3.118309145	-1.68294	1.68293666
Freeman-1	8101.00	34.6	4900	2360	3.372912	3.148077649	6.665883	6.665882598
Freeman-1	8102.00	34.2	7460	3185	3.50310944	3.339528482	4.669593	4.669593039
Freeman-1	8103.60	34.3	5990	1930	3.28555731	3.239565251	1.399825	1.399825155
Freeman-1	8104.90	34.3	6340	2529	3.40294883	3.265431214	4.041131	4.041130871
Freeman-1	8106.20	34.4	4620	1872	3.27230584	3.121276504	4.61538	4.615379724
Freeman-1	8106.95	34.3	5520	2891	3.46104809	3.202345705	7.474683	7.474683393
Freeman-1	8107.95	33.5	7690	1970	3.29446623	3.353359545	-1.78764	1.787643733
Freeman-1	8109.55	33.0	5920	1250	3.09691001	3.234211006	-4.43348	4.433483454
Freeman-1	8110.30	34.3	5460	1879	3.27392678	3.197367644	2.33845	2.338449867
Freeman-1	8111.05	33.1	8160	3678	3.56561172	3.380380639	5.194931	5.194931493
				average error	2.590528	4.027630908		

Table 3. Application of equation 2 to FREEMAN-1 at a depth range of (8100.15ft - 8111.05 ft) and pressure of 3000psi

well	depth	por_3000	ka_3000	kb_3000	Log kb_3000	Log Kbrine	error %	absolute error
Freeman-1	8100.15	32.0	3280	852	2.93043959	2.96524849	-1.18784	1.187838595
Freeman-1	8101.00	32.8	3690	1820	3.26007139	3.01889725	7.397818	7.397817608
Freeman-1	8102.00	32.0	5250	2083	3.31868927	3.17950308	4.194011	4.194010985
Freeman-1	8103.60	33.1	4250	1460	3.16435286	3.08325431	2.562879	2.562879351
Freeman-1	8104.90	31.8	4590	1659	3.21984639	3.11830914	3.153481	3.15348092
Freeman-1	8106.20	32.7	3470	1248	3.09621459	2.99089755	3.401477	3.401477168
Freeman-1	8106.95	32.5	4160	2230	3.34830486	3.07350509	8.207131	8.207131343
Freeman-1	8107.95	32.0	5620	1547	3.18949031	3.21052345	-0.65945	0.65945126
Freeman-1	8109.55	31.1	4760	960	2.98227123	3.13487417	-5.117	5.117004023
Freeman-1	8110.30	32.0	4560	1600	3.20411998	3.11532233	2.771359	2.77135863
Freeman-1	8111.05	31.8	7200	2705	3.43216727	3.32337032	3.16992	3.169919723
					average error	2.535798	3.802033601	

Table 4. Application of equation 2 to FREEMAN-1 at a depth range of (8100.15ft - 8111.05 ft) and pressure of 4500psi

well	depth	por_4500	ka_4500	kb_4500	Log kb_4500	Log Kbrine	error %	absolute error
Freeman-1	8100.15	30.6	2560	586	2.7678976	2.852362076	-3.05157	3.051574564
Freeman-1	8101.00	30.7	2920	1250	3.09691	2.912293535	5.961312	5.961312329
Freeman-1	8102.00	30.5	4670	1859	3.2692794	3.126179544	4.377107	4.377106646
Freeman-1	8103.60	31.6	2480	1005	3.0021661	2.837900923	5.471554	5.471554056
Freeman-1	8104.90	30.5	3360	1094	3.0390173	2.976224634	2.066217	2.066216846
Freeman-1	8106.20	30.6	2730	963	2.9836263	2.881647384	3.417952	3.417951616
Freeman-1	8106.95	30.2	3220	1654	3.2185355	2.956839238	8.130911	8.130911297
Freeman-1	8107.95	31.2	4320	1204	3.0806265	3.090695354	-0.32684	0.326844776
Freeman-1	8109.55	29.0	3000	860	2.9344985	2.924604772	0.337151	0.337150605
Freeman-1	8110.30	29.9	2540	1021	3.0090257	2.848789602	5.325183	5.325183426
Freeman-1	8111.05	30.8	6640	2069	3.3157605	3.286489882	0.882772	0.882772115
					average error		2.962885	3.57714348

Table 5. Application of equation 2 to FREEMAN-2ST1 at a depth range of (9351.20ft – 9364.20 ft) and pressure of 1000psi

well	depth	por_1000	ka_1000	kb_1000	Log kb_1000	Log Kbrine	error %	absolute error
Freeman-2ST1	9351.20	36.9	1540	454	2.65705585	2.620871732	1.361813	1.361812579
Freeman-2ST1	9352.25	32.3	4560	3420	3.53402611	3.115322327	11.84778	11.84778399
Freeman-2ST1	9353.10	32.9	6260	5090	3.70671778	3.259647161	12.06109	12.06109145
Freeman-2ST1	9354.00	30.2	4780	2910	3.46389299	3.136783978	9.443393	9.443392508
Freeman-2ST1	9356.85	33.6	3460	2000	3.30103	2.989583012	9.434843	9.434842569
Freeman-2ST1	9357.55	35.2	3310	1800	3.25527251	2.9693956	8.781965	8.781965405
Freeman-2ST1	9358.15	32.2	2460	1220	3.08635983	2.83421274	8.169724	8.169724341
Freeman-2ST1	9359.45	32.9	2480	1310	3.1172713	2.837900923	8.962017	8.962016658
Freeman-2ST1	9361.55	31.8	3260	1640	3.21484385	2.962462619	7.850497	7.850497288
Freeman-2ST1	9362.30	32.9	4170	2560	3.40823997	3.074598694	9.789254	9.789254109
Freeman-2ST1	9363.50	32.1	2670	1820	3.26007139	2.871525011	11.91834	11.91833953
Freeman-2ST1	9364.20	31.6	3370	1920	3.28330123	2.97757824	9.311451	9.311451109
					average error		9.077681	9.077680962

Table 6. Application of equation 2 to FREEMAN-2ST1 at a depth range of (9351.20ft – 9364.20 ft) and pressure of 3000psi

well	depth	por_3000	ka_3000	kb_3000	Logkb_3000	Log Kbrine	error %	absolute error
Freeman-2ST1	9351.20	34.2	955	379	2.57863921	2.40322754	6.80249	6.802489979
Freeman-2ST1	9352.25	31.1	3400	2100	3.32221929	2.98161509	10.25231	10.25230957
Freeman-2ST1	9353.10	29.9	3380	2380	3.37657696	2.97892784	11.77669	11.77669358
Freeman-2ST1	9354.00	29.4	4010	1310	3.1172713	3.05677782	1.940591	1.940590725
Freeman-2ST1	9356.85	31.8	2320	1380	3.13987909	2.8075238	10.58497	10.58497091
Freeman-2ST1	9357.55	32.4	2320	1060	3.02530587	2.8075238	7.198679	7.198679288
Freeman-2ST1	9358.15	30.1	1870	1120	3.04921802	2.70930748	11.14747	11.14746611
Freeman-2ST1	9359.45	30.2	1310	811	2.90902085	2.54719413	12.43809	12.438093
Freeman-2ST1	9361.55	30.4	2250	1330	3.12385164	2.79356902	10.57293	10.572929
Freeman-2ST1	9362.30	30.4	3040	1810	3.25767857	2.93063781	10.03907	10.03907393
Freeman-2ST1	9363.50	29.7	1840	1160	3.06445799	2.70194093	11.82973	11.82972838
Freeman-2ST1	9364.20	30.2	2420	1530	3.18469143	2.82674556	11.23958	11.23957792
					average error		9.651884	9.651883532

Table 7. Application of equation 2 to FREEMAN-2ST1 at a depth range of (9351.20ft – 9364.20 ft) and pressure of 4500psi

well	depth	por_4500	ka_4500	kb_4500	Log kb_4500	Log Kbrine	error %	absolute error
Freeman-2ST1	9351.20	32.0	741	353	2.5477747	2.287665337	10.20928	10.20927668
Freeman-2ST1	9352.25	30.8	3090	1610	3.2068259	2.938068453	8.380793	8.380792509
Freeman-2ST1	9353.10	28.6	2920	1610	3.2068259	2.912293535	9.184544	9.184544245
Freeman-2ST1	9354.00	28.6	3640	918	2.9628427	3.012683131	-1.68218	1.682183475
Freeman-2ST1	9356.85	30.8	1920	1120	3.049218	2.721326329	10.7533	10.75330434
Freeman-2ST1	9357.55	31.6	2070	901	2.9547248	2.755589698	6.739548	6.739547902
Freeman-2ST1	9358.15	29.1	1640	1070	3.0293838	2.649528228	12.53904	12.5390369
Freeman-2ST1	9359.45	29.0	960	639	2.8055009	2.405606069	14.25395	14.25395354
Freeman-2ST1	9361.55	29.8	2070	1220	3.0863598	2.755589698	10.71716	10.71716036
Freeman-2ST1	9362.30	29.6	2740	1550	3.1903317	2.88331279	9.623417	9.623416526
Freeman-2ST1	9363.50	28.3	1540	928	2.967548	2.620871732	11.68225	11.68224564
Freeman-2ST1	9364.20	28.8	2040	1350	3.1303338	2.74894012	12.1838	12.18380138
					average error		9.548741	9.829105293

Table 8. Application of equation 2 to FREEMAN-3ST1 at a depth range of (9363.65ft – 9557.30ft) and pressure of 1000psi

well	depth	por_1000	ka_1000	kb_1000	Log kb_1000	Log Kbrine	error %	absolute error
Freeman-3ST1	9363.65	28.1	321	39	1.59106461	1.9066224	-19.8331	19.8331274
Freeman-3ST1	9367.50	30.0	2040	811	2.90902085	2.7489401	5.50290	5.50290777
Freeman-3ST1	9373.50	33.3	9610	1500	3.17609126	3.4548802	-8.77774	8.77773990
Freeman-3ST1	9374.25	31.6	3440	1670	3.22271647	2.9869424	7.31600	7.31600122
Freeman-3ST1	9547.65	33.4	2540	1020	3.00860017	2.8487896	5.31179	5.31179155
Freeman-3ST1	9549.20	30.8	3180	2150	3.33243846	2.9511455	11.4418	11.4418586
Freeman-3ST1	9550.20	32.5	3580	1850	3.26717173	3.0051125	8.02098	8.02098058
Freeman-3ST1	9550.60	30.9	3100	684	2.8350561	2.9395401	-3.68543	3.68543122
Freeman-3ST1	9554.40	33.0	4040	2220	3.34635297	3.0601727	8.55200	8.55200276
Freeman-3ST1	9555.20	25.6	3580	2380	3.37657696	3.0051125	11.0012	11.0012134
Freeman-3ST1	9556.20	32.3	4400	2140	3.33041377	3.0990531	6.94690	6.94690275
Freeman-3ST1	9557.30	32.4	5520	2770	3.44247977	3.2023457	6.97561	6.97561294
					average error		3.23108	8.61379751

Table 9. Application of equation 2 to FREEMAN-3ST1 at a depth range of (9363.65ft – 9557.30ft) and pressure of 3000psi

Freeman-3ST1	9363.65	26.2	226	29	1.462398	1.7467889	-19.4469	19.44689021
Freeman-3ST1	9367.50	27.8	1460	541	2.73319727	2.5965732	4.99868	4.998687497
Freeman-3ST1	9373.50	29.8	5610	928	2.96754798	3.2097122	-8.16042	8.160416432
Freeman-3ST1	9374.25	29.6	2480	861	2.93500315	2.8379009	3.30842	3.308419909
Freeman-3ST1	9547.65	32.5	2290	770	2.88649073	2.8015954	2.94112	2.941123994
Freeman-3ST1	9549.20	30.1	2650	1390	3.1430148	2.8681002	8.74684	8.746841652
Freeman-3ST1	9550.20	30.3	3100	1210	3.08278537	2.9395401	4.64661	4.646616894
Freeman-3ST1	9550.60	30.0	2580	570	2.75587486	2.8559067	-3.62977	3.629769027
Freeman-3ST1	9554.40	31.9	3530	1750	3.24303805	2.9987061	7.53404	7.534044745
Freeman-3ST1	9555.20	24.4	3100	1490	3.17318627	2.9395401	7.36313	7.36313926
Freeman-3ST1	9556.20	31.8	4210	2100	3.32221929	3.0789470	7.32258	7.322582016
Freeman-3ST1	9557.30	31.9	5100	2240	3.35024802	3.1662996	5.49059	5.490591044
					average error		1.75958	6.965760223

Table 10. Application of equation 2 to FREEMAN-3ST1 at a depth range of (9363.65ft – 9557.30ft) and pressure of 4500psi

well	depth	por_4500	ka_4500	kb_4500	Log kb_4500	Log Kbrine	error %	absolute error
Freeman-3ST1	9363.65	23.5	139	25	1.39794	1.52539392	-9.11727	9.11726633
Freeman-3ST1	9367.50	25.1	637	246	2.3909351	2.21878143	7.20026	7.20026528
Freeman-3ST1	9373.50	29.0	4760	750	2.8750613	3.13487417	-9.03678	9.03677817
Freeman-3ST1	9374.25	27.0	1520	636	2.8034571	2.61491755	6.72525	6.72525217
Freeman-3ST1	9547.65	31.5	1840	520	2.7160033	2.70194093	0.51776	0.51776117
Freeman-3ST1	9549.20	29.2	2610	1020	3.0086002	2.86117256	4.90020	4.90020605
Freeman-3ST1	9550.20	29.8	2830	920	2.9637878	2.89803361	2.21858	2.21858707
Freeman-3ST1	9550.60	28.6	2270	315	2.4983106	2.79759999	-11.9797	11.9796702
Freeman-3ST1	9554.40	30.5	2930	1100	3.0413927	2.91385076	4.19353	4.19353691
Freeman-3ST1	9555.20	24.3	2830	1090	3.0374265	2.89803361	4.58917	4.58917720
Freeman-3ST1	9556.20	30.9	3820	1050	3.0211893	3.03466805	-0.44614	0.44614072
Freeman-3ST1	9557.30	30.2	4090	1240	3.0934217	3.06577540	0.89371	0.89371196
					average error		0.05488	5.15152944

APPLICATION OF EQUATION 4 TO SANDSTONE RESERVOIRS

[where* K_l *is liquid (brine) permeability]*

Table 11. Application of equation 4 to FREEMAN-1 at a depth range of (8100.15ft – 8111.05ft) and pressure of 1000psi.

well	depth	por_1000	ka_1000	kb_1000	K_l	error %	absolute error
Freeman-1	8100.15	33.8	4590	1166	6313.684995	-441.482	441.4824181
Freeman-1	8101.00	34.6	4900	2360	6754.304728	-186.199	186.1993529
Freeman-1	8102.00	34.2	7460	3185	10272.32848	-222.522	222.5220874
Freeman-1	8103.60	34.3	5990	1930	8250.324201	-327.478	327.4779379
Freeman-1	8104.90	34.3	6340	2529	8732.396567	-245.29	245.2904929
Freeman-1	8106.20	34.4	4620	1872	6365.022701	-240.012	240.0118964
Freeman-1	8106.95	34.3	5520	2891	7602.969881	-162.988	162.9875435
Freeman-1	8107.95	33.5	7690	1970	10569.34548	-436.515	436.5149991
Freeman-1	8109.55	33.0	5920	1250	8125.604554	-550.048	550.0483643
Freeman-1	8110.30	34.3	5460	1879	7520.328904	-300.23	300.2303834
Freeman-1	8111.05	33.1	8160	3678	11203.20801	-204.601	204.6005441
					average error	-301.579	301.5787291

Table 12. Application of equation 4 to FREEMAN-2ST1 at a depth range of (9315.20ft – 9364.20ft) and pressure of 3000psi

well	depth	por_3000	ka_3000	kb_3000	K_l	error %	absolute error
Freeman-2ST1	9351.20	34.2	955	379	1315.023284	-246.972	246.9718428
Freeman-2ST1	9352.25	31.1	3400	2100	4642.184593	-121.056	121.0564092
Freeman-2ST1	9353.10	29.9	3380	2380	4598.273815	-93.2048	93.20478213
Freeman-2ST1	9354.00	29.4	4010	1310	5447.074985	-315.807	315.8072508
Freeman-2ST1	9356.85	31.8	2320	1380	3173.760475	-129.983	129.9826431
Freeman-2ST1	9357.55	32.4	2320	1060	3179.10416	-199.915	199.9154868
Freeman-2ST1	9358.15	30.1	1870	1120	2545.542267	-127.281	127.2805596
Freeman-2ST1	9359.45	30.2	1310	811	1783.77323	-119.947	119.9473774
Freeman-2ST1	9361.55	30.4	2250	1330	3065.103585	-130.459	130.4589162
Freeman-2ST1	9362.30	30.4	3040	1810	4141.903036	-128.834	128.8344219
Freeman-2ST1	9363.50	29.7	1840	1160	2501.690763	-115.663	115.6629968
Freeman-2ST1	9364.20	30.2	2420	1530	3295.361844	-115.383	115.383127
					average error	-153.709	153.7088178

Table 13. Application of equation 4 to FREEMAN-2ST1 at a depth range of (9315.20ft – 9364.20ft) and pressure of 4500psi

well	depth	por_3000	ka_4500	kb_4500	K_l	error %	absolute error
Freeman-2ST1	9351.20	34.2	741	353	1020.34791	-189.05	189.0503993
Freeman-2ST1	9352.25	31.1	3090	1610	4218.926586	-162.045	162.0451295
Freeman-2ST1	9353.10	29.9	2920	1610	3972.473236	-146.737	146.7374681
Freeman-2ST1	9354.00	29.4	3640	918	4944.477044	-438.614	438.6140571
Freeman-2ST1	9356.85	31.8	1920	1120	2626.560393	-134.514	134.5143208
Freeman-2ST1	9357.55	32.4	2070	901	2836.528281	-214.82	214.8200089
Freeman-2ST1	9358.15	30.1	1640	1070	2232.454181	-108.641	108.6405777
Freeman-2ST1	9359.45	30.2	960	639	1307.192596	-104.568	104.5684814
Freeman-2ST1	9361.55	30.4	2070	1220	2819.895298	-131.139	131.1389589
Freeman-2ST1	9362.30	30.4	2740	1550	3733.162605	-140.849	140.8492003
Freeman-2ST1	9363.50	29.7	1540	928	2093.806399	-125.626	125.6256896
Freeman-2ST1	9364.20	30.2	2040	1350	2777.908331	-105.771	105.7709875
					average error	-166.865	166.8646066

APPLICATION OF EQUATION 2 TO CARBONATE RESERVOIRS

Table 14. Application of equation 2 to data from carbonate reservoirs from locations within the Middle East

Measured K_{air} md	porosity	laboratory K_{liquid}. md	log K_{liquid}.	calculated K_{liquid}. Using equation 4.	calculated K_{liquid}. Using equation 2.	% error
6.9	0.23	5.2	0.716003344	5.12	1.437424114	72.35723
5.1	0.189	3.8	0.579783597	3.62	1.046886503	72.45036
158	0.226	142	2.152288344	147.49	38.34878005	72.99382
34	0.233	28	1.447158031	28.36	7.656232056	72.65631
23.7	0.247	20	1.301029996	19.34	5.243678607	73.78161
64.2	0.2	55	1.740362689	55.4	14.91223494	72.88685
6	0.283	4.5	0.653212514	4.47	1.24143799	72.41249
4.4	0.255	3.3	0.51851394	3.174	0.896712383	72.8269
5.6	0.242	4.2	0.62324929	4.09	1.154780928	72.50522
12.8	0.184	10	1	9.71	2.748158748	72.51841
25	0.188	21	1.322219295	19.99	5.545739698	73.59172
8.4	0.209	6.5	0.812913357	6.25	1.766786675	72.81867
					average error	72.81663

Table 15. Application of equation 2 to data from carbonate reservoirs from locations within the Middle East

Measured K_{air} md	porosity	laboratory K_{liquid}. md	log K_{liquid}.	calculated K_{liquid}. Using equation 4.	calculated K_{liquid}. Using equation 2.	% error
1275.9	0.189	1150.73	3.060973435	1100.5	342.9102677	70.20063
160	0.185	122.714	2.088894113	137.7	38.85805314	68.33446
408.43	0.153	337.728	2.528567068	345.6	103.8341411	69.2551
48.72	0.166	34.1326	1.533169371	41.5	11.16522283	67.28868
52.273	0.174	36.803	1.565883222	44.7	12.02068907	67.33775
1950.7	0.166	1821.34	3.260391026	1662.9	535.2439654	70.61263
2497.4	0.152	2379.81	3.376542285	2112.1	693.5623781	70.8564
1147	0.168	1027.14	3.011629642	978.9	306.6691664	70.14339
1169.2	0.21	1046.08	3.019564899	1018	312.8972747	70.08859
146.24	0.189	111.396	2.046869597	126.1	35.36074512	68.25672
391.34	0.176	322.014	2.507874754	335.4	99.28208466	69.16839
309.07	0.183	249.605	2.397253281	265.8	77.51247897	68.94594
					average error	69.20739

Acknowledgement

We are grateful to the Department of Petroleum Resources, Nigeria and Shell Nigeria Exploration and Production Cooperation for making some of the resources used for this article available to us.

References

[1] Tuttle MLW, Charpentier RR, and Brownfield ME. The Niger Delta Petroleum System: Niger Delta Province, Nigeria, Cameroon, and Equatorial Guinea, Africa, United States Geological Survey, Open-File Report 99-50-H, 1999.

[2] Hyne NJ. Non-technical guide to petroleum geology, exploration, drilling and production. ISBN-13: 978-0878148233 2001.

[3] http://www.slb.com/news/inside_news/2015/2015_0130_defining_permeability.aspx.

[4] Ahmed T and McKinney PD. Advanced Reservoir Engineering. ISBN-13: 978-0750677332.

[5] Ezekwe N. 2010. Petroleum Reservoir Engineering practice. ISBN-13: 978-0137152834.

[6] Lucia FJ. Carbonate reservoir characterization. Berlin, Springer, ISBN 978-3-540-72740-8.

[7] Macary SM. Conversion of Air Permeability to Liquid Permeabilities Extracts Huge Source of Information for Reservoir Studies. SPE 53113-MS, 1999, Egyptian Petroleum Research Institute. http://dx.doi.org/10.2118/53113-MS.

[8] Al-Sudani JA, Kaiser R and Al-Rubeai SJ., 2014. Estimation Liquid Permeability Using Air Permeability Laboratory Data. Iraqi Journal of Chemical and Petroleum Engineering, 2014; 15(1): 43- 50.

[9] Choquette PW, and James NP. 1987. Diagenesis in limestones. The deep burial environment: Geoscience Canada, 1987; 14: 3– 35.

[10] Moore CH. 2001. Carbonate reservoirs porosity evolution and diagenesis in a sequence stratigraphic framework. Amsterdam, Elsevier, ISBN: 9780444508386.

[11] Schlumberger, 2007. Carbonate reservoirs, Meeting Unique challenges to maximize recovery. http://www.slb.com/~/media/Files/industry_challenges/carbonates/brochures/cb_carbonate_reservoirs_07os003.pdf.

[12] Ehrenberg SN and Nadeau PH. Sandstone vs. carbonate petroleum reservoirs: A global perspective on porosity-depth and porosity-permeability relationships. AAPG Bulletin, 2005; 89(4): 435–445.

To whom correspondence should be addressed: Augustine Okechukwu Chukwuemeka, Akwa Ibom State University Ikot Akpaden, Nigeria

Petroleum and Coal

Article **Open Access**

ENHANCING THE PERFORMANCE OF LOCAL CEMENT AS AN ALTERNATIVE FOR OIL AND GAS WELL CEMENTING OPERATION

Eric Broni-Bediako, Richard Amorin

Department of Petroleum Engineering, University of Mines and Technology, Ghana

Received June 23, 2018; Accepted September 3, 2018

Abstract

The biggest identified problems with the use of locally manufactured construction grade cement in Ghana are; unpredictable thickening time, premature gelation of cement slurries and low strength development as compared to imported cementing samples. Locally manufactured cement hardly meet the physical properties exhibited by the imported cement sample, but with proper design of local cement, the important properties required for oil well cementing could be attained. This research focuses mainly on enhancing the physical properties of local cement using oil well cement additives. Laboratory investigations on both local and imported cement to determine physical properties such as thickening time, fluid loss, free fluid and rheology were conducted at bottom hole circulating temperature of 66°C (150°F). The cement slurries were tested in accordance with API Specification 10A and API Recommended Practice 10B. The results show that with the right selection of additives, local cement (CEM A) could be used as an alternative for imported class G cement for cementing operations in terms of the physical properties tested. By working in conjunction with local cement manufactures, oil companies can help ensure local cement maintains consistency.

***Keywords**: Additives; Free Fluid; Fluid Loss; Rheology; Thickening Time.*

1. Introduction

Oil well cementing involves placing cement slurry from the surface to several thousands of feet below the surface of the earth [1-2]. The cement slurry which consists mainly of cement, water and performance-controlling additives [3] is pumped down the casing and up the annulus, where it is allowed to set and harden [4]. In oil well cementing, less error is tolerated as compared to conventional construction work. Oil well cement slurry must, therefore, be carefully designed to meet technical requirements such as optimum thickening time, low viscosity, low free fluid, adequate strength, fluid loss control, high sulphate resistance and overall high durability [5-6]. Oil well cement are formulated to provide the required physical properties at the downhole conditions of pressure and temperature. The high temperatures and pressures encountered downhole impose severe requirements on the setting behaviour of the oil well cement. The premature setting can have disastrous consequences; whereas too long setting times can cause financial losses due to excessive "wait-on-cement (WOC)" times [6]. Due to the important role of cement in oil and gas cementing operations, the oil industry purchases cements manufactured in accordance with American Petroleum Institute (API) specifications for cementing operations. This special class of cement is called Oil Well Cements (OWCs).

In spite of the usage of API specified cement, conventional construction (local) cement have been used for oil well cementing in many parts of the world for various reasons such cost, availability and logistics [7]. However, the situation is not the same in Ghana as all the produced cement goes into the building and the road sectors [8] of the economy. The biggest identified problems with the use of locally manufactured construction grade cement in Ghana are; unpredictable thickening time, premature gelation of cement slurries and low strength development as compared to imported cementing samples [5, 9]. Locally manufactured cement hardly meet the physical properties exhibited by the imported cement sample. However, with the right formulation of locally manufactured cement, the important properties required for oil well cementing would be attained. This research work, therefore, focuses mainly on designing cement slurry using locally manufactured cement and cement additives as alternative for oil and gas cementing operations in Ghana.

2. Universal cement system(UCS) additive

For several years, a service company has identified the value that could be created for its customers by the use of locally manufactured cement, particularly in areas remote from locations where oil well cement are manufactured. To overcome the problems associated with local cement, the service company developed and tested a product that allows non-API specification (local cement) to be used in oil well cementing designs and application and also manages problems associated with the local cement. This product is commonly referred to as Universal Cement System (UCS) additive. In the majority of cement tested worldwide, UCS additive has allowed the formulation of consistent slurry recipes with locally manufactured cement at concentrations that make it economically desirable. The physical properties that a UCS additive can provide include enhances compressive strength, controls fluid loss, controls rheology, imparts chemical resistance, controls premature gelation, and allows use in freshwater and seawater [10].

UCS additive can be added to cement that might not normally be usable in oil well cementing, such as those often produced in developing countries, those with high alkali sulphate and high free-lime content, and ASTM Type I/II construction-grade cement. UCS additive may be available in liquid or powder form (Fig. 1). The application of the powdery UCS is always preblended with the dry cement and not added directly to the mixing water for maximum results. The UCS additives can counteract the difference of the physical properties often seen between different batches of locally manufactured cement, reducing the high gelation effects, imparting chemical resistance, allowing their use at temperatures up to 250°F. The application of Gelation Control Additive (GCA) or UCS-additive of 1% by weight of cement (bwoc) has shown resistance to sulphate attack similar to that of a class G oil well cement. The sulphate resistance testing was based on ASTM C102. The untreated, non-resistant cement used in the study expanded and showed sulphate attack during a 90 day test period [10].

Fig. 1 UCS Additive in Powder and Liquid Form [10]

3. Materials and methods

3.1. Materials

A brand of cement available on the Ghanaian market and commonly used by Ghanaians for construction purposes was purchased from retail outlets for the cement slurry formulation. Fresh water from a company's laboratory was used for the cement slurry formation. Additives such as defoamer, fluid loss additive, retarder and Universal Cement System (UCS) were obtained from a service company in Port Harcourt, Nigeria. The additives used in the cement composition were selected based on the test pressure and temperature conditions. UCS was employed to reduce the premature gelation or to improve upon the rheological properties of the local cement slurry at elevated temperature. Retarder and fluid loss additive were used to increase the setting time and control fluid loss of the cement slurry at high pressures and temperatures respectively. Defoamer was also used to remove slurry foam during cement slurry formulation.

3.2. Experimental design

Laboratory experiments were performed on local CEM A to formulate a cement slurry recipe for oil and gas well cementing operations. The locally manufactured CEM A was blended with different percentages of additives to deal with the premature gelation associated with locally manufactured cement at high temperature. The cement slurry was tested at BHCT of 150°F. The cement slurry and specimen preparation were carried out by closely following API Specification 10A. The physical properties were determined by closely following API Specification 10A, and API Recommended Practice 10B [2, 11]. The physical properties tests conducted included thickening time, free fluid, fluid loss and rheology of the cement slurry (Table 1). Two modified cement slurries for CEM A were also tested for physical properties using the test conditions and slurry composition presented in Table 1.

Table 1 Experimental conditions and slurry composition

Test Condition	Units	CEM G	CEM A	Modified CEM A1	Modified CEM A2
BHST	°F	190	190	190	190
BHCT	°F	150	150	150	150
BHP	psi	7900	7900	7900	7900
Heat Up Time	min	53	53	53	53
Water					
Water Type	-	Fresh Water	Fresh Water	Fresh Water	Fresh Water
Water Requirement	gal/sk	5.03	5.03	5.03	5.03
Chloride Content	ppm	400	400	400	400
Cement					
Cement Weight	% bwoc	100	100	100	100
Slurry Weight	ppg	15.8	15.8	15.8	15.8
Mixing Fluid	gal/sk	5.11	5.11	5.11	5.11
Yield	cu.ft/sk	1.16	1.16	1.16	1.16
Additives					
UCS	% bwoc	-	-	1	1
Defoamer	gal/sk	0.02	0.02	0.02	0.02
Fluid Loss Agent	% bwoc	0.5	0.5	0.5	0.5
Retarder	% bwoc	0.18	0.18	0.3	0.18

3.3. Thickening time testing

The results of the laboratory thickening time tests provide an indication of the length of time that cement slurry remains pumpable [12]. That is, the time after initial mixing when the cement can no longer be pumped [13]. The consistency of cement slurry is expressed in Bearden units of consistency (Bc) [12]. The Thickening Time (TT) test was performed in a High-Pressure High-Temperature (HPHT) Consistometer that is usually rated at pressure up to 30 000 psi and temperatures up to 400°F. The cement slurry was mixed according to API procedures and then placed in a slurry cup into the consistometer for testing. The testing pressure and temperature were controlled to simulate the conditions the slurry will encounter in the well. The test concluded when the slurry reached a consistency considered unpumpable in the well. The maximum consistency during 15 minutes to 30 minutes after the initiation of the test and the time for the cement slurry to reach the consistency of 100 Bc were recorded [2, 11].

3.4. Free fluid testing

The purpose of a free fluid test is to measure the excess fluid in the cement slurry not required to fully mix the dry cement blend [14]. The cement slurries were preconditioned in a Model 165AT Atmospheric Consistometer for thirty minutes. The preconditioned slurry was remixed within 10 seconds and poured into a 500 ml graduated flask according to API Specification 10A [2]. The mouth of the flask was sealed and then placed on a vibration free surface for 2 hours. The slurry was then examined for any free fluid on the top of the cement column. This free fluid was decanted and measured with a syringe to determine the percent of free water (φ) based on the weight and the specific gravity of the cement using Equation (1).

$$\varphi = (V_{FF}) \text{ x } S_g \text{ x } \frac{100}{m_S} \tag{1}$$

where V_{FF} is the volume of free fluid collected (supernatant fluid), expressed in millilitres; S_g is the specific gravity, and m_s is the initially recorded mass of the slurry in grams.

3.5. Fluid Loss Testing

Fluid loss tests are conducted to establish API procedures to help determine the relative amount of fluid loss that will occur in a given cement slurry. The amount of filtrate lost by the fluid under bottomhole temperature and 1 000 psi differential pressure is measured in this test [11]. A differential pressure normally exists to prevent fluid flow from the formation into the wellbore, and most formations have pore throats that are too small to allow cement particles to invade the formation. However, if a differential pressure exists into the formation, the water in the cement slurry can leak into the formation. After conditioning the slurry at the Bottomhole Circulating Temperature (BHCT) for thirty (30) minutes, the slurry was placed in the fluid cell, and a differential pressure of 1 000 psi was applied across the 325 mesh screen for about thirty minutes. For tests that "blowout" before 30 minutes in API fluid loss was determined using Equation (2).

$$\text{Fluid Loss at } Q_{30\text{mins}} = \frac{2 \text{ x } Q_t \text{ x } 5.477}{\sqrt{T}} \tag{2}$$

where Q_t is the volume (mL) of filtrate collected at the Time T (mins) of the "blowout".

3.6. Rheology testing

Rheology of cement slurries is of great importance for the design, construction and quality of primary cementing. Knowledge of the rheological properties is necessary to assess the possibilities for mixing and pumping cement slurries, determine the relationship of pressure to depth during and after repression, return circulation to calculate the phase of "free fall", forecasts temperature profile during pumping a cement slurry, design and capacity required for optimal suppression of cement puree [15]. According to Shahriar [16], the fundamental knowledge of oil well cement slurry rheology is necessary to evaluate the ability to remove mud and optimise slurry placement. Incomplete mud removal can result in poor cement bonding, zone communication and ineffective stimulation treatment [17]. The Rheology of fluids also has a major effect on solids setting and free fluid properties and also on the friction pressures [14]. Because rheological testing is typically conducted at atmospheric pressure, the maximum temperature is limited to about 190°F [11]. The shear stress and shear rate behaviour of the slurry at different temperatures was measured in this test. The rheological properties of the fluid samples used in this study were measured using Fan Viscometer Model 35A. The properties of interest studied included Plastic Viscosity (μ_p) and Yield Point (τ_o). The plastic viscosity and the yield point value were obtained using Equations (3) and (4) respectively [20-21]

$$\mu_p = 1.5(\theta_{300} - \theta_{100}) \tag{3}$$

$$\tau_o = \theta_{300} - \mu_p \tag{4}$$

where θ_{300} is 300 rpm dial reading, and θ_{100} is 100 rpm dial reading.

4. Results and discussions

4.1. Thickening time analysis

According to Broni-Bediako *et al.* [5], locally manufactured cement in Ghana pump shorter as compared to imported class G cement and would require more additives to bring up the thickening time of the local cement. Fig. 1 showed the results of the thickening time of locally manufactured CEM A and imported class G cement mixed with various concentrations of retarder, defoamer, UCS and fluid loss additive and tested at 1 2250 ft, 7 900 psi and 150°F (Table 1). From Figure 1, it could be seen that the modified local cement appeared to have improved and better thickening time than imported class G. The thickening times of locally modified local cement showed longer setting with a slow increase in consistency of the cement slurry. This gives an idea that with the right concentration of additives, locally manufactured cement could be used at elevated temperatures without the cement slurry setting prematurely. The improvement in the value of the thickening time could be due to the right concentrations of UCS that were blended with the local cement. According to Hibbeler *et al.* [7], in choosing between available class G cement or considering the option of using a construction grade cement, the primary performance factors of concern are retarder response and early gelation of the cement slurry.

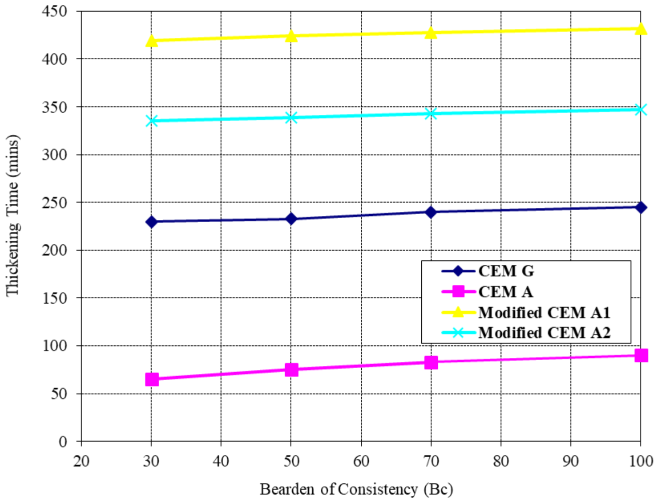

Fig. 1. Thickening time vs. consistency at 150°F

From the result presented in Fig. 1, local cement responded very well to retarder concentrations. Furthermore, the locally manufactured cement was compatible with a fluid loss agent, defoamer and universal cement system used for the cement slurry design. The modified CEM A1 with a retarder of 0.3 by weight of cement (%bwoc), a fluid loss additive of 0.5 %bwoc, defoamer of 0.02 %bwoc and UCS of 1% bwoc (Table 1), the local cement appeared to pump longer and better than the imported class G cement (Fig. 1). The end of thickening time test was considered to be 70 Bc. At the consistency of 70 Bc, the modified CEM A1 pumped about 188 minutes (3 hrs: 8 mins)longer than the imported class G. The results of the thickening time showed that the modified cement slurry had been overdesigned when compared with the imported class G cement. However, the results revealed that the modified locally manufactured cement CEM A1 could be used for cementing oil wells which require operating time of 7 hours or less.

From Fig. 1, the modified CEM A2 appeared to have a better slurry design than the modified CEM A1 when both are compared with the imported class G cement. The modified CEM A2 with a retarder of 0.18 %bwoc, a fluid loss additive of 0.5 %bwoc, defoamer of 0.02 %bwoc and UCS of 1 %bwoc (Table 1), proved to pumped shorter than modified CEM A1. All the concentrations of additives used in the modified CEM A1 were maintained for modified CEM 2 except the retarder's concentration. The addition of UCS of 1 %bwoc and a retarder of 0.18 %bwoc gave a better thickening time results which compared favourably with the imported class G cement. At the consistency of 70 Bc, the modified CEM A2 pumped about 343 minutes (5 hrs: 43 mins) but 85 minutes (1 hr: 25 mins) shorter than the modified CEM A1 (Fig. 1). Comparing the modified CEM A2 and imported cement, the modified CEM A2 pumped 104 minutes (1 hr: 43 mins) longer than imported cement. The increase in the thickening time values was due to the addition of the right concentration of UCS as the UCS played an imperative role by acting as a retarder in addition to its primary function. Normally, a contingency time of 1 hour is added to the pumping time to allow for possible equipment failure [23]. Therefore, modified CEM A2, would be suitable for 283 minutes (4 hrs: 43 mins) cementing job.

4.2. Free fluid and fluid loss analysis

When cement is setting, free fluid separates from the slurry, settling at the top of the cement column or in small water pockets if the well deviates. This water can create channels while moving at the top of cement, resulting in a poor cement bond or casing failure if the water pockets are between the casing to the casing annulus [14]. The results of free fluid between the locally manufactured cement and imported class G at 150°F and 7 900 psi (Table 1) is presented in Table 2. The modified CEM A1 and A2 proved to have no free fluid when mixed with a fluid loss additive at 0.5 %bwoc. In terms of fluid loss, both the imported class G and modified cement samples compared favourably (Table 2). According to Anon [24], under standard laboratory conditions (1 000 psi filter pressure, with a 325 mesh filter) a slurry for a squeeze job and primary cement job should give a fluid loss of 50-200 cc and 250-400 cc within thirty (30) minutes respectively. The results showed at both modified CEM A1 and CEM A2 could be used for squeeze cementing and primary cementing operation per the recommended value by Anon [24].

Again, the results compared favourably with the recommendation by Boškovic *et al*. in 2013. According to Boškovic *et al*. [15], fluid loss for class G cement is not precisely defined by API Specification, but they recommended that within thirty (30) minutes test period up to 1000 cc, 500 cc, less or equal to 100 cc and 30-50 cc respectively is vital for cementing technical casing string, production casing string, liner casing and gas wells. From the results, the modified CEM A1 and CEM A2 could be used for cementing technical and production casing string.

Table 2. Fluid Loss and Free Fluid at 150°F

Cement Type	CEM G	CEM A	Modified CEM A1	Modified CEM A2
Fluid Loss (cc/30 minutes)	90	70	190	136
Free Fluid @ 90 deg incl. (%)	0	0	0	0

4.3. Rheology analysis

The rheological properties of oil well cement (OWC) slurries are important in assuring that such slurries can be mixed at the surface and pumped into the well with minimum pressure drop, thereby achieving effective well cementing operation [22, 23]. The basic reason for determination of rheological properties was to predict plastic viscosity and yield point values. In general, the problem of pumping cement slurry through wellbore occurs when plastic viscosity becomes high [25]. The introduction of 1% bwoc UCS additive to the local cement produced slurries that were pumpable with viscosities that compared favourably with that of the imported class G cement at 150°F. The result of rheological properties of modified local cement and imported class G cement at 150°F is presented in Table 3.

Table 3. Rheological properties of modified local and imported cement samples at 150°F

Rheology @ BHCT of 150 °F	CEM G	CEM A	Modified CEM A1	Modified CEM A2
			Dial Reading	
300 rpm	158	298	100	73
200 rpm	125	240	72	52
100 rpm	90	172	42	31
6 rpm	35	86	5	4
3 rpm	27	71	3	3
Plastic viscosity (cp)	**102**	**189**	**87**	**63**
Yield point (lb/100 ft^2)	**56**	**109**	**13**	**10**

At a BHCT of 150°F, the problem of premature gelation associated with the local cement slurry was dealt with. This could be attributed to the introduction of the right concentration of UCS. The plastic viscosity for all the cement samples was below 100 cp, which according to Abbas *et al.* [25] is desirable to keep cement slurry pumpable. The values of the Yield Point calculated also showed that all the slurries were pumpable at 150°F (Table 3) though a little below 15 lb/100 ft^2 recommended by Salehi and Paiaman [26]. Comparing the imported class G cement sample and the modified CEM A1 and CEM A2, the modified cement appeared to have rheological stability than the imported cement sample. Notwithstanding, both modified cement and imported cement are pumpable. The rheological results for all the local cement after the introduction of 1 %bwoc of UCS additive showed lower rheological values than the imported class G cement at a temperature of 150°F.

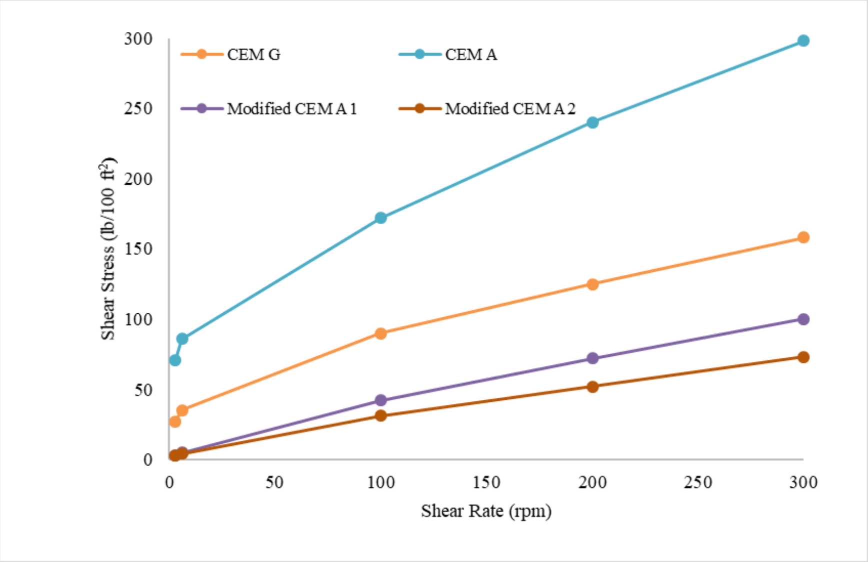

Figure 2 Shear stress vs. shear rate at 150°F

5. Conclusions

From the research, it could be concluded that:

i. Locally manufactured modified CEM A, proved to have better properties suitable for application in oilwell cementing operations, in terms of fluid loss, thickening time, and free water when tested at 150°F.
ii. Locally manufactured CEM A is compatible with Universal Cement System. The addition 1 %bwoc of Universal Cement System additive reduced the premature gelation associated with local cement thereby improving the bulk-flow characteristics at 150°F.
iii. Locally manufactured CEM A responded very well with the retarder used and can be used to achieve the require thickening time for oil and gas well cementing operations.

6. Recommendation

It is recommended that further tests be conducted to ascertain the stability of locally manufactured cement under High Pressure, High Temperature (HPHT) conditions.

References

[1] Shahrudin S, Samsuri A, Suhiami A, Nasir AS, and Ahmad Z. Possibility Studies of Using Local Cement in Oil and Gas Well Cementing Operations in Malaysia. http://eprints.utm.my/id/eprint/4029/1/SKMBT_60007062016310.pdf

[2] Anon. Oil Well Cement. http://www.lafarge-na.com/Well_Cements_v10.pdf. Accessed: March 10, 2013.

[3] Hodne H Rheological Performance of Cementitious Materials used in Well Cementing. PhD Thesis, University of Stavanger 2007, Stavanger, Norway, 8 p.

[4] Zhang J, Weissinger EA, Peethamparan S and Scherer GW. Early Hydration and Setting of Oil Well Cement. Cement and Concrete Research, 2010; 40: 1023 – 1033.

[5] Broni-Bediako E, Joel OF and Ofori-Sarpong G. Comparative Study of Local Cements with Imported Class 'G' Cement at Different Temperatures for Oil Well Cementing Operations in Ghana. Journal of Petroleum and Environmental Biotechnology, 2015; 1 - 7.

[6] Anon Well Engineering. Shell Intensive Training Programme 2014, pp. 1 - 46.

[7] Hibbeler J, Rae P, Gilmore T and Weber L. Using Alternative Sources of Oilwell Cement, International Association of Drilling Contractors. Society of Petroleum Engineers (IADC/SPE) Asia Pacific Drilling Technology Conference 2000, SPE 62746, Kuala Lumpur, Malaysia, pp. 1 – 10

[8] Atiemo E. Studies on the Effect of Selected Local Admixtures on Essential Properties of Cement for Housing Construction. PhD Thesis, Kwame Nkrumah University of Science and Technology 2012, Kumasi, Ghana, 174 pp.

[9] Broni-Bediako E, Joel OF. and Ofori-Sarpong G. (2015), Evaluation of the Performance of Local Cements with Imported Class 'G' Cement for Oil Well Cementing Operations in Ghana. Ghana Mining Journal, 2015; 15(1): 78 - 84.

[10] Broni-Bediako E. and Amorin R. Advances in the Possibility of Utilising Construction Grade Cements (CGCs) for Oil Well Cementing. Journal of Oil and Gas Research, 2017; (3): 1-4.

[11] Anon American Petroleum Institute (API) Recommended Practice 10B for Testing Well Cements, American Petroleum Institute 1997, Washington DC, USA, 134 pp.

[12] Alp B and Akin S. Utilization of Supplementary Cementitious Materials In Geothermal Well Cementing. Proceedings of Thirty-Eighth Workshop on Geothermal Reservoir Engineering 2013, Stanford University, Stanford, California, pp. 1 - 7.

[13] Salam KK, Arinkoola AO, Ajagbe B and Sanni O. Evaluation of Thickening Time of Oil Field Class G Cement Slurry at High Temperature and Pressure using Experimental Design. International Journal of Engineering Sciences, 2013; 2(8): 361 - 367.

[14] Ng'ang'a SI. Cementing Processes In Geothermal Well Drilling: Application and Techniques. Geothermal Training Programme Report 2014, United Nations University, 37 pp.

[15] Boškovic Z, Cebašek V and Gojkovic N. Application of Local Cement for Cementing Oil Wells in the South Eastern Region of the Pannonian Basin. Archives for Technical Sciences, 2013; 8(1): 35 - 39.

[16] Shahriar A. Investigation on Rheology of Oil Well Cement Slurries. Unpublished PhD Thesis, The University of Western Ontario 2011, Ontario, Canada, 251 pp.

[17] Bannister CE. Rheological Evaluation of Cement Slurries: Methods and Models. Society of Petroleum Engineers Annual Technical Conference and Exhibition 1980, SPE 9284, Dallas, Texas, 1-16.

[18] Darley HCH and Gray GR. Composition and Properties of Drilling and Completion Fluid, Gulf Professional Publishing 1983, 5th Edition, USA, 653 pp.

[19] Falode OA, Salam KK, Arinkoola AO and Ajagbe BM. (2013), Prediction of Compressive Strength of Oil Field Class G Cement Slurry using Factorial Design. Journal of Petroleum Exploration Production Technology, 2013; 3: 297 - 302.

[20] Anon Specification for Drilling Fluid Material, American Petroleum Institute (API) Specification 13A, API Publishing Service 2004, Washington DC, 66 pp.

[21] Bett EK. Geothermal Well Cementing, Materials and Placement techniques. Geothermal Training Programme - Report 10, 2010, pp. 99-130.

[22] Gandelman R, Miranda C and Teixeira K. On the Rheological Parameters Governing Oil Well Cement Slurry Stability. Annual Transactions of the Nordic Rheology Society, 2004; 12: 85-91.

[23] Shahriar A and Nehdi M. Modelling Rheological Properties of Oil Well Cement Slurries Using Multiple Regression Analysis and Artificial Neural Networks. International Journal of Material Science, 2013; 3(1): 26-37.

[24] Anon Drilling Engineering. Lecture Notes on Cementing, Institute of Petroleum Engineering 2009, Herriot Watt University, pp. 1-40.

[25] Abbas G, Irawan S, Kumar,S, Memon RK and Khalwar SA. (2014), Characteristics of Oil Well Cement Slurry using Hydroxypropylmethylcellulose. Journal of Applied Sciences, 2014; 14(11): 1154-1160.

[26] Salehi R and Paiaman AM. (2009), A Novel Cement Slurry Design Applicable to Horizontal Well Conditions. Pet Coal, 2009; 51(4): 270-276.

To whom correspondence should be addressed: Dr. Eric Broni-Bediako, Department of Petroleum Engineering, University of Mines and Technology, Ghana

Petroleum and Coal

Article **Open Access**

REMOVAL OF CRUDE OIL FROM AQUEOUS SOLUTION BY ZINC CHLORIDE MODIFIED *DIOSCOREA ROTUNDATA* PEEL CARBON: EQUILIBRIUM, KINETIC AND INTRA-PARTICLE DIFFUSIVITY

*Folasegun A. Dawodu[1], Ugochinyere N. Obioha[1], Kovo G. Akpomie[2]**

[1] Department of Chemistry (Industrial) University of Ibadan, Ibadan, Nigeria
[2] Department of Pure & Industrial Chemistry, University of Nigeria, Nsukka, Nigeria

Received June 19, 2018; Accepted September 28, 2018

Abstract

This study evaluated the potential of unmodified yam peel carbon (UYPC) and Zinc chloride activated yam peel carbon (AYPC) as low cost sorbent for remediation of crude oil from aqueous solution. Their efficiencies on the adsorption of crude oil from the water were investigated through batch adsorption studies. The crude oil obtained was characterized, and properties such as viscosity (kinematic and dynamic), pH, density, specific gravity, and API gravity were determined. Thermal properties such as heat of combustion, thermal conductivity, specific heat capacity and latent heat of vaporization were also determined. Proximate analyses were carried out on the raw yam peels, and the physiochemical properties were examined after carbonization. The AYPC was found to be more efficient than UYPC in removing oil from water under the varied conditions of pH (3 to 13), concentration (2.0 to 5.0 g/L), time (0 to 80 min) and dosage (0.2 to 1.4g). AYPC sorption of crude oil required a much lesser dosage compared to UYPC to obtain maximum removal. The adsorption experiment gave the optimum conditions of pH 7, and contact time of 40 mins for both sorbents. The equilibrium adsorption test conducted showed that the Langmuir isotherm is a better fit for the adsorption of the crude oil on AYPC and the Freundlich model was a better fit for UYPC. The kinetics studies showed that Pseudo-second order kinetics is a better fit for both sorbents than the pseudo first order model. The intra-particle diffusion evaluation revealed the influence of film diffusion and external mass transfer. The sorbents were found to be very effective as low cost materials for treatment of oil spill waters.

***Keywords**: Oil spill; sorption; crude oil; remediation.*

1. Introduction

The oil spill is the main source of oil contamination in water which is a result of the unintentional introduction of oil into the environment during the extraction, production, transportation or storage processes. When the oil is explored, transported and stored and its derivatives are used, there is a risk for spillage with the potential to cause significant environmental impact [1]. In recent times, major environmental pollution of soil and water is due to hydrocarbon contamination resulting from petrochemical industries activities. It can be caused by accidental discharge of petroleum industries products into the environment; it can also be caused by human activity. Hydrocarbon compounds are known for its carcinogenic and neurotoxic behavior. The overall annual intake of petroleum hydrocarbon around the world is very high, and it is approximately about 1012 US gallons [2]. Higher concentration of the hydrocarbon molecules, which are the main constituent of crude oil and petroleum products are highly toxic to living beings, including humans. Petroleum products also comprise trace amounts of sulfur and nitrogen compounds, which are hazardous and can react with the environment to produce secondary poisonous chemicals [3].

The oily wastewaters and produced waters generated from oil and gas exploration activities, crude oil refinery, petrochemical and petroleum refining plants, steel manufacturing and metal works, vehicle repair, and various types of manufacturing plants are other sources of water contamination by oil. The discovery of oil has so much influenced the world's economy that it appears to be one of the major sources of energy in homes and industries. At the same time, it has constituted a huge source of environmental disaster. Contaminated water cannot be used as a municipal water supply in industry, or for irrigation [4]. With oil continuing to pour into the Gulf of Mexico, the Deepwater Horizon drilling rig explosion, which occurred on April 20, 2010, has been described as the worst environmental disaster in U.S history. Every year approximately 5 million tons of petroleum oil is shipped across the oceans in shipping containers which place the marine life and the ecosystem at high risk [5]. Oil spills can also affect marine life, birds, and plantation. In 2010 the BP Deep Horizon rig was lit in flames leading to the death of 11 workers and released approximately 5 million barrels of oil into the Gulf of Mexico. The oil spills lasted for three months which led to the death of a huge population of marine animals and polluted 320 km of shorelines [5]. Oil spills are a common event in Nigeria. Half of all spills occur due to pipeline and tanker accidents (50%), other causes include sabotage (28%) and oil production operations (21%), with 1% of the spills being accounted for by inadequate or non-functional production equipment. Corrosion of pipelines and tankers is the rupturing or leaking of old production infrastructures that often do not receive inspection and maintenance [4]. Oil in water constitutes a major contaminant and research are ongoing to develop techniques for removing these contaminants, especially from low cost agricultural waste. There are many techniques available for oil-in-water separation regardless of being physical, biological or chemical such as gravity separation, chemical treatment methods, flotation system, coagulation, filtration, hydrocyclone, electrical process, reverse osmosis and membrane reactor which offer advantages and drawbacks over others [6]. Some existing methods are expensive, and sometimes some supplementary treatments are needed in order to achieve the stipulated environmental standards. Among these methods, the sorption process has emerged as a highly efficient treatment method due to its simplicity of the design, ease in operation and inert to toxic substances in removing dissolved organic components from water.

The high commercial sorbent costs and stringent environmental regulations have resulted in the need to develop low-cost sorbents derived from biomass materials, such as wheat straw, sawdust, rice residues, corncob, coconut husk, kapok fibers, cotton, wool and wood [7-9]. The advantages of these materials include being low cost, biodegradability, and non-toxicity. Among the main existing oil removal techniques, the sorption process has gained high popularity as it is one of the easiest and most cost effective physiochemical methods for removing contaminants from aqueous solution [10]. Synthetic organic polymers such as polypropylene, polyurethane, and polyethylene have been widely used to remove oil. Synthetic polymers have a high sorption capacity, but their major drawbacks are non-biodegradability and high cost. Over the years, researchers have tried to use adsorption as a technique for the control of environmental pollution from heavy metals and oil spills. Intensive researches have been done on various sorbents for oil spills control, and both their thermodynamic and kinetic studies have been reported. The highly hydrophobic characteristics of biomass combined with its high porosity develop a capillary force towards the adsorption of oils. Vegetal tissues, with the large surface area and big pores, tend to adsorb organic contaminants through physical and chemical mechanisms, in a similar way to charcoal. Several researchers, while studying the adsorption of oil by-products using different types of biomass, have observed the promising character of these materials as adsorbents [11]. it was observed that the application of carbon in the form of commercial activated carbon or charcoal (ACC), which had proved to be very effective in treating most complex industrial wastewater, is exorbitantly expensive and about 10–15% of it, is lost during regeneration [12]. Therefore there is a need to source for a cheap alternative form of effective carbon-based adsorbents. However, the use of yam peel carbon and its zinc chloride activated form for crude oil removal hasn't been established. The aim of this study was therefore to utilize yam peel carbon, and its zinc chloride activated derivative as low cost sorbents for crude oil removal from aqueous solution.

2. Experimental

2.1. Sampling

Waste yam peels were collected, washed and dried in sunlight for one week. The sundried peels were further dried in an oven at 110^0C for one hour. The crude oil was obtained from Warri refinery and petrochemical company (WRPC) in Warri, Delta state of Nigeria.

2.2. Characterization of crude oil and proximate analysis of yam peels

The physical properties of the crude oil such as density, specific gravity, viscosity, and thermal properties were determined using ASTM methods (ASTM D1298-95, ASTM D445-01). The proximate analysis of the yam peels such as moisture content, ash content, crude fibre, crude protein, carbohydrate, and crude fat were determined using standard methods [13].

2.3. Carbonization of the yam peels

The dried yam peels were carbonized in a muffle furnace at 400^0C for 1hr in the absence of air. The charcoal obtained was allowed to cool, grounded, and sieved to obtain a uniform particle size. This was then stored in a plastic container as Unmodified Yam Peel Carbon (UYPC).

2.4. Chemical activation of the carbonized yam peel

Two hundred grams (200g) of the carbonized material was divided into two equal portions. 100g was transferred into a beaker mixed with 150mL 0.1M $ZnCl_2$ until the mixture formed paste. The paste was transferred into a dry crucible, oven dried for 1hr at 105^0C and finally introduced into the muffle furnace and heated at 520^0C for 2 hrs in the absence of air so as to increase the surface area of the sample for the adsorption process. It was then cooled at room temperature, washed with distilled water until the filtrate obtained a pH of about 7. The washed activated carbon was dried for 3hrs in an oven at 105^0C and then stored in a plastic container as the Activated Yam Peel Carbon (AYPC) [14].

2.5. Fourier Transform Infrared spectroscopy analysis

The Infra-Red spectra of the samples were obtained before and after the adsorption analysis for the activated and inactivated portion of the sample using a Fourier transform infra-red spectrometer. This was carried out to identify the functional groups that were responsible for adsorption.

2.6. Batch sorption experiment

The adsorption analysis was carried out by a batch process. A definite concentration of the crude oil was prepared (18g in 2.5L of distilled water). The adsorption experiments were carried out by agitation of AYPC and UYPC in required amounts with 50mL of the oil/water mixture at room temperature in an orbital shaker. Several parameters affect the uptake on the adsorbent, so studies were undertaken to choose the best conditions. The adsorptions were carried out at various pH (3.0 -13.0), the pH of the working mixtures was adjusted to the desired value with 0.1M HCl or 0.1M NaOH, contact time (0-80min), initial crude oil-water concentrations (2.0 – 5.0 g/L) and adsorbent dosage (0.2 – 1.4g). At the end of a preliminarily determined period of time, samples were withdrawn by vacuum filtration and analyzed using UV adsorption spectrophotometer to obtain the final concentrations of the oil in the sample. The amount of crude oil adsorbed per unit mass of adsorbent at equilibrium, (q_e mg/g), or at time t, (q_t) were calculated according to the following relations;

$$q_e = (C_o - C_e)\frac{v}{m} \qquad (1)$$

$$q_t = (C_o - C_e)\,\frac{v}{m} \qquad (2)$$

where C_o and C_e are the initial and final concentrations of crude oil (g/L), v is the volume of the crude oil-water mixture (L), m is the amount of adsorbent used (g). The percentage of oil removed was determined using the equation;

$$\%\ \text{Removal} = (C_o - C_e)\,\frac{100}{Co} \qquad (3)$$

Adsorption data obtained from the effect of initial concentration and contact time were employed in testing the applicability of adsorption isotherm and adsorption kinetics respectively.

3. Results and discussion

3.1. Characterization of the yam peel and sorbents

The result of the proximate analysis of the yam peel as well as the characterization of UYPC and AYPC are shown in Table 1. The proximate analysis presented the low amount of moisture content, ash content, crude fiber, crude protein, and crude fat. The low crude fiber value of the yam peel obtained indicated its usefulness in producing a good activated carbon [15]. Crude protein is an organic compound, and the low organic material is necessary to produce activated carbon with low ash content [16]. The result for the characterization of the sorbents showed a lower bulk density of AYPC than that of UYPC. Generally, the lower the bulk density, the higher the porosity and surface area. This suggests that AYPC would be more efficient as a sorbent for crude oil remediation than UYPC.

Table 1. Proximate analysis of yam peel and sorbents characterization

Parameter	Yam peel	UYPC	AYPC
Moisture content (%)	5.81	0.50	0.48
Ash content (%)	4.99	14.0	13.2
Crude fibre (%)	11.40	-	
Crude protein (%)	10.58×10^{-5}	-	
Crude fat (%)	0.61×10^{-5}	-	
Carbohydrate content (%)	78.01	-	
Bulk density (g/cm^3)	-	0.210	0.192
Carbon yield (%)	-	69.1	71.3

3.2. FTIR analysis

Fourier Transform Infra-Red (FTIR) analysis determined for UYPC and AYPC before and after sorption of crude oil and the absorption bands are presented in Table 2.

Table 2. FTIR spectra absorption bands of the sorbents before and after crude oil uptake

Sample	Functional groups			
	O-H$_{str}$	C-H$_{str}$	C-O$_{str}$	C-N$_{str}$
UYPC before sorption	3404 cm^{-1}	2930 cm^{-1}	1388 cm^{-1} 1122 cm^{-1} 1049 cm^{-1}	2381 cm^{-1}
UYPC after sorption	3420 cm^{-1}	2926 cm^{-1}	1383 cm^{-1} 1267 cm^{-1} 1157 cm^{-1}	2371 cm^{-1}
AYPC before sorption	3431 cm^{-1}	N.D	1434 cm^{-1} 1050 cm^{-1}	2359 cm^{-1}
AYPC after sorption	3430 cm^{-1}	2929 cm^{-1}	1437 cm^{-1} 1050 cm^{-1}	2364 cm^{-1}

Some functional groups were revealed which were responsible for the sorption characteristics of the sorbents. The band at 3404 cm^{-1} (broad peak) was indicative of a hydroxyl functionality of absorbed water which became more intense after activation giving a peak at 3431 cm^{-1} (narrow and sharp). The C-O$_{str}$ peaks observed for UYPC became sharper and more intense after activation, showing two distinct peaks at 1434 cm^{-1} and 1050 cm^{-1}. The peaks observed for the Nitrile functionality also became more intense and distinct after activation. The peaks around 2900 cm^{-1} indicate C-H$_{str}$ of alkane which was not detected after activation. The C-H$_{str}$ was again observed after adsorption which is most likely from the adsorbed crude oil. Slight differences in absorption bands after crude oil sorption showed that the functional groups of both adsorbents were utilized in the removal process.

3.3. Physical and thermal characterization of crude oil

The physical and thermal properties of the crude oil are presented in Table 3. Watson and Nelson [17], depicted a relationship between crude oil gravity and characterization parameter: that lower gravity crudes tend to be more naphthenic, while higher-gravity crudes tend to be more paraffinic. From the experimental data obtained for the crude oil sample, it indicates that it contains more paraffinic components and less naphthenic components.

Table 3. Physical and thermal properties of the crude oil

Parameter	Value
pH	6.203
^{0}API gravity (Degrees)	37.6
Density (g/cm^3)	0.814
Kinematic viscosity (cSt)	1.1
Dynamic viscosity, (cP)	0.895
Heat of combustion, Q_v (cal/g)	10,642.3
Thermal conductivity, K (BTU. ^{0}F^{-1}hr^{-1}ft^{-1})	0.0427
Specific heat, c kcal/(kg°C)	0.495
Latent heat of vaporization, L (kcal/kg)	229.35

3.4. Effect of contact time on crude oil sorption

The effect of contact time on the removal of crude oil from water was studied as shown in Fig.1.

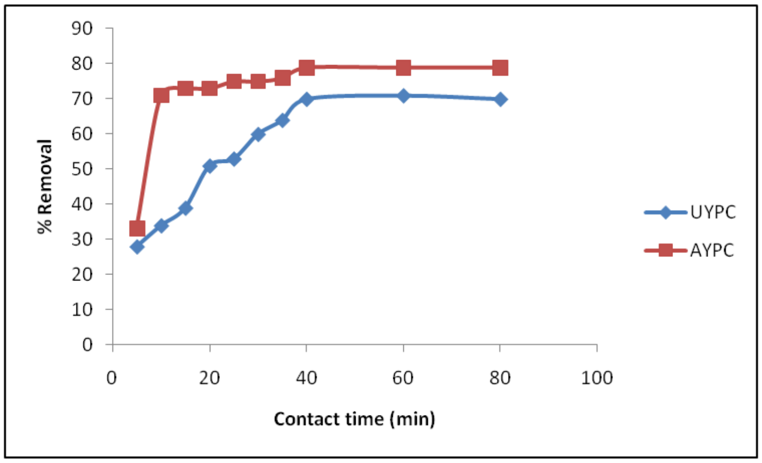

Fig.1. Effect of contact time on crude oil sorption on the sorbent

An initial concentration of 5.0g/L of the crude oil was prepared. 0.3g of UYPC and AYPC was utilized by varying the time from 0 to 80 min at 5 min interval and 20 min interval after 40 min. The adsorption was carried out in the 15mL crude oil-water mixture. The concentrations of the filtrate were obtained by running the absorbance in a UV-Visible spectrophotometer at 320nm and extrapolating from the calibration curve. For UYPC, an increase in the percentage removal from 28 to 71 as the time increased from 5 to 60 min was recorded after which the % removal decreased to 70 at 80 min. This is as a result of desorption of the oil into the solution. Also for AYPC, an increase in the percentage removal as the time increased from 5 to 40 min was obtained with the maximum removal of 79%. During the sorption process, the particles of the crude oil attach to the surface of the adsorbent by forces of attraction and occupy/ clog the available sites. The longer the time of contact, the more the available sites would be occupied until all the adsorbent sites are filled up. This is when the breakthrough time is achieved and no more adsorbate can be sorbed. The plot of percentage removal against time thus became constant.

3.5. Effect of sorbent dosage on crude oil sorption

The effect of sorbent dosage on the removal of crude oil from water by UYPC and AYPC was investigated as shown in Figure 2.

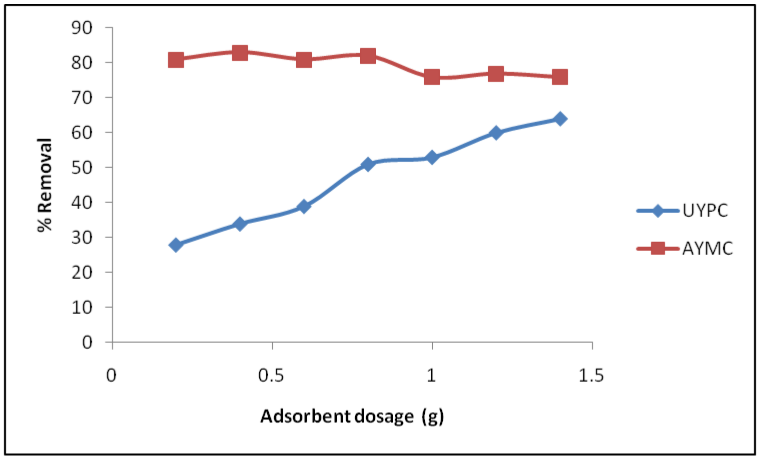

Fig.2. Effect of sorbent dosage on the sorption of crude oil on the sorbents

An initial concentration of 5.0g/L of the crude oil was prepared. The adsorbent dosage was varied from 0.2 to 1.4g at an interval of 0.2g. 20mL of the crude oil- water solution was used and the time was kept constant at 60 min. The percentage removal of crude oil increased steadily UYPC as the adsorbent mass was increased from 0.2 to 1.4g, with the optimum removal of 64%. The percentage removal of crude oil increased steadily as the adsorbent mass was increased from 0.2 to 0.4g for AYPC where the highest percentage removal was attained at 83%. Beyond this, there was a decrease in the % removal depicting desorption. This shows that a smaller adsorbent mass of activated carbon is needed compared to the inactivated carbon. The decrease in the percentage removal after attaining the highest adsorption percentage as the adsorbent increases may be due to the aggregation of adsorption sites resulting in a decrease in the surface area available for adsorption and an increase in the diffusion pathlength. The decrease in percentage removal at 1.0g dosage was due to lack of achieving equilibrium between the amounts of oil adsorbed by the sorbent and the amount of oil remaining in the solution. As a result, active sites of the adsorbent were not fully bound to the oil molecules as a result of the weak van de Waal's force of attraction between the adsorbate and adsorbent.

3.6. Effect of crude oil concentration on the percentage removal

The effect of initial concentrations was studied in order to analyze the sorption concentration dependence, and thus the sorption isotherm which allows describing the nature of interactions between the sorbate and sorbent. The study on the effect of initial concentration on oil sorption onto UYPC and AYPC was carried out by varying the initial oil concentration from 2.0 g/L to 5.0 g/L at 0.5 g/L interval, while other parameters sorbent dosage (20 mg/mL), contact time (60 min) and pH (6.5) were kept constant. The result is shown in Figure 3. It was observed that for UYPC, an increase in the initial concentration of the crude oil- water solution resulted in an increase in the percentage removal of crude oil. As the initial concentration increases, the percentage removal increased from 25% at 2.0g/L to 52% at 4.5g/L after which there was a decrease in the percentage removal. For AYPC it was discovered that an increase in the initial concentration of the crude oil- water solution resulted in an increase in the percentage removal of crude oil. As the initial concentration increases, the percentage removal increased from 35% at 2.0g/L to 73% at 4.5g/L, where there was maximum sorption capacity after which there was a decrease in the percentage removal. This is because all sorption sites on the sorbent surfaces were completely occupied by oil, and this hindered more oil to be sorbed. Increasing the initial concentration would increase the mass transfer driving force, and, therefore, the rate at which molecules pass from the bulk solution to the particle surface. This would result in a higher adsorption capacity. When the sites at the sorbent are occupied, there would be opposition to the mass transfer driving force which would lead to desorption [18].

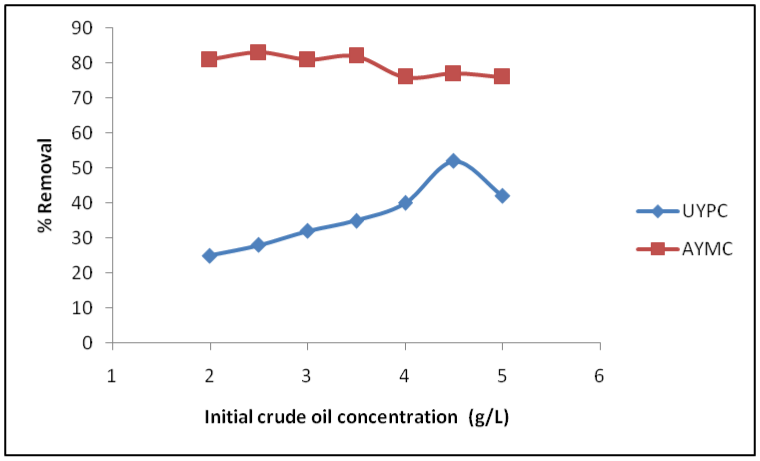

Fig.3. Effect of crude oil concentration on sorption by the sorbents

3.7. Effect of solution pH

The effect of pH on the removal of crude oil from aqueous solution was studied as shown in Figure 4.

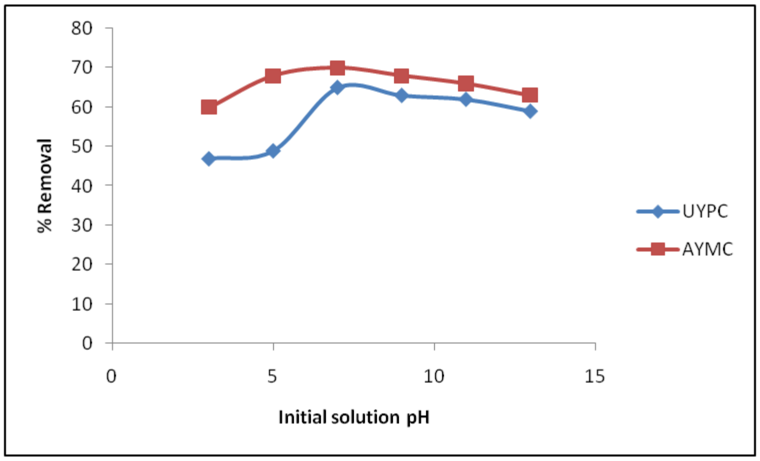

Fig.4. Effect of pH on crude oil sorption on the sorbents

An initial concentration of 5.0 g/L of the crude oil was prepared. The pH was varied from 3.0 to 13.0 at an interval of 2.0 while sorbent dosage (20 mg/mL) and contact time (60 min) were kept constant. An increase in the pH of the crude oil- water solution resulted in an increase in the percentage removal of crude oil for UYPC. As the initial pH increases, the percentage removal increased from 47 % at pH 3 to 65 % at pH 7 after which there was a decrease in the percentage removal. This indicates that under acidic conditions, the carbon could remove oil till a neutral pH where maximum sorption capacity was achieved. In the case of AYPC, it was discovered that an increase in the pH of the crude oil- water solution also resulted in an increase in the percentage removal of crude oil. As the initial concentration increases, the percentage removal increased from 60 % at pH 3 to 70 % at pH 7 after which there was a decrease in the percentage removal. The higher the pH of an adsorbent, the higher the removal efficiency of organic materials by the adsorbent from wastewater. The surface of the adsorbent functional group is usually repulsively associated with hydroxonium ions (H_3O^-) at low pH which invariably reduces the removal efficiency of organics during adsorption. Interestingly, it was observed that a higher percentage crude oil removal was achieved for AYPC than UYPC under all conditions of pH, contact time, sorbent dosage and concentration which indicates the effectiveness of zinc chloride modification.

3.8. Equilibrium isotherm and kinetic modeling of sorption

In this study, Langmuir and Freundlich's models were used to describe the equilibrium between the crude oil adsorbed onto the carbon, and the adsorbate solutions (Table 4).

Table 4. Equilibrium isotherm, kinetic and Intraparticle diffusion constants for sorption

Isotherm Model	UYPC	AYPC
Langmuir		
qm (g g-1)	0.0393	0.0605
KL (L g-1)	0.2728	5.3184
R2	0.6076	0.6698
Freundlich		
KF (g g-1)	0.0100	0.0570
n	0.4202	-12.94
R2	0.7569	0.0152
Pseudo first order		
Ki (min-1)	0.0269	0.0131
qe (g g-1)	0.0798	0.0378
R2	0.246	0.022
Pseudo second order		
K2 (g g-1min-1)	0.3391	1.1654
qe (g g-1)	0.03166	0.3282
R2	0.9693	0.994
Intraparticle diffusion		
Kd (g g-1 min-1/2)	0.0338	0.0327
C	0.0327	0.101
R2	0.9126	0.6653

Equilibrium kinetic study on adsorption provides information on the capacity of the adsorbent. An adsorption isotherm is characterized by certain constant values, which express the surface properties and the affinity of the adsorbents and can also be used to compare the adsorptive capacities of the adsorbent for different pollutants. Equilibrium data can be analyzed using commonly known adsorption isotherms, which provide the basis for the design of adsorption systems. The Langmuir isotherm is valid for monolayer sorption onto a surface with a finite number of identical site, represented by the following equation:

$$q_e = \frac{q_m K_l C_e}{(1+K_l C_e)} \qquad (4)$$

Where, q_m and K_L are Langmuir parameters related to maximum capacity and free energy of adsorption, respectively; Ce is the equilibrium concentration in the aqueous solution and qe is the equilibrium adsorption capacity of adsorbent. The linearized form of Langmuir equation can be expressed as [18]:

$$Ce/qe = 1/q_L K_L + Ce/q_L \qquad (5)$$

The Langmuir constants q_L and K_L can be evaluated by plotting C_e/q_e versus C_e [18]. The low values of the linear regression coefficient obtained showed this model was not appropriate in the description of the process.

The Freundlich isotherm is an empirical equation based on sorption on heterogeneous surface energy systems given as:

$$qe = K_f Ce^{1/n} \quad (6)$$

where K_f and n are the Freundlich constants that indicate adsorption capacity and adsorption intensity. The linear form of Freundlich isotherm can be written as:

$$\log qe = \log K_f + 1/n \log Ce \quad (7)$$

The value of K_f and n can be calculated by plotting log qe versus log Ce. The best isotherm model in describing the sorption process must have the determination coefficient (R^2) closer to 1. According to these criteria on the R^2 results, it was observed that Langmuir isotherm showed a good fit to the experimental data with the highest R^2 for AYPC and Freundlich isotherm was the best fit for the UYPC. In addition, the Langmuir model for AYPC indicates the formation of monolayer coverage of oil onto the homogeneous sorbent surface [19].

The pseudo first order and pseudo second order kinetic models were also applied, and the equation and model constants have been discussed extensively in a previous report [18]. The model constants are given in Table 4. The pseudo second order model was shown to give clearly a better fit than the pseudo first order model as R^2 values obtained were close to one. This pseudo second order model assumes a chemisorptions mechanism between the sorbents and crude oil removal process.

3.9. Intraparticle diffusion model analysis

It is generally known that the sorption process is the rate- controlled process in which the slowest step determines the process rate limiting step. The kinetic data were further analyzed assuming that the mechanism of oil sorption can generally be described by four consecutive rate controlling steps which are external mass transfer (transport from the bulk solution to the sorbent surface), film diffusion (diffusion across the liquid film from the sorbent surface), intraparticle diffusion (pore diffusion, surface diffusion or combination of both mechanisms) and surface interactions at active sites [20]. Most of the time, only film and intraparticle diffusion are considered as the rate limiting steps as the process of external mass transfer, and chemical surface interaction are generally rapid. The rate limiting step of the sorption can be qualitatively determined by analyzing kinetic data using the Weber-Morris model as given by:

$$qt = K_d t^{1/2} + C \quad (8)$$

where k_i is the diffusion coefficient ($g/g/min^{0.5}$), and C is a constant that gives an indication of the thickness of the boundary layer. The constants obtained are presented in Table 4. The sorption process is said to be intraparticle diffusion controlled if the straight line plot passes through the origin, while some boundary layer diffusion (external mass transfer or film diffusion) may be present if it does not pass through the origin [20]. The plot for both UYPC and AYPC did not pass through the origin indicating some external mass transfer or film diffusion in the removal process.

4. Conclusion

The carbonized yam peel and zinc chloride activated yam peel carbon was found to be very efficient low cost materials for the remediation of oil spill polluted waters. The activated of the yam peel carbon by zinc chloride was very effective in improving the removal of crude oil from aqueous solution.

References

[1] Husseien M, Amer AA, El-Maghraby A. and Taha A. Availability of Barley Straw Application on Oil Spill Cleanup. Inter. J. Environ. Sci. Technol.,2009, 6, 123–130.

[2] Hadibarata T. and Tachibana S. 2009. Microbial degradation of crude oil by fungi pre-grown on wood meal. Inter. stud. Environ. Chem., 2009, 15, 317- 322.

[3] Nievas ML, Commendatorea MG, Esteves JL. and Bucal V. Biodegradation pattern of hydrocarbons from a fuel oil-type complex residue by an emulsifier-producing microbial consortium. J. Hazard. Mater., 2008,154, 96–104.

[4] Badejo OT. and Nwilo PC. Management of Oil Spill Dispersal along the Nigerian Coastal Areas. ISPRS Congress, Istanbul, Turkey, 2004.

[5] Corbett JJ. and Winebrake JJ. Sustainable Movement of Goods: Energy and Environmental Implications of Trucks, Trains, Ships, and Planes. Environ. Manage. 2007, 10, 8-12.

[6] Fakhru'l-Razi A, Pendashteh A, Abdullah LC, Biak DRA, Madaeni SS, and Abidin ZZ. Review of technologies for oil and gas produced water treatment. J. Hazard. Mater., 2009,170, 530–551.

[7] Ali N, El-Harbawi M, Jabal AA. and Yin CY. Characteristics and oil sorption effectiveness of Kapok Fibre, sugarcane bagasse and rice husks: Oil removal suitability matrix. Environ. Technol., 2012, 33, 481–486.

[8] Vlaev L, Petkov P, Dimitrov A. and Genieva S. Cleanup of water polluted with crude oil or diesel fuel using rice husks ash. J. Taiwan Institute Chem. Eng., 2011, 42, 957–964.

[9] Ibrahim S, Ang HM, and Wang S. Removal of emulsified food and mineral oils from wastewater using surfactant modified barley straw. Bioresource Technology, 2009, 100, 5744–5749.

[10] Lua AC, Yang T. and Guo J. Effects of pyrolysis conditions on the properties of activated carbons prepared from pistachio-nut shells. J. Analy. App. Pyrolysis, 2004, 72, 279–287.

[11] Aniefiok EI, Udo JI, Margaret UI. and Sunday WP. Petroleum Exploration and Production: Past and Present Environmental Issues in the Nigeria's Niger Delta. Amer J. Environ. Protect., 2013, 1, 78-90.

[12] Tandale JP. and Shide NH. Preparation of low cost adsorbent and its characterization. Poll. Res., 2008, 27, 635-641.

[13] Charles AL, Sriroth K, Huang T. Proximate composition, mineral contents, hydrocarbon cynanide and phytic acid of five cassava genotypes. Food Chem., 2005, 92, 615-620.

[14] Awoyale AA, Eloka-Eboka AC. and Odubiyi AO. Production and experimental efficiency of activated carbon from local waste bamboo for wastewater treatment. Inter. J. Eng. Appl. Sci. 2012, 3, 8–10

[15] Ekpete OA, Horsfall JM. and Tarawou T. Sorption Kinetic Study on the removal of Phenol using Fluted Pumpkin and Commercial Activated Carbon. Inter. J. Bio. Chem. Sci. 2011, 5, 1143-1152

[16] Nwadinigwe CA, and Alumona TN. NAASAR procedure for quantitative assessment of n-alkanes, asphaltenes and resins in crudes. J. Petrol. Explor. Prod. Technol. 2015, 5,383-390.

[17] Watson KM. and Nelson EF. Improved Methods for Approximating Critical and Thermal Properties of Petroleum. Ind. Eng. Chem., 1933, 25, 880-892.

[18] Dawodu FA. and Akpomie KG. Simultaneous adsorption of Ni (II) and Mn (II) ions from aqueous solution unto a Nigerian kaolinite clay. J. Mater. Res. Technol., 2014,3, 129–141

[19] Hameed BH, Mahmoud DK. and Ahmad AL. Sorption equilibrium and kinetics of basic dye from aqueous solution using banana stalk waste. J. Hazard. Mater. 2008, 158, 499–506.

[20] Ho YS, Ng JCY. and McKay G. Kinetics of pollutant sorption by biosorbents: Review. Sep. Purif. Rev., 2000, 29, 189–232.

To whom correspondence should be addressed: Dr. Kovo G. Akpomie, Department of pure and industrial chemistry university of Nigeria, Nsukka

Petroleum and Coal

Article **Open Access**

AUGMENTED WIRELINE BASED LITHOLOGY AND FACIES PREDICTION, FOR UPPER ORDOVICIAN SUCCESSION, MURZUQ BASIN, LIBYA

Abubaker Alansari[1*], *Ahmed Mohammad Ahmed Salim*[1], *Abdul Hadi Bin Abd Rahman*[1], *Nuri Mohamed Fello*[2], *Hammad Tariq Janjuhah*[3]

[1] *Department of Geosciences, University Technology PETRONAS, 32610, Perak, Malaysia*
[2] *National Oil Corporation (NOC), Tripoli, Libya*
3 Department of geology, American University of Beirut, Libanon

Received July 10, 2018; Accepted September 28, 2018

Abstract

The upper Ordovician reservoir is one of the leading producing units in SW part of the Murzuq basin; it has a complex architecture inherited from the glacial effects on the braided fluvial deposits of the late stage at this era. The ultimate target for any petrophysical evaluation is to determine the quantities of water saturation and porosity accurately, but unfortunately, the models for thinly interbedded sand and shale layers are not straightforward. Therefore in this paper, an effort has been made to delineate and distinct between the types of interbedded (shaly-sand and sandy-shale layers), and lithology end members by application compressional compliance versus density cross-plot in the two studied wells. After that, the determination of the thinly interbedded of layers type is augmented by correlating Vp-compliance with Poisson's ratio, effective porosity, and VP/VS. Among all the examined cross-plot; Poison's ratio, VP/VS and effective porosity with compressional compliance enhanced the upper and lower boundaries of the thinly interbedded sand and shale layers of the Ordovician succession in Murzuq basin. The "Mamuniyat" formation (main reservoir) with more clean sand content displays low compressional compliance, low-velocity ratio, and low Poisson's ratio. In contrary, the rich TOC shale (Hot shale) shows high compressional compliance, high-velocity ratio and high Poisson's ratio. While the disputed sandstone, siltstones and silty shales of late Ordovician "Bir Tlacsin" formation has slightly higher compressional compliance, velocity ratio, and Poisson's ratio than the underlying Mamuniyat formation, which enables drawing a clear contact between two gradually graded formations in the areas with no abrupt changes. The estimated petrophysical and elastic and properties are then used as an input for electrofacies prediction in both wells, by using unsupervised neural network classification. The predicted petrophysical facies clusters in both wells failed to differentiate between the various type of shales. However, the petro-elastic facies cluster reliably delineated the interbedded sandy- shale and shaly-sand thin layers without using gamma-ray logs. The results will help to avoid and to reduce the errors made during fluid substitution and rock physics models of shaly-sand formations.

Keywords: *Lithology prediction; Electrofacies; Upper Ordovician reservoir; Murzuq Basin.*

1. Introduction

A principal task of geoscience in reservoir characterization is to determine the diverse lithofacies and elactrofacies clusters of the main zone of interest from the interpretation of wireline and cores obtained from wells. However, for technical and financial causes cores are not always derived for the entire reservoir zone. Besides In old exploration wells, greatly deviated and horizontal wells only wireline data are often available. Thus petrophysical properties, elastic properties, lithology, and facies prediction depend on the interpretation of the wireline logs. With the advent of quantitative seismic interpretation and rock physics modelling been incorporated into the conventional hydrocarbon exploration appraisal and development workflow, it became a necessity to understand the minor component of the reservoir unit. The upper

Ordovician reservoir are the main producing unit in the study area SW part of the Murzuq basin (Fig. 1); it has a complex architecture which has been inherited from the glacial effects on braided fluvial deposits during the Ordovician time.

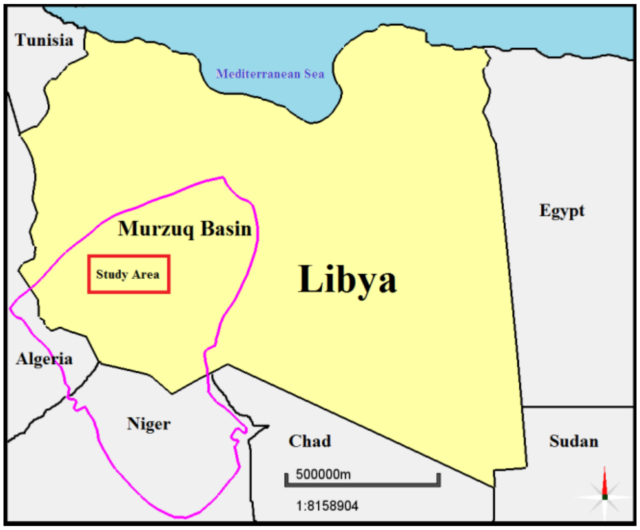

Fig. 1. Location of studied wells, Murzuq Basin, Libya

Consequently, there is no consistency on the lithostratigraphic units that constitute the Ordovician sedimentary infill of the Murzuq Basin. Especially the transitional deposits between the source rock formation and underlying reservoir units that remains accurately undefined [1], They also consider this unit (Bir Tlacsin formation) as non-reservoir rocks which baffles the hydrocarbon flow during migration and production process. Furthermore, the thinning and gradually graded contacts with upper and lower formations masks the identification of this formation boundaries, consequently top reservoir boundary. In the literature, there is an obvious gab in the studies concerned with the use of wireline data to overcome the fore stated problem in this region. A recent study by Abushalah and Serpa [2] have defined the upper and the lower boundary of this formation using seismic amplitude spectrum analysis and inverted density attributes, however, the density the Bir Tlacsin formation overlaps with densities of Mamuniyat and Tanezzuft formation even at wells scale. According to Bhat and Helle [3] the large overlap of the petrophysical properties in clastic rocks limit their effectiveness in accurate facies prediction. Therefore, in-depth integrated petrophysical and elastic analysis to comprehend the lithology end members and facies is required before seismic inversion and reservoir modelling.

According to [4-5], the mixed shale-sand layers should lie in a straight line between the two parent lithology end members (sand and shale). The former [4] has proposed workflow for determining shaly-sand lamination based on VP-compliance and density for a better application of fluid substitution, while the latter [5] improved the interpretation of the fluid substitution models. By modelling the volume of dispersed shale, and its correlation with effective porosity VP. In this paper, the above method has been adopted and developed to enable the delineation of the existence of shaly-sand and sandy-shale layers distribution at the reservoir and well scale through incorporating more petro-elastic correlation applied to study wells. The principal objective of this paper is; 1) to determine the petro-elastic properties of the main lithology end members of the Upper Ordovician reservoir unit. 2) To enhance the separation of interbedded sandy-shale and shaly-sand layers by minimizing the overlap between petrophysical properties of different fluid cases within the zone of interest. 3) Finally, group them into electro-facies derived from both petrophysical and elastic properties.

2. Geological settings

Ordovician reservoirs and their main lithofacies have been investigated in the recent geological record by many researchers namely [6-11]. Based on these studies the Ordovician plays were divided into several underlying sub-groups, but in this paper, the focus will be a shift to upper Ordovician deposits (Fig. 2).

2.1. Upper Ordovician

According to Aziz [6] Najem *et al.* [9] ,El-Ghali [11], Shalbk [12] during the Late Ordovician, Melaz Shuqran Mamuniyat, and Bir Tlacsin formations were alternately deposited and locally covered by the basal Silurian marine deposits. The main Ordovician reservoir (Mamuniyat formation) is typified by three sand-dominated cycles that indicate complex interlace of marine and glacial depositional effects (Fig. 2). The Lower Ordovician reservoirs consist of 3 zones, which are discussed below:

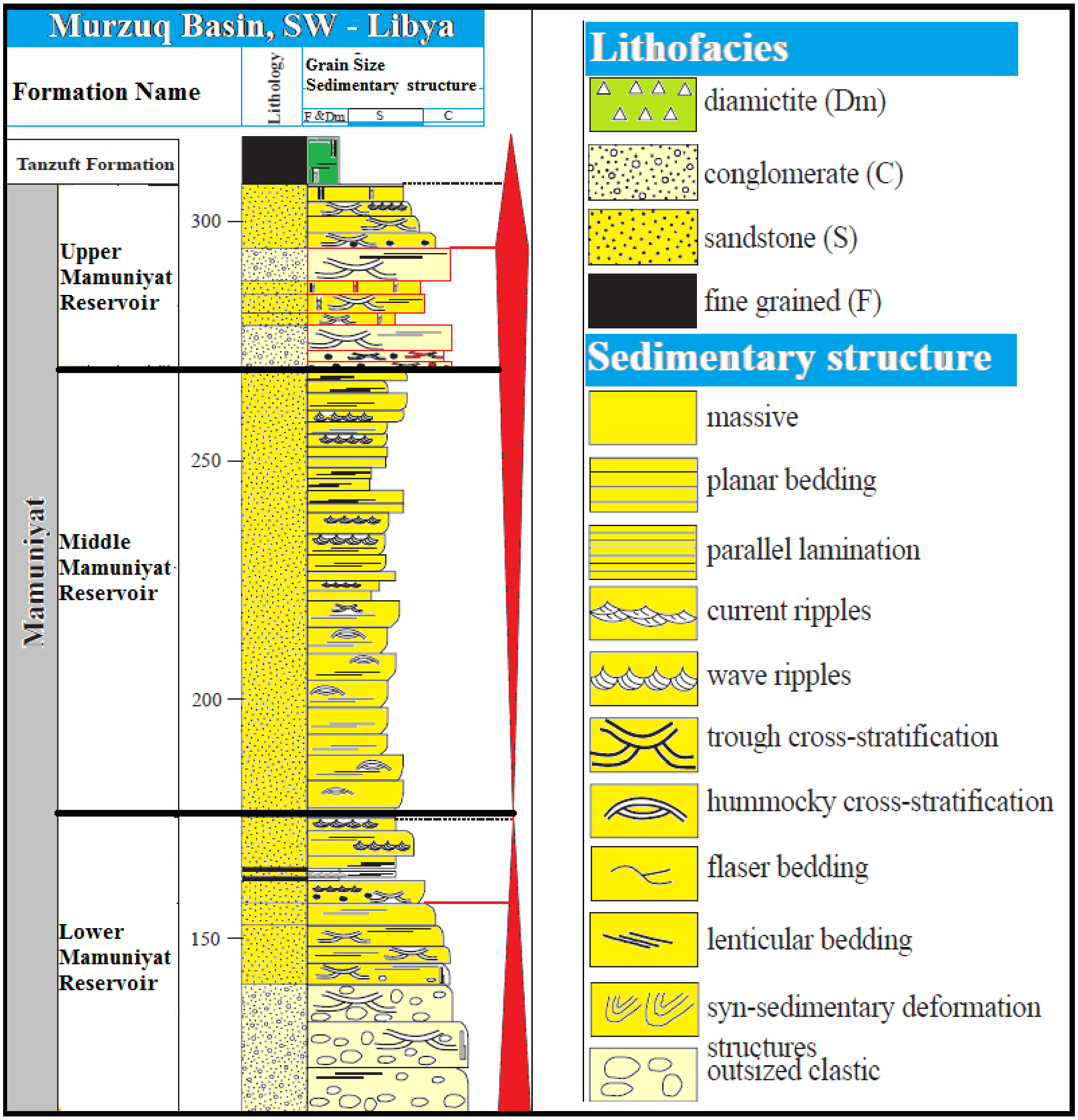

Fig. 2. Representing the upper Ordovician lithostratigraphic column of the studied area (*Modified from* [11])

Lower Mamuniyat: This zone comprises the marine and possibly glacially-influenced Melaz Shuqran Formation, which was typically deposited in shallow to marginal marine settings (Fig. 2). Middle Mamuniyat: This zone covers the Middle Mamuniyat sequence with the deposition of proximal braid deltas. Some studies such as suggest deposition into glacial lakes/ponds that accumulated in ice-formed valleys and may be subjected to a marine transgression. Glacial influence is believed to be the toughest in this zone likened to the others (Fig. 2). Upper Mamuniyat: This zone includes the Upper Mamuniyat series, which typically contains upward coarsening braid-delta and localized shallow marine deposition with glacial influences. Localized burrowing (including Skolithos) testifies to the marine-influenced in this zone, which is typically represented by sub-aqueous deposition of deltas which prograded from glacial sources. The zone is terminated by coarse braid delta deposition and the localized reworking of some deposits by possible aeolian processes. This is typically overlain by a transgressive phase and marine reworking. The contact with the overlying marine Silurian is characteristically distinctive, and may also be unconformable (Fig. 2). Reservoir quality of the Mamuniyat formation is maximum in the medium- to very coarse-grained fluvial sandstones with porosity up to 25% and permeability commonly up to 1000 mD (but locally higher). The glacially-influenced sandstones show reduced reservoir quality, possibly as a result of poorer sorting characteristics.

3. Methodology

Two wells were used for deriving the main petrophysical and elastic properties. Then both properties have been combined using multiple cross-plots to delineate the Lithology end members (sand, shale, sand-shale and shale-sand layers). After that, a set of selected petrophysical and petro-elastic properties have been imported to the unsupervised neural network for electrofacies prediction.

3.1. Petrophysical interpretation

Two wells had relevant wireline logs that include Gamma-ray (GR), Resistivity, Sonic, Neutron and Density logs from which the volume of shale, porosity and water saturation were derived. For V-shale estimation the Linear GR method will be used after best determination GRmax and GRmin using the following equation; For porosity determination, a combination method of neutron porosity, density and sonic logs will be applied to obtain more favourable total porosity (φ total) [13]. After that total porosity will be obtained by using the weighted average of neutron density porosity. The result was also supported by neutron density method. For effective porosity derivation [14] will be used by combining results. Finally, for water saturation estimation Indonesian equation have been used.

3.2. Elastic properties determination

Fortunately, in all the wells compressional sonic log is available but the shear wave sonic exist in only one well. Several methods will be used for Vs estimation, these methods included Castagna "mudrock line", Greenberg-Castagna, correlation regressions and finally multi-set of well logs as an input for supervised neural network method. After that, the above methods will be compared, and one of them will be selected based on its accuracy when compared to the measured Vs from well A. Gassmann fluid substitution is often employed on estimating elastic properties of clean sands with different water saturation for different fluid types and with a different range of porosities. For this paper shaly-sand, the fluid substitution will be applied to well A and B using the average reservoir porosity and pressure values. The mass balance equation will be used for calculating the bulk density of the mixed fluid rock. Moreover, fluid modulus has been estimated by using Wood's

3.3. Compressional-compliance to determination

For defining the main end members of clastic lithology, we will be using the equation suggested by Kathara [4], Backus [15].

$$\rho = \rho_{Sh} * X_{sh} + \rho_{SD} * (1 - X_{Sh}) \qquad (1)$$

$$\frac{1}{\rho Vp^2} = \frac{X_{sh}}{\rho_{Sh*} Vp_{sh2}} + \frac{1-X_{sh}}{\rho_{SD*} Vp_{SD2}} \qquad (2)$$

where ρ = density; Vp is velocity; Sh = shale and subscript SD denotes sand.

The above two equations infer that both density and the compressional compliance ($C=1/(\rho Vp^2)$), are linear functions of shale fraction. Which helped on the initial determination of interbedded sand and shale layers within the reservoir unit. Furthermore, the fluid substituted cases will be plotted against compressional compliance. Hence it is expected to provide more lithology separation especially, for the clean sand gas unit.

3.4. Facies prediction

Finally, the estimated petrophysical and elastic and properties has been used as an input for electrofacies prediction in both wells, by using unsupervised neural network classification. Two inputs will be used; first, petrophysical logs only (GR, NPHI, ROHB and PHI) as an input and it was called petrophysical facies. The second a combination of elastic and petrophysical properties (Poison's ratio, VPVS and effective porosity with compressional compliance), named petro-elastic. Then both facies will be calibrated to litho-facies derived from mud logging and wellbore side-cutting reports. The facies associations will be grouped to fit the facies association introduced by [16]

4. Results

4.1. Shear wave estimation (VS)

Three methods were tested for shear velocity prediction (VS) in well B, and then compared to the measured Vs in Well-A (Fig. 3). The estimated shear velocity using supervised neural networks (blue curves) illustrated an excellent overlap with the measured (VS) represented by the red colour curve in both wells. The result was achieved by using an input of gamma-ray, effective porosity, Compressional compliance, and density logs in a supervised neural network with three hidden layers. While the other two curves represent derived Greenberg-Castagna (black colour) and linear regression resulted from correlating VP measured and Vs measured (dotted purple colour) (Fig. 3). The former is slightly higher than measured shear velocity and slightly different from the other curves. Similarly the latter is noticeably lower than measured Vs (Fig. 3).

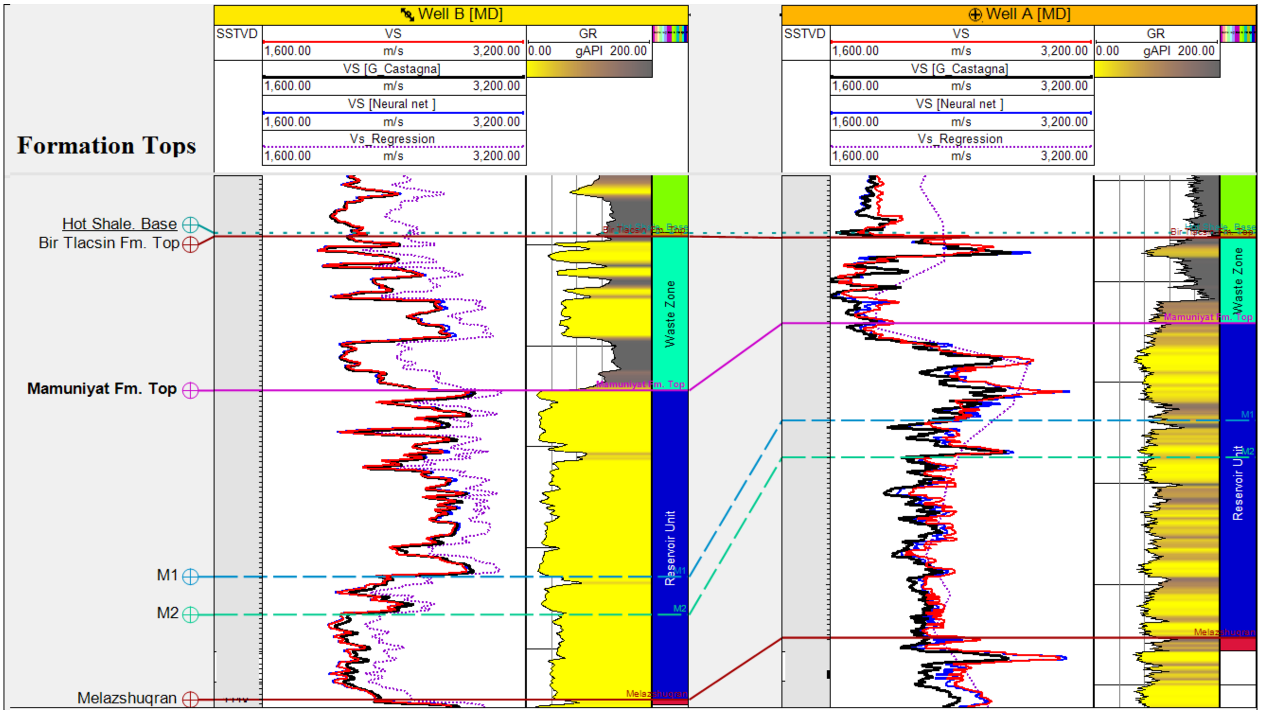

Fig. 3. Vs prediction using three methods in Well A and Well B. (B). Red colour reflecting measured VS value, whereas the black colour representing Greenberg-Castagna derived VS, blue colour denotes the neural-network, and dotted purple is shear velocity estimated using the regression values with VP

4.2. Shale and sand end members' determination

Compressional compliance has been estimated for main reservoir intervals, and entire the wells (A and B) by using the workflow explained in section 3.2.3. Before starting the analysis of defining shale and sand lithology end members, their distribution should be solely understood. Therefore, the volume of shale log (X) was cross-plotted against gamma-ray log (Y) and colour-coded by total porosity in the reservoir zone for both wells (Fig. 5). It showed that; the clean sand cut-off in both wells has ranged between (0 – 0.3) shale percentage in both wells and shale zone considered to be all the values which more than 0.75. The minimum gamma reading in well A is higher than the one in well B (20 to 60 API) and (67 to 110 API) respectively, which means that the gamma-ray log is not reliable lithology represented in well in well A.

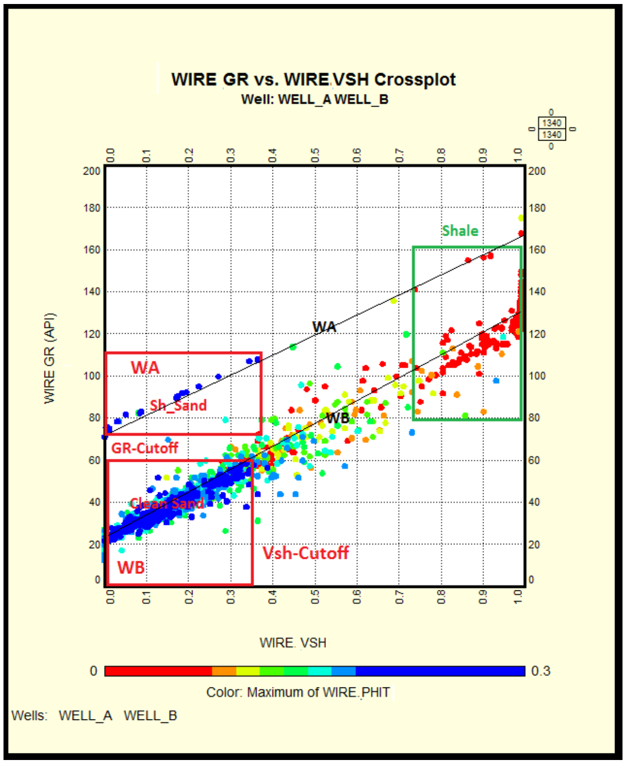

Fig. 4. A cross plot of V-shale and gamma-ray to determine the clean sand and shale cut-off

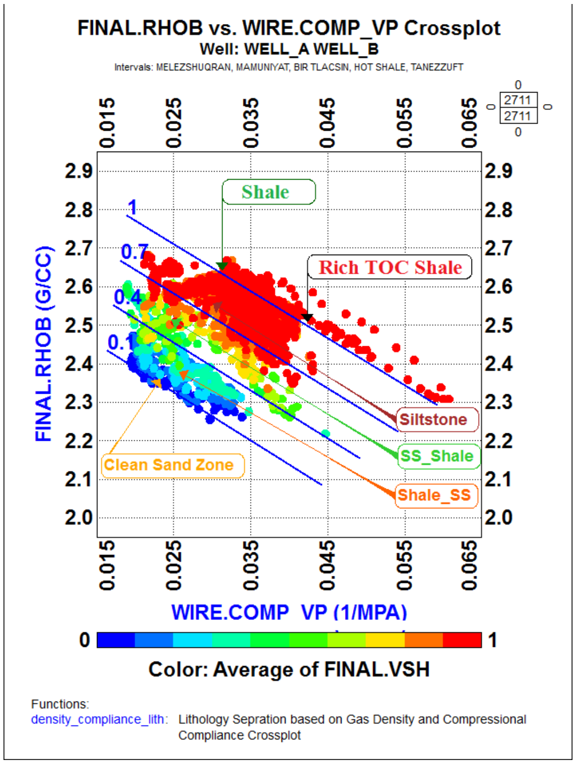

Fig. 5. A cross plot of compressional compliance versus the density (colour-coded by V-shale) reflecting the two main lithology end members (sand is blue and shale red) for the zone of interest in both Wells

4.3. Compressional compliance versus density cross-plot

Once the primary lithology distribution is understood at both wells, the resulted compressional compliance was correlated with density log in both wells (A & B) and colour-coded by the volume of shale (V-Sh). For each cross plot, a function representing the percentage of shale within the sandy layers is drowned with a range of (0 Sand-1 Shale) and an interval of 0.3.

Figure (5) illustrates a cross plot of compressional compliance vs density log annotated by lines showing the percentages of shale in each formation. Where any values higher than 1% considered to be pure shale, more than 0.7% and less than 1% is siltstone with mud layers, between 0.4 and 0.7% is interpreted to be a sandy shale layer. While the lithology points fell below 0.4% and higher than 0.2% is considered to be shaly- sand layers and any percentages lower than that is clean sand (Fig. 5). The lithology end members showed a distinct trend in both wells at the reservoir interval with a very some mixed layers in between (Fig.5).

The above-stated separation is increased when the density of oil used and even more by using the density of gas curve, which has enabled a better selection of the primary lithology end members (sand and shale) and their associated mixed layers (sand-shale and shale-sand) in both wells (Fig. 6). However, with the remaining uncertainty that associated with an allocation of the contact between sand-shale and shale-sand layers.

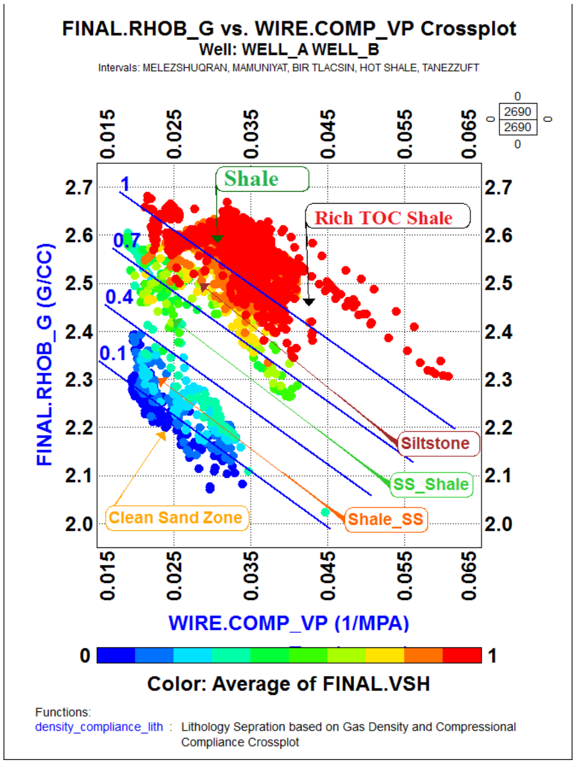

Fig. 6. A cross plot of compressional compliance versus the density of gas case (colour-coded by V-shale) reflecting the two main lithology end members (sand is blue and shale red) for the zone of interest in both Wells

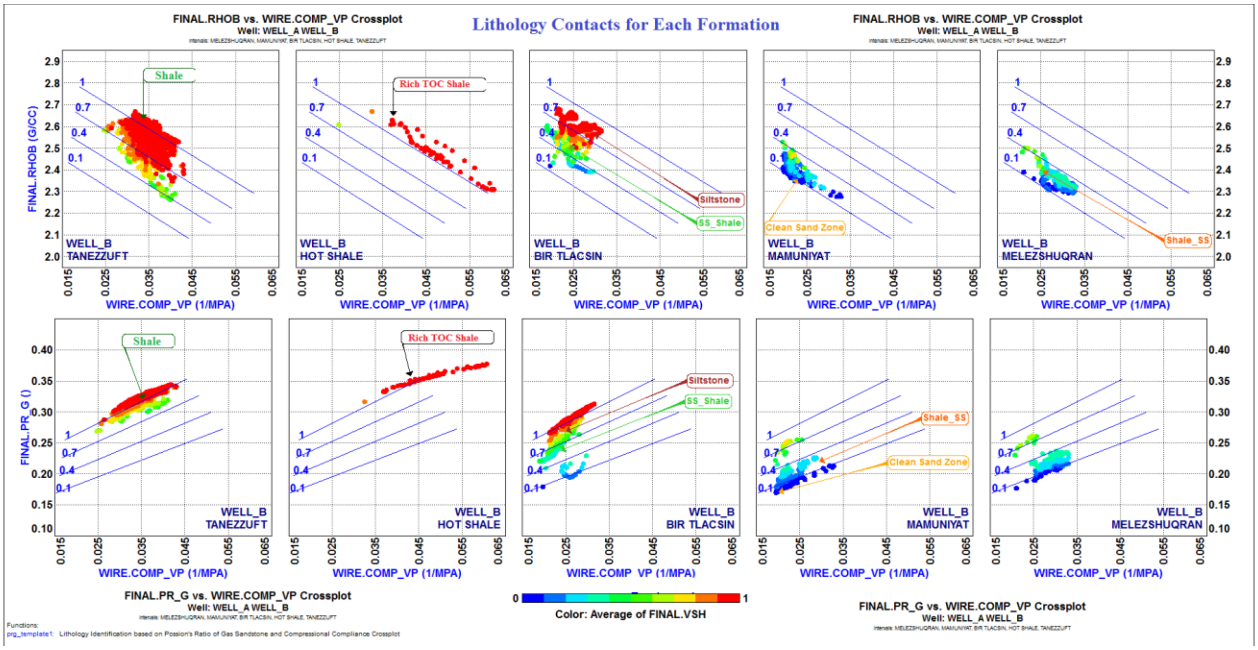

Fig. 7. Compressional compliance versus density cross-plots for each formation within the within the zone of interest, (colour-coded by V-shale) reflecting the percentages and lithology type in both studied wells

To comprehend the composition in the zone of interest, the main formations were investigated individually (Fig. 7). The pure shale (Tanezzuft Silurian shale) annotated by red colour can be outlined in Well A between density range of 2.5 to 2.66 G/CC, and compressional compliance of 0.025 to 0.043 1/MPA. The shalness of the formation in well A is higher than Well B. The cross-plot also enabled an accurate delineation of the rich TOC shale "Hot shale" especially in well B where the formation is characterized with higher compliances and gradual decrease in the density (Fig. 7). The next formation (Bir Tlacsin) is more complicated than others since it contains a range of rock types (shale, siltstone, and mixed shale sand layers) which harden the lithology and facies interpretation of this formation and often confused with upper shale unit (Tanezzuft) and lower reservoir unit (Mamuniyat).

The main reservoir unit (Mamuniyat) showed by dark to light blue colours in both wells; the formation has similar density values with the underlying lower Ordovician formation (Melezshuqran). However, with a definite difference in the compliance values than the lower Mamuniyat reservoir. The Mamuniyat lithology points range lower than 0.026 1/MPA, while Melezshuqran is higher.

4.4. Effective porosity versus compressional compliance cross-plot

Another way for improving the lithology prediction and contacts allocation between different formations at the well scale is to cross-plot the corrected effective porosity vs estimated compressional compliance colour-coded by average shale volume curve (Fig. 8).

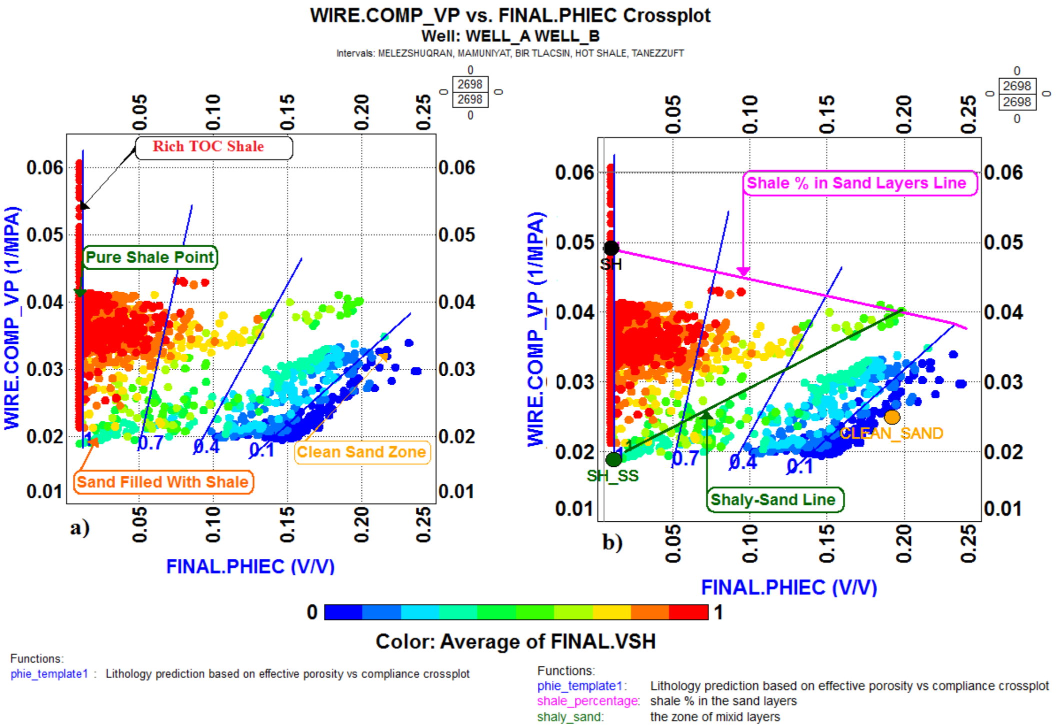

Fig. 8. A cross plot a) effective porosity versus compressional compliance log, b) is the same with a different template. The latter was used for lithology prediction illustrated in the lithology log. The figure represents the primary lithology end members and dispersed shale layers for different formation in the zone of interest of Well A and B

The cross-plot enhanced the ability to define the sandy-shale and shaly-sand layers range. Figure (8a) represents the trend of the main lithology end members drown by the annotated (0 to 1%) blue lines in which the compressional compliance increases in the areas with abundant shales and lower porosities (showed by v-sh colour coding red shale and blue sand). However, it slightly increases in the high porosity clean sandstone zones with shaly contents which can give an apparent difference between lower Ordovician formation "Melezshuqran" and upper Ordovician Mamuniyat". Where they have similar porosities range (0.14 to 0.2 V/V), however the shale content of the former is higher, causing a rise of compressional compliance values (0.023-0.033 1/MPA) (Fig. 8a).

The cross-plot also led to the segregation of the three exist shales which is very hard to accomplish using traditional triple compo logging set. Since all the shale with high clay contents exhibits a very low porosity, the Vp-compliance log is used to differentiate between shale types. The first type is pure shale (Tanezzuft Fm) has a compressional compliance range of (0.028-0.033 1/MPA) that is decreasing with the increase of quartz contents and porosity. Then the shale with compressional compliance higher the 0.045 1/MPA is considered to be shale with high TOC contents or what is known in this area by "Hot shale" (Fig. 8).

The last type is the controversial shale of the late Ordovician known as "Birtlacsin" which is often confused with lower Silurian Formation Tenezuft and the Upper Ordovician Mamuniyat reservoir. The formation (Birtlacsin) has a lower compliance than the fore-stated two types below 0.03 1/MPA which is due to the higher contents of the mixed layers than the pure shale in this formation (Fig. 8b). This observation outlined by the green shaly-sand line in figure (8b). The interpreted lithology log using the above cross-plot suggested a higher percentage of shaly-sand layers within the Upper Ordovician Mamuniyat reservoir overlain by sand-shale layers within the late Ordovician Birtlacsin formation (Fig. 9).

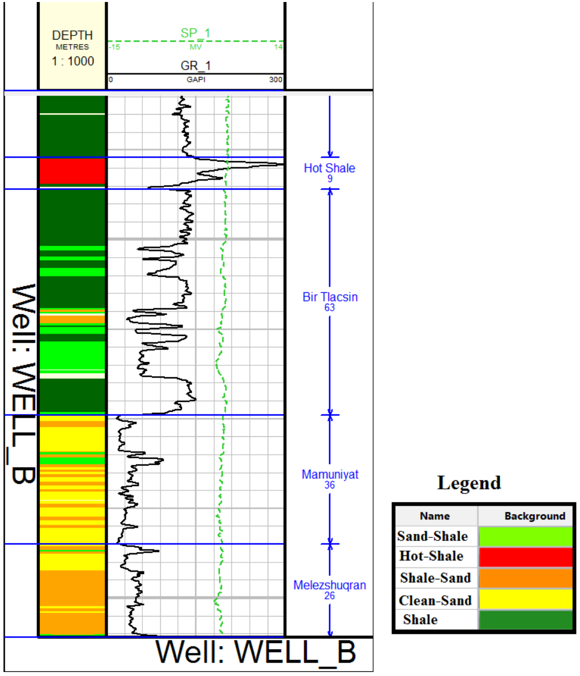

Fig. 9. Representing the prediction of different lithologies (Shale dark green, Sand yellow, sand-shale light green, shale-sand orange and hot-shale is red).using the cross plot of compressional compliance versus effective porosity

←

4.5. Compressional compliance versus velocity and Poisson's ratios cross-plots

The relationship between compressional compliance, poison's ratio and velocity ratio has been investigated in both wells. It was obtained by cross-plotting compressional compliance vs poison's ratio and colour-coded by the volume of shale (Fig. 10). The graph illustrated a consistent continuation of shale (red) and sand (blue) lithology end members, which bound the sand-shale layers (yellow to light green) and shale-sand lamination (light blue) (Fig. 10). The cross-plot was used to generate lithology log which has confirmed the result previously generated using compliance vs density but with a slight improvement in the layers number and type's distribution. The cross-plot of compliance versus Vp/Vs strongly supported the above lithology and contact separation obtained by poison's ratio (Fig. 11).

4.6. Facies prediction

The scheme for classifying the facies of Ordovician succession in this study is entirely based on the response of petrophysical and estimated elastic logs. The scheme classifies Ordovician deposits on the basis of shale percentages within sand layers and vice versa, organic matter contents and wireline log response. Five clusters have been recognized (Fig. 12), namely: (1) sandy-shale dominated layers (FA1), (2) TOC rich deposits (FA2), (3) shaly-sand dominated layers (FA3), (4) clean sand deposits (FA4), and (5) pure shale deposits (FA5). In Well A, only four petrophysical facies associations are present and (FA1) is missing, but in petro-elastic facies the five clusters are present. While in Well B only three petrophysical facies are identified (FA2, FA4 and FA5), however, under the petro-elastic classification all the facies are present. In both wells, the petro-elastic facies shows a closer match to the litho-facies more than petrophysical facies (Fig. 12).

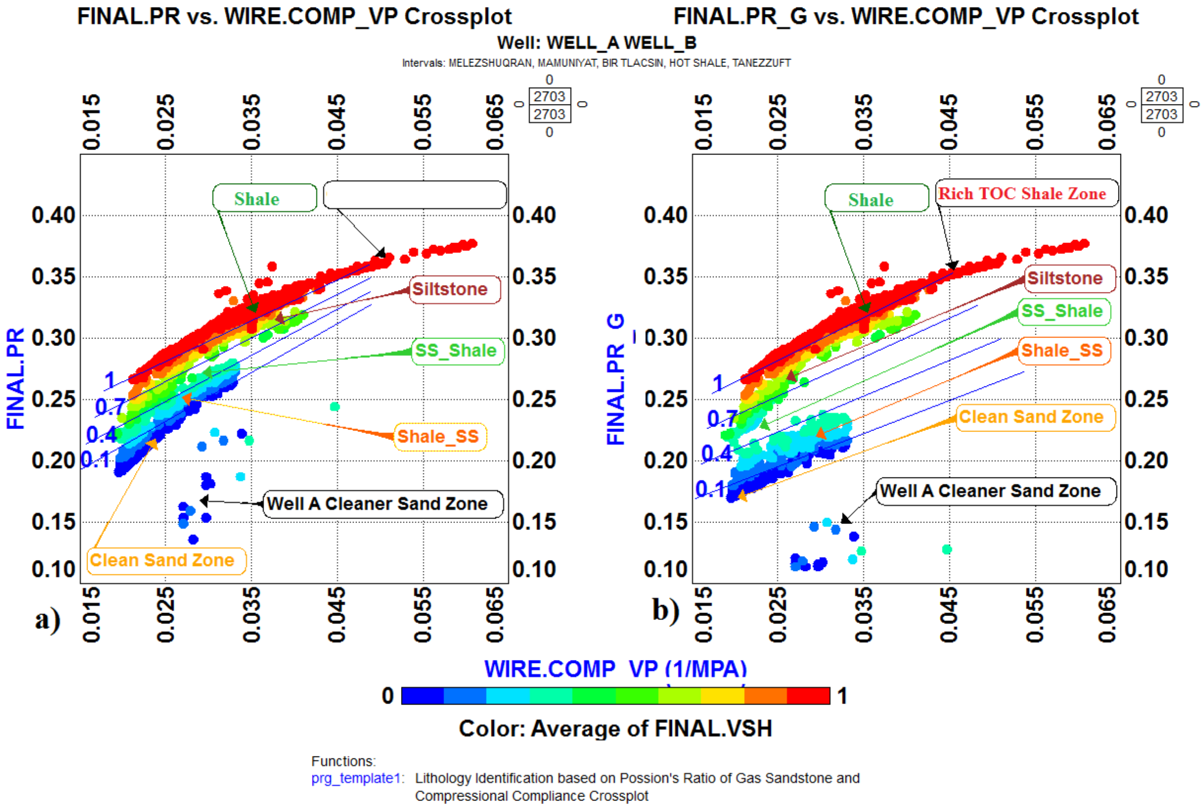

Fig. 10. A cross plot of compressional compliance versus Poisson's ratio (colour-coded by V-shale) showing the main lithology end members

5. Discussion

Precise delineation and understanding of lithology and facies are the primary keys to any successful exploration, appraisal and development operations. However, it still a fundamental obstacle for the subsurface operations [17]. Also, the profitability of any oil or gas field is reliant on the quality and correctness of lithology and associated facies prediction [18]. Before progressing with any elastic properties analysis, a robust estimation of shear wave velocity in all the wells is required. In this study, different methods (section 3.2.1) were tested and supervised neural network proved to be a powerful tool for shear wave estimation if suitable input logs were chosen (Fig. 3). Many input pairs were tested, and the set of gamma-ray, density, Vsh and total porosity logs was best predicted the shear wave with an almost overlay to the measured one in well A (Fig. 3). By investigating the different relation between estimated elastic and petrophysical properties and cross-plot them with each other, color-coded mainly by the volume of shale in the whole wells and zone of interest, it provides treasured information for facies and lithology, from which, also sandy-shale, shaly-sand and TOC content percentages are inferred. All the examined correlations allowed lithology primary end member separation. However, they lack a clear differentiation between the two kinds of thinly interbedded layers (shaly-sand and sandy-shale).

Well B exhibited more than ten thin layers ranging from (0.3-2 m) in thickness. Poison's ratio, velocity ratio and effective porosity cross-plots vs compressional compliance enhanced the allocation of the different lithological types within the zone of interest (Fig. 9, 10, and 11).

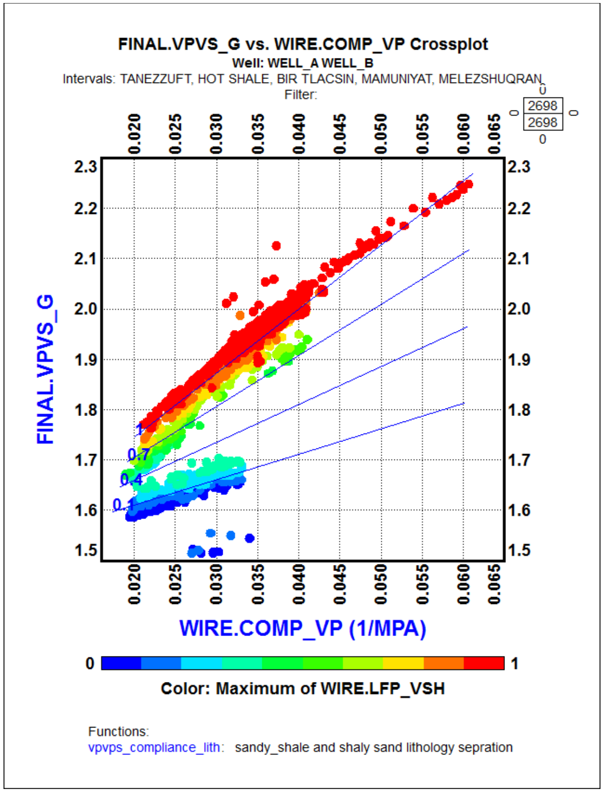

Fig. 11. A cross plot between A) compressional compliance versus VP/VS gas and B) compressional compliance versus VP/VS gas (colour-coded by V-shale) showing the main lithology end members

Shaly-sand fluid substitution for both wells manages to recognise some of the thin layers within shale and sand intervals. However, most of the layers identified within reservoir units have not been taking into account in the fluid substitution estimation. Therefore, erroneous results of fluid substitution application may occur. The "Mamuniyat" formation (main reservoir) with more clean sand content shows low compressional compliance, low-velocity ratio, and low Poisson's ratio. In contrary, the rich TOC shale (Hot shale) shows high compressional compliance, high-velocity ratio and high Poisson's ratio. While the debated sandstone, siltstones and silty shales of late Ordovician "Bir Tlacsin" formation has slightly higher compressional compliance, velocity ratio, and Poisson's ratio than the underlying Mamuniyat formation, which enables drawing a clear contact between two gradually graded formations in the areas with no abrupt changes (Fig. 9, 10, 11,and 12). The pure shale formation "Tanezzuft" has lower compressional compliance, velocity ratio, and Poisson's ratio than the rich TOC "Hot Shale" formation but higher values than the shale in the underlying Bir Tlacsin formation. This has enabled the separation of the three shales (Hot sale, Tanezzuft shale and Bir Tlacsin shale) that often have a higher gamma-ray reading and appears very similar when only petrophysical properties are considered. The thinly interbedded sand and shale layers are bounded between two main identified end members (clean sand of Mamuniyat and pure shale of Tanezzuft formation) and if the percentage of shale increases in the sandy unit the above parameters will move towards the shale end member and vice versa.

According to Bhatt and Helle [3] the Application ANN in clastic rocks for facies prediction "reveals an average hit rate well above 90% in wells unknown to the network".in compression to the other methods the technique proved to be a reliable lithology and facies clustering method. Hence it was favoured in this study for petrophysical and petro-elastic facies prediction. Predicted petrophysical facies clusters in both wells failed to differentiate between the various type of shales as well as sandy-shale and shaly-sand layers (Fig. 12), where the facies association 2 (Hot shale) was considered to exist within the main reservoir unit, which is incorrect. This was due to the overlap between the petrophysical parameters of the clastic sediments and for minimizing its effect elastic properties are invoked in the analysis along with petrophysical properties. The facies is also significantly affected by the high gamma-ray reading in Well A, leading to misinterpretation and confusion of integrated sand-shale and shale layers. (FA3 and FA5).To overcome this issue, a combined petro-elastic facies cluster prediction using the earlier generated logs as input (Vp-compliance, Poisson's ratio, VPVS, PHIE and RHOB) is generated, the cluster accurately determines the Hot shale (FA2) and place it in the correct position within both wells (Fig. 12). Also, reliably delineated the interbedded sandy- shale and shaly-sand thin layers without using gamma-ray logs which have lowered the effect of petrophysical properties values interference for the lithological end members.

Finally, The unsupervised neural network predicted petro-elastic facies using logs (Poison’s ratio, VpVs and effective porosity with compressional compliance) as an input showed a reasonable ability for detecting mixed shale sand layers than the only petrophysical logs (GR, NPHI, ROHB and PHI) clusters (Fig 12). Also illustrated a closer match to the litho-facies derived from mud logging.

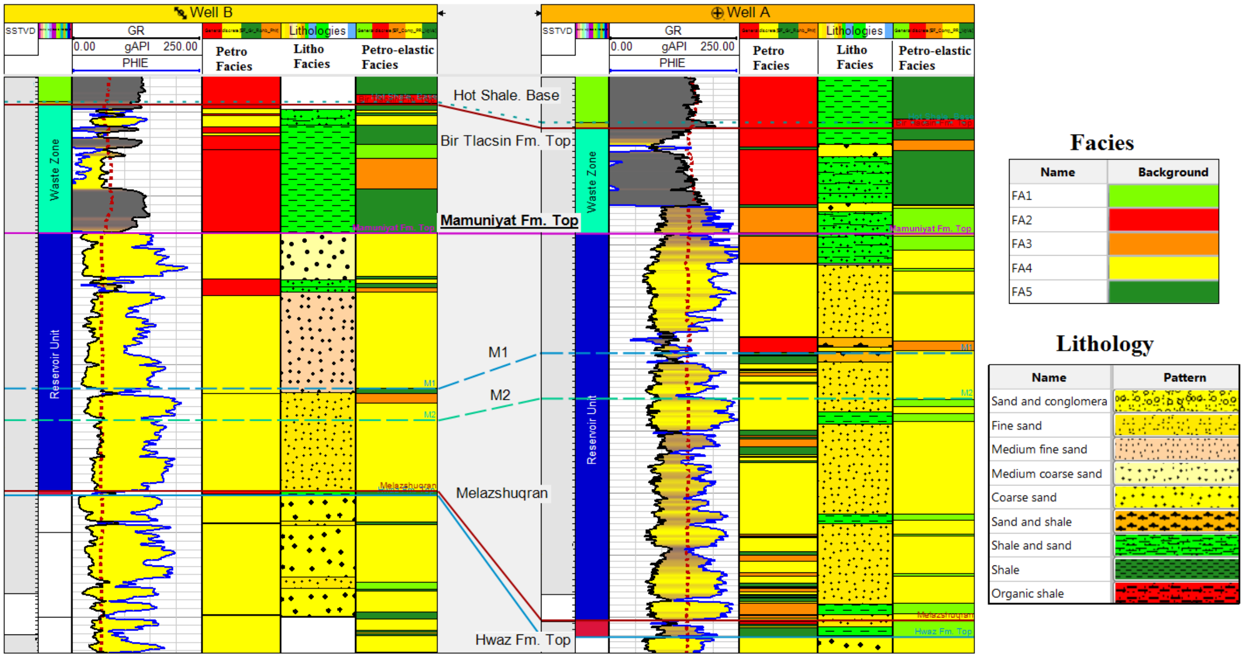

Fig. 12. Illustrate the predicted petrophysical and petro-elastic facies in comparison to the litho-facies for well A and well B

6. Conclusion

Even with the absence of high-resolution data such as image and core data, it is still possible to improve the determination of lithology and facies. In this study, a combination of petrophysical and elastic properties is correlated and used as an input for supervised and unsupervised neural network techniques in an attempt to improve the prediction of shear wave velocity, lithology and facies in the studied wells. The methods relied on a coupling of elastic and petrophysical properties to minimize the overlap of the petrophysical logs response to the clastic rocks. The supervised neural network analysis successfully improved the accuracy of VS estimation in Well B, where the measured one is absent. While the unsupervised neural network aided in the detection of different petrophysical facies clusters and significantly improved the delineation of the upper and lower boundaries of thinly interbedded sand and shale layers under the petro-elastic facies scheme. Application to an Ordovician succession of Murzuq basin revealed a precise five facies clusters. The outcome of this paper will help to improve sandy-shale fluid substitution, rock physics models reservoir model.

Acknowledgement

Our gratitude goes to Akakus Oil company for providing the data and NOC for their cooperation and allowing the publication of this work.

List of abbreviations

V_{sh}	*Shale volume*	C	*Compressional compliance*
GR_{log}	*Gamma ray log reading*	R_t	*Deep resistivity*
GR_{min}	*Gamma ray sand reading*	m	*Cementation exponent*
GR_{max}	*Gamma ray shale reading*	V_p	*Compressional velocity*
ϕ_N	*Neutron Porosity from the logs*	V_s	*Shear velocity*
ϕ_D	*Density porosity*	V_p/V_s	*Velocity ratio*
ρ_{ma}	*Matrix density*	K_{sat}	*Bulk moduli of saturated rock*
ρ_{log}	*Bulk density from log*	K_{dry}	*Bulk moduli of the dry rock*
ρ_{fl}	*Fluid density*	K_f	*Bulk moduli of the fluid*
ϕ_S	*Sonic derived porosity*	K_{ma}	*Bulk moduli of the rock matrix*
Δt_{ma}	*Matrix transit time*	S_w	*Water saturation from logs*
Δt_{log}	*Sonic transit time from log*	ρ_w	*Density of formation water*
Δt_{fl}	*Fluid transit time*	ρ_{hc}	*Density of hydrocarbon*
ϕ_{total}	*Total Porosity*	ρ_g	*Density of formation gas*
ϕ_{Seff}	*Effective porosity*	ρ_b	*Bulk density*
S_w	*Water saturation*	K_{hc}	*Bulk moduli of hydrocarbon*
n	*Saturation exponent*	μ_{sat}	*Shear moduli of saturated rock*
R_w	*Brine resistivity*	ρ_{sat}	*Density of saturated rock*
SD	*Sand Stone*	μ_{dry}	*Shear moduli of dry roc*
SH	*Shale*		

References

[1] Echikh K and Sola M. Geology and hydrocarbon occurrences in the Murzuq Basin, SW Libya. in Geological exploration in Murzuq Basin, ed: Elsevier, 2000, pp. 175-222.

[2] Abushalah Y and Serpa L. Using instantaneous frequency and colored inversion attributes to distinguish and determine the sandstones facies of the Late Ordovician Mamuniyat reservoir, R-field in Murzuq Basin, Libya. Interpretation, 2016; 4: T507-T519.

[3] Bhatt A and Helle HB. Determination of facies from well logs using modular neural networks. Petroleum Geoscience, 2002; 8: 217-228.

[4] Katahara K. Fluid substitution in laminated shaly sands. in SEG Technical Program Expanded Abstracts 2004, ed: Society of Exploration Geophysicists, 2004: 1718-1721.

[5] Dejtrakulwong P and Mavko G. Fluid substitution for laminated sand-shale sequences. in SEG Technical Program Expanded Abstracts 2011, ed: Society of Exploration Geophysicists, 2011, pp. 2183-2187.

[6] Aziz A. Stratigraphy and hydrocarbon potential of the Lower Palaeozoic succession of License NC-115, Murzuq Basin, SW Libya-Chapter 16. 2000.

[7] Davidson L, Beswetherick S, Craig J, Eales M, Fisher A, Himmali A. The structure, stratigraphy and petroleum geology of the Murzuq Basin, Southwest Libya-Chapter 14. 2009.

[8] Grothe B and Park TJ. Structure and function of the bat superior olivary complex. Microscopy Research and Technique, 2000; 51. 382-402.

[9] Najem A, El-Arnauti A, and Bosnina S. Delineation of Paleozoic Tecto-stratigraphic Complexities in the Northern Part of Murzuq Basin-Southwest Libya. in SPE North Africa Technical Conference and Exhibition, 2015.

[10] Le Heron D, Meinhold G, Elgadry M, Abutarruma Y, and Boote D. Early Palaeozoic evolution of Libya: perspectives from Jabal Eghei with implications for hydrocarbon exploration in Al Kufrah Basin. Basin Research, 2015; 27: 60-83.

[11] El-Ghali MAK. Depositional environments and sequence stratigraphy of paralic glacial, paraglacial and postglacial Upper Ordovician siliciclastic deposits in the Murzuq Basin, SW Libya. Sedimentary Geology, 2005; 177: 145-173.

[12] Shalbak FA. Palaeozoic petroleum systems of the Murzuq Basin, Libya. 2015.

[13] Asquith G. with CR Gibson. 1982, Basic Well Log Analysis for Geologist. AAPG Methods in Exploration Series, The American Assoc. of Petroleum Geologists, OK, 1986.

[14] Hill H, Klein G, Shirley O, Thomas E, and Waxman W. Bound Water In Shaly Sands-Its Relation To Q And Other Formation Properties. The log analyst, 1979; 20.

[15] Backus GE. Long-wave elastic anisotropy produced by horizontal layering. Journal of Geophysical Research, 1962; 67: 4427-4440.

[16] Khalifa S, Laksana S, and Schöbel M. Rock Typing Approach for Reservoir Characterization of Ordovician Sandstones, Fields Case Study, Concessions NC115/NC186, Murzuq Basin, Libya. in North Africa Technical Conference and Exhibition, 2010.

[17] Kupecz JA, Gluyas J, and Bloch S. Reservoir quality prediction in sandstones and carbonates: An overview. 1997.

[18] Hami-Eddine K, Klein P, Richard L de Ribet, B, and Grout M. A new technique for lithology and fluid content prediction from prestack data: An application to a carbonate reservoir," Interpretation, 2015; 3: SC19-SC32.

To whom correspondence should be addressed: Dr. Abubaker Alansari, Department of Geosciences, University Technology PETRONAS, 32610, Perak, Malaysia

Petroleum and Coal

Article **Open Access**

ADAPTIVE ARTIFICIAL NEURAL NETWORK APPROACH FOR PERMEABILITY PREDICTION

O. Teslim[1], *O. Akeem*[2]

[1] *African University of Science and Technology, Abuja, Nigeria*
[2] *Ladoke Akintola University of Technology, Nigeria*

Received November 15, 2017; Accepted April 12, 2018

Abstract

Many oil reservoirs have heterogeneity in rock properties. Understanding the form and spatial distribution of these heterogeneities is fundamental to the success of reservoir description. Permeability is one of the fundamental rock properties to characterize flow potentials of the reservoir when subjected to applied pressure gradients. A number of mathematical models have been suggested in the literature to simulate and quantify this property. However, common to them are difficulties in being able to model appropriately various geological variations associated with any reservoir. This study explores the benefits of using the artificial neural network (ANN) and Nuclear Magnetic Resonance (NMR) log in the permeability predictive model development. ANN was used to capture the non-linearity issues between the dependent and independent variables while the transversal relaxation times (T2) data is capable of capturing intrinsic rock properties at pore scale level. Out of verified datasets available, 60% of the datasets were used for the training process and the remainder for testing and validation. The input data was transverse relaxation time data, its mean value of the bins, mean square value of the bins and the maximum value of the bins. The developed ANN was trained, tested and validated using MATLAB Neural network toolbox trained with backward propagation scheme. The result shows a very good performance of ANN when compared with other existing empirical correlations adopted in this study.

Keywords: Permeability; Heterogeneity; Artificial Neural Network; Reservoir; MATLAB.

1. Introduction

Permeability and porosity are among the most important rock properties. Of this two, permeability has been found to be a function of porosity as it measures the ease with which fluids flow through the rocks' pores under the influence of applied pressure gradient. Despite being a critical factor that affects the fluid flow within the rock, there has been no universally acceptable method for its estimation. Having a correct knowledge of permeability variation downhole is very important in reservoir characterization i.e. static modeling and dynamic reservoir modeling.

Many a time, several researchers have made considerable attempts at studying the factors that control permeability and most of them concluded that porosity, grain size, degree of sorting, cementation are among the key parameters accounting for permeability variation. Most of the permeability models are based on the assumption that there is a strong correlation between porosity and permeability [1-3]. Previous works on the prediction of permeability such as Timur-Coates, SDR model, Carman-Kozeny model and FZI concept have suffered from either overestimation or underestimation of the reservoir rock permeability and inability to produce appropriate permeability for specific lithology [3-4].

Furthermore, other researchers have also found that there exists an empirical relationship between capillary pressure, porosity, and permeability. Most of these models have been found to perform to an appreciable degree of confidence in sandstone reservoirs but fail in carbonate reservoirs because of diagenetic effect, grain size variation etc. [3-5]. Because of these setbacks, a better predictor that can handle these inherent unconformities will be good for modeling the reservoir complexities as the accuracy of any model depend upon the objective of the research and level of understanding of reservoir complexities.

Due to the inability of most empirical correlation to correctly model the reservoir rock complexities, an alternative was sought in Artificial Neural Network (ANN). According to Hamada and Elshafei, this model has been found to perform excellently in modeling this complex relationship [5]. Unlike regression analysis used in developing the most empirical correlations, ANN doesn't require the generation of any relationship between the input and output data as it has the ability to deduce the underlying relationship from the given training data. However, using ANN for identification purposes is more useful when a large number of data are available.

This research work unlike no other study the development of a generic artificial neural network model to predict permeability of reservoir rock within the uncored intervals. The outcome of this study will also be compared with existing correlations to compare its relative performance. MATLAB ANN and NMR were used without the addition of conventional log data that have been proved to contain uncertainties.

2. Methodology

2.1. Data collection and analysis

In this study, NMR logs and core data from an XYZ field were collected and analyzed. Furthermore, information gotten from the conventional logs were used to estimate permeability using existing correlations such as the Schlumberger-Dolls-Research and Timur- Coates permeability.

Prior to training the AANN model, the data sets must be analyzed to remove inconsistencies. Here, extreme values of permeability values were included in this study in order to the account for heterogeneity associated with the XYZ reservoir. In this study, the normalization algorithm used for transforming the data is the logarithmic type which has the ability to capture the effect of extreme values such as a low-permeable shale interval within a highly permeable formation. Also, this transformation will help reduces variability and makes the domain of its stochasticity uniform.

Using all the datasets, the first step was to identify different regions such as regions of low permeability, medium permeability, and high permeability. Fig 1 depicts the histogram that shows the skewed distribution of the permeability within the XYZ reservoir.

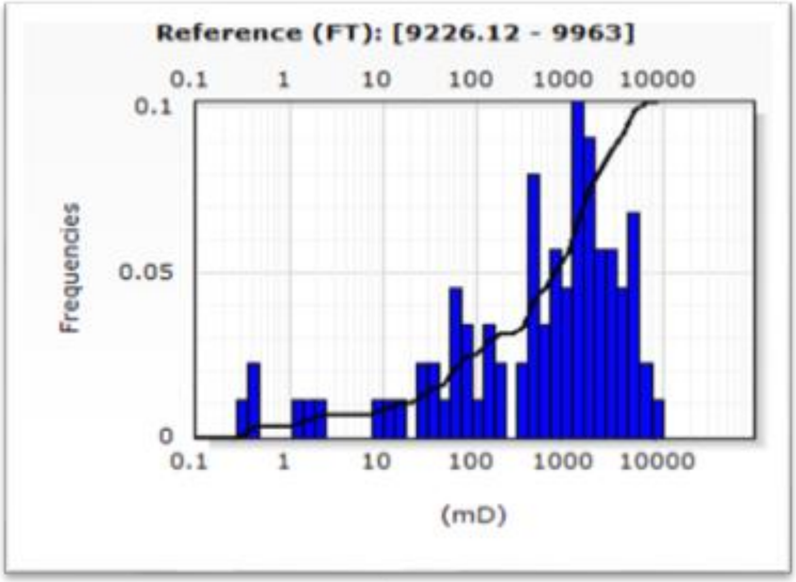

Figure 1. Histogram of the permeability distribution

2.2.Neural Network model development

Inputs, in this case, T_2 distributions, representing the variables that affect the output (permeability) of the network are fed to each of the neurons in the following layers with activation depending on their weighted sum of the inputs. Fig. 2a and 2b show the diagrammatic representation of a typical biological neural network and artificial neural network architecture respectively, depicting various component and characteristics used in model development.

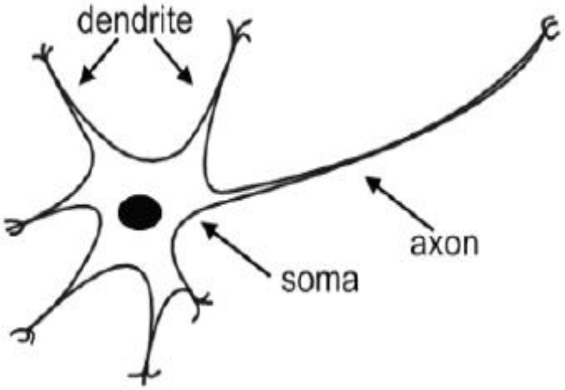

Figure 2b. Typical Artificial neural network

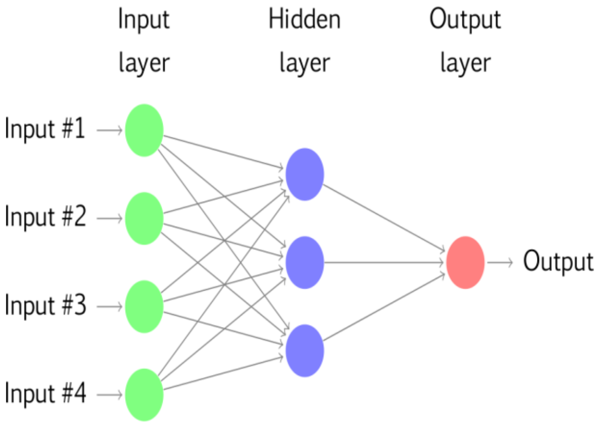

Figure 2b. Typical Artificial neural network

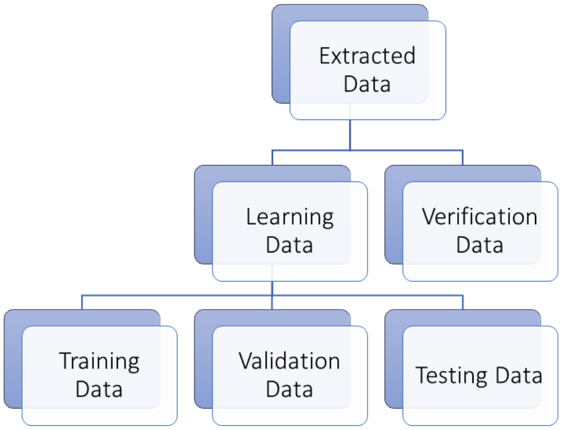

The network was trained to adapt the weights such that the error between the desired output and the network output is minimized. The summary of steps that were used in the development of the neural network model is as shown in fig. 3 The weight used was selected at random by the ANN toolbox itself. Two steps used in training the model include the feedforward computation and weight adaptation. The method of training used in this research is an adaptive training algorithm. Of the 69 available datasets, 60% of the available test data was used to train the network while the remaining data was used for model testing and validation.

The performance indices used to assess the accuracy of the developed model are summarized in Table 1. The model developed was used to predict permeability and statistically, the predictions were compared with the field and core data.

For more confidence and applicability of the developed model, the network was inspected against datasets that were chosen differently from those used to develop the model. It covered all the ranges of the input variables. After this testing and validation phase, the structure of the model earlier predicted was retained because of its acceptable precision. After the network has been validated, the permeability of given interval predicted using network was compared with that obtained from the core and empirical correlations including Schlumberger-Doll research model and Timur-Coates model. After the ANN has been trained and inspected by testing and validation, the final network developed was used to predict the permeability of the un-cored part of the reservoir given its NMR data.

2.3. Statistical analysis

In this phase, the Schlumberger Dolls research, Timur Coates and proposed Artificial Neural Network model were analyzed using performance indices summarized in Table 1.

Table 1. Summary of performance indices *(Arinkoola and Ogbe [6])*

Name of measure	Formula
Absolute deviation(AD)	$AD = \frac{1}{N}\sum_{i=1}^{N}(Pred.-Exp.)$
Average absolute deviation(AAD)	$AAD = \frac{1}{N}\sum_{i=1}^{N}/(Pred.-Exp.)/$
Root mean square error(RMSE)	$RMSE = \sqrt{\frac{1}{N}\sum_{i=1}^{N}(Actual - Predicted)^2}$
Average absolute percentage relative error	$AAPPRE = \frac{1}{N}\left[\sum_{i=1}^{N}/E_i/\right]$
Maximum error(Emax)	$E_{max} = Max/E_i/$ $E_{min} = Min/E_i/$ $E_i = \frac{Pred.-Exp.}{Exp.} \times 100$
Standard deviation(SD)	$SD = \sqrt{\frac{1}{N-1} \times \sum_{i=1}^{N} {E_i}^2}$

3. Results and analysis

As earlier stated that previous works on the estimation of permeability such as Timur-Coates, SDR, and Kozeny-Carman models have suffered from either overestimation or underestimation of the reservoir rock permeability because of their inability to produce appropriate permeability model for specific lithology. To confirm this assertion, a preliminary assessment of these models was performed with the result as shown in fig. 4, 5a and 5b.

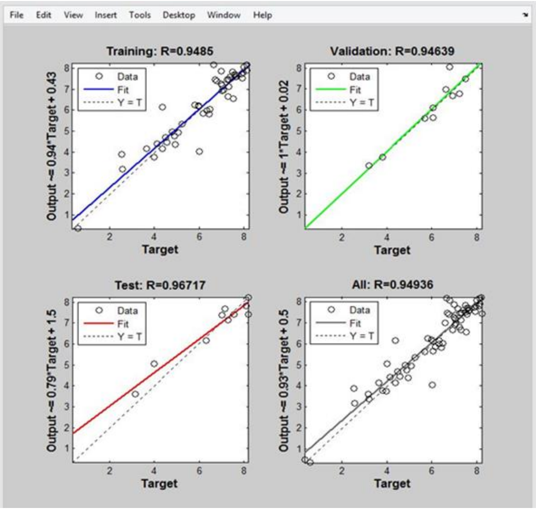

Figure 4. Performance evaluation of ANN training

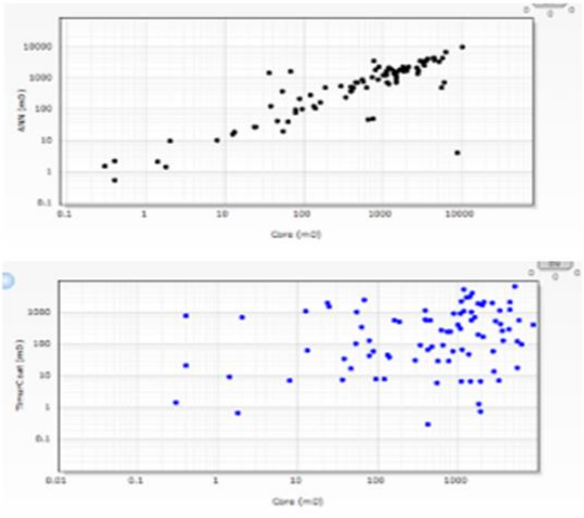

Figure 5a. Preliminary assessment of existing correlations

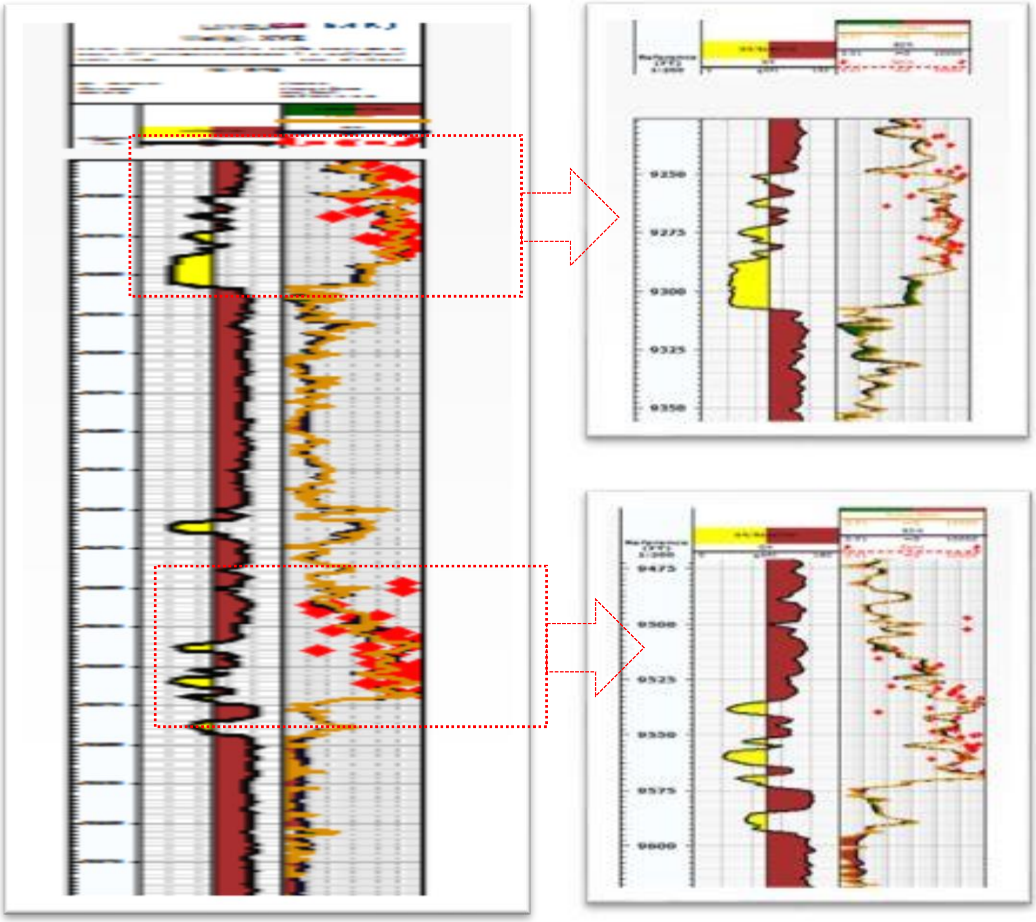

Figure 5b. Preliminary assessment of existing correlations

After the learning process, the following set of results were obtained. The regression plot (fig. 5) displays the network outputs with respect to estimate of the targets during training, validation, and test phase. For a perfect fit, the data should fall along a 45° line, where the network outputs are equal to the targets. From the assessment of this plot, it can be inferred that the neural model manages to properly interpolate the test data and achieves almost uniform performance on the entire log data. The correlation coefficients obtained for training, testing and validation are 0.9485, 0.9672 and 0.9464 respectively. For this problem, these coefficients are reasonably good and the developed model is capable of giving a realistic forecast of permeability where data are not available.

Figure 6a and 6b show the estimate of permeability using the developed model, studied correlations and core data. From the figure, it can be seen that the ANN model was able to model the complex nonlinear relationship between the petrophysical properties and it was also able to generalize the relationship between the properties in different facies. The use of arti-ficial neural network has overcome the problem of non- linearity that has led to underestimation and overestimation associated with the use of other existing empirical correlations. This will surely help petrophysical scientist and oil companies in estimating permeability in un-cored well once the T_2 distribution for each bin are available

The statistical evaluation of the existing correlations coupled with the proposed model is as shown in Table 2. Here, the estimates of permeability of the developed model were compared with each target output. From Table 2, statistical analysis shows the negligible difference between the estimate of using ANN but large differences using SDR and Timur-Coates when compared with the base value (core permeability). Although the model developed prediction is within an acceptable range, it can still do better if additional data are available.

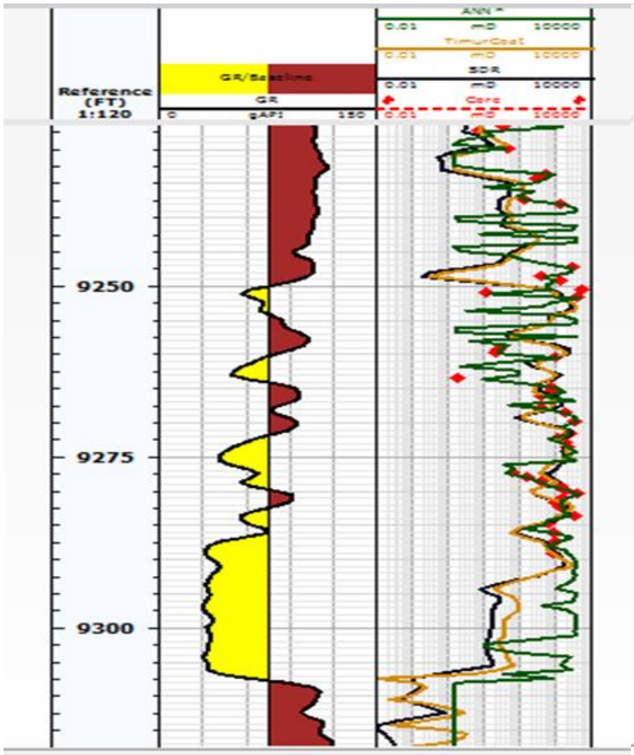

Fig. 6a. Well section 1 using the proposed ANN model

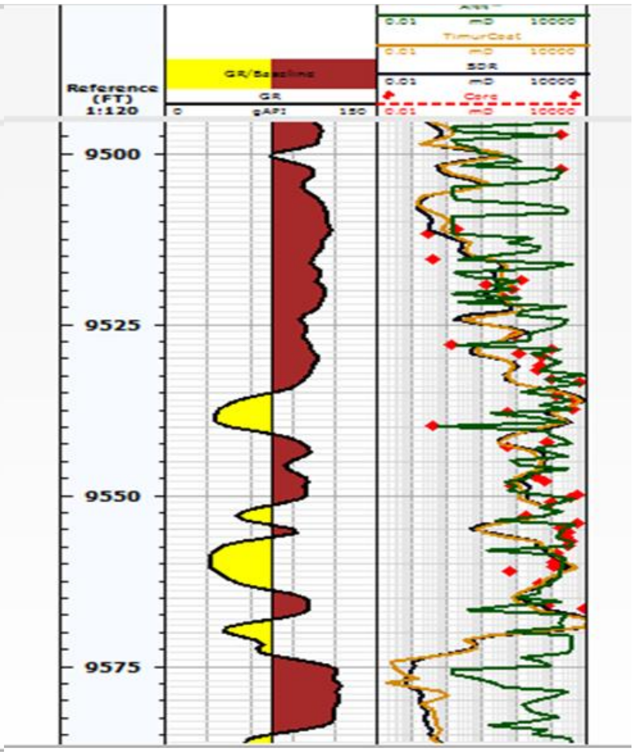

Fig. 6b. Well section 2 using the proposed ANN model

Table 2. Summary of performance indices

Measure	ANN	Timur	SDR
AD	0.02	2.29	2.43
AAD	0.62	2.29	2.43
RMSE	1.51	9.14	10.23
SD	0.61	0.31	0.28
Emax	6.09	16.68	28.48
AAPRE	0.66	0.17	0.32

The model developed using the artificial neural network presents a new and unique way in estimating reservoir permeability. The rock permeability estimated through this process is expected to less error prone because it mimics the way human being learn new things. It is also expected that the heterogeneities usually present in most reservoir were modelled accurately using the ANN.

4. Conclusion

From the results obtained it can be concluded that the prediction of permeability using artificial neural network had provided an accurate model for predicting permeability in oil and gas wells. It was also deduced that NMR derived permeability has shown good matching with core tests results. Also, that NN-predicted permeability from NMR decay times T_2 achieve very close values to the core permeability compared with other models. It is recommended to use the developed NN model to predict permeability from NMR data in other wells so as safe companies from incurring costs that could have been averted if they had used the model. It is also recommended to try different NN structures for possibly achieving improved results than those obtained by Feed Forward Neural Network and also a considerable amount of NMR data should be provided for future research because the NMR data gives a better representation of the hydrocarbon fluid present in the oil and gas bearing rock.

References

[1] Kozeny J. Uber Kapillare Leitung des Wassers im Boden, Stizurgs- berichte. Royal Academy of Science Proc. Class I, Vienna.1927; 136:271–306.

[2] Rose W. Theoretical Generalizations Leading to the Evaluation of Relative Permeability. Trans. AIME. 1936; 186:111.

[3] Amaefule JO, Altunbay M, Tiab D, Kersey DG, Keelan DK. Enhanced Reservoir Description: Using Core and Log Data to Identify Hydraulic (Flow) Units and predict Permeability in Uncored Intervals. SPE paper 26436 Presented at the SPE Annual Technical Conference and Exhibition, Houston Texas, October 3 1993.

[4] Jaya I, Sudaryanto A, Widarsono B. Permeability Prediction Using Pore Throat and Rock Fabric: A Model from Indonesian Reservoirs. SPE Paper 93363 presented at the Asia Pacific Oil & Gas Conference and Exhibition, Jakarta Indonesia, 5-7 April 2005.

[5] Elshafe, M, Hamada GM, 2010. Neural network prediction of porosity and permeability of heterogeneous gas sand reservoirs using NMR and conventional logs. Paper NAFTA 2010; 61(10) 451-460, Dhahran, Saudi Arabia.

[6] Arinkoola AO, Ogbe DO, 2015. Examination of experimental designs and response surface methods for uncertainty analysis of production forecast: A Niger Delta case study. Journal of Petroleum Engineering. 2015; ID 714541, http://dx.doi.org/10.1155/2015/714541.

To whom correspondence should be addressed: Teslim Olayiwola, Department of Petroleum Engineering, African University of Science and Technology, Km 10 Airport road, Galadimawa roundabout, Abuja
olayiwolateslim9@gmail.com

Petroleum and Coal

Article **Open Access**

IMPACT OF POWER PLANT GREENHOUSE GASES EMISSIONS IN AN URBAN ENVIRONMENT

B. S. Fakinle[1], O. B. Okedere[2] , J. A. Sonibare[3]

[1] *Department of Chemical Engineering, Landmark University, Omu-Aran, Kwara State, Nigeria*
[2] *Faculty of Engineering, Osun State University, Osogbo, Nigeria*
[3] *Environmental Engineering Research Laboratory, Department of Chemical Engineering, Obafemi Awolowo University, Ile-Ife, Nigeria*

Received June 24, 2018; Accepted September 28, 2018

Abstract

Greenhouse gases (GHGs) emission profiles of a thermal plant were investigated for different scenarios of fuel utilization. The scenarios were the proposed plant using natural gas only and the existing plant with a mix of low pour fuel oil (LPFO) and natural gas (NG). Emission inventory approach was adopted to quantify annual levels of three key GHGs while global warming potentials were used to determine the carbon dioxide equivalent of the GHGs. Results showed that the existing plant with a mix of LPFO and NG had total carbon dioxide equivalent ($tCO_2 eq$) of 13330961.8 while the proposed plant had 10296349.7 (tCO_2 eq). The discontinuation of LPFO was observed to reduce GHGs emission profile by 22.8%. Given, the desire to reduce GHG emissions and its negative impacts globally, scenario 2 is seen as the preferred alternative.

Keywords: *Thermal plant; urbanization; greenhouse gas; emission inventory; carbon dioxide equivalent; global warming*

1. Introduction

The greenhouse effect is a natural phenomenon in the atmosphere and is essential to maintain the earth's temperature. In fact, without the greenhouse effect, the earth would be about 33°C colder than it is today and would be uninhabitable for humans and most other life forms. However, increasing concentrations of greenhouse gases will result in a continuous increase in earth's temperature, and this increase could significantly impact life on earth [1-2]. The primary causes of climate pattern change are the greenhouse gases (GHGs) which include water vapour (H_2O), carbon dioxide (CO_2), methane (CH_4), nitrous oxide (N_2O), hydrofluorocarbons (HFCs), perfluorocarbons (PFCs) and sulfur hexafluoride (SF_6) [3]. Increasing concentrations of these gases will allow the atmosphere to trap higher than the usual amount of thermal radiation, preventing heat loss into space and resulting in higher surface temperatures [4].

CO_2 is the leading GHG, accounting for about 80% of the impact [5]. CO_2 enters the atmosphere through fossil fuel and coal combustion, agricultural activities, industrial activities, energy use, fertilizer application and as a result of other chemical reactions [6]. It is removed from the atmosphere by the plant during photosynthesis and also by acid rain. CH_4 is emitted during production and transportation of coal, natural gas and petroleum products. It is also emitted from livestock, agricultural activities and decay of organic waste from municipal solid waste landfills. N_2O is emitted during combustion of fossil fuels and solid waste, as well as industrial and agricultural activities while fluorinated gases (HFCs, PFCs, SF_6) are synthetic gases emitted from a variety of industrial processes. They are emitted in smaller quantities but are referred to as High Global warming potential (GWP) gases. GWP is an index that represents the global warming impact of a greenhouse gas relative to carbon dioxide. GWP represents the combined effect of how long the gas remains in the atmosphere and its relative effectiveness in absorbing outgoing infrared heat [7].

While urbanization is a welcome development, it has been identified as the leading force driving anthropogenic activities which are the leading causes of GHG emission [8-10]. It occurs as a result of changes in social wellbeing, in-flow, and concentration of people and activities in cities. The dynamics of urbanization is driven by changes in population, employment opportunities, industrialization, consumption patterns, and availability of energy, international migration, and accessibility. Over the years increase in population growth and human activities in urban areas had led to increasing GHG emission and urban vulnerability to hazards of climate change.

One of the key factors driving urbanization but which is responsible for GHG emission is energy generation. The Nigerian energy generation systems comprise a mix of hydro and thermal plants but the latter forms the bulk of energy generated in Nigeria [11]. The drive to improve energy generation and at the same time limit the emission of GHGs is of major concern. Although most of the thermal plants in Nigeria are natural gas fired, there are still pockets of plants with a mix of natural gas and low pour fuel oil (LPFO). For instance, Egbin thermal station which is the largest contributor to energy generated in Nigeria uses a mix of natural gas and LPFO. Presently, plans are on-going to introduce additional natural gas fired thermal plants while discontinuing the use of LPFO. The present study was carried out to investigate how the proposed addition of gas fired plants and removal of LPFO fired plant from an existing thermal plant will impact on greenhouse gas emission.

2. Methodology

2.1. Study area description

The study area is Egbin thermal power plant located at the suburb of Lagos State, Ijede area of Ikorodu (Figure 1). It is the largest power generating station in Nigeria with an installed capacity of 1,320 MW consisting of 6 units of 220 MW which was commissioned in July 1985. The station is located at latitude 6^0 33′ 48″ North and Longitude 3^0 36′ 55″ East. It is about 40 km north east of the city of Lagos, and is situated on low land in Ijede and bounded by the Lagoon to the south, Agura/Gberigbe to the north and situated in Ijede Local Council Development Area. The station is of reheat type with intermediate low pressure impulse reaction turbine design and a hydrogen cooled generator.

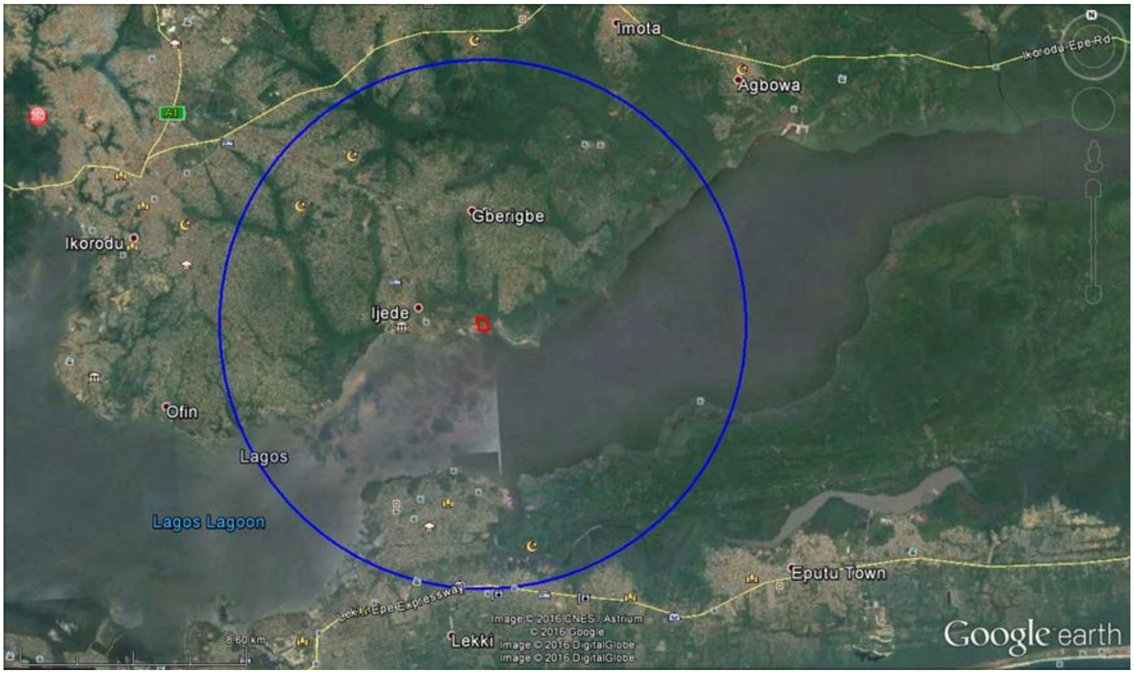

Figure 1. The Power plant location and zone of interest

2.2. Greenhouse gases (GHGs) emission sources

The existing power plants of capacity 1,320 MW in addition to the proposed three (3) units 450 MW capacity plants are the identified main sources of GHGs in the studied project. The existing Egbin power station has six units 220 MW Babcock- Hitachi Power Plants which are in operations to give 1320 MW are already contributing to GHGs. These power plants operate on dual fuel including Low Pour Fuel Oil (LPFO) and natural gas. The proposed three units 450 MW Mitsubishi Hitachi Gas Turbines are also expected to contribute GHGs to the proposed project airshed.

The emissions are as a result of fuel combustion activities in the power plants in addition to the other combustion products including criteria air pollutants and heat. During operation of the three units 450 MW Mitsubishi Hitachi Gas Turbines complete oxidation of carbon compounds available in fuel may result in the formation of carbon dioxide (CO_2) in the presence of complete combustion. It is the principal anthropogenic greenhouse gas that affects the Earth's radiative balance thus the reference gas against which other greenhouse gases are measured. Its duration in the atmosphere is 50 – 200 with 100-year global warming potential of 1. Similarly, N_2O is generated during fuel combustion by oxidation of chemically-bound nitrogen in the fuel and by fixation of nitrogen in the combustion air. At about 600 – 1000 °C temperature during combustion activities in the power plants, the formation of N_2O may be encouraged especially from HCN produced in intermediate reactions. Its duration in the atmosphere is about 120 years with a 100-year Global Warming Potential of 310. The other important greenhouse gas is CH_4 because its molecules survive for about 12 ± 3 years in the atmosphere and it is about 30 times more effective in heat trap than CO_2. In thermal power plant stations, CH_4 sources include natural gas leakage and its escape from combustion activities.

The anticipated annual GHGs emissions from the proposed thermal station expansion were determined using a combination of fuel consumption and the IPCC emission factor for natural gas and LPFO combustion. The natural gas consumption in each of the proposed power plants is 80,234 m^3/h while it is 54,430 m^3/h in each of the existing plants. The LPFO consumption in the existing plant is 45,760 kg/h. Table 1 shows the emission factors for the investigated gases. The scenarios considered include the emission of GHGs from newly proposed power plants (Scenario 1) only, emission of GHGs from a combination of newly proposed power plants and the existing power plants operating on natural gas (Scenario 2) and existing plants running on natural gas and LPFO (Scenario 3). In addition, the total GHG emission (tCO_2 equivalent) which is the standard reporting procedure for GHGs were determined by multiplying the annual GHG (ton/year) with the corresponding global warming potential.

Table 1. Emission factor for GHGs from thermal plants

	EF for GHGs		
	CH_4	N_2O	CO_2
Natural gas	1.00	0.10	56 100.00
LPFO	3.00	0.60	77 400.00

3. Result and discussion

3.1. Annual tonnage of GHGs emission from proposed and existing system

As presented in Table 2 the anticipated greenhouse gases emissions from scenario 1 are 92.7 tons/annum, 9.3 tons/annum and 5.2 million tons/annum for CH_4, N_2O and CO_2 respectively but 183.3 tons/annum, 18.3 tons/annum and 10.3 million tons/annum from scenario 2. The Scenario 3 operations of the existing power plant will generate greenhouse gases of 411.9 tons/annum, 72.9 tons/annum and 13.4 million tons/annum for CH_4, N_2O and CO_2 respectively. While the annual Scenario 1 operation of the proposed project will generate CO_2 level that is 5.36% of the national CO_2 emission from energy generation as reported by CIA [12], its Scenario 2 operation will generate CO_2 level that is 10.61% of the national CO_2 emission from energy generation while CO_2 from its Scenario 3 operation will be 13.85% of the national CO_2 emission from energy generation.

Table 2. Emission sources characteristics of the proposed and existing gas turbines

Emission source	From natural gas (tons/annum)			From LPFO (tons/annum)		
	CH_4	N_2O	CO_2	CH_4	N_2O	CO_2
Proposed 450 MW Mitsubishi Hitachi Power 1	30.90	3.10	1 734 690.90	-	-	-
Proposed 450 MW Mitsubishi Hitachi Power 2	30.90	3.10	1 734 690.90	-	-	-
Proposed 450 MW Mitsubishi Hitachi Power 3	30.90	3.10	1 734 690.90	-	-	-
Sub-Total	**92.70**	**9.30**	**5 204 072.70**	-	-	-
Existing 220 MW Babcock- Hitachi Power Plant 1	15.10	1.50	848 071.10	53.20	10.60	1 372 320.60
Existing 220 MW Babcock- Hitachi Power Plant 2	15.10	1.50	848 071.10	53.20	10.60	1 372 320.60
Existing 220 MW Babcock- Hitachi Power Plant 3	15.10	1.50	848 071.10	53.20	10.60	1 372 320.60
Existing 220 MW Babcock- Hitachi Power Plant 4	15.10	1.50	848 071.10	53.20	10.60	1 372 320.60
Existing 220 MW Babcock- Hitachi Power Plant 5	15.10	1.50	848 071.10	53.20	10.60	1 372 320.60
Existing 220 MW Babcock- Hitachi Power Plant 6	15.10	1.50	848 071.10	53.20	10.60	1 372 320.60
Sub-Total	**90.60**	**9.00**	**5 088 426.60**	**319.20**	**63.60**	**8 233 923.60**
Grand-Total	**183.30**	**18.30**	**10 292 499**	**411.90**	**72.90**	**1 3437 996**

3.2. Carbon dioxide equivalent (tCO2 e) of the GHGs

The standard practice in the reporting of GHGs is to express their emissions in carbon dioxide equivalent (tCO_2 eq). This is to bring all GHGs to a common unit and to facilitate the determination of the total greenhouse gas concentration. The (tCO_2 eq) of GHGs from the individual unit of Egbin thermal plants as well as overall (tCO_{2eq}) from the different scenarios are reported in Table 3 and Table 4, respectively. The total GHG emission (tCO_2 eq) from scenarios 1, 2 and 3 are 5206019.4, 10296349.7 and 13330961.8, respectively. Considering the different scenarios of existing and proposed systems, the introduction of new sets of natural gas fired thermal plants and discontinuation of LPFO fired thermal plants as represented by scenario 2 is expected to result in about 22.8% reduction in the total GHG emission.

Table 3. Total GHG emission from Egbin thermal station

GHGs	Scenario 1* (CO_2 e)	Scenario 2** (CO_2 e)	Scenario 3*** (CO2 e)
CH_4	1 946.7	3 849.7	8 605.8
N20	2883	5 673	22 506
CO_2	5 204 072.7	10 292 500	13 322 356
Total	5 206 019.4	10 296 349.7	13 330 961.8

**Describes the contribution of proposed addition with natural gas only*

***Describes the existing and proposed system with the removal of LPFO utilization*

****Describes the existing system with utilization of natural gas and LPFO*

Table 4. Actual GHG emissions from proposed and existing gas turbines

Emission source	From natural gas (tons/annum)			From LPFO (tons/annum)		
	CH_4	N_2O	CO_2	CH_4	N_2O	CO_2
Proposed 450 MW Mitsubishi Hitachi Power 1	648.9	961	1 734 691	-	-	-
Proposed 450 MW Mitsubishi Hitachi Power 2	648.9	961	1 734 691	-	-	-
Proposed 450 MW Mitsubishi Hitachi Power 3	648.9	961	1 734 691	-	-	-
Sub-Total	**1946.7**	**2883**	**5 204 073**	-	-	-
Existing 220 MW Babcock- Hitachi Power Plant 1	317.1	465	848 071.1	1117.2	3286	1 372 321
Existing 220 MW Babcock- Hitachi Power Plant 2	317.1	465	848 071.1	1117.2	3286	1 372 321
Existing 220 MW Babcock- Hitachi Power Plant 3	317.1	465	848 071.1	1117.2	3286	1 372 321
Existing 220 MW Babcock- Hitachi Power Plant 4	317.1	465	848 071.1	1117.2	3286	1 372 321
Existing 220 MW Babcock- Hitachi Power Plant 5	317.1	465	848 071.1	1117.2	3286	1 372 321
Existing 220 MW Babcock- Hitachi Power Plant 6	317.1	465	848 071.1	1117.2	3286	1 372 321
Sub-Total	**1 902.6**	**2 790**	**5 088 427**	**6 703.2**	**19716**	**8 233 926**
Grand-Total	**3 849.7**	**5 673**	**10 292 500**			

4. Conclusion

The study investigated the impact of discontinuation of LPFO unit and the introduction of the additional natural gas unit on GHG emission profile of a thermal plant. The Scenario 3 operations of the existing power plant were observed to generate greenhouse gases of 411.9 tons/annum, 72.9 tons/annum and 13.4 million tons/annum for CH_4, N_2O and CO_2 respectively. The replacement of LPFO unit with additional units that run on NG was observed to yield 183.3 tons/annum, 18.3 tons/annum and 10.3 million tons/annum for CH_4, N_2O and CO_2 respectively. These values represent a significant reduction in the annual emission rates of these gases. Considering the carbon dioxide equivalent of the three GHGs, the replacement of LPFO unit with additional units of NG was observed to reduce GHGs emission profile of the thermal plant by 22.8%. Given, the desire to reduce GHG emissions and its negative impacts globally, it is concluded that the NG fired thermal plant will be a better alternative.

References

[1] Oreskes N. Beyond the Ivory Tower: The Scientific Consensus on Climate Change. Science, 2004; 306: 1686.

[2] U.S. EPA. Climate Change Science: State of Knowledge. Accessed June, 2018, http://www.epa.gov/climatechange/science/stateofknowledge.html

[3] IPCC (2007a). Climate Change 2007: The Physical Science Basis. Contribution of Working Group I to the Fourth Assessment report of the Intergovernmental Panel on Climate Change [Solomon, S., D. Qin, M. Manning, Z. Chen, M. Marquis, K.B. Averyt, M. Tignor and H.L. Miller (eds.)]. Cambridge University Press, Cambridge, United Kingdom and New York,

[4] Michigan State University (2011) Greenhouse Gas Basics; Climate Change and Agriculture Fact Sheet Series E3148. www.swmpc.org/downloads/e3148_climate_change_1pdf

[5] Freije AM, Hassain T, and Salman EA. (2017) Global warming awareness among the University of Bahrian Science Students. Journal of the Association of Arab Universities for Basic and Applied Sciences, 2017; 22: 9 – 16.

[6] Ozbayrak O, Uyulgan M, Alpat S, Alpat SK, Kartal M. A research on high school students' knowledge related to global warming. Buca Eğitim Fakültesi Dergisi, 2011; 29: 58 – 67.

[7] IPCC (2007b). Climate Change 2007: Synthesis report. Contribution of working Groups I, II and III to the Fourth Assessment report of the Intergovernmental Panel on Climate Change [Core Writing Team, Pachauri, R.K and Reisinger, A. (eds.)]. IPCC, Geneva, Switzerland.

[8] NRC. Advancing science of climate change, National Research Council, The National Academic Press 2010, Washington, DC, USA.

[9] Vaughan A. Global carbon dioxide level breaks 400 ppm milestone. Guardian. Retrieved in May 2015 from www.theguardian.com

[10] Tongwane M, Mdlambuzi T, Moeletsi M, Tsubo M, Mliswa V., and Grootboom L. Greenhouse gas emissions from different Crop Production and Management Practices in South Africa. Environmental Development. 2016; 19: 23 – 35

[11] Sonibare JA. Air pollution implications of Nigeria's present strategy on improved electricity generation, Energy Policy, 2010; 38: 5783 – 5789

[12] CIA. The World Fact Book, Central Intelligence Agency, USA. https://www.cia.gov/library/publications/the-world-factbook/geos/ni.html Accessed on February 28, 2017

To whom correspondence should be addressed: Dr. B. S. Fakinle, Department of Chemical Engineering, Landmark University, Omu-Aran, Kwara State, fakinle.bamidele@lmu.edu.ng, xdales@yahoo.com

Petroleum and Coal

Article **Open Access**

MINERALOGICAL AND PETROGRAPHIC CHARACTERIZATION OF THE PALEOZOIC SHALE IN THE KROH FORMATION, NORTH PERAK, PENINSULAR MALAYSIA

*Monera Adam Shoieb**, *Chow Weng Sum, Mohd Suhaili Ismail, Haylay Tsegab Gebretsadik*

Universiti Teknologi PETRONAS, Department of Geoscience, Perak Darul Ridzuan, 32610 Seri Iskandar, Tronoh- Malaysia

Received July 4, 2018; Accepted September 28, 2018

Abstract

The increasing global demand for clean energy has made it imperative to explore and exploit unconventional oil and gas resources. Twenty-five percent of the sedimentary rocks in Peninsular Malaysia are Paleozoic shales. Nevertheless, no work has been carried out on shales in the Kroh Formation as regards their mineralogical composition and the effect of minerals in the hydraulic fracturing. Representative samples of black shales from the Kroh Formation were analyzed using X-ray diffraction (XRD) and Field Emission Scanning Electron Microscope (FE-SEM) with energy dispersive X-ray (EDX). The mineralogical composition of the shales has an important effect on the competency of rocks, for drilling and for hydrocarbon production. The FESEM results showed that the shale samples mainly comprised kaolinite which appears as booklets and quartz as round grain with small oval depressions of vary grain sizes. The elemental compositions of the shale samples determined by EDX confirm the minerals identified by FESEM. XRD and FESEM results both identified the minerals as illite, chlorite, pyrite, and a minor amount of dolomite, feldspar, and calcite. Knowing the clay minerals composition of the shale can be useful in planning for drilling and hydraulic fracturing.

***Keywords**: Minerology; Petrographic; Paleozoic shale; hydraulic fracturing; morphology.*

1. Introduction

Shale is a fine grain sedimentary rock, containing different types of clay minerals such as illite and kaolinite and non- clay minerals such as quartz and pyrite [1]. Shales are structurally fissile, which give them the tendency to split along relatively smooth surfaces parallel to the bedding plane. Black shale is a dark-colored mud rock containing organic matter, silt- and clay-sized mineral grains that accumulate together [2]. A shale gas reservoir comprises not of a single lithology but a collection of fine-grained rocks capable of storing significant amounts of gas. Most of the black shales are marine and may have a real extent of thousands of square kilometers. Unconventional hydrocarbon resource has become an interesting field of study and especially for it as source rocks which can also turn to be excellent reservoirs for generation and accumulation [3].

Exploration and production of gas from fine-grained rocks such as shale, contemporaneous with technology advancement facilitated exploration of black shale and made them cost benefit. During the last few years, a major concern has been given to unconventional oil and gas shales. Black shales have attracted interest from researchers primarily because of their economic importance in terms of hydrocarbon development potential [4]. Mineral composition and texture can be critical properties that influence the potential of shales, particularly for drilling and production [5]. The mineral contents of the rocks in an unconventional reservoir are important when the operators want to perform hydraulic fracture operations successfully. The presence of expandable clays like smectite causes problems during drilling due to swelling of the clays. Fractures are more common and created more easily in carbonate-rich and silica-rich than in clay-rich shales. Mineralogy alone maybe the first deciding factor when assessing the economic exploitation potential of a shale reservoir [6].

Generally, rocks with low clay and high quartz content have low Poisson's Ratio and high Young's Modulus, thus making them more brittle and more prone to natural fractures and are good for fracking [7]. Many Paleozoic black shales are rich in quartz and can be regarded as siliceous shales or marlstones. Shale can vary considerably in kerogen type, thermal maturity, and mineralogy [8-9]. In spite of the fact that Paleozoic black shales are old and their organic matter and degree of maturation might have been changed by diagenesis/metamorphism, these shales attract attention as potential unconventional oil and gas resources [10-12].

Twenty five percent of sedimentary rocks from Peninsular Malaysia are Paleozoic shales [13]. These black shale formations are exposed in areas such as Langkawi, Kedah, Perlis, North Perak, and many other areas in Malaysia. These areas have been mapped by the Minerals and Geoscience Department, and the lithology and stratigraphy have been studied extensively [14-19]. However, the mineralogy and petrography of these shales have not been studied in detail. Therefore, this study is designed to characterize the mineral composition and petrographic texture of the shale in order to get an idea about the hydraulic fracturing potential based on the minerals that present in the shale.

2. Geological setting

Paleozoic rocks are mainly marine and account for about 25% by area of Peninsular Malaysia. The Paleozoic formations of Peninsular Malaysia are distributed in three northwesterly to northerly trending zones parallel to the general elongation trend of the Peninsula [13]. They are the Western Belt, Central Belt and Eastern Belts (Figure 1). Each of these Belts is characterized by distinctive tectonic, stratigraphy structure and sedimentary history.

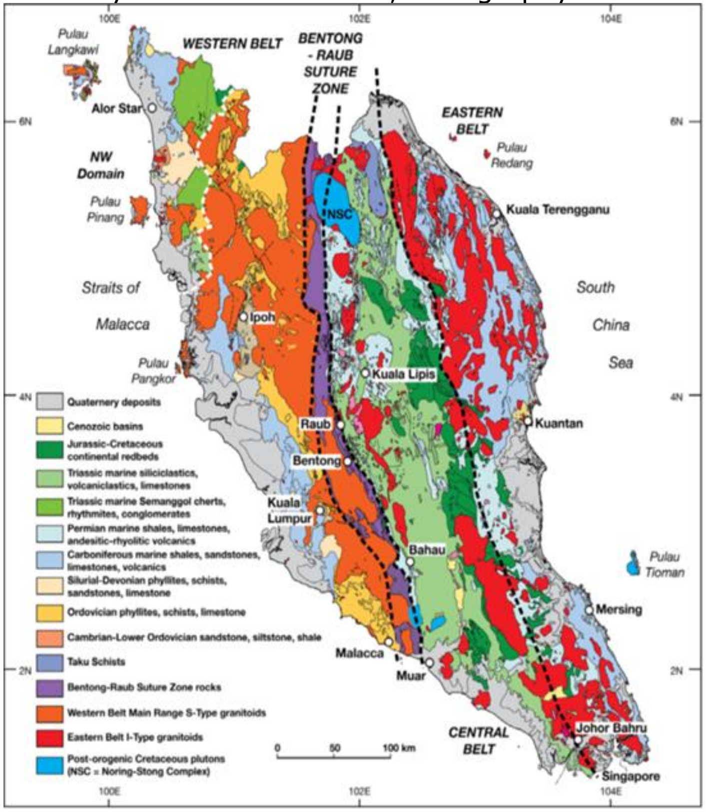

Fig 1. Simplified geological map of the Malay Peninsula showing the study area (*after Tate et al.* [30])

The Western Belt forms a portion of the Sibumasu Terrane, derived from the NW Australian Gondwana margin within the late Cambrian-Early Permian. The Central and Eastern belts represent the Sukhothai Arc constructed within the Late Carboniferous-Early Permian on the margin of the Indochina Block (derived from the Gondwana margin in the Early Devonian) [18].

Paleozoic rocks of the Western Belt are distributed at foothills along both flanks of the Main Range granite batholith stretching from the Malaysian–Thai border southwards to Malacca. The Northwestern Zone of the Western Belt covers Langkawi, Kedah, and Perlis and these are mainly shallow-marine shelf sediments [17]. Lower Paleozoic rocks are confined to the Western Belt, while the Upper Paleozoic rocks occur in the Central and Eastern Belts.

The Kroh Formation is part of the Baling Group. It is characterized by the Early – Middle Silurian and Lower Devonian graptolites, and the Early – Middle Devonian Tentaculites. The Mahang Formation in Kedah is equivalent to the Kroh Formation in Upper Perak. The Kroh Formation is overlain by the Upper Paleozoic rocks. The Upper Paleozoic rocks were deemed as an extension of the Kati Formation [20]. They are extensively exposed in the Pengkalan Hulu, Kelian Intan and Kerunai areas in northern Perak. The rock succession extends eastwards into the Bersia area as mentioned by [21] (Figure 2). Generally, the Kroh Formation is composed of black shale, sub-mature arenite, calcareous shale, and limestone.

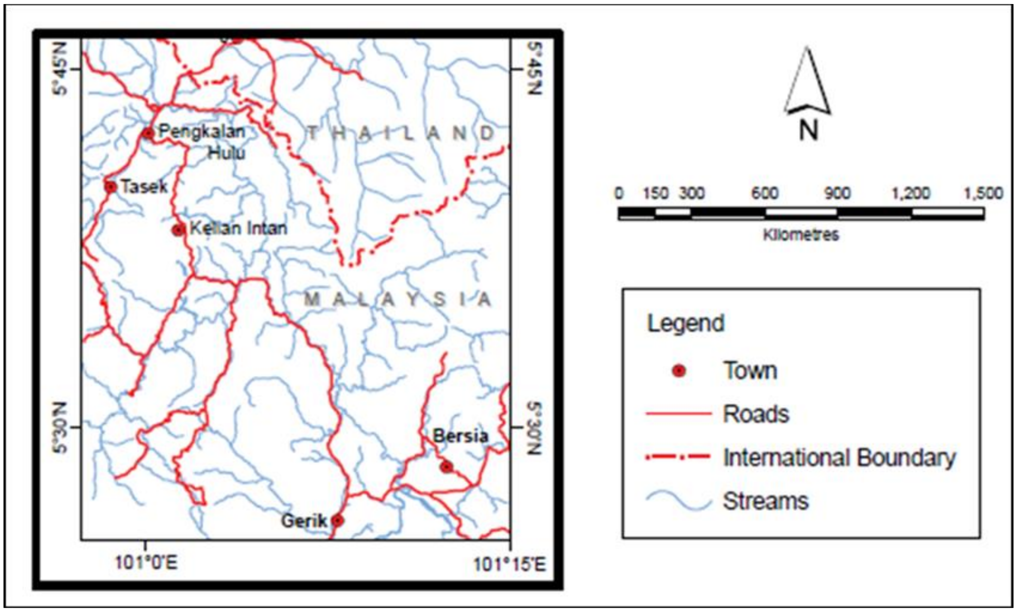

Fig 2. Location map of the study area (*after* [20])

Table 1. Schematic stratigraphic column of the Betong-Pengkalan Hulu Transect area, Malaysia showing the Kroh Formation [19]

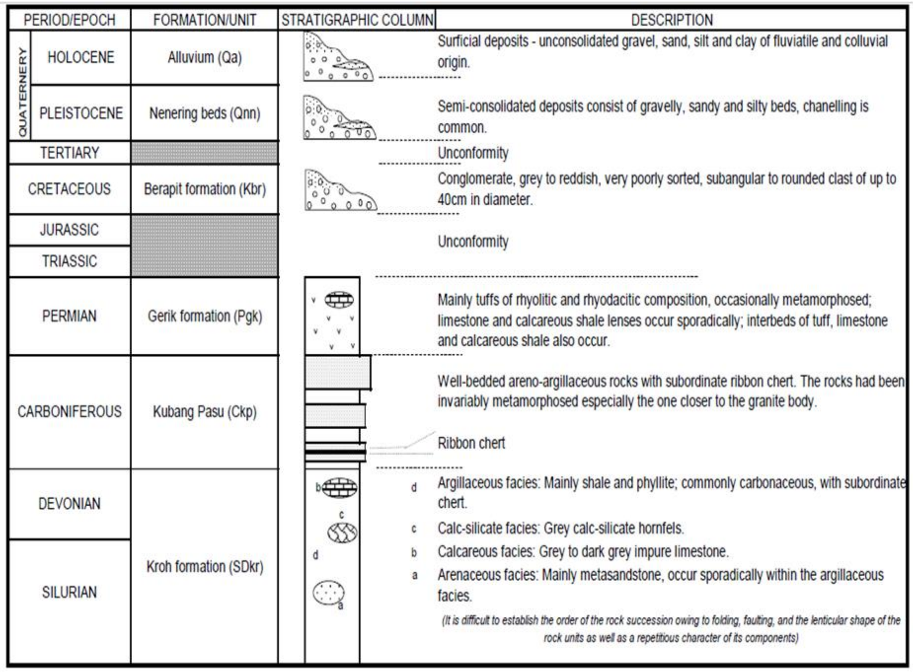

PERIOD/EPOCH		FORMATION/UNIT	STRATIGRAPHIC COLUMN	DESCRIPTION
QUATERNERY	HOLOCENE	Alluvium (Qa)		Surficial deposits - unconsolidated gravel, sand, silt and clay of fluviatile and colluvial origin.
	PLEISTOCENE	Nenering beds (Qnn)		Semi-consolidated deposits consist of gravelly, sandy and silty beds, chanelling is common.
TERTIARY		▨		Unconformity
CRETACEOUS		Berapit formation (Kbr)		Conglomerate, grey to reddish, very poorly sorted, subangular to rounded clast of up to 40cm in diameter.
JURASSIC		▨		Unconformity
TRIASSIC				
PERMIAN		Gerik formation (Pgk)		Mainly tuffs of rhyolitic and rhyodacitic composition, occasionally metamorphosed; limestone and calcareous shale lenses occur sporadically; interbeds of tuff, limestone and calcareous shale also occur.
CARBONIFEROUS		Kubang Pasu (Ckp)		Well-bedded areno-argillaceous rocks with subordinate ribbon chert. The rocks had been invariably metamorphosed especially the one closer to the granite body. Ribbon chert
DEVONIAN		Kroh formation (SDkr)		d Argillaceous facies: Mainly shale and phyllite; commonly carbonaceous, with subordinate chert. c Calc-silicate facies: Grey calc-silicate hornfels. b Calcareous facies: Grey to dark grey impure limestone. a Arenaceous facies: Mainly metasandstone, occur sporadically within the argillaceous facies. *(It is difficult to establish the order of the rock succession owing to folding, faulting, and the lenticular shape of the rock units as well as a repetitious character of its components)*
SILURIAN				

The rocks are divisible into four facies: the argillaceous facies, calc-silicate facies, calcareous facies, and minor arenaceous facies. The widely spread argillaceous facies with a considerable amount of carbonaceous content suggests that the deposition of this rock unit occurred in a euxinic marine environment. Fine-grained materials indicate long distance transportation and the deposition took place in a quiet and undisturbed environment. The absence of benthos fossils and bioturbation indicates that the deposition occurred in a deep marine environment. The calcareous facies and arenaceous facies with subordinate conglomerate might be deposited in the continental shelf, the relatively shallower part of the depositional basin [19].

3. Material and methods

Twelve representative samples were taken from six locations in the Gerik area, Upper Perak (Figure 2). They are carbonaceous shale and have been dated and assigned an Upper Ordovician -Lower Devonian age [22]. All the shale samples were subjected to X-ray diffraction (XRD) and Field emission scanning electron microscope (FESEM) studies. XRD analysis is a useful method to identify minerals that are present in the shales. Shale samples were ground using a milling machine into powder, and the powder was analyzed using a Bruker D8 Discover X-ray Diffractometer according to the Hardy and Tucker method [23]. Field emission scanning electron microscopy (FE-SEM) is a known tool for investigating and imaging the microstructure of rocks [24-27]. The method depends on the interaction of the electrons emitted by the FESEM with the atoms that make up the sample producing signals that contain information about the sample surface topography, composition, and properties such as electrical conductivity. Sample preparation includes polishing the sample into thin blocks and then coating with gold. Energy-dispersive spectrometry(EDX) technique was used to determine the elemental composition of the sample.

4. Results and discussion

4.1. X- Ray diffraction (XRD)

XRD was used to identify the clay minerals and other minerals present in the shale samples. The results of all shale samples from the Kroh Formation have a mineralogical composition which typically consists of kaolinite, illite, and non- clay minerals such as quartz. A large quantity of illite usually indicates older rocks. All of these minerals were identified by the fact that each mineral has unique fingerprints.

Kaolinite is a clay mineral, with the chemical composition ($Al_2Si_2O_5(OH)_4$). It is a layered silicate mineral, with one tetrahedral sheet of silica (SiO_4) linked through oxygen atoms [28], which has diffraction at 7.3Aº basal spacing [23]. Figure 3 shows the XRD result for one sample. Kaolinite is present in variable quantities in all shale samples. The XRD peak suggests that the kaolinite is a clear crystal.

Quartz is very common in shales and is present in all the samples as shown in Figure 3. The quartz has diffractions at 4.2 Aº and 3.3 Aº. The intensities of XRD peaks suggest that quartz is dominant in all the samples. The quartz produced the highest peaks as compared to the other minerals. The height of the peaks produced by a certain mineral does not indicate its quantity. It just shows that the mineral has a good crystalline form [29].

The presence of quartz will be good for hydraulic fracturing because fractures form more readily and more widespread in carbonate-rich and silica-rich shales. Other minerals identified from the XRD analysis include calcite, alkaline feldspar, siderite, dolomite, smectite, muscovite, goethite and pyrite (Figure 3). Table 2 shows the mineralogical composition of 12 rock samples in the Kroh Formation which were analyzed by XRD.

The qualitative analyses of mineral employing a search/match program become increasingly challenging when the mineral is a mixture of several phases, rendering the diffraction pattern complex.

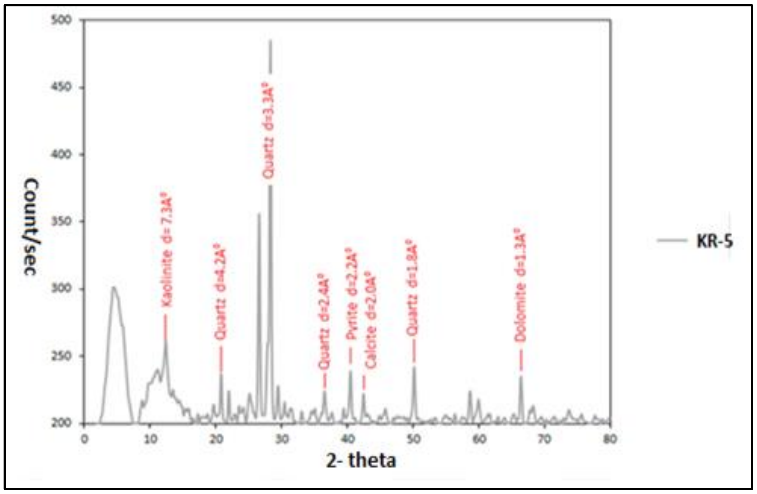

Fig 3. The XRD peak of shale from the Kroh Formation in the KR-3 samples

Table 2. Mineralogical composition of 12 rock samples from the Kroh Formation determined by XRD

Sample ID	Quartz	Kaolinite	Illite	Feldspar	Pyrite	Dolomite	Smectite
KR-1	✓	✓	✓		✓	✓	✓
KR-2	✓	✓					
KR-3	✓	✓		✓	✓		
KR-4	✓	✓			✓	✓	
KR-5	✓	✓	✓	✓			✓
KR-6	✓	✓					
KR-7	✓	✓	✓	✓			✓
KR-8	✓	✓		✓			✓
KR-9	✓	✓				✓	
KR-10	✓	✓					
KR-11	✓	✓		✓			
KR-12	✓	✓					✓

4.2. Field Emission Scanning Electron Microscope with energy dispersive X-ray (SEM-EDX)

Field Emission Scanning electron microscopes (FE-SEM) with energy dispersive X-ray (EDX) were employed to measure the surface topography, microstructure, and chemical composition of rock samples. The FESEM-EDX analysis was carried out on the twelve shale samples from the Kroh Formation. Figure 4 shows the images of shale samples at different magnification factors. The crystal structure can be clearly observed with increasing magnification.

Kaolinite appeared as pseudo hexagonal plates or books in the SEM result (Figure 5 A). The presence of kaolinite was also confirmed by EDX techniques. Results showed that the shale samples are dominated by silica, oxygen, and aluminum ($Al_2Si_2O_5(OH)_4$) and the weight concentration of Si and Al confirmed their identification as kaolinite (Figure 5B). In the SEM, the quartz appeared as rounded grain with small oval depressions and different grain sizes (Figure 6.A). The presence of quartz is also confirmed by EDX techniques. Results showed that the elemental composition of the shale samples is dominated by silica and oxygen (Si-O), and they have high peaks in the spectrum as shown in Figure 6.B. Addition, the weight concentration of these elements is high compared to the other elements present in the samples.

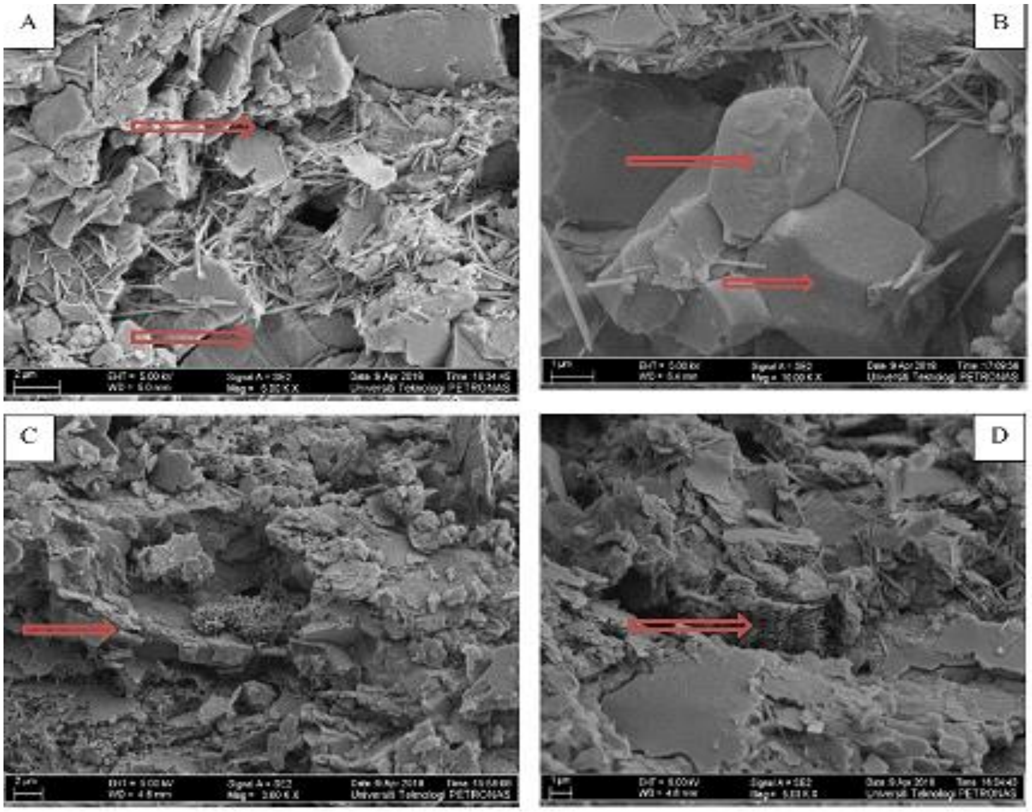

Fig 4. Images of shale samples from the Kroh Formation. (A) Quartz appeared as rounded grain with small oval depressions. (B) Quartz appeared as large grains. (C) Quartz appears as different grain size. (D) Kaolinite appeared as pseudo hexagonal plates or books

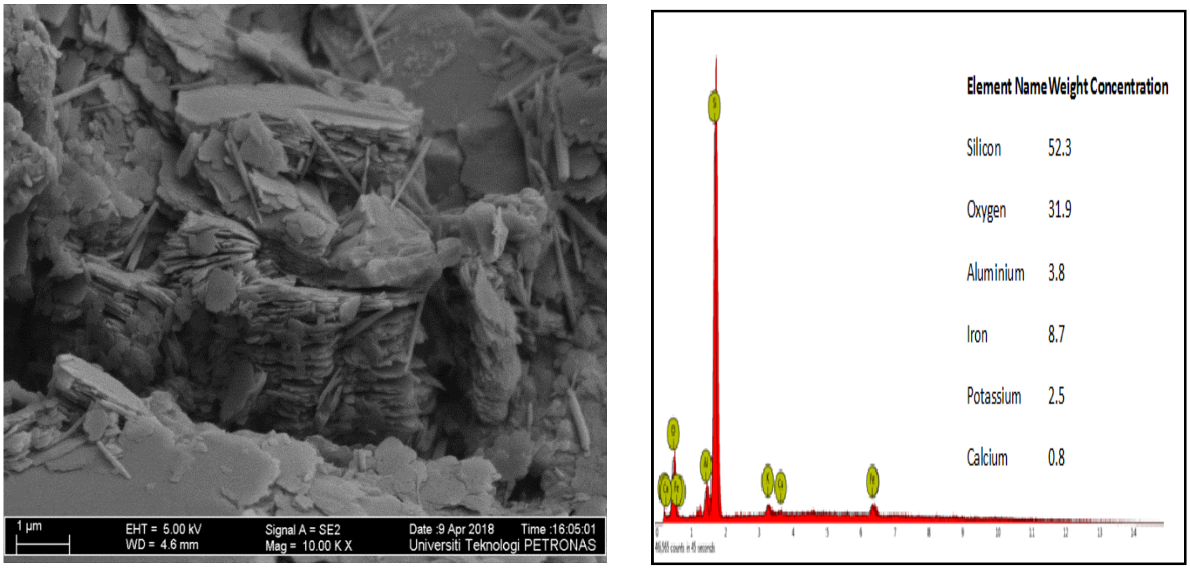

Fig 5. (A). Kaolinite appeared as pseudo hexagonal plates or books in sample KR-3. (B). EDX Spectrum Analysis of KR-3 for kaolinite show the elemental composition of the shale sample

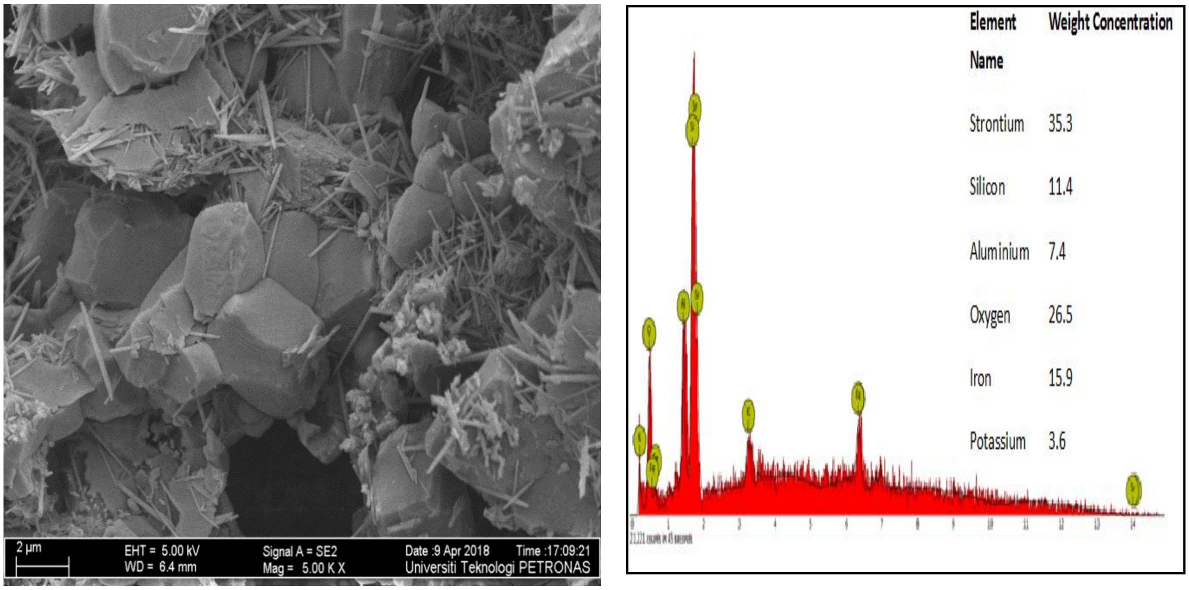

Element Name	Weight Concentration
Strontium	35.3
Silicon	11.4
Aluminium	7.4
Oxygen	26.5
Iron	15.9
Potassium	3.6

Fig 6. (A). SEM image of sample KR-5 shale sample shows the quartz appeared as large grains. (B). EDX Spectrum Analysis of sample KR-5 for quartz

5. Conclusion

An integrated mineralogical and petrographic investigation of the shale samples from the Kroh Formation in the Upper Perak was performed to determine the minerals and the morphology of the minerals present in the shale. Knowing the composition in the shales of the shale can be useful in planning for drilling and hydraulic fracturing.

FESEM were used to identify minerals to determine the chemical composition of the minerals present in the shale. Shale is the most abundant sedimentary rock and is a combination of a wide variety of minerals that clay minerals found in the samples tested are illite, kaolinite and the non- clay minerals are quartz and pyrite. The peaks of the quartz are highly diffracted because quartz has good crystalline form and shows larger peaks. On the other hand, clays do not diffract as well because they do not have good crystalline form and consequently, their peaks are lower than that of quartz.

The peak height of the quartz does not reflect the quantity. It just means that the quartz has a good crystalline form. It is difficult to get the quantitative mineral composition of the clays. The reason is that they do not have good crystalline forms and do not diffract well.

Acknowledgment

The authors would like to acknowledge the support providing by the PRF project "Advanced Shale Gas Extraction Technology Using Electrochemical Methods."

References

[1] Peters EJ. Petrophysics: Department of Petroleum and Geosystems Engineering. The Text note of the University of Texas at Austin 2004.

[2] Swanson VE, Swanson VE. Geology and geochemistry of uranium in marine black shales: a review, US Government Printing Office 1961, Washington, DC.

[3] Shoieb MA, Sum CW, Abidin NSZ, Bhattachary SK. The organic geochemical characterization: An indication of type of kerogen and maturity of early–Mid Jurassic shale in the Blue Nile formation. AIP Conference Proceedings, 2018. AIP Publishing, 030013.

[4] Wignall PB. Black shales. Oxford University Press 1994, USA ISBN0198540388.

[5] Shoieb MA, Abidin NSZ, Sum CW, Ibrahim Y. Mineralogical and Petrographic Characterization: An Indication of Fractability of Shale Gas Reservoir in the Blue Nile Basin, Sudan. ICIPEG 2016, DOI 10.1007/978-981-10-3650-7_21.

[6] Sondhi N. Petrophysical characterization of Eagle Ford shale. Ph.D. Thesis 2011, University of Oklahoma, Oklahoma.
[7] Elgmati M. Shale gas rock characterization and 3D submicron pore network reconstruction. Masters Theses. 6735, http://scholarsmine.mst.edu/masters_theses/6735.
[8] Aplin AC, MacQuaker JH. Mudstone diversity: Origin and implications for source, seal, and reservoir properties in petroleum systems. AAPG bulletin, 2011; 95: 2031-2059.
[9] Eseme E, Krooss B, Littke R. 2012. Evolution of petrophysical properties of oil shales during high-temperature compaction tests: Implications for petroleum expulsion. Marine and petroleum geology, 2012; 31: 110-124.
[10] Pashin JC, Kopaska-Merkel DC, Arnold AC, McIntyre MR, Thomas WA. Gigantic, gaseous mushwads in Cambrian shale: Conasauga Formation, southern Appalachians, USA. International Journal of Coal Geology, 2012; 103: 70-91.
[11] Soua M. Paleozoic oil/gas shale reservoirs in southern Tunisia: An overview. Journal of African Earth Sciences, 2014; 100: 450-492.
[12] Baioumy H, Ulfa Y, Nawawi M, Padmanabhan E, Anuar MNA. Mineralogy and geochemistry of Palaeozoic black shales from Peninsular Malaysia: Implications for their origin and maturation. International Journal of Coal Geology, 2016; 165: 90-105.
[13] Yee FK. The Palaeozoic sedimentary rocks of Peninsular Malaysia-stratigraphy and correlation. Workshop on Stratigraphic Correlation of Thailand abd Malaysia Haad Yai, Thailand 8-10 September, 1983, https://gsm.org.my/file/SCTM_01.pdf.
[14] Burton C. The Baling group/Bannang Sata group of the Malay/Thai Peninsula. Journal of Southeast Asian earth sciences, 1986; 1: 93-106.
[15] Jones CR. The geology and mineral resources of the Grik area, Upper Perak. Geological Survey Headquarters 1970.
[16] Foo KY. Geology and Mineral Resources of the Taiping-Kuala Kangsar Area Perak Darul Ridzuan: By Foo Khong Yee, Geological Survey Headquarters 1990.
[17] Cocks L, Fortey R, Lee C. A review of Lower and Middle Palaeozoic biostratigraphy in west peninsular Malaysia and southern Thailand in its context within the Sibumasu Terrane. Journal of Asian Earth Sciences, 2005; 24: 703-717.
[18] Metcalfe I. Tectonic evolution of the Malay Peninsula. Journal of Asian Earth Sciences, 2013; 76: 195-213.
[19] The Malaysia-Thailand Working Group. Geology of the Pengkalan Hulu-Betong Transect area along the malaysia-thailand border, The Malaysia-Thailand Border Joint Geological Survey Committee (MTJGSC), 2009.
[20] Teh G, Hussin AH. 1994. Field Relationships of Rock Units along the Malaysia-Thai Border, Nenering, Hulu Perak. Warta Geologi, 1994; 20(3):244.
[21] Mohd T, Mohd Zin, Selvarajah. Geology and Mineral Resources of the Kerunai Area, Perak Darul Ridzuan. Proceeding of the 24th Annual Geological Conference, 1993; 5: 92 – 106
[22] Burton CK. The geology and mineral resources of the Baling area, Kedah and Perak. Geol. Sur. Malaysia Dist. Mem., 1972; 12: 1–150.
[23] Hardy R, Tucker M. X-ray powder diffraction of sediments. Techniques in sedimentology, Oxford 1988:191-228, ISBN: 0632013613.
[24] Chalmers G, Bustin R, Powers I. A pore by any other name would be as small: the importance of meso-and microporosity in shale gas capacity. AAPG Annual Convention and Exhibition, Denver, Colorado, 2009.
[25] Wang FP, Reed RM. Pore networks and fluid flow in gas shales. SPE Annual Technical Conference and Exhibition, 2009. Society of Petroleum Engineers.
[26] Curtis ME, Ambrose RJ, Sondergeld CH. Structural characterization of gas shales on the micro-and nano-scales. Canadian Unconventional Resources and International Petroleum Conference, 2010. Society of Petroleum Engineers.
[27] Schieber J. Common themes in the formation and preservation of intrinsic porosity in shales and mudstones-illustrated with examples across the Phanerozoic. SPE Unconventional Gas Conference, 2010. Society of Petroleum Engineers.
[28] Pohl WL Economic geology: principles and practice. Metals, minerals, coal and hydrocarbons--introduction to formation and sustainable exploitation of mineral deposits. Springer Science & Business Media 2011, ISBN 978-1-4443-3662-7.
[29] Butt AS. 2012. Shale Characterization Using X-Ray Diffraction. Master of Engineering Thesis 2012, Dalhousie University, Dalhousie University Halifax, Nova Scotia.
[30] Tate RB, Tan DN, Ng TF. Geological Map of Peninsular Malaysia. Scale. 2008.

To whom correspondence should be addressed: Monera Adam Shoieb, Universiti Teknologi PETRONAS, Department of Geoscience, Perak Darul Ridzuan, 32610 Seri Iskandar, Tronoh- Malaysia

Petroleum and Coal

Article **Open Access**

SUBSURFACE CHARACTERIZATION USING SEISMIC REFRACTION TOMOGRAPHY IN THE UNIVERSITY OF PORT HARCOURT

Rasaq Bello[1], *Jonathan ChineduNwafor*[2]

[1] *Department of Physics, Federal University Kashere, Gombe State, Nigeria*
[2] *Department of Physics, University of Port Harcourt, Port Harcourt, Nigeria*

Received July 5, 2018; Accepted September 28, 2018

Abstract

Seismic refraction tomography survey was carried out in four different sites (profiles) for the subsurface characterization. Results showed that the study areas are made-up of three layers and there is an increase in velocity with depth in the areas. The first layer is the weathered layer and is suggested to be dry sand. It has average thicknesses of 12.49 m, 9.17 m, 11.71 m, and 11.73 m, and velocity ranges from 779 m/s to 1531 m/s, 822 m/s to 1487 m/s, 846 m/s to 1480 m/s and 837 m/s to 1475 m/s respectively for the four profiles. The second layer is thought to be saturated sand (aquifer layer) and has average thicknesses of 2.9 m, 2.8 m, 2.0 m and 2.3 m at depths of 12.49 m, 9.17 m, 11.71 m and 11.73 m with velocities ranges from 1531 m/s to 2068 m/s, 1487 m/s to 2073 m/s, 1480 m/s to 2026 m/s and 1475 m/s to 2006 m/s respectively along the profiles. The third layer which is thought to be sand stone at depths 15.39 m, 11.97 m, 13.66 m and 13.99 m, and has infinite thicknesses with velocities ranges from 2068 m/s to 4216 m/s, 2073 m/s to 4157 m/s, 2026 m/s to 4621 m/s and 2006 m/s to 4237 m/s respectively along the profiles.

Keywords: *Seismic; Refraction; Tomography; Lithology; Profiles.*

1. Introduction

The first geophysical approach used in search of the reservoir is the seismic refraction method, but over the years its relevance in the exploration of oil has reduced because of different types of modern reflection studies. Though, seismic refraction survey is continually relevance on the shallow investigation of the subsurface, especially for civil and geotechnical engineering sites. It remains non negligible exploratory instrument for a shallow survey when applied together with investigative drill [1]. The two ways travel time is measured in a refraction survey at a known place on the Earth along its surface where the seismic primary (P) waves energy is generated via an energy source. The energy source is usually generated through a small explosive charge, vibrosis or accelerated weight drop [2]. The energy which radiates from the shot point traveled via the top layer and refracted on a boundary, and then detected at the surface by geophones (12, 24, 48, or more geophones) that are arranged in linear array whereas travel times are recorded via seismometer. Graphs of geophone distance (starting from the first geophone to the last) against time of those first arrivals are plotted to show the depth to refracting interfaces. "Seismic refraction method is quantitative as it produces depths of various geo-material layers and the compressional wave velocity (V_p) of these layers" [3].

Seismic refraction tomography is a method for examining the Earth's interior with seismic wave generated by earthquakes or explosions. P-, S-, and surface waves can be used for tomographic models of different resolutions based on seismic wavelength, the seismograph array coverage, and wave source distance. The seismic refraction tomography (velocity gradient or diving-wave tomography) employs first arrival travel time of seismic wave for its input. In this method, both forward and reverse shots are taken by firing shots before the first geophone and after the last geophone respectively, and shots are also fired at various points of geophones which make it possible to scan every point of the Earth's interior of the profile line from both forward and reverse shot. Although the depth of probe depends mainly on the energy source (explosive, vibrosis or weight drop) and geophones spacing along the profile, that means the higher the geophone spacing is higher the depth of probe. The spatial variations such as pore fluids, fracturing, or lithology, maybe forecasted from the information obtained from seismic refraction tomography technique. Hence, the technique is of great importance in applications to engineering and greater extent of exploration [4]. Seismic refraction tomography survey was carried out in four different sites in the University of Port Harcourt with a total length of 95 mands 5 m being geophone spacing.

1.1. Geology of the study area

The study area of the first site (behind faculty of Social Sciences) has coordinates of latitude 04°54′28.5″ North and longitude of 006°55′06.8″ East with an elevation of 17.2 m, the second site (front of faculty of humanity) has coordinates of latitude 04°54′29.1″ North and longitude of 006°55′09.3″ East with an elevation of 17.4 m, the third site (behind Gas Engineering Department) has coordinates of latitude 04°54′26.0″ North and longitude of 006°55′25.4″ East with an elevation of 17.0 m, while the fourth site (adjacent to Gas Engineering Department) has coordinates of latitude 04°54′25.1″ North and longitude of 006°55′23.0″ East with an elevation of 17.1 m, all in the University of Port Harcourt, Obio/Akpor Local Government Area of Port Harcourt Metropolis, Rivers State of Nigeria.

1.2. Stratigraphic framework

The sequential order of the Niger Delta layers is made up three wide lithostratigraphic units and they are, (1) Benin Formation (sequence of a continental shallow massive sand), (2) Agbada Formation (a costal marine sequence of alternating sands and shales) and (3) Akata Formation (a basal marine shale unit) [5-8]. Clays and Shales including minor sand intercalations are the components of the Akata Formation. They were deposited prodelta environments and sand deposited here is less than 30% in general.

Sands and shales are the components of Agbada Formation signifying sediments of the transitional environment consist of the lower delta plain (mangrove swamps, marsh, flood plain) and the coastal barrier and fluviomarine realms. In the Agbada Formation sand varies in percentage from 30-70%, which is as a result of more large numbers of depositional offlap cycles. Generally, a complete cycle is made-up of minor fossiliferrous transgressive marine sand, followed by an offlap sequence which commences with marine shale and continues with laminated fluviomarine sediments followed by barriers and/or fluviatile sediments terminated by another transgression [5].

The Benin Formation is made-up of high sand which varies in percentage from 70-100% and forms the outermost Niger Delta layers depositional sequence. The huge sands were placed in a continental setting comprising the fluvial realms (braidedand meandering systems) of the top delta plain.

2. Methodology

2.1. Data acquisition

All the data used in this research were acquired using seismic refraction tomography survey with instruments Seismometer; Twelve geophones, Cable, Weight drop (sledge hammer), Base plate, GPS (Global positioning system), Cutlass, Umbrella, Trigger geophone, Trigger cable realm, Tape and Wooden pegs, in the University of Port Harcourt, Abuja campus. The data were gotten in four different places, behind the Faculty of Social Sciences (first profile), in the front of the Faculty of Humanities (second profile), behind Faculty of Gas Engineering (third profile), and adjacent to the Faculty of Gas Engineering (fourth profile). The data were acquired in a relatively calm environment, and efforts were put in place to assure that random noise was suppressed as much as possible. Though all the obtainable sources of the random noise could not be stopped because of the nature of the environment (school activities), but yet it was controlled to a reasonable extent. The profiles where the data were obtained have approximately zero gradients and structures were erected on the surroundings. The first and second profiles were about 120 m and 170 m respectively away from the road while the third and fourth profiles were 200 m and 100 m respectively away from the road.

Shot points and geophone positions were first marked starting from one end marking 5 m and using wooden pegs to separate them to the other end. A total of twenty points were made for both forward and reverse shots. Twelve geophones were then fixed as shown in figure 1 connecting to the cable with their polarity being observed. The cable and trigger cable realm connecting to trigger geophone positioned in a shot point were connected properly to ABEM seismometre being powered by a DC battery. Vertical geophones were properly placed perpendicular to the Earth's surface in order to pick the vibration made by the ground.

A total length of 95 m was used for each profile line (shown in Figure.1). Sledge hammer was, used as the energy source. In order to reduce the random noise, five stacks were made, and the averathe ges were recorded by the seismometer on each shot point.

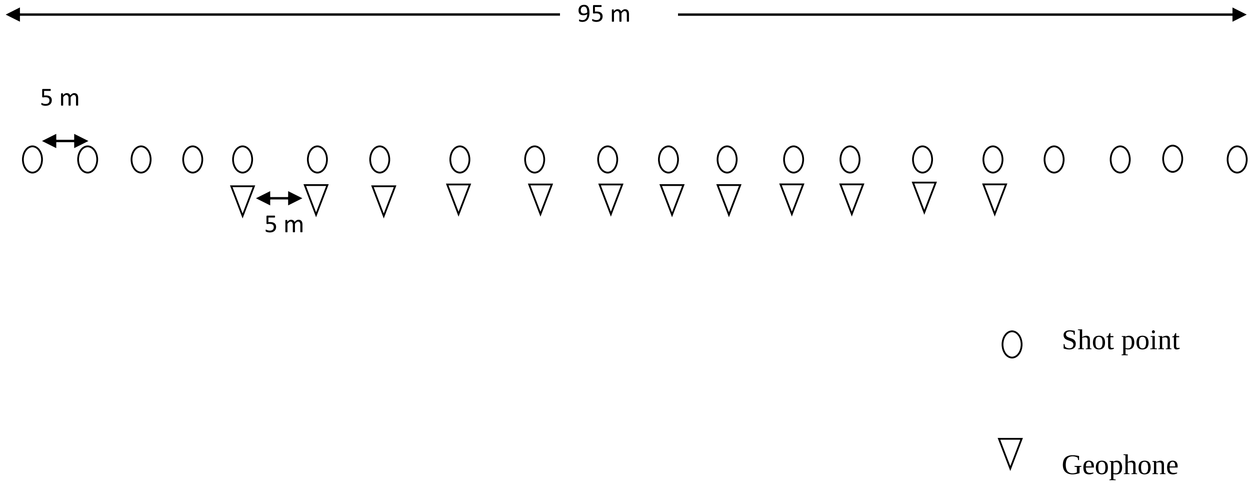

Figure 1. The profile line showing geophone and shot points positions in the site

2.2. Data processing

After the data had been acquired from the field using the adequate instruments listed above, the next step was the extraction of data from the seismometer for processing. The data was extracted by connecting the seismometer into a computer system providing access to the raw data. The raw data which has no value until it was processed by appropriate software like Reflexw is of SEG2 file type. The first step in processing was to import the data in the Reflex as a SEG2 format. The data were imported into the software as a SEG2 format to enable the software to recognize them as seismic data. At this stage, the outline used in the site was provided to the software for proper processing, for example, number of shot points and geophone spacing, number of geophones used and others. After the importation of data, the next stage is to filter out the noise and then gaining.

After importing the data which always comes with random noise, the next stage is to filter out the noise. Both random noise (noise coming from the environment such as vibration caused by car) and coherent noise (noise coming from the instrument maybe due to malfunction) in the data obscure the subsurface imaging, therefore, have to filter out in order to observe a comprehensible image about the subsurface. By filtering, bandpass frequencies of 20 Hz for lower cutoff and 50 Hz for upper cutoff were applied. Gaining (Deconvolution) is applied immediately the data is filtered. By gaining, amplification of the amplitude of the signal which was reduced as it propagates through the Earth and spread its energy over a large surface was achieved.

After enhancing the amplitude of the signal which gives room to identify the first refractor, the next is to careful pick the time it takes each geophone to record signal picked from the first interface by a particular source signal generation known as first arrival travel times or first breaks. This was carried out by manual picking.

From the picking of the first arrival travel times for each shot, time-distance graph for forward and reverse shots were plotted (see Fig. 2). Travel times are recorded in milliseconds for both forward and reverse shots. The average refracted travel time is calculated which we used to assign layers.

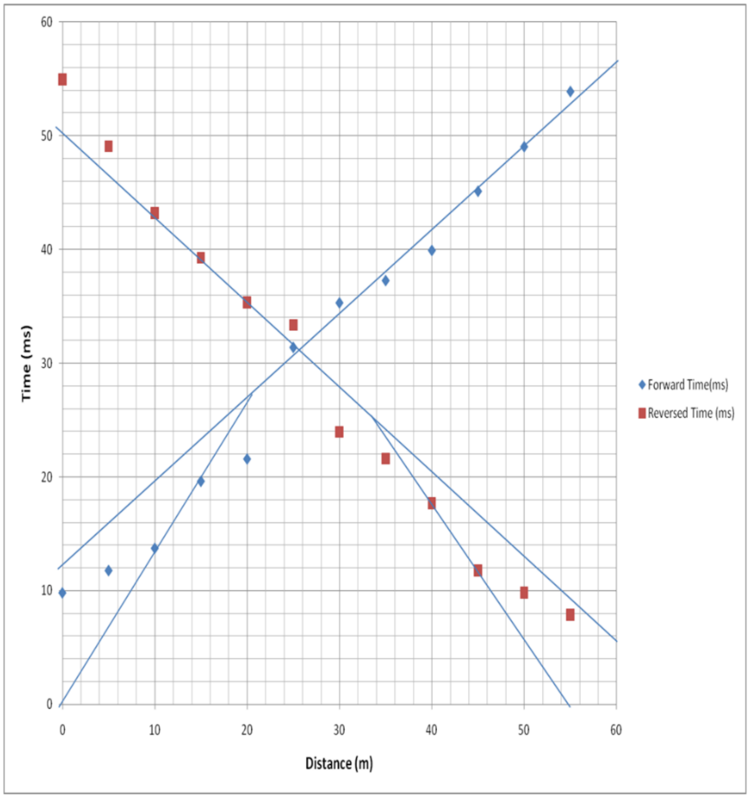

Figure 2. Time-distance graph for first shot arrival travel times picked for both forward and reversed shots of the 1st profile line

The next is the wavefront inversion. By inversion, velocity-depth models directly from the recorded data are produced (see Fig. 3-6). The picked traveltimes of different shots are put together by traveltime processing (the first part) which also assign picks to special layers. The wavefront inversion method is used to invert the combined traveltimes into the underground model and hence allows: interactive back propagation of the wavefronts using finite differences approximation of the eikonal equation; the back propagation is exact, even for very complicated overburdens [9].

After the models were generated by wave front inversion, ray tracing was then applied. In a system which has regions of varying propagating velocity, absorption characteristics, and reflecting surfaces, ray tracing is seen as a technique used to calculate the path of particles or waves. Under these conditions, wave fronts may change direction, bend, or reflect off surfaces, complicating analysis. Ray tracing correct the setback by constantly advancing idealized thin beams called rays through the system by discrete amounts [10]. From this analysis, the tomography models were generated for the four profiles in the study areas.

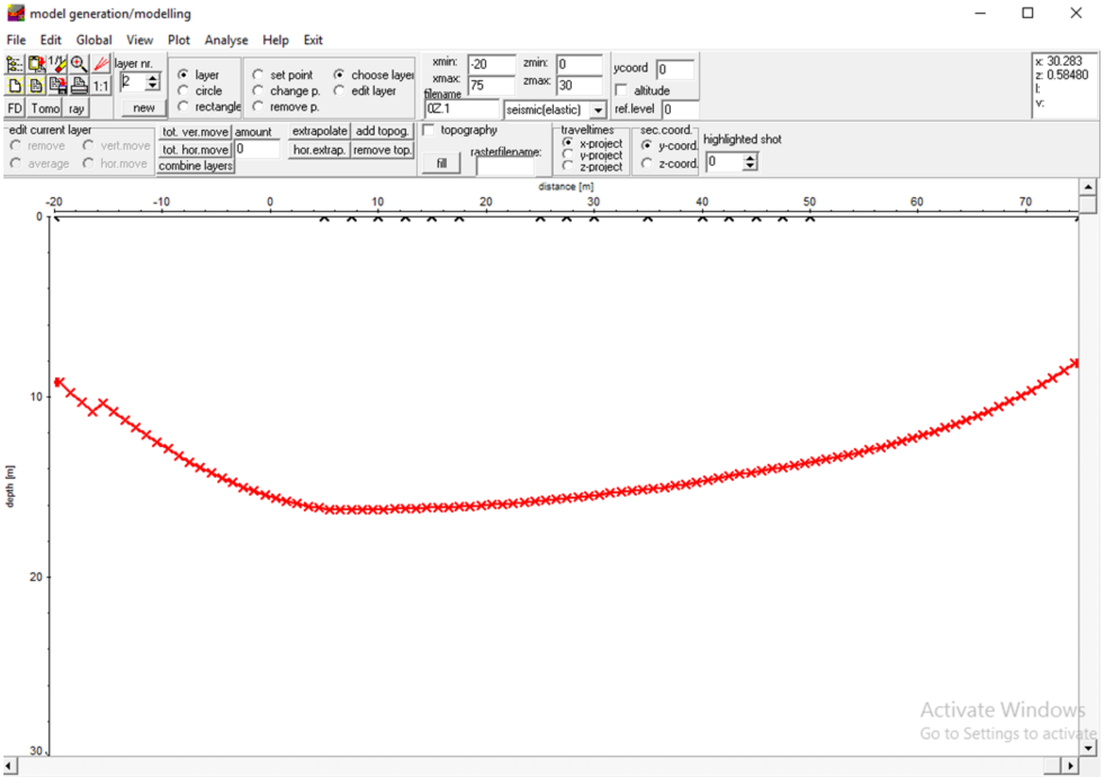

layer nr. 2

xmin: -20

xmax: 75

zmin: 0

zmax: 30

filename 0Z.1

ycoord 0

ref.level 0

amount 0

highlighted shot 0

x: 30.283
z: 0.58480
t:
v:

Figure 3. The first profile inversion process with Reflex software to generate initial first and second layers. The model showing initial depth of the weathered layer in lateral direction of the profile

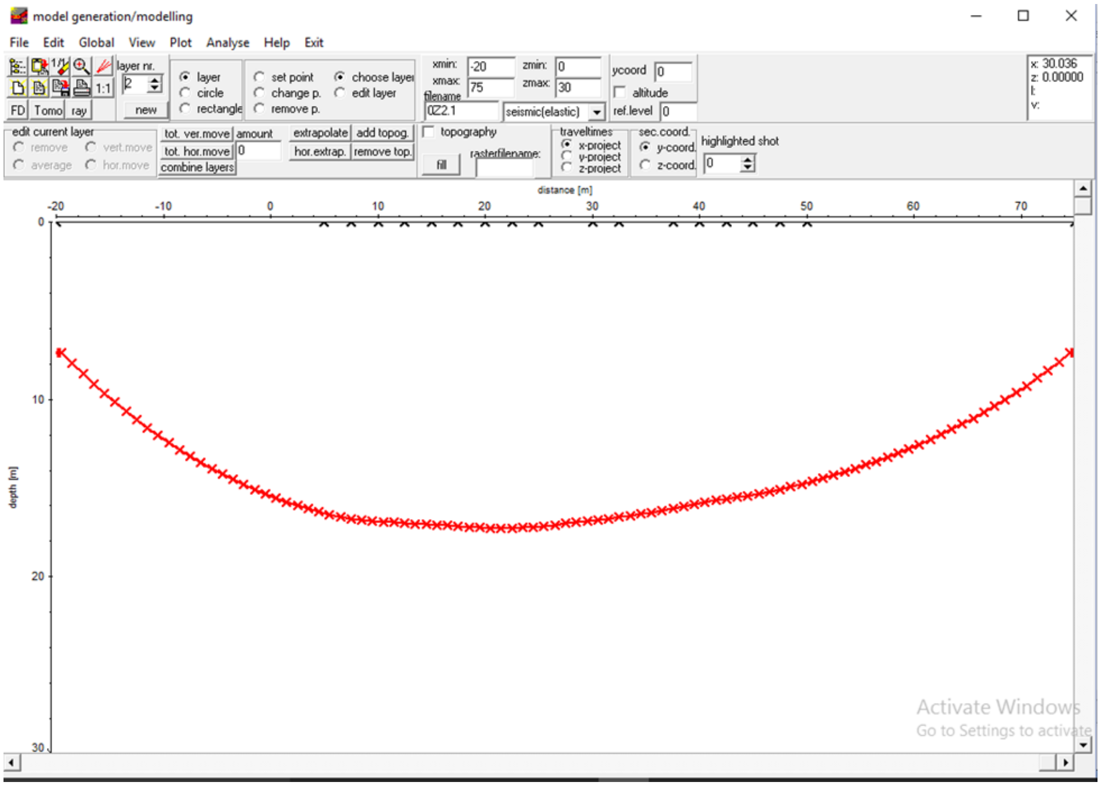

layer nr. 2

xmin: -20

xmax: 75

zmin: 0

zmax: 30

filename 0Z2.1

ycoord 0

ref.level 0

amount 0

highlighted shot 0

x: 30.036
z: 0.00000
t:
v:

Figure 4. Second profile inversion process with Reflex software to generate initial first and second layers. The model showing initial depth of the weathered layer in lateral direction of the profile

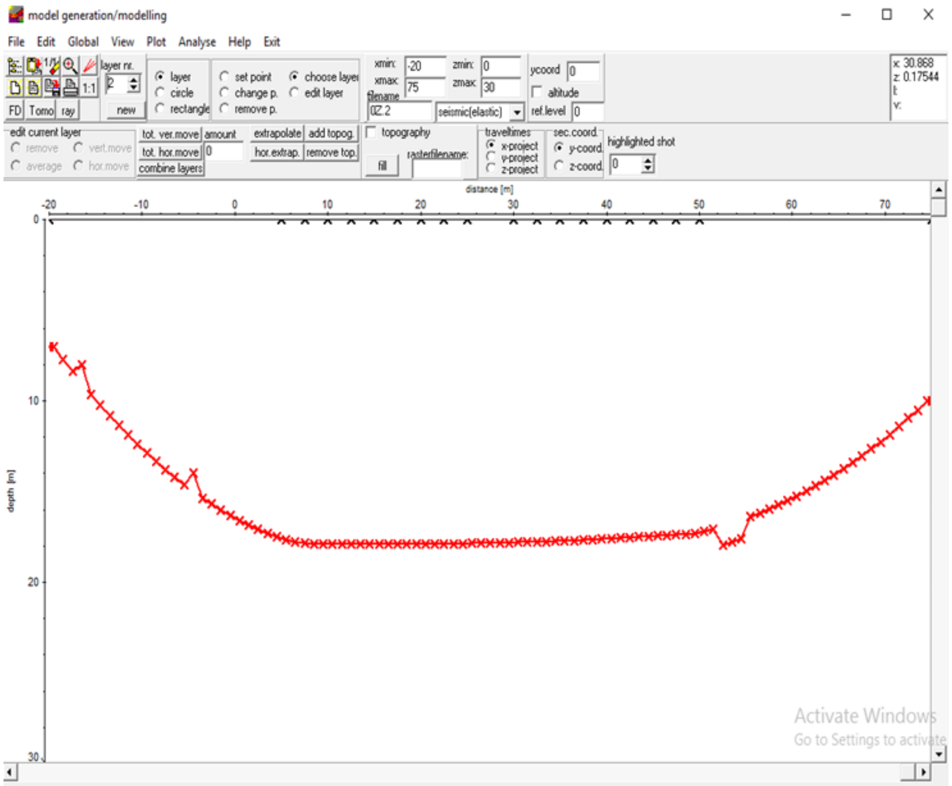

layer nr. 2
● layer ○ circle ○ rectangle
○ set point ○ change p. ○ remove p.
● choose layer ○ edit layer
xmin: -20
xmax: 75
zmin: 0
zmax: 30
filename 0Z.2
seismic(elastic)
ycoord 0
☐ altitude
ref.level 0
amount 0
☐ topography
rasterfilename:
traveltimes ● x-project ○ y-project ○ z-project
sec.coord. ● y-coord. ○ z-coord.
highlighted shot 0
x: 30.868
z: 0.17544
t:
v:

Figure 5. Third profile inversion process with Reflex software to generate initial first and second layers. The model showing initial depth of the weathered layer in lateral direction of the profile

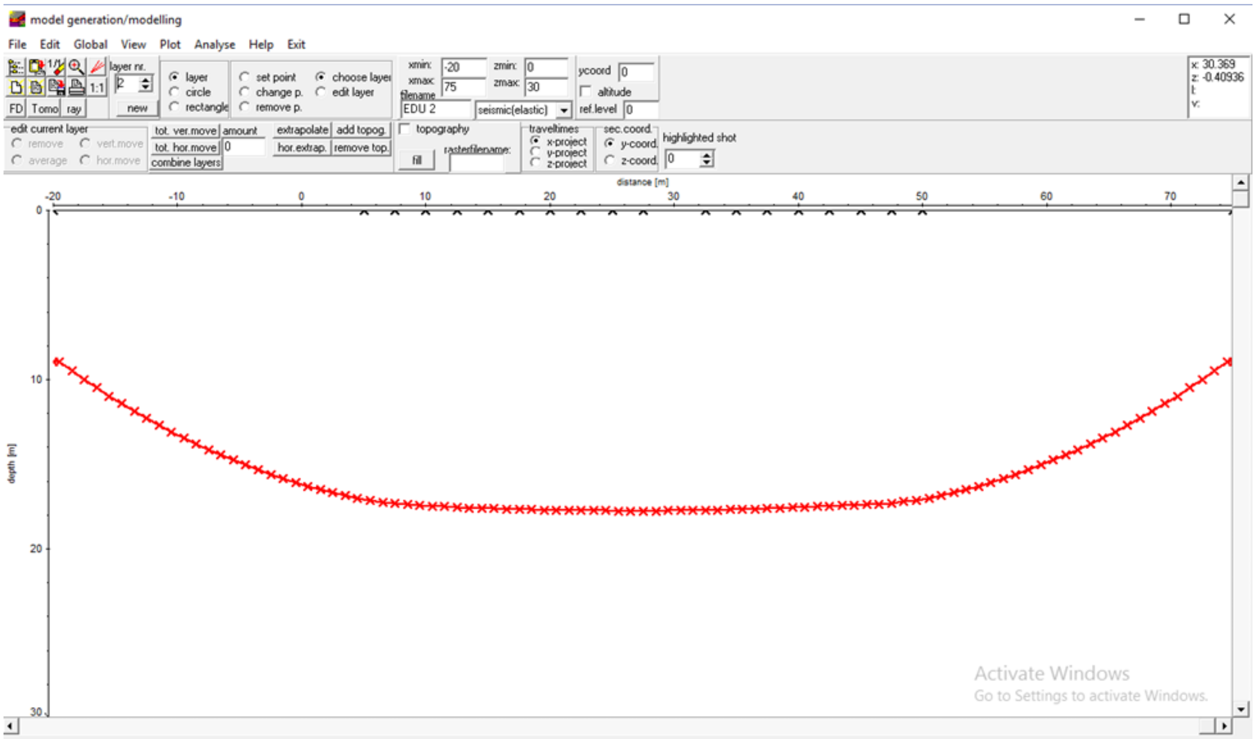

layer nr. 2
● layer ○ circle ○ rectangle
○ set point ○ change p. ○ remove p.
● choose layer ○ edit layer
xmin: -20
xmax: 75
zmin: 0
zmax: 30
filename EDU 2
seismic(elastic)
ycoord 0
☐ altitude
ref.level 0
amount 0
☐ topography
rasterfilename:
traveltimes ● x-project ○ y-project ○ z-project
sec.coord. ● y-coord. ○ z-coord.
highlighted shot 0
x: 30.369
z: -0.40936
t:
v:

Figure 6. Fourth profile inversion process with Reflex software to generate initial first and second layers. The model showing initial depth of the weathered layer in lateral direction of the profile

Table 1. First shot arrival travel times picked for both forward and reversed shots of the 1st profile line

Distance (m)	Forward Time (ms)	Reversed Time (ms)
0	9.81	54.93
5	11.77	49.04
10	13.73	43.16
15	19.62	39.23
20	21.58	35.31
25	31.39	33.35
30	35.31	23.95
35	37.27	21.58
40	39.92	17.66
45	45.12	11.77
50	49.04	9.81
55	53.89	7.85

3. Results and discussion

The velocity tomography models for first to fourth profiles are respectively shown in Figure 7 to Figure 10. The velocity tomography models are presented in different shades of colours. The velocity distributions portrayed by the tomography models show an increase in velocity with depth along the whole profiles. There is no case or evidence where a low velocity layer is overlain with higher velocity layer. By the right hand side of each tomography model, a colour bar is attached to it showing velocity range of each colour. The tomography models are not discussed based on the colour distributions in the models but are discussed according to the velocity distribution attached to a colour from the colour bar. From the tomography models, a horizontal distance along the profile is shown in meters also, a vertical distance showing the depth of probe measured in meters. The tomography models clearly isolated the consolidated from the unconsolidated layer (weathered layer).

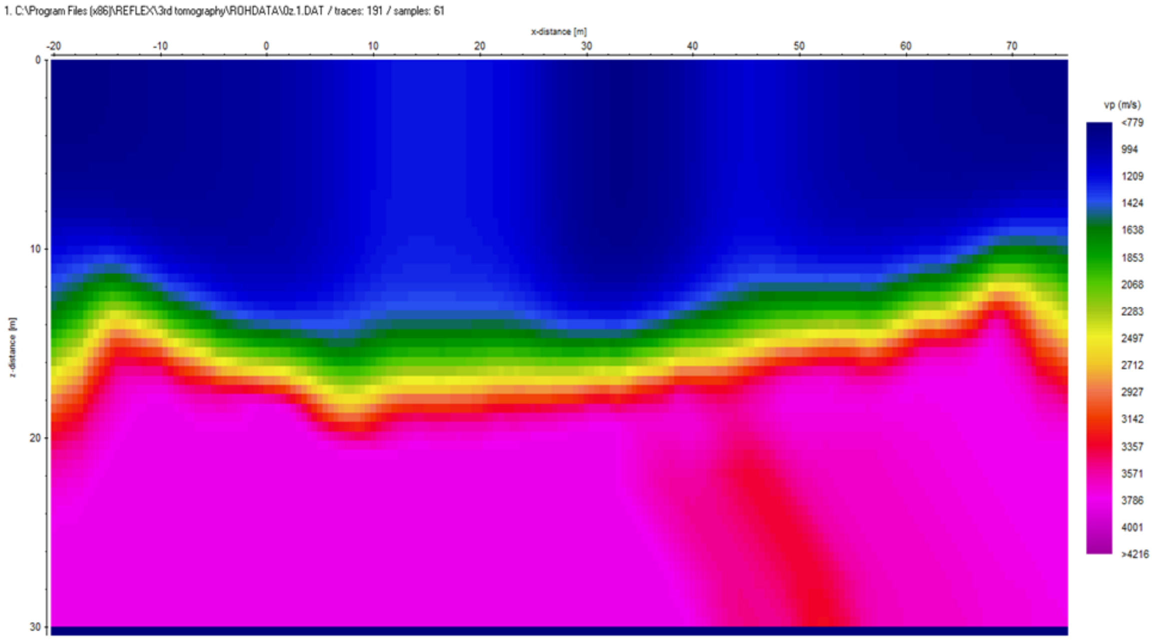

Figure 7. Tomography model of velocity distribution along the first profile

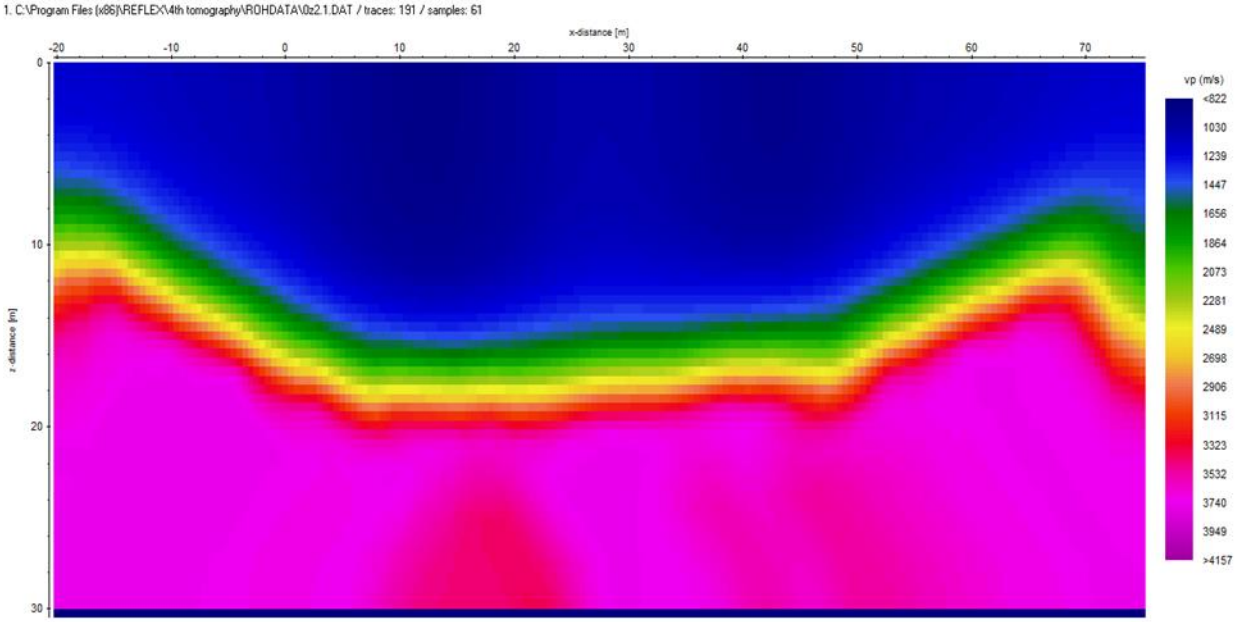

Figure 8. Tomography model of velocity distribution along the second profile

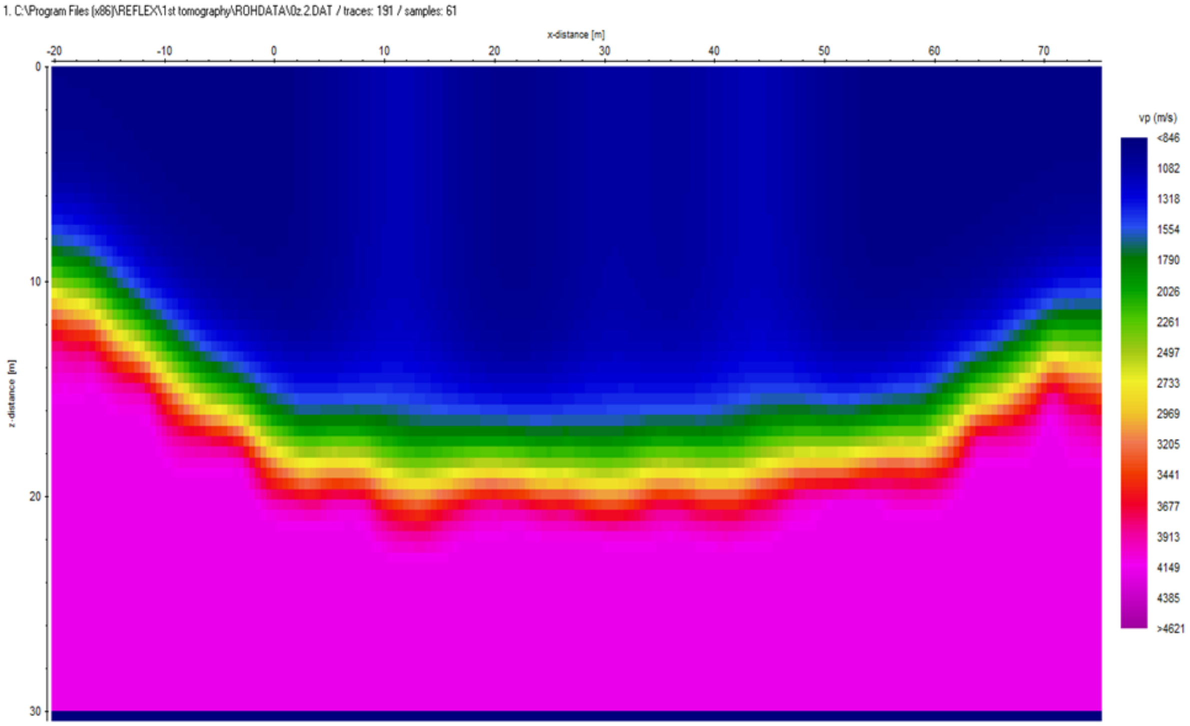

Figure 9. Tomography model of velocity distribution along the third profile

For the first profile, the surface velocity down to the entire depth of the probe from the tomography model as shown in Figure 2 ranges from 779 m/s to 4216 m/s. The model shows the weathered layer primary wave velocity varies from 779 m/s to 1531 m/s. The weathered layer thickness is 11.59 m at the beginning, 14.33 m at the middle, and 9.22 m at the end with an average thickness of 12.49 m. The following layer has p-wave velocity varies from

1531 m/s to 2068 m/s at an average depth of 12.49 m. While the velocity of the third layer varies from 2068 m/s to 4216 m/s at an average depth of 15.39 m along the profile.

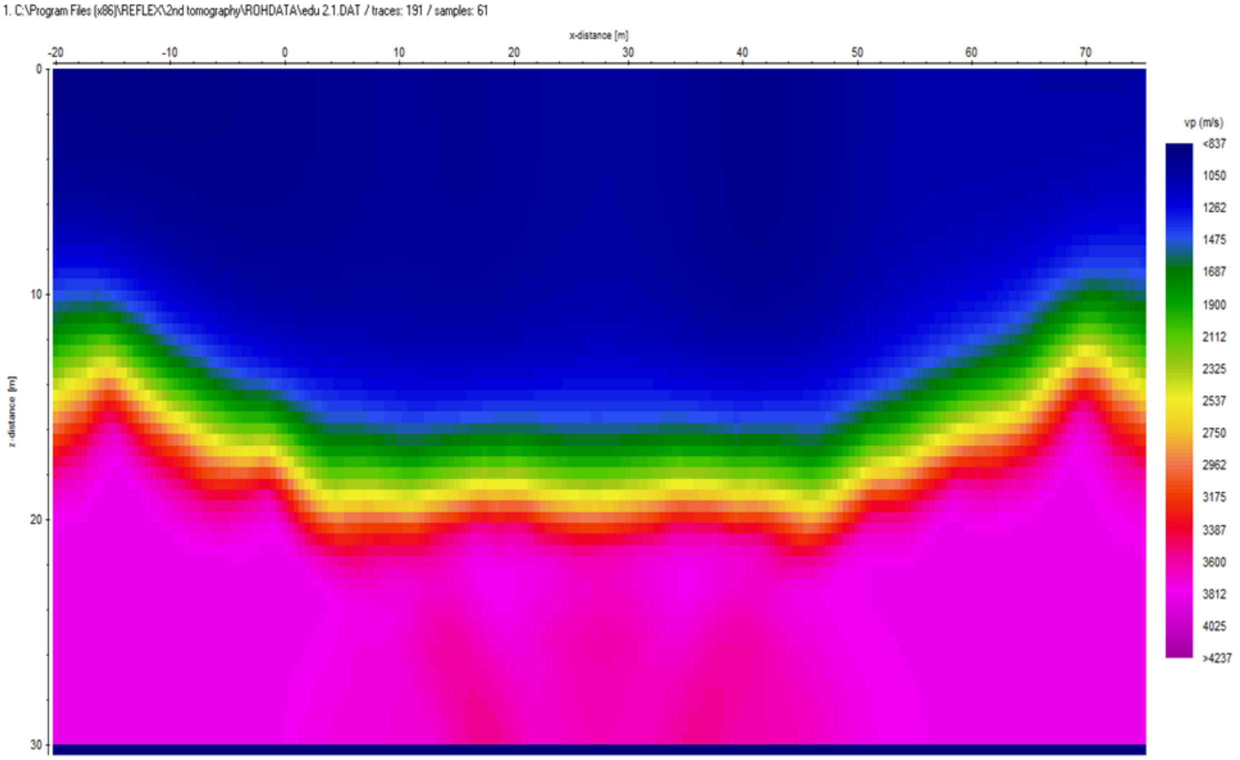

Figure 10. Tomography model of velocity distribution along the fourth Profile

The surface velocity down to the entire depth of the probe from the tomography model of the second profile as shown in Figure 3 ranges from 822 m/s to 4157 m/s. The weathered layer primary wave velocity varies from 822 m/s to 1487 m/s. The weathered layer thickness is 6.27 m at the beginning, 14.01 m at the middle, and 7.22 m at the end with an average thickness of 9.17 m. The following layer has p-wave velocity varies from 1487 m/s to 2073 m/s at an average depth of 9.17 m. While the velocity of the third layer varies from 2073 m/s to 4157 m/s at an average depth of 11.97 m along the profile.

Also, the surface velocity down to the entire depth of the probe from the tomography model of the third profile showed in Figure 4.4 ranges from 846 m/s to 4621 m/s. The weathered layer primary wave velocity varies from 846 m/s to 1480 m/s. The weathered layer thickness is 8.01 m at the beginning, 16.38 m at the middle, and 10.75 m at the end with an average thickness of 11.71 m. The following layer has p-wave velocity varies from 1480 m/s to 2026 m/s at an average depth of 11.71 m. While the velocity of the third layer varies from 2026 m/s to 4621 m/s at an average depth of 13.66 m along the profile.

Then, the surface velocity down to the entire depth of the probe from the tomography model of the fourth profile showed in figure 5 ranges from 837 m/s to 4237 m/s. The weathered layer primary wave velocity varies from 837 m/s to 1475 m/s. The weathered layer thickness is 10.17 m at the beginning, 16.01 m at the middle, and 8.96 m at the end with an average thickness of 11.73 m. The following layer has p-wave velocity varies from 1475 m/s to 2006 m/s at an average depth of 11.73 m. While the velocity of the third layer varies from 2006 m/s to 4237 m/s at an average depth of 13.99 m along the profile.

The four tomographic models have three equivalent layers and comparing the velocities with that of Kearey *et al.* [3], and Azwin *et al.* [1], the first layer is the weathered layer and is likely to be dry sand. It has average thicknesses of 12.49 m, 9.17 m, 11.71 m, and 11.73 m respectively for the four profiles. The second layer is likely to be saturated sand which is the aquifer layer and has average thicknesses of 2.9 m, 2.8 m, 2.0 m and 2.3 m at depths of 12.49 m, 9.17 m, 11.71 m and 11.73 m respectively. The third layer which is likely to be sand stone (the confined aquifer) at depths 15.39 m, 11.97 m, 13.66 m, and 13.99 m, and has infinite thicknesses along the profiles.

4. Conclusion

It is concluded from the 2D seismic refraction results that the weathered layer thickness and aquifer depth varies from the Earth's surface in the four profiles. Though the weathered layer thicknesses and aquifer depths are relatively the same in average along the first, third and fourth profiles, the second profile is considered to reduce cost while sinking a borehole. The layers of the four profiles which are made up mainly sand and sand stones are the same because they have equivalent velocity range. The environments are good for structures, and multi storey buildings erect will not collapse provided the foundations are carried out properly.

References

[1] Azwin IN, Saad R, Nordiana M. Applying the seismic refraction tomography for site characterization. APCBEE Procedia, 2013; 5: 227-231.

[2] Igboekwe MU, Ohaegbuchu HE. Investigation into the weathering layer using up hole method of seismic refraction. J. Geol. Min. Res., 2011; 3: 73-86.

[3] Kearey P, Brooks M, Hill I. An introduction to geophysical exploration (3rded.). Blackwell Science Ltd. 2002.

[4] Cardarelli E, de Nardis R. Seismic refraction, isotropic and anisotropic seismic tomography on an ancient monument (Antoniuo and Faustina temple AD 141). Geophysical Prospecting, 2001; 49. 228 – 241.

[5] Obaje NG. Geology and Mineral Resources of Nigeria. Springer Dordrecht Heidelberg London New York. 2009.

[6] Reijers TJ. A Stratigraphy and sedimentology of the Niger Delta. Geologos, 2011; 17(3): 133–162.

[7] Ajaegwu NE, Odoh BI, Akpunonu EO, Obiadi II, Anakwuba EK. Late Miocene to Early Pliocene Palynostratigraphy and Palaeoenvironmentsof ANE-1 Well, Eastern Niger Delta, Nigeria. Journal of Mining and Geology, 2012; 48 (1): 31–43.

[8] Onema A, Lucas FA, Dada S. Palynocycles, palaeoecology and systems tracts concepts: A Case Study from the Miocene Okan-1 Well, Niger Delta Basin, Nigeria. Applied Ecology and Environmental Sciences, 2015; 3 (3): 66-74.

[9] Sandmeier KJ. Reflexw 3.0 manual, Sandmeier Software, Zipser Strabe 1, D-76227 Karlsruhe, Germany, 2002.

[10] Ray_tracing. In Wikipedia. Retrieved December, 2017, from https://en.m.wikipedia.org/wiki/Ray_tracing_(physics).

To whom correspondence should be addressed: Dr. Rasaq Bello, Department of Physics, Federal University Kashere, Gombe State, Nigeria

Petroleum and Coal

Article **Open Access**

MATHEMATICAL MODELLING OF A TWO-PHASE RADIAL FLOW IN A HYDROCARBON RESERVOIR AND ANALYTICAL SOLUTION FOR NONLINEAR DIFFUSION PROBLEM

Amirabbas Mohammadi[1], *Abdullah Shidfar*[1], *Mostafa Mohammadi*[2], *Amir H. Mohammadi*[3*]

[1] *School of Mathematics, Iran University of Science and Technology, Tehran, Iran*
[2] *Department of Mathematics, Shahid Beheshti University, Tehran, Iran*
[3] *Discipline of Chemical Engineering, School of Engineering, University of KwaZulu-Natal, Howard College Campus, King George V Avenue, Durban 4041, South Africa*

Received April 7, 2018; Accepted June 27, 2018

Abstract

In this work, the radial flow of a two-phase hydrocarbon fluid in a petroleum reservoir is first modeled. Using the mass balance equation and Darcy's law as the governing equations, a nonlinear radial diffusion equation is obtained. We then assume that throughout the reservoir, ${\partial P}/{\partial r}$ is small and ${\partial P}/{\partial r} \neq 0$ also the viscosity (μ) is independent of pressure. The recent hypotheses are true about the radial flow. Accordingly, the resulting nonlinear equation is converted to a linear radial diffusion equation which is a one-dimensional equation (ODE) and it is noticeable to achieve the pressure distribution in the reservoir and adjacent to the well. Descriptions of reservoir processes have motivated a large volume of work on ODEs. Analytical and numerical methods have provided solutions to the problems satisfying a fairly wide range of conditions. However, analytical methods continue to be highly valued for the inherent simplicity, their capacity to convey qualitative information about the physical problem, and as a verification for numerical models. In this work, after obtaining the linear radial diffusion equation, regarding the transient state $({\partial P}/{\partial r} = f(r,t)$ and ${\partial P}/{\partial r} \neq 0)$ for the fluid flow, we apply the related boundary and initial conditions. Afterward, we apply the analytical methods for the resulting model to obtain the pressure distribution. To achieve this goal, we separately apply the separation of variables method (based on Bessel equations) and the method of Laplace transform to solve the problem. In the end of the second method, as for the resulted fraction any inverse value is not found in most of tables, so we apply Heaviside's theorem.

***Keywords**: Radial flow; Darcy's law; Transient state; Bessel equation; Laplace transform.*

1. Introduction

Generally, after digging a well in a petroleum reservoir, the difference in pressure between the reservoir and the wellbore causes to the flow of fluid into the wellbore in three states: transient ($\frac{\partial P}{\partial t} \neq 0$), semi-steady ($\frac{\partial P}{\partial t} = \text{constant}$) and steady ($\frac{\partial P}{\partial t} = 0$) [1].

When digging a well in the middle of the reservoir, the hydrocarbon fluid flows from the surrounding area to the wellbore, then a radial flow occurs (Fig. 1). When numerous wells are digged at a short distance from each other, the flow lines are parallel and a linear flow is created. The spherical flow occurs when the reservoir has a nearly hemispherical shape [2]. In this study, we assumed that the desired fluid has a radial flow in a hydrocarbon reservoir.

The pressure distribution at any time (t) and at any point (r) in a reservoir producing a hydrocarbon fluid with radial flow is an applied function that is used daily by reservoir engineers in order to predict pressure drop and provide methods of stabilizing or increasing the pressure. Therefore, it is significant to provide a suitable model for determining the distribution of this important parameter in a reservoir.

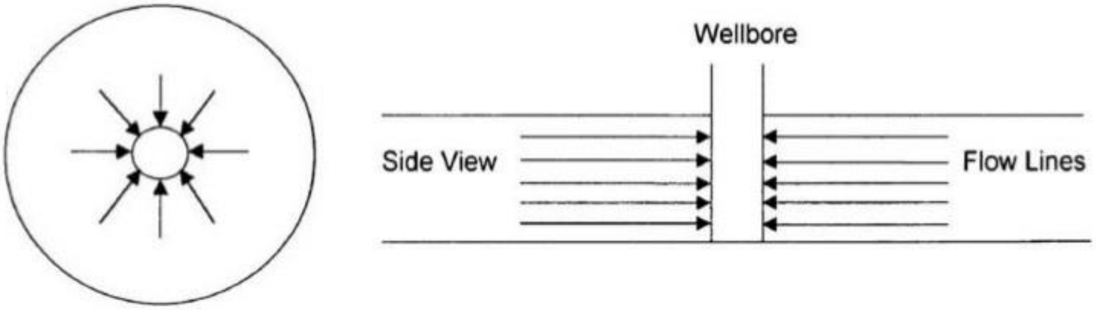

Figure 1. Radial flow into a wellbore

In recent years, various studies have been carried out to calculate the distribution of pressure in the reservoir. In this regard, the use of the diffusion equation in calculations has been of interest to many researchers. It seems that provision of analytical models (if applicable) with mathematical structures can play a decisive role in proving the validity and reliability of numerical models in addition to problem solving. The analytical method of diffusion equation, which is superior in calculation to the existing analytical methods such as the integral transformation method of Fourier or Laplace and/or the variable separation method, was thus established in the parabolic space [3].

In this work, in order to achieve the pressure distribution throughout the reservoir, the problem is only studied in the transient state which is undoubtedly difficult to analyze. The semi-steady and steady states (due to the simplicity of the problem) will not be studied in this work.

2. Mathematical formulation

We consider the following assumptions:

A. In a hydrocarbon reservoir, since deposition of some materials such as asphaltene, causes to changing the porosity in terms of time, so we ignore the deposition and assume that physical properties of the reservoir including porosity and permeability are constant. In general, we assume that the reservoir is homogeneous.

B. Height of drilling well is equal to the reservoir thickness, in this case, assumption of radial flow for the fluid is correct.

C. In a two-phase reservoir, the desired fluid is oil or gas and water is immobile.

The mass balance equation is considered as "rate of mass accumulation = rate of input mass –rate of output mass" [4].

According to Fig. 2 and defined parameters earlier, the mass balance equation can be written as follow:

$$q\rho\big|_{r+dr} - q\rho\big|_{r} = (2\pi rh\varphi dr)\frac{d\rho}{dt} \qquad \text{or} \qquad \frac{q\rho\big|_{r+dr} - q\rho\big|_{r}}{dr} = (2\pi rh\varphi)\frac{d\rho}{dt} \tag{1}$$

where: $2\pi rh\varphi dr$ is the volume of vacant space in the cylindrical layer in which the fluid is placed. Equation (1) can be written as below:

$$\frac{\partial}{\partial r}(q\rho) = (2\pi rh\varphi)\frac{d\rho}{dt} \tag{2}$$

On the other hand, for a radial flow in horizontal mode, Darcy's law is [5-6]:

$$q = \frac{2\pi r k h}{\mu}\frac{\partial \rho}{\partial r} \tag{3}$$

where: $2\pi r h$ is the surface which is perpendicular to the direction of flow. Using equations (2) and (3) we can obtain:

$$\frac{\partial}{\partial r}\left(\frac{2\pi r k h}{\mu}\rho\frac{\partial \rho}{\partial r}\right) = (2\pi r h \varphi)\frac{d\rho}{dt} \tag{4}$$

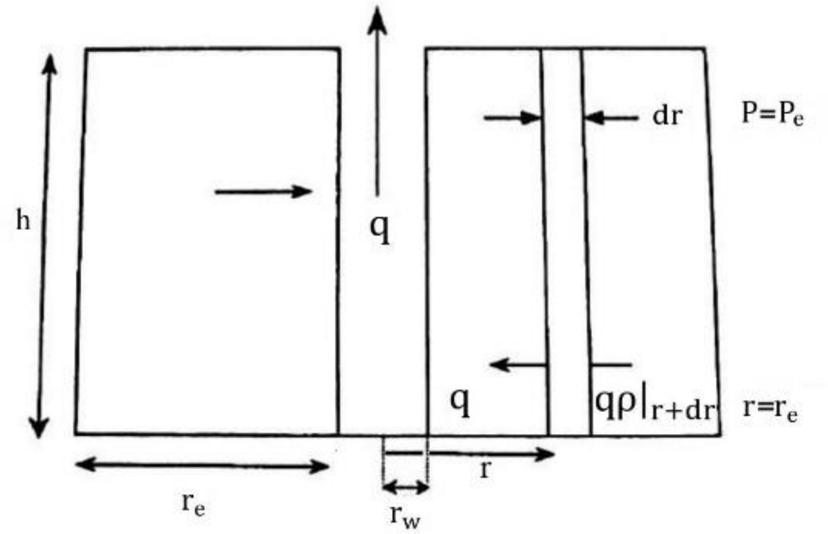

Figure 2. A cylindrical part of a hydrocarbon reservoir with length h (thickness of the reservoir) and thickness dr and inner radius r

The above equation can be written as follow:

$$\frac{1}{r}\frac{\partial}{\partial r}\left(\frac{k\rho}{\mu}r\frac{\partial \rho}{\partial r}\right) = \varphi\frac{d\rho}{dt} \tag{5}$$

Considering the compressibility of fluid is defined as follow:

$$c = -\frac{1}{v}\frac{\partial v}{\partial P} \tag{6}$$

Hence, according to definition of mass density ($\rho = \frac{m}{v}$), we can have:

$$c = -\frac{\rho}{m}\frac{\partial(\frac{m}{\rho})}{\partial P} = \frac{1}{\rho}\frac{\partial \rho}{\partial P} \tag{7}$$

By differentiating of both sides of equation (7) in terms of time, we can have:

$$c\rho\frac{\partial P}{\partial t} = \frac{\partial \rho}{\partial t} \tag{8}$$

By substituting equation (8) in (5):

$$\frac{1}{r}\frac{\partial}{\partial r}\left(\frac{k\rho}{\mu}r\frac{\partial \rho}{\partial r}\right) = \varphi c \rho\frac{\partial P}{\partial t} \tag{9}$$

Equation (9) is called the radial diffusion equation in the reservoir which is nonlinear because the pressure indirectly affects the density, compressibility and viscosity. In general, equation (9) does not have any simple solution but in particular conditions can be linearized and can be solved. After differentiation, equation (9) can be extended as follow:

$$\frac{1}{r}\left\{\frac{\partial}{\partial r}(\frac{k}{\mu})\rho r\frac{\partial \rho}{\partial r}+(\frac{k}{r})\frac{\partial \rho}{\partial r}r\frac{\partial \rho}{\partial r}+(\frac{k\rho}{\mu})\frac{\partial \rho}{\partial r}+(\frac{k\rho}{\mu})r\frac{\partial^2 \rho}{\partial r^2}\right\}=\varphi c\rho\frac{\partial P}{\partial t} \tag{10}$$

On the other hand, equation (7) can be written as follow:

$$\frac{\partial P}{\partial r}=\frac{1}{c\rho}\frac{\partial \rho}{\partial r} \tag{11}$$

In a two-phase reservoir of oil or gas and water (water is considered immobile), the following assumptions are true about the radial flow:

A. Viscosity (μ) is independent of pressure.

B. $\frac{\partial P}{\partial r}$ is very small, so $(\frac{\partial P}{\partial r})^2$ can be ignored. Furthermore, we can ignore $c(\frac{\partial P}{\partial r})^2$, if $c<1$

Substituting equation (11) in equation (10) and according to the assumptions A and B, we can write equation (10) as follows:

$$\frac{\partial^2 P}{\partial r^2}+\frac{1}{r}\frac{\partial P}{\partial r}=\frac{\varphi\mu c}{k}\frac{\partial P}{\partial t} \tag{12}$$

Or:

$$\frac{1}{r}\frac{\partial}{\partial r}\left(r\frac{\partial P}{\partial r}\right)=\frac{\varphi\mu c}{k}\frac{\partial P}{\partial t} \tag{13}$$

Assuming c is constant (independent of pressure), ${\varphi\mu c}/{k}$ is constant and equations (12) and (13) can be linearized. Now, we define η as:

$$\eta=\frac{k}{\varphi\mu c} \tag{14}$$

Equations (12) and (13) can be written as follows:

$$\frac{\partial^2 P}{\partial r^2}+\frac{1}{r}\frac{\partial P}{\partial r}=\frac{1}{\eta}\frac{\partial P}{\partial t} \tag{15}$$

$$\frac{1}{r}\frac{\partial}{\partial r}\left(r\frac{\partial P}{\partial r}\right)=\frac{1}{\eta}\frac{\partial P}{\partial t} \tag{16}$$

This equation is a linear form of the radial diffusion equation and η is known as the diffusion constant [7].

3. Solving the problem in the transient state

In this case, the initial short time is considered and pressure P throughout the reservoir (including $r=r_e$) is a function of time which is not affected by production yet, so $\frac{\partial P}{\partial r}\neq 0$. We consider the followings;

$$P(r,0)=P_0 \qquad r\le r_e \tag{17}$$

$$P(0,t)=P_w \tag{18}$$

$$P(r_w,t)=P_w \tag{19}$$

3.1. Solving the problem by using the separation of variables method

We do the following transform:

$$\Gamma(r,t)=P(r,t)-P_w \tag{20}$$

Hence, we can write equation (15) and conditions (17), (18) and (19) as below:

$$\frac{\partial\Gamma}{\partial t}=\eta\left(\frac{\partial^2\Gamma}{\partial t^2}+\frac{1}{r}\frac{\partial\Gamma}{\partial t}\right) \tag{21}$$

$$\Gamma(r,0)=P_0-P_w=\Gamma_0 \tag{22}$$

$$\Gamma(0,t)=0 \tag{23}$$

$$\Gamma(r_w,t)=0 \tag{24}$$

By using the separation of variables method, we have:

$$\Gamma(r,t)=R(r).Q(t) \tag{25}$$

According to equations (21) and (25):

$$\frac{1}{\eta Q(t)}\frac{dQ}{dt}=\frac{1}{R(r)}\left(\frac{d^2R}{dr^2}+\frac{1}{r}\frac{\partial R}{\partial r}\right)=-\lambda^2 \tag{26}$$

Note that the separation constant is chosen, the function $R(r)$ will be as orthogonal (Bessel). Therefore, from eqaution (26):

$$\frac{dQ}{dt}+\lambda^2\eta Q=0 \tag{27}$$

and:

$$Q(t)=e^{-\eta\lambda^2 t} \tag{28}$$

We can also have:

$$\frac{d^2R}{dr^2}+\frac{1}{r}\frac{\partial R}{\partial r}+\lambda^2 R=0 \tag{29}$$

Equation (29) is a Bessel equation with the following solution [8]:

$$R(r)=AJ_0(\lambda r)+BY_0(\lambda r) \tag{30}$$

From equation (25) and boundary conditions (23) and (24) we can have:

$$\Gamma(r_w,t)=R(r_w).Q(t)=0 \quad\Rightarrow\quad R(r_w)=0 \tag{31}$$

$$\Gamma(0,t)=R(0).Q(t)=0 \quad\Rightarrow\quad R(0)=0 \tag{32}$$

As second-order Bessel functions are not defined at point zero, therefore in equation (30) when $r=0$ and in according to (32), $B=0$. On the other hand:

$$R(r_w)=AJ_0(\lambda r_w)=0$$

The values of λ are obtained by solving $J_0(\lambda r_w)=0$:

$$\lambda_1 r_w=2.405 \quad\Rightarrow\lambda_1=\frac{2.405}{r_w}$$

$$\lambda_2 r_w=5.520 \quad\Rightarrow\lambda_2=\frac{5.520}{r_w}$$

$$\lambda_3 r_w = 8.654 \quad \Rightarrow \lambda_3 = \frac{8.654}{r_w}$$

$$\lambda_4 r_w = 11.792 \quad \Rightarrow \lambda_4 = \frac{11.792}{r_w}$$

Now, we put the values of $Q(t)$ and $R(t)$ in equation (25):

$$\Gamma(r,t) = \sum_{n=1}^{\infty} A_n e^{-\eta \lambda_n^2 t} J_0(\lambda_n r) \tag{33}$$

By applying the condition (22):

$$\Gamma_0 = \sum_{n=1}^{\infty} A_n J_0(\lambda_n r) \tag{34}$$

Therefore, Γ_0 has been expanded in terms of Bessel sentences. Now, we use the orthogonality property of Bessel functions. We multiply two sides of (34) in $rJ_0(\lambda_n r)dr$ and after integrating, we will have:

$$\int_0^{r_w} \Gamma_0 r J_0(\lambda_n r)dr = A_n \int_0^{r_w} r J_0^2(\lambda_n r)dr \tag{35}$$

And:

$$A_n = \frac{\int_0^{r_w} \Gamma_0 r J_0(\lambda_n r)dr}{\int_0^{r_w} r J_0^2(\lambda_n r)dr} = \frac{\frac{\Gamma_0 r_w}{\lambda_n} J_1(\lambda_n r_w)}{\frac{r_w^2}{2} J_1^2(\lambda_n r_w)} \tag{36}$$

Then:

$$A_n = \frac{2\Gamma_0}{\lambda_n r_w J_1(\lambda_n r_w)} \tag{37}$$

Finally, we write (33) as below:

$$\Gamma(r,t) = \frac{2\Gamma_0}{r_w} \sum_{n=1}^{\infty} e^{-\eta \lambda_n^2 t} \frac{J_0(\lambda_n r)}{(\lambda_n r_w) J_1(\lambda_n r_w)} \tag{38}$$

Or:

$$P(r,t) = P_w + \frac{2(P_0 - P_w)}{r_w} \sum_{n=1}^{\infty} e^{-\eta \lambda_n^2 t} \frac{J_0(\lambda_n r)}{(\lambda_n r_w) J_1(\lambda_n r_w)} \tag{39}$$

3.2. Solving the problem by using Laplace transform

First, we do the following transform:

$$\theta(r,t) = P(r,t) - P_0 \tag{40}$$

We can write equation (15) and conditions (17), (18) and (19) as follows:

$$\frac{1}{r}\frac{\partial}{\partial r}\left(r\frac{\partial \theta(r,t)}{\partial r}\right) = \frac{1}{\eta}\frac{\partial \theta(r,t)}{\partial t} \tag{41}$$

$$\theta(r,0) = P_0 - P_0 = 0 \tag{42}$$

$$\theta(0,t) = P_w - P_0 = \theta_w \tag{43}$$

$$\theta(r_w,t) = P_w - P_0 = \theta_w \tag{44}$$

After applying Laplace transform on equation (41), we can have:

$$\frac{1}{r}\frac{\partial}{\partial r}\left(r\frac{d\theta(r,s)}{dr}\right) = \frac{1}{\eta}(s\theta(r,s) - \theta(r,0)) \tag{45}$$

Now, with regards to equation (42) we can write equation (45) as below:

$$\frac{d^2\theta(r,s)}{dr^2} + \frac{1}{r}\frac{d\theta(r,s)}{dr} - \frac{s}{\eta}\theta(r,s) = 0 \tag{46}$$

Or:

$$r^2\theta'' + r\theta' - \frac{s}{\eta}r^2\theta = 0 \tag{47}$$

Equation (47) is a modified Bessel equation. In general, a modified Bessel equation is presented in the form of equation (48), which has a solution such as equation (49) as bellow [8]:

$$x^2y'' + x(a + 2bx^m)y' + (c + dx^{2n} - b(1-a-m)x^m + b^2x^{2m}y = 0 \tag{48}$$

$$y(x) = x^{\frac{1-a}{2}} e^{-\frac{bx^m}{m}} \left\{ AZ_p\left(\frac{\sqrt{|d|}}{n}x^n\right) + BZ_{-p}\left(\frac{\sqrt{|d|}}{n}x^n\right) \right\} \tag{49}$$

where $p = \frac{1}{n}\sqrt{\left(\frac{1-a}{2}\right)^2 - c}$ and Z is one of the functions I, J, Y, K which are determined by using Table 1.

Table 1. Z in the solution of modified Bessel equation

	Z_{-p}	Z_p	p	$\sqrt{d}$
1	J_{-p}	J_p	Non-integer	Real
2	Y_p	J_p	Integer	Real
3	I_{-p}	I_p	Non-integer	Imaginary
4	K_p	I_p	Integer	Imaginary

Accordingly, the solution for equation (47) will be:

$$\theta(r,s) = AI_0\left(r\sqrt{\frac{s}{\eta}}\right) + BK_0\left(r\sqrt{\frac{s}{\eta}}\right) \tag{50}$$

On the other hand, after applying Laplace transform on (43) and (44):

$$\theta(0,s) = \frac{\theta_w}{s} \tag{51}$$

$$\theta(r_w,s) = \frac{\theta_w}{s} \tag{52}$$

Now, we apply the above conditions on equation (50) and we determine the coefficients *A* and *B*. For $r=0$ the left side of equation (50) is defined but K_0 has an undefined value, hence B must be zero. Now, for $r=r_w$ we can have:

$$\frac{\theta_w}{s}=AI_0(r_w\sqrt{\frac{s}{\eta}})$$

And then:

$$A=\frac{\theta_w}{sI_0(r_w\sqrt{\frac{s}{\eta}})}$$

Accordingly, the solution of the equations (46) and (51) and (52) is:

$$\theta(r,s)=\frac{I_0(r\sqrt{\frac{s}{\eta}})}{sI_0(r_w\sqrt{\frac{s}{\eta}})}\theta_w \tag{53}$$

Now, by applying inverse Laplace transform on the equation above, $\theta(r,t)$ is resulted. There are many techniques to find the inverse Laplace transform of a Laplace domain function [9], but its discussion is outside the scope of this study. On the other hand, by referring to most of tables, any inverse value will not be found for the fraction above, thus, we use Heaviside's theorem as follows.

3.3. Heaviside's expansion theorem [10]

If $P(s)$ is a polynomial with degree less than n and α_k is the roots of $Q(s)=0$, as well as $Q'(\alpha_k)$ is derivative of $Q(s)$ in terms of s at $s=\alpha_k$ then:

$$L^{-1}\left\{\frac{P(s)}{Q(s)}\right\}=\sum_{k=1}^{n}\frac{P(\alpha_k)}{Q'(\alpha_k)}e^{\alpha_k t}$$

According to this theorem we can write:

$$L^{-1}\left\{\frac{I_0(r\sqrt{\frac{s}{\eta}})}{sI_0(r_w\sqrt{\frac{s}{\eta}})}\right\}=\sum_{k=0}^{\infty}\frac{P(s_k)}{\left.\frac{dQ}{ds}\right|_{s=s_k}}e^{s_k t} \tag{54}$$

where s_k is the root of the following equation:

$$sI_0(r_w\sqrt{\frac{s}{\eta}})=0$$

In other words:

$$s_0=0$$

$$I_0(r_w\sqrt{\frac{s_k}{\eta}})=0 \qquad k=1,2,3,...$$

There is the following relation between I_n and J_n:

$$I_n(x) = i^{-n} J_n(ix) = e^{\frac{-n\pi i}{2}} J_n(ix) \tag{55}$$

$$J_0(ir_w\sqrt{\frac{s_k}{\eta}}) = 0 \qquad k = 1,2,3,\ldots \tag{56}$$

Or:

$$J_0(\lambda_k) = 0 \qquad s.t \qquad \lambda_k = ir_w\sqrt{\frac{s_k}{\eta}} \qquad k = 1,2,3,\ldots \tag{57}$$

The first four roots of the recent equation are:

$$\lambda_1 = 2.4048 \qquad \Rightarrow s_1 = -\frac{\eta(2.4048)^2}{r_w^2}$$

$$\lambda_2 = 5.5201 \qquad \Rightarrow s_2 = -\frac{\eta(5.5201)^2}{r_w^2}$$

$$\lambda_3 = 8.6537 \qquad \Rightarrow s_3 = -\frac{\eta(8.6537)^2}{r_w^2}$$

$$\lambda_4 = 11.7915 \qquad \Rightarrow s_4 = -\frac{\eta(11.7915)^2}{r_w^2}$$

It can be seen that regarding the values of λ_k, the roots of s_k can be easily obtained.

Now $P(s_k) = I_0(r\sqrt{\frac{s_k}{\eta}})$ must be calculated.

$$P(s_0) = P(0) = I_0(0) = 1$$

$$P(s_k) = I_0(-ir\sqrt{\frac{\lambda_k}{r_w}}) = J_0(\lambda_k \frac{r}{r_w}) \qquad k = 1,2,3,\ldots$$

On the other hand:

$$sI_0(r_w\sqrt{\frac{s}{\eta}}) = 0$$

$$\frac{dQ}{ds} = \frac{d\left(sI_0(r_w\sqrt{\frac{s}{\eta}})\right)}{ds} = I_0(r_w\sqrt{\frac{s}{\eta}}) + \frac{r_w}{2}\sqrt{\frac{s}{\eta}} I_1(r_w\sqrt{\frac{s}{\eta}})$$

$$\left.\frac{dQ}{ds}\right|_{s=0} = I_0(0) = 1$$

$$\left.\frac{dQ}{ds}\right|_{s=s_k} = -\frac{i\lambda_k}{2} I_1(-i\lambda_k) = -\frac{\lambda_k}{2} J_1(\lambda_k) \qquad k = 1,2,3,\ldots$$

Substituting the obtained values in (54) and according to the (53) we can have:

$$\theta(r,t)=\theta_w\left\{1-2\sum_{k=1}^{\infty}\frac{J_0(\lambda_k \frac{r}{r_w})}{\lambda_k J_1(\lambda_k)}e^{\frac{-\eta\lambda_k^2 t}{r_w^2}}\right\} \tag{58}$$

Or:

$$P(r,t)=P_0+(P_w-P_0)\left\{1-2\sum_{k=1}^{\infty}\frac{J_0(\lambda_k \frac{r}{r_w})}{\lambda_k J_1(\lambda_k)}e^{\frac{-\eta\lambda_k^2 t}{r_w^2}}\right\} \tag{59}$$

4. Conclusion

The recent study has provided a nonlinear radial diffusion equation to achieve the pressure distribution in a petroleum reservoir producing a two-phase hydrocarbon fluid with radial flow. This nonlinear equation does not have any simple solution. In particular conditions, this equation is linearized and solved in the transient state of flow by two analytical methods. In the separation of variables method (based on Bessel equation), P is written in the terms of Bessel sentences. In the second method (based on Laplace transform), we obtained a modified Bessel equation whose solution is determined. Applying the inverse Laplace transform based on Heaviside's theorem, we solved the problem and achieved the pressure distribution which is an applied function in a petroleum reservoir. The assumption of an incompressible fluid such as oil in the problem, is equivalent to assuming that pressure is maintained constant at the well radius ($r=r_w$) and at some external radius. In other words, the entire flow into the well passes across the external radius.

In the continuation of this study, it would be interesting to obtain the distribution of pressure in a reservoir producing the fluid by spherical flow.

Nomenclature

h	*Height of a cylindrical part of reservoir*	$q\rho\big\rvert_r$	*Rate of output mass in cylinder*
dr	*Thickness of a cylindrical part of reservoir*	ρ	*Mass density of fluid*
r	*Inner radius of a cylindrical part of reservoir*	P	*Pressure*
r_e	*Outer diameter of the reservoir*	m	*Mass of fluid*
P_e	*Pressure of the reservoir in radius* r_e	c	*Compressibility of fluid*
r_w	*Radius of well*	μ	*Viscosity of fluid*
q	*Amount of fluid flow*	φ	*Porosity degree of reservoir rock*
$q\rho\big\rvert_{r+dr}$	*Rate of input mass in cylinder*	η	*Diffusion constant*

References

[1] Grant MA, Bixley PF. Geothermal Reservoir Engineering. Academic Press, (2nd ed.) (2011) 94-95.

[2] Rezaee R. Fundamentals of Gas Shale Reservoirs. John Wiley & Sons, (2015) 295-296.

[3] Okino T. New mathematical solution for analyzing interdiffusion problems. Mater. Trans., 2011; 52: 2220-2227.

[4] Himmelblau DM. Basic Principles and Calculations in Chemical Engineering. Prentice Hall, (2nd ed.) (1967) 59-62.

[5] Manning JC. Applied Principles of Hydrology. Prentice Hall, (3rd ed.) (1997) 276.

[6] Freeze RA and Cherry JA. Groundwater. Prentice Hall, (1979) 604.

[7] Carslaw HS and Jaeger JC. Conduction of heat in solids. 2nd. Oxford Oxfordshire New York: Clarendon Press; Oxford University Press. 85026963 (1986).

[8] Watson GN. A Treatise on the Theory of Bessel Functions. London: Cambridge University Press, (1944).

[9] Churchill RV. Operational Mathematics. New York: McGraw-Hill Book Co. (Vol. 2) (1972).

[10] Norman LB. Discrete Mathematics. New York: Oxford University Press, (2nd ed.) (1990) 403–407.

To whom correspondence should be addressed: Professor Amir H. Mohammadi, Discipline of Chemical Engineering, School of Engineering, University of KwaZulu-Natal, Howard College Campus, King George V Avenue, Durban 4041, South Africa

Petroleum and Coal

Article **Open Access**

ON THE ASSESSMENT OF PSEUDO STEADY–STATE HORIZONTAL WELL PRODUCTIVITY: APPLICATION IN RECTANGULAR AND SQUARE DRAINAGE AREAS

Arash Kamari[1], Alireza Bahadori[2] Amir H. Mohammadi**[3]*

[1] *Department of Geology, Kansas State University, 108 Thompson Hall, Manhattan, KS, 66506, USA*
[2] *School of Environment, Science & Engineering, Southern Cross University, Lismore, NSW, Australia*
[3] *Discipline of Chemical Engineering, School of Engineering, University of KwaZulu-Natal, Howard College Campus, King George V Avenue, Durban 4041, South Africa*

Received April 4, 2018; Accepted September 28, 2018

Abstract

The productivity index is accounted as one of the main characteristics of well performance, and is of much importance in assessing the production amount/volume of liquids from wells. Furthermore, pseudo skin factor is an effective parameter in calculations related to the productivity index of producing oil/gas wells. In this study, an accurate and reliable method is proposed to estimate the pseudo skin factor as a function of dimensionless length and the ratio of horizontal well length over drainage area in both square and rectangular drainage areas. To measure the accuracy performance of the newly developed method, a smart technique called least square support vector machine algorithm was used as a comparative method. The result demonstrate that the developed method can estimate the pseudo skin factor data with lower average absolute relative deviation compared to the smart technique (9.2 against 11.4%).

Keywords: *Productivity performance; Pseudo skin factor; LSSVM model; Drainage area; Horizontal well.*

1. Introduction

As a matter of fact, the productivity index (PI) which plays a key role in evaluating the production amount/volume of liquids from wells, is accounted as one of the main characteristics of well performance [1]. In other words, productivity index is required for a large number of calculations related to production and reservoir engineering. As a definition with no considering the type of formation and wellbore, the PI is the amount/volume of possible daily production of reservoir fluids from a gas and/or oil well by 1 psi pressure drop [2]. As a result, several parameters (i.e. the reservoir permeability, geometry of drainage area, the length of horizontal wellbore, the properties of reservoir fluid, etc.) have influences on the value of PI for a drilled well particularly horizontal one. Nowadays, use of horizontal wells has gained considerable attention in petroleum industry because it can increase the production of oil/gas from reservoir, and the ability of injection to reservoirs for enhanced oil recovery (EOR) cases. Therefore, it is of great importance to assess the productivity performance of hydrocarbon reservoirs in case of horizontal wells.

Normally, the producing wells partially penetrates the formation of oil fields, so that if an oil and/or gas well is completed as partially penetrating, the streamline converges and the area for flowing the reservoir liquid reduces in the environs of the wellbore, which results in added resistance (pseudo skin factor) [3]. Subsequently, pseudo skin factor is recognized as an effective parameter in calculations related to the PI and performance evaluation of producing oil/gas wells. Therefore, it is needed to estimate the pseudo skin factor due to partial penetration through analytical and empirical methods. Babu and Odeh [4] proposed a complicated equation for estimating the PI of horizontal wells which needed that the drainage volume be approximately box-shaped, and all the boundaries of the drainage volume be sealed. Li *et al.* [5]

proposed a new method to evaluate the productivity performance of fractured reservoirs. They studied the influences of fracture properties on the PI of the wells. Fokker et al. [6] developed a new method for assessing the PI of complex wells. The results indicated that method proposed could be applied in the finite-conductivity wells, well interference, non-homogenous formations, and hydraulically fractured reservoirs. Bahadori *et al.* [7] developed an easy-to-utilize empirical correlation for the evaluation of pseudo steady-state PI of horizontal oil wells. To this end, pseudo skin factor was obtained by their new method. In the equation, they considered pseudo skin factor as a function of dimensionless length and the ratio of horizontal well length over drainage area side. Yu *et al.* [8] conducted a sensitivity analysis using the numerical simulation in order to find the effects of various geometries of multiple transverse hydraulic fractures on gas production.

The aim of present study was to develop a reliable, accurate and applicable method for the evaluation of oil horizontal well productivity through estimation of pseudo skin factor. To this end, the literature data of pseudo skin factor as a function of dimensionless length and the ratio of horizontal well length over drainage area side were collected. Furthermore, the results obtained by the newly proposed method were compared with least square support vector machine (LSSVM). Finally, the influences of dimensionless length and the ratio of horizontal well length over drainage area side on the pseudo skin factor estimated by the newly developed method were evaluated using a sensitivity study technique.

2. Proposing new method

As mentioned earlier, the reservoir properties, geometry of drainage area, the length of horizontal wellbore, and the properties of reservoir fluid, etc., have significant effects on predicting the fluid productivity of wells. Furthermore, pseudo skin factor is accounted as one of the most important parameters in calculations related to well-testing analysis and productivity index. Therefore, a simple method which could rapidly estimate the pseudo skin factor is needed to evaluate the productivity performance of producing wells. To develop such method, the data of pseudo skin factor or shape-related skin factor (S_{CAh}) as a function of dimensionless length (L_D) and the ratio of horizontal well length over drainage area side (U or L/2xe) for square and rectangular shapes with ratios of sides 1, 2, and 5, was collected from literature [9-10]. The collected databank collected in this study covers a wide range of pseudo skin factor from 1.412 to 5.86. Additionally, dimensionless length and the ratio of horizontal well length over drainage area side range from 1 to 100 and 0.2 to 1, respectively.

Regarding issues discussed earlier, a simple method with two variables including dimensionless length and the ratio of horizontal well length over drainage area side should be proposed for the determination of pseudo skin factor or shape-related skin factor. During development of the method, average absolute relative deviation (AARD or E_a) was considered as an error function to measure the accuracy of the newly proposed model. Final form of the method is as follow:

$$S_{CAh} = \frac{2\,U + {L_D}^{0.3767} + 2.6936}{Ln(2.752\ L_D)} \qquad (1)$$

where S_{CAh} stands for pseudo skin factor, L_D expresses dimensionless length, and U is the ratio of horizontal well length over drainage area side (L/2xe). The equation for calculating dimensionless length has previously been reported as follow:

$$L_D = \frac{L}{2h}\sqrt{\frac{k_v}{k_h}} \qquad (2)$$

where L denotes the horizontal well length (ft), h expresses the formation thickness (ft), k_v is vertical permeability (mD), and k_h stands for horizontal permeability (mD). Here, it shoud be noted that the method proposed (Eq. (1)) is applicable for both rectangular and square drainage areas.

3. Sensitivity study

To illustrate the relevancy of the selected variables (*i.e.* dimensionless length and the ratio of horizontal well length over drainage area side) for the estimation of pseudo skin factor, a sensitivity study was carried out in this study. To this end, the relevancy factor (r) approach [11] is employed to measure the influence degree of each variable applied in Eq. (1) for the determination of pseudo skin factor. In this approach, the positive or negative influence of input variables on the pseudo skin factor is however not determined by absolute value of r. The r values are calculated as follow [12]:

$$r(Inp_k,\mu_g)=\frac{\sum_{i=1}^{n}(Inp_{k,i}-\overline{Inp_k})(\mu_i-\overline{\mu})}{\sqrt{\sum_{i=1}^{n}(Inp_{k,i}-\overline{Inp_k})^2\sum_{i=1}^{n}(\mu_i-\overline{\mu})^2}} \qquad (3)$$

where: $Inp_{k,i}$ stands for *i*th value of the *k*th input variables and Inp_k denotes the average value of the *k*th input variables, μ_i indicates the *i*th value of the pseudo skin factor calculated by Eq. (1), and $\bar{\mu}$ is the average value of the pseudo skin factor calculated by Eq. (1).

4. Results and discussion

As a consequence, the LSSVM approach has successfully been implemented for estimation of the different important properties in petroleum and chemical engineering [13-17]. Therefore, LSSVM methodology [18-19] as a smart predictive technique was used in this study for comparing the results obtained by the newly proposed method (Eq. (1)) for the estimation of pseudo skin factor. In the LSSVM algorithm has two tuning parameters including σ^2 and γ which should be optimized through an optimization technique. Hence, the coupled simulated annealing (CSA) [20-22] as an adjusting strategy was applied in the current study. Using the CSA technique, the tuned values of σ^2 and γ for the developed LSSVM model for estimation of the pseudo skin factor are reported as 0.002228 and 27288.14, respectively. Furthermore, some important error parameters are considered to measure the accuracy of methods developed in this study as shown in Table 1. Table 1 also reports the results obtained by both Eq. (1) and LSSVM model for the estimation of pseudo skin factor. As clear in the table, the average absolute relative deviation obtained for the newly developed method is less than LSSVM model. The AARD values reported for Eq. (1) and LSSVM model are 9.2 and 11.4%, respectively. This clearly shows that Eq. (1) is more accurate than LSSVM model for calculation of pseudo skin factor.

Table 1. Statistics error parameters of developed model for prediction of wax deposition rate

Performance	Ea[a] %	Er[b] %	SD[c]	RMSE[d]	R² [e]
LSSVM approach	11.4	-2.7	0.14	0.354	0.90
New method (Eq. (2))	9.2	4.2	0.12	0.382	0.90

[a] $$E_a\%=\frac{1}{n}\sum_{i=1}^{n}|E_i\%| \text{ where } E_i\%=\left[\frac{X_{\exp}-X_{\text{rep./pred}}}{X_{\exp}}\right]\times 100 \Rightarrow i=1,2,3,\ldots,n$$

[b] $$E_r\%=\frac{1}{n}\sum_{i=1}^{n}E_i\%$$

[c] $$SD=\sqrt{\frac{1}{n-1}\sum_{i=1}^{n}\left(\frac{X_{i\exp}-X_{i\,\text{rep./pred}}}{X_{i\exp}}\right)^2}$$

[d] $$RMSE=\sqrt{\frac{1}{n}\sum_{i=1}^{n}\left(X_{i\exp}-X_{i\,\text{rep./pred}}\right)^2}$$

[e] $$R^2=1-\frac{\sum_{i=1}^{N}\left(X_{(i)\exp}-X_{(i)\,\text{rep./pred}}\right)^2}{\sum_{i}^{N}\left(X_{(i)\,\text{rep./pred}}-averageX_{(i)rep/pred}\right)^2}$$

Figs. 1 and 2 illustrate the pseudo skin factor data calculated by Eq. (1) and LSSVM model in comparison with the literature reported records, respectively. Top vies of the two figures shows scatter diagram, and bottom view is considered for illustrating the distribution of relative error calculated for both Eq. (1) and LSSVM model.

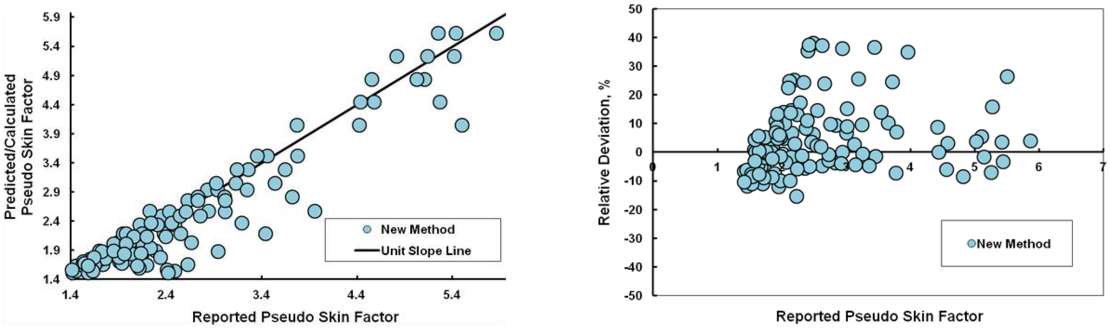

Fig. 1. Graphical error analysis for the proposed method. left: scatter diagram; right: relative error distribution plot

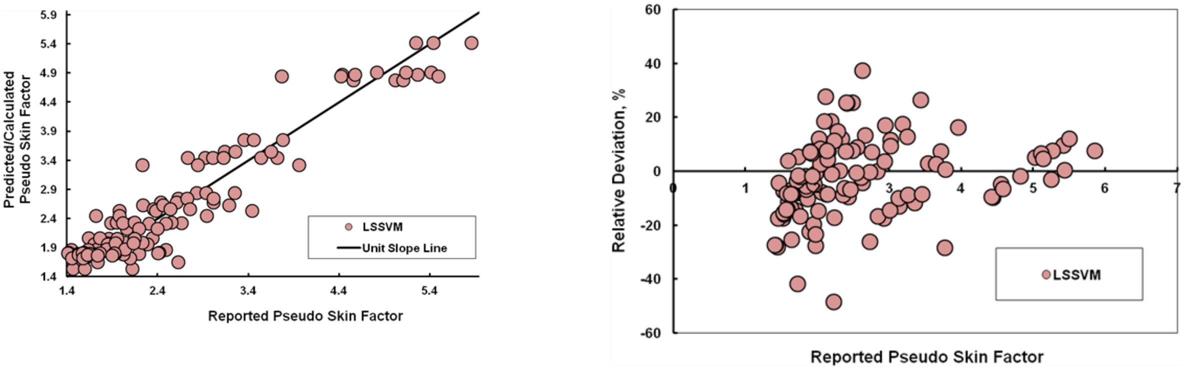

Fig. 2. Graphical error analysis for the developed LSSVM model. Left: scatter diagram; right: relative error distribution plot

As can be seen from the figures, the results obtained by Eq. (1) are in more agreement with the actual data of pseudo skin factor. Additionally, it is clear from the figures that the values obtained by LSSVM model have been more distributed around zero line compared to values calculated by Eq. (1). A further comparison between two methods is displayed in Fig. 3. Fig. 3 indicates the smooth performance of the both Eq. (1) and LSSVM model against actual data of pseudo skin factor. In other words, the figure illustrates the trend plot of pseudo skin factor estimated by Eq. (1) and LSSVM model versus dimensionless length at the ratio of horizontal well length over drainage area side equal to 0.2 (L/2xe=0.2). The figure confirms that the values estimated by Eq. (1) are more matched with the actual data of pseudo skin factor compared to the LSSVM model. This means that the Eq. (1) has an acceptable smoothness trend in estimating pseudo skin factor.

As already mentioned, a relevancy analysis is carried out to see the impacts of dimensionless length and the ratio of horizontal well length over drainage area side on the pseudo skin factor estimated by Eq. (1). Fig. 4 illustrates the results of such sensitivity analysis. This figure shows that the dimensionless length and the ratio of horizontal well length over drainage area side have positive and negative effects on the pseudo skin factor estimated by Eq. (1), respectively. The results obtained in this study demonstrate that the proposed method is capable and reliable for the estimation of pseudo skin factor. Additionally, the method proposed in this study could be applied in reservoir engineering soft wares to estimate the productivity performance of horizontal oil wells with rectangular and square drainage areas. Finally. It is worthwhile to mention that the method proposed in this study is a small equation with few number of coefficients which can be re-optimized if more relevant data become available in future.

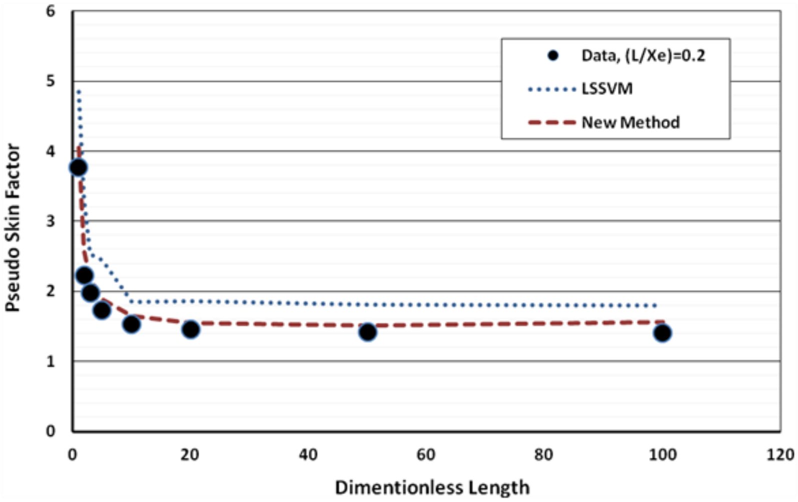

Fig. 3. Smooth performance of the proposed method and LSSVM model in estimating pseudo skin factor at the ratio of horizontal well length over drainage area side equal to 0.2 (L/2xe=0.2)

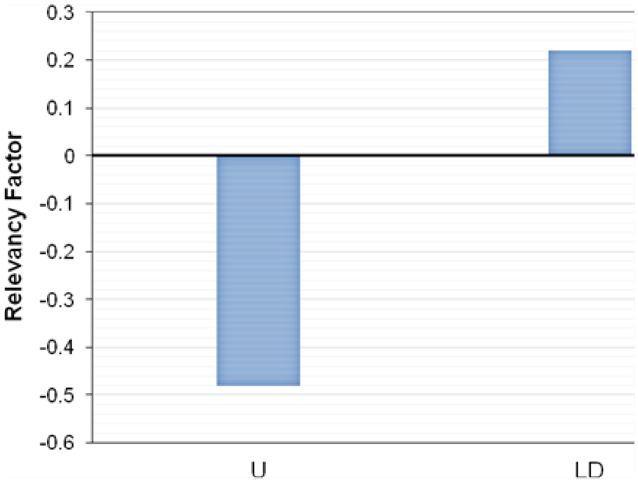

Fig. 4. The impact of variable used in Eq. (1) on pseudo skin factor

5. Conclusions

This study aimed to assess the productivity performance of horizontal oil wells in square and rectangular drainage areas. To this end, an accurate and reliable equation was proposed to estimate the pseudo skin factor. The equation is applicable in both square and rectangular drainage areas. To measure the accuracy performance of the newly developed method, a comparative study was graphically and statistically carried out. Therefore, a smart technique called least square support vector machine algorithm was used to see whether the proposed method is reliable. The result demonstrate that the developed method can estimate the pseudo skin factor data with lower average absolute relative deviation compared to the smart technique (9.2 against 11.4%). Finally, a sensitivity analysis was performed to observe the effects of variables applied in the proposed method. The results indicate that the dimensionless length and the ratio of horizontal well length over drainage area side have positive and negative effects on the pseudo skin factor estimated by the newly proposed method, respectively.

Nomenclature

EOR	*enhance oil recovery*
PI	*productivity index*
LSSVM	*least square support vector machine*
CSA	*coupled simulated annealing*
AARD	*average absolute relative deviation*
R	*relevancy factor*
S_{CAh}	*pseudo skin factor*
L_D	*dimensionless length*
U	*ratio of horizontal well length over drainage area side (L/2xe)*
L	*horizontal well length, ft*
h	*formation thickness, ft*
k_v	*vertical permeability, mD*
k_h	*horizontal permeability, mD*

References

[1] Aulisa E, Ibragimov A, and Walton JR. A new method for evaluating the productivity index of nonlinear flows. SPE J, 2009; 14(4): 693-706.

[2] Al Rbeawi S, and Tiab D, Predicting productivity index of hydraulically fractured formations. Journal of Petroleum Science and Engineering, 2013; 112: 185-197.

[3] Lu J, and Tiab D. Pseudo-Steady-State Productivity Formula for a Partially Penetrating Vertical Well in a Box-Shaped Reservoir. Mathematical Problems in Engineering, 2010.

[4] Babu D, and Odeh AS. Productivity of a Horizontal Well (includes associated papers 20306, 20307, 20394, 20403, 20799, 21307, 21610, 21611, 21623, 21624, 25295, 25408, 26262, 26281, 31025, and 31035). SPE Reservoir Engineering, 1989; 4(04): 417-421.

[5] Li H, Jia Z, and Wei Z. A new method to predict performance of fractured horizontal wells, International three-day conference & trade show on horizontal well technology. 1996; pp. 179-185.

[6] Fokker PA, Verga F, and Egberts P. 2005. New Semi-Analytic Technique to Determine Horizontal Well PI in Fractured Reservoirs. SPE Reservoir Evaluation & Engineering, 2005; 8(02): 123-131.

[7] Bahadori A, Jamili A, and Zendehboudi S. 2013. Calculating pseudo-steady-state horizontal oil well productivity in rectangular drainage areas using a simple method. Chemical Engineering Communications, 2013; 200(2): 222-234.

[8] Yu W, Luo Z, Javadpour F, Varavei A, and Sepehrnoori K. Sensitivity analysis of hydraulic fracture geometry in shale gas reservoirs. Journal of Petroleum Science and Engineering, 2014; 113: 1-7.

[9] Chaudhry A. Oil well testing handbook. Elsevier 2004.

[10] Mutalik P, Godbole S, and Joshi S. Effect of drainage area shapes on horizontal well productivity, SPE 63rd Annual Technical Conference 1988, Houston, Texas, October, pp. 2-5.

[11] Chen G. Fu K, Liang ZZ, Idem R. The genetic algorithm based back propagation neural network for MMP prediction in CO 2-EOR process. Fuel, 2014; 126: 202-212.

[12] Hosseinzadeh M, and Hemmati-Sarapardeh A. Toward a predictive model for estimating viscosity of ternary mixtures containing ionic liquids. Journal of Molecular Liquids, 2014; 200: 340-348.

[13] Kamari A, Bahadori A, and Mohammadi A. A Two-parameter Model for the Determination of Optimum Liquefied Petroleum Gasses (LPG) Storage Volume. Petroleum Science and Technology, 2015; 33(4): 494-501.

[14] Kamari A, Bahadori, A, Mohammadi AH, and Zendehboudi S. Evaluating the Unloading Gradient Pressure in Continuous Gas-lift Systems During Petroleum Production Operations. Petroleum Science and Technology, 2014; 32(24): 2961-2968.

[15] Kamari A, Bahadori A, Mohammadi AH, and Zendehboudi S. New tools predict monoethylene glycol injection rate for natural gas hydrate inhibition. Journal of Loss Prevention in the Process Industries, 2015; 33: 222-231.

[16] Kamari A, Mohammadi A, Bahadori A, and Zendehboudi S. A Reliable Model for Estimating the Wax Deposition Rate During Crude Oil Production and Processing. Petroleum Science and Technology, 2014; 32(23): 2837-2844.

[17] Kamari A, Mohammad, AH, Bahadori A, and Zendehboudi S. Prediction of Air Specific Heat Ratios at Elevated Pressures Using a Novel Modeling Approach. Chemical Engineering & Technology, 2014; 37(12): 2047-2055.

[18] Suykens JAK, and Vandewalle J. Least squares support vector machine classifiers. Neural processing letters, 1999; 9(3): 293-300.

[19] Suykens JAK, van Gestel T, de Brabanter J, de Moor B, and Vandewalle J. Least Squares Support Vector Machines. World Scientific Publishing Company 2002.

[20] Atiqullah MM, and Rao S. 1993. Reliability optimization of communication networks using simulated annealing. Microelectronics Reliability, 1993; 33(9): 1303-1319.

[21] Fabian V. Simulated annealing simulated. Computers & Mathematics with Applications, 1997; 33(1): 81-94.

[22] Vasan A, and Raju KS. 2009. Comparative analysis of simulated annealing, simulated quenching and genetic algorithms for optimal reservoir operation. Applied Soft Computing, 2009; 9(1): 274-281.

To whom correspondence should be addressed: Dr. Alireza Bahadori, School of Environment, Science & Engineering, Southern Cross University, Lismore, NSW, Australia

Prof. Amir H. Mohammadi, Discipline of Chemical Engineering, School of Engineering, University of KwaZulu-Natal, Howard College Campus, King George V Avenue, Durban 4041, South Africa